MOUNTING AN ATTACK ON THE GLIOBLASTOMA TRIAD:

PROLIFERATION, INVASION AND RESISTANCE

Mark C. de Gooijer

Mounting an attack on the glioblastoma triad:
proliferation, invasion and resistance

ISBN: 978-94-6323-427-6

Cover design and lay-out: Lianne Verkerk www.lianneverkerk.nl
Printed by: Gildeprint Drukkerijen, Enschede

MIX
Paper from responsible sources
FSC
www.fsc.org

Printing of this thesis was financially supported by the Onderzoeksschool Oncologie Amsterdam, Stichting STOPHersentumoren.nl and the Utrecht Institute for Pharmaceutical Sciences

Mounting an attack on the glioblastoma triad: proliferation, invasion and resistance

Het opzetten van een aanval tegen de glioblastoma triade:

proliferatie, invasie en resistentie

(met een samenvatting in het Nederlands)

Proefschrift

ter verkrijging van de graad van doctor aan de Universiteit Utrecht op gezag van de rector magnificus, prof.dr. H.R.B.M. Kummeling, ingevolge het besluit van het college voor promoties in het openbaar te verdedigen op woensdag 23 januari 2019 des middags te 2.30 uur

door

Mark Cornelis de Gooijer

geboren op 5 oktober 1989

te Amsterdam

Promotor: Prof. dr. J.H. Beijnen

Copromotor: Dr. O. van Tellingen

TABLE OF CONTENTS

PREFACE

Despite decades of research, glioblastoma (GBM) remains a formidable opponent. Patients suffering from this primary brain tumor still have a dismal prognosis, and although they receive extensive treatment involving surgery, ionizing radiotherapy and temozolomide chemotherapy, the median overall survival is still only roughly 15 months[1]. Fairly recently, large-scale efforts to characterize GBM have delivered major insights into its genomic landscape[2], epigenetic profile[2,3] and micro-environmental context[4]. Together, these studies have revealed that GBM is not one disease, but rather a many-faced beast. Today, we recognize up to 5 different subtypes of glioblastoma based on genomic, epigenomic and expression profiling: classical, proneural, G-CIMP, mesenchymal and neural GBM[2]. Moreover, GBMs are very heterogeneous and typically consist of more than 1 subtype[5]. Importantly, these subtypes appear to exhibit a high level of plasticity, as GBM cells can rapidly change their subtype as a result of selective pressures such as anticancer treatment[6,7].

Although it seems that no two GBM cells are the same, the aforementioned characterization efforts have also pinpointed various commonalities between GBMs that offer new handles for therapeutic approaches. This thesis investigates several of these new approaches, but also studies ways to further improve the efficacy of classical treatment modalities such as chemotherapy and radiotherapy. The ultimate aim is to mount a full-blown attack on three main pillars of GBM biology: uncontrolled proliferation, an unparalleled level of invasion of healthy brain tissue, and tremendous resistance to therapy as a result of protection by the blood-brain barrier (BBB). Together, these properties form the glioblastoma triad. This thesis investigates all three pillars separately and aims to pinpoint efficient ways to attack each individually. Hopefully, this knowledge will aid in designing an intelligent treatment strategy that attacks the entire glioblastoma triad.

In **Section I** of this thesis, several pillars of the glioblastoma triad are introduced. The BBB and its role in protecting GBMs from systemic therapy are discussed in detail, as well as the cellular signaling pathways that are frequently used for its uncontrolled proliferation. **Section II** is the first to zoom in on a specific therapeutic strategy: improving the efficacy of DNA-damaging chemotherapy. This section first demonstrates that drug transport proteins at the BBB still function even when the barrier is physically compromised and subsequently shows that inhibiting these drug transporters improves the efficacy of the alkylating chemotherapeutic temozolomide. Starting from **Section III**, more targeted therapeutic approaches are investigated. This section describes inhibitors of the PI3K signaling pathway, a cellular signaling route that is frequently exploited by GBMs to proliferate uncontrollably, that efficiently cross the BBB. Moreover, it demonstrates that these inhibitors are able to reach the tumor and elicit modest efficacy against experimental GBM models. Importantly, this section also provides the first evidence of this thesis that combination therapies are likely required to achieve meaningful clinical responses. **Section**

IV focuses on a second proliferation pathway that is likely important to therapeutically target: the MAPK pathway. Several inhibitors of components of this pathway have been developed, including MEK inhibitors and BRAF inhibitors. Unfortunately, this section shows that most of these inhibitors developed to date do not cross the BBB, although it identifies one welcome exception. **Section V** moves on from proliferation pathways and instead focuses on a vital cellular process that all GBM cells share: the cell cycle. Careful progression through the cell cycle is absolutely essential for division and cancer cells frequently pay a price for fast proliferation by relying more on cell cycle checkpoints. This section focuses on targeting several of these checkpoints: the G2 checkpoint, the G1 checkpoint and the spindle assembly checkpoint during mitosis. **Section VI** shifts the focus back to the DNA, but does not aim to induce more damage rather than reduce the amount of DNA repair. It shows that inhibiting the DNA repair protein PARP can improve the efficacy of temozolomide, although the BBB remains a limiting factor in this context. It also investigates another PARP inhibitor that is said to be less amenable to drug efflux, but unfortunately demonstrates that this compound will likely not fare any better. **Section VII** is the last section discussing a therapeutic strategy and focuses entirely on an important pillar of the glioblastoma triad: invasion of GBM cells through healthy brain tissue. First, the current knowledge on GBM invasion is discussed as well as the benefits and limitations of the available models to study invasion. Then, it demonstrates using several of these models that GBM invasion can be therapeutically targeted through the CK2–TBK1–IRF3 axis. **Section VIII** completes the main body of the thesis and contains a general discussion and detailed summary of the major findings of each chapter.

In summary, therapeutically targeting glioblastoma has proven to be especially challenging. However, over the years we have increasingly gained knowledge on the complexity of GBM biology that allowed us to more rationally design treatment strategies. Major pillars of the malignancy of GBM are uncontrolled proliferation, unparalleled invasion and tremendous therapy resistance, and together these form the glioblastoma triad. This thesis investigates treatment strategies for all three pillars separately and concludes that while modest efficacy can be achieved by individual targeting, an intelligently designed therapeutic approach that attacks the entire glioblastoma triad will be necessary to provide long-term solutions for patients.

REFERENCES

1. Stupp, R., *et al.* Radiotherapy plus concomitant and adjuvant temozolomide for glioblastoma. *N Engl J Med* **352**, 987-996 (2005).
2. Brennan, C.W., *et al.* The somatic genomic landscape of glioblastoma. *Cell* **155**, 462-477 (2013).
3. Ceccarelli, M., *et al.* Molecular profiling reveals biologically discrete subsets and pathways of progression in diffuse glioma. *Cell* **164**, 550-563 (2016).
4. Wang, Q., *et al.* Tumor evolution of glioma-intrinsic gene expression subtypes associates with immunological changes in the microenvironment. *Cancer Cell* **32**, 42-56 (2017).
5. Patel, A.P., *et al.* Single-cell RNA-seq highlights intratumoral heterogeneity in primary glioblastoma. *Science* **344**, 1396-1401 (2014).
6. Segerman, A., *et al.* Clonal variation in drug and radiation response among glioma-initiating cells is linked to proneural-mesenchymal transition. *Cell Rep* **17**, 2994-3009 (2016).
7. Wang, J., *et al.* Clonal evolution of glioblastoma under therapy. *Nat Genet* **48**, 768-76 (2016).

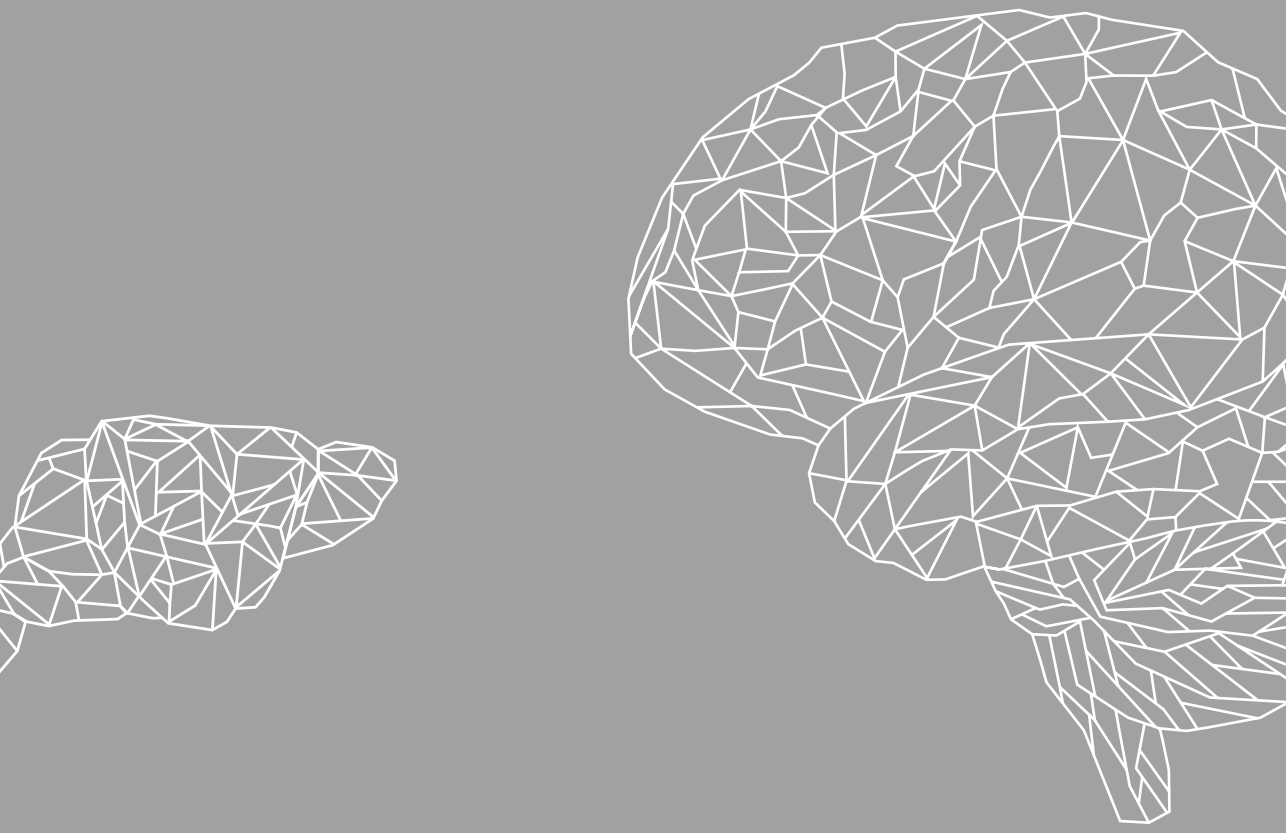

SECTION I

INTRODUCTION: TARGETS IN GBM AND THE IMPORTANCE OF THE BBB

Chapter 1

OVERCOMING THE BLOOD-BRAIN TUMOR BARRIER FOR EFFECTIVE GLIOBLASTOMA TREATMENT

O. van Tellingen*, B. Arik-Yetkin*, M.C. de Gooijer*,
P. Wesseling, T. Wurdinger, and E.H. de Vries

* These authors contributed equally

Drug Resistance Updates. 2015;19:1-12

ABSTRACT

Gliomas are the most common primary brain tumors. Particularly in adult patients, the vast majority of gliomas belong to the heterogeneous group of diffuse gliomas, *i.e.*, glial tumors characterized by diffuse infiltrative growth in the preexistent brain tissue. Unfortunately, glioblastoma, the most aggressive (WHO grade IV) diffuse glioma is also by far the most frequent one. After standard treatment, the 2-year overall survival of glioblastoma patients is approximately only 25%. Advanced knowledge in the molecular pathology underlying malignant transformation has offered new handles and better treatments for several cancer types. Unfortunately, glioblastoma multiforme (GBM) patients have not yet profited as although numerous experimental drugs have been tested in clinical trials, all failed miserably. This grim prognosis for GBM is at least partly due to the lack of successful drug delivery across the blood–brain tumor barrier (BBTB). The human brain comprises over 100 billion capillaries with a total length of 400 miles, a total surface area of 20 m^2 and a median inter-capillary distance of about 50 μm, making it the best perfused organ in the body. The BBTB encompasses existing and newly formed blood vessels that contribute to the delivery of nutrients and oxygen to the tumor and facilitate glioma cell migration to other parts of the brain. The high metabolic demands of high-grade glioma create hypoxic areas that trigger increased expression of VEGF and angiogenesis, leading to the formation of abnormal vessels and a dysfunctional BBTB. Even though the BBTB is considered 'leaky' in the core part of glioblastomas, in large parts of glioblastomas and, even more so, in lower grade diffuse gliomas the BBTB more closely resembles the intact blood–brain barrier (BBB) and prevents efficient passage of cancer therapeutics, including small molecules and antibodies. Thus, many drugs can still be blocked from reaching the many infiltrative glioblastoma cells that demonstrate 'within-organ-metastasis' away from the core part to brain areas displaying a more organized and less leaky BBTB. Hence, drug delivery in glioblastoma deserves explicit attention as otherwise new experimental therapies will continue to fail. In the current review we highlight different aspects of the BBTB in glioma patients and preclinical models and discuss the advantages and drawbacks of drug delivery approaches for the treatment of glioma patients. We provide an overview on methods to overcome the BBTB, including osmotic blood–brain barrier disruption (BBBD), bradykinin receptor-mediated BBTB opening, inhibition of multidrug efflux transporters, receptor-mediated transport systems and physiological circumvention of the BBTB. While our knowledge about the molecular biology of glioma cells is rapidly expanding and is, to some extent, already assisting us in the design of tumor-tailored therapeutics, we are still struggling to develop modalities to expose the entire tumor to such therapeutics at pharmacologically meaningful quantities. Therefore, we must expand our knowledge about the fundamentals of the BBTB as a step towards the design of practical and safe devices and approaches for enhanced drug delivery into the diseased brain area.

GLIOMAS

Gliomas account for approximately 80% of all tumors arising in brain tissue, with an incidence of about 7 per 100,000 individuals worldwide. Patients with gliomas may present with several neurological symptoms such as headaches, seizures, focal neurologic deficits, memory loss, personality changes, vomiting, and visual changes[1-3]. According to the World Health Organization (WHO), gliomas are classified according to their cell type and malignancy grade[4]. The vast majority of gliomas in adult patients are so-called diffuse gliomas, *i.e.*, tumors that are characterized by diffuse infiltration of tumor cells in the preexistent brain tissue. However, diffuse gliomas may also occur in children. Based on the phenotype of the tumor cells diffuse gliomas are according to the WHO 2007 classification typed as astrocytic, oligodendroglial or oligoastrocytic tumors. Furthermore, a malignancy grade (grade II = low grade diffuse glioma; grade III = malignant/ anaplastic diffuse glioma; grade IV = glioblastoma) is assigned to these tumors based on the presence/absence of features like brisk mitotic activity, florid microvascular proliferation and necrosis[4,5]. Glioblastomas are by far the most common and most malignant type[3,6]. Of note, WHO grade I is reserved for more circumscribed glioma variants such as pilocytic astrocytoma that occur especially in children.

Despite their initially often relatively indolent nature, most low-grade diffuse gliomas eventually progress to anaplastic glioma or glioblastoma[6]. Glioblastomas can be further subdivided into primary and secondary glioblastoma and are characterized by marked cellular proliferation, necrosis, florid microvascular proliferation (*i.e.*, a peculiar form of angiogenesis), resistance to apoptosis, and genomic aberrations[7]. Primary glioblastomas comprise the majority of cases (>90%), generally occur in older patients (>50 years) and are considered to be WHO grade IV from the start. In contrast, secondary glioblastomas occur in younger patients and arise from progression of a lower grade glioma[8]. Most lower grade diffuse gliomas carry a mutation in the isocitrate dehydrogenase 1 or 2 (*IDH1/IDH2*) gene, and it was recently proposed to define primary versus secondary glioblastoma based on the *IDH1/IDH2* mutation status of the tumor[9].

MOLECULAR COMPOSITION OF THE BBB AND IMPLICATIONS FOR DRUG ENTRY

The human brain comprises over 100 billion capillaries with a total length of 400 miles, a total surface area of 20 m^2 and a median inter-capillary distance of about 50 μm, making it the best perfused organ in the body[10]. Proper function of the vasculature in the central nervous system (CNS) is essential for adequate brain function, not only to efficiently supply the brain with nutrients and oxygen, but also to protect the brain from potentially neurotoxic compounds. This protective blood barrier known as the blood–brain barrier (BBB), between the blood compartment and the brain is an essential prerequisite to secure correct neuronal functioning of the brain. The BBB is a cellular barrier (**Figure 1**) that regulates the ionic composition for proper synaptic signaling

function, prevents macromolecules and unwanted cells from entering the brain as well as protects the CNS from neurotoxic substances and ensures brain nutrition.

In essence, the BBB is formed by the specialized brain endothelial cells that exert their barrier properties through the continuous interaction with surrounding cells like astrocytes, pericytes, and perivascular macrophages, forming the so-called neurovascular unit[11]. Astrocytic endfeet cover the basal lamina of the brain capillaries and provide the cellular connection to neurons. Astrocytes play a key role in the maintenance of the barrier properties of the endothelium[11,12]. Pericytes cover the endothelium and contribute to the structural integrity of the BBB and the induction of barrier properties during development[13,14]. There is increasing evidence that astrocytes and pericytes secrete soluble developmental cues, like sonic hedgehog, retinoic acid and WNT, that control the onset of barrier properties[15-19].

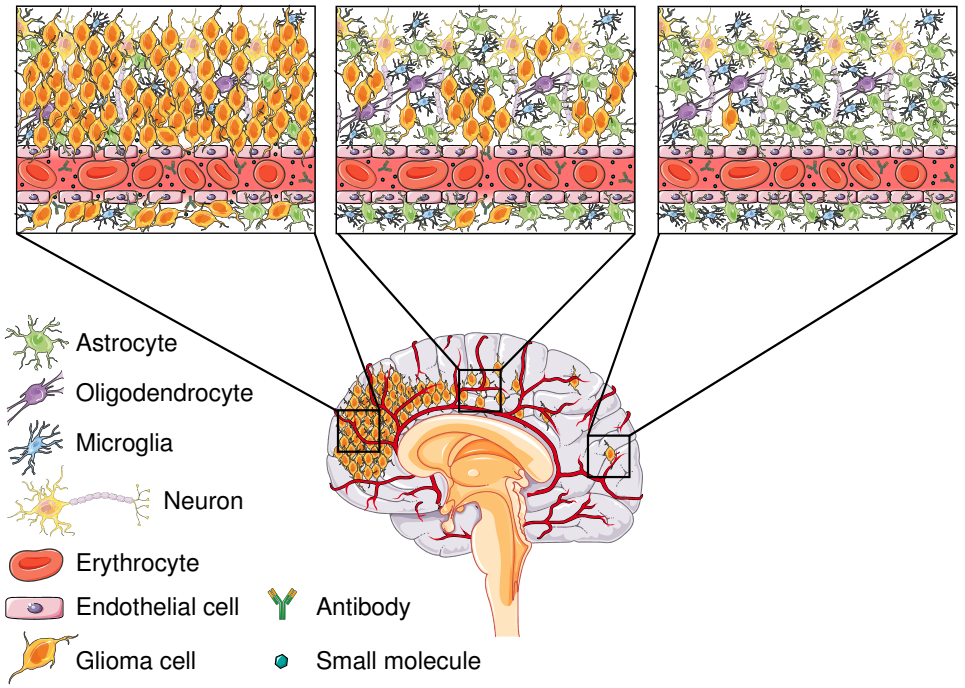

Figure 1 | Glioblastomas consist of different regions characterized by various degrees of BBTB integrity. Heterogeneous BBTB integrity can be found throughout a glioblastoma, varying from completely compromised in bulky tumor areas (*left panel*) to slightly leaky in more invasive peripheral regions (*middle panel*) or even completely intact in sparsely invaded regions distant from the tumor bulk (*right panel*). Where the BBTB is compromised macromolecules (*e.g.*, antibodies) and compounds that are normally efficiently restricted from the brain by efflux transporters can extravasate and engage glioma cells, while an intact BBTB protects isolated invaded tumor cells against efficient delivery of therapeutics. This protection has strong implications for anti-tumor treatment efficacy, especially considering the fact that these regions are unresectable and often give rise to recurrent tumors. Note: **Figure 1** and **Figure 2** have been prepared using Servier Medical Art under a Creative Commons Attribution 3.0 Unported License.

Brain endothelial cells are closely connected by intercellular tight junctions. Except for some very small or gaseous molecules (*e.g.*, water, carbon dioxide) the tight junctions prevent brain entry of molecules via para-cellular trafficking in between the endothelial cells[11]. Tight junction associated proteins include occludin, claudin-1, claudin-5 and junctional adhesion molecules (JAMs)[20,21]. Claudin-1 and occludin are linked via zonula occludens (ZO) protein complexes to tight junction associated proteins (*e.g.,* Cingulin, Jacop, 7H6) that bind to the actin/myosin cytoskeletal system, resulting in modification of the tight junction properties. In adherens junctions that ensure the structural formation of tight junctions, VE-cadherin proteins are linked in the cytoplasm to α-, β- and γ-catenin. The sealing function of tight junctions depends not only on the presence of the proteins, but is also influenced by the organization and interaction of these proteins[22]. As a result of the tight structure of the endothelial cell layer and the lack of fenestrae, the BBB actively regulates the transendothelial passage of soluble substances from the blood to the brain and *vice versa*. Solutes can cross these endothelial barriers by passive diffusion, but the efficiency of this process depends on their physicochemical properties, such as electrical charge, molecular weight, and lipid solubility[10]. Uptake of essential nutrients is actively regulated via carrier-mediated transport using one of the several solute carriers (*e.g.*, SLC2/GLUT-1 for glucose) or receptor-mediated transport (*e.g.*, transferrin) (**Figure 2A and Figure 3**). Solute carriers can also shuttle drugs across membranes, but their impact at the BBB is still not yet clear. For example OATP1A2 and OATP2B1 are expressed at the BBB and may be involved in uptake into and/or efflux from the brain[23-25]. The absence of Oatp1a/1b in mice causes a profound reduction of the hepatic uptake of methotrexate and paclitaxel[26], but effects on the brain penetration of these drugs has not been reported.

In contrast, efficient efflux of unwanted compounds is achieved by the presence of a range of active (ATP Binding cassette (ABC)) efflux transporters, such as ABCB1 (P-glycoprotein) and ABCG2 (breast cancer resistance protein; BCRP). ABCB1 was first discovered by its ability to confer multidrug resistance in tumor cells[27]. ABCB1 recognizes a remarkably wide range of substrates, including about 60% of all marketed drugs and mediates resistance by via its ability to extrude drug molecules out of the cells, thus reducing intracellular drug accumulation and cytotoxicity. It was already known since the late 1980s that ABCB1 was also expressed at the BBB[28], but the true functional impact of its presence became clear only after the generation of the *Abcb1a* knockout mouse model[29]. Most strikingly, the absence of Abcb1a rendered ivermectin, a widely used and safe drug into a lethal neurotoxic agent. Since then numerous papers have confirmed the impact of ABCB1 on the brain penetration of a wide range of agents[30]. At the turn of the millennium, ABCG2, a drug efflux transporter that was also first discovered in tumor cells[31] was also found to be expressed at the BBB[32,33]. The functionality of ABCG2 at the BBB was demonstrated using knockout (KO) mice, but only after the combined *Abcb1a/b;Abcg2* (triple KO) mice were generated, its role in driving the efflux of compounds became apparent[34]. Previous work in single *Abcg2*-deficient mice was not convincing[35], since there is a large overlap in substrate affinity between

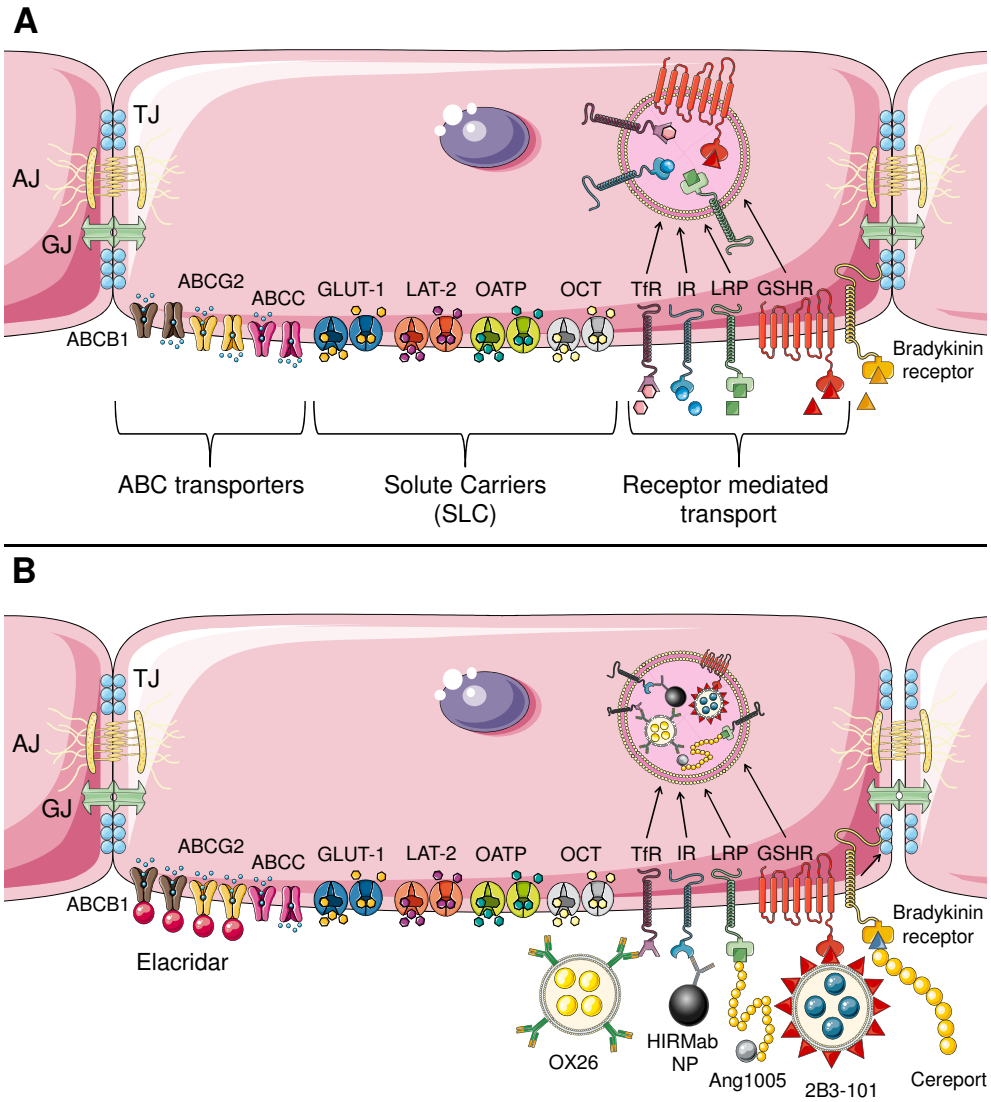

Figure 2 | Therapeutic brain delivery strategies that target the physiological make-up of the BBB. (A) The blood–brain barrier consists of both a physical and physiological barrier, where the physical component consists of tight junctions (TJ), gap junctions (GJ) and adherens junctions (AJ) that together restrict paracellular exchange between the blood and the brain and allow the endothelial cells to cooperate closely by providing channels for direct cytoplasmic exchange. The tight junctions are under regulation by the bradykinin receptor to maintain their stringent barrier character. The physiological aspect of the BBB aims to restrict the brain entry of potentially harmful exogenous compounds while at the same time allows for efficient uptake of essential nutrients. Brain penetration of exogenous compounds is efficiently restricted by ATP-binding cassette (ABC) transporters, a group efflux transport proteins located at the luminal endothelial cell membrane. In contrast, endothelial cells that constitute the BBB are equipped with a wide range of solute carriers (SLC), influx transporters that efficiently facilitate uptake of nutrients such as glucose (GLUT-1), amino acids (LAT-2), anions (the OATP family) and cations (the OCT family). Moreover, a wide range of receptors mediate transport through transcytosis. Among these are the transferrin receptor (TfR), insulin receptor (IR), LDL-receptor-related protein (LRP) and glutathione receptor (GSHR). **(B)** Strategies against various modalities of the intact BBB have been developed for improving therapeutic delivery to the brain. Elacridar inhibits ABCB1 and ABCG2, thereby reducing efflux and allowing increased brain penetration of small molecules. OX26, human insulin receptor monoclonal antibody conjugated nanoparticles (HIRMab NP), Ang1005 and 2B3-101 all target transcytosis pathways while Cereport targets tight junction stringency signaling through the bradykinin receptor.

Abcb1a/b and Abcg2. The action of Abcb1a/b at the BBB of single *Abcg2*-deficient mice was sufficient to expel those substrates out of the brain. The functional impact of Abcg2 at the BBB becomes most evident when comparing the brain penetration of compounds between *Abcb1a/b-vs. Abcb1a/b;Abcg2*-deficient mice. For certain drugs, such as vemurafenib, brain penetration in *Abcb1a/b;Abcg2*-deficient mice increased over 10-fold compared to wild-type controls[36].

Next to ABCB1 and ABCG2, there are several members of the ABCC family of transporters localized at the BBB (*viz.* ABCC1, ABCC2, ABCC4 and ABCC5)[37-39]. These ABCC family members generally transport a range of more polar molecules, including drug conjugates and endogenous metabolites[40]. However, the functional impact of these ABCC transporters has only been demonstrated for Abcc4 with the oseltamivir metabolite RO64-0802)[41], the camptothecin analogs (topotecan, SN-38 and gimatecan)[42] and methotrexate[43]. In these latter cases, the fact that other ABC transporters at the BBB (Abcb1, Abcg2) recognize similar substrates, can (partly) obscure the functional impact of Abcc4 at the BBB. The same may apply for Abcc1 (Mrp1). Whereas *Abcb1;Abcc1* KO mice had similar brain levels of etoposide as *Abcb1a/b* KO[44], this might be due to the affinity of etoposide for Abcg2[45]. The demonstration of functional activity of Abcc2 was hampered by the fact that the FVB mouse strain that is used for backcrosses of ABC transporter knockout genes does not express Abcc2 at the BBB[39]. Apart from active efflux, metabolic degradation may play some role in reducing brain accumulation of compounds[46], however this is still a largely unexplored area. Together, the superfamily of ABC transporters plays a key role in limiting the brain penetration of a wide range of compounds, including many of the targeted agents that may be useful to inhibit aberrant signaling pathways in glioma[47].

THE BLOOD–BRAIN TUMOR BARRIER (BBTB)

The functioning and organization of the BBB can be altered under pathological conditions, such as multiple sclerosis, epilepsy, autoimmune deficiency syndrome (AIDS), dementia, stroke, and brain cancer[11,14,48]. Importantly, alterations in the barrier evoked by tumors in the brain do not link with tumor size, tumor type, or anatomic location and is variable within any single neoplasm (**Figure 1**)[49]. In low-grade gliomas, the normal vascularization and the function of the BBTB remain mostly intact and resemble the BBB as under normal conditions[50]. High-grade gliomas, however, are characterized by major alterations of the normal vascular function resulting in a disrupted, 'leaky' BBTB as manifested by contrast-enhanced MRI[51]. Very recently it was shown that displacement of the astrocytic endfeet from a endothelial cell by a single invading tumor cell would already suffice to cause local breaching of the BBB[52]. However, it is unlikely that the magnitude of this local disruption is sufficient to allow drug penetration in meaningful quantities, taking into account that areas with invasion commonly do not enhance during contrast-enhanced MRI.

The high metabolic demands of high-grade glioma creates hypoxic areas that trigger increased expression of vascular endothelial growth factor (VEGF) and angiogenesis, leading to the formation of abnormal vessels and a dysfunctional BBTB[53,54]. Importantly, however, the invasive potential of glioma causes widespread proliferation of high-grade glioma cells outside regions of the disrupted BBTB and inside areas of otherwise normal brain, where the function of the barrier is still (much more) intact. Typically, this includes the areas that do not show gadolinium enhancement on T1 weighted MRI[55]. As a consequence, both in low-grade and high-grade glioma the BBB and the BBTB barrier form a major obstacle in brain tumor therapy by preventing the delivery of sufficient quantities of potentially effective therapeutic agents[56,57].

The BBTB is formed by brain tumor capillaries and comprises a barrier that is variably distinct from the BBB. Brain tumor capillaries may show overexpression of receptors that mediate ligand dependent drug delivery, which can be exploited to selectively enhance drug delivery to tumor tissues[58,59]. The BBTB can be composed of three distinct microvessel populations, *i.e.*, continuous and non-fenestrated capillaries (resembling normal brain capillaries, *e.g.*, in diffuse low grade gliomas), continuous and fenestrated capillaries, and capillaries containing inter-endothelial gaps[60-62]. Drug efflux transporters expressed at the BBB can also be found in endothelial cells at the BBTB[63-65] (**Figure 2A and Figure 3**). Moreover, ABC transporters can be expressed in a (subset of) tumor cells as well and may confer chemo-resistance to glioblastomas[66] (**Figure 3**), thus forming an additional hurdle towards curative treatment.

CIRCUMVENTING OR OVERCOMING THE BBTB

During the last decades numerous strategies to improve the delivery of agents to brain tumors have been under investigation (**Figure 2B**). Unfortunately, major changes in the landscape of brain tumor therapy have not yet matured from these efforts. In this section, we will briefly discuss the history, pitfalls and potential of developed methodologies.

Osmotic blood–brain barrier disruption (BBBD)

The oldest work to literally breach the BBTB has been pioneered since the early 1970s by Rapoport[67,68]. This strategy of so-called blood–brain barrier disruption (BBBD) is based on intra-arterial infusion of a hyperosmotic solution of mannitol, causing temporary shrinkage of endothelial cells and subsequent opening of the tight junctions for several hours[69]. This time window can then be used for the intra-arterial delivery of the chemotherapeutic agents such as methotrexate or carboplatin. There are substantial technical challenges that limit the feasibility of this procedure and obstacles have been identified that jeopardize patient safety. The non-selective opening of not only the BBTB but also the BBB causes gross and uncontrolled influx of low and high molecular weight compounds and an increase of brain fluid leading to neurological toxicity,

aphasia and hemiparesis[69]. On the other hand, the clinical benefit of this method for treatment of glioma has still not been established, despite more than 40 years of concentrated efforts. A randomized phase III study was announced in 2005[70], but no reports have appeared since then. Only in the case of primary CNS lymphoma, improved efficacy has been claimed, but these studies were all relative small and uncontrolled[71]. More recently, a phase I clinical trial has been reported on the use of BBBD in combination with bevacizumab, a monoclonal antibody directed against VEGF[72]. The rationale of using BBBD for the delivery of bevacizumab in glioblastoma patients remains somewhat unclear and just appears to be a very complicated modality to administer this biological agent. VEGF is mainly produced in areas of florid microvascular proliferation, where disruption of the BBTB is evident. Moreover, the bevacizumab mode of action requires long term presence in order to scavenge VEGF as is already achieved by 3-weekly IV dosing, since bevacizumab has a systemic half-life of about 2 weeks. It is therefore unlikely that the short pulse of extra bevacizumab that may enter during the hours of BBBD will add to this therapy.

Bradykinin receptor-mediated BBTB opening

Another attempt to open up the BBTB/BBB which is more subtle, is based on the stimulation of brain endothelial receptors that induce opening of the tight junctions through utilization of compounds like bradykinin via second messengers[73]. This has led to the clinical development of RMP-7 (Cereport or labramidil), a bradykinin analog with improved systemic exposure following IV injection[74,75]. In several animal studies and uncontrolled phase II studies RMP-7 revealed very promising results. However, a randomized, double blind, placebo controlled phase II study of RMP-7 in combination with carboplatin failed to demonstrate clinical benefit[76]. A few subsequent studies on childhood gliomas also had a negative outcome[77], and further clinical development was discontinued. A potential reason for the negative results was that the dose level of RMP-7 of 300 ng/kg might have been inadequate. Further dose escalation, however, has not been attempted in follow up studies for reasons that have not been published, leaving this issue open ended. Other explanations for the negative outcome might be related to the drug scheduling, since the time lapse of BBTB/BBB opening is relatively short, or the potential insufficient gain of drug influx by opening the BBTB/BBB with RMP-7. In experimental models using the most optimal scheduling in combinatorial treatment and with higher doses of RMP-7, the gain in brain tumor drug concentration was only about 2-fold[78]. Taking into account that carboplatin has no single agent activity; a mere 2-fold increase may still be inadequate to turn this combinatorial therapy into an active treatment regimen.

Inhibition of drug efflux transporters

As outlined above, many drugs exhibit a profoundly enhanced brain penetration when drug efflux transporters are absent (as observed in knockout mice)[47]. Consequently, inhibition of these

multidrug resistance efflux transporters by specific inhibitors seems an appealing strategy to boost drug penetration into the brain without compromising the integrity of the endothelial layer and tight junctions that might cause toxicities as seen with BBBD. Most of the clinically used ABC transporter inhibitors originate from the eighties and nineties of the previous century. At that time all major pharmaceutical companies had active programs aimed at reversing the multidrug resistance phenotype of tumors by concomitant use of chemotherapy and ABCB1 inhibitors. As a consequence, most inhibitors have been developed to target ABCB1, although later studies demonstrated that elacridar and tariquidar (both structurally related) are also ABCG2 transport inhibitors[79]. Unfortunately, clinical trials aimed at reversing multidrug resistance in solid tumors have failed. As a consequence, companies lost their interest and further developments were halted. Plausible explanations for the lack of efficacy are that multidrug resistance is multifactorial and that tumor cells (due to their genomic instability) are "moving targets" that cannot be captured by a single modality[80]. However, the concept of using these reversal agents to improve BBB drug penetration is very different from using these agents to block multidrug resistance in genomically unstable cancer cells. The objective here is to make a sanctuary site more accessible by targeting ABC transporters in genomically stable endothelial cells. Obviously, when attempting to implement this strategy there are still a few challenges to be addressed.

(A) Since most drugs are substrates of both ABCB1 and ABCG2, inhibition of both efflux transporters will be mandatory to yield adequate brain penetration. Based on this criterion, elacridar and tariquidar are currently the two only suitable options. Both have been used in clinical trials for reversing multidrug resistance. Given the lack of interest of pharmaceutical companies, it is unlikely to expect that other clinically applicable and more potent ABC transporter inhibitors will become available.

(B) Inhibition of ABC transporters at the BBB is more difficult than inhibition of ABC transporters in other tissues, such as lymphocytes that are frequently used as surrogate marker[81]. Comparative studies in ABC transporter KO mice demonstrate that first and second generation ABCB1 inhibitors are generally not potent enough to inhibit ABCB1 at the BBB[81,82]. These results underscore the need to use a dedicated and potent inhibitor. Repurposing of-the-shelf drugs such as cyclosporin A will unlikely be successful.

(C) Tariquidar has already been tested in humans to investigate inhibition of ABCB1 and ABCG2 transport at the BBB. In a healthy volunteer study, 150 mg tariquidar given by IV infusion did not evoke central opioid effects of loperamide, whereas it profoundly inhibited ABCB1 in lymphocytes[83]. Tariquidar did enhance the brain penetration of verapamil in rats and humans by 11 and 2.7-fold, respectively, as assessed by positron emission tomography (PET). The lower enhancement in humans was thought to be due to incomplete inhibition of ABCB1 at the BBB[84], however, a recent study using IV infusion resulting in tariquidar plasma levels of 3 μM

demonstrated a similar 2.7-fold increase[85]. The potency of tariquidar to inhibit ABCB1 at the BBB appears to be less than that of elacridar[81,86], suggesting that the latter may be preferred.

(D) The first candidate 'commuter' agents to be used in order to clinically test the concept of enhancing their brain penetration by inhibition of multidrug resistance efflux transporters must also be selected with care. The potency of inhibitors to inhibit efflux in part depends on transport substrate affinity of the candidate agents for ABCB1 and ABCG2. For example, elacridar was able to fully inhibit Abcb1-mediated efflux of topotecan from the brain but not Abcg2-mediated efflux[34]. Similarly, elacridar was not potent enough to fully inhibit gefitinib efflux from the brain[87]. Currently, we do not know what level of inhibition will be required to yield clinical benefit, but initial clinical testing this concept should preferably be done using relatively weak substrates. Preclinical studies have shown promising results using elacridar in combination with dasatinib[88-90], sorafenib[91], sunitinib[92] or temozolomide and veliparib[66]. Ideally, clinical development should be guided by monitoring predictive pharmacodynamic biomarkers as are present for most tyrosine kinase inhibitors. Beyond the treatment of brain tumors there may be opportunities in the treatment of drug resistant epilepsy with phenobarbital or phenytoin[93,94].

(E) The bioavailability (*i.e.*, systemic levels of the inhibitor) should be adequate for inhibition of ABC transporters at the BBB. Tariquidar is available as an IV formulation, which may be good for proof-of-concept testing as plasma levels of 1000 ng/ml can be achieved[84]. However, for therapeutic purposes, an oral formulation will be more preferable. Most of the preclinical studies with elacridar have been performed in mice receiving 100 mg/kg p.o. and resulting in plasma levels of about 400-500 ng/ml for about 24 h[82,95]. Under these conditions the brain penetration of paclitaxel was almost similar as in *Abcb1a/b* knockout mice, whereas lower doses were less effective. Importantly, however, the plasma levels in patients receiving oral elacridar at dose levels between 100 and 1000 mg never exceeded 130 ng/ml[96]. Elacridar is a poorly water soluble and membrane permeable drug and very difficult to formulate into a product with good oral bioavailability. Most likely, the conventional oral formulation as originally designed by GlaxoSmithKline is not sufficiently suitable to yield high enough plasma levels of elacridar. Consequently, better formulations of elacridar are necessary and initiatives are ongoing[95,97]. Given the structural similarities between elacridar and tariquidar, it is likely that development of a good oral formulation of the latter may pose the same challenge as for elacridar.

In summary, for the first proof-of-concept that overcoming the BBB/BTBB by blocking drug efflux transporters will be of benefit for glioma patients there is a need for a potent inhibitor with good systemic bioavailability as well as for a 'commuter' agent with moderate affinity for these efflux transporters. If successful, further optimization is warranted to explore the potential of enhancing brain penetration under more stringent conditions.

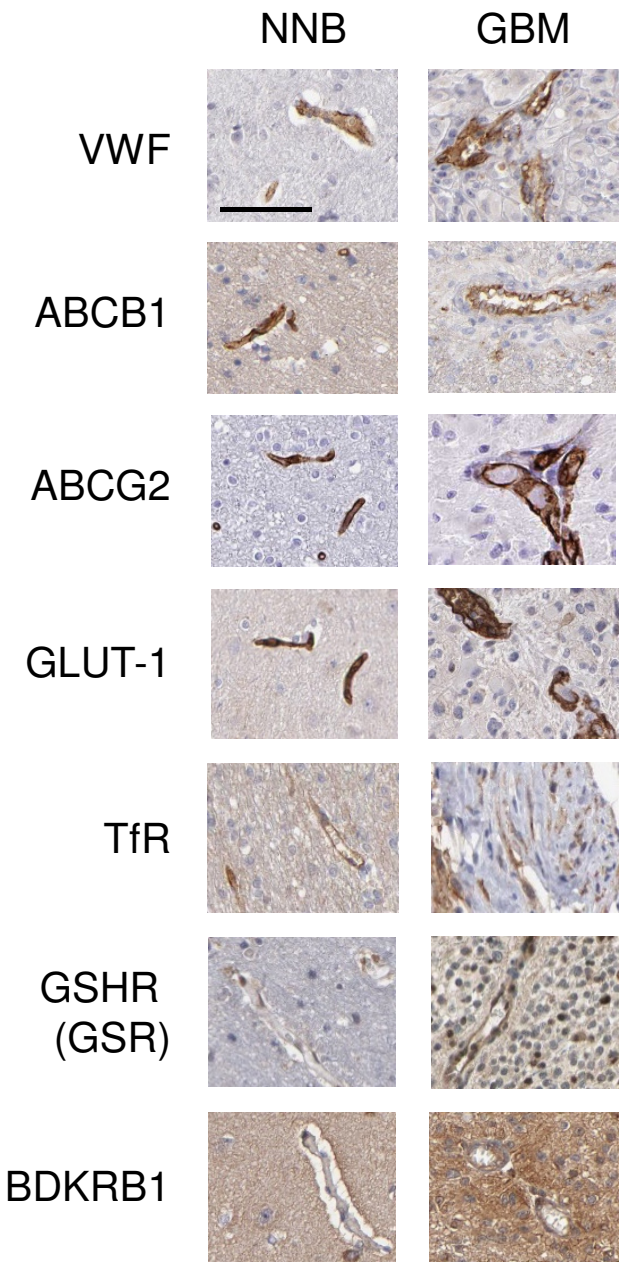

Figure 3 | Immunohistochemistry for ABC transporters, solute carriers, and transport receptors. Examples of immunohistochemical staining for ABC transporters, solute carriers, and transport receptors in non-neoplastic brain (NNB) and glioblastoma (GBM). See **Figure 2** for schematic depiction of these molecules. The immunohistochemical images were retrieved from www.proteinatlas.org.

Exploiting receptor-mediated transport systems

Another strategy to enhance brain penetration without disrupting the tight junctions and integrity of the endothelial layer is to employ receptor-mediated uptake mechanisms. Towards this end, a shuttling factor that targets a receptor (*e.g.*, insulin or transferrin receptor) at the BBB is coupled to a drug (*e.g.*, paclitaxel) or a vehicle (*e.g.*, liposome) containing a drug or radiopharmaceutical (**Figure 2B**). These are classic technology platforms that allow the shuttling of a range of drugs. Several receptor-mediated uptake systems have been described and tested for enhancing the brain uptake of drugs and radiopharmaceuticals as reviewed by Pardridge[98]. We will focus here on two of these strategies that have already yielded products that reached clinical evaluation. The first is GRN1005 (formerly ANG1005) developed by AngioChem, and is a conjugate of paclitaxel and the angiopep-2 peptide that targets the lipoprotein receptor-related protein 1 (LRP1) and crosses the BBB by transcytosis[99]. Although this is of course still in the early days, it is encouraging that responses have been observed in a phase I study. Currently, 3 phase II clinical trials for glioma (ClinicalTrials.gov Identifier NCT01967810) and breast cancer brain metastasis (NCT02048059 and NCT01480583) are accruing. The same angiopep-2 peptide has also been coupled to doxorubicin (ANG1997) and etoposide (ANG1009)[100] or anti-HER2 mAb (ANG4043)[101], demonstrating the versatility of this approach, but these have so far only been tested in preclinical studies.

The other clinically advanced candidate is 2B3-101 (NCT01386580, NCT01818713), which is a PEGylated liposome that is conjugated with glutathione (GSH). Preliminary results are also encouraging[102], but similar to GRN1005, it is far too early to draw any conclusion about the usefulness of this therapeutic approach. Unfortunately, currently there is not an easy surrogate marker to demonstrate better drug delivery to the brain and/or brain tumor. PEGylated liposomes have a long circulation half-life in blood. Consequently, plasma levels of the (encapsulated) drug are very high relative to the actual levels that have been attained in the brain and results of measurement of brain homogenates are flawed by admixing of blood in the tissue specimen. A better alternative would be measurement in brain interstitial fluid via a microdialysis probe. However, technical problems (adsorption to the membrane) markedly decrease the accuracy of this approach. Recently, a cerebral open flow microperfusion method has been presented and used for 2B3-101 *vs.* untargeted PEGylated liposomes and demonstrated a 4.7-fold increase in brain interstitial fluid doxorubicin levels[103].

Very recently an interesting paper appeared, demonstrating that the docosahexanoic transporter Mfsd2a acts by suppressing transcytosis in CNS endothelial cells[104]. Interfering with its function or expression may enhance transcytosis and thereby improve drug delivery via this route.

Circumvention of the BBTB

An apparently straightforward approach to overcome the BBTB is by delivery of therapeutic agents directly into the brain (tumor) parenchyma or into the resection cavity of glioma patients. Intracavitary drug injection, with the use of an intraventricular/intracavitary system such as an ommaya reservoir, allows for such direct delivery of chemotherapeutic agents to the tumor cavity. Injection occurs percutaneously into the subcuteaneous reservoir and the drug is subsequently transferred through the skull into the tumor (cavity) by manual compression of the reservoir. The distribution of the drug is determined by the rate and duration of the injection and by diffusion[105-108]. This method has been applied in various clinical trials for local delivery of drugs such as methotrexate and nitrosourea[107,108]. However, insufficient drug delivery, infections, neurotoxicity, and catheter obstruction has prevented successful application of this method in a routine setting[105,107]. Another direct local delivery approach is the use of gliadel wafers, which are biodegradable polymer wafers loaded with a chemotherapeutic agent implanted into the brain or tumor cavity at the time of surgery[60,109-111]. The biodegradable wafers, 1.45 cm diameter discs that contains 3.85% carmustine (BCNU), provide continuous delivery of therapeutic molecules to the tumor with ideally some control over the release and the spatial distribution of the drug in the course of time[57,112]. The drug is released from the wafer over a limited period of only two to three weeks and is delivered via diffusion from the source into surrounding brain tissue to produce a local anti-neoplastic effect[113]. In 1996, the gliadel wafer was approved by the U.S. Food and Drug Administration (FDA) as the first FDA-approved local treatment for recurrent and newly diagnosed glioblastoma[114]. However, the limitations of this method are significant and include the requirement of surgical placement, increased risk of local neurotoxicity, and local complications such as edema and infections[57,115]. Moreover, the rather diffuse distribution of the drug may well result in insufficient therapeutic drug concentrations at the site of more peripherally located infiltrative glioma cells. Indeed, so far all patients treated with this approach showed glioma progression[114,116].

A technique considered more promising is convection enhanced delivery (CED)[107,108,114,117,118]. CED involves the direct and continuous injection of a therapeutic agent under positive pressure using stereotactically placed intraparenchymal microcatheters, thereby allowing the passage of molecules, regardless of charge and size, into any section of the brain[119-121]. At the tip of the infusion catheter a pressure gradient creates flow of the therapeutic agents through the interstitial spaces of the brain[57,119,122]. Despite the advantages in terms of drug distribution throughout the brain as compared to ommaya reservoirs and wafers and compared to systemic delivery methods, CED remains experimental and several practical challenges need to be resolved, including determining optimal infusion rate and volume, anatomical prerequisites for the infusion site, and approach-related problems such as backflow along the tract[107,119,123]. Recent preclinical efforts using CED in glioma models include the use of radiolabeled monoclonal

antibodies[124], etoposide[125], carmustine[126], carboplatin[127] or an ATM inhibitor[128] in combination with radiotherapy, nanoparticles[129], nanoliposomal formulations with irinotecan[130] or cisplatin[131], and therapeutic stem cells[132]. Neuro-oncological clinical trials with CED have evaluated a wide range of potential therapeutic agents, including conventional chemotherapies such as paclitaxel[133], topotecan[134,135], and nimustine[136], targeted toxins including IL13-PE38QRR[137-139] and IL4-PE38[140,141], TP-38[142,143], oligonucleotides[144], and TGF-ß2 inhibitors[145]. Unfortunately, the results of all these trials were rather disappointing, which is largely attributed to poor drug distribution to more peripheral areas of diffuse gliomas and drug reflux, resulting in side effects and subtherapeutic drug concentrations within the tumor target cells[137-139]. Another major problem in many of these early clinical studies is the lack of visualization of the distribution of the infused drug and unacceptable device-related adverse events. Clinical and preclinical imaging studies are ongoing to further optimize drug distribution via CED[146,147]. In order to obtain efficient delivery of the drugs via CED, it is essential to optimize the CED catheter technology and use therapeutic agents with molecular characteristics suitable for CED, allowing for widespread drug distribution[107,114,117,118]. An additional point of consideration is the effect on CED flow and drug distribution of anatomical cavities in/around the CNS (ventricles, subarachnoid space) and of artificial cavities left after surgical resection of the bulk of the glioblastoma tissue. The issue of suboptimal CED due to resection cavities may be non-existing in the highly malignant diffuse intrinsic pontine gliomas (DIPGs),since in the brainstem bulk resection of such gliomas simply cannot be performed. Hence, DIPGs may provide a more suited tumor type for the evaluation of CED. It is unlikely that by current CED approaches all infiltrative glioblastoma cells will be reached, also not in the case of brainstem gliomas, and glioblastoma recurrences at local and more distal sites can still be expected to occur in most—if not all—patients with glioma. In order to reach more glioma cells, clinical trials are ongoing making use of tumor-selective self-replicative oncolytic viruses[148-152], and several oncolytic viruses have been evaluated preclinically in orthotopic glioma models[153-158]. This may allow for local amplification and spread after the diffuse delivery of the therapeutic agent via CED, and possibly result in a continued attack of the cancer cells. Clearly, further research is warranted towards the use of CED in combination with self-amplifying therapeutic agents.

FUTURE DIRECTIONS

Effective treatment of glioma is hampered by the presence of the BBTB. Especially in areas where the BBTB more closely resembles the BBB, anticancer drugs are denied access to the CNS and the tumor cells that reside therein. In this review, we presented a comprehensive synopsis of all the—also clinically applied—approaches used to date to enhance the permeability of the BBTB. While our knowledge about the molecular biology of glioma cells is rapidly expanding and is, to some extent, already assisting us in the design of tumor-tailored therapeutics, we are still struggling to develop modalities to expose the entire tumor to such therapeutics at pharmacologically

meaningful quantities. Therefore, we need to expand our knowledge about the fundamentals of the BBTB as a step towards the design of practical and safe devices and approaches for improved drug delivery into the diseased brain area. In this respect, the recent discovery of the impact of Mfsd2a on receptor-mediated transcytosis is a remarkable example. The predictive value of pre-clinical testing in *in vivo* models also needs to be improved by implementing animal models that more faithfully recapitulate the BBTB as observed in glioma patients.

As we stand today, some potentially useful technologies based on receptor-mediated transcytosis are currently under clinical evaluation and, when successful, will provide handles for further improvements. Ongoing research will hopefully also lead to the identification of other BBTB selective surface proteins that can be used as receptors for transcytosis or as selective recognition sites that enable targeting of therapeutics to and through the BBTB. Inhibition of drug efflux transporters at the BBTB is also an approach that warrants further exploration in clinical trials. Importantly for treatment of brain tumors, no matter how well the target is selected, there is no benefit if it is not reached.

REFERENCES

1. Chandana, S.R., *et al.* Primary brain tumors in adults. *Am Fam Physician* **77**, 1423-1430 (2008).
2. Ferguson, S.D. Malignant gliomas: diagnosis and treatment. *Dis Mon* **57**, 558-569 (2011).
3. Wen, P.Y. & Kesari, S. Malignant gliomas in adults. *N Engl J Med* **359**, 492-507 (2008).
4. Louis, D.N., *et al.* The 2007 WHO classification of tumours of the central nervous system. *Acta neuropathol* **114**, 97-109 (2007).
5. Sanai, N., *et al.* Low-grade gliomas in adults. *J Neurosurg* **115**, 948-965 (2011).
6. Nupponen, N.N. & Joensuu, H. Molecular pathology of gliomas. *Curr Diagn Pathol* **12**, 394-402 (2006).
7. Furnari, F.B., *et al.* Malignant astrocytic glioma: genetics, biology, and paths to treatment. *Genes Dev* **21**, 2683-2710 (2007).
8. Ohgaki, H. & Kleihues, P. Genetic pathways to primary and secondary glioblastoma. *Am J Pathol* **170**, 1445-1453 (2007).
9. Ohgaki, H. & Kleihues, P. The definition of primary and secondary glioblastoma. *Clin Cancer Res* **19**, 764-772 (2013).
10. Pardridge, W.M. The blood-brain barrier: bottleneck in brain drug development. *NeuroRx.* **2**, 3-14 (2005).
11. Abbott, N.J., *et al.* Astrocyte-endothelial interactions at the blood-brain barrier. *Nat Rev Neurosci* **7**, 41-53 (2006).
12. Alvarez, J.I., *et al.* Glial influence on the blood brain barrier. *Glia* **61**, 1939-1958 (2013).
13. Daneman, R., *et al.* Pericytes are required for blood-brain barrier integrity during embryogenesis. *Nature* **468**, 562-566 (2010).
14. Obermeier, B., *et al.* Development, maintenance and disruption of the blood-brain barrier. *Nat Med* **19**, 1584-1596 (2013).
15. Alvarez, J.I., *et al.* The Hedgehog pathway promotes blood-brain barrier integrity and CNS immune quiescence. *Science* **334**, 1727-1731 (2011).
16. Daneman, R., *et al.* Wnt/beta-catenin signaling is required for CNS, but not non-CNS, angiogenesis. *Proc Natl Acad Sci U S A* **106**, 641-646 (2009).
17. Liebner, S., *et al.* Wnt/beta-catenin signaling controls development of the blood-brain barrier. *J Cell Biol* **183**, 409-417 (2008).
18. Mizee, M.R. & de Vries, H.E. Blood-brain barrier regulation: environmental cues controlling the onset of barrier properties. *Tissue Barriers* **1**, e26882 (2013).
19. Mizee, M.R., *et al.* Retinoic acid induces blood-brain barrier development. *J Neurosci* **33**, 1660-1671 (2013).
20. Wolburg, H. & Lippoldt, A. Tight junctions of the blood-brain barrier: development, composition and regulation. *Vascul Pharmacol* **38**, 323-337 (2002).
21. Abbott, N.J., *et al.* Structure and function of the blood-brain barrier. *Neurobiol Dis* **37**, 13-25 (2010).
22. Hamm, S., *et al.* Astrocyte mediated modulation of blood-brain barrier permeability does not correlate with a loss of tight junction proteins from the cellular contacts. *Cell Tissue Res* **315**, 157-166 (2004).
23. Konig, J., *et al.* Transporters and drug-drug interactions: important determinants of drug disposition and effects. *Pharmacol Rev* **65**, 944-966 (2013).
24. Shitara, Y., *et al.* Clinical significance of organic anion transporting polypeptides (OATPs) in drug disposition: their roles in hepatic clearance and intestinal absorption. *Biopharm Drug Dispos* **34**, 45-78 (2013).
25. Kusuhara, H. & Sugiyama, Y. Active efflux across the blood-brain barrier: role of the solute carrier family. *NeuroRx.* **2**, 73-85 (2005).
26. van de Steeg, E., *et al.* High impact of Oatp1a/1b transporters on in vivo disposition of the hydrophobic anticancer drug paclitaxel. *Clin Cancer Res* **17**, 294-301 (2011).

27. Juliano, R.L. & Ling, V. A surface glycoprotein modulating drug permeability in Chinese hamster ovary cell mutants. *Biochim Biophys Acta* **455**, 152-162 (1976).
28. Cordon-Cardo, C., *et al.* Multidrug-resistance gene (P-glycoprotein) is expressed by endothelial cells at blood-brain barrier sites. *Proc Natl Acad Sci U S A* **86**, 695-698 (1989).
29. Schinkel, A.H., *et al.* Disruption of the mouse mdr1a P-glycoprotein gene leads to a deficiency in the blood-brain barrier and to increased sensitivity to drugs. *Cell* **77**, 491-502 (1994).
30. Demeule, M., *et al.* Drug transport to the brain: key roles for the efflux pump P-glycoprotein in the blood-brain barrier. *Vascul Pharmacol* **38**, 339-348 (2002).
31. Doyle, L.A., *et al.* A multidrug resistance transporter from human MCF-7 breast cancer cells. *Proc Natl Acad Sci U S A* **95**, 15665-15670 (1998).
32. Cooray, H.C., *et al.* Localisation of breast cancer resistance protein in microvessel endothelium of human brain. *Neuroreport* **13**, 2059-2063 (2002).
33. Eisenblatter, T. & Galla, H.J. A new multidrug resistance protein at the blood-brain barrier. *Biochem Biophys Res Commun* **293**, 1273-1278 (2002).
34. de Vries, N.A., *et al.* P-glycoprotein and breast cancer resistance protein: two dominant transporters working together in limiting the brain penetration of topotecan. *Clin Cancer Res* **13**, 6440-6449 (2007).
35. Lee, Y.J., *et al.* Investigation of efflux transport of dehydroepiandrosterone sulfate and mitoxantrone at the mouse blood-brain barrier: a minor role of breast cancer resistance protein. *J Pharmacol Exp Ther* **312**, 44-52 (2005).
36. Durmus, S., *et al.* Oral availability and brain penetration of the B-RAFV600E inhibitor vemurafenib can be enhanced by the P-glycoprotein (ABCB1) and breast cancer resistance protein (ABCG2) inhibitor elacridar. *Mol Pharm* **9**, 3236-3245 (2012).
37. Zhang, Y., *et al.* Plasma membrane localization of multidrug resistance-associated protein (MRP) homologues in brain capillary endothelial cells. *J Pharmacol Exp Ther* **311**, 449-455 (2004).
38. Potschka, H., *et al.* Multidrug resistance protein MRP2 contributes to blood-brain barrier function and restricts antiepileptic drug activity. *J Pharmacol Exp Ther* **306**, 124-131 (2003).
39. Soontornmalai, A., *et al.* Differential, strain-specific cellular and subcellular distribution of multidrug transporters in murine choroid plexus and blood-brain barrier. *Neuroscience* **138**, 159-169 (2006).
40. Slot, A.J., *et al.* Mammalian multidrug-resistance proteins (MRPs). *Essays Biochem* **50**, 179-207 (2011).
41. Ose, A., *et al.* Limited brain distribution of [3R,4R,5S]-4-acetamido-5-amino-3-(1-ethylpropoxy)-1-cyclohexene-1-carboxylate phosphate (Ro 64-0802), a pharmacologically active form of oseltamivir, by active efflux across the blood-brain barrier mediated by organic anion transporter 3 (Oat3/Slc22a8) and multidrug resistance-associated protein 4 (Mrp4/Abcc4). *Drug Metab Dispos* **37**, 315-321 (2009).
42. Lin, F., *et al.* Abcc4 together with abcb1 and abcg2 form a robust cooperative drug efflux system that restricts the brain entry of camptothecin analogues. *Clin Cancer Res* **19**, 2084-2095 (2013).
43. Sane, R., *et al.* The effect of ABCG2 and ABCC4 on the pharmacokinetics of methotrexate in the brain. *Drug Metab Dispos* **42**, 537-540 (2014).
44. Wijnholds, J., *et al.* Multidrug resistance protein 1 protects the choroid plexus epithelium and contributes to the blood-cerebrospinal fluid barrier. *J Clin Invest* **105**, 279-285 (2000).
45. Allen, J.D., *et al.* Mouse breast cancer resistance protein (Bcrp1/Abcg2) mediates etoposide resistance and transport, but etoposide oral availability is limited primarily by P-glycoprotein. *Cancer Res* **63**, 1339-1344 (2003).
46. Robillard, K.R., *et al.* Role of P-glycoprotein in the distribution of the HIV protease inhibitor atazanavir in the brain and male genital tract. *Antimicrob Agents Chemother* **58**, 1713-1722 (2014).
47. Lin, F., *et al.* Targeting core (mutated) pathways of high-grade gliomas: challenges of intrinsic resistance and drug efflux. *CNS Oncol* **2**, 271-288 (2013).
48. de Vries, H.E., *et al.* Inflammatory events at blood-brain barrier in neuroinflammatory and neurodegenerative disorders: implications for clinical disease. *Epilepsia* **53 Suppl 6**, 45-52 (2012).
49. Groothuis, D.R., *et al.* Regional blood flow and blood-to-tissue transport in five brain tumor models: implications for chemotherapy. *Prog Exp Tumor Res* **27**, 132-153 (1984).
50. Machein, M.R., *et al.* Vascular endothelial growth factor expression, vascular volume, and, capillary permeability in human brain tumors. *Neurosurgery* **44**, 732-740 (1999).
51. Dhermain, F.G., *et al.* Advanced MRI and PET imaging for assessment of treatment response in patients with gliomas. *Lancet Neurol* **9**, 906-920 (2010).
52. Watkins, S., *et al.* Disruption of astrocyte-vascular coupling and the blood-brain barrier by invading glioma cells. *Nat Commun* **5**, 4196 (2014).
53. Plate, K.H., *et al.* Tumor angiogenesis and anti-angiogenic therapy in malignant gliomas revisited. *Acta Neuropathol* **124**, 763-775 (2012).
54. Hardee, M.E. & Zagzag, D. Mechanisms of glioma-associated neovascularization. *Am J Pathol* **181**, 1126-1141 (2012).
55. la Fougere, C., *et al.* Molecular imaging of gliomas with PET: opportunities and limitations. *Neuro Oncol* **13**, 806-819 (2011).
56. Juillerat-Jeanneret, L. The targeted delivery of cancer drugs across the blood-brain barrier: chemical modifications of drugs or drug-nanoparticles? *Drug Discov Today* **13**, 1099-1106 (2008).
57. Korfel, A. & Thiel, E. Targeted therapy and blood-brain barrier. *Recent Results Cancer Res* **176**, 123-133 (2007).
58. Nishio, S., *et al.* Microvascular abnormalities in ethylnitrosourea (ENU)-induced rat brain tumors: structural basis for altered blood-brain barrier function. *Acta Neuropathol* **59**, 1-10 (1983).
59. Ningaraj, N.S., *et al.* Regulation of blood-brain tumor barrier permeability by calcium-activated potassium channels. *J Pharmacol Exp Ther* **301**, 838-851 (2002).
60. Groothuis, D.R. The blood-brain and blood-tumor barriers: a review of strategies for increasing drug delivery. *Neuro Oncol* **2**, 45-59 (2000).
61. Schlageter, K.E., *et al.* Microvessel organization and structure in experimental brain tumors: microvessel populations with distinctive structural and functional properties. *Microvasc Res* **58**, 312-328 (1999).
62. Blasberg, R.G., *et al.* Regional localization of a glioma-associated antigen defined by monoclonal antibody 81C6 in vivo: kinetics and implications for diagnosis and therapy. *Cancer Res* **47**, 4432-4443 (1987).
63. Tanaka, Y., *et al.* Ultrastructural localization of P-glycoprotein on capillary endothelial cells in human gliomas. *Virchows Archiv* **425**, 133-138 (1994).
64. Takamiya, Y., *et al.* Murine P-glycoprotein on stromal vessels mediates multidrug resistance in intracerebral human glioma xenografts. *Br J Cancer* **76**, 445-450 (1997).
65. Aronica, E., *et al.* Localization of breast cancer resistance protein (BCRP) in microvessel endothelium of human

control and epileptic brain. *Epilepsia* **46**, 849-857 (2005).
66. Lin, F., *et al.* ABCB1, ABCG2, and PTEN determine the response of glioblastoma to temozolomide and ABT-888 therapy. *Clin Cancer Res* **20**, 2703-2713 (2014).
67. Rapoport, S.I. Effect of concentrated solutions on blood-brain barrier. *Am J Physiol* **219**, 270-274 (1970).
68. Rapoport, S.I., *et al.* Testing of a hypothesis for osmotic opening of the blood-brain barrier. *Am J Physiol* **223**, 323-331 (1972).
69. Siegal, T., *et al.* In vivo assessment of the window of barrier opening after osmotic blood-brain barrier disruption in humans. *J Neurosurg* **92**, 599-605 (2000).
70. Fortin, D., *et al.* Enhanced chemotherapy delivery by intraarterial infusion and blood-brain barrier disruption in malignant brain tumors: the Sherbrooke experience. *Cancer* **103**, 2606-2615 (2005).
71. Angelov, L., *et al.* Blood-brain barrier disruption and intra-arterial methotrexate-based therapy for newly diagnosed primary CNS lymphoma: a multi-institutional experience. *J Clin Oncol* **27**, 3503-3509 (2009).
72. Burkhardt, J.K., *et al.* Intra-arterial delivery of bevacizumab after blood-brain barrier disruption for the treatment of recurrent glioblastoma: progression-free survival and overall survival. *World Neurosurg* **77**, 130-134 (2012).
73. Raymond, J.J., *et al.* Pharmacological modification of bradykinin induced breakdown of the blood-brain barrier. *Can J Neurol Sci* **13**, 214-220 (1986).
74. Inamura, T., *et al.* Intracarotid infusion of RMP-7, a bradykinin analog: a method for selective drug delivery to brain tumors. *J Neurosurg* **81**, 752-758 (1994).
75. Elliott, P.J., *et al.* Unlocking the blood-brain barrier: a role for RMP-7 in brain tumor therapy. *Exp Neurol* **141**, 214-224 (1996).
76. Prados, M.D., *et al.* A randomized, double-blind, placebo-controlled, phase 2 study of RMP-7 in combination with carboplatin administered intravenously for the treatment of recurrent malignant glioma. *Neuro Oncol* **5**, 96-103 (2003).
77. Warren, K., *et al.* Phase II trial of intravenous lobradimil and carboplatin in childhood brain tumors: a report from the Children's Oncology Group. *Cancer Chemother Pharmacol* **58**, 343-347 (2006).
78. Emerich, D.F., *et al.* Enhanced delivery of carboplatin into brain tumours with intravenous Cereport (RMP-7): dramatic differences and insight gained from dosing parameters. *Br J Cancer* **80**, 964-970 (1999).
79. de Bruin, M., *et al.* Reversal of resistance by GF120918 in cell lines expressing the ABC half-transporter, MXR. *Cancer Lett* **146**, 117-126 (1999).
80. Stein, W.D., *et al.* Intractable cancers: the many faces of multidrug resistance and the many targets it presents for therapeutic attack. *Curr Drug Targets* **5**, 333-346 (2004).
81. Choo, E.F., *et al.* Differential in vivo sensitivity to inhibition of P-glycoprotein located in lymphocytes, testes, and the blood-brain barrier. *J Pharmacol Exp Ther* **317**, 1012-1018 (2006).
82. Kemper, E.M., *et al.* Increased penetration of paclitaxel into the brain by inhibition of P-glycoprotein. *Clin Cancer Res* **9**, 2849-2855 (2003).
83. Kurnik, D., *et al.* Tariquidar, a selective P-glycoprotein inhibitor, does not potentiate loperamide's opioid brain effects in humans despite full inhibition of lymphocyte P-glycoprotein. *Anesthesiology* **109**, 1092-1099 (2008).
84. Bauer, M., *et al.* Pgp-mediated interaction between (R)-[11C]verapamil and tariquidar at the human blood-brain barrier: a comparison with rat data. *Clin Pharmacol Ther* **91**, 227-233 (2012).
85. Bauer, M., *et al.* Approaching complete inhibition of P-glycoprotein at the human blood-brain barrier: an (R)-[C] verapamil PET study. *J Cereb Blood Flow Metab* **35**, 743-746 (2015).
86. Kuntner, C., *et al.* Dose-response assessment of tariquidar and elacridar and regional quantification of P-glycoprotein inhibition at the rat blood-brain barrier using (R)-[(11)C]verapamil PET. *Eur J Nucl Med Mol Imaging* **37**, 942-953 (2010).
87. Agarwal, S., *et al.* Distribution of gefitinib to the brain is limited by P-glycoprotein (ABCB1) and breast cancer resistance protein (ABCG2)-mediated active efflux. *J Pharmacol Exp Ther* **334**, 147-155 (2010).
88. Lagas, J.S., *et al.* Brain accumulation of dasatinib is restricted by P-glycoprotein (ABCB1) and breast cancer resistance protein (ABCG2) and can be enhanced by elacridar treatment. *Clin Cancer Res* **15**, 2344-2351 (2009).
89. Agarwal, S., *et al.* Active efflux of Dasatinib from the brain limits efficacy against murine glioblastoma: broad implications for the clinical use of molecularly targeted agents. *Mol Cancer Ther* **11**, 2183-2192 (2012).
90. Becher, O.J., *et al.* ABCG2 and MDR promote brainstem gliomagenesis and limit the efficacy of dasatinib in a diffuse intrinsic pontine glioma (DIPG) mouse model. *Neuro Oncol* **16 suppl 3**, iii25 (2014).
91. Lagas, J.S., *et al.* Breast cancer resistance protein and P-glycoprotein limit sorafenib brain accumulation. *Mol Cancer Ther* **9**, 319-326 (2010).
92. Oberoi, R.K., *et al.* Pharmacokinetic assessment of efflux transport in sunitinib distribution to the brain. *J Pharmacol Exp Ther* **347**, 755-764 (2013).
93. Brandt, C., *et al.* The multidrug transporter hypothesis of drug resistance in epilepsy: proof-of-principle in a rat model of temporal lobe epilepsy. *Neurobiol Dis* **24**, 202-211 (2006).
94. van Vliet, E.A., *et al.* Region-specific overexpression of P-glycoprotein at the blood-brain barrier affects brain uptake of phenytoin in epileptic rats. *J Pharmacol Exp Ther* **322**, 141-147 (2007).
95. Sane, R., *et al.* Development and evaluation of a novel microemulsion formulation of elacridar to improve its bioavailability. *J Pharm Sci* **102**, 1343-1354 (2013).
96. Kuppens, I.E., *et al.* A Phase I, Randomized, Open-Label, Parallel-Cohort, Dose-Finding Study of Elacridar (GF120918) and Oral Topotecan in Cancer Patients. *Clin Cancer Res* **13**, 3276-3285 (2007).
97. Bunt, A.M.G. & van Tellingen, O. Efflux inhibitor compositions and methods of treatment using the same. Vol. WO2014018932 A2 (2014).
98. Pardridge, W.M. Drug transport across the blood-brain barrier. *J Cereb Blood Flow Metab* **32**, 1959-1972 (2012).
99. Drappatz, J., *et al.* Phase I study of GRN1005 in recurrent malignant glioma. *Clin Cancer Res* **19**, 1567-1576 (2013).
100. Che, C., *et al.* New Angiopep-modified doxorubicin (ANG1007) and etoposide (ANG1009) chemotherapeutics with increased brain penetration. *J Med Chem* **53**, 2814-2824 (2010).
101. Lachowicz, J., *et al.* ANG4043, a brain-penetrant anti-HER2 mAb increases survival in mice bearing intracranial BT-474 breast tumor cells. *Cancer Res* **73**, P6-11-05 (2013).
102. Gaillard, P.J., *et al.* Phase I dose escalating study of 2B3-101, glutathione PEGylated liposomal doxorubicin, in patients with solid tumors and brain metastases or recurrent malignant glioma. *Cancer Res* **74**, CT216 (2014).
103. Birngruber, T., *et al.* Enhanced doxorubicin delivery to the brain administered through glutathione PEGylated liposomal doxorubicin (2B3-101) as compared with generic Caelyx,((R))/Doxil((R))—a cerebral open flow microperfusion pilot study. *J Pharm Sci* **103**, 1945-1948 (2014).

104. Ben-Zvi, A., *et al.* Mfsd2a is critical for the formation and function of the blood-brain barrier. *Nature* **509**, 507-511 (2014).
105. Tomita, T. Interstitial chemotherapy for brain tumors: review. *J Neurooncol* **10**, 57-74 (1991).
106. Jacobs, A., *et al.* The Ommaya reservoir in chemotherapy for malignant disease in the CNS. *Clin Oncol* **7**, 123-129 (1981).
107. Bidros, D.S., *et al.* Future of convection-enhanced delivery in the treatment of brain tumors. *Future Oncol* **6**, 117-125 (2010).
108. Allhenn, D., *et al.* Drug delivery strategies for the treatment of malignant gliomas. *Int J Pharm* **436**, 299-310 (2012).
109. Brem, H., *et al.* Placebo-controlled trial of safety and efficacy of intraoperative controlled delivery by biodegradable polymers of chemotherapy for recurrent gliomas. *Lancet* **345**, 1008-1012 (1995).
110. Westphal, M., *et al.* A phase 3 trial of local chemotherapy with biodegradable carmustine (BCNU) wafers (Gliadel wafers) in patients with primary malignant glioma. *Neuro Oncol* **5**, 79-88 (2003).
111. Cao, X. & Schoichet, M.S. Delivering neuroactive molecules from biodegradable microspheres for application in central nervous system disorders. *Biomaterials* **20**, 329-339 (1999).
112. Avgeropoulos, N.G. & Batchelor, T.T. New treatment strategies for malignant gliomas. *Oncologist* **4**, 209-224 (1999).
113. Valtonen, S., *et al.* Interstitial chemotherapy with carmustine-loaded polymers for high-grade gliomas: a randomized double-blind study. *Neurosurgery* **41**, 44-48 (1997).
114. Buonerba, C., *et al.* A comprehensive outlook on intracerebral therapy of malignant gliomas. *Crit Rev Oncol Hematol* **80**, 54-68 (2011).
115. Bidros, D.S. & Vogelbaum, M.A. Novel drug delivery strategies in neuro-oncology. *Neurotherapeutics* **6**, 539-546 (2009).
116. Fung, L.K., *et al.* Pharmacokinetics of interstitial delivery of carmustine, 4-hydroperoxycyclophosphamide, and paclitaxel from a biodegradable polymer implant in the monkey brain. *Cancer Res* **58**, 672-684 (1998).
117. Barua, N.U., *et al.* Convection-enhanced drug delivery to the brain: therapeutic potential and neuropathological considerations. *Brain Pathol* **24**, 117-127 (2014).
118. Saito, R. & Tominaga, T. Convection-enhanced delivery: from mechanisms to clinical drug delivery for diseases of the central nervous system. *Neurol Med Chir* **52**, 531-538 (2012).
119. Westphal, M. & Lamszus, K. The neurobiology of gliomas: from cell biology to the development of therapeutic approaches. *Nat Rev Neurosci* **12**, 495-508 (2011).
120. Yamashita, Y., *et al.* Convection-enhanced delivery of a topoisomerase I inhibitor (nanoliposomal topotecan) and a topoisomerase II inhibitor (pegylated liposomal doxorubicin) in intracranial brain tumor xenografts. *Neuro Oncol* **9**, 20-28 (2007).
121. Lonser, R.R., *et al.* Real-time image-guided direct convective perfusion of intrinsic brainstem lesions. Technical note. *J Neurosurg* **107**, 190-197 (2007).
122. Jordan, A. & Maier-Hauff, K. *Regional therapy of brain tumors*, *Human Press Inc*, New Jersey (2007).
123. Kesari, S. Understanding glioblastoma tumor biology: the potential to improve current diagnosis and treatments. *Semin Oncol* **38 Suppl 4**, S2-10 (2011).
124. Luther, N., *et al.* The potential of theragnostic (1)(2)(4)I-8H9 convection-enhanced delivery in diffuse intrinsic pontine glioma. *Neuro Oncol* **16**, 800-806 (2014).
125. Sonabend, A.M., *et al.* Convection-enhanced delivery of etoposide is effective against murine proneural glioblastoma. *Neuro Oncol* **16**, 1210-1219 (2014).
126. Sewing, A.C., *et al.* Convection enhanced delivery of carmustine to the murine brainstem: A feasibility study. *J Neurosci Methods* **238**, 88-94 (2014).
127. Yang, W., *et al.* Radiation therapy combined with intracerebral administration of carboplatin for the treatment of brain tumors. *Radiat Oncol* **9**, 25 (2014).
128. Vecchio, D., *et al.* Pharmacokinetics, pharmacodynamics and efficacy on pediatric tumors of the glioma radiosensitizer KU60019. *Int J Cancer* **136**, 1445-1457 (2014).
129. Bernal, G.M., *et al.* Convection-enhanced delivery and in vivo imaging of polymeric nanoparticles for the treatment of malignant glioma. *Nanomedicine* **10**, 149-157 (2014).
130. Chen, P.Y., *et al.* Comparing routes of delivery for nanoliposomal irinotecan shows superior anti-tumor activity of local administration in treating intracranial glioblastoma xenografts. *Neuro Oncol* **15**, 189-197 (2013).
131. Huo, T., *et al.* Preparation, biodistribution and neurotoxicity of liposomal cisplatin following convection enhanced delivery in normal and F98 glioma bearing rats. *PLoS One* **7**, e48752 (2012).
132. Duebgen, M., *et al.* Stem cells loaded with multimechanistic oncolytic herpes simplex virus variants for brain tumor therapy. *J Natl Cancer Inst* **106**, dju090 (2014).
133. Lidar, Z., *et al.* Convection-enhanced delivery of paclitaxel for the treatment of recurrent malignant glioma: a phase I/II clinical study. *J Neurosurg* **100**, 472-479 (2004).
134. Bruce, J.N., *et al.* Regression of recurrent malignant gliomas with convection-enhanced delivery of topotecan. *Neurosurgery* **69**, 1272-1279 (2011).
135. Anderson, R.C., *et al.* Convection-enhanced delivery of topotecan into diffuse intrinsic brainstem tumors in children. *J Neurosurg Pediatr* **11**, 289-295 (2013).
136. Saito, R., *et al.* Regression of recurrent glioblastoma infiltrating the brainstem after convection-enhanced delivery of nimustine hydrochloride. *J Neurosurg Pediatr* **7**, 522-526 (2011).
137. Kunwar, S., *et al.* Phase III randomized trial of CED of IL13-PE38QQR vs Gliadel wafers for recurrent glioblastoma. *Neuro Oncol* **12**, 871-881 (2010).
138. Sampson, J.H., *et al.* Poor drug distribution as a possible explanation for the results of the PRECISE trial. *J Neurosurg* **113**, 301-309 (2010).
139. Mueller, S., *et al.* Effect of imaging and catheter characteristics on clinical outcome for patients in the PRECISE study. *J Neurooncol* **101**, 267-277 (2011).
140. Rand, R.W., *et al.* Intratumoral administration of recombinant circularly permuted interleukin-4-Pseudomonas exotoxin in patients with high-grade glioma. *Clin Cancer Res* **6**, 2157-2165 (2000).
141. Shimamura, T., *et al.* The IL-4 and IL-13 pseudomonas exotoxins: new hope for brain tumor therapy. *Neurosurg Focus* **20**, E11 (2006).
142. Rainov, N.G. & Heidecke, V. Long term survival in a patient with recurrent malignant glioma treated with intratumoral infusion of an IL4-targeted toxin (NBI-3001). *J Neurooncol* **66**, 197-201 (2004).
143. Sampson, J.H., *et al.* Sustained radiographic and clinical response in patient with bifrontal recurrent glioblastoma

multiforme with intracerebral infusion of the recombinant targeted toxin TP-38: case study. *Neuro Oncol* **7**, 90-96 (2005).
144. Carpentier, A., *et al.* Intracerebral administration of CpG oligonucleotide for patients with recurrent glioblastoma: a phase II study. *Neuro Oncol* **12**, 401-408 (2010).
145. Bogdahn, U., *et al.* Targeted therapy for high-grade glioma with the TGF-beta2 inhibitor trabedersen: results of a randomized and controlled phase IIb study. *Neuro Oncol* **13**, 132-142 (2011).
146. Chittiboina, P., *et al.* Magnetic resonance imaging properties of convective delivery in diffuse intrinsic pontine gliomas. *J Neurosurg Pediatr* **13**, 276-282 (2014).
147. Suzuki, A., *et al.* Analysis of biodistribution of intracranially infused radiolabeled interleukin-13 receptor-targeted immunotoxin IL-13PE by SPECT/CT in an orthotopic mouse model of human glioma. *J Nucl Med* **55**, 1323-1329 (2014).
148. Kicielinski, K.P., *et al.* Phase 1 clinical trial of intratumoral reovirus infusion for the treatment of recurrent malignant gliomas in adults. *Mol Ther* **22**, 1056-1062 (2014).
149. Markert, J.M., *et al.* A phase 1 trial of oncolytic HSV-1, G207, given in combination with radiation for recurrent GBM demonstrates safety and radiographic responses. *Mol Ther* **22**, 1048-1055 (2014).
150. Geletneky, K., *et al.* Phase I/IIa study of intratumoral/intracerebral or intravenous/intracerebral administration of Parvovirus H-1 (ParvOryx) in patients with progressive primary or recurrent glioblastoma multiforme: ParvOryx01 protocol. *BMC Cancer* **12**, 99 (2012).
151. Forsyth, P., *et al.* A phase I trial of intratumoral administration of reovirus in patients with histologically confirmed recurrent malignant gliomas. *Mol Ther* **16**, 627-632 (2008).
152. Chiocca, E.A., *et al.* A phase I open-label, dose-escalation, multi-institutional trial of injection with an E1B-Attenuated adenovirus, ONYX-015, into the peritumoral region of recurrent malignant gliomas, in the adjuvant setting. *Mol Ther* **10**, 958-966 (2004).
153. Muik, A., *et al.* Re-engineering vesicular stomatitis virus to abrogate neurotoxicity, circumvent humoral immunity, and enhance oncolytic potency. *Cancer Res* **74**, 3567-3578 (2014).
154. Allen, C., *et al.* Oncolytic measles virus strains have significant antitumor activity against glioma stem cells. *Gene Ther* **20**, 444-449 (2013).
155. White, E., *et al.*. Evaluation and optimization of the administration of a selectively replicating herpes simplex viral vector to the brain by convection-enhanced delivery. *Cancer Gene Ther* **18**, 358-369 (2011).
156. Idema, S., *et al.* Anatomical differences determine distribution of adenovirus after convection-enhanced delivery to the rat brain. *PLoS One* **6**, e24396 (2011).
157. Lun, X., *et al.* Myxoma virus virotherapy for glioma in immunocompetent animal models: optimizing administration routes and synergy with rapamycin. *Cancer Res* **70**, 598-608 (2010).
158. Verheije, M.H., *et al.* Coronavirus genetically redirected to the epidermal growth factor receptor exhibits effective antitumor activity against a malignant glioblastoma. *J Virol* **83**, 7507-7516 (2009).

Chapter 2

TARGETING CORE (MUTATED) PATHWAYS OF HIGH-GRADE GLIOMAS: CHALLENGES OF INTRINSIC RESISTANCE AND DRUG EFFLUX TRANSPORTERS

F. Lin, M.C. de Gooijer, D. Hanekamp, D. Brandsma, J.H. Beijnen, and O. van Tellingen

CNS Oncology. 2013;2(3):271-288

ABSTRACT

High-grade gliomas are the most common type of primary brain tumors and are among the most lethal types of human cancers. Most patients with a high-grade glioma have a glioblastoma multiforme (GBM), the most malignant glioma subtype that is associated with a very aggressive course and short overall survival. Standard treatment of newly diagnosed GBM involves surgery followed by chemoradiation with temozolomide. However, despite this extensive treatment the mean overall survival is still only 14.6 months and more effective treatments are urgently needed. Although different types of GBMs are indistinguishable by histopathology, novel molecular pathological techniques allow the discrimination between four main GBM subtypes. Targeting the aberrations in the molecular pathways underlying these subtypes holds promise for improved therapies. Here, we will discuss the potential avenues and pitfalls of molecular targeted therapies for treatment of GBM.

Practice points:

- GBMs are characterized by a collection of mutated signaling pathways
- Three core pathways are affected in a substantial fraction of patients
- Therapy directed against just a single mutated pathway is unlikely to be successful
- Instead, the combination of targeted therapeutics should be explored
- Because of its invasive character, GBM is a disease that affects the whole brain.
- Consequently, therapeutics against GBM should cross the BBB to also reach the more remote areas containing tumor cells.
- Most targeted agents have been designed for other cancers than GBM and many of them will not fulfill the demand of sufficient BBB penetration
- Candidate agents that are not or very weak substrates of ABC transporters have an advantage with respect to BBB penetration.
- Alternatively, inhibitors of ABC transporters may be used to enhance the BBB penetration of substrate drugs.

INTRODUCTION

High-grade gliomas are the most common type of primary brain tumors and are among the most lethal types of human cancers[1]. High-grade gliomas are classified by the World Health Organization (WHO) in grade III: anaplastic astrocytoma, anaplastic oligodendroglioma, and anaplastic oligoastrocytoma; and grade IV: gliosarcoma and glioblastoma multiforme (GBM)[2]. Unfortunately, the majority of high-grade glioma patients are diagnosed with GBM, the most malignant subtype that is associated with a very aggressive course and less than 3 months overall survival if left untreated[2]. Standard treatment of newly diagnosed GBM includes surgery, followed by radiotherapy (30x2 Gy) plus temozolomide (75 mg/m^2, daily) for 6 weeks and maintenance temozolomide therapy (150–200 mg/m^2 x5 per 28 days) during 6 months. However, despite this extensive treatment the mean overall survival is still only 14.6 months and more effective treatments are thus urgently needed[3].

In contrast to conventional chemotherapies that work by interfering with DNA synthesis or cell metabolism, targeted therapies work by inhibition of the deregulated cell signaling pathways in cancer cells by small molecules or antibodies. The underlying concept is that these signaling pathways are more critical for survival and growth of cancer cells than for normal cells. Consequently, targeted therapy holds the promise of being effective with less toxicity than conventional chemotherapies. Despite the emerging success in some other tumor types; *e.g.*, imatinib for chronic myelogenous leukemia[4] or vemurafenib in melanoma[5], the development of molecular targeted therapy for gliomas appear to be extra challenging. Two small molecule inhibitors of epidermal growth factor receptor (EGFR) tyrosine kinase that received regulatory approval for the treatment of lung cancer, erlotinib (Tarceva®, OSI-774; Genentech, Inc) and gefitinib (Iressa®, ZD1839; AstraZeneca), have extensively been evaluated for GBM treatment with high expectations, since EGFR overexpression and *EGFR* mutations are common in GBM. The results of the first phase I studies with erlotinib were exciting[6,7] and a phase II, single institution study showed that erlotinib plus temozolomide before and after radiation significantly increased median survival of GBM patients to 19.3 months in comparison of 14.1 months in historical controls[8]. However, results of subsequent clinical trials with EGFR inhibitors were all disappointing[9-14]. In particular, a randomised controlled phase II study carried out by the European Organisation for Research and Treatment of Cancer (EORTC) demonstrated no clear benefit in progressive GBM patients treated with erlotinib compared to a control group receiving temozolomide or carmustine[10].

The failures of targeted therapy in the treatment of GBM are not limited to EGFR inhibitors. Inhibitors of the mammalian target of rapamycin (mTOR) have also been regarded as a promising target for GBM as the frequently deregulated PI3K–AKT–mTOR signaling is considered to be a key mediator of GBM cell survival and growth. Rapamycin (sirolimus) and its analogues (rapalogs)

temsirolimus (CCI-779) and everolimus (RAD001) are the three mTOR inhibitors that have undergone extensive clinical evaluation for their therapeutic effect in GBMs[15-22]. Similar to the EGFR inhibitors, most trials with mTOR inhibitors as a single agent in GBM, have failed to show any significant therapeutic benefit.

Despite these disappointing results, important lessons have been learned from translational studies with these agents. This review will focus on the recent development of targeted therapies on the core mutated pathways of GBM. Moreover several major putative resistance mechanisms of GBM to the earlier studied targeted therapies will be discussed.

GENETIC ALTERATIONS AND CLASSIFICATION OF GBM

The majority of patients with GBM suffer from primary (or *de novo*) GBM. In comparison with secondary GBM that evolve from low-grade gliomas, primary GBM usually develops without pre-existing precursor lesions. Primary and secondary GBMs are histopathologically indistinguishable and are characterized by a high proliferative index, serpentine pseudopallisading necrosis and microvascular proliferation. Nevertheless, primary and secondary GBM are associated with differences in age of onset, clinical history, median survival and genetic changes (**Table 1**).

Primary and secondary GBMs develop as a result of multiple genetic alterations that are distinct between the two types of GBM. Secondary GBM is more frequently a result of an early mutation of *TP53*, whereas primary GBM much more often harbors mutations in the *EGFR* (epidermal growth factor receptor) gene, deletions within the *CDKN2* (cyclin-dependent kinase inhibitor 2) locus that codes for $p14^{ARF}$, $p16^{INK4A}$ and $p15^{INK4B}$ and a homozygous loss of chromosome 10q23, which houses the phosphatase and tensin homolog (*PTEN*) gene. Overall, loss of chromosome 10q, *EGFR* amplification and deletion of $p16^{INK4A}$ have shown to be the most frequent genetic alterations in primary GBM[1,23-26].

Subtype	Incidence	Origin	Alterations	Clinical history	Median overall survival*
Primary or *de novo* GBM	95%	No recognizable precursor lesions	LOH 10q (70%) *EGFR* amplification (36%) *P16INK4A* deletion (31%) *TP53* mutation (28%) *PTEN* mutation (25%)	<3 months (68%) <6 months (84%)	4.7 months
Secondary GBM	5%	Developed from diffuse astrocytoma or anaplastic astrocytoma	LOH 10q (63%) *EGFR* amplification (8%) *P16INK4A* deletion (19%) *TP53* mutation (65%) *PTEN* mutation (4%)	Low-grade astrocytoma origin: 5.1 years; Anaplastic astrocytoma: 1.9 years.	7.8 months

Table 1 | The classic classification of glioblastoma multiforme. The classic classification includes primary and secondary GBM. GBM, glioblastoma multiforme. * median overall survival without treatment.

The Cancer Genome Atlas project in GBMs

By implementation of large-scale multi-dimensional analytic platforms, a comprehensive characterization of the molecular basis of malignant gliomas recently became available. The Cancer Genome Atlas (TCGA) is a project aimed to catalogue genetic mutations responsible for cancer. In 2008, TCGA published the results of their first cancer project on the analysis of genomic abnormalities in human GBM (mostly primary GBM)[27]. This work not only confirmed the common genetic aberrations reported previously, but also provided new insight into the roles of some known tumor related genes as *ERBB2/HER2* (human epidermal growth factor receptor 2), *NF1* (neurofibromin 1) and *TP53*, and uncovered new mutations. More importantly, it provided a network view of the pathways altered in the development of GBM which can be instructive for future therapeutic decisions and facilitate the search for more efficacious targeted therapies. As shown in **Figure 1**, frequent genetic alterations of GBM occur in three core pathways: RTK/RAS/PI3K signaling and p53 and RB tumor suppressor pathway were mapped based on genetic analyses of 206 GBM samples.

Another important outcome of TCGA is the molecular classification of GBM[28]. Four GBM subtypes: proneural, neural, classical, and mesenchymal subtypes described in this study showed strong correlations with GBM cells of origin, clinical characteristics, and response to standard chemoradiation (**Table 2**). For example, the proneural subtype was associated with younger age and *IDH1* (isocitrate dehydrogenase 1) and *TP53* mutations, with a trend to longer survival for these patients. Intriguingly, however, patients with proneural type GBM did not have an improved survival when receiving aggressive treatment. On the contrary, the classical subtype GBM usually harboring *EGFR* amplification and homozygous deletion of *CDKN2* and *PTEN* had the greatest benefit from standard treatment among all subtypes. Given the fact that each subtype harbors specific aberrations in molecular pathways, one may expect that targeting these pathways by specific inhibitors may provide new avenues for improved therapies.

THE BLOOD–BRAIN BARRIER AND DRUG EFFLUX TRANSPORTERS

The brain is often referred as a pharmacological sanctuary site since most drugs are unable to cross the blood–brain barrier (BBB)[29-31]. The BBB represents one of the major challenges to the chemotherapy efficacy against GBM. The BBB is formed by endothelial cells that are closely linked by tight junctions disabling the paracellular movement of substances (**Figure 2A**). Moreover, in contrast to most endothelial cells elsewhere in the body they lack fenestrae and have low endocytic activity. Consequently, entry of substances into the brain can only occur by transcellular passage of the endothelium. Moreover, the pericytes and astrocytes intimately surrounding the endothelial cells form a secondary lipid layer, which further enforces the impermeability of the BBB[32]. Entry of essential nutrients (*e.g.*, glucose) is strictly regulated by a range of uptake transporters. Other

substances can only enter the brain by passive diffusion across the BBB, and the ability to do so is determined by a series of molecular parameters such as sufficient lipid solubility (octanol:water partition coefficient), molecular weight, degree of ionization, plasma protein binding and tissue binding. Nevertheless, even compounds that comply with molecular characteristics in favor of passive diffusion demonstrate a much lower brain penetration than expected[31], due to the activity of drug efflux transporters.

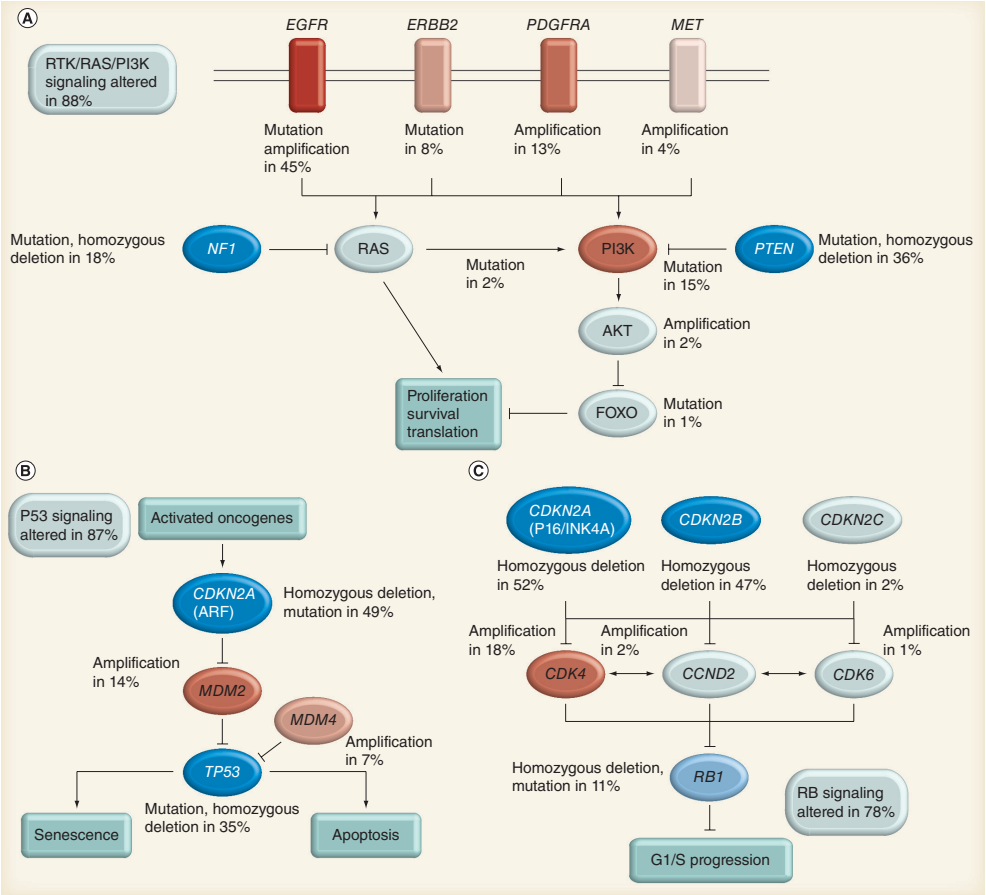

Figure 1 | The Cancer Genome Atlas of glioblastoma multiforme. Primary sequence alterations and significant copy number changes for components of the (**A**) RTK–RAS–PI3K, (**B**) p53 and (**C**) RB signaling pathways are shown. Red indicates activating genetic alterations, with frequently altered genes showing deeper shades of red. Conversely, blue indicates inactivating alterations, with darker shades of blue corresponding to a higher percentage of alteration. For each altered component of a particular pathway, the nature of the alteration and the percentage of tumors affected are indicated. Boxes contain the final percentages of glioblastoma multiformes with alterations in at least one known component gene of the designated pathway. Reprinted with permission from[27]. © Macmillan Publishers Ltd (2008).

ATP-binding cassette (ABC) drug transporters expressed at the BBB have well-known roles in the restriction of therapeutic agents into the brain[33]. Of all efflux transporters present in the BBB, two transporters are in particular responsible for the efflux of anticancer agents back into the blood capillaries. These proteins are ABCB1 (ATP-binding cassette transporter B1) and ABCG2 (ATP-binding cassette transporter G2) (**Figure 2B**).

Subtype	Biomarker	Signature	Major alterations	Treatment response
Classical	Neuro embryonic stem cell	Astrocytic	*EGFR*, *CDKN2A/2B*, *PTEN*	Good
Mesenchymal	Mesenchymal markers	Astroglial	*NF1*, *PTEN*, *CHI3L1*, *MET*	Modest
Proneural	Oligodendrocytic development genes	Oligodendrocytic	*TP53*, *PDGFRA* or *PI3KCA/PIK3R1*, *IDH1*, *PTEN*	Poor or no response
Neural	Neural markers	Neuronal and astrocytic	*EGFR*	Marginal

Table 2 | The Cancer Genome Atlas genomic classification of glioblastoma multiforme. The Cancer Genome Atlas classification reveals four clinically relevant subtypes based on the genomic profiles of glioblastoma multiforme and their correlations with biomarker expression, cellular lineages and response to standard chemoradiation therapy.

ABCB1

ABCB1 (also named Permeability-glycoprotein, P-gp, or multidrug resistance transporter protein 1, MDR1) is a 170-kDa membrane associated protein, expressed at high levels in normal human tissues, including the brain capillaries (**Figure 2C**). It was first discovered by its ability to confer multidrug resistance in cultured tumor cells[34]. ABCB1 is a highly promiscuous transporter, recognizing an amazing range of drugs. Like all members of the ATP-binding cassette transporter superfamily, the energy for active transport of compound is provided by hydrolysis of ATP at the nucleotide binding domains (NBDs)[31,35].

Besides affecting cellular drug accumulation in tumor cells, ABC drug efflux transporters also actively affect the drug disposition by its expression at various barrier sites (BBB, intestinal epithelium, blood–testis barrier)[36-40]. ABCB1 was the first drug efflux transporter showing a remarkable impact on the brain delivery of substrate agents. Mice have two genes that are equivalent to *ABCB1*, namely *Abcb1a* and *Abcb1b*. Abcb1a is the subtype that is expressed in the BBB and *Abcb1a*-deficient mice demonstrate a dramatic sensitivity to the neurotoxic pesticide ivermectin and to the cytotoxic drug vinblastine[41]. The role of ABCB1/Abcb1a in limiting drug brain penetration has been extended to a plethora of agents, including many novel targeted agents.

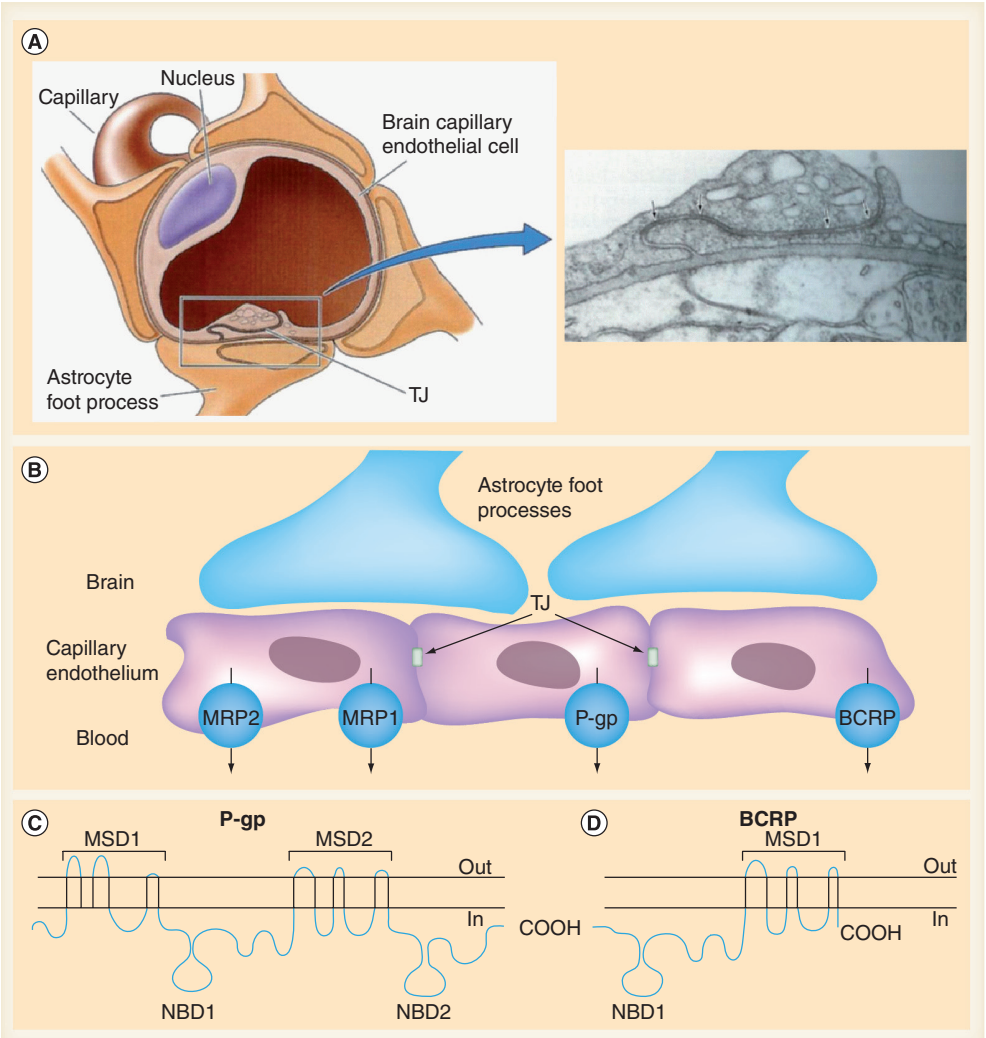

Figure 2 | The blood–brain barrier. (**A and B**) Blood–brain barrier and ABC drug efflux transporters at the blood–brain barrier. (**C and D**) Secondary structures of P-gp and BCRP, respectively. MSD, membrane-spanning domain; NBD, nucleotide-binding domain; TJ, tight junction. Right-hand panel in (**A**) reproduced with permission from[118] © Oxford University Press (1991). Left-hand panel in (**A**) and (**B**) adapted with permission from[119]. (**C and D**) Adapted with permission from[35].

ABCG2

ABCG2 (murine subtype Abcg2), also known as BCRP (breast cancer resistance protein), is a 72-kDa ABC transporter. Similar to ABCB1, it plays an important role in drug disposition and distribution in the body (**Figure 2D**). ABCG2 is expressed in many tissues of the body including the apical side of the intestinal lumen, the bile canaliculus in liver hepatocytes, and the capillaries of the BBB. ABCG2 also transports a broad range of endogenous and exogenous compounds[31,35].

However, pharmacokinetic studies using *Abcg2* knockout mice showed little effect on the brain penetration of drugs, with a few exceptions, such as sorafenib[42]. The reason is that most drugs are substrates of both ABC transporters and the brain accumulation of these substances is limited by Abcb1 that is still present in *Abcg2* knockout mice. The absence of both Abcb1 and Abcg2, however, results in a profound increase in brain uptake compared with the absence of each transporter alone. Due to the extremely broad substrate specificities of these two transporters, the concerted action of ABCB1 and ABCG2 is not restricted to only a few drugs, but represents a common mechanism to limit the brain entry of many drugs and thus potentially conferring resistance to chemotherapies of brain tumors (**Table 3**).

TARGETING EGFR AND LESSONS LEARNED FROM ERLOTINIB TRIALS IN GBM

EGFR (ERBB1) is a member of the ErbB family of transmembrane receptor tyrosine kinases (RTK) and binds to at least six different ligands, including EGF (epidermal growth factor) and TGF-α (transforming growth factor-α). After binding of a ligand, dimerization of EGFR takes place and the complex is activated and recruits phosphatidylinositol 3-kinase (PI3K). This activates the PI3K–AKT–mTOR pathway transducing a proliferation signal to the cell. In tumor cells, *EGFR* amplification is often present as small fragments of extrachromosomal DNA (double minutes) and is often associated with structural mutations in the *EGFR* gene, of which several variants have been identified. *EGFRvIII* or *ΔEGFR* is the most commonly occurring mutation in GBM derived by a non-random 801 bp in-frame deletion of exons 2–7, and codes for a truncated and constitutively activated protein[43-45]. Overall, EGFRvIII expression in the presence of *EGFR* amplification plays an important role in enhanced tumorigenicity and indicates a poor survival prognosis in GBM patients[46].

Although *EGFR* amplification and mutation is considered to be an important factor, none of the currently tested EGFR inhibitors has shown any clinical efficacy against GBM. The contrast between the more successful application of EGFR inhibitors in other types of cancer such as lung cancer, and the failure in GBM has been extensively studied. These studies suggest that the lack of response to EGFR inhibitors in GBM is multifactorial. A first issue is related to the drug delivery: *i.e.*, can a therapeutic level of erlotinib be reached in the glioma tissue? Erlotinib is a substrate of both ABCB1 and ABCG2, and the two drug efflux transporters together resulted in a 7-fold reduction of brain–plasma ratio in wild-type compared to *Abcb1;Abcg2* knockout mice[47,48]. Thus, the limited BBB penetration of erlotinib caused by ABCB1 and ABCG2 may at least be partly responsible for the resistance of GBM to erlotinib treatment. Unfortunately, the bare fact is that ABCB1 and ABCG2 have a long list of overlapping substrates, including most EGFR/tyrosine kinase inhibitors such as gefitinib[49], sunitinib[50], sorafenib[42], dasatinib[51,52], imatinib[53] and lapatinib[54] and the brain penetration of these compounds is also markedly restricted by these two transporters (**Table 3**).

Agent	Target protein(s)	Brain penetration limited by Abcb1?	Brain penetration limited by Abcg2?	Reference
Sirolimus	mTOR	Yes	No	Lin *et al*, unpublished data
Palomid 529	mTOR	No	No	(110)
Erlotinib	EGFR	Yes	Yes	(111,47)
Gefitinib	EGFR	Yes	Yes	(49)
Sunitinib	VEGFR-2 and -3, c-KIT, FLT3, PDGFR	Yes	Yes	(50)
Cediranib	VEGFR	Yes	Yes	(112)
Axitinib	VEGFR	Yes	Yes	(113)
Sorafenib	c-KIT, PDGFR, RAF	Yes	Yes	(42)
Dasatinib	BCR–ABL, c-KIT, PDGFR, SRC	Yes	Yes	(52)
Vemurafenib	B-RAF^{V600E}	Yes	Yes	(114,115)
Dabrafenib	B-RAF^{V600E}	Yes	Yes	(116)
Imatinib	BCR–ABL, c-KIT, PDGFR	Yes	Yes	(53,105)
Lapatinib	HER2 (ERBB2), EGFR	Yes	Yes	(54)
GDC-0941	PI3K	Yes	Yes	(69)
Tandutinib	c-KIT, FLT3, PDGFRβ	Yes	Yes	(117)

Table 3 | Impact of Abcb1 and Abcg2 on the brain penetration of targeted agents as demonstrated in *Abcb1*- and/or *Abcg2*-deficient mice. EGFR, EGF receptor; PDGFR, PDGF receptor; VEGFR, VEGF receptor.

A second issue is that deregulated components downstream of EGFR could abolish the effects of EGFR inhibition. For example, Mellinghoff *et al.* reported that *PTEN* loss in GBM cells would be a cause of resistance to erlotinib[55]. However, this is not the only reason as the randomized EORTC study also found tumors with expression of PTEN and EGFR and/or EGFRvIII that

responded poorly[10]. Only low levels of phosphorylated PKB/AKT appear to have a (weak) relation with outcome to erlotinib treatment. As we know, PTEN is not the only key factor controlling the signaling downstream of EGFR. Also *PI3K* mutation and *AKT* amplification can lead to activation of the PI3K pathway. Furthermore, there is active crosstalk between the PI3K and RAS pathways[56,57] and activation of the RAS–RAF–MEK–ERK pathway is common in GBM[58]. This pathway activation can be caused by a mutation or deletion of *NF1* or (more rarely) by mutation of *RAS*. Besides, mutation and amplification of other parallel receptor tyrosine kinases such as *ERBB2*, *PDGFR* and *c-MET*, could also activate signaling via the PI3K–mTOR and RAS pathway, thereby conferring resistance to EGFR inhibition[59]. Last but not least, another explanation for the disappointing clinical activity of erlotinib in GBM versus lung cancer was delivered by a recent study of Vivanco *et al.*[60]. They showed that distinct types of *EGFR* mutations in lung cancer and GBMs responded differently to EGFR inhibitors. Importantly, they found that the first-generation EGFR inhibitor erlotinib effectively inhibits EGFR carrying mutations in the kinase domain, as found in lung cancer, whereas it performs very poorly against EGFR with mutations or deletions in the extracellular domain as in GBM[60]. The putative resistance of GBM to erlotinib caused by drug efflux transporters and/or intrinsic molecular mechanisms are illustrated in **Figure 3**.

TARGETING THE PI3K–AKT–MTOR PATHWAY

The PI3K–AKT–mTOR pathway, activated by extracellular survival signaling factors via RTKs, is a major cell signaling pathway involved in regulating a variety of cellular processes including cell proliferation, survival, growth, glucose metabolism and protein synthesis[61]. The most frequent alteration responsible for the deregulation of this pathway in GBM is the loss of *PTEN* (36%). In addition, mutation of *PIK3CA* (15%), and occasionally *AKT* amplification (2%) or *FOXO* mutation (1%) also contribute to the activation of the downstream signaling[27,62,63] (**Figure 1 and Figure 4**). Constitutive PI3K–AKT–mTOR pathway activation is a hallmark of GBM.

The class IA phosphatidylinositol 3-kinase (PI3K) is a heterodimer composed of an 85 kDa regulatory subunit (p85α) and a 110 kDa catalytic subunit (p110α). Once an RTK recruits PI3K to the cellular membrane, the PI3K subunit converts inactive PIP_2 (Phosphatidylinositol 4,5-bisphosphate) into active PIP_3 (phosphatidylinositol 3,4,5-trisphosphate). Next, PIP_3 recruits AKT to the membrane together with phosphoinositide-dependent kinase 1 (PDK1). On the contrary, PTEN counteracts PI3K by converting PIP_3 back into PIP_2 and functions as a tumor suppressor. Unlike for other components of cellular pathways with multiple protein family members, there is no PTEN related protein present in the cells that can compensate for its loss. Therefore, it is not surprising that the loss of PTEN function plays a pivotal role in tumorigenesis[64].

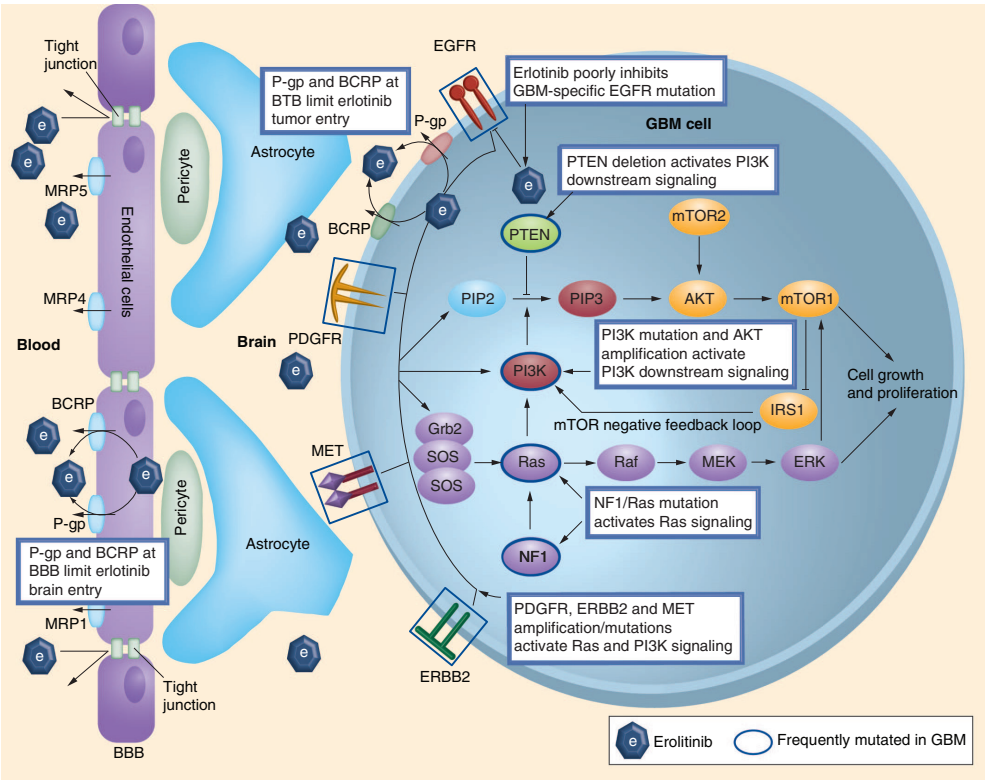

Figure 3 | Putative mechanisms of glioblastoma multiforme resistance to erlotinib treatment. Erlotinib acts on EGFR causing downstream signaling of the PI3K–mTOR and RAS–MEK–ERK pathways. However, the glioblastoma multiforme-specific mutation *EGFRvIII* is less susceptible to erlotinib, and redundant receptor tyrosine kinases (PDGFR, ERBB2 and MET) may also cause downstream signaling. Moreover, the activity of the drug transporters (ABCB1 and ABCG2) located at the BBB and in the tumor cell may cause insufficient entry of erlotinib to elicit target inhibition. BBB, blood–brain barrier; BBTB, blood–brain tumor barrier; EGFR, EGF receptor; GBM, glioblastoma multiforme; PDGFR, PDGF receptor.

PI3K inhibitors

Due to the high mutation rates of *PTEN* and *PIK3CA* (the gene that encodes the catalytic subunit p110α of PI3K) and the importance of this pathway in GBM, PI3K and especially its subunit P110α, provides an attractive drug target. The first generation of PI3K inhibitors (LY294002 and wortmannin) showed *in vivo* antitumor efficacy, but were associated with poor stability or solubility, undesirable toxicities and cross-over inhibition of other lipid and protein kinases[65,66]. Therefore, clinical trials with these compounds have never been initiated. After the crystal structure of PI3K was elucidated, the development of new PI3K inhibitors has been accelerated. More selective PI3K inhibitors have been developed, with promising antitumor efficacy and low toxicity in preclinical research. For example, GDC-0941 is a potent and selective ATP-competitive

PI3K inhibitor. It inhibits the PI3K p110α subunit with an IC_{50} < 10 nM and inhibits phosphorylation of AKT with an IC_{50} value of 28 nM[67]. GDC-0941 treatment has led to an increase of apoptosis and inhibition of endothelial growth in a subset of tumor cell lines. *In vivo* antitumor activity with daily oral dosing at 150 mg/kg of GDC-0941 achieved 98% growth inhibition of subcutaneous U87MG xenografts[65,68]. Unfortunately, GDC-0941 is also a substrate of both ABCB1 and ABCG2. After intravenous or oral administration, the GDC-0941 brain–plasma ratio in *Abcb1;Abcg2*$^{-/-}$ mice was about 30-fold higher than in the wild-type mice. The PI3K pathway was markedly inhibited as evidenced by a 60% suppression of the phosphorylated AKT in the brain of *Abcb1;Abcg2*$^{-/-}$ mice, whereas no inhibition was detected in the brain of wild-type mice[69]. Therefore, the potential efficacy of GDC-0941 as a targeted agent for treatment of GBM is limited due to ABCB1 and ABCG2.

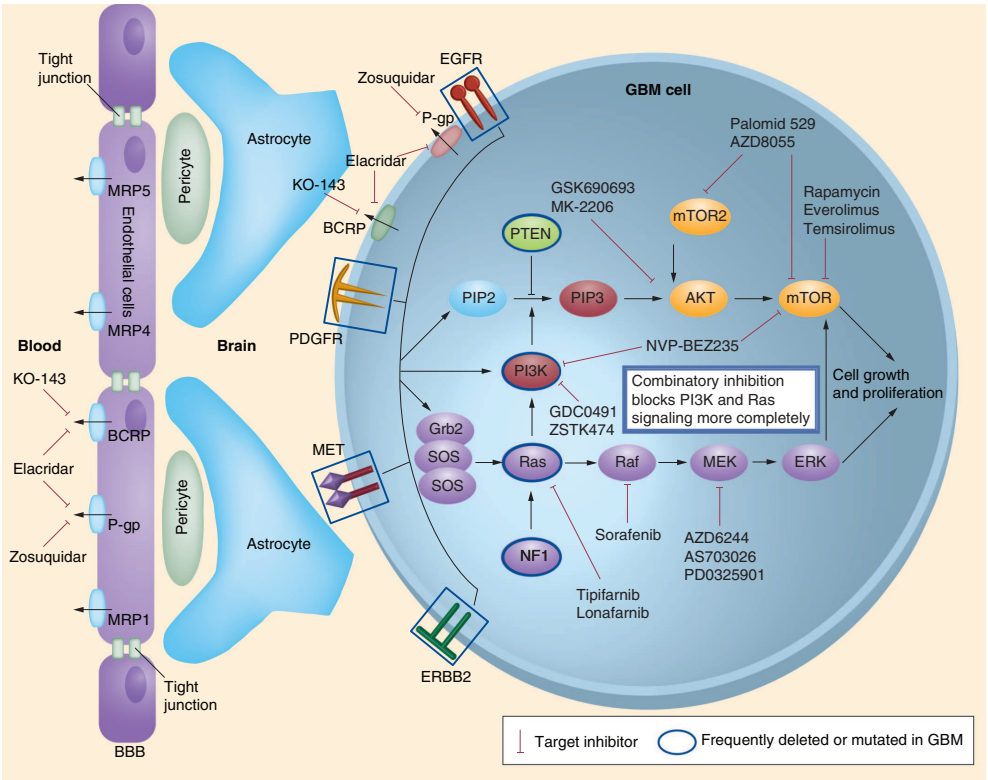

Figure 4 | Core pathways involved in glioblastoma multiforme. RTK–PI3K–AKT–mTOR and RTK–RAS-RAF–MEK–ERK signaling pathways and putative inhibitors. BBB, blood–brain barrier; EGFR, EGF receptor; GBM, glioblastoma multiforme; PDGFR, PDGF receptor.

AKT is a serine/threonine protein kinase which can be activated by phosphorylation at the Threonine-308 (T308) by PDK1, or Serine-473 (S473) by mTORC2 (mammalian target of rapamycin complex 2). The mechanism by which the latter phosphorylation occurs is not fully understood but recent work suggested that activation of mTORC2 kinase activity is induced

by EGFRvIII in GBM cells and that abnormal mTORC2 signaling can promote GBM growth and survival[70]. When phosphorylated, AKT in turn phosphorylates a variety of downstream effector proteins, of which mTORC1 (mammalian target of rapamycin complex 1) is one of the most important ones. There are very few trials with AKT inhibitors in GBM. The planned clinical trial with MK-2206 has been canceled by Merck due to a reprioritization within their oncology program (see ClinicalTrials.gov Identifier NCT01249105).

mTORC1 and mTORC2 inhibitors

mTORC1 is regarded as a central regulator of cell growth and has a critical role in tumor development. Via two major downstream targets S6K (p70 S6 kinases) and 4EBP1 (4E-binding protein), mTORC1 triggers protein synthesis, which is essential for cell survival, growth and proliferation[71-73]. Mutations of the *MTOR* gene are rare in GBM, but frequently deregulated upstream signaling drives mTORC1 activation. Inhibition of mTORC1 by rapamycin or other rapalogs have shown efficacy in a subset of cancers[74,75]. However, rapamycin and other rapalogs only inhibit mTORC1 and not mTORC2[76]. This can lead to an activation of AKT via an mTORC2 driven positive feedback loop[74,77,78]. The novel generation of mTOR inhibitors are multi-targeting agents, which are capable of inhibiting dual targets in the PI3K pathway or even more targets, to more completely block the feedback loop activation caused by inhibition of mTORC1. Dual mTORC1 and mTORC2 inhibitors that disrupt the downstream signaling of mTORC1 and at the same time inhibit the AKT activation by blocking the mTORC2 activity, thus are interesting candidates for evaluation of treatment efficacy in GBM. AZD8055, a dual mTORC1 and mTORC2 inhibitor, is a highly potent, ATP-competitive, and specific mTOR kinase inhibitor. *In vivo*, AZD8055 showed potent single-agent antitumor activity against a range of subcutaneous xenografts including U87 malignant glioma[79]. AZD8055 is currently evaluated in clinical trial in adults with recurrent glioma (NCT01316809). Thus far no data has been presented in orthotopic brain tumor models, or whether AZD8055 is able to cross the BBB. Like AZD8055, Palomid 529 is another dual mTORC1/mTOR2 inhibitor that markedly reduces the phosphorylation of AKT ($pAKT^{S473}$) signaling by inhibition of both mTORC1 and mTORC2 activity. *In vivo* studies showed that Palomid 529 reduced angiogenesis, vascular permeability and tumor growth[80]. Moreover, Palomid 529 was shown to enhance the anti-proliferative effect of radiotherapy in GBM in an orthotopic model[81] as well as in prostate tumor models[82]. Another way to interrupt the mTORC2–PI3K positive feedback loop is by combined inhibition of mTORC1 and PI3K. Particularly, the imidazo[4,5-c] quinoline derivative NVP-BEZ235 selectively inhibits both PI3K and mTOR kinase activity by binding the ATP-binding cleft of these enzymes, thus resulting into G1 arrest and autophagy in tumor cells. It displayed remarkable anti-tumor activity in U87MG GBM xenograft models with a dose dependent effect, and could further enhance the efficacy of temozolomide[83]. Further studies using U87 intracranial xenograft models again confirmed the anti-tumor potency of NVP-BEZ235 in treatment of GBM[84]. NVP-BEZ235 is not tested clinically against glioma, most likely because the

company (Novartis) has prioritized NVP-BKM120 for development in glioma. BKM120 is a pan-class 1 PI3K inhibitor but has no inhibitory activity against mTOR[85]. This compound is assumed to penetrate the BBB[86].

TARGETING THE RAS–RAF–MEK–ERK PATHWAY

The RAS–RAF–MEK–ERK (MAPK, mitogen-activated protein kinase) pathway is activated in the majority of GBMs via various ways, such as *EGFR* mutation or amplification (45%) or *PDGFR* amplification (13%) and deletion of *NF1* (18%)[27] (**Figure 1 and Figure 4**). Upon activation, the growth factor receptors generate binding sites for adaptor proteins like GRB2 (growth factor receptor-bound protein 2) containing an SH2 domain. Next, GRB2 recruits SOS (son of sevenless) to the membrane, which in turn activate RAS through the replacement of inactive GDP (guanosine diphosphate) with active GTP (guanosine triphosphate). As a result, RAS is able to recruit RAF kinases (A-RAF, B-RAF, C-RAF) to the plasma membrane, where they are activated. RAF is able to phosphorylate and thereby activate MEK1 and MEK2 (mitogen-activated protein kinase kinase 1 and 2), which in turn activate ERK1 and ERK2 (extracellular-signal-regulated kinase 1 and 2). Activation of ERK leads to activation of a variety of nuclear and cytoplasmic substrates associated with gene regulation, cell cycle progression, differentiation and cell division[27,87,88]. Due to the important role in cell proliferation and survival, the MAPK pathway is frequently altered in a variety of tumors. *KRAS*, one of the three *RAS* genes, is often mutated in leukemia, colon cancer, pancreatic cancer and lung cancer. Although human GBMs rarely show *RAS* mutations (2%), almost all malignant human gliomas show elevated levels of activated RAS as a result of other upstream molecular alterations.

MEK inhibitors

Inhibition of MEK is an effective strategy to prevent the subsequent downstream signaling of the RAS pathway, and consequently induces tumor regression and/or stasis. A recent study by See *et al.* demonstrated that PD0325901 and AZD6244 as a single agent, suppressed the growth of *NF1*-deficient and MEK inhibitor-sensitive glioma cells both *in vitro* and *in vivo*[89]. Their findings indicate that a subset of *NF1*-deficient GBMs may be responsive to MEK inhibitors. Moreover, they found that *NF1*-deficient glioma cells that are intrinsically resistant to MEK inhibition were sensitized by the addition of the dual PI3K/mTOR inhibitor PI-103. Many commonly used MEK inhibitors are benzohydroxamate derivatives sharing many similarities in chemical structure. These inhibitors result in MEK-specific inhibition by binding to the hydrophobic pocket, adjacent to the ATP binding site of the MEK protein which keeps the kinase in a catalytically inactive state. This allosteric mechanism contributes to a high selectivity for MEK without affecting other protein kinases that have structurally similar ATP binding pockets. Therefore, MEK inhibitors are usually highly specific and non-ATP-competitive inhibitors. PD-0325901 was the first clinically

tested MEK inhibitor. *In vivo* results demonstrated that PD-0325901 potently inhibits growth of human tumor xenografts bearing activating mutations of *BRAF*, concomitant with suppression of ERK1/2 phosphorylation[90]. Interestingly, during the phase I and II clinical trials in advanced cancers anti-tumor activity was seen between 4 to 30 mg bidaily dosing[91,92]. However, besides the more common side effects like rash, diarrhea and fatigue, the drug also caused ocular and central nervous system (CNS) toxicities at doses above 15 mg and Pfizer has suspended its further evaluation. Notably, a similar ocular toxicity has been observed with the MEK1 inhibitor AZD6244 (Selumetinib), albeit to a lesser extent than PD-0325901. Whether these CNS toxicities are a direct consequence of MEK inhibition in the brain or caused by off-target drug effects is still unclear; both are possible regarding the structural similarities of the MEK inhibitors tested so far. Clearly, these CNS toxicities suggest that MEK inhibitors like PD-0325901 are able to enter the CNS, which would qualify these as candidates for testing in GBM. However, MEK inhibitors are predominantly evaluated against non-CNS tumors and the selection of novel candidates is narrowed to those having a low BBB permeability, to avoid CNS toxicities. It should be noted that this strategy holds the risk that a complete class of targeted agents may become useless for treating GBM. The central role of an activated RAS pathway in GBM argues in favor of using MEK inhibitors, although it is obvious that finding the optimal dose level will be a challenging task.

THE RB PATHWAY AND CDK INHIBITON

Deregulation of the G1/S checkpoint is very common in GBM. Cyclin-dependent kinases (CDKs) are serine/threonine protein kinases, whose activity depends on binding and activation by cyclin partners and they are required for cell cycle progression. CDK4 and CDK6, which are both under control of $p16^{INK4A}$ and $p15^{INK4A}$, bind to cyclin D, phosphorylate the retinoblastoma protein (RB), causing subsequent release of the transcription factor E2F and synthesis of proteins that are needed in S phase. The most common alteration of the RB pathway in GBM (52% of cases) is a homozygous deletion of parts of the *CDKN2* locus that codes for $P16^{INK4A}$ and $P15^{INK4B}$. Other alterations include amplification and overexpression of *CDK4* (15–20%) and homozygous deletion/mutation of the *RB1* gene (≈10%) (**Figure 1 and Figure 5**). Deletion of *CDKN2A* (or amplification of *CDK4*), *CDKN2B* and *CDKN2C* leads to loss of cell cycle control and increased cell proliferation. Co-deletion of *CDKN2A* and *CDKN2C* serves as a strong predictor of sensitivity to a selective inhibitor of CDK4/6[93]. Amplification of *CDK6* and individual D-type cyclins, and homozygous deletion of *CDKN2C* encoding $P18^{INK4C}$ are less common[27].

THE CDK inhibitor PD-0332991

CDK4 is a logical target, taking into consideration that loss of *CDKN2A/B* or amplification of *CDK4* is a frequent event in GBM. PD0332991 is an orally bio-available CDK inhibitor, which selectively inhibits cyclin-dependent kinases CDK4 and CDK6. Antiproliferative activity has

been demonstrated in luminal breast cancer, myeloma and GBM cell lines[94,95]. As expected, *RB1*-deficient tumors were resistant to PD0332991. Michaud *et al.*[94] demonstrated that PD-0332991 was effective in suppressing the growth of intracranial U87MG tumors, including those that recurred after initial therapy with temozolomide. The combination of PD0332991 and radiation therapy resulted in a significantly increased survival compared with either therapy alone. Based on these results, it was argued that this compound can efficiently cross the blood–brain barrier[94]. It should be noted, however, that the BBB in U87MG tumors is very leaky[96].

Two completed phase I trials showed that PD0332991 is generally well tolerated and neutropenia was the sole significant toxicity at maximum tolerated dose (125 mg once daily)[97,98]. A phase II clinical study to test PD0332991 in patients with recurrent RB positive GBM is currently ongoing (NCT01227434).

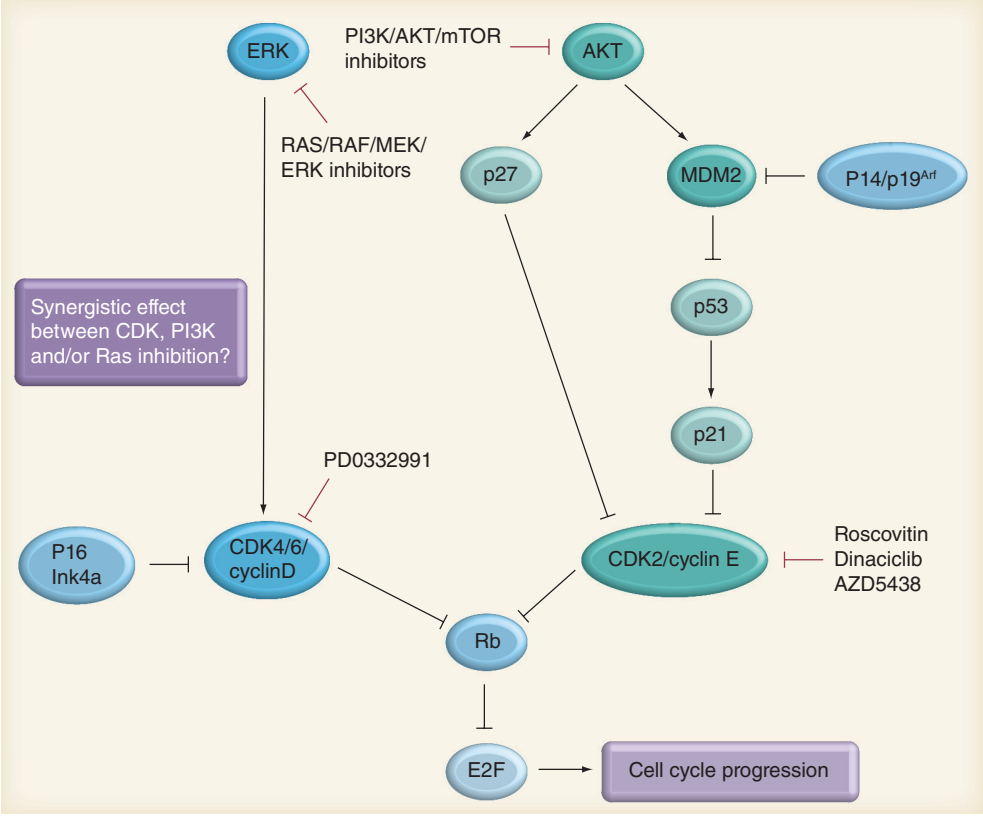

Figure 5 | Core pathways involved in glioblastoma multiforme. The RB pathway and a listing of some example drugs that have been developed to inhibit these pathways.

FUTURE STRATEGIES FOR TARGETED THERAPY

Combined inhibition of multiple pathways

As outlined above, at least three core signaling pathways (RAS–RAF–MEK–ERK, PI3K–AKT–mTOR and CDKN2–CDK4/6–RB) are jointly activated in the majority of GBM's through different mechanisms and targeting just one of these components may be insufficient to achieve a meaningful effect on tumor progression. In addition, crosstalk between different molecules of two or more pathways increases the plasticity of tumor survival signaling and reduces the oncogene addiction[56].

As depicted in **Figure 3**, inhibition of EGFR will not be able to suppress the activation of PI3K and RAS pathways in case other oncogenic alterations in parallel (*e.g.*, other RTKs) and/or downstream components (*e.g.*, PI3K activation) have occurred. Similarly, as shown by the examples of mTOR inhibitors, treatment with an inhibitor of a single pathway may also not sufficiently block parallel signaling pathways to reach a significant anti-proliferative effect. For example, Di Nicolatonio *et al.* have shown that a number of human cancer cell lines carrying alterations in the PI3K pathway responded to everolimus, but only when there was no concomitant *KRAS* mutation[99].

Although several studies with PI3K and RAS inhibitors, given as a single agent, have shown promising tumor growth inhibitory potencies by *in vitro* or *in vivo* models using established GBM cell lines such as U87MG, it should be taken into account that these GBM cells have been cultured for many generations. When grown *in vivo*, they form homogenous non-invasive lesions with a relative stable genome, unlike the highly heterogeneous GBMs that are typically found in patients. This discrepancy may be a plausible explanation for their poor predictive value on the usefulness of these agents against GBM in the clinic.

The considerations above argue in favor of targeting multiple pathways simultaneously, by analogy with the poly-pharmacy that is commonly applied in anti-retroviral therapy. Ideally, this would include targeting all three core signaling pathways simultaneously. Although it will be a challenging to design combination therapies that result in sufficient inhibition of these three core pathways simultaneously with acceptable toxicities, this concept would have the intrinsic potential to be beneficial for a substantial fraction of GBM patients. To date, just a few studies on combinations of targeted agents have been reported. Clinical trials combining EGFR inhibitors and mTOR inhibitors[100,101] reported considerable toxicities and the potential of drug–drug interactions, highlighting some of the issues that may be encountered. However, whereas cytotoxic drugs in oncology are traditionally dosed at the maximum tolerated dose level (MTD), this "more = better" strategy is most likely suboptimal for targeted agents. Taking into consideration the basic principles of pharmacokinetic-pharmacodynamic relationships, the optimal dose should

be determined by verifying target inhibition, since higher dose levels may not contribute to improved efficacy, but may increase toxicities due to off-target effects. Implementing methods to verify target inhibition in tumor tissue will be crucial to the further development of combination therapy with targeted agents, not just in glioma but in all cancers.

Targeted therapy combined with drug efflux transporters inhibitors

The important roles of ABCB1 and ABCG2 in drug resistance and in limiting the brain penetration of therapeutic drugs are well established. However, surprisingly little attention has been paid to this fact when designing clinical trials with targeted agents in GBM. Erlotinib, lapatinib and most other newly developed kinase inhibitors are substrates of ABCB1 and/or ABCG2 and as a consequence, their usefulness in treatment of GBM growth might be compromised by an inadequate brain penetration. The reality is that most targeted agents are in first place developed for treatment of major tumor types like lung and breast cancer, where good BBB penetration is irrelevant or considered undesirable (*e.g.*, MEK inhibitors). Consequently, however, agents from this panel that are being considered for further evaluation in GBM may not be the best BBB permeable drugs.

Elacridar (GF120918) and tariquidar are both dual ABCB1 and ABCG2 inhibitors that have been developed in the 1990s to improve the treatment of ABCB1-mediated multidrug-resistant tumors. Due to the lack of success in this area, this concept is not receiving much attention nowadays. These same agents, however, have the potential to enhance the brain penetration of targeted therapies by blocking the efflux of drugs by these two transporters at the BBB, and perhaps also at the blood–brain tumor barrier. Co-administration of elacridar with a number of anti-cancer drugs have been proven to be an effective strategy to enhance the brain accumulation of these drugs including a range of potentially effective targeted therapeutics[49-52, 102-109]. Therefore, the use of elacridar might represent a feasible strategy to improve the brain entry of potentially effective targeted therapeutics for GBM.

CONCLUSIONS AND FUTURE PERSPECTIVES

The TCGA project and other collaborative research efforts have revealed how the oncogenetic processes of GBM are driven by multiple deregulated core signaling pathways and will provide new avenues for more effective targeted therapies in the treatment of GBM. Because the crosstalk between these molecular pathways fuels the plasticity of these processes, targeting a single, prevalent target that promotes and dominates GBM proliferation will—at best—provide only very short-lived effects. Consequently, the next generation of targeted therapies should focus on multi-targeting agents or combinations of single-targeting agents against these core pathways.

Importantly, when selecting the most appropriate candidates of targeted therapeutics, the brain penetration of such candidates and in particular their interactions with the drug efflux transporters ABCB1 and ABCG2 should be taken into consideration. No matter how potent an agent is in inhibiting or activating its target, it has to reach that target at a therapeutic level, which is more difficult to achieve in the brain than in other tissues. Ideally, substances should be designed to have a low affinity for drug efflux transporters. Alternatively, co-adminstration of targeted agents together with inhibitors of these drug efflux transporters (*e.g.*, elacridar) may be helpful and should also be considered.

The progress that has been made in the treatment of GBM during the last decades has been very modest. Therapies that are based on targeting core signaling pathways underlying the processes of malignant transformation is an emerging therapeutic strategy that hold great potential and receives a lot of attention. However, if we continue testing such agents against GBM one-by-one and without considering whether the candidate drugs are able to cross the BBB sufficiently, it is likely that again little progress will have been made in 5–10 years from now.

REFERENCES

1. Furnari, F.B., *et al.* Malignant astrocytic glioma: genetics, biology, and paths to treatment. *Genes Dev* **21**, 2683-2710 (2007).
2. Louis, D.N,, *et al.* WHO Classification of Tumours of the Central Nervous System. IARC (2007)
3. Stupp, R., *et al.* Radiotherapy plus concomitant and adjuvant temozolomide for glioblastoma. *N Engl J Med* **352**, 987-996 (2005).
4. O'Brien, S.G., *et al.* Imatinib compared with interferon and low-dose cytarabine for newly diagnosed chronic-phase chronic myeloid leukemia. *N Engl J Med* **348**, 994-1004 (2003).
5. Sosman, J.A., *et al.* Survival in BRAF V600-mutant advanced melanoma treated with vemurafenib. *N Engl J Med* **366**, 707-714 (2012).
6. Prados, M.D., *et al.* Phase 1 study of erlotinib HCl alone and combined with temozolomide in patients with stable or recurrent malignant glioma. *Neuro Oncol* **8**, 67-78 (2006).
7. Krishnan, S., *et al.* Phase I trial of erlotinib with radiation therapy in patients with glioblastoma multiforme: results of North Central Cancer Treatment Group protocol N0177. *Int J Radiat Oncol Biol Phys* **65**, 1192-1199 (2006).
8. Prados, M.D., *et al.* Phase II study of erlotinib plus temozolomide during and after radiation therapy in patients with newly diagnosed glioblastoma multiforme or gliosarcoma. *J Clin Oncol* **27**, 579-584 (2009).
9. Brown, P.D., *et al.* Phase I/II trial of erlotinib and temozolomide with radiation therapy in the treatment of newly diagnosed glioblastoma multiforme: North Central Cancer Treatment Group Study N0177. *J Clin Oncol* **26**, 5603-5609 (2008).
10. van den Bent, M.J., *et al.* Randomized phase II trial of erlotinib versus temozolomide or carmustine in recurrent glioblastoma: EORTC brain tumor group study 26034. *J Clin Oncol* **27**, 1268-1274 (2009).
11. Peereboom, D.M., *et al.* Phase II trial of erlotinib with temozolomide and radiation in patients with newly diagnosed glioblastoma multiforme. *J Neurooncol* **98**, 93-99 (2010).
12. Brandes, A.A., Epidermal growth factor receptor inhibitors in neuro-oncology: hopes and disappointments. *Clin Cancer Res* **14**, 957-960 (2008).
13. Franceschi, E., *et al.* Gefitinib in patients with progressive high-grade gliomas: a multicentre phase II study by Gruppo Italiano Cooperativo di Neuro-Oncologia (GICNO). *Br J Cancer* **96**, 1047-1051 (2007).
14. Rich, J.N., *et al.* Phase II trial of gefitinib in recurrent glioblastoma. *J Clin Oncol* **22**, 133-142 (2004).
15. Chang, S.M., *et al.* Phase II study of CCI-779 in patients with recurrent glioblastoma multiforme. *Invest New Drugs* **23**, 357-361 (2005).
16. Galanis, E., *et al.* Phase II trial of temsirolimus (CCI-779) in recurrent glioblastoma multiforme: a North Central Cancer Treatment Group Study. *J Clin Oncol* **23**, 5294-5304 (2005).
17. Chang, S.M., *et al.* Phase I/pharmacokinetic study of CCI-779 in patients with recurrent malignant glioma on enzyme-inducing antiepileptic drugs. *Invest New Drugs* **22**, 427-435 (2004).
18. Mason, W.P., *et al.* A phase I study of temozolomide and everolimus (RAD001) in patients with newly diagnosed and progressive glioblastoma either receiving or not receiving enzyme-inducing anticonvulsants: an NCIC CTG study. *Invest New Drugs* **30**, 2344-2351 (2012).
19. Sarkaria, J.N., *et al.* North Central Cancer Treatment Group Phase I trial N057K of everolimus (RAD001) and temozolomide in combination with radiation therapy in patients with newly diagnosed glioblastoma multiforme. *Int J Radiat Oncol Biol Phys* **81**, 468-475 (2011).
20. Hainsworth, J.D., *et al.* Phase II study of concurrent radiation therapy, temozolomide, and bevacizumab followed by bevacizumab/everolimus as first-line treatment for patients with glioblastoma. *Clin Adv Hematol Oncol* **10**,

240-246 (2012).
21. Reardon, D.A., *et al.* Phase 2 trial of erlotinib plus sirolimus in adults with recurrent glioblastoma. *J Neurooncol* **96**, 219-230 (2010).
22. Cloughesy, T.F., *et al.* Antitumor activity of rapamycin in a Phase I trial for patients with recurrent PTEN-deficient glioblastoma. *PLoS Med* **5**, e8 (2008).
23. Ohgaki, H., *et al.* Genetic pathways to glioblastoma: a population-based study. *Cancer Res* **64**, 6892-6899 (2004).
24. Parsons, D.W., *et al.* An integrated genomic analysis of human glioblastoma multiforme. *Science* **321**, 1807-1812 (2008).
25. Lang, F.F., Pathways leading to glioblastoma multiforme: a molecular analysis of genetic alterations in 65 astrocytic tumors. *J Neurosurg* **81**, 427-436 (1994).
26. von Deimling, A., Subsets of glioblastoma multiforme defined by molecular genetic analysis. *Brain Pathol* **3**, 19-26 (1993).
27. The Cancer Genome Atlas Research Network, Comprehensive genomic characterization defines human glioblastoma genes and core pathways. *Nature* **455**, 1061-1068 (2008).
28. Verhaak R.G., *et al.* Integrated genomic analysis identifies clinically relevant subtypes of glioblastoma characterized by abnormalities in PDGFRA, IDH1, EGFR, and NF1. *Cancer Cell* **17**, 98-110 (2010).
29. Agarwal, S., *et al.* Delivery of molecularly targeted therapy to malignant glioma, a disease of the whole brain. *Expert Rev Mol Med* **13**, e17 (2011).
30. Muldoon, L.L., *et al.* Chemotherapy delivery issues in central nervous system malignancy: a reality check. *J Clin Oncol* **25**, 2295-2305 (2007).
31. de Vries, N.A., *et al.* Blood-brain barrier and chemotherapeutic treatment of brain tumors. *Expert Rev Neurother* **6**, 1199-1209 (2006).
32. Urquhart, B.L. & Kim, R.B. Blood-brain barrier transporters and response to CNS-active drugs. *Eur J Clin Pharmacol* **65**, 1063-1070 (2009).
33. Deeken, J.F. & Loscher, W. The blood-brain barrier and cancer: transporters, treatment, and trojan horses. *Clin Cancer Res* **13**, 1663-1674 (2007).
34. Juliano, R.L. & Ling, V. A surface glycoprotein modulating drug permeability in Chinese hamster ovary cell mutants. *Biochim Biophys Acta* 455(1), 152-162 (1976).
35. Leslie, E.M., *et al.* Multidrug resistance proteins: role of P-glycoprotein, MRP1, MRP2, and BCRP (ABCG2) in tissue defense. *Toxicol Appl Pharmacol* **204**, 216-237 (2005).
36. Dietrich, C.G., *et al.* ABC of oral bioavailability: transporters as gatekeepers in the gut. *Gut* **52**, 1788-1795 (2003).
37. Szakacs, G., *et al.* The role of ABC transporters in drug absorption, distribution, metabolism, excretion and toxicity (ADME-Tox). *Drug Discov Today* **13**, 379-393 (2008).
38. Ayrton, A. & Morgan, P. Role of transport proteins in drug absorption, distribution and excretion. *Xenobiotica* **31**, 469-497 (2001).
39. Schinkel, A.H. & Jonker, J.W. Mammalian drug efflux transporters of the ATP binding cassette (ABC) family: an overview. *Adv Drug Deliv Rev* **55**, 3-29 (2003).
40. Enokizono, J., *et al.* Quantitative investigation of the role of breast cancer resistance protein (Bcrp/Abcg2) in limiting brain and testis penetration of xenobiotic compounds. *Drug Metab Dispos* **36**, 995-1002 (2008).
41. Schinkel, A.H., *et al.* Disruption of the mouse mdr1a P-glycoprotein gene leads to a deficiency in the blood-brain barrier and to increased sensitivity to drugs. *Cell* **77**, 491-502 (1994).
42. Lagas, J.S., *et al.* Breast cancer resistance protein and P-glycoprotein limit sorafenib brain accumulation. *Mol Cancer Ther* **9**, 319-326 (2010).
43. Aldape, K.D., *et al.* Immunohistochemical detection of EGFRvIII in high malignancy grade astrocytomas and evaluation of prognostic significance. *J Neuropathol Exp Neurol* **63**, 700-707 (2004).
44. Frederick, L., *et al.* Diversity and frequency of epidermal growth factor receptor mutations in human glioblastomas. *Cancer Res* **60**, 1383-1387 (2000).
45. Wong, A.J., *et al.* Structural alterations of the epidermal growth factor receptor gene in human gliomas. *Proc Natl Acad Sci U S A* **89**, 2965-2969 (1992).
46. Shinojima, N., *et al.* Prognostic value of epidermal growth factor receptor in patients with glioblastoma multiforme. *Cancer Res* **63**, 6962-6970 (2003).
47. Kodaira, H., *et al.* Kinetic analysis of the cooperation of P-glycoprotein (P-gp/Abcb1) and breast cancer resistance protein (Bcrp/Abcg2) in limiting the brain and testis penetration of erlotinib, flavopiridol, and mitoxantrone. *J Pharmacol Exp Ther* **333**, 788-796 (2010).
48. de Vries, N.A., *et al.* Restricted brain penetration of the tyrosine kinase inhibitor erlotinib due to the drug transporters P-gp and BCRP. *Invest New Drugs* **30**, 443-449 (2012).
49. Agarwal, S., *et al.* Distribution of gefitinib to the brain is limited by P-glycoprotein (ABCB1) and breast cancer resistance protein (ABCG2)-mediated active efflux. *J Pharmacol Exp Ther* **334**, 147-155 (2010).
50. Tang, S.C., *et al.* Brain accumulation of sunitinib is restricted by P-glycoprotein (ABCB1) and breast cancer resistance protein (ABCG2) and can be enhanced by oral elacridar and sunitinib coadministration. *Int J Cancer* **130**, 223-233 (2012).
51. Chen, Y., *et al.* P-glycoprotein and breast cancer resistance protein influence brain distribution of dasatinib. *J Pharmacol Exp Ther* **330**, 956-963 (2009).
52. Lagas, J.S., *et al.* Brain accumulation of dasatinib is restricted by P-glycoprotein (ABCB1) and breast cancer resistance protein (ABCG2) and can be enhanced by elacridar treatment. *Clin Cancer Res* **15**, 2344-2351 (2009).
53. Zhou, L., *et al.* The effect of breast cancer resistance protein and P-glycoprotein on the brain penetration of flavopiridol, imatinib mesylate (Gleevec), prazosin, and 2-methoxy-3-(4-(2-(5-methyl-2-phenyloxazol-4-yl) ethoxy)phenyl)propanoic acid (PF-407288) in mice. *Drug Metab Dispos* **37**, 946-955 (2009).
54. Polli, J.W., *et al.* An unexpected synergist role of P-glycoprotein and breast cancer resistance protein on the central nervous system penetration of the tyrosine kinase inhibitor lapatinib (N-{3-chloro-4-[(3-fluorobenzyl)oxy] phenyl}-6-[5-({[2-(methylsulfonyl)ethyl]amino }methyl)-2-furyl]-4-quinazolinamine; GW572016). *Drug Metab Dispos* **37**, 439-442 (2009).
55. Mellinghoff, I.K., *et al.* Molecular determinants of the response of glioblastomas to EGFR kinase inhibitors. *N Engl J Med* **353**, 2012-2024 (2005).
56. Mendoza, M.C., *et al.* The Ras-ERK and PI3K-mTOR pathways: cross-talk and compensation. *Trends Biochem Sci* **36**, 320-328 (2011).
57. To, M.D., *et al.* Crosstalk between Pten and Ras signaling pathways in tumor development. *Cell Cycle* **4**, 1185-1188 (2005).

58. Jeuken, J., *et al.* RAS/RAF pathway activation in gliomas: the result of copy number gains rather than activating mutations. *Acta Neuropathol* **114**, 121-133 (2007).
59. Stommel, J.M., *et al.* Coactivation of receptor tyrosine kinases affects the response of tumor cells to targeted therapies. *Science* **318**, 287-290 (2007).
60. Vivanco, I., *et al.* Differential sensitivity of glioma- versus lung cancer-specific EGFR mutations to EGFR kinase inhibitors. *Cancer Discov* **2**, 458-471 (2012).
61. Cheng, C.K., *et al.* PI3K signaling in glioma—animal models and therapeutic challenges. *Brain Pathol* **19**, 112-120 (2009).
62. Vivanco, I. & Sawyers, C.L. The phosphatidylinositol 3-Kinase AKT pathway in human cancer. *Nat Rev Cancer* **2**, 489-501 (2002).
63. Courtney, K.D., *et al.* The PI3K pathway as drug target in human cancer. *J Clin Oncol* **28**, 1075-1083 (2010).
64. Bader, A.G., *et al.* Oncogenic PI3K deregulates transcription and translation. *Nat Rev Cancer* **5**, 921-929 (2005).
65. Yap, T.A., *et al.* Targeting the PI3K-AKT-mTOR pathway: progress, pitfalls, and promises. *Curr Opin Pharmacol* **8**, 393-412 (2008).
66. Carnero, A., *et al.* The PTEN/PI3K/AKT signalling pathway in cancer, therapeutic implications. *Curr Cancer Drug Targets* **8**, 187-198 (2008).
67. Folkes, A.J., *et al.* The identification of 2-(1H-indazol-4-yl)-6-(4-methanesulfonyl-piperazin-1-ylmethyl)-4-morpholin-4-yl-t hieno[3,2-d]pyrimidine (GDC-0941) as a potent, selective, orally bioavailable inhibitor of class I PI3 kinase for the treatment of cancer. *J Med Chem* **51**, 5522-5532 (2008).
68. Raynaud, F.I., *et al.* Biological properties of potent inhibitors of class I phosphatidylinositide 3-kinases: from PI-103 through PI-540, PI-620 to the oral agent GDC-0941. *Mol Cancer Ther* **8**, 1725-1738 (2009).
69. Salphati, L., *et al.* Role of P-glycoprotein and breast cancer resistance protein-1 in the brain penetration and brain pharmacodynamic activity of the novel phosphatidylinositol 3-kinase inhibitor GDC-0941. *Drug Metab Dispos* **38**, 1422-1426 (2010).
70. Tanaka, K., *et al.* Oncogenic EGFR signaling activates an mTORC2-NF-kappaB pathway that promotes chemotherapy resistance. *Cancer Discov* **1**, 524-538 (2011).
71. Shor, B., *et al.* Targeting mTOR globally in cancer: thinking beyond rapamycin. *Cell Cycle* **8**, 3831-3837 (2009).
72. Samuels, Y., *et al.* High frequency of mutations of the PIK3CA gene in human cancers. *Science* **304**, 554- (2004).
73. Petroulakis, E., *et al.* mTOR signaling: implications for cancer and anticancer therapy. *Br J Cancer* **94**, 195-199 (2006).
74. Abraham, R.T. & Gibbons, J.J. The mammalian target of rapamycin signaling pathway: twists and turns in the road to cancer therapy. *Clin Cancer Res* **13**, 3109-3114 (2007).
75. Easton, J.B. & Houghton, P.J. mTOR and cancer therapy. *Oncogene* **25**, 6436-6446 (2006).
76. Sarbassov, D.D., *et al.* Phosphorylation and regulation of Akt/PKB by the rictor-mTOR complex. *Science* **307**, 1098-1101 (2005).
77. Phung, T.L., *et al.* Endothelial Akt signaling is rate-limiting for rapamycin inhibition of mouse mammary tumor progression. *Cancer Res* **67**, 5070-5075 (2007).
78. O'Reilly, K.E., *et al.* mTOR inhibition induces upstream receptor tyrosine kinase signaling and activates Akt. *Cancer Res* **66**, 1500-1508 (2006).
79. Chresta, C.M., *et al.* AZD8055 is a potent, selective, and orally bioavailable ATP-competitive mammalian target of rapamycin kinase inhibitor with in vitro and in vivo antitumor activity. *Cancer Res* **70**, 288-298 (2010).
80. Xue, Q., *et al.* Palomid 529, a novel small-molecule drug, is a TORC1/TORC2 inhibitor that reduces tumor growth, tumor angiogenesis, and vascular permeability. *Cancer Res* **68**, 9551-9557 (2008).
81. Cerna, D., *et al.* Palomid 529, a PI3K/Akt/mTOR dual TORC1/2 inhibitor, is a radiosensitizer with effect in both subcutaneous and orthotopic U251 glioblastoma tumor xenograft models. *Cancer Res* **70 Suppl 8**, 2506 (2010)
82. Diaz, R., *et al.* The novel Akt inhibitor Palomid 529 (P529) enhances the effect of radiotherapy in prostate cancer. *Br J Cancer* **100**, 932-940 (2009).
83. Maira, S.M., *et al.* Identification and characterization of NVP-BEZ235, a new orally available dual phosphatidylinositol 3-kinase/mammalian target of rapamycin inhibitor with potent in vivo antitumor activity. *Mol Cancer Ther* **7**, 1851-1863 (2008).
84. Liu, T.J., *et al.* NVP-BEZ235, a novel dual phosphatidylinositol 3-kinase/mammalian target of rapamycin inhibitor, elicits multifaceted antitumor activities in human gliomas. *Mol Cancer Ther* **8**, 2204-2210 (2009).
85. Bendell, J.C., *et al.* Phase I, dose-escalation study of BKM120, an oral pan-Class I PI3K inhibitor, in patients with advanced solid tumors. *J Clin Oncol* **30**, 282-290 (2012).
86. Wen, P.Y., *et al.* Current clinical development of PI3K pathway inhibitors in glioblastoma. *Neuro Oncol* **14**, 819-829 (2012).
87. Rodriguez-Viciana, P., *et al.* Cancer targets in the Ras pathway. *Cold Spring Harb Symp Quant Biol* **70**, 461-467 (2005).
88. Peyssonnaux, C. & Eychene, A. The Raf/MEK/ERK pathway: new concepts of activation. *Biol Cell* **93**, 53-62 (2001).
89. See, W.L., *et al.* Sensitivity of glioblastomas to clinically available MEK inhibitors is defined by Neurofibromin 1 deficiency. *Cancer Res* **72**, 3350-3359 (2012).
90. Solit, D.B., *et al.* BRAF mutation predicts sensitivity to MEK inhibition. *Nature* **439**, 358-362 (2006).
91. Haura, E.B., *et al.* A phase II study of PD-0325901, an oral MEK inhibitor, in previously treated patients with advanced non-small cell lung cancer. *Clin Cancer Res* **16**, 2450-2457 (2010).
92. LoRusso, P.M., *et al.* Phase I pharmacokinetic and pharmacodynamic study of the oral MAPK/ERK kinase inhibitor PD-0325901 in patients with advanced cancers. *Clin Cancer Res* **16**, 1924-1937 (2010).
93. Wiedemeyer, W.R., *et al.* Pattern of retinoblastoma pathway inactivation dictates response to CDK4/6 inhibition in GBM. *Proc Natl Acad Sci U S A* **107**, 11501-11506 (2010).
94. Michaud, K., *et al.* Pharmacologic inhibition of cyclin-dependent kinases 4 and 6 arrests the growth of glioblastoma multiforme intracranial xenografts. *Cancer Res* **70**, 3228-3238 (2010).
95. Konecny, G.E., *et al.* Expression of p16 and retinoblastoma determines response to CDK4/6 inhibition in ovarian cancer. *Clin Cancer Res* **17**, 1591-1602 (2011).
96. Kemper, E.M., *et al.* Development of luciferase tagged brain tumour models in mice for chemotherapy intervention studies. *Eur J Cancer* **42**, 3294-3303 (2006).
97. Schwartz, G.K., *et al.* Phase I study of PD 0332991, a cyclin-dependent kinase inhibitor, administered in 3-week cycles (Schedule 2/1). *Br J Cancer* **104**, 1862-1868 (2011).
98. Flaherty, K.T., *et al.* Phase I, dose-escalation trial of the oral cyclin-dependent kinase 4/6 inhibitor PD 0332991, administered using a 21-day schedule in patients with advanced cancer. *Clin Cancer Res* **18**, 568-576 (2012).

99. Di Nicolantonio, F., *et al.* Deregulation of the PI3K and KRAS signaling pathways in human cancer cells determines their response to everolimus. *J Clin Invest* **120**, 2858-2866 (2010).
100. Nghiemphu, P.L., *et al.* A dose escalation trial for the combination of erlotinib and sirolimus for recurrent malignant gliomas. *J Neurooncol* **110**, 245-250 (2012).
101. Reardon, D.A., *et al.* Pharmacokinetic drug interaction between AEE788 and RAD001 causing thrombocytopenia in patients with glioblastoma. *Cancer Chemother Pharmacol* **69**, 281-287 (2012).
102. de Vries, N.A., *et al.* P-glycoprotein and breast cancer resistance protein: two dominant transporters working together in limiting the brain penetration of topotecan. *Clin Cancer Res* **13**, 6440-6449 (2007).
103. Bihorel, S., *et al.* Modulation of the brain distribution of imatinib and its metabolites in mice by valspodar, zosuquidar and elacridar. *Pharm Res* **24**, 1720-1728 (2007).
104. Sane, R., *et al.* Brain distribution and bioavailability of elacridar after different routes of administration in the mouse. *Drug Metab Dispos* **40**, 1612-1619 (2012).
105. Oostendorp, R.L., *et al.* The effect of P-gp (Mdr1a/1b), BCRP (Bcrp1) and P-gp/BCRP inhibitors on the in vivo absorption, distribution, metabolism and excretion of imatinib. *Invest New Drugs* **27**, 31-40 (2009).
106. Minocha, M., *et al.* Co-administration strategy to enhance brain accumulation of vandetanib by modulating P-glycoprotein (P-gp/Abcb1) and breast cancer resistance protein (Bcrp1/Abcg2) mediated efflux with m-TOR inhibitors. *Int J Pharm* **434**, 306-314 (2012).
107. Lee, Y.J., *et al.* Investigation of efflux transport of dehydroepiandrosterone sulfate and mitoxantrone at the mouse blood-brain barrier: a minor role of breast cancer resistance protein. *J Pharmacol Exp Ther* **312**, 44-52 (2005).
108. Breedveld, P., *et al.* The effect of Bcrp1 (Abcg2) on the in vivo pharmacokinetics and brain penetration of imatinib mesylate (Gleevec): implications for the use of breast cancer resistance protein and P-glycoprotein inhibitors to enable the brain penetration of imatinib in patients. *Cancer Res* **65**, 2577-2582 (2005).
109. Agarwal, S., *et al.* Active efflux of dasatinib from the brain limits efficacy against murine glioblastoma: broad implications for the clinical use of molecularly-targeted agents. *Mol Cancer Ther* **11**, 2183-2192 (2012).
110. Lin, F., *et al.* Dual mTORC1 and mTORC2 inhibitor Palomid 529 penetrates the blood-brain barrier without restriction by ABCB1 and ABCG2. *Int J Cancer* **5**, 1222-1233 (2013).
111. Marchetti, S., *et al.* Effect of the ATP-binding cassette drug transporters ABCB1, ABCG2, and ABCC2 on erlotinib hydrochloride (Tarceva) disposition in in vitro and in vivo pharmacokinetic studies employing Bcrp1-/-/ Mdr1a/1b-/- (triple-knockout) and wild-type mice. *Mol Cancer Ther* **7**, 2280-2287 (2008).
112. Wang, T., *et al.* Brain distribution of cediranib is limited by active efflux at the blood-brain barrier. *J Pharmacol Exp Ther* **341**, 386-395 (2012).
113. Poller, B., *et al.* Differential impact of P-glycoprotein (ABCB1) and breast cancer resistance protein (ABCG2) on axitinib brain accumulation and oral plasma pharmacokinetics. *Drug Metab Dispos* **39**, 729-735 (2011).
114. Durmus, S., *et al.* Oral availability and brain penetration of the B-RAFV600E inhibitor vemurafenib can be enhanced by the P-glycoprotein (ABCB1) and breast cancer resistance protein (ABCG2) inhibitor elacridar. *Mol Pharm* **9**, 3236-3245 (2012).
115. Mittapalli, R.K., *et al.* Impact of P-glycoprotein (ABCB1) and breast cancer resistance protein (ABCG2) on the brain distribution of a novel BRAF inhibitor: vemurafenib (PLX4032). *J Pharmacol Exp Ther* **342**, 33-40 (2012).
116. Mittapalli, R.K., *et al.* Mechanisms limiting distribution of the threonine-protein kinase B-RAFV600E inhibitor dabrafenib to the brain: implications for the treatment of melanoma brain metastases. *J Pharmacol Exp Ther* **344**, 655-664 (2013).
117. Yang, J.J., *et al.* P-glycoprotein and breast cancer resistance protein affect disposition of tandutinib, a tyrosine kinase inhibitor. *Drug Metab Lett* **4**, 201-212 (2010).
118. Peters, A., *et al.* Fine structure of the nervous system: neurons and their supporting cells (3rd Edition). Oxford University Press (1991).
119. Purves, D., *et al*. Neuroscience. Sinauer Associates (2008)

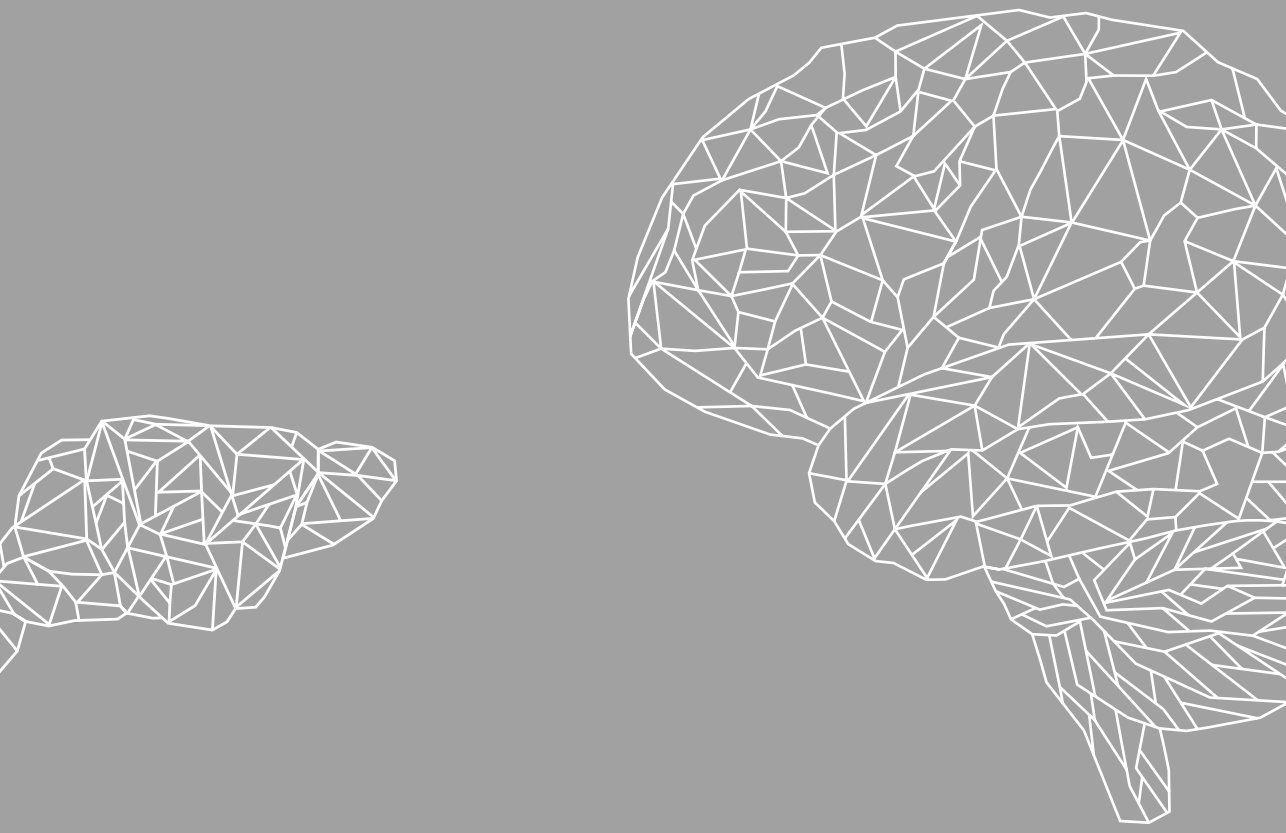

SECTION II

CHEMOTHERAPEUTIC STRATEGIES: INDUCING DNA DAMAGE

Chapter 3

ABC TRANSPORTERS RESTRICT THE BRAIN PENETRATION AND INTACRANIAL EFFICACY OF ANTICANCER AGENTS EVEN WHEN BLOOD-BRAIN BARRIER INTEGRITY IS LOST

M.C. de Gooijer, E.M. Kemper, L.C.M. Buil, T. Buckle, J.H. Beijnen, and O. van Tellingen

Manuscript submitted

ABSTRACT

Background: The impact of the blood–brain barrier (BBB) in brain tumors on the efficacy of anticancer drug therapy is controversial. In primary as well as metastatic brain tumors, the BBB is often disrupted. Yet, many intracranial cancers respond poorly to systemic therapies. ***Methods:*** We characterized the integrity of the BBB in a series of experimental intracranial tumor models using magnetic resonance imaging (MRI), fluorescent dyes and autoradiography. We also assessed the distribution and efficacy of docetaxel in healthy brain tissue and brain tumors that were grafted into P-glycoprotein proficient wild-type (WT) and deficient *Abcb1a/b*$^{-/-}$ recipient nude mice. ***Results:*** Leakiness of the tumor vasculature varied from extensive to almost absent. Tumor blood vessels expressed P-gp and BCRP. The leakiness of the vasculature resulted in higher docetaxel levels in tumors compared to normal brain. However, P-gp expression in tumor vessels reduced the drug distribution in tumors, which also translated into a reduced efficacy. ***Conclusions:*** Leakiness of the BBB does not necessarily imply good accessibility of drugs to brain tumors. Although therapeutic responses may be observed, the full potential of such therapeutics may still be attenuated by drug efflux pumps in the tumor vasculature. Therefore, good BBB penetration of drugs remains an important requirement when used against intracranial tumors.

INTRODUCTION

High-grade gliomas, and in particular glioblastoma (GBM), are the most common primary brain tumors in adults and invariably lethal. The established treatment consists of surgical resection to a maximum safe extent, followed by external beam radiotherapy and temozolomide chemotherapy[1]. Because of the wide-spread infiltration of tumor cells into the surrounding brain structures, complete surgical resection of malignant glioma is impossible. Therefore, the challenge of improving GBM therapy is to design therapies that are able to track and kill those residual tumor cells left within the brain following surgery[2]. So far, however, no systemic chemotherapeutic drugs other than temozolomide have shown significant efficacy in the treatment of malignant glioma, neither as monotherapy nor in combination strategies. A likely contributing factor to the low efficacy of chemotherapy is the presence of the blood–brain barrier (BBB), which limits the brain penetration of many anti-cancer drugs[3]. Improving drug delivery into the brain will therefore be an important first step when considering chemotherapeutic treatment of GBM[4]. The BBB is physically formed by the brain endothelial cells, which lack fenestrations and are closely linked by tight junctions. Besides these passive constraints, active efflux of compounds from the brain by the ATP binding cassette (ABC) transporters P-glycoprotein (P-gp; ABCB1), breast cancer resistance protein (BCRP; ABCG2) and multidrug resistance-associated protein 4 (MRP4; ABCC4) has been well-established[5,6].

GBM is known to disrupt BBB integrity as is visualized by gadolinium contrast-enhanced magnetic resonance imaging (MRI). Penetration of this small molecular contrast agent to the tumor fuels the notion that other small molecule drugs may have similar good access to the tumor. Notably, however, the disruption of the BBB is heterogeneous with the enhancing regions mainly the core of the tumor, where microvascular proliferation results in newly formed leaky blood vessels. In contrast, the BBB is more intact in the peripheral zones and brain adjacent to tumor areas where numerous infiltrating tumor cells reside that are typically left behind following surgery[4]. It is therefore very likely that the BBB remains a hurdle, limiting the entry of therapeutics into substantial areas of GBM tumor tissue in patients[2].

Paclitaxel and docetaxel are efficacious in the treatment of patients with various extracranial malignancies such as ovary, breast, and lung cancer[7], but not against malignant gliomas[8,9]. In general, cell lines derived from malignant glioma are equally sensitive to low nanomolar concentrations of paclitaxel and docetaxel as cell lines of other origin[10,11], showing that malignant glioma cells are not intrinsically resistant. Paclitaxel and docetaxel are effective substrates of the drug efflux pump P-gp, and the brain penetration of docetaxel and paclitaxel in P-gp knockout mice is more than 5- to 10-fold higher than in wild-type (WT) mice[12,13]. We have characterized the BBB in a series of intracranial xenograft tumor models, which encompass various degrees of BBB leakiness. By using recipient nude mice that are proficient or deficient in P-gp in combination with

a P-gp substrate chemotherapeutic drug, we were able to determine the potential impact of drug transporters in leaky and non-leaky tumor areas on drug distribution and efficacy. Importantly, our work shows that ABC transporters in the tumor vasculature are functionally important and protect areas of tumors that are evidently leaky. This result emphasizes the need to use BBB-penetrable drugs when treating intracranial tumors.

METHODS

Cell culture

The melanoma cell line Mel57 and its VEGF-A165 transfected subline Mel57VEGF were kindly provided by dr. W.P. Leenders (Radboud University Medical Center, Nijmegen, The Netherlands) and the GBM8 cell line expressing firefly luciferase and mCherry by dr. B.A. Tannous (Massachusetts General Hospital, Boston, MA). The U87 cell line was obtained from the American Type Culture Collection (ATCC; Manassas, VA). With the exception of the GBM8 glioma stem-like cells, all cell lines were cultured in Minimum Essential Medium, supplemented with 1% L-glutamine, 1% sodium-pyruvate, 1% MEM vitamins, 1% penicillin/streptomycin, 1% non-essential amino acids and 10% fetal calf serum (all from Life Technologies, Carlsbad, CA) and maintained in 5% CO_2 in humidified air at 37°C. GBM8 cells were cultured in 50% Neurobasal medium and 50% DMEM/F12 GlutaMAX supplemented with 2% B-27 without vitamin A (all from Life Technologies) and 10 ng/mL bFGF and EGF (both from PeproTech; London, UK)[14]. All serum-cultured cell lines were stably transfected with firefly luciferase and GFP as described previously[15].

Drugs and compounds

Paclitaxel was purchased from Bristol–Myers Squibb (New York, NY). Docetaxel was obtained from Sanofi (Paris, France), 14C-AIB from Tjaden Biosciences (Burlington, IA) and TexasRed (Sulfurodamine 101) and 3kD-Dextran–FITC both from Life Technologies.

Animals

All mice were bred at the Netherlands Cancer Institute. Male and female nude mice aged between 8 and 15 weeks of wild-type (WT) FVB, *Abcb1a/b*$^{-/-}$ and *Abcb1a/b;Abcg2*$^{-/-}$ background were used. Mice were housed in individually ventilated cages. Animals had access to food and water *ad libitum*. Experiments with animals were carried out according to Institutional guidelines, conform the code of practice for animal research in oncology and in line with Dutch and European legislation. All animal experiments were approved by the local Animal Experiments Committee.

Experimental in vivo tumor models

Adherent cells were harvested by treatment with trypsin/EDTA (0.05%/0.02%) and washed twice with Hanks Balanced Salt Solution (HBSS; Life Technologies). Cells were maintained on ice and used within 6 hours. Neurosphere-cultured cell lines were processed to a near single cell suspension by repeated trituration. Experimental intracranial brain tumors were established by intracranial injection of a 2 µl cell suspension containing $1x10^5$ cells (Mel57–Fluc, U87–Fluc and GBM8–Fluc) or $5x10^3$ cells (Mel57VEGF–Fluc) as described previously[15]. To establish extracranial tumor models, $5x10^5$ Mel57 cells were injected in a volume of 20 µl of HBSS under the renal subcapsule as described previously[16]. A small incision was made in the mouse left flank. The kidney was lifted out of the peritoneum and a 30 g needle was inserted into the lower pole and advanced until its tip reached just under the renal subcapsule. For all extracranial tumor models, tumor size was measured using calipers and volumes were calculated in mm^3 by the formula: $V = 0.5 \times length \times width^2$.

Magnetic resonance imaging

Magnetic resonance imaging was done on a BioSpec 70/20 USR (Bruker; Billerica, MA) system using a sequence consisting of T2-weighted, T1-weighted pre-contrast and T1-weighted post-gadoterate meglumine (Dotarem®; Guerbet; Villepinte, France) contrast imaging, as described previously[17].

Blood–brain barrier permeability analysis

Mice bearing established orthotopic brain tumors were administered 25 µCi of ^{14}C-aminoisobutyrate (AIB) in 100 µl of saline, Texas Red (TxRed; 6 mg/kg) or 3kD-Dextran–FITC (5 mg/kg) and after 30 minutes anesthetized with hypnorm/dormicum and subsequently perfused with saline. The brain was immediately frozen on dry ice in Tissue-Tek® (Sakura Finetek Europe BV; Alphen aan den Rijn, The Netherlands) and kept at -70ºC until sectioning. ^{14}C-AIB extravasation was visualized by autoradiography using a FLA-3000 phospho-imager (Fujifilm; Tokyo, Japan), whereas TxRed and 3kD-Dextran–FITC were analyzed by fluorescence microscopy using a Axiovert 135 system coupled to an Axiocam 512 (both Carl Zeiss; Oberkochen, Germany)

Histology and immunohistochemistry

Tumor-bearing mouse brains were fixed in 4% (v/v) formaldehyde, paraffin embedded and cut into 4 µm coronal sections that were stained with hematoxylin and eosin (H&E), and for P-gp (1:200; 13978; Cell Signaling Technology; Danvers, MA) and BCRP (1:400; ab24115; Abcam; Cambridge, UK). Sections were scanned and processed using an Aperio AT2 system and

ImageScope software v12 (both Leica; Wetzlar, Germany).

Drug concentration measurements

Tumor-bearing mice received 33 mg/kg docetaxel i.v. once. Four hours after administration, animals were sacrificed and the brains were collected and divided into four parts: tumor, right (ipsilateral) hemisphere, left (contralateral) hemisphere and cerebellum. Taxane concentrations in brain and brain tumor tissue samples were analyzed by LC–MS/MS.

***In vivo* efficacy studies**

Paclitaxel was administered i.v. twice at a dose of 20 mg/kg or six times at 10 mg/kg and docetaxel was applied i.v. twice at a dose of 33 mg/kg, as indicated by arrows in each appropriate figure. The drug solutions were prepared with sterile saline to yield final concentrations of 2.0 and 3.3 mg/ml of paclitaxel and docetaxel, respectively and were administered by i.v. bolus injection into the tail vein using 5 or 10 µl per gram body weight.

Bioluminescence images were acquired following i.p. D-luciferin (150 mg/kg; Promega; Madison, WI) using an IVIS Spectrum system with Living Image software v4.5 (both PerkinElmer; Waltham, MA). Animals were stratified into treatment groups (WT, *Abcb1a/b*$^{-/-}$ and *Abcb1a/b;Abcg2*$^{-/-}$ mice) and untreated controls (mix of strains) to achieve a similar mean bioluminescence reading within each cohort. The bioluminescence intensity of each individual animal at the day of start of treatment (day 0) was arbitrarily set at 100%. All subsequent measurements were recorded relative to this first measurement and converted to their logarithmic values. Mean ± SE values were calculated and plotted in graphs. Mice were weighed daily weighed examined for abnormalities. The mice were humanely sacrificed based on bioluminescence imaging results or when weight loss exceeded 20% of the initial body weight. Following sacrifice, brains were collected in formalin and used to qualitatively assess the tumor size by histology.

Statistical analysis

Statistical calculations were done using the software package SPSS (v22; SPSS Inc; Chicago, IL). *In vivo* tumor growth curves were compared using the General Linear Model repeated measured procedure. All comparisons of docetaxel concentrations involving more two experimental groups and multiple brain regions were done using two-way analysis of variance (ANOVA) followed by *post hoc* Bonferroni tests.

RESULTS

Characterization of the leakiness of intracranial tumor models

In order to assess the impact of the leakiness of the tumor vasculature on the efficacy of drug treatment, we first characterized a series of intracranial tumor models by contrast-enhanced MRI with gadolinium as well as by autoradiography with ^{14}C-labeled aminoisobutyrate (AIB) and fluorescence microscopy following the injection of Texas Red (TxRed). We selected four models for our further studies, since these recapitulate the spectrum from minimally to highly leaky tumors (**Figure 1**).

GBM8 is a neurobasal medium-cultured glioblastoma stem cell-like line of the proneural subtype. It is a highly invasive tumor that invades the contralateral hemisphere and displays only a very minimal contrast-enhancement on MRI and only in the more central core of the lesion. Also the other leakiness markers, AIB and 3kD-Dextran–FITC, indicate minimal to no leakiness. Mel57 is a melanoma cell line that forms more compact tumors, which are not very rich in blood vessels. Also this tumor showed some contrast enhancement on MRI, whereas TxRed fluorescence distribution was not detectable. The AIB distribution in this tumor was clearly higher than in the surrounding brain tissue. Together these results suggest that the BBB in Mel57 is not completely intact, although the extent of leakiness is limited. The same Mel57 cell line transduced with VEGF resulted in highly vascularized, compact tumors. The MRI showed ring-enhancement whereas the core was less enhanced, indicative of high interstitial pressure in the tumor. Extensive distribution of TxRed as well as uptake of AIB was found throughout the tumor, indicating profound leakiness of the BBB in these tumors. U87 is a serum-cultured GBM cell line that forms compact tumors that were also well vascularized. These tumor vessels were leaky, as judged by MRI, TxRed and AIB distribution.

Notably, all brain tumor lesions express murine P-gp and BCRP in the tumor vessels, whether the tumor cells originate from GBM or extracranial tumor types. Of note, immunohistochemical staining of P-gp on mouse tissue slides is not straight-forward. We have tested many antibodies over the last years without much success. In most cases, there was either no staining of the vessels or the vessels stained nicely, but the same vessel staining was then also found in P-gp knockout mice. The current antibody gives some non-specific staining of normal brain cells since this was also found in *Abcb1a/b*$^{-/-}$ mice, but the typical vascular staining of P-gp is only present in mice proficient for P-gp (**Supplementary Figure 1**). The antibody for BCRP gives much cleaner results. Note that besides the specific staining of the vessels there is also a more diffuse staining throughout the normal brain parenchyma in BCRP-proficient mice that is absent in *Abcb1a/b; Abcg2*$^{-/-}$ mice.

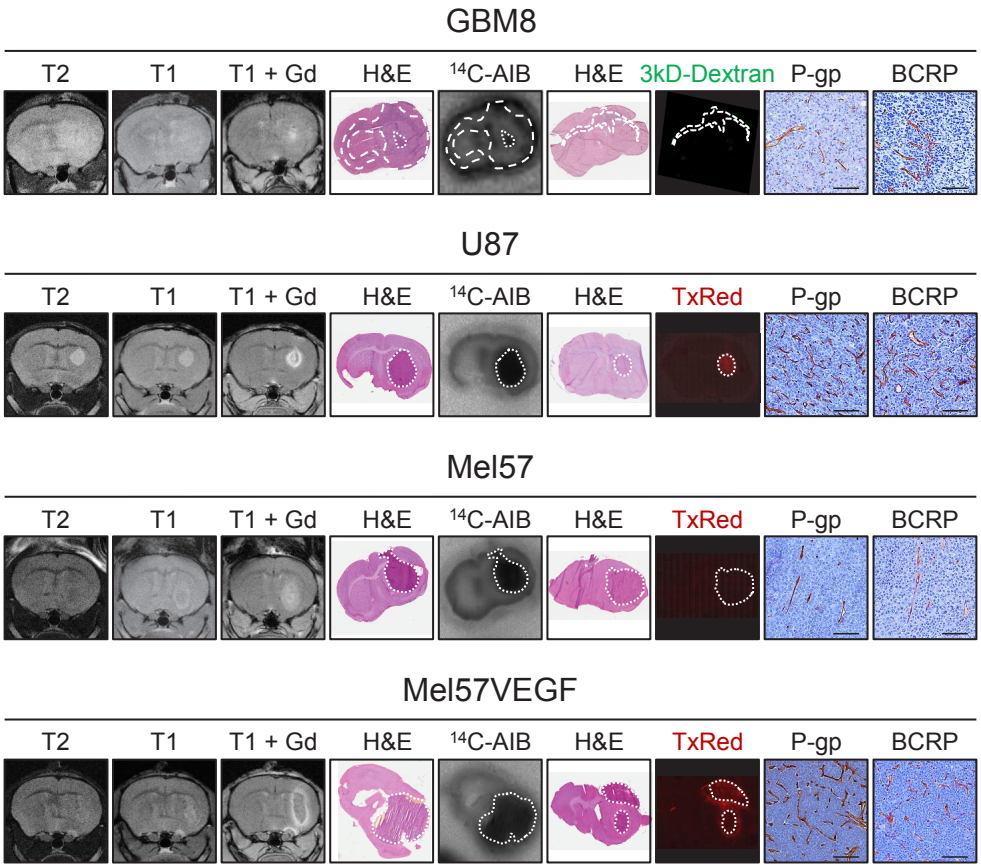

Figure 1 | Characterization of the vasculature of intracranial tumor models. The leakiness of the vasculature of intracranial GBM8, U87, Mel57 and Mel57VEGF tumors was assessed by T2-weighted, T1-weighted pre-contrast and T1-weighted post-gadolinium (Gd) contrast magnetic resonance imaging, by autoradiography following i.v. administration of ^{14}C-aminoisobutyrate (AIB) and by fluorescence microscopy following i.v. Texas Red (TxRed) or 3kD-Dextran–FITC. Histochemical hematoxylin and eosin (H&E) staining was used as a reference for tumor location. P-glycoprotein (P-gp) and breast cancer resistance protein (BCRP) expression was demonstrated by immunohistochemistry.

P-glycoprotein limits the distribution of docetaxel in brain tumors

We assessed the impact of the BBB in the distribution of docetaxel into our panel of intracranial tumor models as well as in ipsilateral (right) and contralateral (left) brain hemispheres and cerebellum. Tumor cells were injected into the striatum in the right hemisphere and were allowed to grow to a size that allowed visual recognition and isolation of sufficient material for analysis. U87 tumors form solid spherical structures that are easy to isolate without any adjacent normal brain tissue. Mel57VEGF tumors were soft, but rich in blood vessels and therefore easy to distinguish and isolate from normal brain. Mel57 and GBM8 were more difficult to discern from normal tissue.

The concentration of docetaxel in GBM8 tumor tissue was equal to the concentration in normal brain and the concentration of the same tumor in *Abcb1a/b*$^{-/-}$ mice was about 5-fold higher (**Figure 2**). This result is in line with the findings by MRI and AIB and TxRed that show that GBM8 tumors have an almost intact BBB. However, in Mel57 tumors that also appear to have a non-leaky BBB, the concentration of docetaxel was about 5-fold higher than in the normal brain of WT mice. Mel57 tumors in *Abcb1a/b*$^{-/-}$ mice accumulated about 2.5-fold more docetaxel than tumors in WT mice. This result demonstrates that docetaxel is able to accumulate into the tumor, but that despite this leakiness, P-gp is still capable to reduce the accumulation in the tumor. A much higher concentration of docetaxel was observed in Mel57VEGF tumors and the concentrations were similar in WT and *Abcb1a/b*$^{-/-}$ mice. This result suggests that the leakiness of vasculature in this tumor is too much for P-gp to effectively counter the distribution of docetaxel into the tumor. The ipsilateral brain hemisphere also contained 2- to 3-fold more docetaxel than contralateral brain, which may be due to more distant leaking of docetaxel into adjacent brain. The finding that the concentration in Mel57 tumors in *Abcb1a/b*$^{-/-}$ mice is only about 40% of the level in Mel57VEGF tumors indicates that the BBB in the Mel57 is still more functional albeit not completely tight. The leaky U87 tumors also accumulate 10-fold more docetaxel than normal brain, which is also further enhanced in *Abcb1a/b*$^{-/-}$ mice, again showing that P-gp can reduce the entry of drugs even when vessels are leaky.

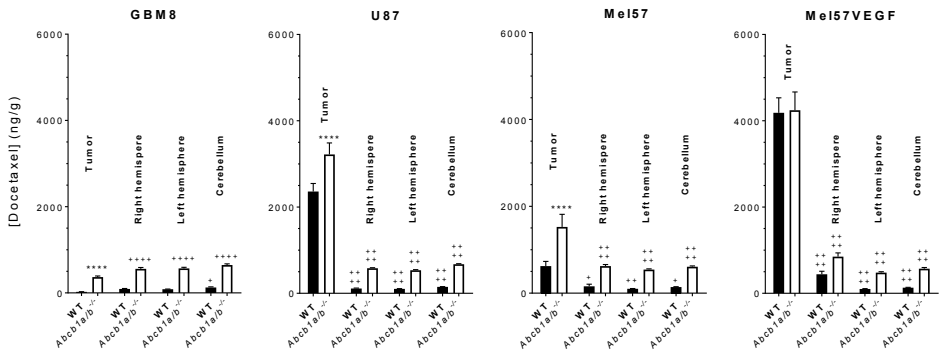

Figure 2 | Docetaxel distribution in brain tumors. The docetaxel concentration was lower in Mel57, U87 and GBM8 tumors of wild-type (WT) mice compared to *Abcb1a/b*$^{-/-}$ mice but considerably higher than in surrounding normal tissues (right hemisphere, left hemisphere and cerebellum) in all tumors but GBM8. Tissues were harvested at 4 h after 30 mg/kg i.v. docetaxel. Data are represented as mean ± SE (n ≥ 6); **** $p < 0.0001$, compared to WT; $^{+}$ $p < 0.05$, $^{++}$ $p < 0.01$, $^{++++}$ $p < 0.0001$ compared to tumor in the same genotype.

A leaky BBB can still protect brain tumors and reduce the efficacy of therapeutics

We used tumor cells expressing luciferase to allow non-invasive longitudinal bioluminescence imaging (BLI) as a readout of tumor growth for this study. Treatment started about 10 to 14 days after tumor cell injection. When we challenged Mel57 tumors with paclitaxel or docetaxel the tumors did not show any response to the treatment, even in *Abcb1a/b*$^{-/-}$ mice (**Figures 3A-B**).

Apparently the about 2.5-fold higher docetaxel accumulation in the tumors in *Abcb1a/b*$^{-/-}$ mice was still insufficient to elicit a therapeutic effect. When Mel57VEGF tumors were treated with docetaxel, a robust response was observed, which was similar in WT and *Abcb1a/b*$^{-/-}$ mice (**Figure 3C**). This is in line with the finding of a similar docetaxel distribution in the tumors grafted in both strains, which was also more than 2-fold higher than in Mel57 tumors (**Figure 2**). Further evidence that the poor response of intracranial Mel57 tumors is due to protection by the BBB comes from the finding that Mel57 tumors are very responsive to docetaxel when placed under the renal subcapsule (**Figure 3D**).

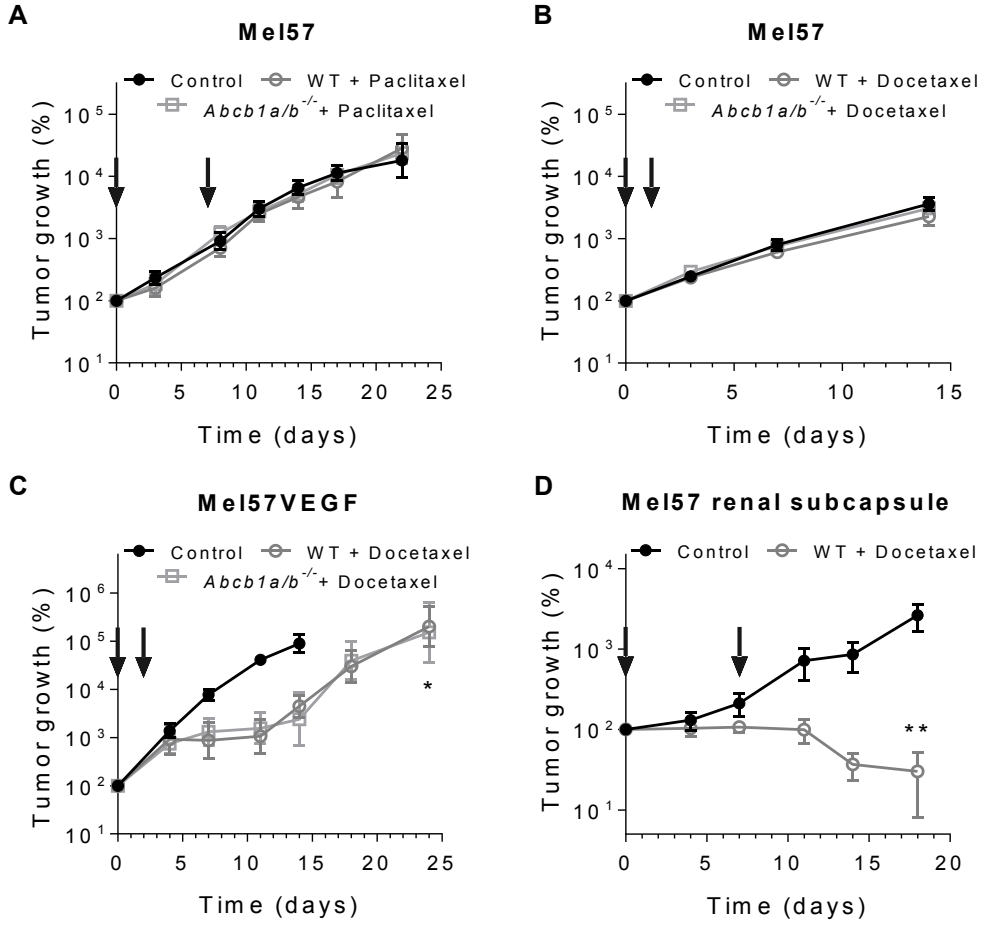

Figure 3. BBB permeability impacts the efficacy of treatment against intracranial Mel57 tumors. (**A**) Efficacy of paclitaxel against intracranial Mel57 tumors grafted in wild-type (WT) or *Abcb1a/b*$^{-/-}$ mice. Data are represented as mean ± SE (n ≥ 6). (**B**) Efficacy of docetaxel against intracranial Mel57 tumors grafted in WT or *Abcb1a/b*$^{-/-}$ mice. Data are represented as mean ± SE (n ≥ 9). (**C**) Efficacy of docetaxel against intracranial Mel57VEGF tumors grafted in WT or *Abcb1a/b*$^{-/-}$ mice. Data are represented as mean ± SE (n ≥ 7); * $p < 0.05$. (**D**) Efficacy of docetaxel against Mel57 tumors grafted in the renal subcapsule of WT mice. Data are represented as mean ± SE (n ≥ 5); ** $p < 0.01$. In all panels, arrows indicate days of taxane administration.

GBM8 tumors do not respond to docetaxel treatment, even not in *Abcb1a/b;Abcg2*$^{-/-}$ mice, which is in line with the finding that the accumulation of docetaxel is very low in these tumors (**Figure 2 and Figure 4A**). In contrast, we observed a response in WT mice when we treated U87 tumors with docetaxel or paclitaxel, in line with the finding that these tumors are very leaky (**Figure 1, Figure 2 and Figures 4B–C**). Notably, however, despite the fact that U87 tumors have very leaky vessels, the response observed in tumors in *Abcb1a/b*$^{-/-}$ mice was much more profound. This finding demonstrates that the activity of P-gp in otherwise leaky vessels can diminish the efficacy of a drug.

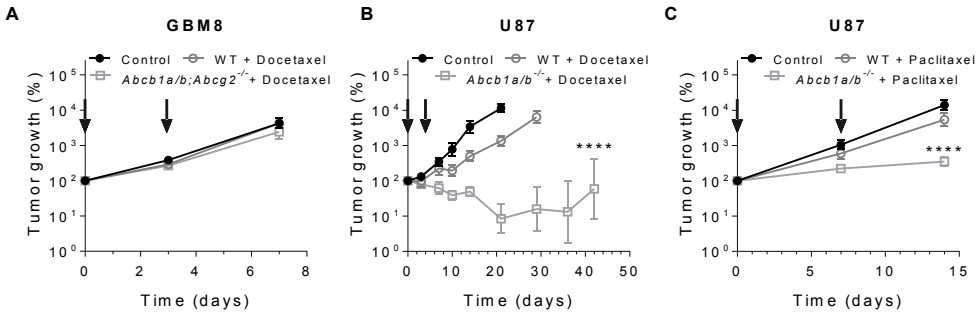

Figure 4. BBB permeability affects the efficacy of treatment against intracranial GBM tumors. (**A**) Efficacy of docetaxel against intracranial GBM8 tumors grafted in wild-type (WT) or *Abcb1a/b;Abcg2*$^{-/-}$ mice. Data are represented as mean ± SE (n ≥ 6). (**B**) Efficacy of docetaxel against intracranial U87 tumors grafted in WT or *Abcb1a/b*$^{-/-}$ mice. Data are represented as mean ± SE (n ≥ 6); **** $p < 0.0001$. (**C**) Efficacy of paclitaxel against intracranial U87 tumors grafted in WT or *Abcb1a/b*$^{-/-}$ mice. Data are represented as mean ± SD (n ≥ 7); **** $p < 0.0001$. In all panels, arrows indicate days of taxane administration.

DISCUSSION

By using our series of orthotopic brain tumor models engrafted into paired sets of P-gp deficient *vs.* proficient nude mice, we show that intracranial tumors that preserve the integrity of the BBB are very well protected against treatment with taxanes even when P-gp is absent. Intracranial tumors that have leakier BBB properties and are thus more accessible can be more responsive to chemotherapy. Importantly, however, the accumulation of docetaxel in tumors that have leaky blood vessels, is significantly higher in *Abcb1a/b*$^{-/-}$ mice compared to WT mice. Moreover, this also translates into a better efficacy. This result indicates that drug efflux transporters expressed in tumor vessels may still compromise chemotherapy efficacy, even when tumor blood vessels are leaky. Thus, leakiness of the BBB as determined by MRI does not imply unimpeded access of drugs into brain tumor lesions.

Fellner *et al*. previously showed that the efficacy of paclitaxel against an experimental U118MG brain tumor model was improved when given in combination with the P-gp inhibitor valspodar[18]. They also tested U87 with paclitaxel and valspodar but only at a dose of 4 mg/kg, which was too low for a response. Results by Gallo *et al.*[19], who analyzed the distribution of paclitaxel in

intracranially grafted B16 melanoma in WT and *Abcb1a/b*$^{-/-}$ FVB mice, suggested that P-gp limited drug entry in these tumors, although the impact on efficacy was not tested.

We have designed this study in order to establish the impact of BBB integrity and the role of P-gp in blood vessels on drug distribution and antitumor efficacy using multiple intracranial models. We have first characterized the integrity of tumor blood vessels in a range of brain tumor models and used paired cohorts of nude mice strains that were deficient or proficient for P-gp. We have used docetaxel, because it is a substrate of P-gp but not of BCRP. Moreover, the effect on the plasma clearance by P-gp is minimal, as elimination of docetaxel occurs mainly through CYP450-mediated metabolic degradation[13,20].

The expression of P-gp and other ABC transporters in the tumor vessels of GBM is well documented[21-23]. Blood vessels of primary brain tumors generally express P-gp levels that are equal or higher compared to vessels in normal brain tissue, whereas the expression in vessels of metastatic lesions is more diverse[24-26]. Based on these results, it was postulated that expression of drug efflux transporters would compromise the distribution and efficacy of chemotherapy. Our results demonstrate that this is indeed the case. All our intracranial tumor models, whether of glial or other origin, expressed both P-gp and BCRP in the tumor vasculature (**Figure 1**). Tumor cells can also express these drug efflux transporters, but these two ABC transporters were not detected in tumor cells used in our studies. It is well established that astrocyte–endothelial cell interactions are crucial for the formation and maintenance of the BBB properties, including the expression of ABC transporters[27]. The finding of ABC transporter expression in non-glial tumors therefore suggests that these tumors grow at least in part via co-option of the pre-existing vasculature. Invasion of the brain by GBM cells may occur via various routes, including the perivascular space[28]. Interestingly, it has been shown that focal breaches of the BBB may already occur when invading tumor cells displace the astrocytic endfeet from the endothelial cells[29]. Obviously, most of the vessels in the our models are surrounded by tumor cells and will have lost the connection with astrocytes, yet this does not compromise the expression of ABC transporters. In fact, even tumor vessel in non-glial Mel57VEGF tumors stained intensely. Notably, however, although large and lethal for mice, the actual size of the tumor lesions in mouse brain is very small and likely reflects the size of asymptomatic lesions in patients that are undetectable by MRI. The absence of P-gp and BCRP in blood vessels of surgical samples of brain metastases may be due to the fact that these tumor will be larger and that expression has been lost during their progression from micro-metastasis to clinically overt lesions. Clinical responses in patients with brain metastases occur[30]. In line with this, Fine *et al*., who have studied the distribution of paclitaxel in primary and metastatic brain tumors in patients, reported that a higher drug accumulation of paclitaxel was found in metastatic tumors relative to primary brain tumors[31]. Nevertheless the usefulness of systemic chemotherapy for brain metastases remains controversial[32,33]

Although the literature suggests that under some conditions compounds can enter brain tumors, our results show that the entry and, consequently, efficacy of substrate drugs may still be limited by drug efflux transporters. Concordant with paclitaxel and docetaxel, other small molecules will be subjected to the same principles. Temozolomide is a relatively BBB-penetrable drug and is able to achieve therapeutic levels in GBM, albeit that we recently showed that even the distribution and efficacy of temozolomide is impeded by drug efflux transporters[17]. In this case, the gain in brain distribution in the absence of P-gp and BCRP was only very small. On the other hand, many of the novel targeted agents that have shown profound responses in patients with extra-cranial malignancies are excellent substrates for P-gp and/or BCRP and are efficiently extruded from the brain[34]. Consequently, it will clearly be advantageous for treatment of intracranial tumors to focus on those candidate drugs that readily cross the BBB.

In conclusion, leakiness of the BBB does not guarantee good accessibility of drugs to brain tumors. Although therapeutics may be able to exert a response against brain tumors, the full potential of the therapy may still be attenuated by drug efflux pumps in the tumor vessels.

REFERENCES

1. Stupp, R., *et al.* Radiotherapy plus concomitant and adjuvant temozolomide for glioblastoma. *N Engl J Med* **352**, 987-996 (2005).
2. Sarkaria, J.N., *et al.* Is the blood-brain barrier really disrupted in all glioblastomas? A critical assessment of existing clinical data. *Neuro Oncol* **20**, 184-191 (2018).
3. Durmus, S., *et al.* Apical ABC transporters and cancer chemotherapeutic drug disposition. *Adv Cancer Res* **125**, 1-41 (2015).
4. van Tellingen, O., *et al.* Overcoming the blood-brain tumor barrier for effective glioblastoma treatment. *Drug Resist Updat* **19**, 1-12 (2015).
5. Abbott, N.J., *et al.* Structure and function of the blood-brain barrier. *Neurobiol Dis* **37**, 13-25 (2010).
6. Lin, F., *et al.* Abcc4 together with Abcb1 and Abcg2 form a robust co-operative drug efflux system that restricts the brain entry of camptothecin analogs. *Clin Cancer Res* **19**, 2084-2095 (2013).
7. Huizing, M.T., *et al.* Taxanes: a new class of antitumor agents. *Cancer Invest* **13**, 381-404 (1995).
8. Prados, M.D., *et al.* Phase II study of paclitaxel in patients with recurrent malignant glioma. *J Clin Oncol* **14**, 2316-2321 (1996).
9. Chamberlain, M.C. & Kormanik, P. Salvage chemotherapy with taxol for recurrent anaplastic astrocytomas. *J Neurooncol* **43**, 71-78 (1999).
10. Cahan, M.A., *et al.* Cytotoxicity of taxol in vitro against human and rat malignant brain tumors. *Cancer Chemother Pharmacol* **33**, 441-444 (1994).
11. Terzis, A.J., *et al.* Proliferation, migration and invasion of human glioma cells exposed to paclitaxel (Taxol) in vitro. *Br J Cancer* **75**, 1744-1752 (1997).
12. Kemper, E.M., *et al.* Increased penetration of paclitaxel into the brain by inhibition of p-glycoprotein. *Clin Cancer Res* **9**, 2849-2855 (2003).
13. Kemper, E.M., *et al.* Improved penetration of docetaxel into the brain by co-administration of inhibitors of P-glycoprotein. *Eur J Cancer* **40**, 1269-1274 (2004).
14. Xie, Y., *et al.* The human glioblastoma cell culture resource: validated cell models representing all molecular subtypes. *EBioMedicine* **2**, 1351-1363 (2015).
15. Kemper, E.M., *et al.* Development of luciferase tagged brain tumour models in mice for chemotherapy intervention studies. *Eur J Cancer* **42**, 3294-3303 (2006).
16. Singh, R.K., *et al.* Organ site-dependent expression of basic fibroblast growth factor in human renal cell carcinoma cells. *Am J Pathol* **145**, 365-374 (1994).
17. de Gooijer, M.C., *et al.* Improved brain penetration and antitumor efficacy of temozolomide by inhibition of ABCB1 and ABCG2. *Neoplasia* **20**, 710-720 (2018).
18. Fellner, S., *et al.* Transport of paclitaxel (Taxol) across the blood-brain barrier in vitro and in vivo. *J Clin Invest* **110**, 1309-1318 (2002).
19. Gallo, J.M., Li, S., Guo, P., Reed, K. & Ma, J. The effect of P-glycoprotein on paclitaxel brain and brain tumor distribution in mice. *Cancer Res* **63**, 5114-5117 (2003).
20. van Waterschoot, R.A., *et al.* Absence of both cytochrome P450 3A and P-glycoprotein dramatically increases docetaxel oral bioavailability and risk of intestinal toxicity. *Cancer Res* **69**, 8996-9002 (2009).
21. Demeule, M., *et al.* Expression of multidrug-resistance P-glycoprotein (MDR1) in human brain tumors. *Int J Cancer* **93**, 62-66 (2001).
22. Fattori, S., *et al.* Human brain tumors: multidrug-resistance P-glycoprotein expression in tumor cells and intratumoral capillary endothelial cells. *Virchows Arch* **451**, 81-87 (2007).

23. Emery, I.F., *et al.* Expression and function of ABCG2 and XIAP in glioblastomas. *J Neurooncol* **133**, 47-57 (2017).
24. Toth, K., *et al.* MDR1 P-glycoprotein is expressed by endothelial cells of newly formed capillaries in human gliomas but is not expressed in the neovasculature of other primary tumors. *Am J Pathol* **149**, 853-858 (1996).
25. Yonemori, K., *et al.* Disruption of the blood brain barrier by brain metastases of triple-negative and basal-type breast cancer but not HER2/neu-positive breast cancer. *Cancer* (2009).
26. Richtig, E., *et al.* Lack of P-glycoprotein expression in melanoma brain metastases of different melanoma types. *Clin Neuropathol* **35**, 89-92 (2016).
27. Abbott, N.J., *et al.* Astrocyte-endothelial interactions at the blood-brain barrier. *Nat Rev Neurosci* **7**, 41-53 (2006).
28. de Gooijer, M.C., *et al.* An experimenter's guide to glioblastoma invasion pathways. *Trends Mol Med* **24**, 763-780 (2018).
29. Watkins, S., *et al.* Disruption of astrocyte-vascular coupling and the blood-brain barrier by invading glioma cells. *Nature Commun* **5**, 4196 (2014).
30. Davies, M.A., *et al.* Dabrafenib plus trametinib in patients with BRAF V600 -mutant melanoma brain metastases (COMBI-MB): a multicentre, multicohort, open-label, phase 2 trial. *Lancet Oncol* **18**, 863-873 (2017).
31. Fine, R.L., *et al.* Randomized study of paclitaxel and tamoxifen deposition into human brain tumors: implications for the treatment of metastatic brain tumors. *Clin Cancer Res* **12**, 5770-5776 (2006).
32. Fortin, D. The blood-brain barrier: its influence in the treatment of brain tumors metastases. *Curr Cancer Drug Targets* **12**, 247-259 (2012).
33. Mehta, M.P., *et al.* The role of chemotherapy in the management of newly diagnosed brain metastases: a systematic review and evidence-based clinical practice guideline. *J Neurooncol* **96**, 71-83 (2010).
34. Kim, M., *et al.* Barriers to effective drug treatment for brain metastases: a multifactorial problem in the delivery of precision medicine. *Pharm Res* **35**, 177 (2018).

SUPPLEMENTARY FIGURES

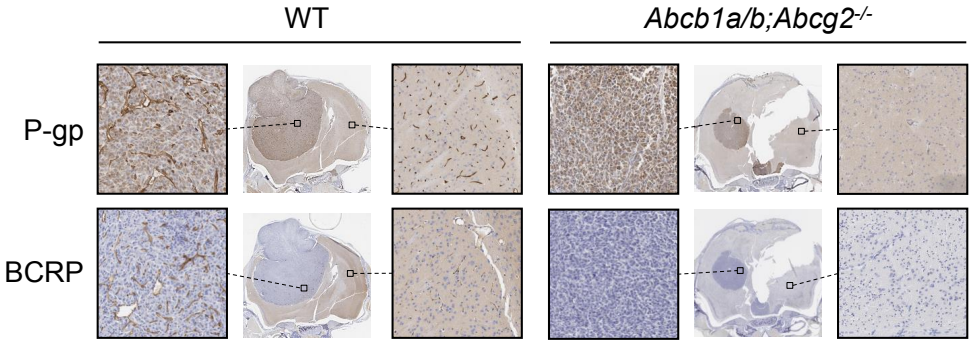

Supplementary Figure 1 | Validation of ABC transporter immunohistochemistry staining. Immunohistochemical staining of P-glycoprotein (P-gp) and breast cancer resistance protein (BCRP) in U87 tumor regions and healthy brain tissue of wild-type (WT) and *Abcb1a/b;Abcg2*$^{-/-}$ mice.

Chapter 4

IMPROVED BRAIN PENETRATION AND ANTITUMOR EFFICACY OF TEMOZOLOMIDE BY INHIBITION OF ABCB1 AND ABCG2

M.C. de Gooijer, N.A. de Vries, T. Buckle, L.C.M. Buil, J.H. Beijnen, W. Boogerd, and O. van Tellingen

Neoplasia. 2018;20(7):210-220

ABSTRACT

The anticancer drug temozolomide is the only drug with proven activity against high-grade gliomas and has therefore become a part of the standard treatment of these tumors. P-glycoprotein (P-gp; ABCB1) and breast cancer resistance protein (BCRP; ABCG2) are transport proteins, which are present at the blood–brain barrier and limit the brain uptake of substrate drugs. We have studied the effect of P-gp and BCRP on the pharmacokinetics and pharmacodynamics of temozolomide, making use of a comprehensive set of *in vitro* transport experiments and *in vivo* pharmacokinetic and antitumor efficacy experiments using wild-type, *Abcg2*$^{-/-}$, *Abcb1a/b*$^{-/-}$ and *Abcb1a/b;Abcg2*$^{-/-}$ mice. We here show that the combined deletion of Abcb1a/b and Abcg2 increases the brain penetration of temozolomide by 1.5-fold compared to wild-type controls ($p < 0.001$), without changing the systemic drug exposure. Moreover, the same increase was achieved when temozolomide was given to wild-type mice in combination with the dual P-gp/BCRP inhibitor elacridar (GF120918). The antitumor efficacy of temozolomide against three different intracranial tumor models was significantly enhanced when Abcb1a/b and Abcg2 were genetically deficient or pharmacologically inhibited in recipient mice. These findings call for further clinical testing of temozolomide in combination with elacridar for the treatment of gliomas, as this offers the perspective of further improving the antitumor efficacy of this already active agent.

INTRODUCTION

High-grade gliomas, and in particular glioblastoma (GBM), are refractory to virtually all chemotherapy regimens. Whereas it is possible that the heterogeneity within these tumors favors the presence of innately resistant tumor cells, inadequate drug-exposure of tumor cells because of the blood–brain barrier (BBB) is most likely also a major cause of the general lack of efficacy of chemotherapy[1]. The BBB restricts the entry of nearly all commonly used agents. Although this barrier is often disrupted in more central tumor areas, where leakiness can be visualized by contrast-enhanced MRI, it is still functional in the more peripheral and surgically unresectable tumor regions that harbor many viable and proliferating tumor cells. Moreover, glioma tumor cells have the propensity to migrate deep into the surrounding normal brain tissue, where the BBB is also fully intact[2,3].

The principal components of the BBB are the endothelial cells that are linked together by tight junctions, limiting the paracellular movement of substances[4]. Moreover, transcellular routing is further restricted by the absence of fenestrae and the low endocytic activity of brain endothelial cells. Besides these more or less passive restraints, the BBB is also equipped with ATP-binding cassette (ABC) efflux transporters such as P-glycoprotein (P-gp, ABCB1) and breast cancer resistance protein (BCRP, ABCG2) that together limit the brain penetration of almost all classical chemotherapeutics and novel targeted anticancer drugs[5,6].

For a long time, the standard treatment of GBM consisted of surgical resection followed by local radiotherapy, with or without nitrosourea-based chemotherapy. However, a large number of adjuvant nitrosourea-based chemotherapy trials have been conducted, but did not demonstrate significant survival benefit[7,8]. At the last turn of the century however, the orally bioavailable alkylating agent temozolomide was reported to have significant activity in the treatment of recurrent grade 3 and grade 4 gliomas, outperforming procarbazine in one study[9-11]. Then, about a decade ago, a large phase III trial showed a significant survival benefit for radiotherapy in combination with concomitant and adjuvant temozolomide compared to radiotherapy alone[12]. This landmark study set the basis for the new standard treatment of newly diagnosed GBM, where patients start temozolomide (75 mg/m^2/day for 42 days) concomitantly with radiotherapy, subsequently followed by 6 courses of temozolomide monotherapy (150 to 200 mg/m^2/day for 5 days with a 23 day rest period). Epigenetic silencing of the O^6-methylguanine-DNA methyltransferase (MGMT) promoter has been demonstrated to predict benefit to temozolomide chemotherapy[13]. Nevertheless, this drug is currently being prescribed to most GBM patients since it is generally well tolerated, a small survival benefit is seen in patients carrying non-silenced MGMT promotors and there is no real alternative[14].

Temozolomide is generally believed to penetrate the BBB relatively well. Indeed, the brain penetration is apparently high enough to improve the median survival of GBM patients from 12.1 to 14.6 months[12]. Nevertheless, we here show that P-gp and BCRP collectively limit the brain penetration of this drug. Using drug transporter knockout mouse models, we show that the temozolomide brain penetration is increased when these two drug transporters are absent or inhibited, while the plasma clearance of the drug remains unaffected. Importantly, we show that the efficacy of temozolomide against three independent experimental intracranial tumor models is significantly improved when P-gp and BCRP are genetically absent or pharmacologically inhibited.

METHODS

Reagents

Temozolomide (Temodal® 20 mg hard capsules) originated from Schering Plough BV (Utrecht, The Netherlands). Elacridar (GF120918) was a generous gift from GlaxoSmithKline Inc. (Research Triangle Park, NC). Erlotinib was kindly provided by OSI Pharmaceuticals, Inc., (Melville, NY). Zosuquidar was a generous gift of Eli Lilly (Indianapolis, IN). Gefitinib was purchased from Sequoia Research Products Ltd (Pangbourne, UK). Bovine serum albumin (BSA) fraction V was purchased from Roche Diagnostics GmbH (Mannheim, Germany). All other chemicals were purchased from Merck (Darmstadt, Germany) and were used as supplied.

Preparation of drug solutions

The content of a temozolomide capsule containing 20 mg of active substance was dissolved in 0.4 mL ethanol and 3.6 mL saline to yield a solution of 5.0 mg/mL and was used within 60 minutes after preparation. Elacridar was prepared freshly the day before each experiment and suspended at 5 mg/mL in a mixture of hydroxypropyl methylcellulose (0.5 g/L)/1% polysorbate 80 (v/v). The suspension was mixed for 2 minutes using a Polytron PT1200 homogenizer (Kinematica AG, Littau, Switzerland). Additionally, the suspension was kept protected from light and stirred continuously before and during administration. Gefitinib was suspended in 0.5% (v/v) Tween 20 and 0.25% (w/v) carboxymethylcellulose in water at a concentration of 10 mg/mL.

Analytical methods

Based on previous work by Kim *et al.*[15], we have developed a high-performance liquid chromatographic (HPLC) assay for the determination of temozolomide in medium used for *in vitro* transport experiments and in mouse plasma and brain tissue homogenates for *in vivo* pharmacokinetic studies. Separation and quantification was achieved using a SymmetryÒ C_{18}

column (150 x 2.0 mm; ID) together with a mobile phase of 7.5% of methanol in 0.5% acetic acid in water, delivered at a flow rate of 0.2 mL/min and UV detection at 330 nm (PDA996 photodiode array detector; Waters; Milford, MA or SF 757 detector; Kratos; Ramsey, NJ). Medium from transwell experiments was diluted 10-fold with 0.2% acetic acid in water and 50 µL was injected directly into the HPLC system. Temozolomide was extracted from the acidified plasma and brain tissue homogenate samples (200 µL) with 1.0 ml ethyl acetate. The dried extracts were subsequently dissolved in 100 µL of 5% methanol in 0.2% acetic acid in water and 50 µL was injected into the HPLC system. External calibration was used. The lower and upper limit of quantitation was 0.020 µg/mL and 10.0 µg/mL, respectively. Samples above the upper limit of quantification were first diluted with acidified blank human plasma. All samples from *in vivo* studies were analyzed twice in 2 independent analytical series and repeated once more when the duplicates differed by more than 10%.

In vitro transport experiments

The parental LLC porcine kidney (PK1) cell line and its Mdr1a transduced subline[16] and the parental Madine–Darby Canine Kidney (MDCKII) cell line and its Bcrp1 transduced subline[17] were used to establish whether temozolomide is a substrate of Mdr1a (P-gp) and Bcrp1, respectively. Cells were seeded on Transwell microporous polycarbonate membrane filters (3.0 µm pore size, 24 mm diameter; Costar Corning; Corning, NY) at a density of $1x10^6$ cells per well in 2 mL of MEM medium (Invitrogen; Carlsbad, CA) containing 10% v/v fetal bovine serum. Cells were incubated at 37 °C in 5% CO_2 for three days with one medium replacement after the first day. Two hours before the start of the experiment the medium in both compartments was replaced with 2 mL of OptiMEM medium (Invitrogen). At the start of the experiment the medium in the apical or basolateral compartment was replaced with 2 mL of freshly prepared OptiMEM medium containing 40 µg/mL of temozolomide. The P-gp and/or BCRP inhibitors elacridar (5 mM), gefitinib (5, 10 µM), erlotinib (5, 10 and 20 mM) or novobiocin (10 and 50 µM) were added to both the apical and basolateral compartment. Zosuquidar (LY335979, 5 µM) was always added to the medium when doing experiments with MDCK cell lines to inhibit endogenous canine P-gp. Samples of 50 µL were collected every 30 min, for up to 2 h after start of the experiment. Because temozolomide is instable in medium at 37°C, we replaced 1 mL of the donor compartment by a freshly prepared aliquot every 30 min. [^{3}H]-inulin (approximately 7 kBq per well) was added to the same compartment as temozolomide to check the integrity of the cell layer. Wells showing a leakage of more than 1.5% per hour were excluded from analysis.

Animals

Animals used in the pharmacokinetics studies were male wild-type (WT), *Abcg2*$^{-/-}$, *Abcb1a/b*$^{-/-}$ and *Abcb1a/b;Abcg2*$^{-/-}$ mice of a FVB genetic background within the age of 8 to 15 weeks as described

before [18]. Animals used for efficacy studies were WT or *Abcb1a/b;Abcg2*$^{-/-}$ athymic nude mice of FVB background or Cre-LoxP conditional *Tp53*$^{F/F}$*;p16*^{Ink4a}*/p19*$^{ArfF/F}$*;LoxP–Stop–LoxP (LSL)–K-ras*^{V12}*;Luc* as previously described[19]. Animals were housed and handled according to institutional guidelines complying with Dutch and European law. The mice were kept in a temperature-controlled environment with a 12 hour light-dark cycle and were given a standard diet (AM-II; Hope Farms B.V.; Woerden, The Netherlands) and acidified water *ad libitum*. All experiments involving animals were approved by the local animal ethics committee.

In vivo pharmacokinetics studies

The brain penetration study comprised cohorts of WT, *Abcg2*$^{-/-}$, *Abcb1a/b*$^{-/-}$ and *Abcb1a/b;Abcg2*$^{-/-}$ mice receiving temozolomide (50 mg/kg) by intravenous injection in the tail vein. Each cohort consisted of at least 40 animals in which at least 6 animals were used per time point (t = 15 min, 1, 2, 4 and 7 hours post temozolomide administration). Separate cohorts of WT and *Abcb1a/b;Abcg2*$^{-/-}$ mice received temozolomide (50 mg/kg) either as single agent or 2 h after elacridar (100 mg/kg) or 1 h after gefitinib (100 mg/kg) administered orally by gavage into the stomach. At the different time points, the mice were anesthetized with methoxyflurane and blood samples were obtained by cardiac puncture and collected on ice in tubes containing potassium EDTA as anticoagulant. The tubes were immediately cooled in melting ice and centrifuged within 60 min (10 min, 5000 g, 4 °C) to separate the plasma fraction, which was transferred into clean vials. Subsequently, plasma fraction was mixed with 1 M hydrochloric acid (10 + 1; v/v) and stored at -20 °C until analysis. Immediately after cardiac puncture the mice were killed by cervical dislocation and the brains were dissected and placed on ice. Within 60 min they were weighed and homogenized in 3 mL of ice-cold 1% of BSA in 0.05 M phosphate buffer adjusted to pH = 2 and stored at -20 °C until further analysis.

We next established the drug exposure in WT (n = 18) and *Abcb1a/b;Abcg2*$^{-/-}$ mice (n = 19) receiving an oral dose of 100 mg/kg temozolomide by gavage. Blood was sampled from the tail at 15, 30 min and 1, 4 and 7 h post drug administration to obtain a full curve from each animal.

Intracranial tumor models

Three different intracranial tumor models were used in this study. First, Mel57–luc cells (100,000 cells/2 µL) were injected stereotactically in the brains of FVB nude mice as previously described in detail[20]. Next, murine GSC457 glioblastoma cells previously isolated from a Cre–LoxP conditional *Tp53*$^{F/F}$*;p16*^{Ink4a}*/p19*$^{ArfF/F}$*;LSL–K-ras*^{V12}*;Luc* high-grade glioma[19] were injected (5,000 cells/2 µL) in the brains of recipient FVB nude mice. Lastly, we examined the results in spontaneous murine gliomas induced by injecting lentiviral CMV–Cre (2 µL) in the brains of *Tp53*$^{F/F}$*;p16*^{Ink4a}*/p19*$^{ArfF/F}$*; LSL–K-ras*^{V12}*;Luc* mice[19]. All stereotactic injections (tumor cells and virus) were done at 2 mm

lateral and 1 mm anterior to the bregma, 3 mm below the skull.

Magnetic resonance imaging

Magnetic resonance imaging was done using a BioSpec 70/20 USR (Bruker; Billerica, MA) using a sequence of T2-weighted, T1-weighted pre-contrast and T1-weighted post-contrast. Gadoterate meglumine (Dotarem®; 0,5 mmol/ml; Guerbet; Villepinte, France) diluted 5-fold with saline was used as a contrasting agent and delivered via an intravenous cannula inserted in the tail vein. Mice were anesthetized using isoflurane (Pharmachemie B.V.; Haarlem, The Netherlands) delivered via a customized mouse holder and heart rate and breathing frequency were monitored throughout the entire procedure. Paravision software (v 6.0.1; Bruker) was used for image acquisition.

Blood–brain barrier integrity characterization

Mice bearing orthotopic GSC457 or *Tp53*$^{-/-}$*;p16*^{Ink4a}*/p19*$^{Arf-/-}$*;K-ras*^{V12}*;Luc* tumors were intravenously injected with 6 mg/kg TexasRed (Sulforhodamine 101; Invitrogen) in saline. After 30 minutes, the animal was anesthetized with hypnorm/dormicum and perfused with saline. The brain was immediately frozen on dry ice in Tissue-Tek® (Sakura Finetek Europe BV; Alphen aan den Rijn, The Netherlands) and kept at –70 °C until sectioning. Fluorescence microscopy analysis of the brain slices was done using an Axio Observer Z1 system (Zeiss; Oberkochen, Germany) equipped with an ORCA-AG CCD camera (Hamamatsu Photonics KK; Hamamatsu, Japan).

In vivo efficacy studies

Bioluminescence imaging using an IVIS200 camera (PerkinElmer; Waltham, MA) was used to establish tumor load in each animal at the start of therapy. Depending on the experiment, the animals were stratified between oral temozolomide (100 mg/kg/day for 5 or 7 days as indicated), no treatment (control) or temozolomide with concomitant oral elacridar (100 mg/kg/day for 5 or 7 days) given 20–30 minutes prior to temozolomide. Bioluminescence imaging was repeated at subsequent days to establish the efficacy of the therapy. The amount of bioluminescence in each animal was calculated relative to the first measurement when therapy was initiated and was logarithmically converted prior to data analysis.

Data analysis

All statistical analyses in this study were carried out using GraphPad Prism v7.03 (GraphPad Inc.; La Jolla, CA) unless otherwise stated. To determine the differences of brain and plasma concentrations among multiple strains or conditions over time, two-way analysis of variance (ANOVA) was performed. All single time point analyses with multiple groups were analyzed by

one-way ANOVA. All ANOVA analyses were corrected for multiple comparisons using the post-hoc Bonferroni procedure. Plasma and brain $AUC_{0\text{-}7h}$ values and standard errors were calculated by the linear trapezoidal rule using standard equations[21]. The plasma half-life of temozolomide was calculated by linear regression analysis after log transformation of the concentration data using Microsoft Excel 2010. The brain–plasma ratio was calculated for each individual animal. *In vivo* tumor growth curves were compared using the General Linear Model repeated measured procedure using SPSS (v22; SPSS Inc; Chicago, IL). Kaplan–Meier curves were drawn using GraphPad Prism v7.03 and the log-rank test was used to determine whether survival curves were significantly different. All differences were considered statistically significant when $p < 0.05$.

RESULTS

In vitro transport assays

Because the stability of temozolomide in culture medium at 37°C is limited by its short half-life of approximately 30 minutes, *in vitro* transport experiments were carried out slightly differently than usual for this kind of experiment[22]. First, we took samples every 30 minutes for up to 2 hours instead of every hour for up to 4 hours. Secondly, to maintain adequate temozolomide levels at the donor side throughout the experiment, we replaced 1 mL of the 2 mL of medium at the donor side of the transwell at each sampling time by 1 mL of a freshly prepared temozolomide solution in medium. We have investigated P-gp-mediated transport of temozolomide (40 mg/mL) using polarized monolayers of porcine kidney (LLC–PK1) cells and its murine P-gp transduced subclone (LLC–Mdr1a). Our results show very limited, if any, evidence for transport by P-gp (**Figures 1A–B**). Similar experiments were conducted in the parental canine MDCKII cells and its Bcrp1 transduced (MDCKII–Bcrp1) subline and showed clear vectorial transport by Bcrp1 (**Figures 1C–D**). This Bcrp1-mediated transport was almost completely abrogated when elacridar (5 mM), gefitinib (10 mM) or erlotinib (10 mM) was present in the medium (**Figures 1E**–**H**). A concentration of 50 μM of novobiocin was not sufficient (**Figures 1I–J**). These *in vitro* results clearly show that whereas temozolomide is a good substrate of Bcrp1 it appears to be transported less efficiently by P-gp.

In vivo pharmacokinetics

To investigate the impact of BCRP and P-gp on the disposition of temozolomide i*n vivo* we have performed experiments in wild-type (WT), *Abcg2*$^{-/-}$, *Abcb1a/b*$^{-/-}$ and *Abcb1a/b;Abcg2*$^{-/-}$ mice. All animals received temozolomide by i.v. injection in the tail vein. This route was chosen to minimize the inter-animal variability that might be higher after oral dosing and because the systemic exposure may be higher in ABC transporter knockout mice. Interestingly, the brain penetration of temozolomide was significantly ($p < 0.01$) higher in both of the single knockout mouse strains compared to the WT control group (**Table 1**). Although the *in vitro* results suggested that P-gp

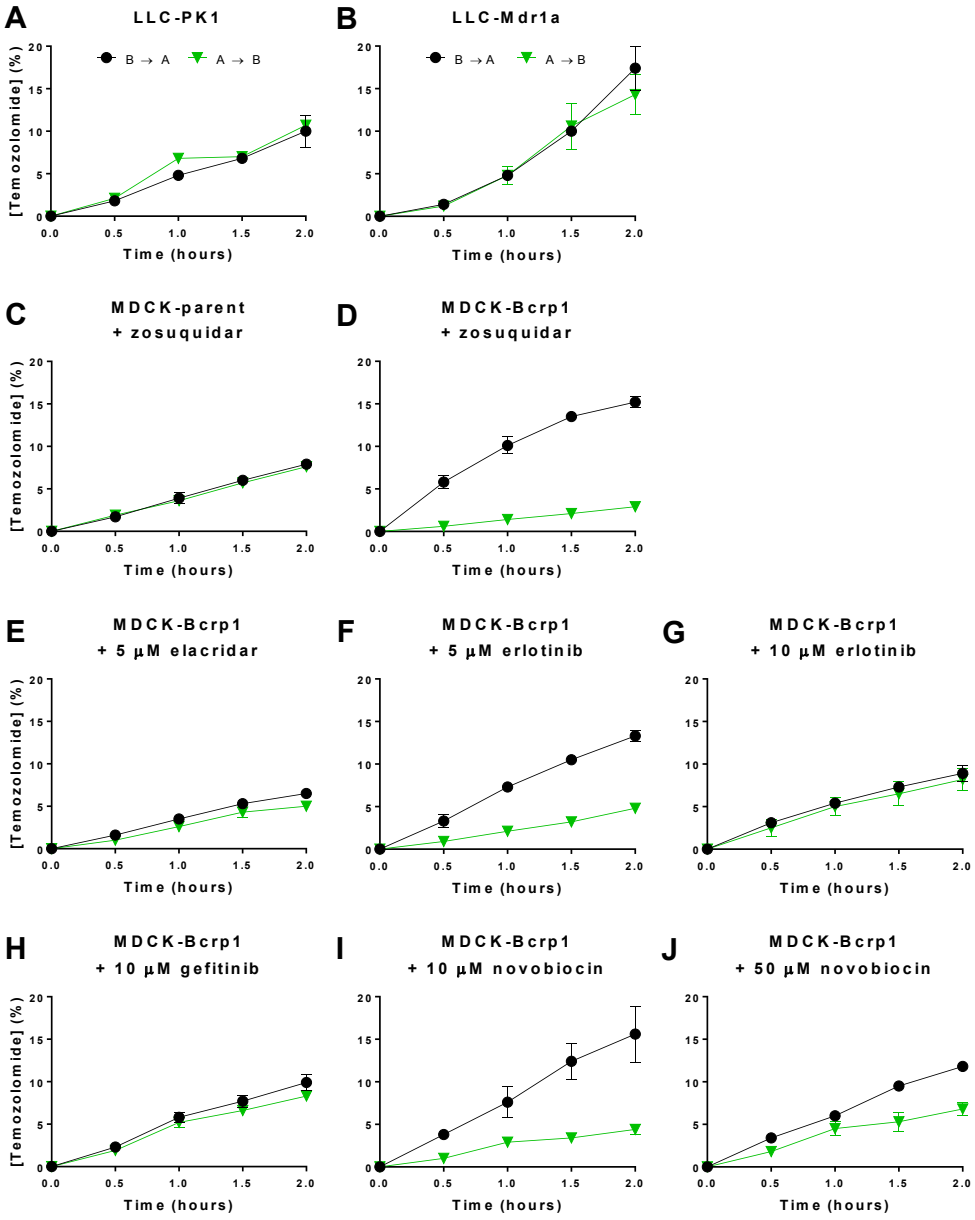

Figure 1 | *In vitro* temozolomide transport experiments. Temozolomide was added to the basolateral or apical compartment of the transwell to measure basolateral-to-apical (B→A) or apical-to-basolateral (A→B) transport, respectively, using LLC-PK1 (parent) versus the Mdr1a subline or using MDCKII (parent) versus the Bcrp1 transduced sublines. The transport of temozolomide is depicted as percentage of temozolomide initially present at the donor compartment (mean ± SD). Because degradation will also take place in the acceptor compartment during the experiment, this value will be an underestimation of the fraction that is actually translocated. Temozolomide transport by Mdr1a was not readily detected by this assay whereas transport by Bcrp1 was evident. The dual P-gp–BCRP inhibitor elacridar and the presumed Bcrp1 inhibitors gefitinib, erlotinib and novobiocin were added at the depicted concentrations.

(Abcb1a/b) does not transport temozolomide, the brains of *Abcb1a/b*$^{-/-}$ mice accumulated about 20% more temozolomide than those of WT mice. The same enhancement was seen in *Abcg2*$^{-/-}$ mice, whereas *Abcb1a/b;Abcg2*$^{-/-}$ mice accumulated 50% more ($p < 0.001$) drug in the brain (**Figure 2A**). Although a 1.5-fold increase for temozolomide is less than observed previously with several other substrate drugs, temozolomide already has proven activity against high-grade glioma. We therefore expect that this 1.5-fold gain in the brain penetration will be highly relevant for treatment of brain cancer patients. The absence of drug transporters did not affect the plasma clearance of this drug (**Table 1 and Figure 2B**), nullifying the chance that the higher brain level is due to higher plasma levels. In fact, the decline of temozolomide from plasma follows first-order elimination kinetics with a half-life of 0.7 hours, in line with the fact that temozolomide is unstable at physiological pH due to non-enzymatic degradation into its metabolite 3-methyl-(triazen-1-yl)imidazole-4-carboximide[23].

Genotype	$AUC_{0\text{-}7\ h,\ brain}$ (μg/g.h)	$AUC_{0\text{-}7\ h\ plasma}$ (μg/mL.h)	$t_{½\ plasma}$ (h)
Wild-type	36.81 ± 1.11	65.40 ± 2.00	0.689 ± 0.019
Abcg2$^{-/-}$	44.78 ± 1.88*	62.96 ± 2.14	0.719 ± 0.017
Abcb1a/b$^{-/-}$	44.51 ± 1.56*	62.16 ± 2.05	0.757 ± 0.021
Abcb1a/b;Abcg2$^{-/-}$	57.09 ± 1.32**/#	64.47 ± 1.29	0.705 ± 0.014

Table 1 | Pharmacokinetic parameters of temozolomide after intravenous administration of 50 mg/kg. AUC, area under the plasma concentration–time curve; $t_{1/2}$, elimination half-life. Data are represented as mean ± SE; n ≥ 7; * $p < 0.01$ relative to wild-type mice, ** $p < 0.001$ relative to wild-type mice, # $p < 0.01$ relative to *Abcb1a/b;Abcg2*$^{-/-}$ mice.

To investigate the possibility of pharmacologically enhancing the brain accumulation of temozolomide by inhibition of P-gp and BCRP we have used the dual P-gp/BCRP inhibitor elacridar. Elacridar significantly ($p = 0.001$) enhanced the brain penetration of temozolomide in WT mice when given at a single oral dose of 100 mg/kg, reaching similar levels as those achieved in *Abcb1a/b;Abcg2*$^{-/-}$ mice (**Figure 2C**). Moreover, no further significant enhancement in the brain penetration of temozolomide was seen when elacridar was given to *Abcb1a/b;Abcg2*$^{-/-}$ mice, demonstrating that the interaction by elacridar was selective for BCRP and P-gp. In contrast, gefitinib given at 100 mg/kg, did not significantly enhance the brain–plasma ratio of temozolomide (**Figure 2D**), even though a previous report suggested it to be a potent P-gp/BCRP inhibitor[24].

Temozolomide is orally administered to patients. Since both P-gp and BCRP may limit the oral bioavailability of substrate drugs, we have investigated the drug exposure of oral temozolomide in WT versus *Abcb1a/b;Abcg2*$^{-/-}$ mice using the dose that would be used in the subsequent *in vivo* efficacy study against intracranial xenografts (**Figure 3A**). While using relatively large cohorts of animals (WT n = 18, *Abcb1a/b;Abcg2*$^{-/-}$ n = 19) for sufficient statistical power, the plasma AUC

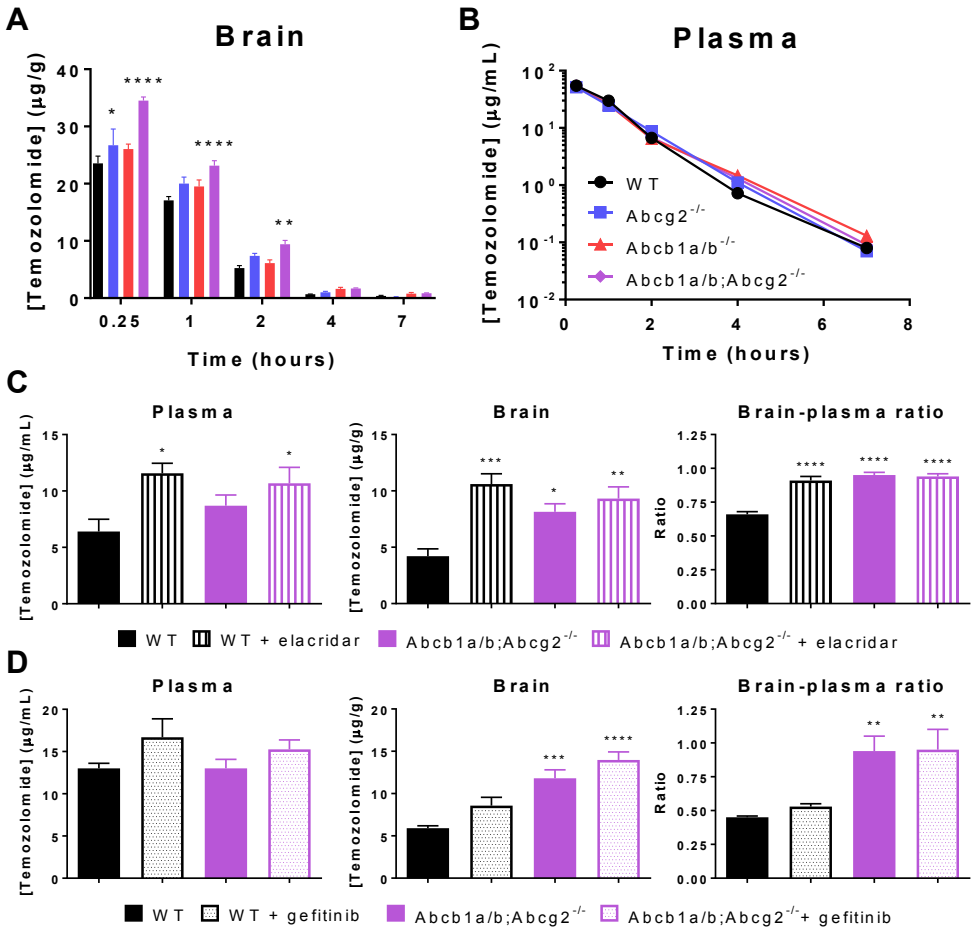

Figure 2 | The impact of Abcb1a/b and Abcg2 on the brain and plasma concentration of temozolomide after intravenous administration. (**A**) Brain and (**B**) plasma concentrations of temozolomide in wild-type (WT), *Abcg2*$^{-/-}$, *Abcb1a/b*$^{-/-}$ and *Abcb1a/b;Abcg2*$^{-/-}$ FVB mice that received 50 mg/kg of temozolomide by intravenous injection. Both *Abcg2*$^{-/-}$ and *Abcb1a/b*$^{-/-}$ mice accumulated 20% more temozolomide in the brain compared to WT mice, whereas *Abcb1a/b;Abcg2*$^{-/-}$ mice even accumulated 50% ($p < 0.001$) more drug in the brain. The absence of the drug transporters Abcb1a/b and Abcg2 did not affect the plasma levels (see also **Table 1**). Data are depicted as mean ± SE; n ≥ 7. (**C**) Elacridar (100 mg/kg) and (**D**) gefitinib (100 mg/kg) were orally administered to WT and *Abcb1a/b;Abcg2*$^{-/-}$ mice 2h (elacridar) or 1h (gefitinib) prior to intravenous temozolomide and blood and brain samples were collected 2h after temozolomide administration. Elacridar significantly enhanced the brain penetration (brain–plasma ratio) in WT mice ($p = 0.001$) to levels that were similar to those observed in *Abcb1a/b;Abcg2*$^{-/-}$ mice, whereas the brain–plasma ratio was not significantly different between *Abcb1a/b;Abcg2*$^{-/-}$ mice with or without elacridar. Administration of gefitinib did not result in a significantly enhanced brain penetration of temozolomide in WT mice. Data are depicted as mean ± SE; n = 5; * $p < 0.05$, ** $p < 0.01$, *** $p < 0.001$, **** $p < 0.0001$.

was not significantly different in *Abcb1a/b;Abcg2*$^{-/-}$ mice (**Table 2**). This result is in line with the almost complete oral bioavailability of temozolomide in C57BL x DBA/2 F1 mice that was previously reported by Stevens *et al.*[25]. Moreover, we neither could find any impact of elacridar on the plasma kinetics of oral temozolomide in brain tumor-bearing animals (**Figure 3B**).

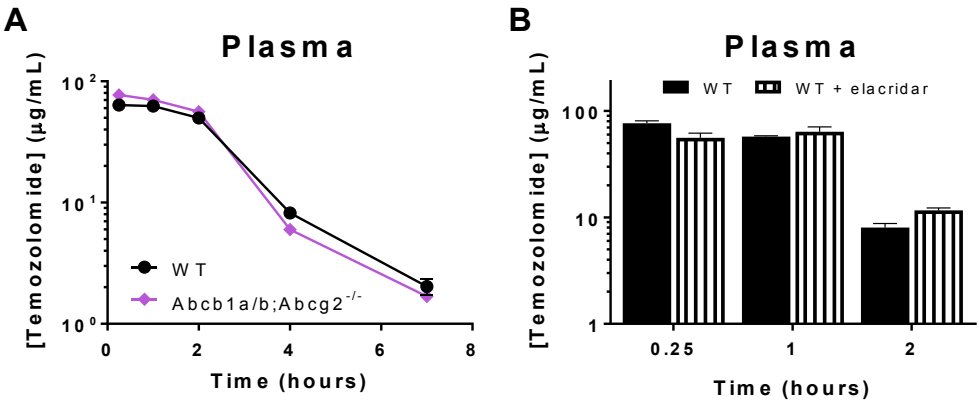

Figure 3 | Plasma concentration-time curves of orally administered temozolomide. (**A**) Temozolomide (100 mg/kg) was given orally to wild-type (WT) and *Abcb1a/b;Abcg2*$^{-/-}$ mice, after which serial blood samples were drawn from the tail vein at various time points. The plasma curves of temozolomide were similar in both mouse strains. Depicted are the curves of the mean ± SE concentrations; n ≥ 18. (**B**) Plasma levels of temozolomide in intracranial Mel57 tumor-bearing mice following oral temozolomide administration (100 mg/kg) with or without orally co-administered elacridar (100 mg/kg). Blood samples were collected from the tail vein of the mice used in the study depicted in **Figure 5B**. Elacridar did not significantly affect the plasma pharmacokinetics of orally given temozolomide. Data are depicted as mean ± SE; n = 8.

In vivo efficacy studies

To investigate the relevance of the higher brain penetration of temozolomide for treatment of intracranial tumors we performed *in vivo* efficacy studies in three different intracranial tumor mouse models. The first model mimicked melanoma brain metastases by stereotactically implanting Mel57 cells in the brains of recipient nude mice[20]. As a second model, we injected murine GSC457 glioma stem-cell like cells that were derived from the a spontaneous transgenic mouse model[26]. Lastly, we used this transgenic mouse model where tumors were induced by stereotactic injection of a Lenti–Cre vector in the brains of *Tp53*$^{F/F}$*;p16*^{Ink4a}*/p19*$^{ArfF/F}$*;LSL–K-ras*^{V12}*;Luc* mice. These mice spontaneously develop high-grade gliomas within a couple of weeks after vector injection.

Using gadolinium-DTPA magnetic resonance imaging (MRI), we have previously shown that the BBB in brain tumors from the Mel57 cell line is relatively intact, rendering this tumor model especially suited to explore the impact of the BBB on antitumor efficacy[20]. In contrast, the BBB integrity of the GSC457 and *Tp53*$^{-/-}$*;p16*^{Ink4a}*/p19*$^{Arf-/-}$*;K-ras*^{V12}*;Luc* glioma models appeared to more compromised, as indicated by the moderate contrast enhancement we observed on post-gadolinium T1-weighted MRI (**Figures 4A–B**). We further characterized the BBB integrity by i.v. injection of tumor-bearing mice with TexasRed just prior to brain tissue collection. TexasRed is a fluorescent small molecule compound with very little penetration into healthy brain tissue. TexasRed extravasation in our orthotopic brain tumor models is quite heterogeneous, with some regions of the tumors showing mild to moderate and other parts little to no extravasation (**Figures 4C–D**).

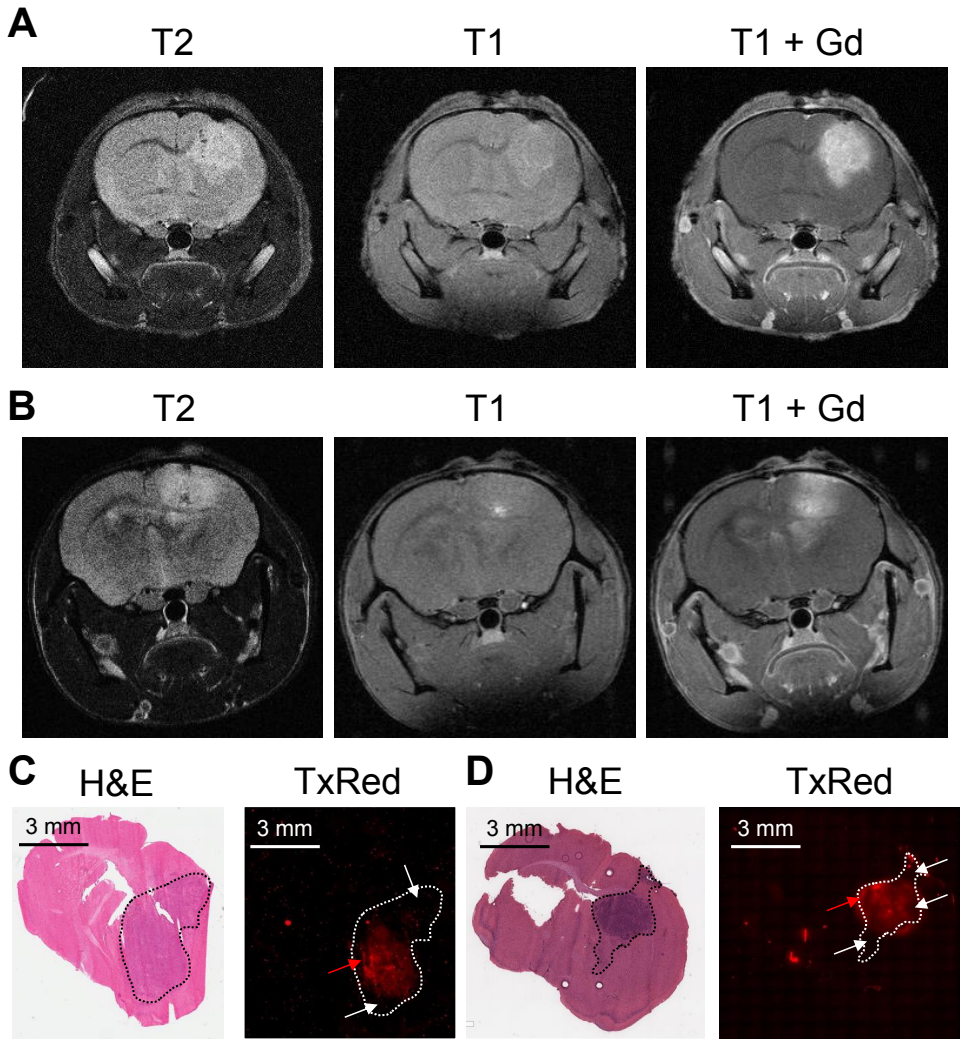

Figure 4 | Characterization of the blood-brain barrier integrity of the orthotopic murine glioma models. T2- and T1-weighted magnetic resonance imaging of orthotopic (**A**) GSC457 and (**B**) *Tp53*$^{-/-}$;*p16*^{Ink4a}/*p19*$^{Arf-/-}$;*K-ras*^{V12};*Luc* tumors. Some contrast enhancement was observed in both tumor models on T1-weighted images after gadolinium (Gd) administration. (**C**) GSC457 and (**D**) *Tp53*$^{-/-}$;*p16*^{Ink4a}/*p19*$^{Arf-/-}$;*K-ras*^{V12};*Luc* glioma-bearing wild-type mice received TexasRed shortly prior to being sacrificed. Comparison of the hematoxylin and eosin (H&E) staining with fluorescence microscopy of coronal brain sections revealed heterogeneous TexasRed (TxRed) extravasation in the tumor regions (dashed circumscribed area) of both models, with some regions showing moderate extravasation (red arrows) and others showing little to no extravasation (white arrows).

We first used Mel57 and employed two strategies to investigate the impact of P-gp and BCRP activity at the BBB on the efficacy of temozolomide, namely by administration of temozolomide to WT mice *vs.* genetic knockouts (*Abcb1a/b;Abcg2*$^{-/-}$ mice) and by using WT mice receiving temozolomide alone or in combination with elacridar; a pharmacological inhibitor of P-gp and BCRP. Interestingly, the modest efficacy of temozolomide against intracranial Mel57 tumors

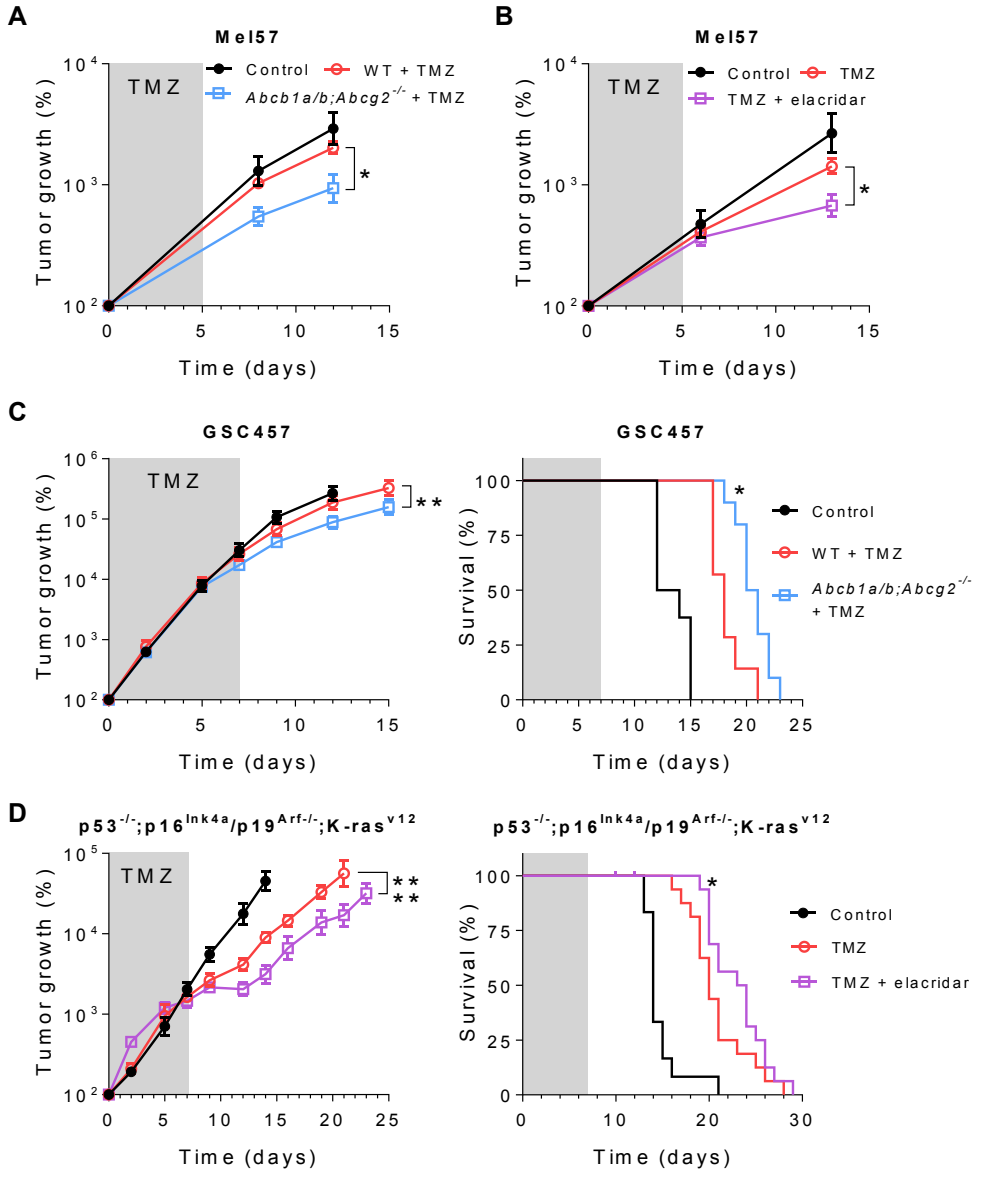

Figure 5. The impact of Abcb1a/b and Abcg2 on the efficacy of temozolomide against intracranial tumors. (**A**) The efficacy of temozolomide (TMZ) against intracranial Mel57–luc tumors in WT and *Abcb1a/b;Abcg2*$^{-/-}$ mice. A significantly better response to treatment with oral temozolomide (100 mg/kg/day x5) was observed in *Abcb1a/b;Abcg2*$^{-/-}$ mice compared to wild-type mice. Data are depicted as mean ± SE; n ≥ 6. (**B**) Intracranial Mel57–luc tumors treated with the combination of temozolomide (100 mg/kg/day x5) and elacridar (100 mg/kg/day x5) grew considerably slower in wild-type mice than tumors treated with temozolomide alone. Data are depicted as mean ± SE; n ≥ 3. (**C**) Wild-type and *Abcb1a/b;Abcg2*$^{-/-}$ mice were orthotopically grafted with GSC457 cells and monitored using *in vivo* bioluminescence imaging. Oral treatment with temozolomide (TMZ; 100 mg/kg/day x7) reduced tumor growth and significantly improved survival of *Abcb1a/b;Abcg2*$^{-/-}$ mice compared to wild-type mice. Data are depicted as mean ± SE; n ≥ 7. (**D**) Spontaneous *Tp53*$^{-/-}$*;p16*^{Ink4a}*/p19*$^{Arf-/-}$*;K-ras*^{V12}*;Luc* gliomas were induced in wild-type mice using a lenti–Cre vector. As is apparent from previously reported data[19], elacridar and temozolomide co-administration significantly reduced tumor growth and prolonged survival compared to TMZ monotherapy. Data are depicted as mean ± SE; n ≥ 11; * $p < 0.05$, ** $p < 0.01$, **** $p < 0.0001$.

grafted in WT mice was significantly higher when grafted in *Abcb1a/b;Abcg2*$^{-/-}$ mice (**Figure 5A**). Furthermore, Mel57 tumors grafted in WT responded significantly better when concomitantly treated with elacridar compared to temozolomide treatment alone (**Figure 5B**). These results suggest that P-gp and BCRP at the BBB at least partly attenuate the efficacy of temozolomide in the brain.

To confirm these findings, we compared the efficacy of temozolomide against the orthotopic GSC457 model grafted in WT and *Abcb1a/b;Abcg2*$^{-/-}$ mice. In this case, we compared the tumor growth and survival and also found that temozolomide treatment resulted in significantly slower tumor growth and longer survival in *Abcb1a/b;Abcg2*$^{-/-}$ mice compared to WT mice (**Figure 5C**).

Lastly, we re-assessed data from a previously published animal cohort and found further support for the notion that the efficacy of temozolomide is diminished by the BBB[19]. In this earlier study, we demonstrated the negative impact of P-gp and BCRP on the brain penetration and intracranial antitumor efficacy of the PARP inhibitor veliparib. However, the data in this study also demonstrate that chemical inhibition of P-gp and BCRP by elacridar improved the effects of single agent temozolomide on tumor growth and survival of the *Tp53*$^{-/-}$*;p16*^{Ink4a}*/p19*$^{Arf-/-}$*;K-ras*^{V12} spontaneous murine glioma model (**Figure 5D**).

Together, these studies demonstrate that P-gp and BCRP at the BBB diminish the efficacy of temozolomide against intracranial tumors and that concomitant inhibition of these transporters by elacridar can improve survival by counteracting this attenuation of temozolomide efficacy.

Genotype	$AUC_{0\text{-}7\ h,\ plasma}$ (μg/mL.h)
Wild-type	154.2 ± 4.1
Abcb1a/b;Abcg2$^{-/-}$	164.5 ± 4.5

Table 2 | Pharmacokinetic parameters of temozolomide after oral administration of 100 mg/kg. AUC, area under the plasma concentration–time curve. Data are represented as mean ± SE; n ≥ 18.

DISCUSSION

This study shows that the absence of both P-gp and Bcrp1 enhances the brain penetration of temozolomide by 1.5-fold without reducing the clearance of this drug. A similar effect on the brain penetration was seen in wild-type mice that received the dual P-gp and BCRP inhibitor elacridar. The increased brain penetration translated into a significantly better antitumor response in experimental intracranial tumor models. As temozolomide has proven activity against high-grade glioma, we expect that this further 1.5-fold gain in the brain penetration of this drug may further enhance the efficacy of temozolomide treatment. Moreover, since the systemic clearance

is not altered this enhanced efficacy may come without enhanced side effects. Consequently, our results provide a basis for further clinical testing of combinations of elacridar and temozolomide in patients suffering from high-grade glioma.

The finding that temozolomide is a substrate of P-gp was not obvious from the *in vitro* results. In contrast, temozolomide was clearly transported by Bcrp1 in our *in vitro* transport assay. Most likely, temozolomide is a relatively weak substrate of P-gp and the *in vitro* system is not sensitive enough to detect small changes in drug translocation. Moreover, the *in vitro* transport assay is also complicated by the instability of temozolomide in the transport medium that has a pH of 7.4. Because of this instability of temozolomide in transport medium, it is also not possible to calculate the permeability in moles per cm^2. But taking into account this instability, the finding that at least 5% of the donor concentration was recovered in the acceptor compartment after 30 minutes suggests that temozolomide readily permeates membranes, which is an important characteristic for a compound to be able to penetrate the BBB at all[27]. However, despite this relatively weak affinity for P-gp, the combined presence of P-gp and Bcrp1 at the BBB significantly reduces the brain penetration of temozolomide (**Figure 2A**). In contrast, we could not observe any effect of P-gp and BCRP on the oral bioavailability of temozolomide. As seen previously, drug efflux transporters appear to be much more capable of restricting the entry of substrate drugs into the brain than preventing uptake from the gut. For example, the substrate drug imatinib has an excellent oral bioavailability (>90%[28]), but a poor brain penetration that is significantly enhanced in *Abcb1a/b;Abcg2*$^{-/-}$ mice[29]. Similar discrepancies are seen for other drugs, including dabrafenib and regorafenib[30-32].

Many studies have demonstrated that the brain penetration of drugs, classic chemotherapeutics and novel targeted anticancer agents alike, can be substantially reduced by drug transporters at the BBB[5]. For example, we and others found a strikingly higher brain penetration of the chemotherapeutic paclitaxel (5-fold) and the small molecule CDK4/6 inhibitor palbociclib (approximately 15-fold) in *Abcb1a/b*$^{-/-}$ compared to WT controls[21,33,34]. In that perspective, the 1.5-fold (*i.e.*, 50%) enhancement of the brain penetration of temozolomide may appear less impressive. Importantly however, in contrast to these other agents, temozolomide is an agent with proven activity against high-grade glioma and in the clinical context a 50% higher drug level in tumor tissue could signify a clinically meaningful improvement of efficacy. Importantly, our proposed strategy of concomitantly inhibiting P-gp and BCRP would provide a 50% temozolomide dose-intensification specifically to the brain without enhancing the systemic exposure to this drug.

The improved BBB penetration of temozolomide translated into a better antitumor response in three different intracranial tumor models. This was not only the case when we used an intracranial Mel57 model that has a very tight BBB[20], but also with tumors that have leakier vasculature based

on MRI (**Figures 4A–B**). Importantly, the TexasRed extravasation data reported here demonstrates that both the GSC457 and the *Tp53*$^{-/-}$;*p16*^{Ink4a}/*p19*$^{Arf-/-}$;*K-ras*^{V12} spontaneous murine glioma model have a heterogeneous BBB integrity (**Figures 4C–D**). This heterogeneity is particularly clinically relevant. GBM contains regions where the BBB is disrupted due to VEGF-driven microvascular proliferation, but is also composed of tumor cells that deeply infiltrate into the surrounding brain tissue where the BBB is still functional. Especially this invasive component of the tumor renders this disease incurable by current treatment modalities. In order to target these invasive tumor cells, agents should be capable to penetrate the BBB.

Obviously, the finding that P-gp and BCRP attenuate the brain penetration and intracranial antitumor efficacy of temozolomide can only be exploited in patients when inhibitors of P-gp and BCRP are clinically available. Fortunately, the BBB penetration and antitumor efficacy of temozolomide was improved by using the dual P-gp/BCRP inhibitor elacridar. We have also tested several other proposed inhibitors of P-gp and BCRP, including the EGFR inhibitor gefitinib. However, even at a dose level of 100 mg/kg, which will results in plasma levels of about 10 μM[35], this compound was not able to increase the brain penetration of temozolomide. These results indicate that the capacity of gefitinib to inhibit Abcb1a/b and Abcg2 *in vivo* at the BBB is insufficient and discount gefitinib as a candidate for clinical testing, in particular because the plasma levels that can be achieved in patients are about 10-fold lower[36].

In general, pharmacological inhibition of P-gp and BCRP could present an interesting potential extra benefit. Whereas this study only focuses on the impact of P-gp and BCRP expression in the blood vessels building the BBB, it is known that GBM tumor cells may themselves also express these transporters, which may further contribute to the multidrug resistant phenotype of GBM[37]. Consequently, inhibition of P-gp and BCRP may also increase the sensitivity of tumor cells to temozolomide chemotherapy. We have previously observed this phenomenon when studying the PARP inhibitor veliparib against intracranial tumors in *Abcb1a/b;Abcg2*$^{-/-}$ mice[19]. Although these mice lack P-gp and BCRP at the BBB, the grafted tumors expressed these transporters and inhibition by elacridar enhanced the antitumor response.

Temozolomide has a good safety profile, with bone marrow toxicity as main dose-limiting toxicity[38]. Although the clearance of temozolomide was unaffected in mice that received concomitant elacridar, the combined use of temozolomide with P-gp and BCRP inhibitors may have an impact on the toxicity profile. Given that P-gp and BCRP are expressed in bone marrow stem cells[39,40], their inhibition in combination with the administration of a cytotoxic drug may enhance the myelotoxic effects. Obviously, the effect a P-gp/BCRP inhibitor on the toxicity of temozolomide needs to be monitored closely when such a combination is tested in a clinical trial.

In conclusion, we have demonstrated that the brain penetration and antitumor efficacy of

temozolomide is limited by P-gp and BCRP and can be increased by concomitant use of the dual P-gp/BCRP inhibitor elacridar. We expect that this combination may further enhance the efficacy of temozolomide against GBM, which should be explored in subsequent clinical trials.

REFERENCES

1. Sarkaria, J.N., *et al.* Is the blood–brain barrier really disrupted in all glioblastomas? A critical assessment of existing clinical data. *Neuro Oncol* **20**, 184-191 (2018).
2. van Tellingen, O., *et al.* Overcoming the blood-brain tumor barrier for effective glioblastoma treatment. *Drug Resist Updat* **19**, 1-12 (2015).
3. Pencheva, N., *et al.* Identification of a druggable pathway controlling glioblastoma invasiveness. *Cell Rep* **20**, 48-60 (2017).
4. Abbott, N.J., *et al.* Structure and function of the blood-brain barrier. *Neurobiol Dis* **37**, 13-25 (2010).
5. Durmus, S., *et al.* Apical ABC transporters and cancer chemotherapeutic drug disposition. *Adv Cancer Res* **125**, 1-41 (2015).
6. Schinkel, A.H. & Jonker, J.W. Mammalian drug efflux transporters of the ATP binding cassette (ABC) family: an overview. *Adv Drug Deliv Rev* **64**, 138-153 (2012).
7. Glioma Meta-analysis Trialists Group. Chemotherapy in adult high-grade glioma: a systematic review and meta-analysis of individual patient data from 12 randomised trials. *Lancet* **359**, 1011-1018 (2002).
8. Medical Research Council Brain Tumour Working Party. Randomized trial of procarbazine, lomustine, and vincristine in the adjuvant treatment of high-grade astrocytoma: a Medical Research Council trial. *J Clin Oncol* **19**, 509-518 (2001).
9. Brada, M., *et al.* Multicenter phase II trial of temozolomide in patients with glioblastoma multiforme at first relapse. *Ann Oncol* **12**, 259-266 (2001).
10. Yung, W.K.A., *et al.* A phase II study of temozolomide vs. procarbazine in patients with glioblastoma multiforme at first relapse. *Br J Cancer* **83**, 588-593 (2000).
11. Yung, W.K.A., *et al.* Multicenter phase II trial of temozolomide in patients with anaplastic astrocytoma or anaplastic oligoastrocytoma at first relapse. *J Clin Oncol* **17**, 2762-2771 (1999).
12. Stupp, R., *et al.* Effects of radiotherapy with concomitant and adjuvant temozolomide versus radiotherapy alone on survival in glioblastoma in a randomised phase III study: 5-year analysis of the EORTC-NCIC trial. *Lancet Oncol* **10**, 459-466 (2009).
13. Hegi, M.E., *et al.* MGMT gene silencing and benefit from temozolomide in glioblastoma. *N Engl J Med* **352**, 997-1003 (2005).
14. Weller, M., *et al.* EANO guideline for the diagnosis and treatment of anaplastic gliomas and glioblastoma. *Lancet Oncol* **15**, e395-e403 (2014).
15. Kim, H., *et al.* High-performance liquid chromatographic analysis and stability of anti-tumor agent temozolomide in human plasma. *J Pharm Biomed Anal* **24**, 461-468 (2001).
16. Schinkel, A.H., *et al.* Absence of the mdr1a P-glycoprotein in mice affects tissue distribution and pharmacokinetics of dexamethasone, digoxin, and cyclosporin A. *J Clin Invest* **96**, 1698-1705 (1995).
17. Jonker, J.W., *et al.* Role of breast cancer resistance protein in the bioavailability and fetal penetration of topotecan. *J Natl Cancer Inst* **92**, 1651-1656 (2000).
18. de Vries, N.A., *et al.* P-glycoprotein and breast cancer resistance protein: two dominant transporters working together in limiting the brain penetration of topotecan. *Clin Cancer Res* **13**, 6440-6449 (2007).
19. Lin, F., *et al.* ABCB1, ABCG2, and PTEN determine the response of glioblastoma to temozolomide and ABT-888 therapy. *Clin Cancer Res* **20**, 2703-2713 (2014).
20. Kemper, E.M., *et al.* Development of luciferase tagged brain tumour models in mice for chemotherapy intervention studies. *Eur J Cancer* **42**, 3294-3303 (2006).
21. Kemper, E.M., *et al.* Increased penetration of paclitaxel into the brain by inhibition of P-glycoprotein. *Clin Cancer Res* **9**, 2849-2855 (2003).
22. Zhang, P., *et al.* ABCB1 and ABCG2 restrict the brain penetration of a panel of novel EZH2-inhibitors. *Int J Cancer* **137**, 2007-2018 (2015).
23. Tsang, L.L.H., *et al.* Comparison of the cytotoxicity in vitro of temozolomide and dacarbazine, prodrugs of 3-methyl-(triazen-1-yl)imidazole-4-carboxamide. *Cancer Chemother Pharmacol* **27**, 342-346 (1991).
24. Yang, C.H., *et al.* Gefitinib reverses chemotherapy resistance in gefitinib-insensitive multidrug resistant cancer cells expressing ATP-binding cassette family protein. *Cancer Res* **65**, 6943-6949 (2005).
25. Stevens, M.F.G., *et al.* Antitumor activity and pharmacokinetics in mice of 8-carbamoyl-3-methyl-imidazo[5,1-*d*]-1,2,3,5-tetrazin-4(3*H*)-one (CCRG 81045; M & B 39831), a novel drug with potential as an alternative to dacarbazine. *Cancer Res* **47**, 5846-5852 (1987).
26. de Vries, N.A., *et al.* Rapid and robust transgenic high-grade glioma mouse models for therapy intervention studies. *Clin Cancer Res* **16**, 3431-3441 (2010).
27. Seelig, A. The role of size and charge for blood–brain barrier permeation of drugs and fatty acids. *J Mol Neurosci* **33**, 32-41 (2007).
28. Peng, B., *et al.* Absolute bioavailability of imatinib (Glivec®) orally versus intravenous infusion. *J Clin Pharmacol* **44**, 158-162 (2004).
29. Oostendorp, R.L., *et al.* The effect of P-gp (Mdr1a/1b), BCRP (Bcrp1) and P-gp/BCRP inhibitors on the in vivo absorption, distribution, metabolism and excretion of imatinib. *Invest New Drugs* **27**, 31-40 (2009).
30. Herbrink, M., *et al.* Variability in bioavailability of small molecular tyrosine kinase inhibitors. *Cancer Treat Rev* **41**, 412-422 (2015).
31. Mittapalli, R.K., *et al.* Mechanisms limiting distribution of the threonine-protein kinase B-RAFV600E inhibitor dabrafenib to the brain: implications for the treatment of melanoma brain metastases. *J Pharmacol Exp Ther* **344**, 655-664 (2012).
32. Kort, A., *et al.* Brain and testis accumulation of regorafenib is restricted by breast cancer resistance protein

(BCRP/ABCG2) and P-glycoprotein (P-gp/ABCB1). *Pharm Res* **32**, 2205-2216 (2015).
33. de Gooijer, M.C., *et al.* P-glycoprotein and breast cancer resistance protein restrict the brain penetration of the CDK4/6 inhibitor palbociclib. *Invest New Drugs* **33**, 1012-1019 (2015).
34. Parrish, K.E., *et al.* Efflux transporters at the blood-brain barrier limit delivery and efficacy of cyclin-dependent kinase 4/6 inhibitor palbociclib (PD-0332991) in an orthotopic brain tumor model. *J Pharmacol Exp Ther* **355**, 264-271 (2015).
35. Zhuang, Y., *et al.* Topotecan central nervous system penetration is altered by a tyrosine kinase inhibitor. *Cancer Res* **66**, 11305-11313 (2006).
36. Herbst, R.S., *et al.* Selective oral epidermal growth factor receptor tyrosine kinase inhibitor ZD1839 is generally well-tolerated and has activity in non–small-cell lung cancer and other solid tumors: results of a Phase I trial. *J Clin Oncol* **20**, 3815-3825 (2002).
37. Xavier, D., *et al.* Role of ABC transporters in the chemoresistance of human gliomas. *Curr Cancer Drug Targets* **6**, 433-445 (2006).
38. Mason, W.P. & Cairncross, J.G. Drug insight: temozolomide as a treatment for malignant glioma—impact of a recent trial. *Nat Clin Pract Neurol* **1**, 88-95 (2005).
39. Schinkel, A.H., *et al.* Normal viability and altered pharmacokinetics in mice lacking mdr1-type (drug-transporting) P-glycoproteins. *Proc Natl Acad Sci U S A* **94**, 4028-4033 (1997).
40. Zhou, S., *et al.* The ABC transporter Bcrp1/ABCG2 is expressed in a wide variety of stem cells and is a molecular determinant of the side-population phenotype. *Nat Med* **7**, 1028-1034 (2001).

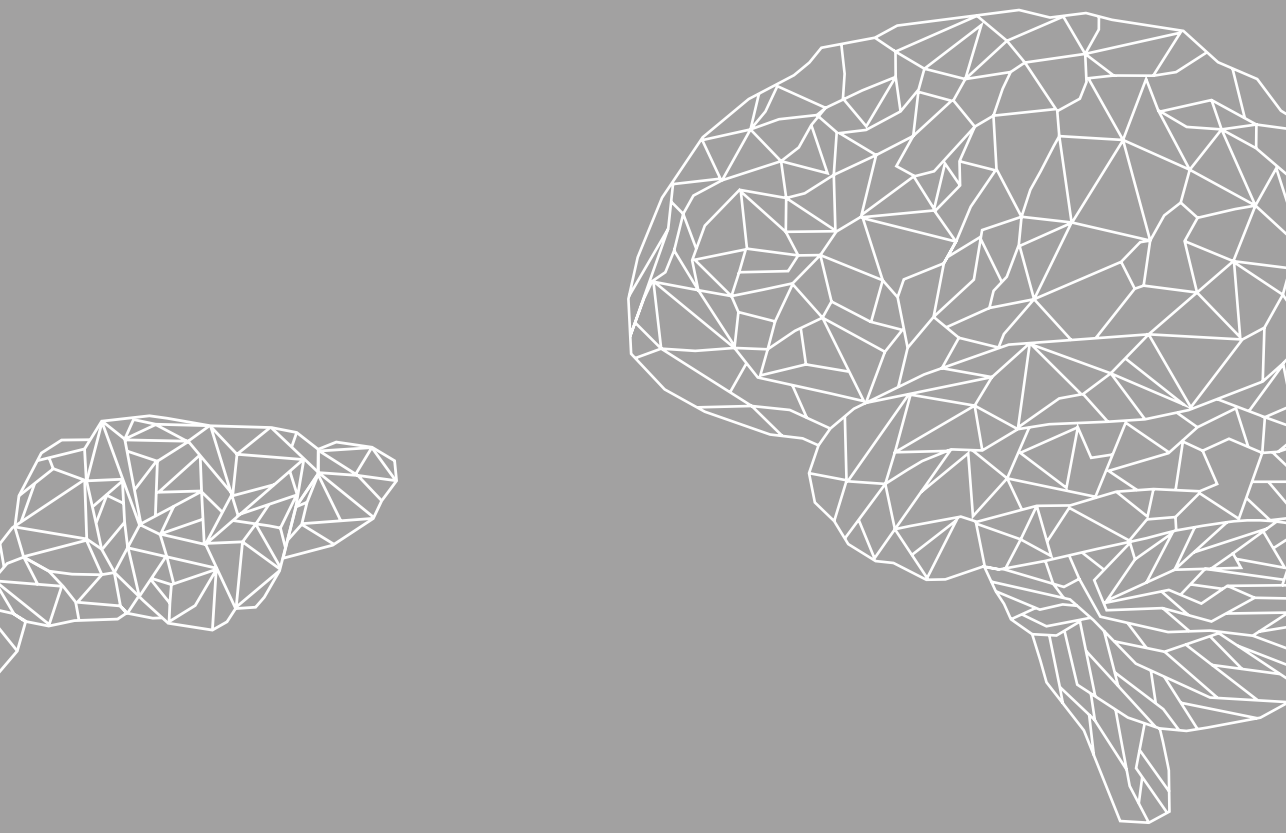

SECTION III

TARGETING THE PI3K PATHWAY: STOPPING GROWTH SIGNALING

Chapter 5

BUPARLISIB IS A BRAIN PENETRABLE PAN-PI3K INHIBITOR

M.C. de Gooijer, P. Zhang, L.C.M. Buil, C.H. Çitirikkaya, N. Thota, J.H. Beijnen, and O. van Tellingen

Scientific Reports. 2018;8(1):10784

ABSTRACT

Characterization of the genomic landscapes of intracranial tumors has revealed a clear role for the PI3K–AKT–mTOR pathway in tumorigenesis and tumor maintenance of these malignancies, making phosphatidylinositol 3-kinase (PI3K) inhibition a promising therapeutic strategy for these tumors. Buparlisib is a novel pan-PI3K inhibitor that is currently in clinical development for various cancers, including primary and secondary brain tumors. Importantly however, earlier studies have revealed that sufficient brain penetration is a prerequisite for antitumor efficacy against intracranial tumors. We therefore investigated the brain penetration of buparlisib using a comprehensive set of *in vitro* and *in vivo* mouse models. We demonstrate that buparlisib has an excellent brain penetration that is unaffected by efflux transporters at the blood–brain barrier, complete oral bioavailability and efficient intracranial target inhibition at clinically achievable plasma concentrations. Together, these characteristics make buparlisib the ideal candidate for intracranially-targeted therapeutic strategies that involve PI3K inhibition.

INTRODUCTION

Phosphatidylinositol 3-kinase (PI3K) is a key component of the PI3K–AKT–mTOR pathway and as such important for cell proliferation and survival[1]. The pivotal role of PI3K in this signaling makes it an attractive anticancer target, especially in tumors harboring an overactivated PI3K pathway[2]. Overactivation of the PI3K pathway is seen in many cancers, including primary intracranial cancers such as glioblastoma (GBM)[3], diffuse intrinsic pontine glioma[4] and pediatric high-grade glioma[4], and cancers that frequently metastasize to the brain such as cutaneous melanoma[5] and breast cancer[6]. PI3K inhibition has thus been proposed as a promising treatment strategy for various intracranial tumors[7-9].

We and others have previously demonstrated that modest efficacy of PI3K inhibition can be achieved in preclinical mouse models of glioblastoma and brain metastases, but only if the compound used to inhibit PI3K exhibits sufficient brain penetration[10-14]. Therefore, it is important to assess whether a PI3K inhibitor has sufficient brain penetration prior to starting its development for treatment of intracranial cancers.

The brain penetration of a small molecular compound is generally restricted by the blood–brain barrier (BBB), which is composed of the brain endothelial cells (BECs) that are being supported by astrocytes and pericytes[15]. BECs abundantly express ATP-binding cassette (ABC) efflux transporters on their apical membranes that very efficiently pump xenobiotics back into the bloodstream, thereby protecting the brain parenchyma from potentially harmful substances. Among these transporters, P-glycoprotein (P-gp) and breast cancer resistance protein (BCRP) are the most dominant. Together, these efflux transporters are responsible for restricting the brain penetration of many anticancer drugs, be it classical chemotherapeutics or novel targeted agents[16]. In line with this, almost all PI3K inhibitors that have been analyzed to date were demonstrated to be transported, ZSTK474 and GNE-317 appearing to be exceptions[12,13].

Buparlisib is a novel pan-PI3K inhibitor that has been developed to inhibit all class I PI3K isoforms[17]. It has shown preclinical efficacy in various PI3K pathway overactivated cancer models, including GBM[18-20]. Buparlisib has thus far proceeded through phase I and phase II clinical trials in various extracranial solid tumors[21,22] and is now also being tested in primary and secondary intracranial cancers (*e.g.*, ClinicalTrials.gov Identifiers NCT02000882, NCT02452294, NCT01339052).

Despite some reports mentioning that buparlisib is BBB penetrable[17,18,21,23], there are no pharmacokinetic data in the public domain supporting this claim. We here report a detailed analysis of the BBB penetration and oral bioavailability of buparlisib and demonstrate that it is a blood–brain barrier penetrable PI3K inhibitor with excellent oral bioavailability and intracranial target engagement.

METHODS

Drugs

Buparlisib (NVP-BKM120) and AZD8055 were purchased from Selleck Chemicals (Houston, TX) and zosuquidar from Eli Lilly (Indianapolis, IN). Elacridar was generously made available by GlaxoSmithKline (Research Triangle Park, NC).

Cell culture

All cell lines used in this study were previously generated in our institute and generously provided by dr. A.H. Schinkel[24-26]. All cells were cultured in MEM supplemented with 10% FBS, 1% L-glutamine, 1% sodium pyruvate, 1% MEM vitamins, 1% non-essential amino acids and 1% penicillin/streptomycin (all from Life Technologies; Carlsbad, CA) under 37 °C and 5% CO_2 conditions.

Concentration equilibrium transport assays

Conventional bidirectional transport assays (CTAs) and concentration equilibrium transport assays (CETAs) were performed as described previously[27]. Buparlisib was used at a concentration of 100 nM and, when appropriate, specific transport was inhibited using the P-gp inhibitor zosuquidar (5 μM) or the dual P-gp/BCRP inhibitor elacridar (5 μM). Transwell leakiness was determined as Carboxyl-[^{14}C]-inulin translocation exceeding 1.5% per hour and these wells were excluded from the analysis.

To prepare buparlisib transport assay samples for LC–MS/MS analysis, 10 μL medium samples were mixed with 30 μL of acetonitrile:formic acid (100:1 v/v). After centrifugation, the supernatant was 5-fold diluted in water and the buparlisib concentration was measured using an LC–MS/MS system as described below.

Animals

All animal housing and studies were approved by the Animal Experimental Committee of the Netherlands Cancer Institute and conducted according to national law and institutional guidelines. Mice were housed at 20.9 °C on a 12 hour light/dark cycle with food and water *ad libitum*.

Pharmacokinetic studies

The pharmacokinetics of buparlisib were analyzed in WT, *Abcg2*$^{-/-}$, *Abcb1a/b*$^{-/-}$ and *Abcb1a/*

b;Abcg2$^{-/-}$ FVB mice. All knockout mice strains have been developed within our institute[28-30]. For i.v. administration, buparlisib was dissolved in DMSO and injected at a dose of 2 mg/kg. For oral administration, buparlisib was formulated in DMSO:Cremophor EL:water (1:1:8 v/v/v) and administered at 1, 2 or 5 mg/kg as indicated. Tail vein bleeding was used to collect blood at intermediate time points, whereas at the last time point blood was drawn by cardiac puncture and various tissue were collected. Plasma was obtained from whole blood by centrifugation (5 min, 5,000 rpm, 4 °C). After weighing, tissues were homogenized using a FastPrep®-24 (MP Biomedicals; Santa Ana, CA) in 1% (w/v) bovine serum albumin in water. Buparlisib was extracted from plasma and tissue homogenate by liquid–liquid extraction with ethyl acetate using AZD8055 as an internal standard.

LC–MS/MS analysis

Buparlisib was measured in samples from *in vitro* transport assays and *in vivo* pharmacokinetic studies using an LC-MS/MS system comprised of an UltiMate 3000 LC Systems (Dionex; Sunnyvale, CA) and an API 4000 mass spectrometer (Sciex; Framingham, MA). Samples were run through a Securityguard C18 pre-column (Phenomenex; Utrecht, The Netherlands) prior to separation on a ZORBAX Extend-C18 column (Agilent; Santa Clara, CA). Elution was done using a in a 5 minute gradient from 20% to 95% B (mobile phase A was 0.1% HCOOH in water (v/v) and mobile phase B was methanol). 95% B was maintained for 3 min followed by re-equilibration at 20% B. Multiple reaction monitoring was performed at 411.3/367.2 (buparlisib) and 418.2/138.4 (AZD8055). Analyst® 1.6.2 software (AB Sciex; Foster City, CA) was used for system control and data analysis.

Western blotting

Mouse brains were homogenized in RIPA buffer supplemented with sodium fluoride (2 mM), sodium orthovanadate (1 mM), sodium pyrophosphate (1 mM), β-glycerophosphate (2.5 mM), PMSF (1 mM), DTT (1 mM) and protein inhibitor cocktail (Roche; Basel, Switzerland). The primary antibodies that were used in this study are phospho-Akt^{S473} (1:1000; D9E, #4060), total Akt (1:1000; #9272; both Cell Signaling Technology; Danvers, MA), phospho-Erk1$^{T202/204}$/Erk2$^{T183/Y185}$ (1:1000; sc-16982), total Erk1/2 (1:1000; C16, sc-93; both Santa Cruz Biotechnology, Santa Cruz, CA) and β–tubulin (1:1000; T3952; Sigma-Aldrich, St. Louis, MO). Goat-anti-rabbit-HRP (1:2000; DAKO, Glostrup, Denmark) was used a secondary antibody.

Pharmacokinetic and statistical analysis

As described in detail before, CETA results were analyzed with the General linear model repeated measures procedure of SPSS (v22; SPSS Inc; Chicago, IL)[27]. PK solver was used to determine pharmacokinetic parameters[31]. The standard error of the oral bioavailability was calculated using

the formula below:

$$SE_F = F\sqrt{\left(\frac{SE_{AUC_{p.o.}}}{AUC_{p.o.}}\right)^2 + \left(\frac{SE_{AUC_{i.v.}}}{AUC_{i.v.}}\right)^2}$$

Buparlisib concentrations in WT and transporter knockout mice *in vivo* were compared using one-way analysis of variance followed by *post hoc* Bonferroni tests. Statistical differences between the buparlisib PK parameters in male and female mice were calculated as Bonferroni corrected *p*-values using multiple Student's t-tests. Differences were considered statistically significant when $p < 0.05$.

RESULTS

Buparlisib is only very weakly transported by murine BCRP in vitro

We first sought to investigate whether buparlisib (**Figure 1A**) is transported by P-gp or BCRP *in vitro* using concentration equilibrium transport assays (CETAs). CETAs are sensitive assays to determine translocation over a cellular monolayer and are frequently used to determine substrate affinity for ABC transporters by comparing cell lines that overexpress ABC transporters with their parental counterparts[27,32,33]. Since P-gp and BCRP are apically located transporters, a prerequisite for detecting substrate affinity for these transporters in a CETA is the capacity of a molecule to penetrate cell membranes. We therefore first confirmed that buparlisib could efficiently diffuse over a cellular monolayer using a conventional transwell set-up. In this set-up, buparlisib plateaued to almost complete equilibrium between the apical and basal compartments within 4 hours, independent of the direction of diffusion (**Figure 1B**). This diffusion was studied in the parental LLC–PK1 cell line and in presence of the P-gp inhibitor zosuquidar to avoid any confounding effects of porcine P-gp on buparlisib diffusion.

Next, we studied buparlisib translocation in CETAs using cell lines that overexpress murine P-gp (Abcb1a/Mdr1a), murine BCRP (Abcg2/Bcrp1) or their human orthologs (ABCB1/MDR1, ABCG2). Only a minimal buparlisib translocation was observed in the MDCK–Bcrp1 CETA, whereas no translocation was found in any of the other CETAs, indicating that buparlisib is not a substrate of human P-gp, murine P-gp and human BCRP and a very weak substrate of murine BCRP (**Figure 1C**). Note that functionality of the cell lines was confirmed as these assays were also performed in parallel using other compounds that did show basolateral to apical translocation.

Buparlisib brain penetration is not restricted by P-gp and BCRP in vivo

To study whether P-gp and BCRP attenuate buparlisib brain penetration *in vivo*, we measured the

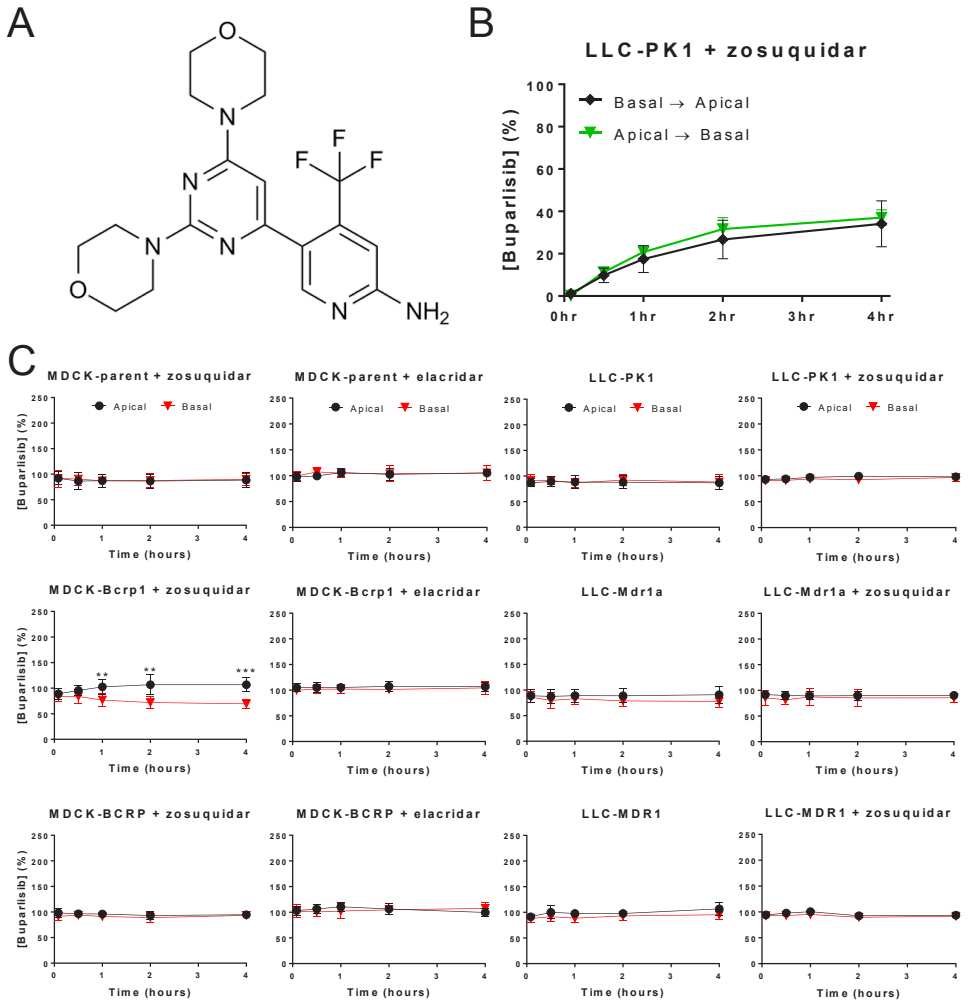

Figure 1 | Analysis of buparlisib substrate affinity for ABC transporters using *in vitro* transport assays. (**A**) The chemical structure of buparlisib. (**B**) A conventional transport assay (CTA) using LLC–PK1 cells in presence of zosuquidar to block endogenous (porcine) P-gp activity. Buparlisib efficiently diffuses over a cellular monolayer irrespective of direction, plateauing to near-equilibrium in 4 hours. (**C**) Concentration equilibrium transport assays (CETAs) using MDCK or LLC cells that overexpress murine BCRP, (Bcrp1), human BCRP, murine P-gp (Mdr1a) or human P-gp (MDR1). No substrate affinity of buparlisib for BCRP, Mdr1a or MDR1 could be observed, whereas very minimal buparlisib transport was found in the MDCK–Bcrp1 cell line. The P-gp inhibitor zosuquidar was used in all MDCK cell lines to inhibit endogenous P-gp activity and in LLC cell lines to validate possible P-gp-mediated translocations. The dual BCRP/P-gp inhibitor elacridar was used to confirm possible BCRP-mediated translocations by abolishing buparlisib translocation in presence of elacridar. Data are represented as mean ± SD (n ≥ 4); ** $p < 0.01$, *** $p < 0.001$.

brain and plasma concentration in wildtype (WT), *Abcg2*$^{-/-}$, *Abcb1a/b*$^{-/-}$ and *Abcb1a/b;Abcg2*$^{-/-}$ mice 1 hour after i.v. administration of 2 mg/kg buparlisib. No differences could be observed among the mouse strains in both the plasma and brain concentrations of buparlisib (**Figures 2A-B**). These results demonstrate that P-gp and BCRP do not restrict the brain penetration of buparlisib *in vivo*. Interestingly, the brain–plasma ratio was between 1.5 and 2 in all strains, indicating that

buparlisib exhibits excellent brain penetration (**Figure 2C**). Remarkably, the brain concentration of buparlisib was even slightly higher than the concentrations in other well-perfused organs that contain fenestrated endothelium such as the liver, kidney and spleen (**Figures 2D-F**).

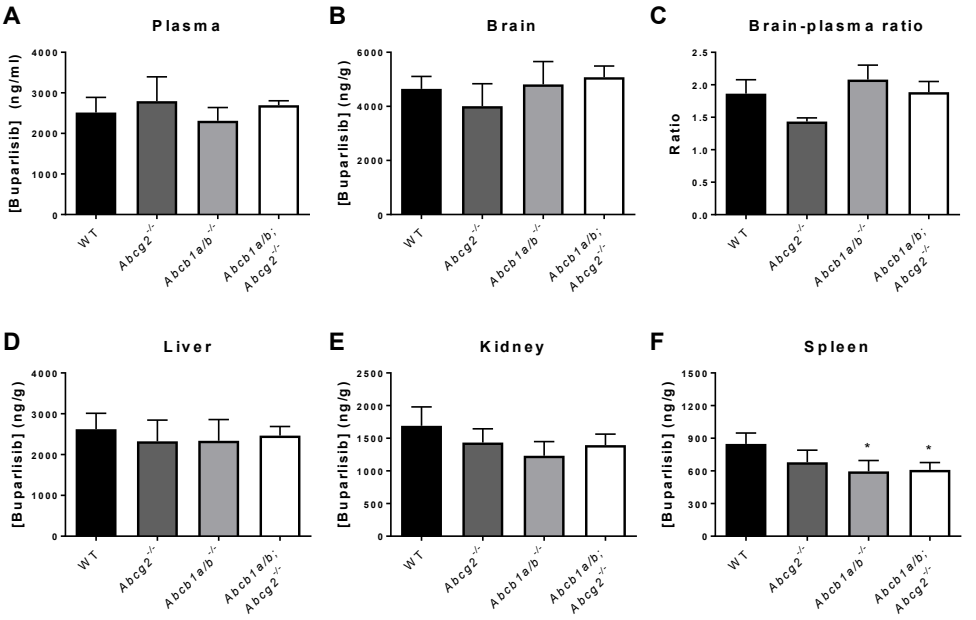

Figure 2 | The impact of P-gp and BCRP on the brain and tissue penetration of buparlisib. Buparlisib was administered intravenously to wildtype, *Abcg2*$^{-/-}$, *Abcb1a/b*$^{-/-}$ and *Abcb1a/b;Abcg2*$^{-/-}$ mice at a dose of 2 mg/kg. One hour after injection, blood and tissues were collected for LC–MS/MS analysis. No difference in buparlisib (**A**) plasma concentration, (**B**) brain concentration, (**C**) brain–plasma ratio, (**D**) liver concentration, (**E**) kidney concentration and (**F**) spleen concentration could be observed among the different mouse strains. All data are represented as mean ± SD (n = 4).

Buparlisib exhibits excellent oral bioavailability and achieves intracranial target inhibition

Buparlisib is given orally in both preclinical[19] and clinical studies[21], since it is claimed to have excellent oral bioavailability[17,18,21]. However, no data supporting this claim are available in the public domain. We therefore set out to determine the systemic exposure and brain concentrations after oral administration of buparlisib in mice.

First, we could confirm that buparlisib also achieves excellent brain penetration after oral administration, since the observed brain–plasma ratio in WT FVB mice was in line with those obtained following i.v. administration (**Figure 2C and Figure 3A**). Interestingly, a dose-proportional increase in plasma and brain concentrations was observed, yielding similar brain–plasma ratios at three different dose levels. Although we only measured one time point, these data suggest that buparlisib displays linear pharmacokinetics between the 1 mg/kg and 5 mg/kg dose levels in mice.

Next, we studied the intracranial pharmacodynamics of buparlisib in WT FVB mice as measured by target inhibition. Immunoblotting of brain lysates revealed that buparlisib dose-dependently decreased the phosphorylation of AKT, the main target of PI3K, without affecting signaling through ERK (**Figure 3B**). Importantly, efficient intracranial target inhibition could be reached in mice at clinically relevant plasma concentrations, since 5 mg/kg oral buparlisib resulted in plasma levels of approximately 1200 ng/mL (**Figure 3A**)[21].

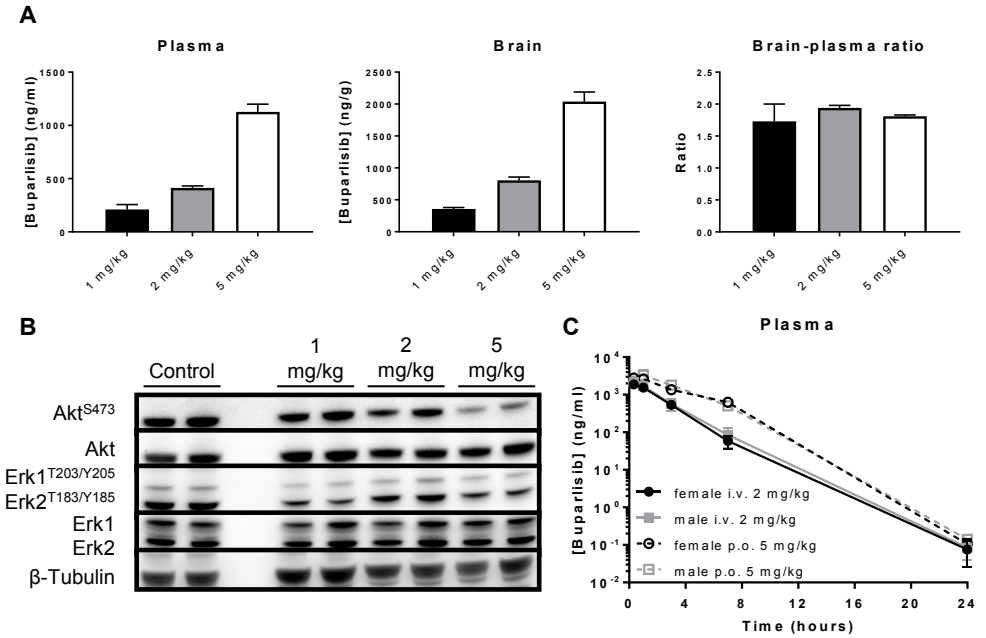

Figure 3 | Buparlisib has excellent intracranial target engagement and oral bioavailability. (**A**) Buparlisib was orally administered to wildtype mice at a dose of 1 mg/kg, 2 mg/kg or 5 mg/kg. One hour after injection, blood and tissues were collected for LC–MS/MS analysis. Buparlisib plasma and brain levels increase dose-dependently, yielding similar and excellent brain–plasma ratios at all dose levels that were tested. (**B**) Immunoblotting of brain tissue lysates from (**A**). Buparlisib efficiently inhibited phosphorylation of Akt^{S473} in the brains of wildtype mice following oral administration at a dose of 5 mg/kg, without affecting signaling through ERK. (**C**) Plasma–time curves of male and female wildtype mice following intravenous (2 mg/kg) or oral (5 mg/kg) administration. No differences could be observed in buparlisib plasma pharmacokinetics among both genders. The oral bioavailability of buparlisib is excellent, since oral and intravenous administration yielded similar dose-adjusted AUCs (see **Table 1**). All data are represented as mean ± SD (n = 4).

Finally, we studied the pharmacokinetics of buparlisib in male and female mice and assessed the oral bioavailability in both genders by comparing the area–under–the–plasma concentration–time–curves (AUCs) following intravenous and oral administration. Both after oral and i.v. administration there was no difference in pharmacokinetics between male and female mice (**Figure 3C and Table 1**). Strikingly, buparlisib displayed complete oral bioavailability since no difference in dose-corrected AUC could be observed between i.v. and oral administration in both genders. Interestingly, buparlisib exhibits a relatively small volume of distribution being less than

1 L/kg (**Table 1**), which is unusual for a small-molecule kinase inhibitor[34]. We therefore also assessed the buparlisib concentrations in a range of other tissues and indeed found that the levels were equal (liver) or even lower (kidney, spleen) than concurrent plasma levels (**Figures 2D-F**). Thus, the brain contains the highest concentration of all tissues included in this study, suggesting that buparlisib may be a very suitable PI3K inhibitor candidate for treatment of intracranial tumors.

Administration route	Parameter	Time (h)	Gender	
			female	male
i.v. (2 mg/kg)	Plasma AUC (ng/ml·h)	0-∞	5600 ± 860	6300 ± 1500
	C_{max} (ng/ml)		1900 ± 410	2100 ± 190
	$t_{1/2}$ (h)		1.60 ± 0.07	1.67 ± 0.07
	V_z (L/kg)		0.86 ± 0.14	0.80 ± 0.23
	CL (L/kg·h)		0.37 ± 0.06	0.33 ± 0.09
p.o. (5 mg/kg)	Plasma AUC (ng/ml·h)	0-∞	16000 ± 1700	16000 ± 1200
	C_{max} (ng/ml)		3000 ± 490	3300 ± 1300
	t_{max} (h)		0.67 ± 0.39	1.00 ± 0.00
	$t_{1/2}$ (h)		1.40 ± 0.04	1.44 ± 0.06
	F (%)		112 ± 21.1	103 ± 26.1
	V_z/F (L/kg)		0.63 ± 0.08	0.64 ± 0.03
	CL/F (L/kg·h)		0.32 ± 0.04	0.31 ± 0.02

Table 1 | Pharmacokinetic parameters of buparlisib after oral and i.v. administration to male and female FVB mice. AUC, area under the curve; C_{max}, maximum concentration in plasma; t_{max}, time to reach maximum plasma concentration; $t_{1/2}$, elimination half-life; V_z, apparent volume of distribution; CL, apparent clearance, F, oral bioavailability; V_z/F, apparent volume of distribution after oral administration; CL/F, apparent clearance after oral administration. Data are represented as mean ± SD (n = 4).

DISCUSSION

This study demonstrates that buparlisib has pharmacokinetic properties that make it an attractive candidate for treatment of intracranial malignancies in patients. The accumulation of buparlisib in the brain is higher than in most other organs and buparlisib inhibits PI3K in the brain at clinically achievable plasma concentrations.

Characterization of the genomic landscapes of intracranial tumors has revealed a clear role for the PI3K–AKT–mTOR pathway in tumorigenesis and tumor maintenance of these malignancies[3-6]. Further work also supports that PI3K pathway hyperactivated tumors are vulnerable to PI3K inhition[2,18-20]. Thus, targeting this pathway is expected to be a promising therapeutic strategy for these tumors. Importantly however, sufficient brain penetration of any therapeutic agent is a

prerequisite for antitumor efficacy against intracranial tumors[10-14,35].

The ability of a compound to access the brain is largely determined by two factors, namely the ability to diffuse over cellular membranes and the affinity for the drug efflux transporters P-gp and BCRP that are expressed at the BBB. Of all PI3K inhibitors that have thus far been reported, buparlisib shows by far the best brain penetration. The brain–plasma ratio ranges between 1.5 and 2 (**Figure 2C and Figure 3A**), whereas the brain–plasma ratio of several other PI3K inhibitors that are considered brain penetrable (NVP-BEZ235, ZSTK474 and GNE-317) do not exceed 1[12,13]. Importantly, the buparlisib brain concentration is also higher than in most other tissues, which is in line with the relatively low distribution volume of this drug (< 1 L/kg; **Table 1**)[34]. The reason why buparlisib distributes more to the brain than to other tissues is unclear, but could be related to more preferential protein binding in the brain or substrate affinity for uptake transporters that are present at the BBB. Regardless of the cause, this characteristic makes buparlisib a clear frontrunner among all PI3K inhibitors for development against intracranial tumors provided that the mouse mimics the human in this respect.

The plasma concentration–time profiles of buparlisib in mice and humans are very different. The peak plasma levels in humans receiving the maximum tolerated dose of buparlisib of 100 mg per day is about 1700 ng/ml (4.15 μM) and remains above 800 ng/ml (1.95 μM) for the remaining period of 24 h until the next dose[21]. By contrast, the peak plasma level in mice receiving 5 mg/kg is in the same range as in humans, but steeply declines to below 1 ng/ml (2.4 nM) after 24 h. Notably, a plasma concentration between 500 and 1000 nM was needed for inhibition of PI3K in the brain of WT mice (**Figure 3A**). Single agent antitumor efficacy in preclinical models has already been shown, but only at 30 to 50 mg/kg dose levels[17,18]. The lack of efficacy at lower doses is likely due to the short duration of pharmacologically active plasma levels. However, high dose levels will cause high and non-clinically relevant plasma levels during the first hours and create the risk that some of the profound single agent antitumor activities observed in mice are in fact due to off-target effects[36].

Thus far, only one PI3K inhibitor has received FDA approval. Idelalisib is a class I PI3Kδ inhibitor and has been approved as monotherapy for treatment of follicular lymphoma and small lymphocytic lymphoma[37]. Buparlisib inhibits all class I PI3K isoforms. Next to the canonical function of class I PI3Kα in regulating tumor cell proliferation and survival, roles for other class I PI3K isoforms in the immune system, including tumor-induced immune suppression, are emerging[38,39]. Thus, pan-PI3K inhibition may be advantageous for antitumor efficacy. Buparlisib is at an advanced stage of development, with several phase III trials underway in extracranial malignancies (*e.g.*, NCT01633060, NCT02756247) and phase II trials ongoing for primary and secondary intracranial tumors (*e.g.*, NCT02000882, NCT01339052).

There is a growing body of clinical and preclinical evidence that PI3K inhibitors used in combination with other drugs may even be more promising for broader antitumor efficacy[40]. For instance in orthotopic mouse models of glioblastoma, the efficacy of PI3K inhibition as monotherapy has previously been shown to be modest at best, even when sufficient brain penetration and intracranial target inhibition could be reached[12,13]. Several preclinical studies have already pinpointed interesting strategies for combination treatment involving buparlisib, for instance combination with a MEK inhibitor[41], Bcl-2 inhibitor[42] and CSF-1R inhibitor[43] in GBM or a Smo antagonist in medulloblastoma[44]. The finding that pharmacologically relevant plasma levels of buparlisib are achieved in patients warrants further clinical investigation of such combination therapies.

In summary, buparlisib is a pan-PI3K inhibitor with excellent brain penetration, complete oral bioavailability and efficient intracranial target inhibition at clinically achievable plasma concentrations, making it the attractive candidate for intracranially-targeted therapeutic strategies involving PI3K inhibition.

REFERENCES

1. Thorpe, L.M., *et al.* PI3K in cancer: divergent roles of isoforms, modes of activation and therapeutic targeting. *Nat Rev Cancer* **15**, 7-24 (2015).
2. Engelman, J.A. Targeting PI3K signalling in cancer: opportunities, challenges and limitations. *Nat Rev Cancer* **9**, 550-562 (2009).
3. Brennan, C.W., *et al.* The somatic genomic landscape of glioblastoma. *Cell* **155**, 462-477 (2013).
4. Mackay, A., *et al.* Integrated molecular meta-analysis of 1,000 pediatric high-grade and diffuse intrinsic pontine glioma. *Cancer Cell* **32**, 520-537.e525 (2017).
5. The Cancer Genome Atlas Network. Genomic classification of cutaneous melanoma. *Cell* **161**, 1681-1696 (2015).
6. The Cancer Genome Atlas Network. Comprehensive molecular portraits of human breast tumours. *Nature* **490**, 61-70 (2012).
7. Lin, F., *et al.* Targeting core (mutated) pathways of high-grade gliomas: challenges of intrinsic resistance and drug efflux. *CNS Oncol* **2**, 271-288 (2013).
8. Niessner, H., *et al.* PI3K pathway inhibition achieves potent antitumor activity in melanoma brain metastases *in vitro* and *in vivo*. *Clin Cancer Res* **22**, 5818-5828 (2016).
9. Ni, J., *et al.* Combination inhibition of PI3K and mTORC1 yields durable remissions in mice bearing orthotopic patient-derived xenografts of HER2-positive breast cancer brain metastases. *Nat Med* **22**, 723-726, (2016).
10. Heffron, T.P., *et al.* Discovery of clinical development candidate GDC-0084, a brain penetrant inhibitor of PI3K and mTOR. *ACS Med Chem Lett* **7**, 351-356 (2016).
11. Salphati, L., *et al.* Targeting the PI3K pathway in the brain—efficacy of a PI3K inhibitor optimized to cross the blood-brain barrier. *Clin Cancer Res* **18**, 6239-6248 (2012).
12. Lin, F., *et al.* PI3K–mTOR pathway inhibition exhibits efficacy against high-grade glioma in clinically relevant mouse models. *Clin Cancer Res* **23**, 1286-1298 (2017).
13. Becker, C.M., *et al.* Decreased affinity for efflux transporters increases brain penetrance and molecular targeting of a PI3K/mTOR inhibitor in a mouse model of glioblastoma. *Neuro Oncol* **17**, 1210-1219 (2015).
14. Osswald, M., *et al.* Impact of blood-brain barrier integrity on tumor growth and therapy response in brain metastases. *Clin Cancer Res* **22**, 6078-6087 (2016).
15. van Tellingen, O., *et al.* Overcoming the blood-brain tumor barrier for effective glioblastoma treatment. *Drug Resist Updat* **19**, 1-12 (2015).
16. Durmus, S., *et al.* Apical ABC transporters and cancer chemotherapeutic drug disposition. *Adv Cancer Res* **125**, 1-41 (2015).
17. Maira, S.M., *et al.* Identification and characterization of NVP-BKM120, an orally available pan-class I PI3-kinase inhibitor. *Mol Cancer Ther* **11**, 317-328 (2012).
18. Burger, M.T., *et al.* Identification of NVP-BKM120 as a potent, selective, orally bioavailable class I PI3 kinase inhibitor for treating cancer. *ACS Med Chem Lett* **2**, 774-779 (2011).
19. Koul, D., *et al.* Antitumor activity of NVP-BKM120—a selective pan class I PI3 kinase inhibitor showed differential forms of cell death based on p53 status of glioma cells. *Clin Cancer Res* **18**, 184-195 (2012).
20. Speranza, M.C., *et al.* BKM-120 (buparlisib): a phosphatidyl-inositol-3 kinase inhibitor with anti-invasive properties in glioblastoma. *Sci Rep* **6**, 20189 (2016).
21. Bendell, J.C., *et al.* Phase I, dose-escalation study of BKM120, an oral pan-class I PI3K inhibitor, in patients with advanced solid tumors. *J Clin Oncol* **30**, 282-290 (2011).
22. Soulières, D., *et al.* Buparlisib and paclitaxel in patients with platinum-pretreated recurrent or metastatic squamous cell carcinoma of the head and neck (BERIL-1): a randomised, double-blind, placebo-controlled phase

2 trial. *Lancet Oncol* **18**, 323-335 (2017).
23. Cho, C.F., *et al.* Blood-brain-barrier spheroids as an in vitro screening platform for brain-penetrating agents. *Nat Commun* **8**, 15623 (2017).
24. Schinkel, A.H., *et al.* Absence of the mdr1a P-glycoprotein in mice affects tissue distribution and pharmacokinetics of dexamethasone, digoxin, and cyclosporin A. *J Clin Invest* **96**, 1698-1705 (1995).
25. Jonker, J.W., *et al.* Role of breast cancer resistance protein in the bioavailability and fetal penetration of topotecan. *J Natl Cancer Inst* **92**, 1651-1656 (2000).
26. Pavek, P., *et al.* Human breast cancer resistance protein: interactions with steroid drugs, hormones, the dietary carcinogen 2-amino-1-methyl-6-phenylimidazo(4,5-*b*)pyridine, and transport of cimetidine. *J Pharmacol Exp Ther* **312**, 144-152 (2005).
27. Zhang, P., *et al.* ABCB1 and ABCG2 restrict the brain penetration of a panel of novel EZH2-inhibitors. *Int J Cancer* **137**, 2007-2018 (2015).
28. Schinkel, A.H. *et al.* Disruption of the mouse mdr1a P-glycoprotein gene leads to a deficiency in the blood-brain barrier and to increased sensitivity to drugs. *Cell* **77**, 491-502 (1994).
29. Jonker, J.W., *et al.* The breast cancer resistance protein protects against a major chlorophyll-derived dietary phototoxin and protoporphyria. *Proc Natl Acad Sci U S A* **99**, 15649-15654 (2002).
30. Jonker, J.W., *et al.* Contribution of the ABC transporters Bcrp1 and Mdr1a/1b to the side population phenotype in mammary gland and bone marrow of mice. *Stem Cells* **23**, 1059-1065 (2005).
31. Zhang, Y., *et al.* PKSolver: an add-in program for pharmacokinetic and pharmacodynamic data analysis in Microsoft Excel. *Comput Methods Programs Biomed* **99**, 306-314 (2010).
32. Luna-Tortós, C., *et al.* Several major antiepileptic drugs are substrates for human P-glycoprotein. *Neuropharmacology* **55**, 1364-1375 (2008).
33. Zhang, C., *et al. In vitro* transport profile of carbamazepine, oxcarbazepine, eslicarbazepine acetate, and their active metabolites by human P-glycoprotein. *Epilepsia* **52**, 1894-1904 (2011).
34. Di Gion, P., *et al.* Clinical pharmacokinetics of tyrosine kinase inhibitors. *Clin Pharmacokinet* **50**, 551-603 (2011).
35. Sarkaria, J.N., *et al.* Is the blood–brain barrier really disrupted in all glioblastomas? A critical assessment of existing clinical data. *Neuro Oncol* **20**, 184-191 (2018).
36. Brachmann, S.M., *et al.* Characterization of the mechanism of action of the pan class I PI3K inhibitor NVP-BKM120 across a broad range of concentrations. *Mol Cancer Ther* **11**, 1747-1757 (2012).
37. Miller, B.W., *et al.* FDA approval: idelalisib monotherapy for the treatment of patients with follicular lymphoma and small lymphocytic lymphoma. *Clin Cancer Res* **21**, 1525-1529 (2015).
38. Kaneda, M.M., *et al.* PI3Kγ is a molecular switch that controls immune suppression. *Nature* **539**, 437-442 (2016).
39. Uehara, M., *et al.* Regulation of T cell alloimmunity by PI3Kγ and PI3Kδ. *Nat Commun* **8**, 951 (2017).
40. Fruman, D.A. & Rommel, C. PI3K and cancer: lessons, challenges and opportunities. *Nat Rev Drug Discov* **13**, 140-156 (2014).
41. El Meskini, R., *et al.* A preclinical orthotopic model for glioblastoma recapitulates key features of human tumors and demonstrates sensitivity to a combination of MEK and PI3K pathway inhibitors. *Dis Model Mech* **8**, 45-56 (2014).
42. Jane, E.P., *et al.* Inhibition of phosphatidylinositol 3-kinase/AKT signaling by NVP-BKM120 promotes ABT-737-induced toxicity in a caspase-dependent manner through mitochondrial dysfunction and DNA damage response in established and primary cultured glioblastoma cells. *J Pharmacol Exp Ther* **350**, 22-35 (2014).
43. Quail, D.F., *et al.* The tumor microenvironment underlies acquired resistance to CSF-1R inhibition in gliomas. *Science* **352**, aad3018 (2016).
44. Buonamici, S., *et al.* Interfering with resistance to smoothened antagonists by inhibition of the PI3K pathway in medulloblastoma. *Sci Transl Med* **2**, 51ra70 (2010).

Chapter 6

PI3K-MTOR PATHWAY INHIBITION EXHIBITS EFFICACY AGAINST HIGH-GRADE GLIOMA IN CLINICALLY RELEVANT MOUSE MODELS

F. Lin*, M.C. de Gooijer*, D. Hanekamp,
G. Chandrasekaran, L.C.M. Buil, N. Thota, R.W. Sparidans,
J.H. Beijnen, T. Wurdinger, and O. van Tellingen

* These authors contributed equally

Clinical Cancer Research. 2017;23(5):1286-1298

ABSTRACT

Purpose: The PI3K–AKT–mTOR signaling pathway is frequently activated in glioblastoma (GBM) and offers several druggable targets. However, clinical efficacy of PI3K/mTOR inhibitors in GBM has not yet been demonstrated. Insufficient drug delivery may limit the efficacy of PI3K/mTOR inhibitors against GBM. The presence of the efflux transporters ABCB1/Abcb1 (P-glycoprotein, MDR1) and ABCG2/Abcg2 (BCRP) at the blood–brain barrier (BBB) restricts the brain penetration of many drugs. ***Experimental design:*** We used *in vitro* drug transport assays and performed pharmacokinetic/pharmacodynamic studies in wild-type and ABC transporter knockout mice. The efficacy of PI3K–mTOR inhibition was established using orthotopic allograft and genetically engineered spontaneous glioblastoma mouse models. ***Results:*** The mTOR inhibitors rapamycin and AZD8055 are substrates of ABCB1 whereas the dual PI3K/mTOR inhibitor NVP-BEZ235 and the PI3K inhibitor ZSTK474 are not. Moreover, ABCG2 transports NVP-BEZ235 and AZD8055 but not ZSTK474 or rapamycin. Concordantly, *Abcb1a/b;Abcg2*$^{-/-}$ mice revealed increased brain penetration of rapamycin (13-fold), AZD8055 (7.7-fold) and NVP-BEZ235 (4.5-fold) but not ZSTK474 relative to wild-type mice. Importantly, ABC transporters limited rapamycin brain penetration to sub-therapeutic levels, while the reduction in NVP-BEZ235 brain penetration did not prevent target inhibition. NVP-BEZ235 and ZSTK474 demonstrated antitumor efficacy with improved survival against U87 orthotopic gliomas, although the effect of ZSTK474 was more pronounced. Lastly, ZSTK474 prolonged overall survival in Cre–LoxP conditional transgenic *Pten*$^{F/F}$*;p16*^{Ink4a}*/p19*$^{ArfF/F}$*;K-Ras*^{V12}*;Luc* mice, mainly by delaying tumor onset. ***Conclusions:*** PI3K/mTOR inhibitors with weak affinities for ABC transporters can achieve target inhibition in brain tumors, but have modest single agent efficacy and combinations with BBB penetrable inhibitors of other activated pathways may be required.

Translational relevance: Glioblastomas are almost uniformly lethal central nervous system tumors and better treatments are desperately needed. Although GBMs frequently harbor an activated PI3K-pathway, clinical trials using PI3K-pathway inhibitors conducted thus far have failed. We demonstrate that the BBB is a major hurdle in GBM treatment, in particular due to ABCB1 and ABCG2 limiting the brain accumulation of many small molecule drugs. From a panel of PI3K-pathway inhibitors, we identified ZSTK474 as a BBB permeable candidate. At clinically relevant plasma levels ZSKT474 achieved target inhibition in orthotopic xenograft and transgenic glioma models. Antitumor efficacy was also observed albeit that the effect size was relatively modest. Our data suggest that BBB penetrable PI3K inhibitors may play a role in the treatment of GBM, but that single agent efficacy is modest, hence they may need to be used in combination with agents that inhibit other proliferation signals present in GBM tumor cells.

INTRODUCTION

Glioblastomas (GBM; WHO Grade IV) are the most common primary brain tumors with a median survival of only 15 months, despite intensive treatment including surgery and chemo-radiation. Common molecular alterations in GBM include overexpression of EGFR, PDGFR and cMET, activating mutations in *PI3K* and *EGFR* (*EGFRvIII*) and loss of function of PTEN by deletion or mutations[1,2]. These alterations lead to constitutive activation of PI3K and further downstream effectors such as mTOR (mammalian target of rapamycin), which are crucial for tumor cell growth, proliferation and survival[3]. Preclinical studies suggest that inhibition of this pathway results in either direct inhibition of tumor growth or in sensitizing cells to conventional chemotherapy and radiotherapy[4,5]. Activation of the PI3K–mTOR signaling pathway is a very common event in solid tumors, which triggered the development of numerous small molecule inhibitors. Although these PI3K inhibitors have been developed mainly for other more common solid tumors, they are now also being tested against GBM (*e.g.*, ClinicalTrials.gov Identifiers NCT01339052, NCT00085566, NCT01240460, NCT02430363, NCT01316809)[6]. Unfortunately, however, the outcomes of clinical studies with agents that target the PI3K pathway in GBM have been disappointing so far. The prototype mTOR inhibitor rapamycin (sirolimus) and its analogs (so called rapalogs) temsirolimus and everolimus were considered promising targeted agents for GBM, but a number of phase I and II trials applying them either as monotherapy or in combination with an EGFR inhibitor failed to demonstrate meaningful clinical efficacy in recurrent GBM[7,8]. Possible explanations for this lack of efficacy include a lack of mTORC2 inhibition by rapalogs[9], increased upstream signaling of AKT through negative feedback loops following mTOR inhibition[10,11], and *PTEN* status[12]. Although these events, which focus on PI3K–mTOR signaling itself, may have contributed to the failures, a frequently underappreciated but critical issue is the presence of the blood–brain barrier (BBB) that may have hampered drug delivery to tumor cells in quantities required to elicit a meaningful pharmacological response. Especially those GBM cells that escaped surgical resection due to their migration away from the tumor core into adjacent regions of the brain will be shielded by a more intact BBB[13,14].

It is well known that the intact BBB restricts the brain entry of the majority of xenobiotics by its unique structure[13]. In particular, the drug efflux transporters expressed at the BBB play a very important role in limiting the brain penetration of a wide variety of compounds including frequently used chemotherapeutics and novel targeted agents. Two well-established drug efflux transporters, ABCB1 (P-glycoprotein, P-gp, MDR1) and ABCG2 (breast cancer resistance protein, BCRP), are abundantly expressed in the human and murine BBB and restrict most newly developed kinase inhibitors such as erlotinib, lapatinib and palbociclib[15-17]. As a consequence, the usefulness of such agents in GBM treatment might be attenuated by an inadequate brain penetration.

In the present study, we have compared the affinity for ABCB1 and ABCG2 as well as their impacts

on brain penetration of the mTOR inhibitors rapamycin and AZD8055, the PI3K/mTOR inhibitor NVP-BEZ235 and the PI3K inhibitor ZSTK474. All these inhibitors are under investigation for treatment of GBM[18-20]. We have used the orthotopic U87 brain tumor model to evaluate the antitumor efficacy of the inhibitors and further investigated ZSTK474, being the PI3K inhibitor with the most favorable brain penetration, in a more clinically relevant transgenic GBM model[21].

METHODS

See also **Supplementary Methods**.

Reagents

The PI3K inhibitors rapamycin and ZSTK474 were purchased from LC Laboratories (Woburn, MA). NVP-BEZ235 was purchased from Selleck Chemicals (Houston, TX). AZD8055 was purchased from Active Biochem (Wan Chai, Hong Kong). These compounds were dissolved in dimethyl sulfoxide (DMSO; Sigma–Aldrich; St. Louis, MO) to yield 10 nM and 4 nM working solutions and were stored at 4 °C. Elacridar was kindly provided by GlaxoSmithKline (Research Triangle Park, NC). Zosuquidar (LY335979) was kindly provided by Eli Lilly (Indianapolis, IN). Modified Eagles medium (MEM), Opti-MEM reduced serum medium, HBSS (Hank's Balanced Salt Solution), L-glutamine, non-essential amino acids, MEM vitamins, penicillin–streptomycin, fetal calf serum, trypsin–EDTA and other reagents for cell culture were purchased from Invitrogen (Carlsbad, CA). All other chemicals were purchased from Merck (Darmstadt, Germany).

Cell lines

LLC and MDCK cell lines used for in vitro transport experiments (see below) have been generated in our institute. U87MG human glioma cells have been obtained from ATCC and have been transfected with luciferase in house to obtain clone U87lucB5. All cell lines have been cryopreserved in stocks and aliquots are thawed and used for a maximum period of about 45 days (10–15 passages). Mycoplasma testing and testing for absence of mouse pathogens of the stocks is performed by PCR. The human U87lucB5 line was last authenticated by STR analysis on January 2013 (Identicell, Denmark).

Animals

Mice were housed and handled according to institutional guidelines complying with Dutch legislation. All experiments with animals were approved by the animal experiment committee of the institute. The animals used for pharmacokinetics studies were female wild-type (WT), *Abcb1a/b*$^{-/-}$, *Abcg2*$^{-/-}$, and *Abcb1a/b;Abcg2*$^{-/-}$ mice of FVB genetic background, between 9 and

14 weeks of age. *p16^{Ink4a}/p19$^{ArfF/F}$;K-Ras^{V12};Luc*, *Pten$^{F/F}$;p16^{Ink4a}/p19$^{ArfF/F}$;K-Ras^{V12};Luc*, *Tp53$^{F/F}$;p16^{Ink4a}/p19$^{ArfF/F}$;K-Ras^{V12};Luc* and *Tp53$^{F/F}$;Pten;p16^{Ink4a}/p19$^{ArfF/F}$;K-Ras^{V12};Luc* conditional mice for generation of GBM cell lines and efficacy studies were genotyped as described previously[21]. The animals were kept in a temperature-controlled environment with a 12 h dark/ 12 h light cycle and received a standard diet (AM–II; Hope Farm B.B.; Woerden, The Netherlands) and acidified water *ad libitum*.

In vitro transport experiments

To determine whether rapamycin, AZD8055, NVP-BEZ235 and ZSTK474 are substrates of murine Abcb1a (Mdr1a), human ABCB1 (MDR1), murine Abcg2 and/or human ABCG2 we analyzed the translocation of these compounds in concentration equilibrium transport assays (CETAs) as previously described[22]. To this end, we used the parental LLC pig-kidney cell line (LLC–PK1) and sub-lines transduced with murine Abcb1a (LLC–Mdr1a) or human ABCB1 (LLC–MDR1) and the parental Madine–Darby Canine Kidney (MDCK) type II cell line (MDCK–parent) and murine Abcg2 (MDCK–Bcrp1) or human ABCG2 transduced sub-lines (MDCK–BCRP). Cells were seeded on Transwell microporous polycarbonate membrane filters (3.0 μm pore size, 24 mm diameter; Costar Corning; Corning, NY) at a density of 2×10^6 cells per well in 2 ml MEM medium. When confluency was reached, the transport experiment was started by replacing the drug free medium with Opti-MEM medium containing 0.5 μM Rapamycin, or MEM medium containing 1 μM AZD8055, 0.5 μM ZSTK474 or 0.5 μM NVP-BEZ235. Zosuquidar (5 μM) or Elacridar (5 μM) was added when appropriate to inhibit either Abcb1 alone or both Abcb1 and Abcg2 respectively. [^{14}C]-inulin (approximately 1.6×10^6 DPM/ml) was added to check the integrity of the membrane. Samples of 50 μl were taken at 30, 120, 180 and 240 min and used for drug analysis.

Colony formation assays

U87 human glioma cells were seeded in 24-well plates and exposed to various concentrations of NVP-BEZ235 or ZSTK474. Upon reaching confluency in the control wells, all cells were fixed and stained using a glutaraldehyde (6% v/v; Sigma-Aldrich) and crystal violet (0.5% w/v; Sigma-Aldrich) solution. Plates were imaged using a Chemi-Doc MP system (Bio-rad; Veenendaal, The Netherlands) and well confluency was measured using the ImageJ plugin ColonyArea as described elsewhere[23]. Curves were plotted, fitted with a 'log(inhibitor) vs. response - Variable slope (four parameters)' curve and IC_{50}s were determined using GraphPad Prism 5.01 (GraphPad Software, Inc.; La Jolla, CA).

Drug formulations

For pharmacokinetic studies, rapamycin was first dissolved in 100% ethanol and further diluted

in HBSS to yield a solution of 0.05 mg/ml. AZD8055 was dissolved in DMSO at a concentration of 10 mg/ml. For p.o. administration, ZSTK474 was mixed with water and sonicated, suspended in a mixture of hydroxypropyl methylcellulose (4%, v/v) and Tween 80 (polysorbate 80; 0.75%, v/v) to yield a drug suspension of 20 mg/ml. For i.v. administration, ZSTK474 was dissolved in DMSO to yield a solution of 10 mg/ml. NVP-BEZ235 was dissolved in DMSO to yield a solution of 5 mg/ml and further mixed with PEG400 to yield a solution of 1 mg/ml.

Plasma and brain pharmacokinetics

Rapamycin (1.5 mg/kg, i.p.), AZD8055 (10 mg/kg, i.v.), NVP-BEZ235 (10 mg/kg, p.o.) and ZSTK474 (10 mg/kg i.v.; 200 mg/kg p.o.) were administered to WT and *Abcb1a/b;Abcg2*$^{-/-}$ mice and/or *Abcb1a/b*$^{-/-}$ and *Abcg2*$^{-/-}$ mice. Elacridar, prepared as described earlier[24], was given p.o. at a dose of 100 mg/kg 15 min. prior to rapamycin. Blood sampling was performed either by collecting tail vein blood or by cardiac puncture at different time points. Brains were dissected after mice were sacrificed and were homogenized in 3 ml 1% (w/v) bovine serum albumin (BSA). Both plasma and brain homogenates were stored at −20 °C until analysis.

Drug analytical method

Rapamycin (MRM 936.6/409.2) was measured using LC–ESI–MS/MS with tacrolimus (826.5/616.2) as internal standard and protein precipitation with methanol for sample pretreatment. Samples of 5 µl were injected onto an Atlantis dC18 column (Waters, Milford) coupled with a Polaris 3 C18-A pre-column (Varian; Middelburg, The Netherlands). The gradient elution of methanol ranged from 65% to 100% (v/v) in 1% (v/v) formic acid. Spray voltage was set to 3900 V, capillary temperature to a 400 °C and argon collision pressure to 2.0 mTorr. Collision energies were at 54 and 36 V, respectively.

AZD8055 (MRM 466.4/450.3) was measured using LC–ESI–MS/MS with buparlisib (411.3/367.2) as internal standard and ethyl acetate extraction as sample pretreatment. Samples of 50 µl were injected onto an Agilent C18 column (Santa Clara, CA) coupled with a Phenomenex analytical securityguard C18 pre-column (Utrecht, The Netherlands). The gradient elution of methanol ranged from 65% to 100% (v/v) in 0.1% (v/v) formic acid. Declustering potential was 100 V and collision energy 59 eV.

For quantification of ZSTK474 in plasma and brain samples, a reversed-phase high-performance liquid chromatographic (HPLC) assay with fluorometric detection was used. Following tert-butyl methyl ether extraction, ZSTK474 and its internal standard NVP-BEZ235 were chromatographically separated using XBridge BEH130 C18 column (Waters) by isocratic elution with a mobile phase which consisted of acetonitrile, and 0.1% triethylamine adjusted with hydrochloric acid to pH 9.5

(50:50, v/v). Fluorescence detection was used with excitation and emission wavelengths of 240 and 425 nm, respectively. NVP-BEZ235 concentration in biological samples was measured using an HPLC assay as described previously[25].

Stereotactic intracranial injections and bioluminescence imaging

The detailed procedures of stereotactic intracranial injection and bioluminescence imaging have been described previously[26]. In short, FVB nude mice or *p16^{Ink4a}/p19$^{ArfF/F}$;K-Ras^{V12};Luc*, *Pten$^{F/F}$;p16^{Ink4a}/p19$^{ArfF/F}$;K-Ras^{V12};Luc*, *Tp53$^{F/F}$;p16^{Ink4a}/p19$^{ArfF/F}$;K-Ras^{V12};Luc* or *Tp53$^{F/F}$;Pten$^{F/F}$;p16^{Ink4a}/p19$^{ArfF/F}$;K-Ras^{V12};Luc* mice were anaesthetized and placed in a stereotactic frame, 10^5 U87–luc cells or CMV–Cre lentivirus suspension in 2 µl was injected 2 mm lateral and 1 mm anterior to the bregma, 3 mm below the skull cap. After the initial tumor load was established, tumor development was monitored by bioluminescence using the IVIS 200 Imaging system (PerkinElmer; Waltham, MA). Mice were sacrificed when clear neurological symptoms occurred or weight loss (≥ 20%) was observed. Brain tissue was fixed in an ethanol-glacial acetic acid mixture containing 4% formaldehyde (EAF), embedded in paraffin and cut into coronal slices of 4 µm. Sections were hematoxylin & eosin (H&E) stained for verification of tumor growth.

Glioma mouse models intervention study

For the U87 xenograft model drug intervention study, animals were stratified based on bioluminescence signal at day 12 after tumor cell injection into three groups receiving daily vehicle control solution (p.o. 200 µl saline per mouse), NVP-BEZ235 (p.o. 10 mg/kg) or ZSTK474 (p.o. 200 mg/kg), respectively, until the day of sacrifice. For the spontaneous GBM model drug intervention study, animals received a dose of 200 mg/kg q.d. of ZSTK474, starting 3 days after lentiviral injection until the day of sacrifice.

Histology and Immunohistochemistry

Brain tissue was fixed in 4% formaldehyde; paraffin embedded and cut into 4 µm coronal sections that were stained with H&E and for pAKT (D9E), pERK (D13.14.4E) and p4EBP1 (236B4; all Cell Signaling Technology; Danvers, MA).

Pharmacokinetic calculations and statistical analysis

As previously described, the General Linear Model repeated measures procedure was used to determine whether the basolateral-to-apical differences of the drugs levels were significantly increased by the factor of time and at which time point(s) these differences became significant[27]. For *in vivo* pharmacokinetic experiments, pharmacokinetic parameters were calculated using an

add-in program for Microsoft Excel PKSolver[28]. To determine the differences of brain and plasma concentrations among multiple strains, one-way analysis of variance (ANOVA) with Bonferroni post-hoc test was performed. Differences were considered statistically significant when $p < 0.05$. For *in vivo* efficacy studies, survival fractions were calculated using Kaplan–Meier method using GraphPad Prism 5.01 (GraphPad Software). The log–rank test was used to compare survival of groups.

RESULTS

Abcb1 severely impairs the brain penetration of rapamycin

To determine substrate affinity of rapamycin for Abcb1a (Mdr1a) and Abcg2 (Bcrp1), a concentration equilibrium transport assay (CETA) was performed using murine Mdr1a and Bcrp1 transduced cells and their parental cell lines as previously described[29]. Rapamycin was significantly translocated from the basolateral to apical (B-to-A) compartment by LLC–PK1 cells (**Figure 1A**). Endogenously expressed porcine Abcb1 was responsible for this translocation, as translocation was abrogated when the specific Abcb1 inhibitor zosuquidar was added. Rapamycin B-to-A translocation in Abcb1a overexpressing LLC–Mdr1a cells was more pronounced than in LLC–PK1 cells and was also completely inhibited by zosuquidar., showing that rapamycin is a good Abcb1 substrate. In contrast, rapamycin is not a substrate of Abcg2 since no B-to-A translocation was observed in Bcrp1-overexpressing MDCK cells (MDCK–Bcrp1).

Next, we assessed the impact of Abcb1 and Abcg2 on rapamycin pharmacokinetics using WT, *Abcb1a/b*$^{-/-}$, *Abcg2*$^{-/-}$ and *Abcb1a/b;Abcg2*$^{-/-}$ mice. Surprisingly, administration of 1.5 mg/kg rapamycin p.o. resulted in 35 to 52-fold higher AUC_{blood} values in all different knockout mice compared to WT mice (**Figure 1B**). However, no differences in rapamycin levels between WT and knockout mice were found in well perfused organs such as the kidney or liver, where drug levels are usually well equilibrated with systemic blood levels. In the brain, Abcb1 is clearly a dominant factor because the brain AUC of rapamycin in *Abcb1a/b*$^{-/-}$ mice was at least 10-fold higher than in WT mice. The levels in brain samples of WT mice were below the lower limit of quantification (LLQ) of the assay (10 ng/g), whereas the levels in brain samples from *Abcg2*$^{-/-}$ mice taken at the earlier time points were above the LLQ (**Figure 1B**), This is most likely due to the presence of some remnant blood in the homogenized brain tissue and the much higher blood levels of rapamycin in this strain. No significant difference was found between the *Abcb1a/b*$^{-/-}$ and *Abcb1a/b;Abcg2*$^{-/-}$ mice, suggesting Abcg2 is not involved in restricting rapamycin from the brain.

To further investigate if Abcb1- and/or Abcg2-mediated transport is responsible for the differences of plasma and brain levels between WT and knockout mice, the dual Abcb1 and Abcg2 inhibitor elacridar was co-administrated to WT mice 30 min prior to i.p. administration of rapamycin.

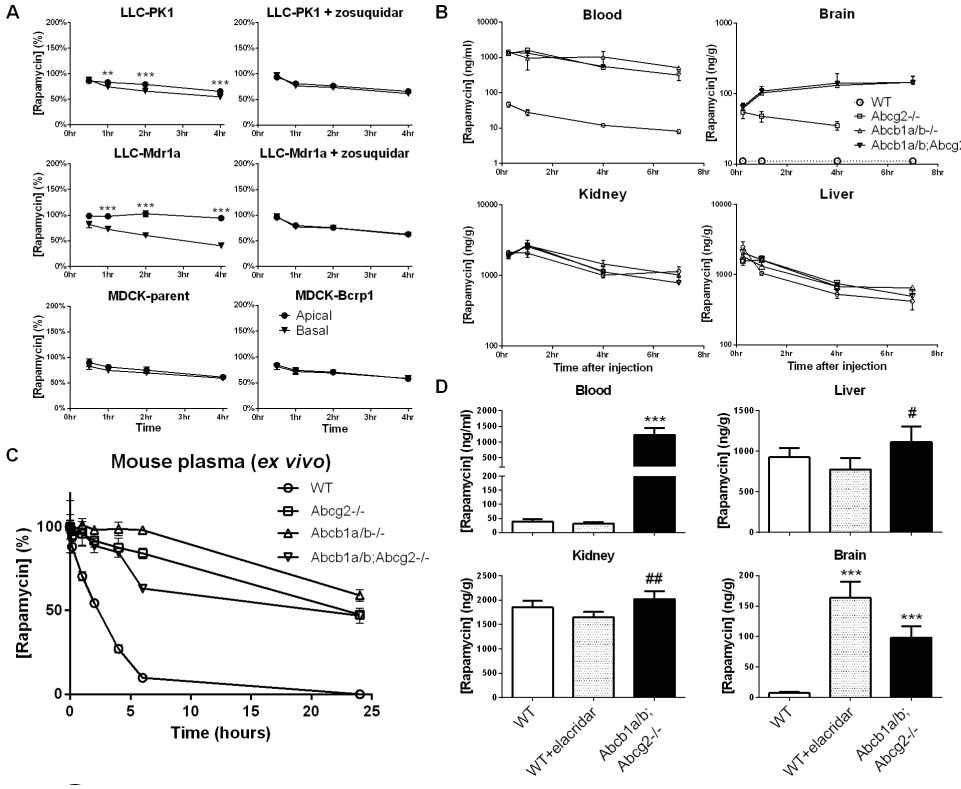

Figure 1 | *In vitro* transport, *in vivo* pharmacokinetics and *ex vivo* stability of rapamycin. (**A**) Concentration equilibrium transport assays (CETA) for rapamycin using Mdr1a and Bcrp1 overexpressing cell lines and their parental counterparts (LLC–PK1 and MDCK–parent, respectively). In CETA, the same drug solution is added to both compartments and this concentration is designated 100%. Zosuquidar (5 μM) was used to specifically inhibit P-gp mediated transport. Data are means ± SD; n = 6; ** $p < 0.01$, *** $p < 0.001$. (**B**) Rapamycin levels in blood, brain, kidney and liver of WT, *Abcb1a/b*$^{-/-}$, *Abcg2*$^{-/-}$ and *Abcb1a/b;Abcg2*$^{-/-}$ mice following i.p. administration of 1.5 mg/kg rapamycin. Data are means ± SD; n = 3–4. (**C**) Effect of elacridar on rapamycin levels in blood, brain, kidney and liver of WT mice and *Abcb1a/b;Abcg2*$^{-/-}$ mice receiving rapamycin alone. 100 mg/kg elacridar was p.o. administered to WT mice 15 min prior to rapamycin (1.5 mg/kg i.p.) administration and samples were taken at 1 h after rapamycin. Data are means ± SD; n = 5; *** $p < 0.001$, compared to WT mice without elacridar; $^{\#}p < 0.05$, $^{\#\#}p < 0.01$, compared with WT mice with elacridar. (**D**) *Ex vivo* stability of rapamycin at 37 °C in plasma of WT, *Abcb1a/b*$^{-/-}$, *Abcg2*$^{-/-}$, and *Abcb1a/b*$^{-/-}$*;Abcg2*$^{-/-}$ mice. Data are means ± SD; n = 3.

Moreover, the LC–MS/MS assay was adapted to improve the LLQ and allow accurate quantification in brain samples of WT mice. Interestingly, elacridar enhanced the brain concentration of rapamycin in WT mice by about 23-fold, but did not cause any alteration of rapamycin levels in blood and kidney, indicating that Abcb1a/b and Abcg2 are not responsible for the differences observed in blood of knockout mice (**Figure 1C**). Together, these results demonstrate that Abcb1 at the BBB profoundly impairs the brain penetration of rapamycin.

It has previously been reported that rapamycin is unstable in plasma and whole blood of human, rabbit and rat[30]. In contrast to plasma, rapamycin levels in the kidney and liver in our study were

not different between WT and knockout mice. Therefore we tested the stability of rapamycin in murine plasma *ex vivo* and indeed found a much more rapid degradation in plasma of WT compared to ABC transporter knockout mice. After 6 h incubation of rapamycin with freshly collected plasma from mice of different knockout strains, we observed that about 85% of the added rapamycin was recovered in plasma of *Abcb1a/b*$^{-/-}$, *Abcg2*$^{-/-}$ and *Abcb1a/b;Abcg2*$^{-/-}$ mice, but about 10% in plasma of WT mice (**Figure 1D**). Recent work with rapamycin's analog everolimus has demonstrated that carboxyl esterase 1c is more abundantly present in ABC transporter knockout mice and responsible for enhanced stability in plasma[31]. It is very likely that the higher blood level of rapamycin in knockout mice is similarly caused by avid binding of rapamycin to a serum factor, possibly Ces1c, which is more abundantly present in plasma of knockout mice. Due to this avid binding, only a small fraction of rapamycin is available for degradation and for tissue distribution.

Abcb1 and Abcg2 restrict AZD8055 brain penetration

AZD8055 was transported *in vitro* by human and murine MDR1/Mdr1a and BCRP/Bcrp1 (**Figure 2A**). B-to-A translocation was observed in CETAs with Abcb1a, ABCB1, Abcg2 and ABCG2 overexpressing cell lines but not parental control lines. Inhibition with zosuquidar or elacridar diminished translocation in all cases and validated AZD8055 transport by MDR1/Mdr1a and BCRP, although Bcrp1 mediated translocation was not completely inhibited by elacridar, indicative of very efficient transport.

Compared to WT mice, the AZD8055 brain concentrations were 3.7- ($p < 0.01$) and 7.7-fold ($p < 0.0001$) higher in *Abcb1a/b*$^{-/-}$ and *Abcb1a/b;Abcg2*$^{-/-}$ mice, respectively (**Figure 2B**), whereas the levels in liver and kidney were not different (not shown). Interestingly, a similar plasma retention effect in ABC transporter knockout mice was found as observed for rapamycin albeit that the effect size was much more modest. Consequently, the brain-plasma ratios do not correctly reflect AZD8055 brain penetration in WT mice vs. the knockout mice. However, the increased ratio in *Abcb1a/b;Abcg2*$^{-/-}$ mice in comparison to each of the single knockout strains clearly demonstrates that both Abcb1a/b and Abcg2 restrict the BBB penetration of AZD8055.

NVP-BEZ235 is a substrate of Abcg2 but its brain penetration is mainly limited by Abcb1

Using *in vitro* CETAs, neither LLC–PK1, LLC–Mdr1a nor LLC–MDR1 cells displayed significant basolateral to apical translocation of NVP-BEZ235, suggesting that NVP-BEZ235 is not transported by murine or human Abcb1/ABCB1 (**Figure 3A**). In contrast, NVP-BEZ235 was significantly translocated by MDCK–Bcrp1 cells but not MDCK-parent or MDCK-BCRP cells, and this translocation was inhibited by elacridar, indicating that NVP-BEZ235 is transported by murine Abcg2 but not human ABCG2 .

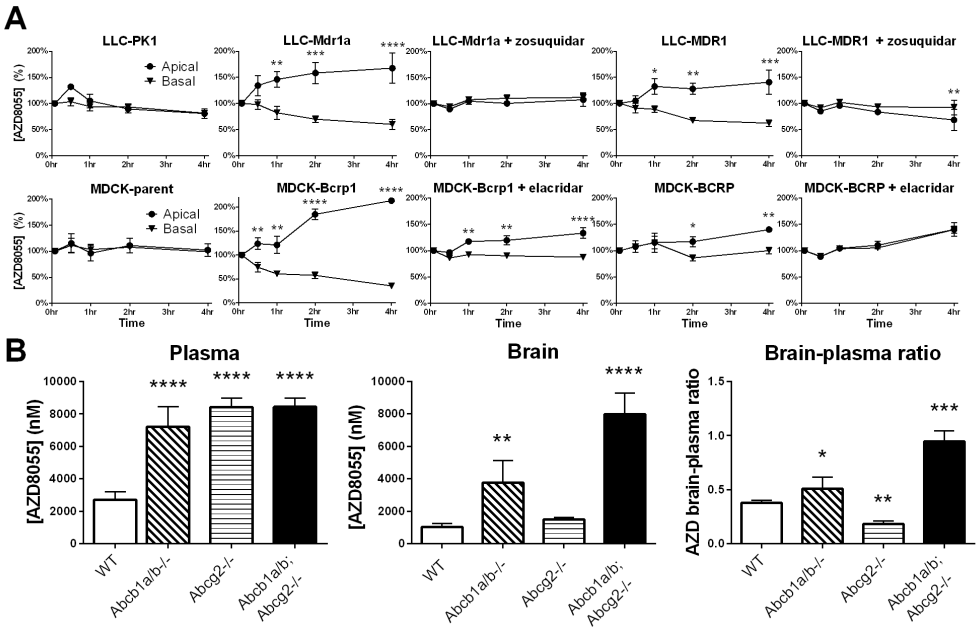

Figure 2 | *In vitro* transport and *in vivo* pharmacokinetics of AZD8055. (**A**) Concentration equilibrium transport assays for AZD8055 using Mdr1a/MDR1 and Bcrp1/BCRP overexpressing cell lines and their parental counterparts (LLC–PK1 and MDCK–parent, respectively). Zosuquidar or elacridar (5 μM) was used to specifically inhibit P-gp or P-gp/BCRP mediated transport, respectively. Data are means ± SD; n = 6; * $p < 0.05$, ** $p < 0.01$, *** $p < 0.001$, **** $p < 0.0001$. (**B**) AZD8055 plasma concentration, brain concentration and brain–plasma ratios in WT, *Abcb1a/b*$^{-/-}$, *Abcg2*$^{-/-}$ and *Abcb1a/b;Abcg2*$^{-/-}$ mice 1 h after 10 mg/kg i.v. administration. Data are means ± SD; n = 4; * $p < 0.05$, ** $p < 0.01$, *** $p < 0.001$, **** $p < 0.0001$.

The roles of Abcb1 and Abcg2 in limiting the brain penetration of NVP-BEZ235 were investigated using WT and *Abcb1a/b;Abcg2*$^{-/-}$ mice. We administered NVP-BEZ235 orally at a dose of 10 mg/kg. As shown in **Figure 3B**, both plasma and brain levels of NVP-BEZ235 were significantly higher in *Abcb1a/b;Abcg2*$^{-/-}$ mice than those in WT mice at multiple time points. Moreover, the brain–plasma ratio of *Abcb1a/b;Abcg2*$^{-/-}$ mice was 2.0 ($p < 0.01$) and 1.6-fold ($p < 0.01$) higher than that of WT mice at 1 and 4 hours, respectively. These data suggests that the higher brain level of NVP-BEZ235 was due to the absence of active brain efflux mediated by Abcb1 and Abcg2 and not only a consequence of higher plasma levels in *Abcb1a/b;Abcg2*$^{-/-}$ mice. Interestingly, in contrast to results obtained from the CETAs, pharmacokinetic experiments with single transporter knockouts showed the brain penetration of NVP-BEZ235 to be predominantly impaired by Abcb1a/b (**Figure 3C**). The brain concentration and brain–plasma ratio in WT mice were 3.6 ($p < 0.05$) and 1.7-fold ($p < 0.01$) lower than those of *Abcb1a/b*$^{-/-}$ mice and 4.5 ($p < 0.01$) and 2.0-fold ($p < 0.001$) lower than those of *Abcb1a/b;Abcg2*$^{-/-}$ mice, but similar to *Abcg2*$^{-/-}$ mice. Similar to AZD8055, and to a lesser extent to rapamycin, the plasma levels in all knockout strains were higher than in WT mice.

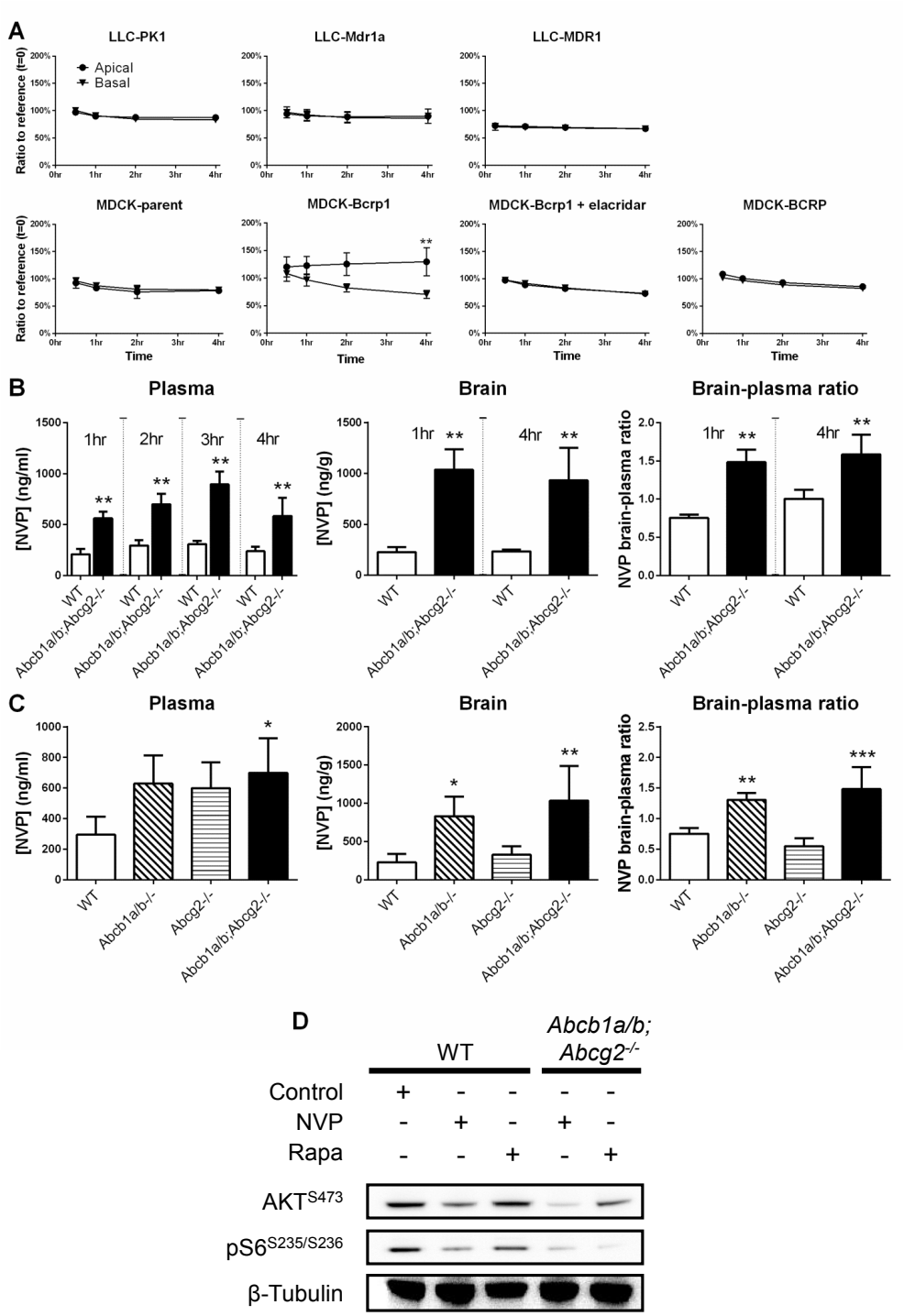
A
LLC-PK1
LLC-Mdr1a
LLC-MDR1
Apical
Basal
Ratio to reference (t=0)
MDCK-parent
MDCK-Bcrp1
MDCK-Bcrp1 + elacridar
MDCK-BCRP
Time
B
Plasma
Brain
Brain-plasma ratio
[NVP] (ng/ml)
[NVP] (ng/g)
NVP brain-plasma ratio
1hr
2hr
3hr
4hr
WT
Abcb1a/b;Abcg2-/-
C
Abcb1a/b-/-
Abcg2-/-
D
Control
NVP
Rapa
AKTS473
pS6S235/S236
β-Tubulin

Figure 3 | *In vitro* transport, *in vivo* pharmacokinetics and target inhibition of NVP-BEZ235. (**A**) Concentration equilibrium transport assays for NVP-BEZ235 using Mdr1a/MDR1 and Bcrp1/BCRP overexpressing cell lines and their parental counterparts (LLC–PK1 and MDCK–parent, respectively). Elacridar (5 μM) was used to specifically inhibit P-gp/BCRP mediated transport, respectively. Data are means ± SD; n = 6; ** $p < 0.01$. (**B**) NVP-BEZ235 plasma concentration, brain concentration and brain–plasma ratios in WT and *Abcb1a/b;Abcg2*$^{-/-}$ mice 1 and 4 hours after 10 mg/kg p.o. administration. Data are means ± SEM; n = 5; ** $p < 0.01$. (**C**) NVP-BEZ235 plasma concentration, brain concentration and brain–plasma ratios in WT, *Abcb1a/b*$^{-/-}$, *Abcg2*$^{-/-}$ and *Abcb1a/b;Abcg2*$^{-/-}$ mice 1 h after 10 mg/kg p.o. administration. Data are means ± SD; n = 4; * $p < 0.05$, ** $p < 0.01$, *** $p < 0.001$. (**D**) Western blotting of PI3K–mTOR signaling in brains of healthy WT and *Abcb1a/b;Abcg2*$^{-/-}$ mice that received 1.5 mg/kg rapamycin (Rapa) i.p., 10 mg/kg NVP-BEZ235 (NVP) p.o. or no treatment. See supplemental methods for details on antibodies.

To assess the pharmacodynamic implications of the impaired brain penetration of both NVP-BEZ235 and rapamycin, target engagement was compared between healthy brain tissue of WT and *Abcb1a/b;Abcg2*$^{-/-}$ mice. At clinically achievable plasma exposures, both rapamycin and NVP-BEZ235 were not very efficient in reducing the phosphorylation levels of the downstream mTOR target pS6 in WT mice relative to control. In contrast, both compounds did inhibit pS6 phosphorylation in *Abcb1a/b;Abcg2*$^{-/-}$ mice, with NVP-BEZ235 also reducing the phospho-AKT^{S473} levels (**Figure 3D**). In summary, these data show that Abcb1a/b at the BBB can impair rapamycin and NVP-BEZ235 brain penetration, resulting in hampered intracranial target engagement and thus likely restricting therapeutic efficacy.

ZSTK474 brain penetration is not restricted by Abcb1 and Abcg2

No significant directional translocation of ZSTK474 was found *in vitro*, although a minor ZSTK474 concentration difference was observed at 4 hours in the MDCK–Bcrp1 CETA (**Figure 4A**). These data indicate that ZSTK-474 is not transported by Abcb1/ABCB1 or Abcg2/ABCG2.

Since the ABC transporter affinities of a drug can be underestimated when using *in vitro* CETA (see for example NVP-BEZ235), we further investigated the roles of Abcb1 and Abcg2 on brain and plasma pharmacokinetics by p.o. administration of 200 mg/kg of ZSTK474 to WT and *Abcb1a/b;Abcg2*$^{-/-}$ mice. ZSTK474 plasma and brain concentrations as well as its brain–plasma ratio were similar in WT and *Abcb1a/b;Abcg2*$^{-/-}$ mice (**Figure 4B**). Moreover, oral administration of ZSTK474 greatly diminished PI3K pathway signaling in brain of both WT and *Abcb1a/b;Abcg2*$^{-/-}$ mice, suggesting that sufficient ZSTK474 was delivered to inhibit its target in the brain even in presence of Abcb1 and Abcg2 (**Figure 4C**).

We repeated the brain penetration study with ZSTK474 at a lower i.v. dose (10 mg/kg). Again, we did not find any significant difference in plasma, brain concentration or brain–plasma ratio between WT and *Abcb1a/b;Abcg2*$^{-/-}$ mice, confirming that neither systemic clearance nor brain penetration are limited by Abcb1 and Abcg2 (**Figure 4D**).

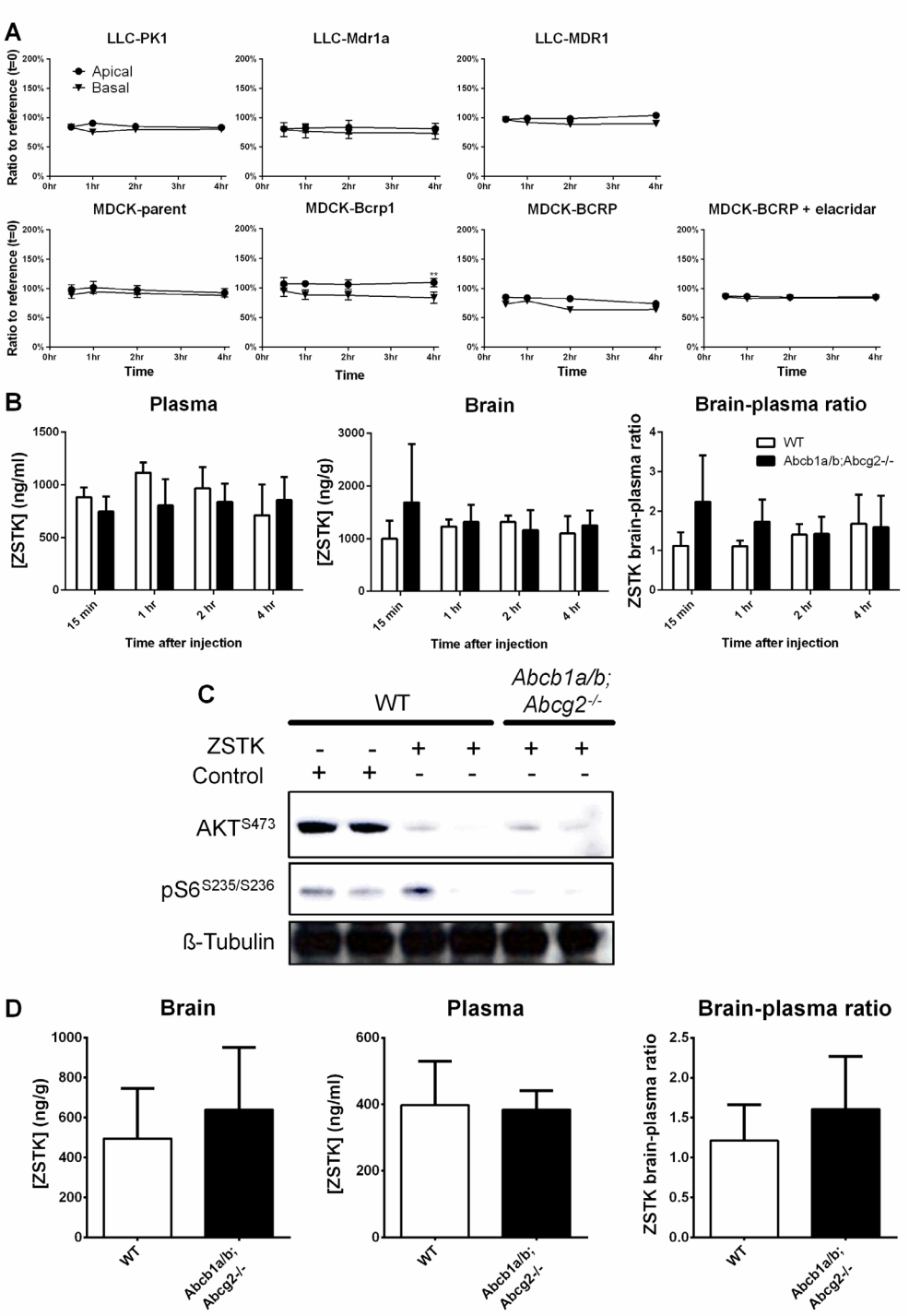
A
LLC-PK1
LLC-Mdr1a
LLC-MDR1
Apical
Basal
Ratio to reference (t=0)
MDCK-parent
MDCK-Bcrp1
MDCK-BCRP
MDCK-BCRP + elacridar
Time
B
Plasma
Brain
Brain-plasma ratio
[ZSTK] (ng/ml)
[ZSTK] (ng/g)
ZSTK brain-plasma ratio
WT
Abcb1a/b;Abcg2-/-
15 min
1 hr
2 hr
4 hr
Time after injection
C
WT
Abcb1a/b; Abcg2-/-
ZSTK
Control
AKTS473
pS6S235/S236
ß-Tubulin
D
Brain
Plasma
Brain-plasma ratio
[ZSTK] (ng/g)
[ZSTK] (ng/ml)
ZSTK brain-plasma ratio
WT
Abcb1a/b; Abcg2-/-

Figure 4 | *In vitro* transport, *in vivo* pharmacokinetics and target inhibition of ZSTK474. (**A**) Concentration equilibrium transport assays for ZSTK474 using Mdr1a/MDR1 and Bcrp1/BCRP overexpressing cell lines and their parental counterparts (LLC–PK1 and MDCK–parent, respectively). Elacridar (5 μM) was used to specifically inhibit P-gp/BCRP mediated transport, respectively. Data are means ± SD; n = 6; ** $p < 0.01$. (**B**) ZSTK474 plasma concentration, brain concentration and brain–plasma ratios in WT and *Abcb1a/b;Abcg2*$^{-/-}$ mice at various time points after 200 mg/kg p.o. administration. Data are means ± SD; n = 5. (**C**) Western blotting of PI3K–mTOR signaling in brains of healthy WT and *Abcb1a/b;Abcg2*$^{-/-}$ mice that received 200 mg/kg ZSTK474 (ZSTK) p.o. or no treatment. Data are shown for two independent animals per group. (**D**) ZSTK474 plasma concentration, brain concentration and brain–plasma ratios in WT and *Abcb1a/b;Abcg2*$^{-/-}$ mice 1 h following 10 mg/kg i.v. administration. Data are means ± SD; n = 7–9.

Brain penetrable PI3K/mTOR inhibitors display efficacy against orthotopic U87

The antitumor efficacy of the brain penetrable inhibitors NVP-BEZ235 (IC_{50} = 17 nM; **Figure 5A**) and ZSTK474 (IC_{50} = 630 nM; **Figure 5B**) was investigated in the U87 orthotopic xenograft model. Daily administration of NVP-BEZ235 (10 mg/kg p.o.) and ZSTK474 (200 mg/kg p.o.) profoundly reduced tumor growth compared to control (**Figure 5C**), without diminishing body weight (data not shown). Possibly in line with the slightly lower effect on tumor growth inhibition, NVP-BEZ235 treated mice survival did not significantly differ from control mice, whereas ZSTK474 demonstrated a markedly longer survival than control (median survival 25.0 *vs.* 17.5 days; p = 0.0019).

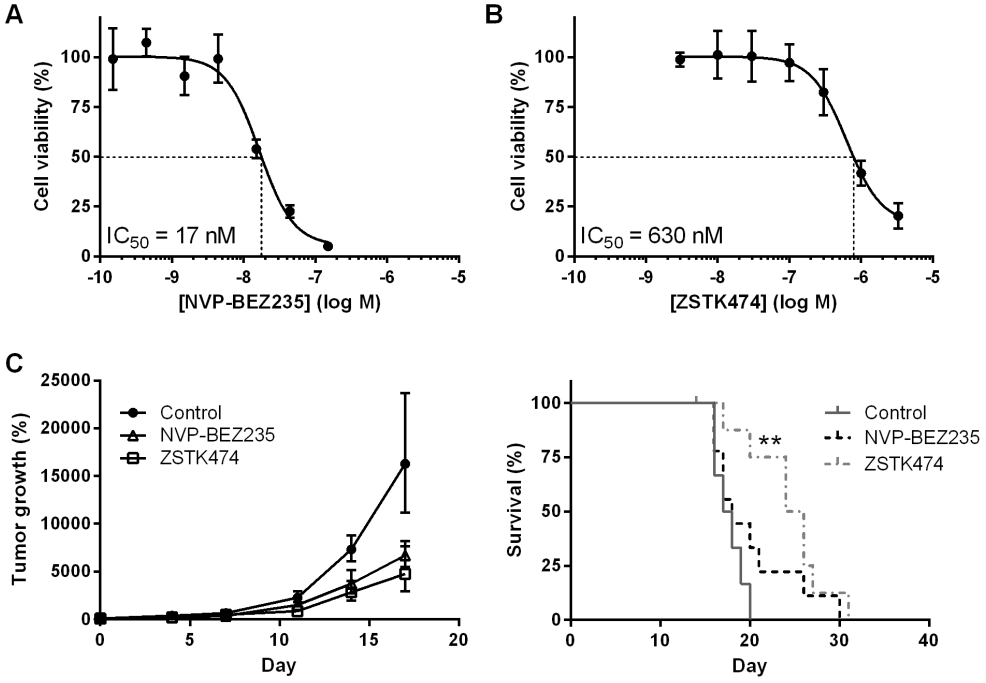

Figure 5 | *In vitro* and *in vivo* efficacy of NVP-BEZ235 and ZSTK474 against the U87 orthotopic xenograft model. Colony formation assay to establish the IC_{50} of (**A**) NVP-BEZ235 (17 nM) and (**B**) ZSTK474 (630 nM) against U87 cells *in vitro*. Data are means ± SD; n = 6. (**C**) Efficacy of NVP-BEZ235 and ZSTK474 against the U87 orthotopic xenograft mouse model. Three groups of WT mice bearing orthotopic U87 tumors received vehicle control, 200 mg/kg *q.d.* ZSTK474 or 10 mg/kg *q.d.* NVP-BEZ235, respectively. Data are means ± SD; n = 6, 9 and 9 for Control, ZSTK474 and NVP-BEZ235 groups, respectively; ** $p < 0.01$.

Inhibiting the PI3K signaling in GBM cells and spontaneous GBM models

The anti-proliferative activities of NVP-BEZ235 and ZSTK474 were assessed *in vitro* using GBM cells derived from spontaneous transgenic high-grade glioma mouse models as previously described[21] (see also **Supplementary methods**). These cells harbor a combination of genetic deletions that are common in human GBM, including $p16^{Ink4a}/p19^{Arf}$, *Tp53* and/or *Pten* together with an activated RAS–MAPK pathway. Both agents showed a dose-dependent growth inhibitory activity in line with target inhibition against all GBM cell lines, with NVP-BEZ235 being approximately 10-fold more potent than ZSTK474 (**Supplementary Figure 1**). *Pten* deficiency did not render these GBM cell lines sensitive to PI3K pathway inhibition, since no clear difference in response was found between the different genotypes.

Traditional xenograft models such as the U87 model fail to recapitulate many important features of human glioma, including BBB integrity. We previously established spontaneous high-grade gliomas models using conditional mice of different genetic backgrounds: *viz*. $p16^{Ink4a}/p19^{ArfF/F}$; $K\text{-}Ras^{V12}$;*Luc*, $Pten^{F/F}$;$p16^{Ink4a}/p19^{ArfF/F}$;$K\text{-}Ras^{V12}$;*Luc*, $Tp53^{F/F}$;$p16^{Ink4a}/p19^{ArfF/F}$;$K\text{-}Ras^{V12}$;*Luc* and $Tp53^{F/F}$; $Pten^{F/F}$;$p16^{Ink4a}/p19^{ArfF/F}$;$K\text{-}Ras^{V12}$;*Luc*[21]. All of these mice spontaneously develop Grade III or IV gliomas after intracranial CMV–Cre lentivirus injection that exhibit many histopathological and biological features of high-grade gliomas. In comparison, our GBM models that are deficient for *Pten* proliferated much more rapidly *in vivo* than *Pten*-proficient $p16^{Ink4a}/p19^{Arf-/-}$;$K\text{-}Ras^{V12}$ tumors (**Figure 6A**). As a result, $p16^{Ink4a}/p19^{ArfF/F}$;$K\text{-}Ras^{V12}$ mice that develop gliomas survived significantly longer than $Pten^{-/-}$;$p16^{Ink4a}/p19^{Arf-/-}$;$K\text{-}Ras^{V12}$ mice (median survival 45 *vs.* 26 days; $p < 0.001$). Similarly, the deletion of *Pten* in mice with *Tp53*-null tumors also had an accelerated tumor onset and progression ($Tp53^{-/-}$;$p16^{Ink4a}/p19^{Arf-/-}$;$K\text{-}Ras^{V12}$ and $Tp53^{-/-}$;$Pten^{-/-}$;$p16^{Ink4a}/p19^{Arf-/-}$; $K\text{-}Ras^{V12}$ gliomas; 28 *vs.* 20 days, respectively; $p < 0.0001$). These data suggest that activation of PI3K pathway signaling by PTEN deletion is important in the transformation of cells into high-grade gliomas. We, therefore decided to treat $Pten^{-/-}$;$p16^{Ink4a}/p19^{Arf-/-}$;$K\text{-}Ras^{V12}$ mice daily with 200 mg/kg of ZSTK474, starting 2 days after lentiviral injection. In line with these expectations, ZSTK474 treatment delayed $Pten^{-/-}$;$p16^{Ink4a}/p19^{Arf-/-}$;$K\text{-}Ras^{V12}$;*Luc* tumor onset. However, ZSTK474 was not able to reduce the proliferation rate of these tumors at a more advanced stage (**Figure 6B**). Overall, ZSTK474 treatment increased median survival from 26 to 32 days ($p = 0.0002$). Concordantly, PI3K signaling in these tumors was markedly reduced two hours after ZSTK474 treatment, while MAPK signaling was unaffected (**Figure 6C**). These results suggest that glioma PI3K signaling can be inhibited by ZSTK474 *in vivo*, leading to prolonged survival.

Figure 6 | Efficacy and target inhibition by ZSK474 in a spontaneous GBM mouse model. (**A**) Tumor growth and survival of mice spontaneously developing GBM with different genotypes: $p16^{Ink4a}/p19^{Arf-/-}$; $K\text{-}Ras^{V12}$;*Luc*, $Pten^{-/-}$;$p16^{Ink4a}/p19^{Arf-/-}$;$K\text{-}Ras^{V12}$;*Luc*, $Tp53^{-/-}$;$p16^{Ink4a}/p19^{Arf-/-}$;$K\text{-}Ras^{V12}$;*Luc* and $Tp53^{-/-}$;$Pten^{-/-}$; $p16^{Ink4a}/p19^{Arf-/-}$;$K\text{-}Ras^{V12}$;*Luc*. Data are means ± SD; n = 9-12. (**B**) $Pten^{F/F}$;$p16^{Ink4a}/p19^{ArfF/F}$;$K\text{-}Ras^{V12}$ conditional mice with spontaneous GBM induced by intracranial injection of lenti-Cre virus received 200 mg/kg q.d. ZSTK474 or vehicle control starting from day 3 after lentivirus injection. Data are means ± SD; n = 6 and 13 for ZSTK and Control groups, respectively; *** $p < 0.001$. (**C**) Representative (immuno-) histochemical analyses of coronal brain sections from Control and ZSTK474 treated mice from (**B**).

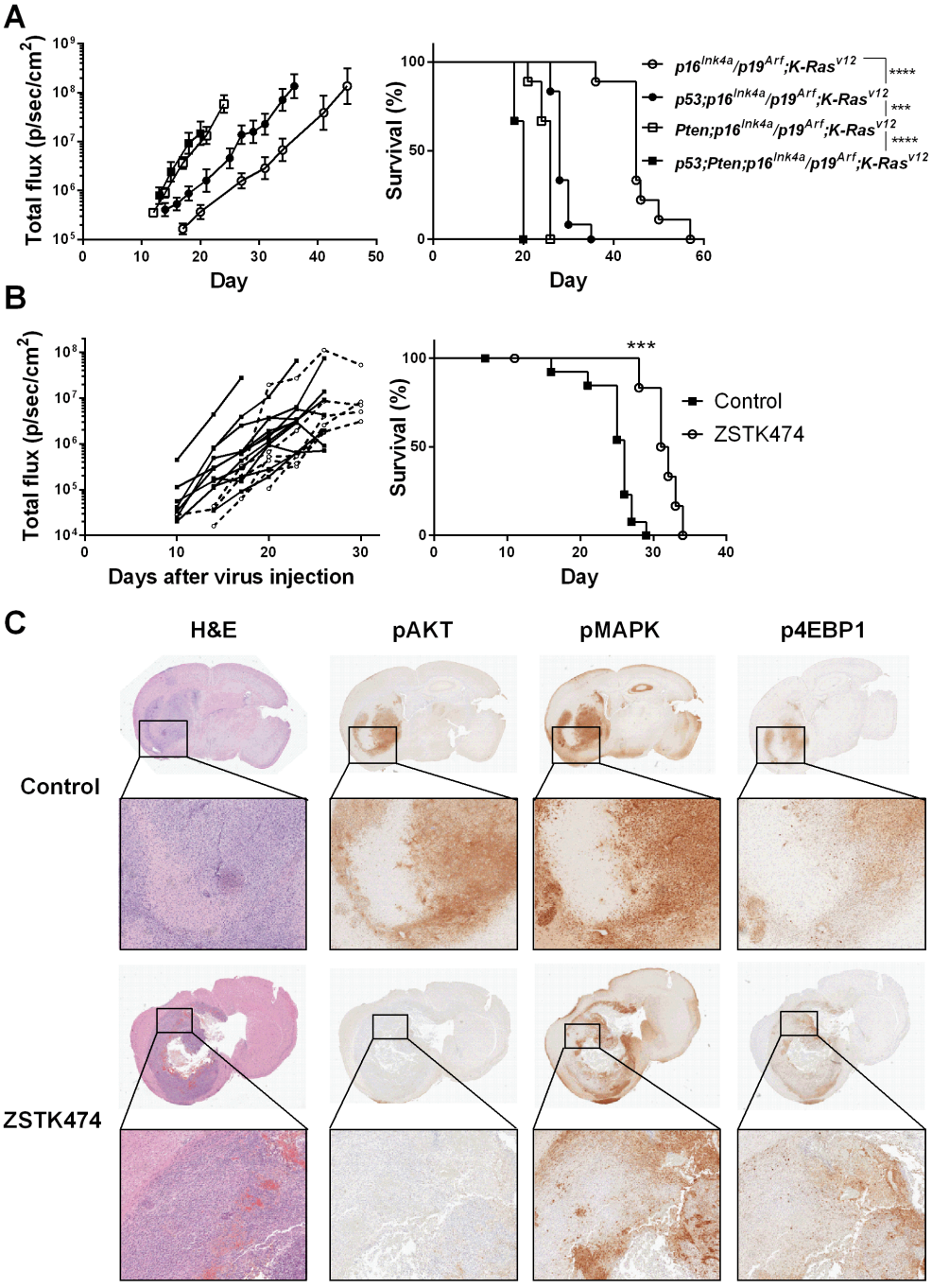
A
Total flux (p/sec/cm2)
Day
Survival (%)
Day
p16Ink4a/p19Arf;K-Rasv12
p53;p16Ink4a/p19Arf;K-Rasv12
Pten;p16Ink4a/p19Arf;K-Rasv12
p53;Pten;p16Ink4a/p19Arf;K-Rasv12
****
***
****
B
Total flux (p/sec/cm2)
Days after virus injection
Survival (%)
Day
***
Control
ZSTK474
C
H&E
pAKT
pMAPK
p4EBP1
Control
ZSTK474

DISCUSSION

This study demonstrates that PI3K inhibitors that are sufficiently brain penetrable can reach levels in GBM that are sufficient for target inhibition and growth delay. Importantly, for ZSTK474 these effects occur at dose levels providing plasma concentrations that are in the range of those achievable in patients[32]. However, this work using our spontaneous *Pten*-deficient GBM model also shows that inhibition of the PI3K–mTOR pathway alone has very modest activity, most likely due to the fact that, next to the PI3K–mTOR cascade, several other signaling pathways are concomitantly active in GBM.

As manifested by the number of ongoing clinical trials, small-molecule targeted therapies are thought to hold promise for treatment of malignant gliomas. But in order to be efficacious, these agents need to penetrate the BBB. Besides the more central areas in GBM where the vasculature is leakier, GBM also harbors many tumor cells that have invaded into adjacent normal brain tissue where the BBB is still more or less intact. By using *in vitro* and *in vivo* mouse models, we determined the impact of Abcb1 and Abcg2, two well established drug efflux transporters expressed at BBB, on the brain penetration of rapamycin, AZD8055, NVP-BEZ235 and ZSTK474. Importantly, for all *in vivo* work with these agents, we have taken the clinical achievable plasma levels into consideration.

Rapamycin is the prototype inhibitor of mTOR and has been tested in clinical trials against GBM without success[33]. Due to Abcb1-mediated brain efflux, the brain concentration of rapamycin (**Figure 1C**) remained very low in mice receiving a dose that has previously been used in other preclinical models of cancer[34,35]. In patients, the maximum tolerated dose (MTD) of daily oral rapamycin is 6 mg/day and results in whole blood levels of about 30 ng/ml[36], thus in the same range as we achieved in WT mice. At this plasma level, however, the brain penetration was insufficient for target inhibition ($pS6^{S235/S236}$) in normal brain tissue of WT mice. Similarly, Mendiburu-Elicabe *et al.* already showed that neither target inhibition nor improved survival was achieved in the U87 xenografts even at a higher dose of 3 mg/kg of rapamycin, while further dose escalation caused severe weight loss[37]. In patients undergoing resection of their tumor following rapamycin treatment the levels in tumor tissue was also in the same range as in the WT mice[38]. Rapamycin is not a substrate of Abcg2. The higher level of rapamycin measured in the brain homogenates of *Abcg2*$^{-/-}$ mice is a consequence of the high plasma level. The brain–plasma ratio is 0.04, which is close to the fraction of blood that is present in the brain vasculature and that will end up in the brain homogenate[39]. Similar as shown before for the rapamycin analog everolimus, the much higher levels of rapamycin in the plasma of the knockout strains is most likely due to the instability of rapamycin in plasma[31] and binding of rapamycin to carboxyl esterase 1c (Ces1c), which protects rapamycin from degradation. Higher plasma levels in knockout mouse strains were also observed with AZD8055 and NVP-BEZ235, albeit that the effect size was much smaller. This

may be due to a similar higher binding to a plasma protein that is more abundant in knockouts. Due to this higher plasma protein binding, the brain–plasma ratio will underestimate the brain retention. For rapamycin the brain–blood ratio in *Abcb1a/b* and *Abcb1a/b;Abcg2* knockout mice is about 0.10. The Abcb1/Abcg2 inhibitor elacridar is able to increase the brain level of rapamycin without the increasing the blood level, which results in an increased brain–blood ratio from 0.18 to 5.2 in WT *vs.* WT + elacridar animals, respectively. Notably, rapamycin is also strongly retained in brain tissue of *Abcb1a/b* and *Abcb1a/b;Abcg2* knockout mice and causes a profound target inhibition ($pS6^{S235/S236}$) in these strains (**Figure 3D**).

Besides insufficient drug exposure, resistance to rapamycin can also be due to the fact that this compound inhibits the formation of the mTORC1 complex, while still causing feedback activation by phosphorylation of AKT at Ser473 by mTORC2[10,11]. This feedback loop activation of AKT can be negated by using a dual mTORC1/2 inhibitor like AZD8055 or a PI3K/mTOR inhibitor like NVP-BEZ235. AZD8055 appeared to be a very good substrate of both Abcb1 and Abcg2, which is in line with previous work showing that AZD8055 (10 mg/kg *b.i.d.*) alone was inactive against intracranial glioma[40]. Because the plasma levels in mice receiving 10 mg/kg are also considerably higher than can be achieved in patients receiving the MTD[40,41], we have not further evaluated this compound *in vivo*. Interestingly, the *in vitro* transwell experiments for NVP-BEZ235 did not show transport by Abcb1 and relatively weak transport by Abcg2. In line with these *in vitro* findings, the impact of Abcg2 on the brain penetration of NVP-BEZ235 was minimal as based on the difference between *Abcb1a/b*$^{-/-}$ and *Abcb1a/b;Abcg2*$^{-/-}$ mice. However, Abcb1 significantly decreased the brain concentration and caused incomplete target inhibition in brains of WT mice. Discordance between *in vitro* transwell and *in vivo* brain penetration has been observed before[29]. In general, the *in vitro* transport model is very effective to identify substrates as shown for rapamycin and AZD8055, but a lack of transport does not always accurately predict the impact of Abcb1 at the BBB. Consequently, *in vivo* studies remain necessary to accurately assess the role of this transporter in drug delivery to the brain. In the case of ZSTK474, the absence of transport by Abcb1 and/or Abcg2 *in vitro* nicely reflected the *in vivo* negligible impact at the BBB. The brain penetration of ZSTK474 was similar between WT and *Abcb1a/b;Abcg2*$^{-/-}$ mice with a brain–plasma ratio of 1.5 and profoundly reduced AKT^{S473} phosphorylation even in brains of WT mice. Importantly, this target inhibition occurred at plasma levels that are in the range as those achievable in patients, given that the first-in-man phase I study reported that the plasma level of ZSTK474 in patients who received the MTD (150 mg/kg *q.d.*x21) ranged between 200 and 500 ng/ml[32].

Based on these results, we assessed the *in vivo* efficacy of ZSTK474 against orthotopic U87 GBM and included NVP-BEZ235 as a reference, since previously studies have shown that NVP-BEZ235 is active against ectopic (s.c.) and orthotopic U87 when given at a daily oral dose of 25 or 45 mg/kg[19,42]. We also found a modest efficacy of NVP-BEZ235 against intracranial U87, even at a lower dose of 10 mg/kg. The plasma concentration in our WT mice was 200 ng/ml in line with

the 1000 ng/ml (peak) and 15 ng/ml (trough) plasma level at a dose of 50 mg/kg as reported by Maira *et al.*[42]. Notably, this appears to be considerably lower than the 1800 ng/ml found in patients as has been presented in a meeting report[43]. No other (full) reports on the plasma pharmacokinetics of NVP-BEZ235 have been published, but apparently patients tolerate higher plasma levels than mice, and the efficacy of NVP-BEZ235 will likely be better at higher doses. On the other hand, intracranial U87 gliomas have a very open (leaky) vasculature, which renders the tumor highly accessible for systemically administered drugs. Although it is being used a lot in preclinical research, it is not the most predictive model for clinical efficacy against glioma. Therefore, we decided to test ZSTK474 in one of our spontaneous transgenic glioma models[21]. We have used the *Pten*$^{F/F}$;*p16*^{Ink4a}/*p19*$^{ArfF/F}$;*K-Ras*^{V12} spontaneous tumors because *Pten*-deficient tumors developed much more rapidly than *Pten*-proficient tumors in *p16*^{Ink4a}/*p19*$^{ArfF/F}$;*K-Ras*^{V12} mice. Based on this finding, we expected that inhibiting the PI3K pathway in *Pten*$^{F/F}$;*p16*^{Ink4a}/*p19*$^{ArfF/F}$;*K-Ras*^{V12} mice carrying spontaneous GBM may extend their survival to be comparable as *p16*^{Ink4a}/*p19*$^{ArfF/F}$;*K-Ras*^{V12} mice. Indeed, we found that treatment with ZSTK474 significantly improved survival and caused inhibition of AKT^{S473} and pS6$^{S235/S236}$ in tumors and surrounding brain. However, the response was much more modest than might have been expected based on the notion that *Pten* loss is an important factor driving this model. GBM is characterized by multiple parallel aberrant signaling pathways[1], and therefore, single target treatment efficacy will be limited. Combinations with other drugs targeting these other pathways (*e.g.*, MAPK, CDK4/6–RB) may be necessary. Obviously, these drugs will also need to cross the BBB sufficiently to reach tumor cells in pharmacologically relevant levels. In conclusion, its excellent brain penetration renders ZSTK474 the most promising candidate among the PI3K pathway inhibitors included in this study for future multiple pathway targeting studies.

REFERENCES

1. Brennan, C.W., *et al.* The somatic genomic landscape of glioblastoma. *Cell* **155**, 462-477 (2013).
2. Parsons, D.W., *et al.* An integrated genomic analysis of human glioblastoma multiforme. *Science* **321** (2008).
3. Song, M.S., *et al.* The functions and regulation of the PTEN tumour suppressor. *Nat Rev Mol Cell Biol* **13**, 283-296 (2012).
4. Engelman, J.A. Targeting PI3K signalling in cancer: opportunities, challenges and limitations. *Nat Rev Cancer* **9**, 550-562 (2009).
5. LoPiccolo, J., *et al.* Targeting the PI3K/Akt/mTOR pathway: effective combinations and clinical considerations. *Drug Resist Updat* **11**, 32-50 (2008).
6. Thorpe, L.M., *et al.* PI3K in cancer: divergent roles of isoforms, modes of activation and therapeutic targeting. *Nat Rev Cancer* **15**, 7-24 (2015).
7. Kreisl, T.N., *et al.* A pilot study of everolimus and gefitinib in the treatment of recurrent glioblastoma (GBM). *J Neurooncol* **92**, 99-105 (2009).
8. Chang, S.M., *et al.* Phase II study of CCI-779 in patients with recurrent glioblastoma multiforme. *Invest New Drugs* **23**, 357-361 (2005).
9. Wang, X., *et al.* Enhancing mammalian target of rapamycin (mTOR)-targeted cancer therapy by preventing mTOR/raptor inhibition-initiated, mTOR/rictor-independent Akt activation. *Cancer Res* **68**, 7409-7418 (2008).
10. Stoeltzing, O., *et al.* Intracellular signaling in tumor and endothelial cells: the expected and, yet again, the unexpected. *Cancer Cell* **10**, 89-91 (2006).
11. O'Reilly, K.E., *et al.* mTOR inhibition induces upstream receptor tyrosine kinase signaling and activates Akt. *Cancer Res* **66**, 1500-1508 (2006).
12. Yilmaz, O.H., *et al.* Pten dependence distinguishes haematopoietic stem cells from leukaemia-initiating cells. *Nature* **441**, 475-482 (2006).
13. van Tellingen, O., *et al.* Overcoming the blood-brain tumor barrier for effective glioblastoma treatment. *Drug Resist Updat* **19**, 1-12 (2015).
14. la Fougere, C., *et al.* Molecular imaging of gliomas with PET: opportunities and limitations. *Neuro Oncol* **13**, 806-819 (2011).

15. de Gooijer, M.C., *et al.* P-glycoprotein and breast cancer resistance protein restrict the brain penetration of the CDK4/6 inhibitor palbociclib. *Invest New Drugs* **33**, 1012-1019 (2015).
16. Polli, J.W., *et al.* An unexpected synergist role of P-glycoprotein and breast cancer resistance protein on the central nervous system penetration of the tyrosine kinase inhibitor lapatinib (N-{3-chloro-4-[(3-fluorobenzyl)oxy] phenyl}-6-[5-({[2-(methylsulfonyl)ethyl]amino }methyl)-2-furyl]-4-quinazolinamine; GW572016). *Drug Metab Dispos* **37**, 439-442 (2009).
17. de Vries, N.A., *et al.* Restricted brain penetration of the tyrosine kinase inhibitor erlotinib due to the drug transporters P-gp and BCRP. *Invest New Drugs* **30**, 443-449 (2012).
18. Keen, H.G., *et al.* Examining changes in [^{18}F]FDG and [^{18}F]FLT uptake in U87-MG glioma xenografts as early response biomarkers to treatment with the dual mTOR1/2 inhibitor AZD8055. *Mol Imaging Biol* **16**, 421-430 (2014).
19. Liu, T.J., *et al.* NVP-BEZ235, a novel dual phosphatidylinositol 3-kinase/mammalian target of rapamycin inhibitor, elicits multifaceted antitumor activities in human gliomas. *Mol Cancer Ther* **8**, 2204-2210 (2009).
20. Kong, D., *et al.* Inhibition profiles of phosphatidylinositol 3-kinase inhibitors against PI3K superfamily and human cancer cell line panel JFCR39. *Eur J Cancer* **46**, 1111-1121 (2010).
21. de Vries, N.A., *et al.* Rapid and robust transgenic high-grade glioma mouse models for therapy intervention studies. *Clin Cancer Res.* **16**, 3431-3441 (2010).
22. Lin, F., *et al.* Dual mTORC1 and mTORC2 inhibitor Palomid 529 penetrates the blood-brain barrier without restriction by ABCB1 and ABCG2. *Int J Cancer* **133**, 1222-1233 (2013).
23. Guzman, C., *et al.* ColonyArea: an ImageJ plugin to automatically quantify colony formation in clonogenic assays. *PloS One* **9**, e92444 (2014).
24. de Vries, N.A., *et al.* P-glycoprotein and breast cancer resistance protein: two dominant transporters working together in limiting the brain penetration of topotecan. *Clin Cancer Res.* **13**, 6440-6449 (2007).
25. Lin, F., *et al.* Determination of NVP-BEZ235, a dual PI3K and mTOR inhibitor, in human and mouse plasma and in mouse tissue homogenates by reversed-phase high-performance liquid chromatography with fluorescence detection. *J Chromatogr B Analyt Technol Biomed Life Sci* **901**, 9-17 (2012).
26. Kemper, E.M., *et al.* Development of luciferase tagged brain tumour models in mice for chemotherapy intervention studies. *Eur J Cancer* **42**, 3294-3303 (2006).
27. Zhang, P., *et al.* ABCB1 and ABCG2 restrict the brain penetration of a panel of novel EZH2-Inhibitors. *Int J Cancer* **137**, 2007-2018 (2015).
28. Zhang, Y., *et al.* PKSolver: an add-in program for pharmacokinetic and pharmacodynamic data analysis in Microsoft Excel. *Comput Methods Programs Biomed* **99**, 306-314 (2010).
29. Luna-Tortós, C., Fedrowitz, M. & Loscher, W. Several major antiepileptic drugs are substrates for human P-glycoprotein. *Neuropharmacology* **55**, 1364-1375 (2008).
30. Ferron, G.M. & Jusko, W.J. Species differences in sirolimus stability in humans, rabbits, and rats. *Drug Metab Dispos* **26**, 83-84 (1998).
31. Tang, S.C., *et al.* P-glycoprotein, CYP3A, and plasma carboxylesterase determine brain and blood disposition of the mTOR Inhibitor everolimus (Afinitor) in mice. *Clin Cancer Res.* **20**, 3133-3145 (2014).
32. Lockhart, A.C., *et al.* A first-in-human Phase I study of ZSTK474, an oral pan-PI3K inhibitor, in patients with advanced solid malignancies. *Mol Cancer Ther* **12 Suppl 11**, B271 (2013).
33. Reardon, D.A., *et al.* Phase 2 trial of erlotinib plus sirolimus in adults with recurrent glioblastoma. *J Neurooncol* **96**, 219-230 (2010).
34. Lang, S.A., *et al.* Mammalian target of rapamycin is activated in human gastric cancer and serves as a target for therapy in an experimental model. *Int J Cancer* **120**, 1803-1810 (2007).
35. Thallinger, C., *et al.* Orally administered rapamycin, dacarbazine or both for treatment of human melanoma evaluated in severe combined immunodeficiency mice. *Pharmacology* **82**, 233-238 (2008).
36. Jimeno, A., *et al.* Pharmacodynamic-guided modified continuous reassessment method–based, dose-finding study of rapamycin in adult patients with solid tumors. *J Clin Oncol* **26**, 4172-4179 (2008).
37. Mendiburu-Elicabe, M., *et al.* Systemic rapamycin alone may not be a treatment option for malignant glioma: evidence from an in vivo study. *J Neurooncol* **108**, 53-58 (2012).
38. Cloughesy, T.F., *et al.* Antitumor activity of rapamycin in a Phase I trial for patients with recurrent PTEN-deficient glioblastoma. *PLoS Med* **5**, e8 (2008).
39. Dai, H., *et al.* Distribution of STI-571 to the brain is limited by P-glycoprotein-mediated efflux. *J Pharmacol Exp Ther* **304**, 1085-1092 (2003).
40. Luchman, H.A., *et al.* Dual mTORC1/2 blockade inhibits glioblastoma brain tumor initiating cells in vitro and in vivo and synergizes with temozolomide to increase orthotopic xenograft survival. *Clin Cancer Res* **20**, 5756-5767 (2014).
41. Naing, A., *et al.* Safety, tolerability, pharmacokinetics and pharmacodynamics of AZD8055 in advanced solid tumours and lymphoma. *Br J Cancer* **107**, 1093-1099 (2012).
42. Maira, S.M., *et al.* Identification and characterization of NVP-BEZ235, a new orally available dual phosphatidylinositol 3-kinase/mammalian target of rapamycin inhibitor with potent in vivo antitumor activity. *Mol Cancer Ther* **7**, 1851-1863 (2008).
43. Peyton, J.D., *et al.* A dose-escalation study with the novel formulation of the oral pan-class I PI3K inhibitor BEZ235, solid dispersion system (SDS) sachet, in patients with advanced solid tumors. *J Clin Oncol* **29 Suppl 15**, 3066 (2011).
44. Bruggeman, S.W., *et al.* Bmi1 controls tumor development in an Ink4a/Arf-independent manner in a mouse model for glioma. *Cancer Cell* **12**, 328-341 (2007).

SUPPLEMENTARY METHODS

Establishment of GBM cell culture, anti-proliferation assay and Western blotting

GBM cells lines have been created from tumors generated in *p16^{Ink4a}/p19$^{ArfF/F}$;K-Ras^{V12};Luc*, *Pten$^{F/F}$;p16^{Ink4a}/p19$^{ArfF/F}$;K-Ras^{V12};Luc*, *Tp53$^{F/F}$;p16^{Ink4a}/p19$^{ArfF/F}$;K-Ras^{V12};Luc* and *Tp53$^{F/F}$;Pten$^{F/F}$;p16^{Ink4a}/p19$^{ArfF/F}$;K-Ras^{V12};Luc* conditional mice after lentiviral injection into the brain. Small amounts of tumor tissue were transferred in ice-cold Ca^{2+} and Mg^{2+} free HBSS and subsequently triturated mechanically. Cell suspensions were prepared in ultra-low binding 6 well plates (Corning) in serum-free MHM (medium hormone mix) medium (DMEM/F12 supplemented with modified N2 medium composed of 100 mg/L apo-transferrin, 25 mg/L recombinant human insulin, 100 μM putrescine, 20 nM progesterone, and 30 nM sodium selenite, 2 mM glutamine, 6 mg/ml glucose, 14 mM $NaHCO_3$ and 5mM HEPES) supplemented with 20 ng/ml EGF and bFGF as described previously[44].

For proliferation assays, cells from the above established GBM culture were seeded in laminin coated 96-well black-well/clear-bottom plate (Greiner Bio-One; Alphen, The Netherlands) at a density of 2,000 cells/well in MHM medium. Treatment was started after one to two days when about 3–5% cell confluence was reached. Next, the medium was replaced by MHM medium containing 0.1% DMSO as a control, ZSTK474 at concentrations of 100, 500, 1000 or 2000 nM, or NVP-BEZ235 at concentrations of 1, 10, 100 and 1000 nm. Cell viability was determined on day 0 (treatment start) and day 2 using bioluminescence imaging on an IVIS Lumina II Imaging System (PerkinElmer) with 150 μg/ml of luciferin in each well.

For Western blotting, GBM cells or healthy brain tissues collected from mice which have been treated with rapamycin (1.5 mg/kg i.p.), NVP-BEZ235 (10 mg/kg p.o.) or ZSTK474 (200 mg/kg p.o.) prior to sample collection were lysed with complete RIPA buffer containing phosphatase inhibitors. Cell lysate was processed for Western blotting. Primary antibodies used in this study are pErk1/2 (Thr202/Tyr204), Erk1 (C16; both Santa Cruz Biotechnology; Santa Cruz, CA), pmTor (Ser2448), pAkt (Ser473), Akt, pS6 (Ser235/236) Ribosomal protein (all Cell Signaling Technology) and mouse β-tubulin isotype III (Sigma-Aldrich).

SUPPLEMENTARY FIGURES

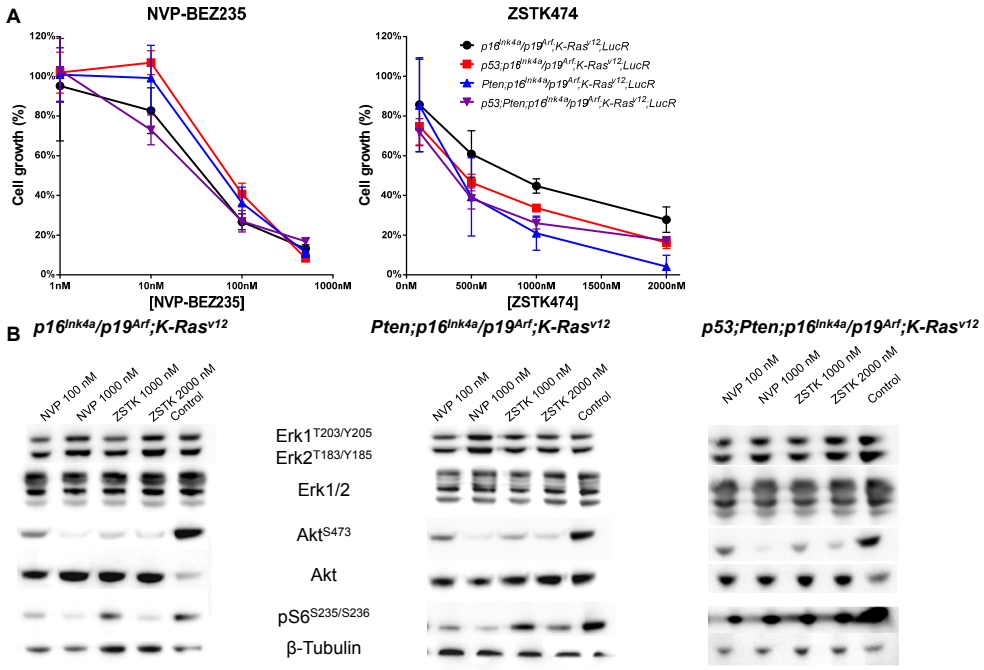

Supplementary Figure 1 | Efficacy and target inhibition by NVP-BEZ235 and ZSK474 against murine GBM cell lines of various genetic backgrounds. (**A**) Growth inhibition of GBM cells with various genotypes by NVP-BEZ235 and ZSTK474. Data are means ± SD; n = 4. (**B**) Immunoblotting analysis of various MAPK and PI3K pathway components in murine GBM cell lines of various genetic backgrounds following 4 hours of treatment with NVPBEZ235 (NVP) or ZSTK474 (ZSTK).

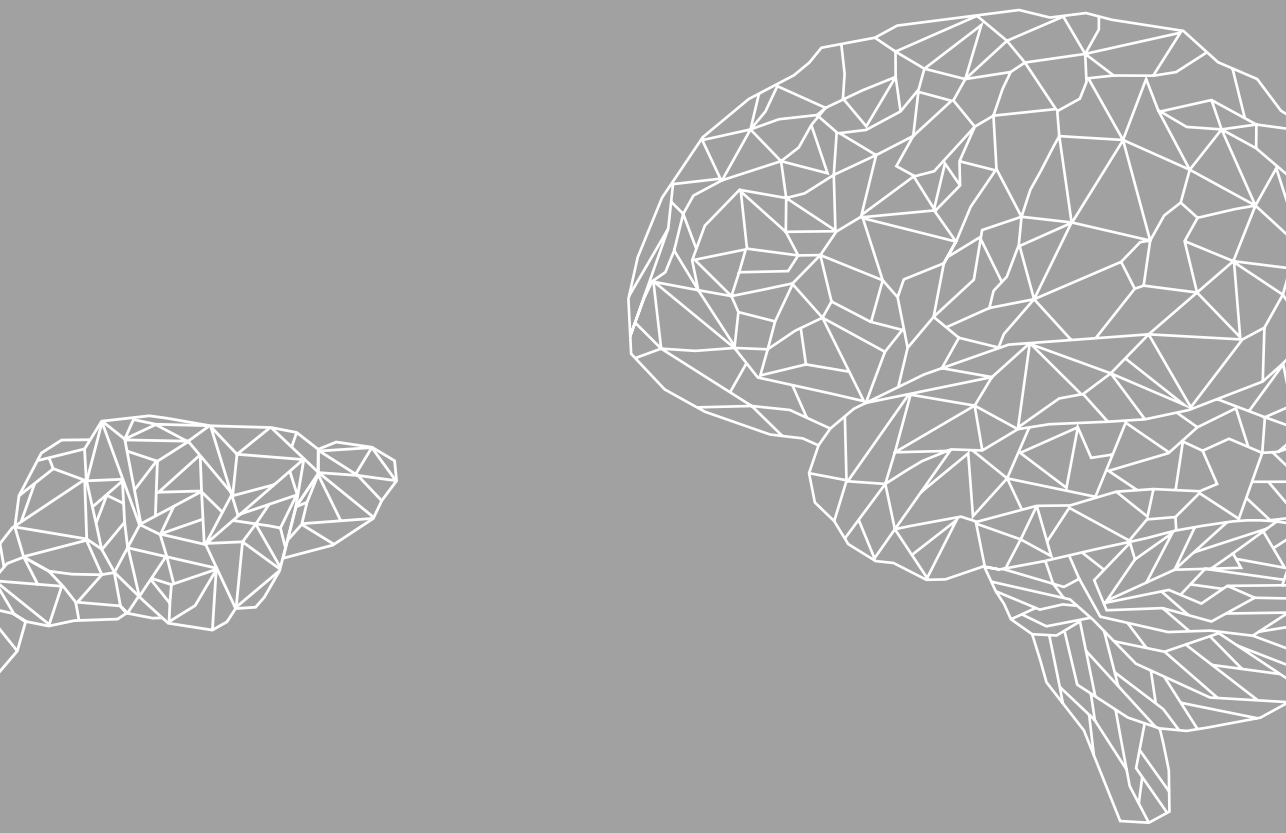

SECTION IV

INHIBITING THE MAPK PATHWAY: BLOCKING PROLIFERATION

Chapter 7

THE IMPACT OF P-GLYCOPROTEIN AND BREAST CANCER RESISTANCE PROTEIN ON THE BRAIN PHARMACOKINETICS AND PHARMACODYNAMICS OF A PANEL OF MEK INHIBITORS

M.C. de Gooijer, P. Zhang, R. Weijer, L.C.M. Buil, J.H. Beijnen, and O. van Tellingen

International Journal of Cancer. 2018;142(2):381-391

ABSTRACT

Mitogen/extracellular signal-regulated kinase (MEK) inhibitors have been tested in clinical trials for treatment of intracranial neoplasms, including glioblastoma (GBM), but efficacy of these drugs has not yet been demonstrated. The blood–brain barrier (BBB) is a major impediment to adequate delivery of drugs into the brain and may thereby also limit the successful implementation of MEK inhibitors against intracranial malignancies. The BBB is equipped with a range of ATP-dependent efflux transport proteins, of which P-gp (ABCB1) and BCRP (ABCG2) are the two most dominant for drug efflux from the brain. We investigated their impact on the pharmacokinetics and target engagement of a panel of clinically applied MEK inhibitors, in order to select the most promising candidate for brain cancers in the context of clinical pharmacokinetics and inhibitor characteristics. To this end, we used *in vitro* drug transport assays and conducted pharmacokinetic and pharmacodynamic studies in wild-type and ABC transporter knockout mice. PD0325901 displayed more promising characteristics than trametinib (GSK1120212), binimetinib (MEK162), selumetinib (AZD6244) and pimasertib (AS703026): PD0325901 was the weakest substrate of P-gp and BCRP *in vitro*, its brain penetration was only marginally higher in *Abcb1a/b;Abcg2*$^{-/-}$ mice, and efficient target inhibition in the brain could be achieved at clinically relevant plasma levels. Notably, target inhibition could also be demonstrated for selumetinib, but only at plasma levels far above levels in patients receiving the maximum tolerated dose. In summary, this study recommends further development of PD0325901 for the treatment of intracranial neoplasms.

What's new?: Almost all brain cancers—adult and pediatric, primary and secondary—harbor an overactivated MAPK pathway, making MEK an attractive therapeutic target. However, the blood–brain barrier is a major impediment to the brain penetration and intracranial efficacy of drugs. To support successful clinical implementation of MEK inhibitors against intracranial neoplasms, we investigated the brain penetration of five clinically applied MEK inhibitors in mice and select PD0325901 as the most promising candidate for treatment of intracranial tumors.

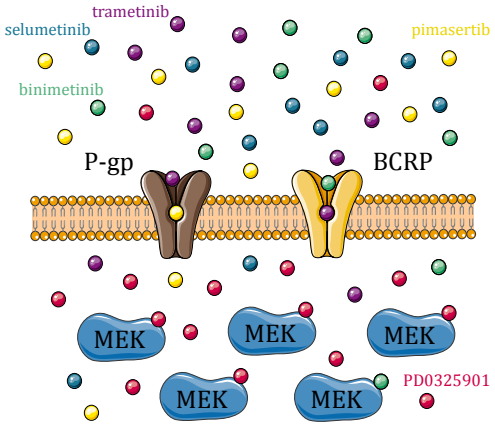

INTRODUCTION

The mitogen-activated protein kinase (MAPK) pathway has emerged as a druggable target in various primary and secondary intracranial neoplasms. First, the vast majority (85%) of glioblastomas (GBM) is characterized by a hyper-activated MAPK pathway[1]. Second, *IDH* wild-type low-grade gliomas often have alterations in *NF1*, *EGFR* and *PTPN11*[2]. Third, pediatric gliomas such as diffuse intrinsic pontine glioma, non-brainstem high-grade glioma, and pleomorphic xanthoastrocytoma frequently harbor alterations in the *NTRK* receptor family and *MET*[3,4]. Finally, cancers that frequently metastasize to the brain, *e.g.*, melanoma and non-small cell lung cancer, are known to carry MAPK pathway activating alterations such as the $BRAF^{V600E}$ and $KRAS^{G12}$ mutation[5,6]. Although activating mutations can occur at different levels in the canonical pathway, they all require signaling via mitogen/extracellular signal-regulated kinase (MEK) in order to increase proliferation and survival[7]. The common activation of the MAPK pathway in malignancies and the central and downstream location of MEK render MEK inhibitors of potential interest for the treatment of intracranial neoplasms.

The MAPK pathway comprises two isotypes of MEK (MEK1 and MEK2) that are 86% homologous in the catalytic domain and have narrow substrate specificities for ERK1 and ERK2. All MEK inhibitors that are now under development are highly specific, because they do not bind to the kinase domain, but to a hydrophobic pocket that is unique for MEK1/2[8]. As a consequence, there is great structural overlap between the MEK inhibitors originating from different pharmaceutical companies (**Figure 1**).

Although MEK inhibitors may be important for treating intracranial tumors, there are only very few clinical studies ongoing that specifically address the treatment of intracranial tumors, including glioblastoma. Importantly, these malignancies are all to some degree protected by the blood–brain barrier (BBB). The BBB is formed by the brain endothelial cells (BECs). Drug trafficking of hydrophilic substances is restricted by the presence of tight junctions, absence of fenestrae and low pinocytic activity of BECs. Uptake of nutrients is mediated by selective uptake carriers, such as glucose by GLUT-1 (SLC2A1), whereas other compounds depend on passive diffusion. Although more lipophilic substances may enter the brain relatively easily by passive diffusion, this is frequently restricted by ATP-Binding Cassette (ABC) transporters located at the apical membrane of BECs[9]. In particular P-gp (ABCB1/MDR1) and BCRP (ABCG2) are the two most dominant drug efflux transporters in the BBB where they restrict the brain penetration of numerous anticancer agents, including many of the novel small molecule targeted inhibitors[10-12]. Importantly, this impaired brain penetration can attenuate target engagement and thereby therapeutic efficacy against intracranially located tumors[13-15]. As it is thus of paramount importance to select the most appropriate candidate drugs for treatment of intracranial neoplasms with respect to their brain penetration, we have first determined the substrate affinities of PD0325901, trametinib

(GSK1120212), binimetinib (MEK162), selumetinib (AZD6244) and pimasertib (AS703026) for P-gp and BCRP by *in vitro* transwell assays. Based on these data, we investigated the brain penetration of PD0325901, selumetinib and pimasertib in wild-type (WT) and transporter knockout mice and intracranial target engagement in WT mice following oral administration of drugs at doses that result in clinically relevant plasma levels.

METHODS

Drugs

PD0325901 and binimetinib (MEK162) were purchased from LC Laboratories (Woburn, MA) and Active Biochem (Bonn, Germany), respectively. Selumetinib (AZD6244), pimasertib (AS703026), trametinib (GSK1120212) and buparlisib (NVP-BKM120) were obtained from Selleck Chemicals (Houston, TX). Zosuquidar was purchased from Eli Lilly (Indianapolis, IN). Elacridar and Palomid 529 were kindly provided by GlaxoSmithKline (Research Triangle Park, NC) and Paloma Pharmaceuticals Inc. (Jamaica Plain, MA), respectively. All drugs were dissolved in DMSO for *in vitro* experiments.

Cell culture

All cell lines were previously generated in-house and were kindly provided by dr. A.H. Schinkel[16-18]. MDCK–Bcrp1, MDCK–BCRP, LLC–Mdr1a and LLC–MDR1 cells as well as their parental counterparts were cultured in MEM supplemented with 10% FBS, 1% L-glutamine, 1% sodium pyruvate, 1% MEM vitamins, 1% non-essential amino acids and 1% penicillin/streptomycin (all Life Technologies, Carlsbad, CA) under 37 °C and 5% CO_2 conditions.

Concentration equilibrium transport assays

Concentration equilibrium transport assays (CETAs) were performed as described previously[19]. In short, MDCK or LLC cells were seeded onto Transwell microporous polycarbonate membrane filters (Costar Corning; Corning, NY) and allowed to grow into a monolayer. The experiment was started by replacing medium in the apical and basolateral compartment by MEK inhibitor containing medium (100 nM or 1 μM) and samples were taken from both compartments at specific time points. When appropriate, specific transport was inhibited using the P-gp inhibitor zosuquidar (5 μM) or the dual P-gp/BCRP inhibitor elacridar (5 μM). Monolayer integrity was assessed by translocation of Carboxyl-[^{14}C]-inulin. Wells demonstrating leakiness exceeding 1.5% per hour were excluded from analysis.

PD0325901, selumetinib and pimasertib samples were mixed with 4 parts of acetonitrile. After

centrifugation, the supernatant was 3-fold diluted in water and the drug concentration was measured by High Performance Liquid Chromatography (HPLC) with UV detection at 275 nm (PD0325901), 257 nm (selumetinib) or 282 nm (pimasertib) using a GraceSmart RP18 5µm column (Grace; Deerfield, IL). The mobile phases comprised of 0.1% (v/v) formic acid in water and 80% (v/v) methanol in water. Elution was done at different ratios (v/v) for PD0325901 (25/75), selumetinib (15/85) and pimasertib (17.5/82.5) delivered at a flow rate of 0.2 ml/min. Data analysis was performed using Chromeleon® 6.80 software (Dionex; Sunnyvale, CA).

Binimetinib and trametinib were extracted from medium using ethyl acetate for liquid–liquid extraction and buparlisib as internal standard. Samples were reconstituted in acetonitrile:water (30:70 v/v) and measured in a LC–MS/MS setup consisting of an Ultimate 3000 LC System (Dionex) and an API 3000 mass spectrometer (AB Sciex; Framingham, MA). Separation was performed on a ZORBAX Extend-C18 column (Agilent Technologies; Santa Clara, CA). Mobile phase A (0.1% formic acid in water) and B (methanol) was used in a 5 min gradient from 30%B to 95%B maintained for 3 min followed by re-equilibration at 30%B. Multiple reaction monitoring (MRM) ion pairs were 443.0/381.0 (binimetinib) and 616.2/491.2 (trametinib). Data was analyzed using Analyst® 1.5.1 software (AB Sciex).

Animals

All animal housing and studies were conducted according to national law and institutional guidelines and approved by the animal experimental committee. Housing environment was temperature-controlled, on a 12 h light/dark cycle and food and water were provided *ad libitum*.

Pharmacokinetic studies

Pharmacokinetic studies were conducted using WT, *Abcg2*$^{-/-}$, *Abcb1a/b*$^{-/-}$ and *Abcb1a/b;Abcg2*$^{-/-}$ FVB mice. All knockout mouse strains were previously generated and characterized within the Netherlands Cancer Institute[20-22]. PD0325901, selumetinib and pimasertib were either dissolved in DMSO and administered i.v. at a dose of 5 mg/kg or given p.o. at various doses in a formulation consisting of DMSO:Cremophor EL:water (1:1:8). Blood was collected from the tip of the tail at serial time points, while terminal bleeding was done by cardiac puncture under isoflurane anesthesia, followed by tissue collection. Plasma was obtained by centrifugation (5 min, 5,000 rpm, 4 °C). Tissues were weighed and homogenized using a FastPrep®-24 (MP-Biomedicals; Santa Ana, CA) in 1% (w/v) bovine serum albumin in water. Samples were analyzed using an LC–MS/MS method as described for trametinib and binimetinib CETAs. Palomid 529 was used as internal standard for PD0325901 analysis, while selumetinib and pimasertib were used as reciprocal internal standards. MRM ion pairs were 483.1/249.1 (PD0325901), 459.1/397.0 (selumetinib) and 432.1/214.1 (pimasertib).

Western blotting

Brain tissues were homogenized in complete RIPA buffer containing phosphatase inhibitors. Primary antibodies used in this study are phospho-Erk1/2 (pErk1$^{T202/204}$ and pErk2$^{T183/Y185}$) and total Erk1/2 (C16; Santa Cruz Biotechnology; Santa Cruz, CA). Blots were quantified using Image Lab v5.2.1 (Bio-Rad; Hercules, CA).

Pharmacokinetic and statistical analysis

CETA results were analyzed using the General linear model repeated measures procedure of SPSS (v20; SPSS Inc; Chicago, IL) as described previously[12]. For *in vivo* experiments one-way analysis of variance and *post hoc* Tukey was performed. Differences were considered statistically significant when $p < 0.05$.

RESULTS

Selumetinib is transported and restricted from the brain by P-gp and BCRP

ABC transporter knockout mice and concentration equilibrium transport assays (CETAs) together form a comprehensive set of experiments to investigate the impact of P-gp and BCRP on the brain penetration of small molecules and have been extensively used for these purposes in the past[11-13,23,24]. Here, we used these methods to study a panel of MEK inhibitors (**Figure 1**). First, selumetinib was demonstrated to be a substrate of human and murine P-gp (ABCB1/MDR1) and BCRP (ABCG2). Species differences in substrate affinities between murine and human transport proteins may exist. However, selumetinib was efficiently transported by cells transduced with either transporter, but much less by their untransduced (parent; PK1) counterparts (**Figures 2A–B and Table 1**). Near-complete transport inhibition by either zosuquidar or elacridar in the transduced cells confirmed that P-gp and BCRP were mostly responsible for the observed drug translocation. The translocation of selumetinib in the LLC–PK1 cells was not reduced by zosuquidar, indicating that this might be caused by another transporter that seems absent in the LLC–Mdr1a cells. The residual translocation in the MDCK–Bcrp1 cells in the presence of elacridar suggests incomplete inhibition of Bcrp1.

Pharmacokinetic studies revealed a marked impact of P-gp and BCRP on selumetinib brain penetration. Whereas plasma levels were similar in wild-type and transporter knockout mice, the brain concentration of selumetinib was 3.5-fold increased in *Abcb1a/b;Abcg2*$^{-/-}$ mice following i.v. administration (**Figure 2C and Table 1**). Interestingly, neither single knockout mouse strain demonstrated any increased brain penetration, indicative of redundancy between P-gp and BCRP as has been observed for various other compounds[11,24,25]. The brain–plasma ratio was only about

0.02, which is close to the fraction of blood in brain samples. The selumetinib brain–plasma ratio increased in *Abcb1a/b;Abcg2*$^{-/-}$ mice, but remained very poor (0.06).

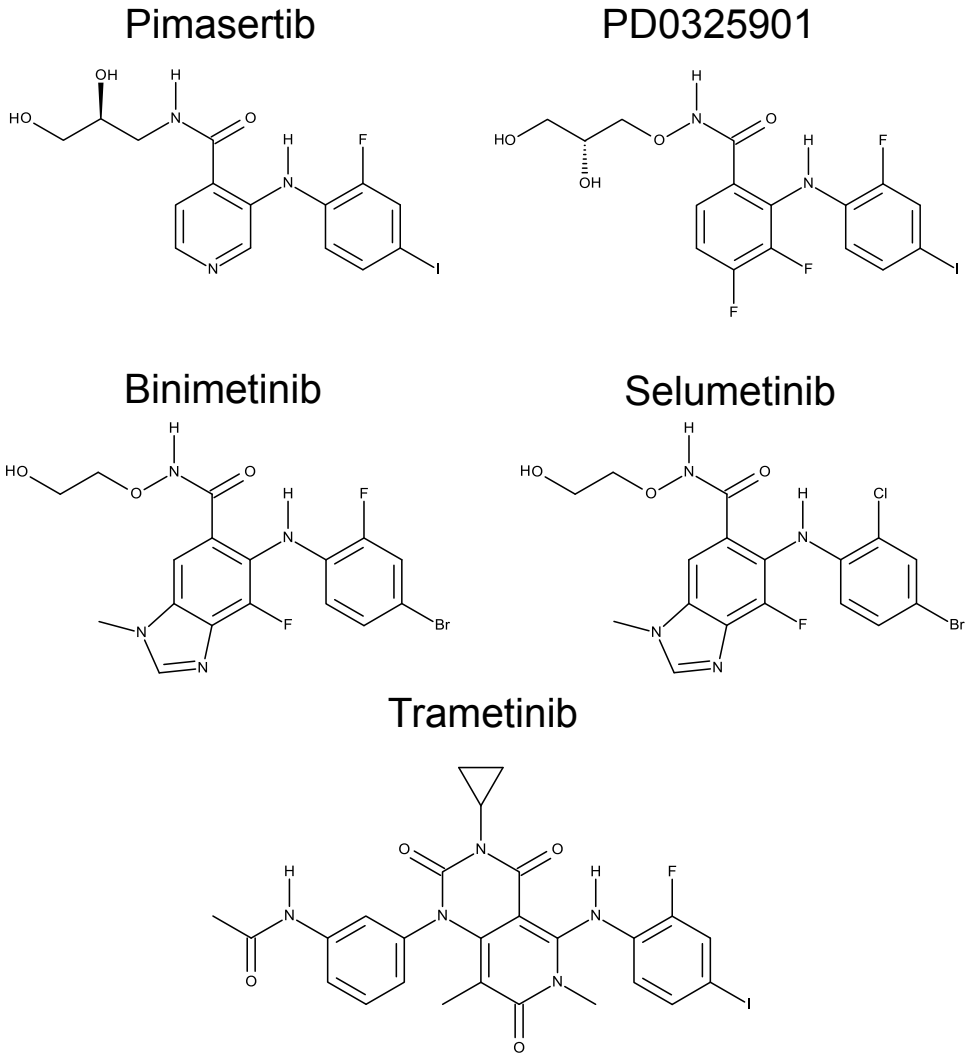

Figure 1 | Chemical structures of the panel of five MEK inhibitors. This study investigates five MEK inhibitors that are in clinical development: pimasertib (AS703026), PD0325901, binimetinib (MEK162), selumetinib (AZD6244) and trametinib (GSK1120212). As can be seen from the chemical structures, all inhibitors share a common backbone.

Since small molecules are mostly administered p.o. in preclinical efficacy studies and clinical trials, we sought to determine the brain concentration that could be reached in wild-type mice following oral administration of a range of dose levels that yielded clinically relevant plasma concentrations. A dose-dependent increase in both plasma and brain selumetinib concentration

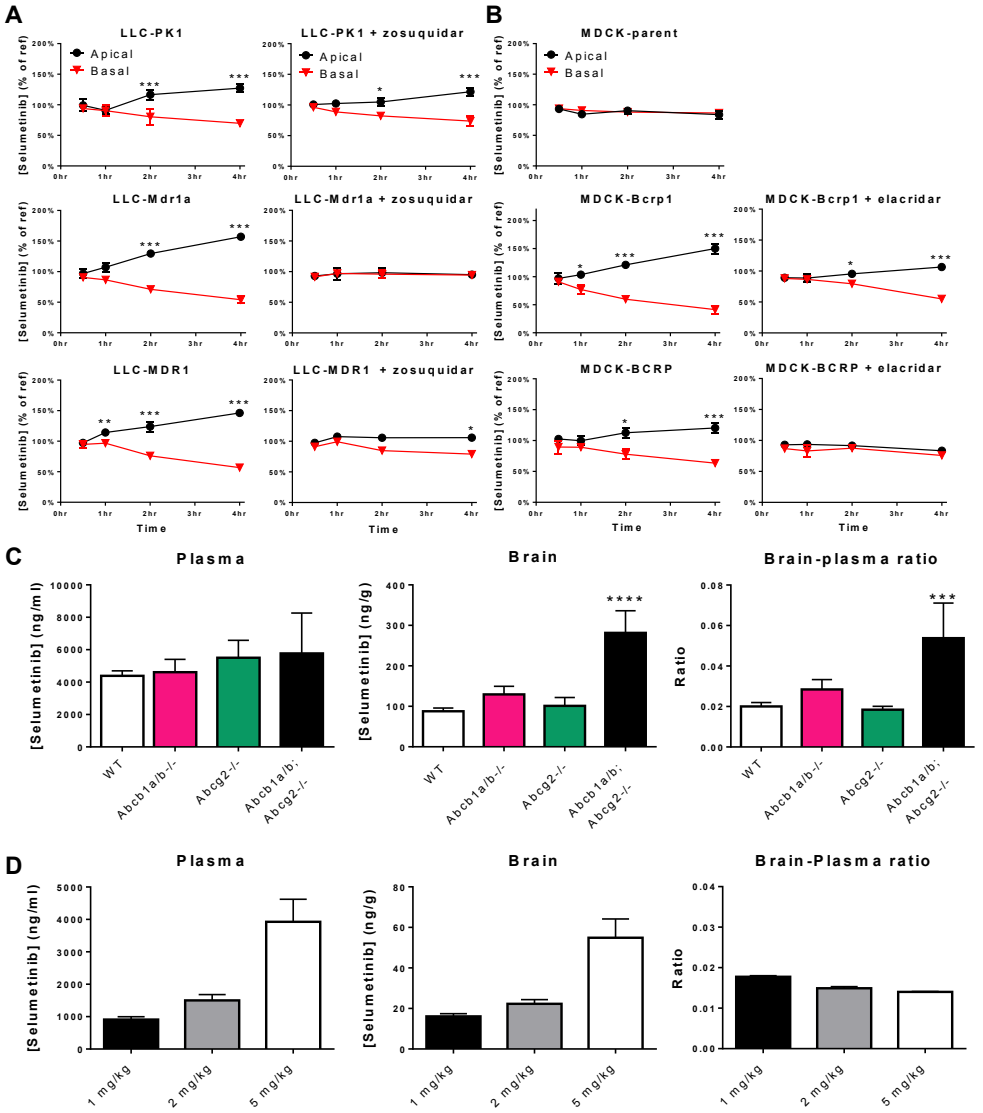

Figure 2 | The impact of P-gp and BCRP on the brain penetration of selumetinib. (**A**) Concentration equilibrium transport assays (CETAs) for selumetinib using parental and (murine) Mdr1a or (human) MDR1 overexpressing LLC cells. Zosuquidar (5 μM) was used to specifically inhibit P-gp mediated transport. Data are means ± SD; n = 6; ** $p < 0.01$, *** $p < 0.001$. (**B**) CETAs for selumetinib using parental (non-transduced) MDCK cells and sublines that overexpress the murine Bcrp1 or human BCRP protein. Elacridar (5 μM) was used to specifically inhibit P-gp and BCRP mediated transport. Data are means ± SD; n = 6; * $p < 0.05$, *** $p < 0.001$. (**C**) Selumetinib plasma concentration, brain concentration and brain–plasma ratios in WT, *Abcb1a/b*$^{-/-}$, *Abcg2*$^{-/-}$ and *Abcb1a/b;Abcg2*$^{-/-}$ mice 1 h after 5 mg/kg i.v. administration. Data are means ± SD; n = 4; *** $p < 0.001$, **** $p < 0.0001$. (**D**) Selumetinib plasma concentration, brain concentration and brain–plasma ratios in WT mice 1 h after p.o. administration of 1, 2, or 5 mg/kg. Data are means ± SD; n = 2.

was observed 1 hour after doses ranging from 1 to 5 mg/kg, in all cases yielding a brain–plasma ratio similar to that following i.v. administration (**Figure 2D and Table 1**). Unfortunately however, dose levels higher than 1 mg/kg resulted in a plasma concentration above clinically achievable levels and thus 15 ng/g seems to be highest feasible brain concentration in the clinic (**Table 1**).

Pimasertib is very efficiently transported by P-gp and BCRP, profoundly impacting its brain penetration

Pimasertib displayed a similar pattern of results as selumetinib, although the extent and efficiency of transport was even more pronounced as CETAs showed very efficient translocation in all transduced sublines. Translocation was inhibited by zosuquidar in LLC–MDR1 cells, but not in LLC–PK1 (**Figures 3A–B and Table 1**), again suggesting the presence of an alternative transporter. Elacridar appears to be unable to inhibit transport by Bcrp1. *In vivo*, a 4.4-fold increased brain concentration was found in *Abcb1a/b;Abcg2*$^{-/-}$ mice compared to wild-type mice, while no difference was seen in single knockout mice due to transporter redundancy (**Figure 3C and Table 1**). Importantly, already in wild-type mice pimasertib demonstrated a quite reasonable brain–plasma ratio of 0.6, which was further increased to 2.4 in *Abcb1a/b;Abcg2*$^{-/-}$ mice. The brain–plasma ratio was about 2-fold lower after oral administration. Oral administration in wild-type mice indicated that 75 ng/g is likely the highest clinically achievable brain concentration since 2 mg/kg was the highest dose at which the plasma concentration did not exceed those in patients receiving the clinical maximum tolerated dose (MTD) (**Figure 3D and Table 1**).

PD0325901 is a weak substrate of P-gp and BCRP and reaches reasonable brain levels in wild-type mice

Of all five MEK inhibitors that were analyzed, PD0325901 was least efficiently transported in CETAs, although it still exhibited substrate affinity towards P-gp and BCRP (**Figures 4A–B, Table 1 and Supplementary Figure 1**). Following i.v. administration, PD0325901 has a similar brain–plasma ratio as pimasertib (0.6). The brain penetration of PD0325901 is the least restricted by P-gp and BCRP as it is 2-fold higher in *Abcb1a/b;Abcg2*$^{-/-}$ mice (**Figure 4C and Table 1**). Finally, PD0325901 achieved the highest brain concentration (82 ng/g) following oral administration of a dose that resulted in a clinically feasible plasma concentration, despite a strongly reduced brain–plasma ratio compared to i.v. administration (**Figure 4D and Table 1**).

PD0325901 and pimasertib achieve the highest clinically relevant target inhibition

To understand the impact of brain pharmacokinetics on therapeutic efficacy it is imperative to assess target engagement of selective inhibitors. To this end, phosphorylation of ERK1/2, directly downstream of MEK, was analyzed in the brains of the mice in the pharmacokinetic studies

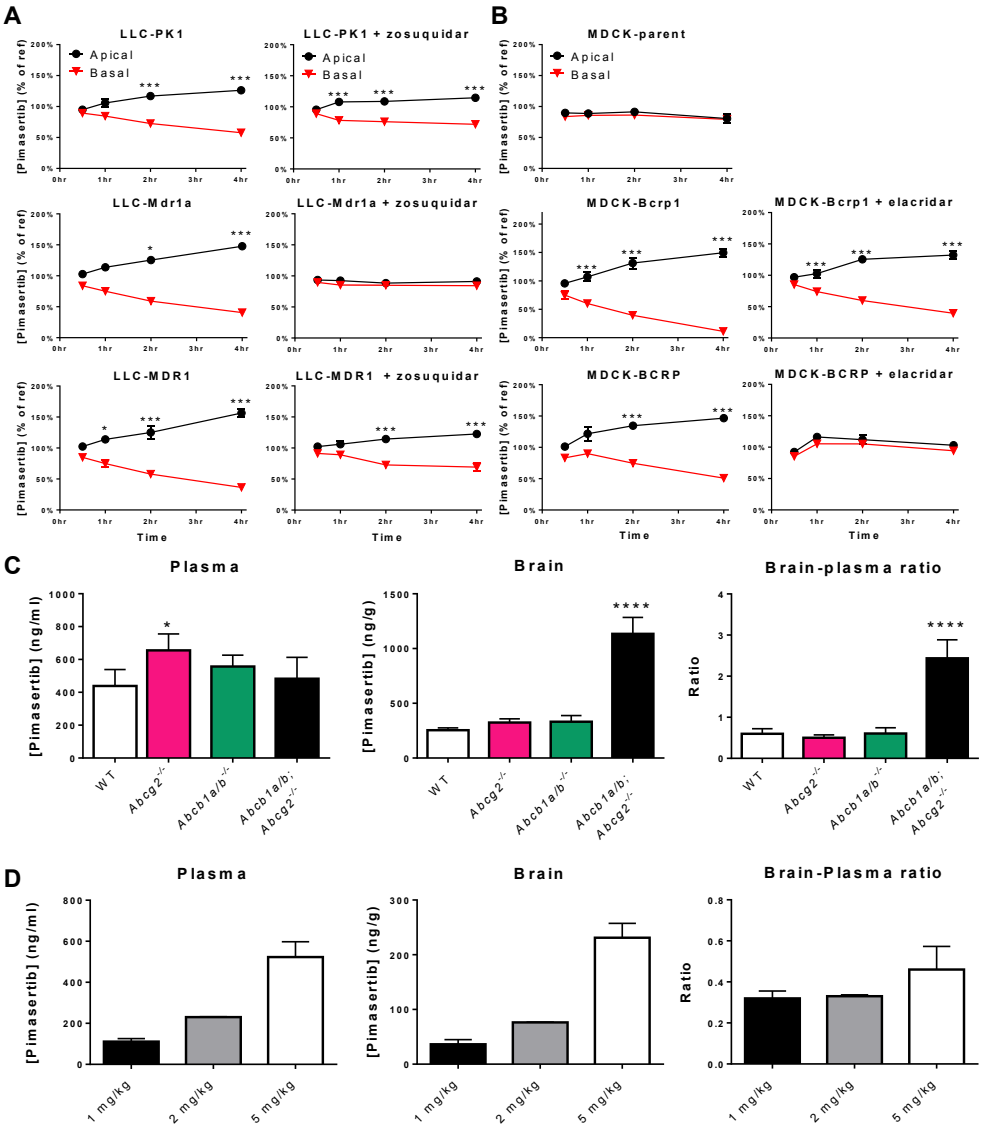

Figure 3 | The impact of P-gp and BCRP on the brain penetration of pimasertib. (**A**) Concentration equilibrium transport assays (CETAs) for pimasertib using parental and Mdr1a or MDR1 overexpressing LLC cells. Zosuquidar (5 µM) was used to specifically inhibit P-gp mediated transport. Data are means ± SD; n = 6; * $p < 0.05$, ** $p < 0.01$, *** $p < 0.001$. (**B**) CETAs for pimasertib using parental and Bcrp1/BCRP overexpressing MDCK cells. Elacridar (5 µM) was used to specifically inhibit P-gp and BCRP mediated transport. Data are means ± SD; n = 6; *** $p < 0.001$. (**C**) Pimasertib plasma concentration, brain concentration and brain–plasma ratios in WT, *Abcb1a/b*$^{-/-}$, *Abcg2*$^{-/-}$ and *Abcb1a/b;Abcg2*$^{-/-}$ mice 1 h after 5 mg/kg i.v. administration. Data are means ± SD; n = 4; * $p < 0.05$, **** $p < 0.0001$. (**D**) Pimasertib plasma concentration, brain concentration and brain–plasma ratios in WT mice 1 h after p.o. administration of 1, 2, or 5 mg/kg. Data are means ± SD; n = 2.

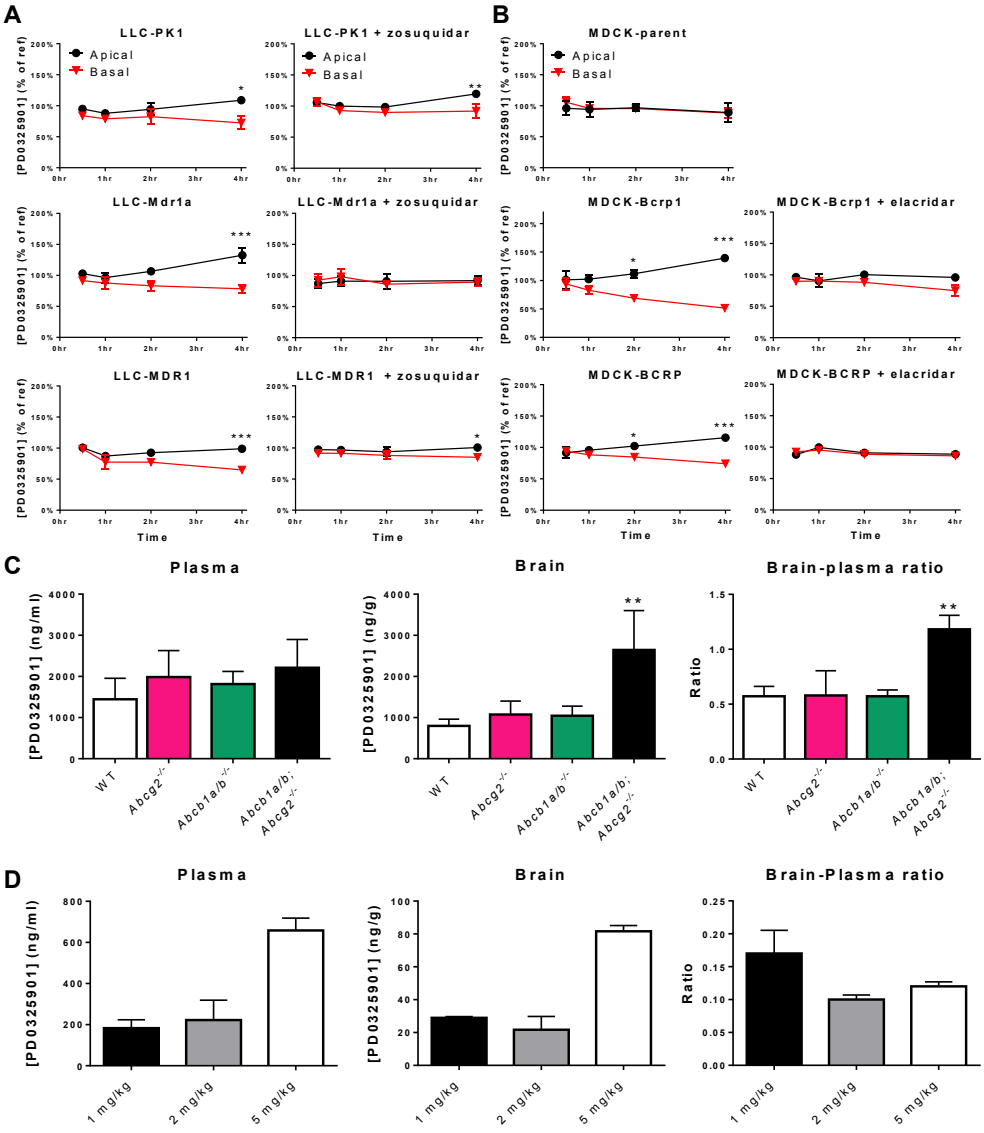

Figure 4 | The impact of P-gp and BCRP on the brain penetration of PD0325901. (**A**) Concentration equilibrium transport assays (CETAs) for PD0325901 using parental and Mdr1a or MDR1 overexpressing LLC cells. Zosuquidar (5 μM) was used to specifically inhibit P-gp mediated transport. Data are means ± SD; n = 6; * $p < 0.05$, ** $p < 0.01$, *** $p < 0.001$. (**B**) CETAs for PD0325901 using parental and Bcrp1/BCRP overexpressing MDCK cells. Elacridar (5 μM) was used to specifically inhibit P-gp and BCRP mediated transport. Data are means ± SD; n = 6; * $p < 0.05$, *** $p < 0.001$. (**C**) PD0325901 plasma concentration, brain concentration and brain–plasma ratios in WT, *Abcb1a/b*$^{-/-}$, *Abcg2*$^{-/-}$ and *Abcb1a/b;Abcg2*$^{-/-}$ mice 1 h after 5 mg/kg i.v. administration. Data are means ± SD; n = 4; ** $p < 0.01$. (**D**) PD0325901 plasma concentration, brain concentration and brain–plasma ratios in WT mice 1 h after p.o. administration of 1, 2, or 5 mg/kg. Data are means ± SD; n = 2.

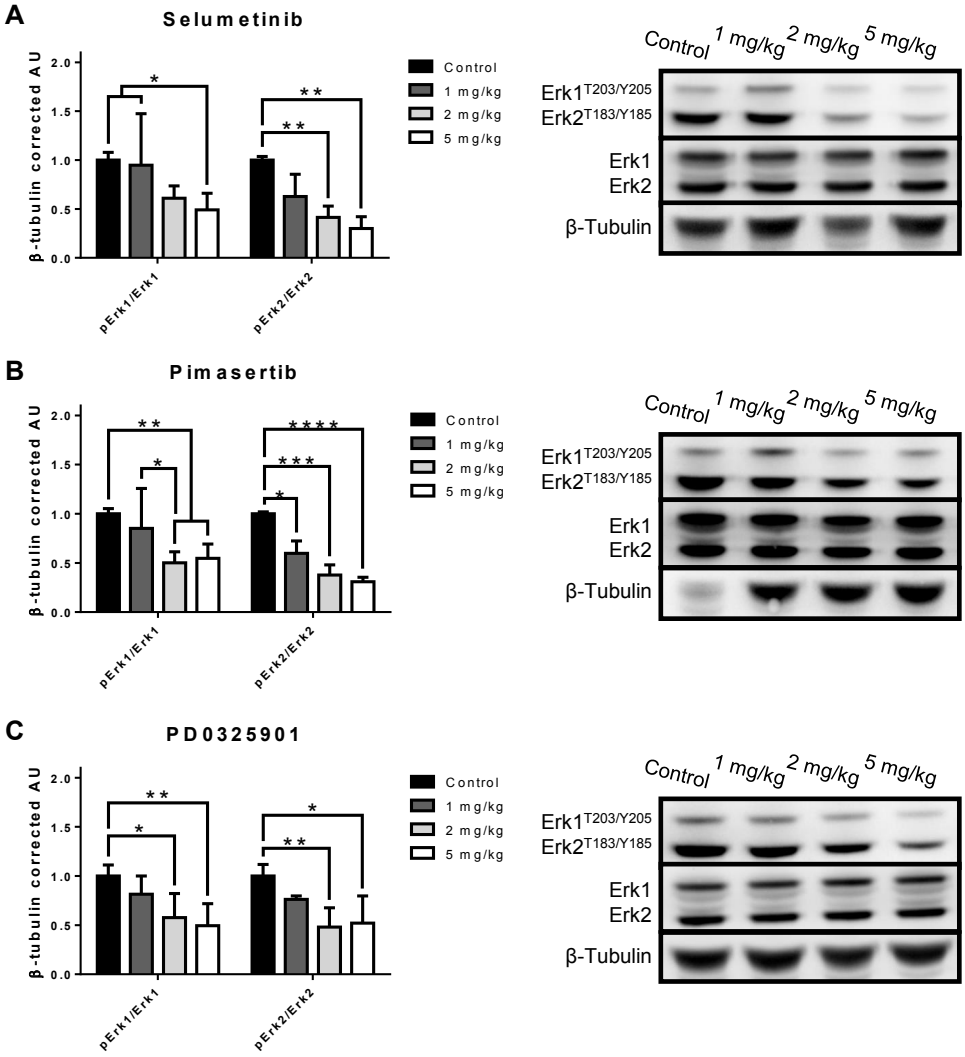

Figure 5 | Intracranial target engagement of selumetinib, pimasertib and PD0325901 following oral administration. (**A**) Western blot of brains of mice from **Figure 2D** that have received p.o. selumetinib. Erk1/2 phosphorylation levels (pErk1$^{T202/204}$ and pErk2$^{T183/Y185}$) are quantified in arbitrary units (AU) based on band intensity and corrected for total Erk1/2. Data are means ± SD; n = 4; * $p < 0.05$, ** $p < 0.01$. (**B**) Western blot of brains of mice from **Figure 3D** that have received p.o. pimasertib. Data are means ± SD; n = 4; * $p < 0.05$, ** $p < 0.01$, *** $p < 0.001$, **** $p < 0.0001$. (**C**) Western blot of brains of mice from **Figure 4D** that have received p.o. PD0325901. Data are means ± SD; n = 4; * $p < 0.05$, ** $p < 0.01$.

receiving various oral doses of the MEK inhibitors**.** Target inhibition was dose-dependent for all inhibitors, with the greatest inhibition achieved by 5 mg/kg of selumetinib (**Figure 5 and Table 1**). However, as mentioned previously, the highest dose levels that yielded plasma concentrations that are clinically achievable in patients were 1 mg/kg for selumetinib, 2 mg/kg for pimasertib and 5 mg/kg for PD0325901 (**Table 1**). When comparing these dose levels, pimasertib and

PD0325901 achieved a better target inhibition levels than selumetinib. Both MEK inhibitors achieved approximately 50% inhibition of both ERK1 and ERK2.

DISCUSSION

In recent years, characterization of the genomic landscapes of various primary and secondary intracranial neoplasms has demonstrated that MAPK pathway overactivation is a common hallmark of these tumors[1-3,5,6]. The potential importance of MEK inhibitors for the treatment of intracranial neoplasms calls for careful selection of the most appropriate candidate inhibitor, since focusing resources on the MEK inhibitor with the greatest potential to achieve a clinical benefit would ensure the most rapid clinical implementation if efficacy can be confirmed. In this study, we select PD0235901 as the most promising candidate out of a panel of five MEK inhibitors that are in clinical development (**Table 1**).

Only very few clinical studies investigating MEK inhibitors against intracranial tumors are ongoing or have been conducted. The clinical development of MEK inhibitors is slightly more advanced for secondary brain tumors (*e.g.*, ClinicalTrials.gov Identifiers NCT02015117, NCT01245062, NCT01693068) than for primary brain tumors (*e.g.*, NCT01089101, NCT02285439, NCT02124772). MEK inhibitors have found their place in anticancer therapy. For example, a phase III trial on trametinib in patients with $BRAF^{V600E}$-postive metastatic melanoma demonstrated improved survival for metastatic patients[26]. However, in this study patients with prior brain metastases were excluded from the analysis. In general, intracranial metastases are a negative prognostic factor, as a consequence of the more advanced disease state and the complications of drug delivery through the blood–brain barrier. As has been demonstrated in mice, P-gp and BCRP at the blood–brain barrier can limit the access and thus efficacy of anticancer agents against tumors in the brain, whereas genetically similar extracranial tumors are responsive[27].

Despite the similarities in molecular structures of the different MEK inhibitors, there are major distinctions in their affinity for P-gp and BCRP and the ability to permeate the BBB, underscoring the need to make a careful choice. Based on our preclinical data, we demonstrate that brain access of selumetinib is efficiently restricted (brain–plasma ratio of only 0.02 to 0.06) and results in just a marginal inhibition of intracranial MEK at clinically achievable plasma concentrations. In fact, the selumetinib brain–plasma ratio in WT mice is not much higher than the value that we would obtain when all drug in the sample originates from blood in the sample[28], suggesting that selumetinib is near-incapable of penetrating the BBB. In contrast, both pimasertib and PD0325901 displayed much better pharmacokinetic/pharmacodynamic (PK/PD) characteristics, although PD0325901 outperformed pimasertib in some respects. Of all five MEK inhibitors that were analyzed by *in vitro* transwell assays, PD0325901 was the weakest substrate of P-gp and BCRP (**Table 1, Figures 2A–B, 3A–B, 4A–B and Supplementary Figure 1**), whereas the affinities of the other

Experiment	Parameter / Condition	MEK inhibitor				
		Selumetinib	Pimasertib	PD0325901	Trametinib	Binimetinib
IC_{50} (nM)	MEK1 / MEK2 K_i	14 / NA [37]	ND	0.33 [38]	0.92 / 1.8 [40]	12 [42]
	Cell (MAPK act.)	50-2,000 [31,37]	5-2,000 [31]	10-100 [32,33]	0.5-175 [40]	2.5-10,000 [41]
	Cell (MAPK WT)	>20,000 [37]	2-2,000 [31]	2,000-4,000 [39]	>10,000 [40]	28-3,500 [41]
Patient	Regimen	100 mg *b.i.d.*	45 mg *q.d.*	15 mg *b.i.d.*	2 mg *q.d.*	60 mg *b.i.d.*
MTD	C_{max} (ng/ml)	900 [44]	200 [34]	840 [30]	22 [43]	500 [42]
Plasma PK	$t_{1/2}$ (h)	ND	5.1 [34]	5.2 [30]	90 [43]	3.6 [42]
Concentration	Mdr1a / Abcb1a	+++	+++	++	+++	+++
equilibrium	MDR1 / ABCB1	+++	+++	+	+++	+++
transport	Bcrp1 / Abcg2	+++	+++	++	++	+++
assay	BCRP / ABCG2	++	+++	+	++	++
Plasma 1 h	WT	4400±320	440±99	1400±510	≈1200 [29]	NA
(ng/ml)	*Abcb1a/b*$^{-/-}$	4600±790	660±100	2000±690	≈1200 [29]	NA
i.v. 5 mg/kg	*Abcg2*$^{-/-}$	5500±1100	560±70	1800±310	≈1200 [29]	NA
	Abcb1a/b;Abcg2$^{-/-}$	5800±2500	480±130	2200±690	≈1200 [29]	NA
Brain 1 h	WT	88±8.1	250±21	800±160	≈85 [29]	NA
(ng/g)	*Abcb1a/b*$^{-/-}$	130±20	320±34	1100±330	≈1500 [29]	NA
i.v. 5 mg/kg	*Abcg2*$^{-/-}$	100±21	330±56	1000±230	≈60 [29]	NA
	Abcb1a/b;Abcg2$^{-/-}$	280±55	1100±150	2600±960	≈1400 [29]	NA
Plasma 1 h	1 mg/kg	910±130	110±21	180±58	NA	NA
(ng/ml)	2 mg/kg	(1500±250)	230±3.5	220±140	NA	NA
p.o.	5 mg/kg	(3900±980)	(520±110)	660±85	NA	NA
Brain 1 h	1 mg/kg	16±1.9	36±12	29±1.0	NA	NA
(ng/g)	2 mg/kg	(22±2.9)	76±0.6	22±11	NA	NA
p.o.	5 mg/kg	(55±13)	(230±37)	82±5.0	NA	NA
pErk1/pErk2	1 mg/kg	95±53/63±23	85±41/60±13	81±19/76±3.5	NA	NA
signaling (%)	2 mg/kg	(61±13/41±12)	50±11/38±10	57±25/48±20	NA	NA
in vivo	5 mg/kg	(49±17/30±12)	(55±15/31±4.5)	49±22/52±28	NA	NA

Table 1 | Preclinical and clinical parameters of the panel of MEK inhibitors. Overview table of preclinical and clinical characteristics of the panel of MEK inhibitors studied here. Data are from this study or obtained from references[29-34, 37-44] as indicated. The potency of these drugs (IC_{50} values) is provided in cell free systems (K_i) and in cells with activated or wild-type MAPK pathway. Affinity for P-gp an BCRP in concentration equilibrium transport assays was graded as + (mild affinity), ++ (moderate affinity), or +++ (strong affinity). Plasma concentrations, brain concentrations and target inhibition levels in brain that occurred at levels that are not clinically achievable are put between parentheses. IC_{50}, 50% inhibitory concentration; act., activated; WT, wild-type; NA, not applicable; ND, not determined; MTD, maximum tolerated dose; PK, pharmacokinetics; C_{max}, maximum concentration; *q.d.*, *quaque die* (once daily) *b.i.d.*, *bis in die* (bidaily); $t_{1/2}$, half-life; i.v., intravenously; p.o., *per os* (orally). Data are represented as mean ± SD. NA, data not available.

compounds were quite similar. Based on these, we also took pimasertib and PD0325901 to *in vivo* studies with ABC transporter knockout mice that showed that P-gp and Bcrp1 alone can reduce brain entry to the level in WT mice. Intriguingly, a recent study with trametinib reports that the brain penetration of this compound in WT mice is only 5 to 10% of the levels in knockout mice but in this case only Abcb1 is limiting drug entry into the brain (**Table 1**)[29]. Pimasertib and PD0325901 achieved similar intracranial MEK inhibition levels at clinically feasible plasma concentrations, although the inhibition level by PD0325901 might be slightly underestimated since the highest PD0325901 plasma level achieved in this study was lower than the C_{max} of patients receiving the MTD (660 *vs.* 840 ng/mL)[29]. Even though target inhibition was similar for pimasertib, PD0325901 could still be considered a more favorable candidate for the following three reasons. First, because of its lower affinity for P-gp and BCRP, PD0325901 could be less prone to ABC transporter-mediated acquired resistance. Second, it has a lower IC_{50} against MAPK pathway overactivated cancer cell lines (**Table 1**), making it intrinsically more effective against cancer cells[31-33]. Third, PD0325901 demonstrates a considerably smaller inter-patient variability in plasma PK profiles, with a coefficient of variation in C_{max} following oral administration of 30% for PD0325901 and 100% for pimasertib[30,34]. A more homogeneous PK profile among patients is clearly more favorable for treatment accuracy, especially when considering that patients with the lowest exposure to pimasertib (C_{max} of 70 ng/mL) will have plasma levels above the intended target inhibition concentration for only a very short duration. The much higher inter-patient variability of pimasertib may indicate a more problematic uptake after oral intake. In line with this reasoning, pimasertib reaches a 4-fold lower C_{max} compared to PD0325901, even though the daily intake is 1.5-fold higher (45 mg *q.d. vs.* 15 mg *b.i.d.*).

Just like many other MEK inhibitors that have been tested in the clinic, ocular toxicity was the dose limiting toxicity for PD0325901, raising the question of a possible class-effect of these targeted agents[30,35]. However, the ocular toxicity was manageable and reversible at the MTD of 15 mg *b.i.d.* when given in a schedule of 5 days on/2 days off for 3 weeks followed by 1 week off[30]. Importantly, the trough plasma levels of PD0325901 (170 ng/mL) remained well over the intended target concentration (16.5 ng/mL), despite this dosing schedule containing days off the drug. PD0325901 is currently in clinical trials for treatment of extracranial solid tumors (NCT02022982, NCT02510001, NCT02039336).

In conclusion, *in vitro* and *in vivo* studies demonstrate that among a panel of five MEK inhibitors that are in clinical development, PD0325901 possesses the most favorable pharmacokinetic and pharmacodynamics properties to reach efficacy in the brain. These characteristics make PD0325901 the most promising candidate for further development as treatment for intracranial malignancies.

REFERENCES

1. Brennan, C.W., *et al.* The somatic genomic landscape of glioblastoma. *Cell* **155**, 462-477 (2013).
2. The Cancer Genome Atlas Research Network. Comprehensive, integrative genomic analysis of diffuse lower-grade gliomas. *N Engl J Med* **372**, 2481-2498 (2015).
3. Wu, G., *et al.* The genomic landscape of diffuse intrinsic pontine glioma and pediatric non-brainstem high-grade glioma. *Nat Genet* **46**, 444-450 (2014).
4. Bender, S., *et al.* Recurrent MET fusion genes represent a drug target in pediatric glioblastoma. *Nat Med* **22**, 1314-1320 (2016).
5. The Cancer Genome Atlas Research Network. Genomic classification of cutaneous melanoma. *Cell* **161**, 1681-1696 (2015).
6. Govindan, R., *et al.* Genomic landscape of non-small cell lung cancer in smokers and never-smokers. *Cell* **150**, 1121-1134 (2012).
7. Schubbert, S., *et al.* Hyperactive Ras in developmental disorders and cancer. *Nat Rev Cancer* **7**, 295-308 (2007).
8. Frémin, C. & Meloche, S. From basic research to clinical development of MEK1/2 inhibitors for cancer therapy. *J Hematol Oncol* **3**, 8 (2010).
9. van Tellingen, O., *et al.* Overcoming the blood-brain tumor barrier for effective glioblastoma treatment. *Drug Resist Updat* **19**, 1-12 (2015).
10. Durmus, S., *et al.* Apical ABC transporters and cancer chemotherapeutic drug disposition. *Adv Cancer Res* **125**, 1-41 (2015).
11. Zhang, P., *et al.* ABCB1 and ABCG2 restrict the brain penetration of a panel of novel EZH2-inhibitors. *Int J Cancer* **137**, 2007-2018 (2015).
12. de Gooijer, M.C., *et al.* P-glycoprotein and breast cancer resistance protein restrict the brain penetration of the CDK4/6 inhibitor palbociclib. *Invest New Drugs* **33**, 1012-1019 (2015).
13. Lin, F., *et al.* ABCB1, ABCG2, and PTEN determine the response of glioblastoma to temozolomide and ABT-888 therapy. *Clin Cancer Res* **20**, 2703-2713 (2014).
14. Becker, C.M., *et al.* Decreased affinity for efflux transporters increases brain penetrance and molecular targeting of a PI3K/mTOR inhibitor in a mouse model of glioblastoma. *Neuro Oncol* **17**, 1210-1219 (2015).
15. Parrish, K.E., *et al.* Efficacy of PARP inhibitor rucaparib in orthotopic glioblastoma xenografts is limited by ineffective drug penetration into the central nervous system. *Mol Cancer Ther* **14**, 2735-2743 (2015).
16. Schinkel, A.H., *et al.* Absence of the mdr1a P-glycoprotein in mice affects tissue distribution and pharmacokinetics of dexamethasone, digoxin, and cyclosporin A. *J Clin Invest* **96**, 1698-1705 (1995).
17. Jonker, J.W., *et al.* Role of breast cancer resistance protein in the bioavailability and fetal penetration of topotecan. *J Natl Cancer Inst* **92**, 1651-1656 (2000).
18. Pavek, P., *et al.* Human breast cancer resistance protein: interactions with steroid drugs, hormones, the dietary carcinogen 2-amino-1-methyl-6-phenylimidazo(4,5-*b*)pyridine, and transport of cimetidine. *J Pharm Exp Ther* **312**, 144-152 (2005).
19. Lin, F., *et al.* Dual mTORC1 and mTORC2 inhibitor Palomid 529 penetrates the blood-brain barrier without restriction by ABCB1 and ABCG2. *Int J Cancer* **133**, 1222-1233 (2013).
20. Schinkel, A.H., *et al.* Disruption of the mouse mdr1a P-glycoprotein gene leads to a deficiency in the blood-brain barrier and to increased sensitivity to drugs. *Cell* **77**, 491-502 (1994).
21. Jonker, J.W., *et al.* The breast cancer resistance protein protects against a major chlorophyll-derived dietary phototoxin and protoporphyria. *Proc Natl Acad Sci U S A* **99**, 15649-15654 (2002).
22. Jonker, J.W., *et al.* Contribution of the ABC transporters Bcrp1 and Mdr1a/1b to the side population phenotype in mammary gland and bone marrow of mice. *Stem Cells* **23**, 1059-1065 (2005).
23. Luna-Tortós, C., *et al.* Several major antiepileptic drugs are substrates for human P-glycoprotein. *Neuropharmacology* **55**, 1364-1375 (2008).
24. Durmus, S., *et al.* Breast cancer resistance protein (BCRP/ABCG2) and P-glycoprotein (P-gp/ABCB1) restrict oral availability and brain accumulation of the PARP inhibitor rucaparib (AG-014699). *Pharm Res* **32**, 37-46 (2015).
25. Agarwal, S., *et al.* Distribution of gefitinib to the brain is limited by P-glycoprotein (ABCB1) and breast cancer resistance protein (ABCG2)-mediated active efflux. *J Pharmacol Exp Ther* **334**, 147-155 (2010).
26. Flaherty, K.T., *et al.* Improved survival with MEK inhibition in BRAF-mutated melanoma. *N Engl J Med* **367**, 107-114 (2012).
27. Parrish, K.E., *et al.* Efflux transporters at the blood-brain barrier limit delivery and efficacy of cyclin-dependent kinase 4/6 inhibitor palbociclib (PD-0332991) in an orthotopic brain tumor model. *J Pharmacol Exp Ther* **355**, 264-271 (2015).
28. Dagenais, C., *et al.* Development of an in situ mouse brain perfusion model and its application to mdr1a P-glycoprotein-deficient mice. *J Cereb Blood Flow Metab* **20**, 381-386 (2000).
29. LoRusso, P.M. *et al.* Phase I pharmacokinetic and pharmacodynamic study of the oral MAPK/ERK kinase inhibitor PD-0325901 in patients with advanced cancers. *Clin Cancer Res* **16**, 1924-1937 (2010).
30. Haura, E.B., *et al.* A phase II study of PD-0325901, an oral MEK inhibitor, in previously treated patients with advanced non-small cell lung cancer. *Clin Cancer Res* **16**, 2450-2457 (2010).

SUPPLEMENTARY FIGURES

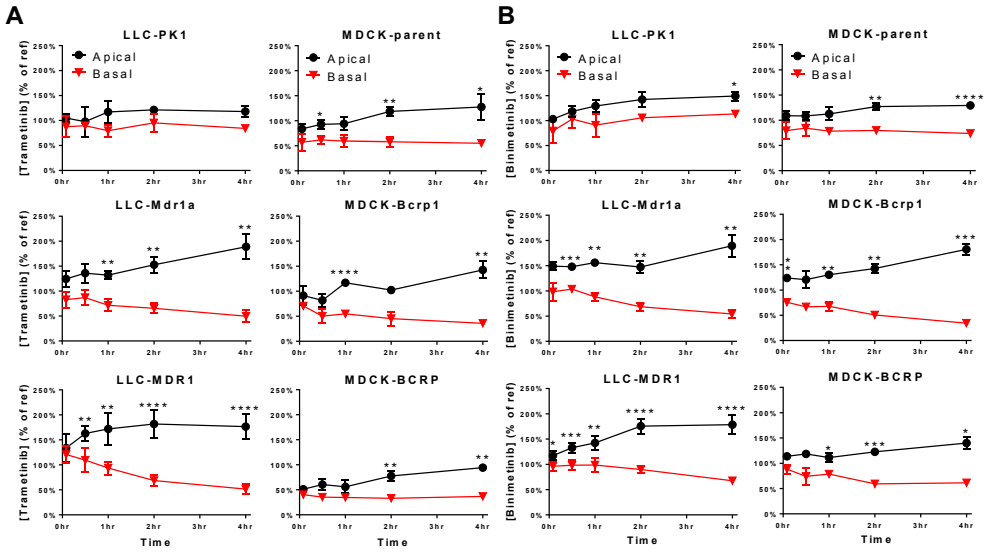

Supplementary Figure 1 | *In vitro* transport of trametinib and binimetinib by P-gp and BCRP. (**A**) Concentration equilibrium transport assays (CETAs) for trametinib using Mdr1a/MDR1 and Bcrp1/BCRP overexpressing cell lines and their parental counterparts (LLC–PK1 and MDCK–parent, respectively). Data are means ± SD; n = 3; * $p < 0.05$, ** $p < 0.01$, **** $p < 0.0001$. (**B**) CETAs for binimetinib using Mdr1a/MDR1 and Bcrp1/BCRP overexpressing cell lines and their parental counterparts. Data are means ± SD; n = 3; * $p < 0.05$, ** $p < 0.01$, *** $p < 0.001$, **** $p < 0.0001$.

Chapter 8

ACQUIRED AND INTRINSIC RESISTANCE TO VEMURAFENIB IN BRAFV600E-DRIVEN MELANOMA BRAIN METASTASES

M.C. de Gooijer*, P. Zhang*, L.C.M. Buil, S. Freriks, J.H. Beijnen, and O. van Tellingen

* These authors contributed equally

Manuscript submitted

ABSTRACT

The introduction of BRAF and MEK inhibitors has improved the survival of metastatic melanoma patients. Melanoma brain metastases (MBMs) also respond, albeit that responses are generally less durable than of extracranial metastases. MBMs may find protection by the blood–brain barrier (BBB). Notably, the drug efflux proteins P-glycoprotein (P-gp; ABCB1) and breast cancer resistance protein (BCRP; ABCG2) are expressed in brain endothelium and limit the brain penetration of many agents. We have used the *BRAF*-mutated A375 tumor model to investigate whether the BBB impacts the efficacy of vemurafenib. Although A375 tumors disrupt the integrity of the BBB, as shown by contrast-enhanced MRI, vemurafenib achieves greater antitumor efficacy against A375 MBMs in *Abcb1a/b;Abcg2*$^{-/-}$ mice compared to wild-type mice. P-gp and BCRP in brain tumor vessels limit vemurafenib penetration into A375 MBMs. Vemurafenib efficacy in both strains was similar against subcutaneous A375 tumors. Intriguingly, although initially responsive, A375 MBMs rapidly developed therapy resistance, even in *Abcb1a/b;Abcg2*$^{-/-}$ mice, and this was unrelated to pharmacokinetic or target inhibition issues. Rather, MBMs likely resorted to non-canonical growth signaling, as target inhibition of canonical MAPK and PI3K pathway signaling components was maintained in resistant intracranial A375 tumors. Taken together, this study demonstrates that BRAF^{V600E}-positive MBMs are not only less responsive to vemurafenib because they are partly protected by the BBB, but they also rapidly acquire further resistance by resorting to non-canonical growth signaling.

INTRODUCTION

Metastatic melanoma patients historically have a poor survival, mostly due to a lack of available effective chemotherapeutics[1]. However, significant advances have been made in the last decade that considerably improved the outlook for metastatic melanoma patients. These advances were kick-started by the discovery of oncogenic *BRAF* mutations as an important driver in melanoma[2]. The vast majority of *BRAF* mutations are in codon 600, substituting a valine for either a glutamic acid, lysine, arginine or aspartic acid, and result in constitutively active BRAF$^{V600E/K/R/D}$ oncoproteins[3]. BRAF^{V600}-positive melanoma cells can therefore proliferate independently from external growth stimuli[2]. Importantly, BRAF^{V600} can be therapeutically targeted, and three drugs have now been approved for treatment of metastatic melanoma: vemurafenib[4], dabrafenib[5] and encorafenib[6]. All three BRAF^{V600} inhibitors have generated striking clinical responses and significantly improved survival of metastatic melanoma patients[7-9]. However, therapy resistance invariably occurs, in most cases due to selection and outgrowth of clones that carry additional mutations more downstream in the MAPK signaling pathway[10]. Therefore, BRAF inhibitors are currently successfully combined with MEK inhibitors (vemurafenib and cobimetinib[11], dabrafenib and trametinib[12], encorafenib and binimetinib[6]), yielding further improved response rates and survival[13-15].

Despite all the recent success in treatment of metastatic melanoma, it is still unclear if patients with melanoma brain metastases (MBMs) benefit similarly from BRAF^{V600} inhibitors as metastatic melanoma patients with extracranial metastases. In the clinical studies that led to the approval of BRAF^{V600} inhibitors for metastatic melanoma, MBM patients were excluded from study participation. Only recently, clinical trials focusing specifically on MBM patients have been set up, and the results from several phase II trials appear to suggest that BRAF^{V600} inhibitors also induce responses in MBMs[16,17]. However, these responses were generally shorter than those achieved in extracranial metastases, suggesting that resistance occurs in MBMs even more rapidly than in extracranial metastases[17]. The reason for this rapid resistance in MBMs in unclear, but could be related to the brain environment. Several preclinical studies have demonstrated that vemurafenib[18,19], dabrafenib[20] and encorafenib[21] exhibit very poor brain penetration in mice as a result of efficient efflux by P-glycoprotein (P-gp; ABCB1) and breast cancer resistance protein (BCRP; ABCG2) at the blood–brain barrier (BBB). These observations seem to be corroborated by a clinical study showing that the concentration of vemurafenib in cerebrospinal fluid (CSF) was less than 1% of the plasma concentration[22].

The BBB limits the brain penetration of many xenobiotics, including many anticancer agents[23], and can consequently impact the intracranial anticancer efficacy of small molecule drugs[24,25]. We here investigate the impact of P-gp and BCRP on the efficacy of vemurafenib against MBMs in an intracranial mouse model of BRAF^{V600E}-driven melanoma. In line with the clinical data,

we find that MBMs can respond to vemurafenib, most likely as a result of compromised BBB integrity. However, vemurafenib achieved greater antitumor responses in *Abcb1a/b;Abcg2*$^{-/-}$ mice, indicating that P-gp and BCRP still play a protective role at the compromised BBB of MBMs. Moreover, vemurafenib efficacy could also be improved by co-administration of the P-gp/BCRP inhibitor elacridar, offering a potential clinical strategy for increasing vemurafenib efficacy against MBMs. Intriguingly, we also observed much more rapid therapy resistance in the preclinical MBM model compared to previously published extracranial melanoma mouse models, analogous to clinical observations. We conclude that $BRAF^{V600}$-positive MBMs are not only less responsive to vemurafenib because of limited drug penetration by drug efflux transporters, but also rapidly acquire resistance during treatment. Therefore, P-gp/BCRP inhibitors might help to improve the clinical response of MBMs to vemurafenib by increasing its brain penetration, but pinpointing the mechanism behind the brain-specific acquired resistance will likely be necessary to produce durable responses.

METHODS

Cell culture and drugs

A375 cells expressing firefly luciferase and mCherry (A375–FM) were cultured in minimum essential medium (MEM) supplemented with 10% fetal bovine serum (FBS), 1% penicillin/streptomycin, L-glutamine, nonessential amino acids, sodium pyruvate and MEM vitamins (all Life Technologies; Carlsbad, CA). Vemurafenib was purchased from LC Laboratories (Woburn, MA), vemurafenib-^{13}C6 was obtained from the Slotervaart Hospital pharmacy and elacridar was generously provided by GlaxoSmithKline (Research Triangle Park, NC).

Animals

Mice were housed and handled according to institutional guidelines complying with Dutch and European legislation. All experiments with animals were approved by the animal experiment committee of the institute. The animals were athymic (nude) mice of a > 99% FVB background with wild-type (WT) or *Abcb1a/b;Abcg2*$^{-/-}$ genotype, between 8 and 12 weeks of age. The animals were kept in a temperature-controlled environment at 20.9 °C on a 12 hour light/dark cycle and received chow and acidified water *ad libitum*.

Drug formulations

A stock solution (25 mg/ml or 10 mg/ml) of vemurafenib was dissolved in dimethyl sulfoxide (DMSO) and Cremophor EL (1:1; both Sigma–Aldrich; St, Louis, MO). The working solution (2.5 mg/ml or 1 mg/ml) was freshly prepared prior to administration by diluting the stock solution

with saline on the day of administration. Elacridar (5mg/ml) was formulated in DMSO:Cremophor EL:water (1:2:7) and prepared similarly.

Xenograft models and tumor growth monitoring

For subcutaneous xenograft models, 30 µL of cell suspension containing 3 × 10^6 A375–FM cells were injected into both flanks of WT and *Abcb1a/b;Abcg2*$^{-/-}$ nude mice. Stereotactic intracranial injections of melanoma cells were performed as described previously[24]. Briefly, WT and *Abcb1a/b;Abcg2*$^{-/-}$ nude mice were injected intracranially with 2 µL of A375-FM cell suspension containing 1 × 10^5 cells 2 mm lateral, 1 mm anterior and 3 mm ventral from the bregma. Tumor growth was measured by bioluminescence imaging (BLI) using the IVIS 200 imaging system (PerkinElmer; Waltham, MA) for intracranial tumors and by caliper for subcutaneous tumors. The volume of subcutaneous tumors was calculated in mm^3 using the modified ellipsoid formula (volume = 0.5 x length x $width^2$).

Magnetic resonance imaging

A BioSpec 70/20 USR (Bruker; Billerica, MA) system was used for magnetic resonance imaging (MRI), as described previously[24]. The MRI sequence consisted of T2-weighted, T1-weighted pre-contrast and T1-weighted post-gadoterate meglumine (Dotarem®; Guerbet; Villepinte, France) contrast imaging.

Pharmacokinetic studies

To establish vemurafenib plasma kinetics, tumor-free FVB WT and *Abcb1a/b;Abcg2*$^{-/-}$ nude mice received vemurafenib orally (p.o.). Elacridar (100 mg/kg) was administrated p.o. by gavage four hours before vemurafenib. Blood was sampled from the tail vein at 15 min, 1 h, 2 h, 4 h, 8 h and 24 h after the administration. The plasma was obtained by centrifugation (5 min, 5,000 rpm, 4°C). Vemurafenib was extracted from plasma by diethyl ether liquid–liquid extraction. Extracts were dried using a Savant SpeedVac Concentrator (Thermo Fisher Scientific; Waltham, MA), reconstituted in MeCN:water (30:70) and subjected to liquid chromatography/tandem mass spectrometry (LC/MS–MS) analysis. Vemurafenib-^{13}C6 was used as an internal standard.

To study its distribution in tumor-bearing mice, vemurafenib was administered p.o. to tumor-bearing mice for three days at a dose of 10 mg/kg or 25 mg/kg *q.d.*, starting 14 days after intracranial tumor cell injection. One group of mice received 10 mg/kg vemurafenib 4 hours after administration of 100 mg/kg elacridar. Four hours after the third administration, blood was collected by heart puncture, whole brains were dissected and divided into four parts: ipsilateral hemisphere (tissue from the tumor-bearing hemisphere that was free of macroscopic tumor

tissue), contralateral hemisphere (the tumor-free hemisphere), cerebellum and macroscopic tumor. In a follow-up experiment tissues and plasma were collected 4 hours after 5 and 10 consecutive daily p.o. administrations of vemurafenib. All tissues were weighed and subsequently homogenized using a FastPrep®-24 (MP-Bio-medicals; New York, NY) in 3 ml 1% (w/v) bovine serum albumin. All tissue samples were prepared for LC–MS/MS analysis as described above for plasma samples.

LC–MS/MS analysis

The LC–MS/MS system consisted of an API 3000 mass spectrometer (Sciex; Framingham, MA) coupled to an UltiMate 3000 LC System (Dionex; Sunnyvale, CA). Samples were separated using a ZORBAX Extend-C18 column (Agilent; Santa Clara, CA), preceded by a Securityguard C18 pre-column (Phenomenex; Utrecht, The Netherlands). Elution was done using a mixture of mobile phase A (0.1% formic acid in water (v/v)) and mobile phase B (methanol) in a 5 minute gradient from 20% to 95%B, followed by 95%B that was maintained for 3 min and then re-equilibrated at 20%B. Multiple reaction monitoring parameters were 490.2/383.1 (vemurafenib) and 496.2/389.1 (vemurafenib-^{13}C6). System control and data analysis was done using Analyst® 1.6.2 software (AB Sciex; Foster City, CA).

Efficacy studies in xenograft models

For the subcutaneous tumor model, therapy was initiated two weeks after implantation, when the tumor volume exceeded 40 mm^3. FVB WT and *Abcb1a/b;Abcg2*$^{-/-}$ nude mice (n = 8) received 25 mg/kg and 10 mg/kg of vemurafenib daily, respectively. Control mice (n = 8) received vehicle. Tumor development was assessed by caliper twice a week. For the intracranial tumor model, treatment was started about two weeks after intracranial injection of tumor cells, when full-blown tumors were present in all animals. WT and *Abcb1a/b;Abcg2*$^{-/-}$ nude mice received vehicle, 25 mg/kg vemurafenib, 10 mg/kg vemurafenib plus 100 mg/kg elacridar or 10 mg/kg vemurafenib once daily for 10 consecutive days or in a 5 days on/2 days off/5 days on schedule, as indicated in the figures. Tumor growth was monitored by BLI every four or five days.

Histology and immunohistochemistry

Mouse brains were fixed in 4% (v/v) formaldehyde. Alternatively, whole heads without skin were fixed in 4% (v/v) formaldehyde and 5% (v/v) glacial acetic acid and subsequently decalcified using a 6.5 % (v/v) formic acid solution for 3 days at 37 °C. After fixation, samples were paraffin embedded and sliced into 4 µm thick sections. Whole head slides were stained for hematoxylin and eosin (H&E), human vimentin (1:4,000; M0725; DakoCytomation; Glostrup, Denmark), P-gp (1:200; 13978; Cell Signaling Technology; Danvers, MA) and BCRP (1:400; ab24115;

Abcam; Cambridge, UK). Brain slides were stained for H&E, PDGFRβ (1:50; 3169; Cell Signaling Technology), phospho-MET (1:150; 3077; Cell Signaling Technology), MET (1:100; AF527; R&D Systems; Minneapolis, MN), phospho-IGF1R (1:40,000; sc-101703; Santa Cruz Biotechnology; Dallas, TX), AXL (1:100; 8661; Cell Signaling Technology), NGFR (1:400; 8238; Cell Signaling Technology), phospho-EGFR (1:600; ab40815; Abcam), EGFR (1:200; ab52894; Abcam), BRAF^{V600E} (1:100; E19290; SpringBioscience; Pleasanton, CA), phospho-ERK1/2 (1:200; 4370; Cell Signaling Technology), phospho-AKT (1:8,000; 4060; Cell Signaling Technology, phospho-S6 (1:1,000; 2211; Cell Signaling Technology), phospho-4EBP1 (1:100; 2855; Cell Signaling Technology), 4EBP1 (1:1,200; 9644; Cell Signaling Technology), SOX10 (1:100; sc-17342; Santa Cruz Biotechnology), MITF (1:100; 284M-94; Cell Marque; Rocklin, CA) and Ki-67 (1:3,000; ab15580; Abcam).

Pharmacokinetic calculations and statistical analysis

Pharmacokinetic parameters were calculated with PKSolver[26]. All comparisons involving more than two groups were analyzed by one-way ANOVA followed by Bonferroni *post hoc* tests. Kaplan–Meier curves were drawn using GraphPad Prism v7 (GraphPad Software; La Jolla, CA) and statistically significant survival differences were determined using the log–rank test. Statistical significance was accepted in all tests when $p < 0.05$.

RESULTS

Characterization of the A375 melanoma brain metastasis model

To characterize the BBB integrity of the A375 MBM model, we subjected mice that were orthotopically injected with A375–FM cells to magnetic resonance imaging and (immuno) histochemical analysis. Similar to the clinical presentation of MBMs, intracranial A375 tumors were visible on T2-weighted and T1-weighted post-gadolinium contrast MRI sequences (**Figure 1A**). Enhancement on T1-weighted MR images after intravenous adminstration of a contrast agent indicates a reduction in BBB integrity. However, the BBB is not only a physical barrier but also a physiological barrier because of the expression of a range of efflux transporters, of which P-gp and BCRP are the most dominant. Immunohistochemical staining of these transporters in intracranial A375 tumors revealed that the vasculature in these tumors expresses P-gp and BCRP, suggesting that the physiological component of its BBB may still be functional (**Figure 1B**). Interestingly, intracranial A375 tumors were also characterized by large infiltrations of cells that resembled neutrophils, as apparent from their morphology and lack of staining for human vimentin. Melanomas are generally considered to be highly immunogenic, and widespread neutrophil infiltration could be a result of the immunogenicity of the A375 model.

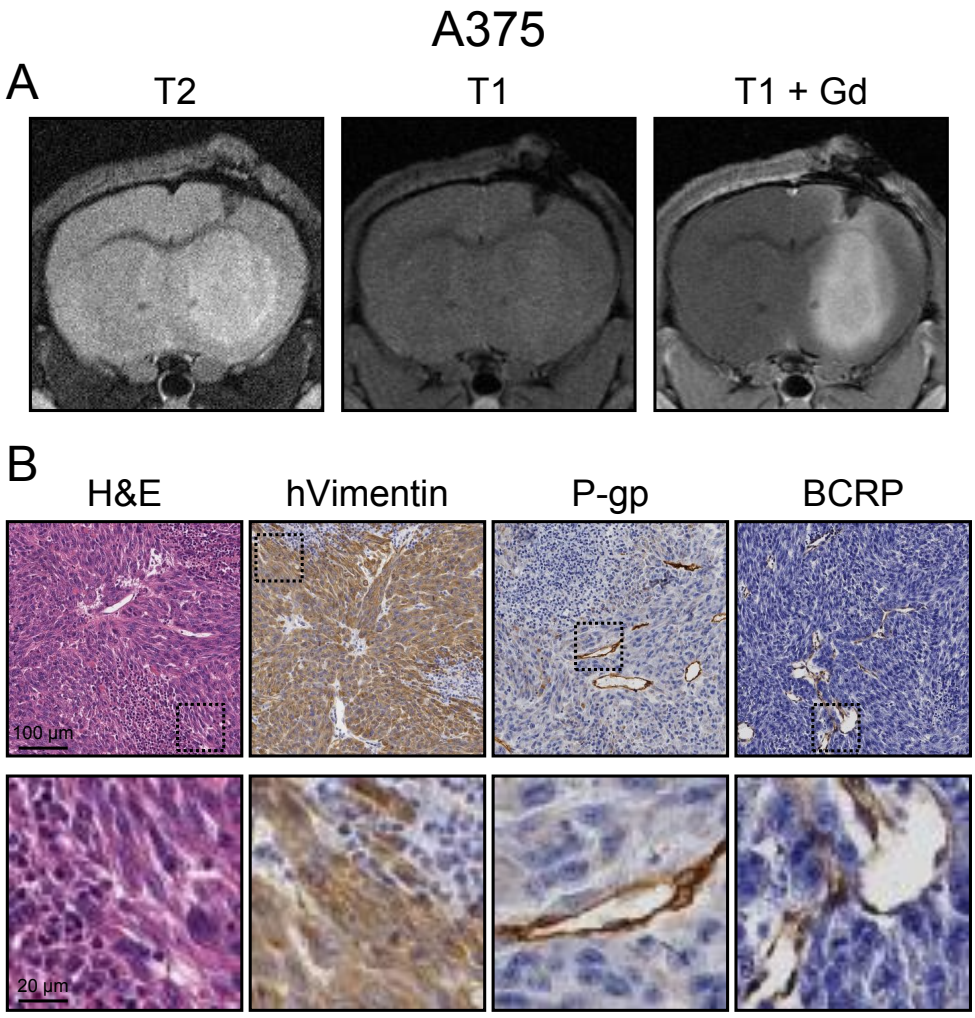

Figure 1 | Characterization of the A375 melanoma brain metastasis model. (**A**) T2-weighted, T1-weighted pre-contrast and T1-weighted post-gadolinium (Gd) contrast magnetic resonance imaging of A375 tumors grafted in the brains of WT nude mice. (**B**) Histochemical staining with hematoxylin and eosin (H&E) and immunohistochemical staining of human vimentin (hVimentin), P-glycoprotein (P-gp) and breast cancer resistance protein (BCRP) of intracranial A375 melanoma tumors.

Vemurafenib has intrinsic antitumor potential against intracranial A375 tumors

The brain penetration of vemurafenib was previously reported to be significantly higher (between approximately 20- and 80-fold) in *Abcb1a/b;Abcg2*$^{-/-}$ compared to WT mice[18,19]. We therefore first studied the efficacy of vemurafenib treatment against A375 tumors implanted in the brains of *Abcb1a/b;Abcg2*$^{-/-}$ mice, as we expected these mice to be the most pharmacologically favorable recipients to establish the intrinsic antitumor potential of vemurafenib against MBMs. Indeed,two

cycles of 5 days of 25 mg/kg daily oral vemurafenib induced regression and subsequent tumor stasis of A375 tumors in these mice (**Figure 2A**). When the treatment was stopped, tumor growth started at a similar speed as untreated tumors, but a survival difference was already established (**Figure 2B**), indicating that vemurafenib is intrinsically potent against MBMs.

Parameter	Time (h)	WT 25mg/kg	*Abcb1a/b;Abcg2*$^{-/-}$ *25*mg/kg	WT 10mg/kg + elacridar	*Abcb1a/b;Abcg2*$^{-/-}$ 10mg/kg
AUC_{plasma} (μg/ml·h)	0–4	147 ± 28	140 ± 16	38 ± 5.7	56 ± 7.2*
AUC_{plasma} (μg/ml·h)	0–24	390 ± 98	530 ± 68*	180 ± 24	230 ± 35
AUC_{plasma} (μg/ml·h)	0–∞	390 ± 99	610 ± 84**	190 ± 23	250 ± 49
C_{max} (μg/ml)		42 ± 7.7	41 ± 4.5	12 ± 1.7	17 ± 1.7*
t_{max} (h)		2.6 ± 1.3	1.9 ± 0.9	3.6 ± 0.9	2.8 ± 1.1
$t_{1/2}$ (h)		2.1 ± 0.2	8.5 ± 1.2****	5.8 ± 0.6	6.7 ± 1.4
CL/F (L/kg·h)		0.07 ± 0.017	0.04 ± 0.006**	0.05 ± 0.006	0.04 ± 0.006

Table 1 | Pharmacokinetic parameters of vemurafenib after oral administration of different doses to WT and *Abcb1a/b;Abcg2*$^{-/-}$ FVB mice. AUC, area under the curve; C_{max}, maximum concentration in plasma; t_{max}, time to reach maximum plasma concentration; $t_{1/2}$, elimination half-life; *CL/F*, apparent clearance after oral administration. Data are represented as mean ± SD (n ≥ 5); * $p < 0.05$, ** $p < 0.01$, **** $p < 0.0001$, compared to WT mice receiving the same vemurafenib dose.

Dose adaptions between WT and Abcb1a/b;Abcg2*$^{-/-}$ *mice are needed to level the systemic exposure of vemurafenib between strains

The aim of this study was to assess the impact of P-gp and BCRP at the BBB on the intracranial efficacy of vemurafenib against MBMs by comparing WT and *Abcb1a/b;Abcg2*$^{-/-}$ mice, The systemic exposure and oral bioavailability of vemurafenib is known to be attenuated by P-gp and BCRP[18,19]. This difference in systemic exposure may confound a fair comparison between the strains and a reduction of the dose in *Abcb1a/b;Abcg2*$^{-/-}$ mice was deemed necessary. The previous pharmacokinetic studies were conducted in tumor-free mice and used different formulations than the Cremophor-based formulation utilized in this study. Therefore, we first assessed the plasma exposure in tumor-free WT and *Abcb1a/b;Abcg2*$^{-/-}$ mice receiving vemurafenib in a Cremophor-based formulation. *Abcb1a/b;Abcg2*$^{-/-}$ mice received the same dose as WT mice (25 mg/kg) or a reduced dose (10 mg/kg). WT mice received the full dose (25 mg/kg) or the reduced dose (10 mg/kg) with concomitant administration of the P-gp/BCRP inhibitor elacridar (**Figure 2C**). We administered vemurafenib 4 hours after elacridar, as this is approximately the t_{max} of oral elacridar in mice. Similar to earlier studies, the plasma area under the curve (AUC) was significantly higher in *Abcb1a/b;Abcg2*$^{-/-}$ mice compared to WT mice receiving the same dose (**Table 1**). Notably, the terminal half-life of vemurafenib was considerably shorter in WT mice making accurate leveling between strains by dose adjustments difficult. Reducing the dose to 10 mg/kg in *Abcb1a/b;Abcg2*$^{-/-}$ mice resulted in a lower plasma AUC than WT at 25 mg/kg, but

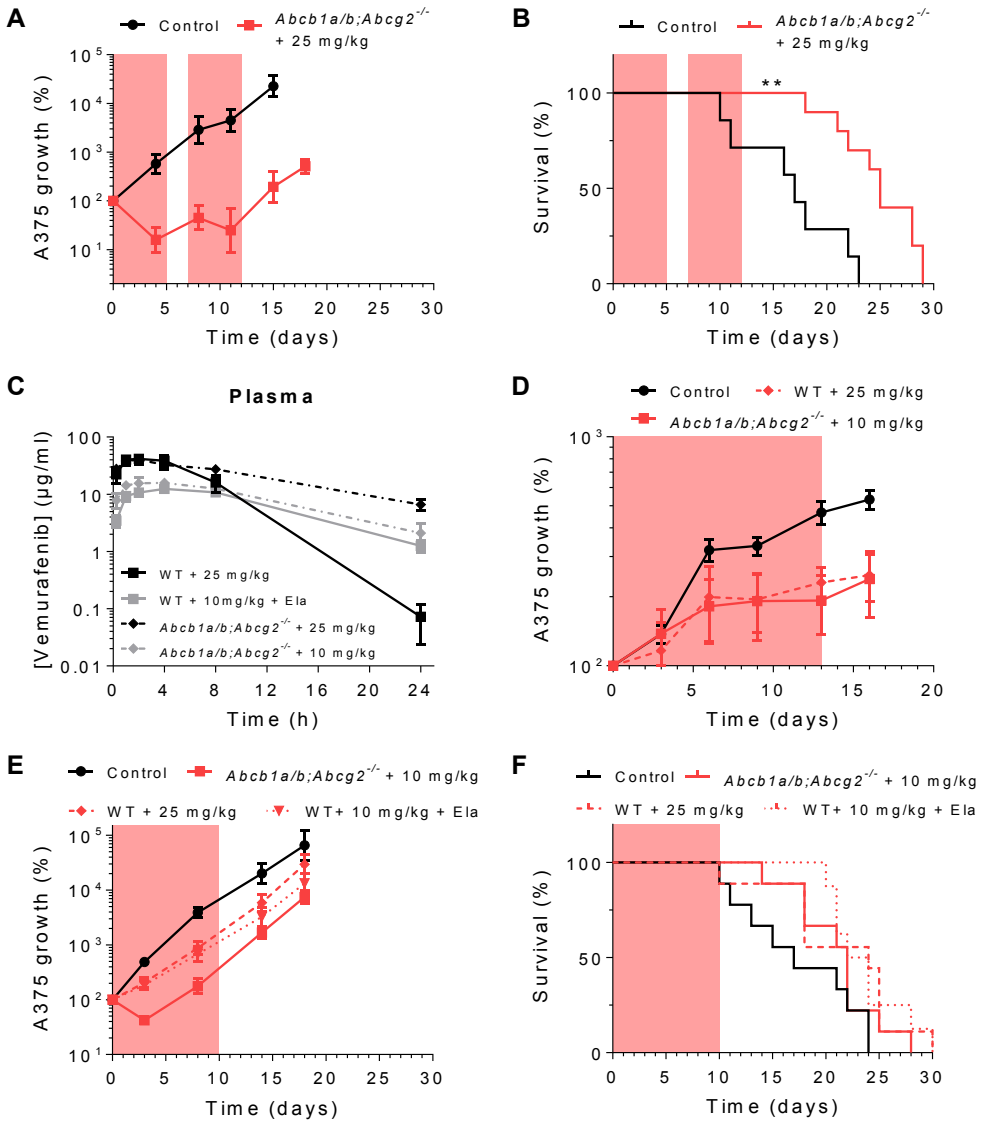

Figure 2 | Intrinsic and acquired resistance of A375 tumors against vemurafenib *in vivo*. (**A**) Tumor growth and (**B**) survival of *Abcb1a/b;Abcg2*$^{-/-}$ mice bearing intracranial A375 melanoma tumors treated with two rounds of 25 mg/kg vemurafenib *q.d.*x5d or vehicle control. Treatment periods are shaded in red. Data are represented as mean ± SD (n ≥ 7); ** $p < 0.01$. (**C**) Oral vemurafenib plasma concentration–time curves in WT mice receiving 25 mg/kg, WT mice receiving 10 mg/kg 4 hours after administration of the P-gp/BCRP inhibitor elacridar (Ela), *Abcb1a/b;Abcg2*$^{-/-}$ mice receiving 25 mg/kg and *Abcb1a/b;Abcg2*$^{-/-}$ mice receiving 10 mg/kg. Data are represented as mean ± SD (n ≥ 5). (**D**) Tumor growth of subcutaneous A375 tumors grafted in WT or *Abcb1a/b;Abcg2*$^{-/-}$ mice treated with various doses of vemurafenib administered *q.d.*x13d or vehicle control. Treatment periods are shaded in red. Data are represented as mean ± SD (n ≥ 7). (**E**) Tumor growth and (**F**) survival of WT and *Abcb1a/b;Abcg2*$^{-/-}$ mice bearing intracranial A375 melanoma tumors treated with 25 mg/kg, 10 mg/kg and 100 mg/kg elacridar (Ela) or 10 mg/kg vemurafenib *q.d.*x10d or vehicle control. Treatment periods are shaded in red. Data are represented as mean ± SD (n ≥ 8).

the trough levels were significantly higher. Co-administration of elacridar to WT mice yielded a vemurafenib plasma exposure similar to that in *Abcb1a/b;Abcg2*$^{-/-}$ mice, suggesting that elacridar efficiently inhibits systemic clearance mediated by P-gp and BCRP.

In order to assess if the dose leveling between the strains was appropriate, we treated subcutaneously grafted A375 tumors with 25 mg/kg vemurafenib in WT mice and 10 mg/kg vemurafenib in *Abcb1a/b;Abcg2*$^{-/-}$ mice for 13 consecutive days. Subcutaneous tumors are similarly accessible in WT and *Abcb1a/b;Abcg2*$^{-/-}$ mice and as we found that vemurafenib was similarly effective (**Figure 2D**), we selected these dose regimens for the efficacy study against intracranial A375 tumors.

P-gp and BCRP limit vemurafenib efficacy against intracranial tumors

We next grafted WT and *Abcb1a/b;Abcg2*$^{-/-}$ mice with intracranial A375 tumors, to study whether P-gp and BCRP at the BBB affect antitumor efficacy in an MBM model. We again treated WT mice with 25 mg/kg and used 10 mg/kg vemurafenib for *Abcb1a/b;Abcg2*$^{-/-}$ mice. We also added a group of WT mice receiving 10 mg/kg with concomitant elacridar. In this case, we now found that vemurafenib was more effective in *Abcb1a/b;Abcg2*$^{-/-}$ than in WT mice (**Figure 2E**). While vemurafenib only reduced A375 growth speed in WT mice, it induced tumor regression in *Abcb1a/b;Abcg2*$^{-/-}$ mice during the first three days of treatment. Notably, however, while still under therapy, regrowth occurred in these mice reaching a similar tumor growth speed as in untreated animals before the completion of treatment. As a result, survival was not significantly extended (**Figure 2F**). Pharmacological inhibition of P-gp and BCRP by elacridar even was less efficacious, as the vemurafenib antitumor efficacy was greater in *Abcb1a/b;Abcg2*$^{-/-}$ mice receiving 10 mg/kg than in WT mice receiving elacridar and the same dose of vemurafenib (**Figure 2E**). Taken together, these data indicate that P-gp and BCRP at the BBB can diminish the efficacy of vemurafenib against MBMs.

P-gp and BCRP reduce vemurafenib penetration in MBMs

P-gp and BCRP limit the brain penetration of vemurafenib by virtue of their efflux function at the BBB[18,19]. However, it is unknown if the penetration into MBMs is similarly affected, as these lesions display signs of a compromised BBB on contrast-enhanced MRI. We therefore measured the vemurafenib distribution in tumor-bearing WT and *Abcb1a/b;Abcg2*$^{-/-}$ mice after 3 daily administrations of vemurafenib. We collected brain, tumor and plasma samples at approximately the t_{max} of vemurafenib (4 hours after the last administration). The vemurafenib plasma concentration in WT mice receiving 25 mg/kg was about 2-fold lower than observed in our previous pharmacokinetic experiment (**Figure 2C and Figure 3A**), whereas such discrepancies were not observed in *Abcb1a/b;Abcg2*$^{-/-}$ mice and WT mice that also received elacridar. Notably,

these tumor-bearing mice in the later experiment received three administrations of vemurafenib and the tumor-free mice in the earlier experiment only one. Therefore, these data could suggest induction of P-gp and BCRP by repeated vemurafenib administration, resulting in increased clearance.

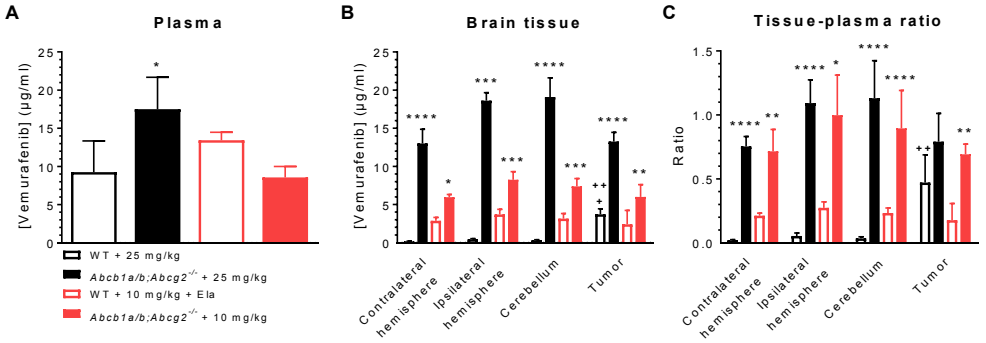

Figure 3 | Vemurafenib concentrations in tumor and healthy brain of WT and *Abcb1a/b;Abcg2*$^{-/-}$ mice. (**A**) Plasma concentrations, (**B**) brain tissue concentrations and (**C**) tissue–plasma ratios in WT and *Abcb1a/b;Abcg2*$^{-/-}$ mice 4 hours after receiving oral vemurafenib at doses of 25 mg/kg, 10 mg/kg or 10 mg/kg 4 hours after receiving 100 mg/kg oral elacridar (Ela). The contralateral hemisphere represents the tumor-free hemisphere. The ipsilateral hemisphere is the hemisphere where the tumor was injected, from which all macroscopic tumor was removed. Data are represented as mean ± SD (n ≥ 3); * $p < 0.05$, ** $p < 0.01$, **** $p < 0.0001$, compared to WT mice receiving 25 mg/kg vemurafenib; $^{++}$ $p < 0.01$, compared to the contralateral hemisphere level of the same group.

The apparent discrepancies in plasma concentration do not affect the results of the brain penetration. The vemurafenib concentrations in different brain regions differed greatly amongst all treatment groups (**Figure 3B**). In general, the highest concentrations were reached in *Abcb1a/b;Abcg2*$^{-/-}$ mice receiving 25 mg/kg vemurafenib. The concentrations were lower in *Abcb1a/b;Abcg2*$^{-/-}$ mice receiving 10 mg/kg vemurafenib, but this was only a result of the lower dose, as tissue–plasma ratios were similar between both dose levels in *Abcb1a/b;Abcg2*$^{-/-}$ mice (**Figure 3C**). In line with previous reports, the vemurafenib penetration in normal brain regions of WT mice was negligible. The tissue–plasma ratios were very close to the total blood volume of the murine brain (approximately 2%). Elacridar increased the vemurafenib concentration in healthy brain regions, but inhibition of P-gp and BCRP was incomplete, since the levels and brain–plasma ratios were significantly lower than in *Abcb1a/b;Abcg2*$^{-/-}$ mice. Vemurafenib penetrated into the tumor core in WT mice, but the levels were approximately half of those achieved in *Abcb1a/b;Abcg2*$^{-/-}$ mice. Elacridar was also not able to improve the penetration of vemurafenib into the tumor core to the same level as in *Abcb1a/b;Abcg2*$^{-/-}$ mice. These data show that P-gp and BCRP can still diminish vemurafenib penetration into MBMs, even when the tumor lesion has compromised BBB integrity. These drug distribution data are in line with the observed intracranial antitumor efficacy (**Figure 2E**), as vemurafenib tumor concentrations were similar between WT mice receiving 25 mg/kg and WT mice receiving 10 mg/kg with concomitant elacridar, but lower than in *Abcb1a/b;Abcg2*$^{-/-}$ mice receiving 10 mg/kg.

Intracranial A375 tumors develop therapy resistance despite sufficient vemurafenib tumor penetration and target inhibition

As mentioned above, the A375 MBM model is sensitive to vemurafenib, but developed therapy resistance after just a few days of treatment in *Abcb1a/b;Abcg2*$^{-/-}$ mice. Since P-gp and BCRP is absent in these mice, we reasoned that P-gp/BCRP-unrelated pharmacokinetic phenomena may underlie the observed resistance. For instance, induction of vemurafenib pre-systemic metabolism, systemic clearance or efflux at the BBB by other ABC transporters might result in diminished vemurafenib brain concentrations after repeated administrations. However, the vemurafenib concentrations in various brain regions in tumor-bearing mice treated for a short (5 days) or long (10 days) period, were not different in *Abcb1a/b;Abcg2*$^{-/-}$ mice and WT mice also receiving elacridar (**Figure 4**). Notably, we did find a considerably lower vemurafenib concentration in plasma in long-term treated WT mice compared to short-term treated WT mice. Brain and tumor concentrations were also lower as a consequence of the lower plasma concentration, as the tissue–plasma ratios were not affected (**Figure 2C, Figure 3A and Figure 4**). Again, we found no reduction in vemurafenib plasma concentration in *Abcb1a/b;Abcg2*$^{-/-}$ mice or WT mice also receiving elacridar, indicating that the reduction in WT mice was mediated by P-gp and/or BCRP.

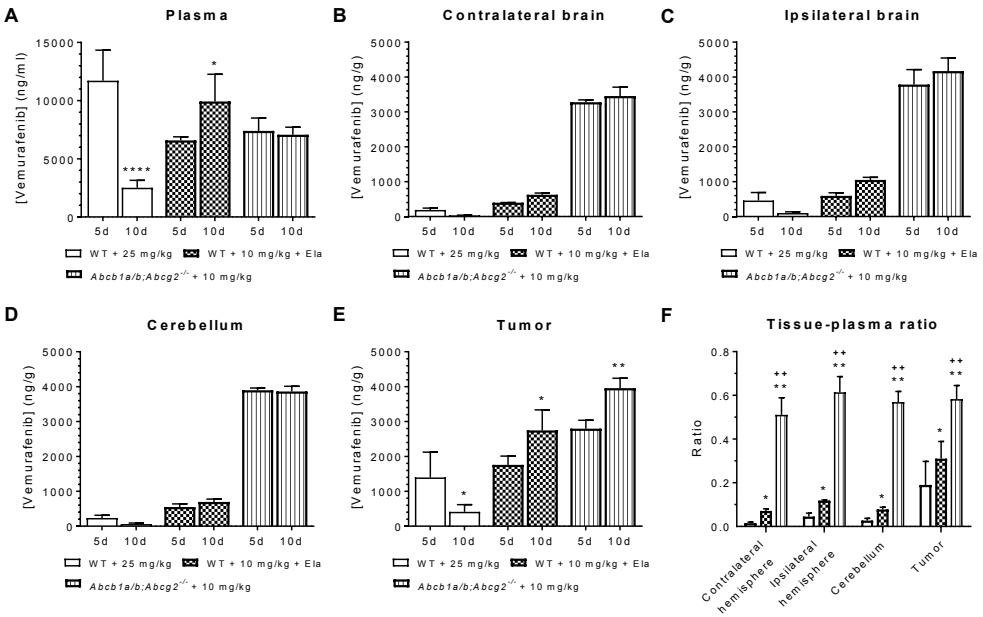

Figure 4 | Vemurafenib concentrations in short-term and long-term treated intracranial A375 tumors. Vemurafenib concentrations in (**A**) plasma, (**B**) contralateral brain, (**C**) ipsilateral brain, (**D**) cerebellum and (**E**) tumor after short-term (5 days; 5d) and long-term treatment (10 days; 10d) of A375 melanomas brain metastases. Tumor-bearing WT or *Abcb1a/b;Abcg2*$^{-/-}$ mice orally received 25 mg/kg, 10 mg/kg or 10 mg/kg vemurafenib and 100 mg/kg oral elacridar (Ela). Data are represented as mean ± SD (n ≥ 3); * $p < 0.05$, ** $p < 0.01$, **** $p < 0.0001$, compared to short-term treated tumors of the same group. (**F**) Vemurafenib tissue–plasma ratios for different brain regions in pooled 5 and 10 day-treated tumors.

Since the vemurafenib concentration in responsive short-term treated tumors and resistant long-term treated tumors was similar, we explored alternative ways by which intracranial A375 tumor may acquire resistance. We still observed pathway inhibition in resistant MBMs, as indicated by reduced immunohistochemical staining of downstream $BRAF^{V600E}$ targets phospho-S6 and phospho-4EBP1 (**Figure 5**). $BRAF^{V600E}$,phospho-ERK and phospho-AKT were still low or unaffected, suggesting that resistance occurred via non-canonical growth signaling, as the proliferation marker Ki-67 was similarly unaffected. Upstream growth factor receptors are likely candidates for such a mechanism and have been demonstrated to mediate resistance to $BRAF^{V600}$ inhibitors before[27-29]. However, PDGFRβ, MET, IGF1R, AXL, NGFR and EGFR signaling were not increased in resistant tumors. In fact, PDGFRβ expression appeared to be diminished by vemurafenib treatment. Furthermore, transcription factors that have been implicated in acquired resistance mechanisms such as SOX10[27] and MITF[29] were likewise unaffected. Taken together, these findings indicate that rapid resistance in intracranial A375 tumors does not occur via pharmacological processes but through acquiring non-canonical growth signaling.

DISCUSSION

The introduction of BRAF and MEK inhibitors has dramatically improved the survival of metastatic melanoma patients. However, clinical responses in melanoma brain metastases are less durable than those in extracranial metastases, suggesting MBMs may be intrinsically resistant to therapy[17]. By using a preclinical mouse model, we here show that although $BRAF^{V600E}$-positive MBMs cause a disruption of BBB integrity, P-gp and BCRP are expressed in the tumor blood vessels and reduce the distribution of vemurafenib into these lesions. Moreover, we find that these MBMs rapidly acquire resistance to therapy by resorting to non-canonical proliferation signaling.

The BBB limits the brain penetration and antitumor efficacy of treatment for primary brain tumors such as glioblastoma and diffuse intrinsic pontine glioma [30]. However, its impact on the treatment of brain metastases is less well established[31]. Brain metastases usually demonstrate contrast enhancement on T1-weighted MR imaging, indicating a loss of BBB integrity. Moreover, MBMs grow as relatively circumscribed lesions without much invasion of surrounding brain and remain in the vicinity of the vasculature[32,33]. Consequently, MBM cells are rarely found outside of the contrast-enhanced brain regions where the BBB is intact. Therefore, clinical responses can be observed with poorly brain-penetrable drugs such as vemurafenib. These responses lead some to conclude that the relevance of the BBB is limited in brain metastases. Contrast enhancement on MR images indeed indicates a physical disruption of the BBB integrity, as tight junctions normally prevent paracellular diffusion of contrast agents. However, despite this loss of integrity, the drug efflux transporters P-gp and BCRP can still be functional in these brain lesions. In line with this hypothesis, we observed increased efficacy of vemurafenib against a $BRAF^{V600E}$-positive MBM model that displays T1-weighted MRI contrast enhancement when these tumors were grafted

in *Abcb1a/b;Abcg2*$^{-/-}$ mice and when vemurafenib was combined with the P-gp/BCRP inhibitor elacridar in WT mice.

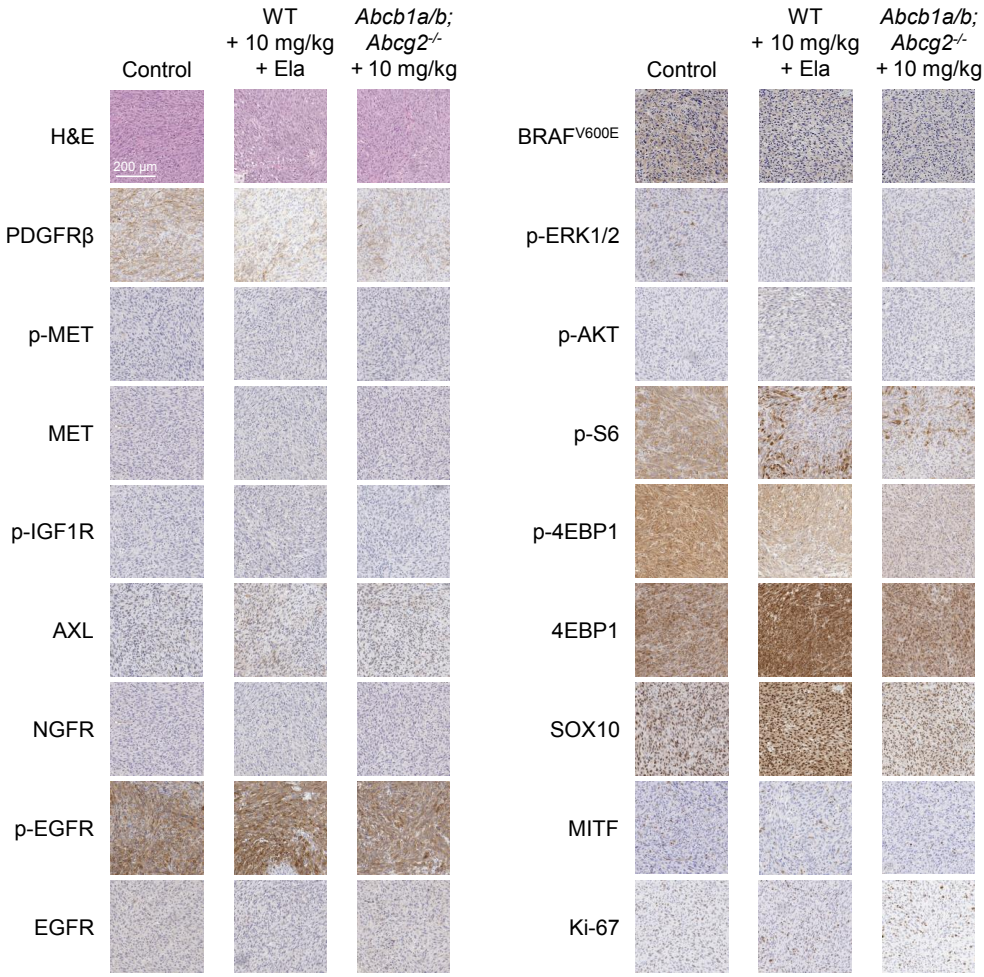

Figure 5 | Target inhibition by vemurafenib in late stage A375 melanoma brain metastases. Tumors growing in WT mice treated orally with 10 mg/kg vemurafenib and 100 mg/kg elacridar (Ela) *q.d.*x10d and in *Abcb1a/b;Abcg2*$^{-/-}$ mice treated orally with 10 mg/kg vemurafenib *q.d.*x10d were stained for various markers and compared to untreated tumors. H&E, hematoxylin and eosin; PDGFRβ, platelet-derived growth factor receptor β; p-MET, phospho-MET; p-IGF1R, phospho-insulin-like growth factor 1 receptor; AXL, tyrosine-protein kinase receptor UFO; NGFR, neural growth factor receptor; p-EGFR, phospho epidermal growth factor receptor; p-ERK, phospho-extracellular single-regulated kinase; p-AKT, phospho-AKT; p-S6, phospho-ribosomal protein S6; p-4EBP1, phospho-eukaryotic translation initiation factor 4E-binding protein 1; SOX10, sex determining region Y-box 10; MITF, microphtalmia transcription factor; Ki-67, proliferation marker protein Ki-67.

The BBB may thus limit the efficacy of BRAF inhibitors against BRAF-mutated tumors residing in the brain. These not only include brain metastases of melanoma[34] and non-small cell lung cancer[35], but also subsets of several different of primary adult[36] and pediatric[37] brain tumors.

The expression of P-gp and BCRP in vessels of primary brain tumors is well-documented[30,38]. Unfortunately, there are only two papers on P-gp or BCRP expression in blood vessels of brain metastatic lesions. Richtig *et al*. reported a general lack of P-gp expression in MBMs[39], whereas the blood vessels of various subtypes of breast cancer brain metastases were positive for BCRP[40]. The results in human MBMs are not in line with our results in mice. This may be related to the size of the lesion. Stainings were all done on relatively large lesions that may depend more on angiogenesis. Notably, BCRP may be a more important drug efflux transporter in humans than in mice, since it is more abundantly expressed[41].

To maximize the potential of BRAF inhibitor therapy against intracranial malignancies, it is important to optimize its pharmakinetic and pharmacodynamic parameters. In that regard, vemurafenib does not appear to be the superior BRAF inhibitor. Pharmacokinetically, the brain–plasma ratios of oral vemurafenib in WT mice are around 0.02[18,19], for encorafenib roughly 0.004[21] and for dabrafenib approximately 0.1[20]. While a brain–plasma ratio of 0.1 for dabrafenib is still quite poor, it is clearly better than those of vemurafenib and encorafenib. Dabrafenib is also pharmacodynamically superior, as its IC_{50} against A375 cells is 4 nM[42]. Encorafenib is similary potent against A375 cells (IC_{50} = 4 nM), but the IC_{50} of vemurafenib is approximately 100-fold higher at rougly 500 nM[43,44]. As a consequence of the higher potency, plasma levels of dabrafenib given at therapeutic doses are about 20- to 50-fold lower[45]. Nevertheless, these data suggest that dabrafenib may the inhibitor of choice for treatment of BRAF-mutated intracranial tumors. This notion seems to be supported by clinical data. MBM patietns receiving vemurafenib had a median overall survival of 4.3 months[46], compared to 7 months for dabrafenib treatment alone[16]. To what extent this superior overall survival can be attributed to the higher intrinsic potency of dabrafenib and how much to its higher brain penetration is unclear, but both characteristics are likely to have contributed. In summary, the currently available data seems to suggest that dabrafenib-based treatment regimens have superior efficacy and that co-adminstration of P-gp/BCRP inhibitors such as elacridar may further enhance their efficacy.

Next to reduced sensitivity caused by the BBB, we observed a striking development of acquired resistance that occurred much more rapidly than is typically reported for extracranial tumor models[47]. Interestingly, these data seem to be in line with observations in metastastatic melanoma patients. In a phase II study investigating dabrafenib and trametinib combination therapy in metastatic melonoma patients with brain metastases, similar intracranial and extracranial response rates (approximately 50%) were observed[17]. However, the duration of response was considerably shorter for intracranial metastases (6.5 months) than for extracranial metastases (10.2 months). The reason why MBMs acquire therapy resistance more rapidly is not yet understood. Several resistance mechanisms to BRAF inhibitors have been described to date[48]. Notable mechanisms include increased EGFR signaling[27], increased PDGFRβ signaling[28] and a low MITF/AXL ratio[29]. These mechanisms do not appear to occur in this study, since we

could not find these changes in resistant intracranial A375 tumors (**Figure 5**). A very recently discovered resistance mechanism is the acquisition of a secondary *BRAF* mutation resulting in a BRAF$^{V600E/L514V}$ oncoprotein[49], but this is unlikely to occur in our A375 MBM model as this mutation would lead to increased canonical MAPK pathway signaling. Microenvironment-related resistance mechanisms exerted by reactive astrocytes have also been proposed[33]. For instance, factors secreted by astrocytes have been demonstrated to increase AKT signaling in melanoma cells *in vitro*[50]. This specific mechanism is unlikely to have occurred in our study, as we did not observed increased p-AKT levels in resistant tumors (**Figure 5**). However, it does indicate that the microenvironment can contribute to acquired therapy resistance. Indeed, a potential role for the MBM microenvironment may also help to explain the observed differential clinical responses of intracranial and extracranial metastases[17].

Taken together, this study demonstrates that BRAF^{V600E}-positive MBMs are not only less sensitive to vemurafenib because they still protected by expression of P-gp and BCRP in the disrupted BBB, but they also rapidly acquire resistance by resorting to non-canonical growth signaling. Adding elacridar to BRAF inhibitor therapy may therefore improve survival by overcoming intrinsic resistance of MBMs, but understanding the mechanism behind the apparent brain-specific acquired resistance will likely be necessary to induce long-term responses.

REFERENCES

1. Sloot, S., *et al.* Improved survival of patients with melanoma brain metastases in the era of targeted BRAF and immune checkpoint therapies. *Cancer* **124**, 297-305 (2018).
2. Davies, H., *et al.* Mutations of the BRAF gene in human cancer. *Nature* **417**, 949-954 (2002).
3. Hodis, E., *et al.* A landscape of driver mutations in melanoma. *Cell* **150**, 251-263 (2012).
4. Kim, G., *et al.* FDA approval summary: vemurafenib for treatment of unresectable or metastatic melanoma with the BRAFV600E mutation. *Clin Cancer Res* **20**, 4994-5000 (2014).
5. Ballantyne, A.D. & Garnock-Jones, K.P. Dabrafenib: first global approval. *Drugs* **73**, 1367-1376 (2013).
6. Shirley, M. Encorafenib and binimetinib: First global approvals. *Drugs* **78**, 1277-1284 (2018).
7. Chapman, P.B., *et al.* Improved survival with vemurafenib in melanoma with BRAF V600E mutation. *N Engl J Med* **364**, 2507-2516 (2011).
8. Hauschild, A., *et al.* Dabrafenib in BRAF-mutated metastatic melanoma: a multicentre, open-label, phase 3 randomised controlled trial. *Lancet* **380**, 358-365 (2012).
9. Delord, J.P., *et al.* Phase I dose-escalation and -expansion study of the BRAF inhibitor encorafenib (LGX818) in metastatic BRAF-mutant melanoma. *Clin Cancer Res* **23**, 5339-5348 (2017).
10. Van Allen, E.M., *et al.* The genetic landscape of clinical resistance to RAF inhibition in metastatic melanoma. *Cancer Discov* **4**, 94-109 (2014).
11. Signorelli, J. & Shah Gandhi, A. Cobimetinib. *Ann Pharmacother* **51**, 146-153 (2017).
12. Odogwu, L., *et al.* FDA approval summary: dabrafenib and trametinib for the treatment of metastatic non-small cell lung cancers harboring BRAF V600E mutations. *Oncologist* **23**, 740-745 (2018).
13. Dummer, R., *et al.* Encorafenib plus binimetinib versus vemurafenib or encorafenib in patients with BRAF-mutant melanoma (COLUMBUS): a multicentre, open-label, randomised phase 3 trial. *Lancet Oncol* **19**, 603-615 (2018).
14. Ascierto, P.A., *et al.* Cobimetinib combined with vemurafenib in advanced BRAF(V600)-mutant melanoma (coBRIM): updated efficacy results from a randomised, double-blind, phase 3 trial. *Lancet Oncol* **17**, 1248-1260 (2016).
15. Long, G.V., *et al.* Dabrafenib and trametinib versus dabrafenib and placebo for Val600 BRAF-mutant melanoma: a multicentre, double-blind, phase 3 randomised controlled trial. *Lancet* **386**, 444-451 (2015).
16. Long, G.V., *et al.* Dabrafenib in patients with Val600Glu or Val600Lys BRAF-mutant melanoma metastatic to the brain (BREAK-MB): a multicentre, open-label, phase 2 trial. *Lancet Oncol* **13**, 1087-1095 (2012).
17. Davies, M.A., *et al.* Dabrafenib plus trametinib in patients with BRAF(V600)-mutant melanoma brain metastases (COMBI-MB): a multicentre, multicohort, open-label, phase 2 trial. *Lancet Oncol* **18**, 863-873 (2017).
18. Durmus, S., *et al.* Oral availability and brain penetration of the B-RAFV600E inhibitor vemurafenib can be enhanced by the P-glycoprotein (ABCB1) and breast cancer resistance protein (ABCG2) inhibitor elacridar. *Mol Pharm* **9**, 3236-3245 (2012).
19. Mittapalli, R.K., *et al.* Impact of P-glycoprotein (ABCB1) and breast cancer resistance protein (ABCG2) on the brain distribution of a novel BRAF inhibitor: vemurafenib (PLX4032). *J Pharmacol Exp Ther* **342**, 33-40 (2012).
20. Mittapalli, R.K., *et al.* Mechanisms limiting distribution of the threonine-protein kinase B-RAFV600E inhibitor

dabrafenib to the brain: implications for the treatment of melanoma brain metastases. *J Pharmacol Exp Ther* **344**, 655-664 (2012).
21. Wang, J., *et al.* P-glycoprotein (MDR1/ABCB1) and breast cancer resistance protein (BCRP/ABCG2) affect brain accumulation and intestinal disposition of encorafenib in mice. *Pharmacol Res* **129**, 414-423 (2018).
22. Sakji-Dupre, L., *et al.* Cerebrospinal fluid concentrations of vemurafenib in patients treated for brain metastatic BRAF-V600 mutated melanoma. *Melanoma Res* **25**, 302-305 (2015).
23. Durmus, S., *et al.* Apical ABC transporters and cancer chemotherapeutic drug disposition. *Adv Cancer Res* **125**, 1-41 (2015).
24. de Gooijer, M.C., *et al.* Improved brain penetration and antitumor efficacy of temozolomide by inhibition of ABCB1 and ABCG2. *Neoplasia* **20**, 710-720 (2018).
25. Kim, M., *et al.* Efficacy of the MDM2 Inhibitor SAR405838 in glioblastoma is limited by poor distribution across the blood-brain barrier. *Mol Cancer Ther* **17**, 1893-1901 (2018).
26. Zhang, Y., *et al.* PKSolver: An add-in program for pharmacokinetic and pharmacodynamic data analysis in Microsoft Excel. *Comput Methods Programs Biomed* **99**, 306-314 (2010).
27. Sun, C., *et al.* Reversible and adaptive resistance to BRAF(V600E) inhibition in melanoma. *Nature* **508**, 118-122 (2014).
28. Nazarian, R., *et al.* Melanomas acquire resistance to B-RAF(V600E) inhibition by RTK or N-RAS upregulation. *Nature* **468**, 973-977 (2010).
29. Muller, J., *et al.* Low MITF/AXL ratio predicts early resistance to multiple targeted drugs in melanoma. *Nat Commun* **5**, 5712 (2014).
30. van Tellingen, O., *et al.* Overcoming the blood-brain tumor barrier for effective glioblastoma treatment. *Drug Resist Updat* **19**, 1-12 (2015).
31. Gampa, G., *et al.* Drug delivery to melanoma brain metastases: Can current challenges lead to new opportunities? *Pharmacol Res* **123**, 10-25 (2017).
32. Preusser, M., *et al.* Brain metastases: pathobiology and emerging targeted therapies. *Acta Neuropathol* **123**, 205-222 (2012).
33. Fidler, I.J. The role of the organ microenvironment in brain metastasis. *Semin Cancer Biol* **21**, 107-112 (2011).
34. Capper, D., *et al.* Immunohistochemical testing of BRAF V600E status in 1,120 tumor tissue samples of patients with brain metastases. *Acta Neuropathol* **123**, 223-233 (2012).
35. Dagogo-Jack, I., *et al.* Impact of BRAF mutation class on disease characteristics and clinical outcomes in BRAF-mutant lung cancer. *Clin Cancer Res* (2018).
36. Behling, F., *et al.* Frequency of BRAF V600E mutations in 969 central nervous system neoplasms. *Diagn Pathol* **11**, 55 (2016).
37. Wu, G., *et al.* The genomic landscape of diffuse intrinsic pontine glioma and pediatric non-brainstem high-grade glioma. *Nat Genet* **46**, 444-450 (2014).
38. Tanaka, Y., *et al.* Ultrastructural localization of P-glycoprotein on capillary endothelial cells in human gliomas. *Virchows Arch* **425**, 133-138 (1994).
39. Richtig, E., *et al.* Lack of P-glycoprotein expression in melanoma brain metastases of different melanoma types. *Clin Neuropathol* **35**, 89-92 (2016).
40. Yonemori, K., *et al.* Disruption of the blood brain barrier by brain metastases of triple-negative and basal-type breast cancer but not HER2/neu-positive breast cancer. *Cancer* **116**, 302-308 (2010).
41. Uchida, Y., *et al.* Quantitative targeted absolute proteomics of human blood-brain barrier transporters and receptors. *J Neurochem* **117**, 333-345 (2011).
42. King, A.J., *et al.* Dabrafenib; preclinical characterization, increased efficacy when combined with trametinib, while BRAF/MEK tool combination reduced skin lesions. *PloS One* **8**, e67583 (2013).
43. Stuart, D.D., *et al.* Preclinical profile of LGX818: A potent and selective RAF kinase inhibitor. *Cancer Res* **72 Suppl 8**, 3790-3790 (2012).
44. Tsai, J., *et al.* Discovery of a selective inhibitor of oncogenic B-Raf kinase with potent antimelanoma activity. *Proc Natl Acad Sci U S A* **105**, 3041-3046 (2008).
45. Falchook, G.S., *et al.* Dose selection, pharmacokinetics, and pharmacodynamics of BRAF inhibitor dabrafenib (GSK2118436). *Clin Cancer Res* **20**, 4449-4458 (2014).
46. Fennira, F., *et al.* Vemurafenib in the French temporary authorization for use metastatic melanoma cohort: a single-centre trial. *Melanoma Res* **24**, 75-82 (2014).
47. Yadav, V., *et al.* The CDK4/6 inhibitor LY2835219 overcomes vemurafenib resistance resulting from MAPK reactivation and cyclin D1 upregulation. *Mol Cancer Ther* **13**, 2253-2263 (2014).
48. Rizos, H., *et al.* BRAF inhibitor resistance mechanisms in metastatic melanoma: spectrum and clinical impact. *Clin Cancer Res* **20**, 1965-1977 (2014).
49. Wang, J., *et al.* A secondary mutation in *BRAF* confers resistance to RAF inhibition in a *BRAF*^{V600E}-mutant brain tumor. *Cancer Discov* **8**, 1130-1141 (2018).
50. Niessner, H., *et al.* Targeting hyperactivation of the AKT survival pathway to overcome therapy resistance of melanoma brain metastases. *Cancer Med* **2**, 76-85 (2013).

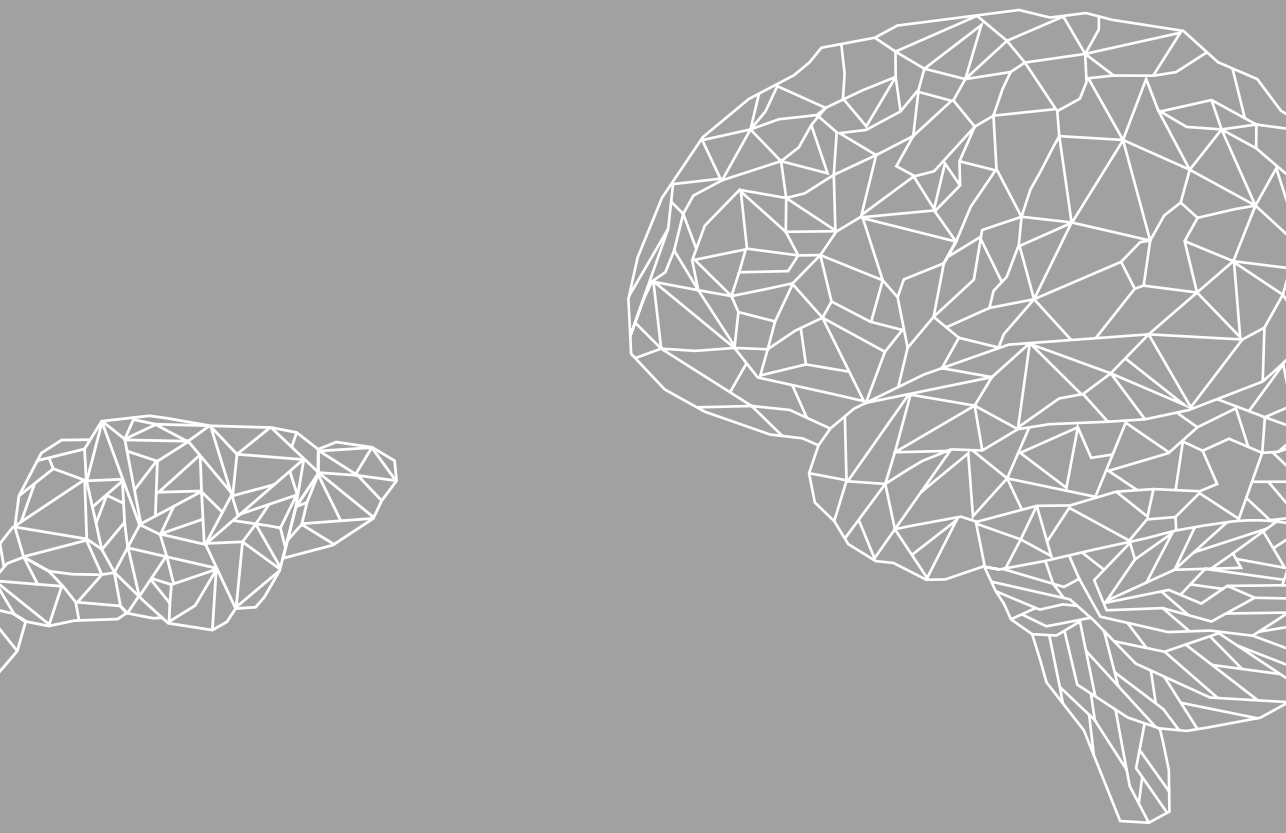

SECTION V

TARGETING THE CELL CYCLE: EXPLOITING VITAL CELLULAR PROCESSES

Chapter 9

THE G2 CHECKPOINT: A NODE-BASED MOLECULAR SWITCH

M.C. de Gooijer, A. van den Top, I. Bockaj, J.H. Beijnen, T. Wurdinger, and O. van Tellingen

FEBS Open Bio. 2017;7(5):439-455

ABSTRACT

Tight regulation of the eukaryotic cell cycle is paramount to ensure genomic integrity throughout life. Cell cycle checkpoints are present in each phase of the cell cycle and prevent cell cycle progression when genomic integrity is compromised. The G2 checkpoint is an intricate signaling network that regulates the progression of G2 to mitosis (M). We propose here a node-based model of G2 checkpoint regulation, in which the action of the central CDK1–cyclin B1 node is determined by the concerted but opposing activities of the Wee1 and CDC25C nodes. Phosphorylation of both Wee1 and CDC25C at specific sites determines their subcellular localization, driving them either towards activity within the nucleus or to the cytoplasm and subsequent ubiquitin-mediated proteasomal degradation. In turn, this subcellular balance of the Wee1 and CDC25C nodes is directed by the action of the PLK1 and CHK1 nodes via what we have termed the 'nuclear and cytoplasmic decision states' of Wee1 and CDC25C. The proposed node-based model provides an intelligible structure of the complex interactions that govern the decision to delay or continue G2/M progression. The model may also aid in predicting the effects of agents that target these G2 checkpoint nodes.

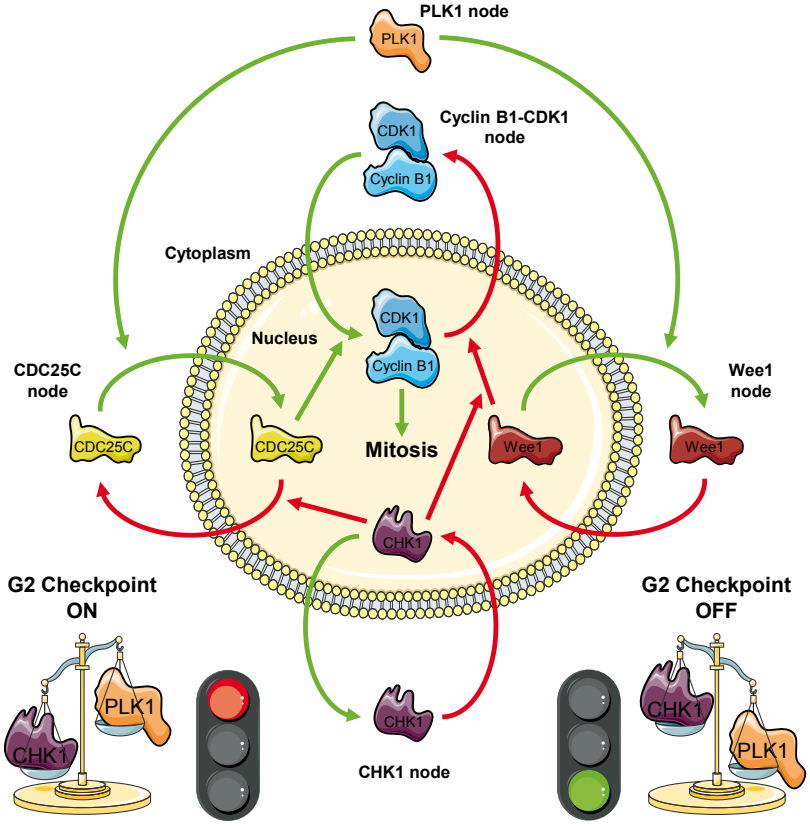

INTRODUCTION

The eukaryotic cell cycle is tightly regulated and encompasses checkpoints in each of its different phases[1]. Cellular checkpoint control is pivotal in minimizing DNA damage accumulation and ensuring genomic integrity during cell cycle progression[2]. Thus, not surprisingly, checkpoint deregulation and resulting DNA damage have been implicated in many diseases, including cancer and neurodegenerative disorders[3,4].

Research conducted during the last two decades supports that nuclear–cytoplasmic cycling of important G2 checkpoint proteins—such as cyclin-dependent kinase 1 (CDK1), cyclin B1, Wee1 kinase (Wee1) and cell division control protein 25C (CDC25C)—is a key mechanism of G2 checkpoint regulation[5-8]. An elaborate understanding has been established of the various types of protein interactions involved in cellular checkpoint control and the DNA damage response (reviewed by Reinhardt and Yaffe[9]). However, a comprehensive spatiotemporal overview of cellular checkpoint dynamics has not yet been reported. Here, we will focus on the human G2 checkpoint as a model checkpoint utilizing the plethora of protein interactions and modifications to regulate nuclear–cytoplasmic protein cycling. We identify the diverse post-translationally modified states of each G2 checkpoint protein undergoing nuclear–cytoplasmic cycling. Competing factors determine their state and thereby the subcellular localization and thus the activity of the protein. The outcome of all of these competitions will determine the status of the G2 checkpoint at any given time. Therefore, we propose to call these states the nuclear decision state (NDS) and cytoplasmic decision state (CDS) of a protein. We will describe the G2 checkpoint as a node-based biomolecular switch in great detail, underlining the importance of various protein interactions and emphasizing subcellular protein localization as a pivotal regulatory factor during checkpoint regulation.

THE NODULAR BASIS OF CHECKPOINTS

The G1 and G2 checkpoints, although differing in the involvement of specific checkpoint proteins, are in essence node-based systems revolving around a pivotal cyclin-dependent kinase (CDK) node that controls cell cycle progression (**Figure 1**). The central CDK2 node regulates the progression to S phase at the G1/S transition, while CDK1 (also known as cell division control protein 2, CDC2) comprises the central checkpoint node of the G2 checkpoint and is responsible for entry into mitosis[4]. The central CDK1 node is directly regulated by the primary regulatory Wee1 and CDC25C nodes, which respectively phosphorylate and dephosphorylate CDK1[10]. In the nucleus, Wee1 phosphorylates CDK1 on Tyr15, inactivating the kinase and thus inducing a G2 arrest, resulting in cell cycle progression inhibition[11,12]. In contrast, the phosphatase CDC25C mirrors Wee1 function by dephosphorylating the inactivating phosphorylation of CDK1 on Tyr15, reactivating CDK1 in the nucleus and promoting mitotic entry[13,14].

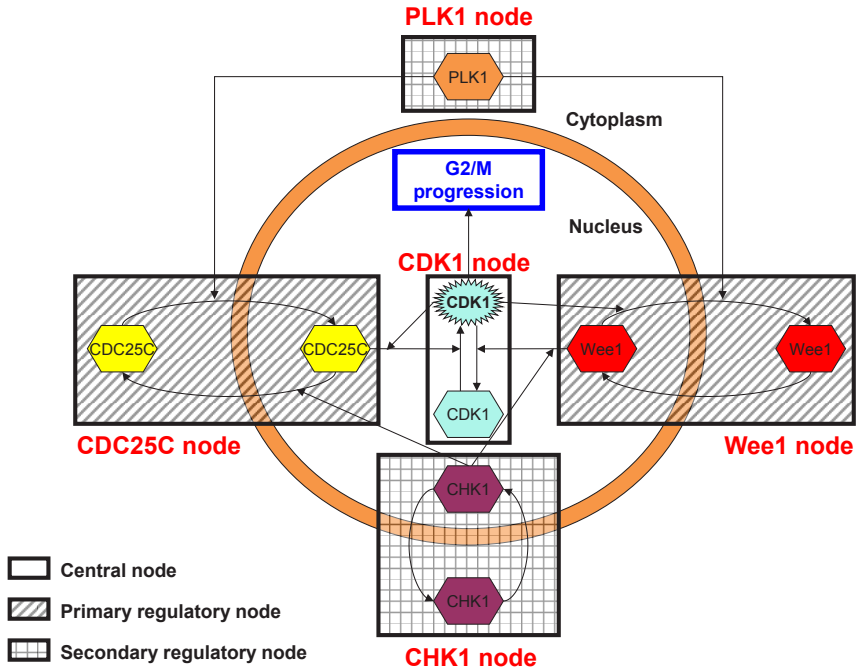

Figure 1 | The nodal basis of the G2 checkpoint. The action of the central CDK1–cyclin B1 node (clear box) is determined by the concerted but opposing activities of the Wee1 and CDC25C primary regulatory nodes (dashed boxes). In their turn, the PLK1 and CHK1 secondary regulatory nodes (gridded boxes) direct the action of the Wee1 and CDC25C nodes by phosphorylation at specific sites that determine their subcellular localization, either driving them towards nuclear accumulation and activity or cytoplasmic localization and subsequent ubiquitin-mediated proteasomal degradation.

In turn, the primary regulatory nodes Wee1 and CDC25C are regulated by three regulatory nodes. First, the central CDK1 node itself regulates these nodes. Active CDK1 can phosphorylate both Wee1 and CDC25C resulting in nuclear exclusion of Wee1 and promotion of CDC25C phosphatase activity[14,15]. Via these two activities CDK1 augments the further formation of active CDK1 through both its regulatory nodes. The result of this mechanism is a truly ingenious molecular switch, where active CDK1, once a certain threshold level is reached, triggers a snowball effect culminating into G2/M progression in a fashion that is irreversible by components of the cellular checkpoint machinery. Obviously, this mechanism calls for meticulous regulation of the CDK1 activation balance.

Secondly, the primary regulatory nodes Wee1 and CDC25C are regulated by two secondary regulatory nodes. The polo-like kinase 1 (PLK1) and checkpoint kinase 1 (CHK1) nodes dictate the cellular localization balance of the Wee1 and CDC25C nodes. PLK1 paves the way for degradation of Wee1 by phosphorylating its Ser53 residue[16]. Similarly, the translocation of CDC25C to the nucleus is promoted by phosphorylation on Ser198 by PLK1[17]. Taken together, PLK1 promotes G2/M progression through affecting the subcellular localization of both CDK1

regulatory checkpoint nodes. In contrast, CHK1 activity is directly counteractive to that of PLK1 activity. CHK1 promotes the nuclear localization of Wee1 through phosphorylation on Ser642 and prepares CDC25C for cytoplasmic translocation through phosphorylation on Ser216, thus enforcing G2 arrest through both primary regulatory nodes. Below we will discuss in more detail the different nodes and their spatiotemporal role in the G2 checkpoint starting with the secondary regulatory nodes, followed by the primary regulatory nodes and finishing with the central CDK1 node (for a complete overview of all nodes and their spatiotemporal interplay see **Supplementary Figure 1 and Supplementary Video 1**).

THE PLK1 NODE

As a result of various replication events, even in absence of genotoxic stress, healthy eukaryotic cells acquire basal levels of DNA damage during S phase that may not be resolved until late G2 phase[18-21]. With successful repair of each DNA damage lesion, signaling through PLK1 increases, ultimately resulting in checkpoint recovery and subsequent G2/M progression[22,23]. hBora associates with PLK1, inducing a conformational change between the protein binding domain (PBD) and kinase domain (KD) of PLK1 that exposes the Thr210 site of PLK1 to phosphorylation by active aurora kinase A (AURKA)[24]. Activated PLK1 can then phosphorylate CDC25C on Ser198[17], promoting cytoplasmic-to-nuclear CDC25C translocation, and Wee1 on Ser53[16], priming Wee1 for ubiquitin-mediated proteasomal degradation (**Figure 2**). Signaling through the secondary regulatory PLK1 node, therefore, is actively driving cells through the G2/M transition by influencing the subcellular distribution of both CDK1 regulatory nodes.

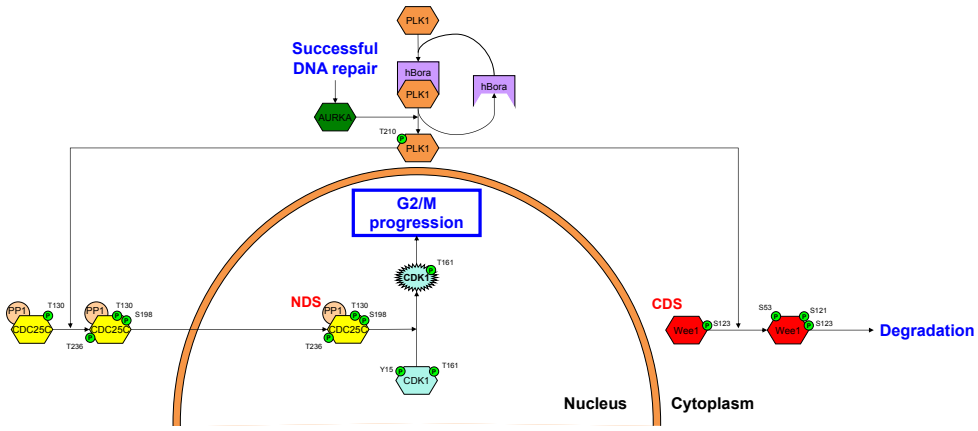

Figure 2 | The PLK1 node. Upon successful DNA repair completion, PLK1 is activated by aurora kinase A (AURKA) in cooperation with hBora through phosphorylation of its Threonine-210 residue. Following activation, PLK1 can promote G2/M progression by driving nuclear accumulation and CDK1 target activity of CDC25C and signaling Wee1 for ubiquitin-mediated proteasomal degradation.

PLK1 has been described as harboring a nuclear translocation signal that allows for tight regulation of its subcellular localization during the cell cycle[25]. Already in 1994 Golsteyn *et al.* showed that PLK1 is diffusely localized throughout the cell during interphase[26]. It has been extensively described that PLK1 is involved in the spindle assembly checkpoint (SAC) during M phase, confirming the importance of active PLK1 at the kinetochore during early mitosis[27-29]. Moreover, a recent study demonstrated that despite being cytoplasmically activated, PLK1 activity is first detected in the nucleus in early G2 phase[30]. However, based on current literature it is still conjecture whether nuclear or cytoplasmic PLK1 is predominantly responsible for the role of PLK1 in the G2 checkpoint later in the phase. Here, we propose a model in which cytoplasmic—and not nuclear—PLK1 is the major contributor for its regulatory function in the G2 checkpoint. The effects of PLK1 on nuclear accumulation of CDC25C[17] and Wee1[31]—by providing a phosphorylation-mediated nuclear translocation signal or nuclear stabilization of CDC25C and Wee1—can be explained by both cytoplasmic and nuclear PLK1. However, the finding that myelin transcription factor 1 (MYT1)—a kinase targeting CDK1 and further detailed in '**The CDK1 node**' section described below—is targeted by PLK1 cannot be attributed to a nuclear role of PLK1 in the G2 checkpoint[32]. MYT1 is a membrane-associated Wee1-like kinase that localizes to the Endoplasmatic Reticulum (ER) and Golgi system[33,34], and therefore targeting of this kinase by PLK1 has to occur in the cytoplasm. Furthermore, cytoplasmic activity of PLK1 is also required to prime the cyclin B1–CDK1 complex for nuclear localization by phosphorylation of serine residues on cyclin B1 (see also **Figure 6**)[35].

THE CHK1 NODE

Detection of DNA damage during S and G2 phase, causes induction of a G2 checkpoint arrest that allows for proper DNA repair and prevention of mitotic catastrophe[1,36]. The DNA damage signal is relayed to the G2 checkpoint through ataxia telangiectasia mutated kinase (ATM), ATM and Rad3-related kinase (ATR) and checkpoint kinase 1 (CHK1) (**Figure 3**). ATM is commonly activated by DNA double strand breaks (DSBs) and is primarily involved in G2 checkpoint arrest[37]. ATR is mostly involved in G1 checkpoint arrest and is activated upon DNA single strand break (SSB) formation[38,39], but has also been implicated in DSB repair as a downstream target of ATM[40]. Following growth signaling through the mitogen activated protein kinase (MAPK) pathway, p90 ribosomal S6 kinase (RSK) phosphorylates CHK1 at the Ser280 residue, promoting its nuclear localization[41]. In the nucleus, both ATM[42,43] and ATR[44] can phosphorylate their downstream target CHK1 on the Ser317 and Ser345 amino acid residues, inducing CHK1 auto-phosphorylation on Ser296[45,46] and enabling CHK1 to carry out its role in inducing G2 checkpoint arrest[47]. In contrast, Ser40 activated wild-type p53-induced phosphatase (WIP1) can prevent CHK1 autophosphorylation by dephosphorylating the Ser345 residue[48], a process that might be autoregulated by a feedback loop similar to that proposed for CHK2[49,50]. The autophosporylated form of CHK1 can best be designated as the CHK1 nuclear decision state (NDS), since it is

competed for by 14-3-3 γ and protein phosphatase 2A (PP2A). Ser296 phosphorylation favors nuclear activity and can be stabilized by association with 14-3-3 γ[51]. In contrast, exhibition of CHK1 activity consumes a phosphorylated residue. We speculate that the phosphorylated Ser296 residue of CHK1 is consumed, thereby inducing dissociation of 14-3-3 γ and again allowing CHK1 to autophosphorylate or be targeted by WIP1.

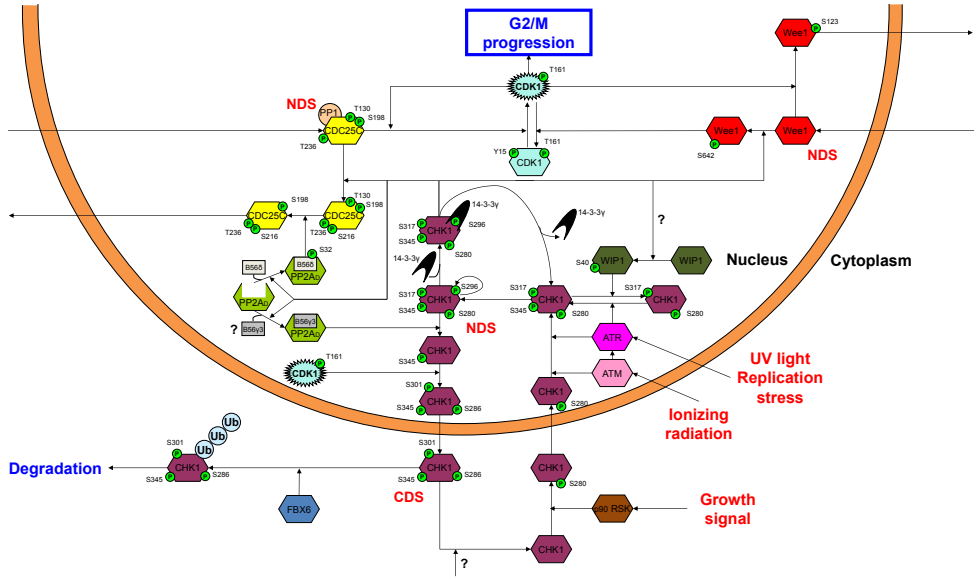

Figure 3 | The CHK1 node. CHK1 is translocated to the nucleus by p90 RSK phosphorylation. In the nucleus, CHK1 is activated following DNA damage, either directly by ataxia teleangiectasia mutated kinase (ATM), or through its downstream target ATM and Rad3-related kinase (ATR). The inhibitory activity of CHK1 on G2/M progression is threefold: through activating and nuclearly stabilizing Wee1, through deactivating CDC25C by direct phosphorylation and through promoting cytoplasmic translocation of CDC25C via activation of PP2A/B56δ. In turn, PP2A/B56γ3 can deactivate CHK1 by dephosphorylation, after which it is primed for nuclear export by CDK1. In the cytoplasm, CHK1 is either targeted for proteasomal degradation by SCF^{Fbx6} or reshuttled to the nucleus by dephosphorylation.

CHK1 controls both CDK1 regulatory nodes by managing the subcellular localization balance of Wee1 as well as CDC25C. CHK1 phosphorylates Wee1 on Ser642, preventing it from being targeted for extra-nuclear translocation and activating its CDK1 directed kinase activity[52,53]. Conversely, CHK1 phosphorylates the Ser216 residue of CDC25C, signaling it for extra-nuclear translocation and preventing activation of its phosphatase activity by CDK1[54]. Moreover, CHK1 also facilitates the second step in extra-nuclear translocation signaling of CDC25C through its effect on PP2A. PP2A is a trimeric dual specific phosphatase that always consists of a structural (A), catalytic (C) and regulatory subunit (B)[55]. As the diversity in A and C isoforms is limited but a range of highly diverse B isoforms exist with different subcellular localizations, substrate recognition of the PP2A complex is generally determined by the regulatory B isoform associated with the AC dimer (PP2AD)[56]. On one hand, CHK1 can phosphorylate the nuclear B56δ regulatory PP2A subunit

on the Ser32 residue, promoting association of the PP2AD/B56δ complex[57]. Subsequently, the PP2AD/B56δ complex can dephosphorylate CDC25C on Thr130 (which is phosphorylated by CDK2, further addressed in '**The CDC25C node**' below), further promoting cytoplasmic translocation of CDC25C. Interestingly, a recent study suggests that Greatwall kinase promotes nuclear CDK1 activity following DNA damage recovery through inhibition of the PP2A complex, specifically in promoting dephosphorylation of $CDK1^{Y15}$ in the nucleus[58]. Since Greatwall is known to inhibit PP2A, we speculate that Greatwall and CHK1 may potentially have antagonistic effects on PP2A complex activity in the context of DNA damage. On the other hand, a negative feedback loop exists between CHK1 and PP2A where CHK1 can promote the association of a nuclear B regulatory subunit with the PP2A dimer[59]. The PP2AD/B trimer can then dephosphorylate the CHK1 NDS, rendering it inactive and compromising G2 arrest[60]. Although the specific PP2A regulatory subunit responsible for dephosphorylation of CHK1 is still unknown, PP2AD/B56γ3 has been described to dephosphorylate checkpoint kinase 2 (CHK2)[61]. Since CHK1 and CHK2 share many downstream targets, encompass similar kinase domains and are both inhibited by AZD7762, the nuclearly localized B56γ3 subunit is a likely candidate to exhibit affinity towards both CHK1 and CHK2[39,62,63]. Thus, PP2AD/B56δ enables cytoplasmic translocation of CDC25C and activates G2 arrest, whereas PP2AD/B56γ3 may prevent CDC25C translocation to the cytoplasm and antagonizes G2 arrest. Importantly, the opposite functions of these two different PP2A complexes downstream of CHK1 may help to explain the recent observation that inhibition of the catalytic subunit of PP2A by okadaic acid resulted in attenuation of G2 arrest whilst increasing phosphorylated CHK1 levels[64].

Following dephosphorylation by PP2A, CHK1 can be targeted by the CDK1–cyclin B1 complex, reinforcing nuclear CDK1 activity. This interaction has been shown to promote Crm-1 (exportin-1) mediated translocation of CHK1 to the cytoplasm by phosphorylation of the Ser286 and Ser301 residues[65]. Interestingly, a reciprocal cytoplasmic interaction also been described for CHK1 in regulating cyclin B1–CDK1 localization to the centrosomes thereby preventing premature mitosis[66]. In the cytoplasm, $CHK1^{S268/S301/S345}$ is competed for by the E3 ubiquitin ligase Skp1–Cul1–Fbox F-box only protein 6 (SCF^{Fbx6}) on one hand and phosphatases on the other hand, designating this form as the cytoplasmic decision state (CDS). Fbx6 targets CHK1 for ubiquitin-mediated proteasomal degradation by phosphodegron recognition of the Ser345 residue[67], whereas phosphatase activity would prime CHK1 for re-entry into the nucleus. The identity of these phosphatases is not established yet but prime candidates include PP2A, WIP1 and protein phosphatase 1 (PP1).

THE WEE1 NODE

Wee1 kinase is the primary negative regulator of the CDK1 node through phosphorylation of active CDK1 on the Tyr15 residue (**Figure 4**)[68,69]. Wee1 has been shown to be differentially localized

throughout the cell cycle[70]. Following its synthesis in the cytoplasm, Wee1 can be shuttled into the nucleus by the phosphorylated chaperone protein heat shock protein 90α (HSP90α)[71,72]. Moreover, complex formation with HSP90α stabilizes cytoplasmic Wee1 by preventing it from degradation[73]. Interestingly, Wee1 facilitates its own nuclear translocation by phosphorylation of the Tyr38 residue of HSP90α[74].

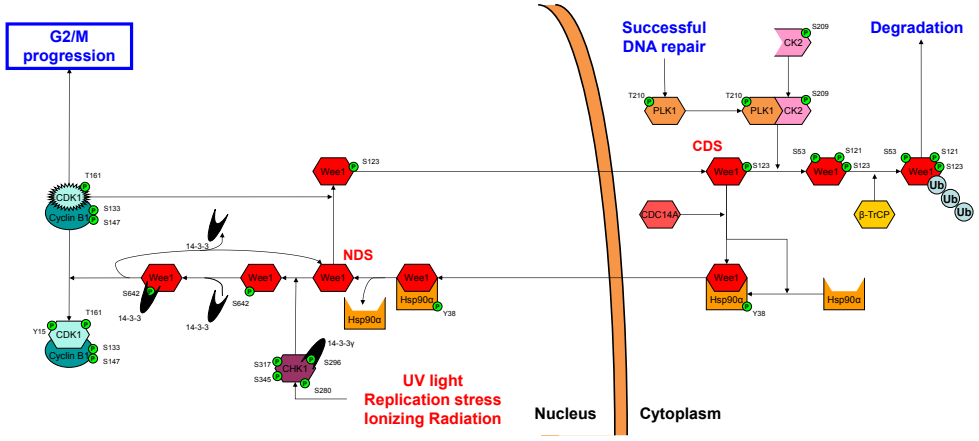

Figure 4 | The Wee1 node. Wee1 undergoes nuclear–cytoplasmic cycling that is important for determining its inhibitory effect on G2/M progression through the CDK1 node. Wee1 is shuttled into the nucleus by heat shock protein 90α (HSP90α), where it reaches its nuclear decision state (NDS). Phosphorylation of the Wee1 NDS by CHK1 promotes CDK1 directed activity of Wee1, while phosphorylation by CDK1 promotes translocation back to the cytoplasm. In the cytoplasm, Wee1 reaches its cytoplasmic decision state (CDS) that is either primed for ubiquitin-mediated proteasomal degradation by phosphorylation by the PLK1–CK2 complex or prepared for re-entry into the nucleus by dephosphorylation by CDC14A.

Once transported into the nucleus, Wee1 needs to be released from HSP90α to carry out its downstream function, which occurs by a mechanism that is not yet elucidated but might involve dephosphorylation of HSP90α by any tyrosine phosphatase. This unbound form of Wee1 can best be designated as the Wee1 NDS since two kinases compete for this unphosphorylated Wee1. On one hand CHK1 targets the Ser642 residue of Wee1, favoring the Wee1 decision towards phosphorylation of CDK1[53]. On the other hand, the active cyclin B1–CDK1 complex targets the Ser123 residue, which favors the fate of the Wee1 decision towards extra-nuclear translocation[15].

Phosphorylation of the Ser642 residue by CHK1 creates a binding site for the cup-shaped phosphorylation stabilization family of 14-3-3 proteins, which shelters the phosphorylated residue and stabilizes Wee1^{S642} in its phosphorylated form[53]. This configuration of Wee1 is the active form that can phosphorylate CDK1 on the Tyr15, maintaining the cyclin B1–CDK complex in the inactive state and preventing G2/M progression. As recently described in yeast, Cks complex formation possibly mediates this targeting of CDK1 by Wee1 by facilitating protein association[75]. Since active Wee1 only harbors one phosphorylated residue, we speculate that Wee1 mediated Tyr15 phosphorylation of CDK1 goes at the expense of the phosphorylated Ser642 residue and

release of 14-3-3, thereby returning Wee1 to the Wee1 NDS. In contrast, phosphorylation of the Wee1 NDS by CDK1 generates a signal for cytoplasmic translocation of Wee1 that also acts as a phosphodegron once Wee1 translocation has been completed[16,76]. Although the mechanism by which translocation is mediated is unclear, one might speculate about the involvement of heat shock proteins since these important cellular chaperone proteins have also been shown to transport Wee1 into the nucleus.

The resulting cytoplasmic phosphorylated $Wee1^{S123}$ can be designated as the Wee1 CDS since, again, two proteins compete for this form. At one end, cell division control protein 14A (CDC14A) dephosphorylates Ser123, undoing the action of CDK1, preventing Wee1 degradation and completing the Wee1 cycle by again enabling complex formation with HSP90α[77]. At the other end, active phosphorylated $PLK1^{Y210}$ in a complex with phosphorylated casein kinase 2 (CK2) competes with CDC14A for the Wee1 CDS. Phosphorylation of the Ser53 residue by PLK1 and the Ser121 residue by CK2 creates two additional phosphodegrons[31,78,79]. Ultimately, the three phosphodegrons generated by CDK1, CK2 and PLK1 fiercely promote docking of the E3 ubiquitin ligase Skp1–Cul1–Fbox β-transducin repeat-containing protein ($SCF^{\beta\text{-}TrCP}$), preparing Wee1 for proteasome mediated degradation[16]. This degradation most likely occurs in the cytoplasm, since the initial phosphodegron that CDK1 generates on Wee1 also acts as a cytoplasmic localization signal.

THE CDC25C NODE

In human cells, three isoforms of CDC25 have been identified that can in part compensate for each other's role upon perturbation of the cell cycle machinery, but also perform distinct functions throughout the cycle under physiological conditions[80-82]. While CDC25A and CDC25B instigate cyclin B1–CDK1 activation, CDC25C is responsible for stimulating and maintaining the full-blown cyclin B1–CDK1 activation that ultimately determines to pass the G2 checkpoint[13]. It is this role that makes CDC25C an essential node in regulating the decision of the G2 checkpoint. The CDC25C node mirrors many features of the Wee1 node, including a nuclear–cytoplasmic cycle, the presence of nuclear and cytoplasmic decision states and an important regulatory role of proteasomal degradation (**Figure 5**). We here propose that nuclear translocation of CDC25C, ultimately promoting G2/M progression, is under control of cytoplasmic CDK2, the cyclin-dependent kinase responsible for the G1/S and S/G2 transitions in complex with Cyclin E and cyclin A respectively[4]. Several findings support this hypothesis. First, as a result of successful S phase completion cellular levels of cyclin A will increase during G2 phase, indicating that high cyclin A–CDK2 levels are correlated with onset of mitosis[7]. Secondly, it has been demonstrated that cyclin A–CDK2 complexes rapidly shuttle between the cytoplasm and the nucleus, allowing cytoplasmic targeting of CDC25C by CDK2[8]. Thirdly, active CDK2 can phosphorylate CDC25C on the Thr130 residue, signaling CDC25C for nuclear translocation and initiating the G2/M transition[83,84].

In turn, this phosphorylation has been shown to cause release of 14-3-3, which shields the phosphorylated Ser216 residue of CDC25C at the CDS of CDC25C, allowing weak association with PP1—a serine/threonine phosphatase—and subsequent Ser216 dephosphorylation. Since 14-3-3 bound CDC25C is rapidly translocated to the cytoplasm, we speculate that such a role for CDK2 can therefore only be cytoplasmically localized[85].

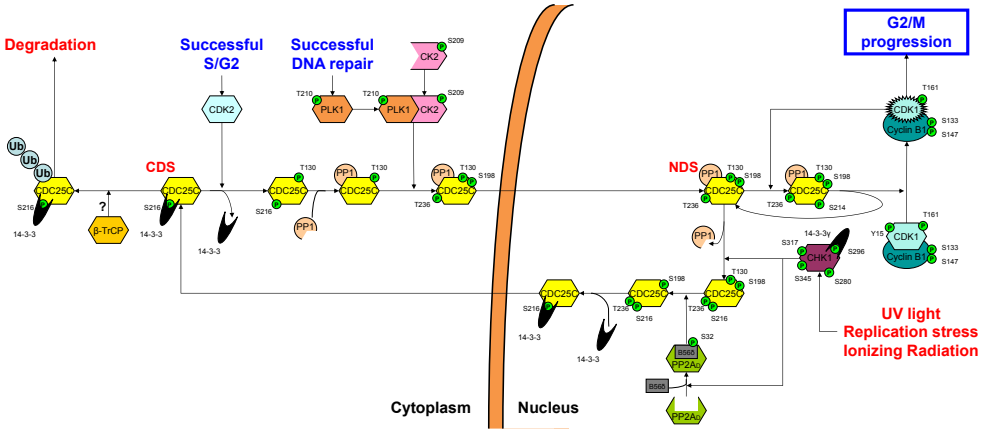

Figure 5 | The CDC25C node. The CDC25C node is characterized by nuclear–cytoplasmic cycling that regulates its effect on promoting G2/M progression. Following successful completion of S and G2 phase, cyclin-dependent kinase 2 (CDK2) primes CDC25C for nuclear translocation that is subsequently facilitated by PP1 and the PLK1–CK2 complex. When it reaches the nuclear decision state (NDS), targeting by activated CDK1 stimulates activity of CDC25C towards the CDK1–cyclin B1 complex while CHK1 drives cytoplasmic translocation both directly and through PP2A/B56δ. Back into the cytoplasm, at the cytoplasmic decision state (CDS), CDC25C can either be primed for re-entry into the nucleus by CDK2 or targeted for ubiquitin-mediated proteasomal degradation.

PP1 remains associated to CDC25C during its nuclear translocation, facilitating its own nuclear shuttling[86]. Dephosphorylation of Ser216 allows dual phosphorylation of CDC25C by a complex consisting of PLK1 and CK2. Activated PLK1 can phosphorylate CDC25C on Ser198. Since this residue is located within the nuclear export signal (NES), PLK1 thereby ultimately promotes nuclear retention by preventing subsequent nuclear exclusion[17]. Moreover, active CK2 phosphorylates the Thr236 residue of CDC25C, creating a nuclear localization signal (NLS) and mediating binding of the importin-α/β complex that subsequently shuttles CDC25C to the nucleus[87].

Nuclear triple phosphorylated CDC25C$^{T130/S198/T236}$ that is weakly associated with PP1 can be designated as the NDS of CDC25C, since both CDK1 and CHK1 compete for phosphorylation to determine its fate. Favoring entry into mitosis, CDK1 can phosphorylate the Ser214 residue as part of a positive feedback loop, enabling CDC25C to carry out its phosphatase function on CDK1[14,88]. Moreover, phosphorylation of Ser214 strengthens association with PP1, further stabilizing the active form of CDC25C[86]. The activating dephosphorylation of its target CDK1 most likely consumes the phosphorylated Ser214 residue of CDC25C, since no phosphatase has been described to target this residue and dephosphorylation of any of the other residues would result

in rapid translocation to the cytoplasm. The consumption of the Ser214 residue of CDC25C again weakens the association with PP1 and effectively returns CDC25C to the NDS of CDC25C.

Opposite to the action of CDK1, CHK1 can phosphorylate the NDS of CDC25C on the Ser216 residue, favoring nuclear exclusion and causing dissociation of PP1[54,86]. Moreover, active CHK1 causes active PP2AD/B56δ complex formation and subsequent dephosphorylation of the Thr130 residue of CDC25C[57]. Subsequently, 14-3-3 binding stabilizes the phosphorylated Ser216 residue and promotes removal of the phosphorylated Ser198 residue through induction of a conformational change[54]. Since this causes the nuclear exclusion signal to become unphosphorylated again, 14-3-3 binding induces cytoplasmic translocation of CDC25C[85,89]. The cytoplasmically localized, 14-3-3 bound, phosphorylated CDC25C can be designated as the CDS of CDC25C, since CDK2 competes for this state with the cellular degradation machinery to again initiate nuclear translocation of CDC25C.

Cytoplasmically located phosphorylated $CDC25C^{S216}$ is recognized by components of the degradation pathways, promoting G2 arrest and implicating the phosphorylated S216 residue as a phosphodegron[90]. In contrast to Wee1, the precise players involved in CDC25C degradation are still unclear. However, several observations argue in favor of CDC25C and Wee1 following identical routes of degradation. First, experiments with Arsenite have confirmed that ubiquitin mediated proteasomal degradation is responsible for CDC25C degradation[91]. Secondly, CDC25A, the homolog of CDC25C that is predominantly active in the G1/S transition, has been reported to be ubiquitinated by the $SCF^{\beta\text{-}TrCP}$ E3-ligase[92], although a role for the anaphase-promoting complex or cyclosome (APC/C) has also been described[93].

THE CDK1 NODE

Even though CDK1 can form a complex with other cyclins earlier in the cell cycle, the cyclin B1–CDK1 complex is responsible for triggering mitotic onset. The cyclin B1–CDK1 complex is localized cytoplasmically during interphase but is rapidly translocated to the nucleus to instigate G2/M transition during prophase[7,94]. CDK1 is activated in the cytoplasm by cyclin-activating kinase (CAK) through phosphorylation of its Thr161 moiety (**Figure 6**), prior to its nuclear translocation[13,95]. CAK is a kinase complex comprised of CDK7 and cyclin H and is regulated by a positive feedback loop through cyclin B1–CDK1[96,97]. This complex activates CAK by phosphorylating the Ser164 and Thr170 residues of CDK7, fortifying its own activation[98,99]. The activated cyclin B1–CDK1 complex is recognized by PLK1, which was originally thought to signal the complex for importin-β mediated nuclear uptake through phosphorylation of the Ser133 and Ser147 residues of cyclin B1[8,100,101]. Later, it was speculated that phosphorylation of the complex by PLK1 prevents subsequent nuclear exclusion since both residues are located within the cyclin B1 NES[8,35,102], although the targeting of the Ser133 residue by PLK1 remained controversial[103].

Complex formation of PLK1 with CK2 might offer an explanation to resolve this controversy, since the Ser133 residue of cyclin B might be targeted by CK2 whereas the Ser147 of cyclin B is targeted by PLK1. First, since the PLK1-mediated regulation of subcellular localization of CDC25C (**Figure 5**) and Wee1 (**Figure 4**) is carried out in complex with CK2, a similar PLK1 mechanism in conjunction with CK2 is not unlikely to be also involved in the cytoplasmic-to-nuclear transport regulation of cyclin B1–CDK1. Moreover, the generation of two phosphorylated residues on cyclin B1 adds to the likelihood of two kinases being involved. More recently, important work has provided important new information on the controversy surrounding the role of PLK1, and possibly CK2, in promoting nuclear localization of cyclin B1–CDK1, by demonstrating that nuclear cyclin B1–CDK1 itself promotes the increased nuclear entry of cytoplasmic cyclin B1–CDK1, although the precise mechanism by which this occurs has not yet been elucidated[104]. Interestingly, the observation that phosphorylated cyclin B1 allows the cyclin B1–CDK1 complex to stably bind to mitotic chromatin could suggest that cyclin B1 phosphorylation by PLK1, and possibly CK2, is important for maintenance of the nuclear cyclin B1–CDK1 fraction[105].

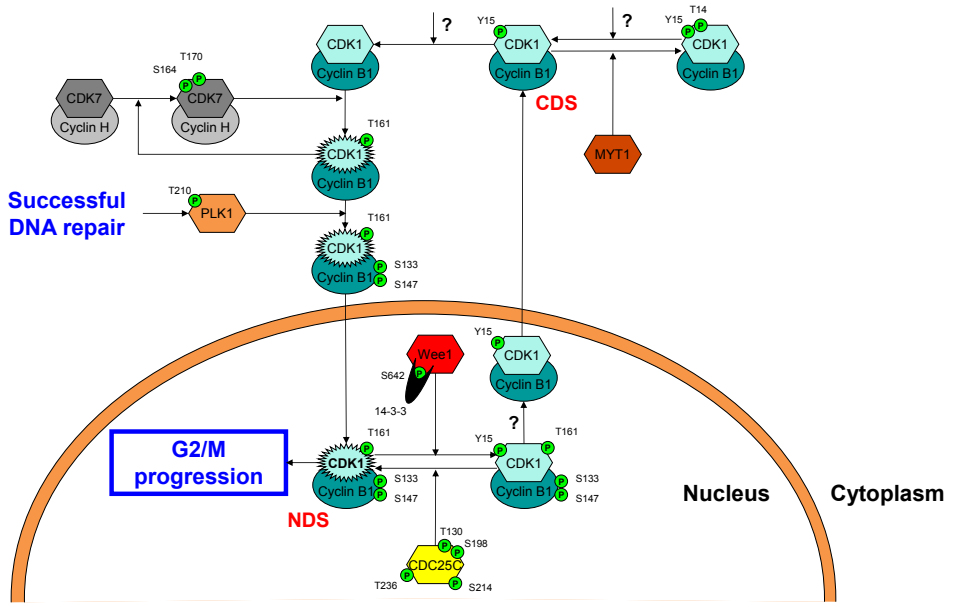

Figure 6 | The CDK1 node. Nuclear–cytoplasmic cycling regulates CDK1 activity. The CDK1–cyclin B1 is cytoplasmically activated by the CDK7–cyclin H complex and subsequently primed for nuclear translocation by PLK1. In the nucleus, the nuclear decision state (NDS) of CDK1 can be deactivated by Wee1-mediated phosphorylation, a process that is counteracted by CDC25C-mediated dephosphorylation. Following Wee1-mediated inactivation, the CDK1–cyclin B1 complex is primed for cytoplasmic translocation, most likely through dephosphorylation of cyclin B1, where it reaches its cytoplasmic decision state (CDS). Here, targeting by MYT1 further inactivates CDK1 while phosphatase activity enables re-entry into the nucleus.

In the nucleus, the active cyclin B1–CDK1 can be designated as the NDS of cyclin B1–CDK1, since Wee1 competes for this state with the mitosis promoting activity of CDK1. Moreover,

the active cyclin B1–CDK1 complex directly counteracts the effects of CHK1 in the nucleus by competing for the NDS of Wee1 and CDC25C and priming CHK1 for nuclear export (**Figure 3**). Wee1 phosphorylates the NDS of cyclin B1–CDK1 on the Tyr15 residue of CDK1, a modification counteracted through dephosphorylation by CDC25C. Tyr15 phosphorylation inactivates CDK1 and signals it for Crm-1 (exportin-1) mediated nuclear exclusion[8,106,107]. Thus far, the mechanism responsible for cytoplasmic translocation has not been identified, but the requirement for dephosphorylation of the cyclin B1 NES points toward abundant nuclear phosphatases such as PP2A and PP1 as likely candidates responsible for this process[108].

In the cytoplasm, MYT1 competes with a yet unidentified phosphatase for the phosphorylated CDS of cyclin B1–CDK1^{Y15}. MYT1 further consolidates the inactivation of CDK1 by phosphorylating the Thr14 residue of CDK1, sequestering it from the nuclear–cytoplasmic cycle[109]. Such a cytoplasmic role for MYT1 explains the observation that it is not essential for cell cycle arrest under normal conditions with low levels of DNA damage, but MYT1 does strengthen the Wee1 induced G2 checkpoint arrest through its effects on CDK1 after extensive DNA damage[110].

Indeed, it was shown that overproduction of MYT1 sequesters CDK1 in the cytoplasm by preventing nuclear import[109]. Whether the phosphorylated Thr14 residue may act as a phosphodegron is not yet clear, but the observation that CDK1 levels are unchanged following over-expression of MYT1 suggests against a role for MYT1 in ubiquitin-mediated proteasomal degradation of CDK1. Rather, cyclin B1–CDK1 regulates cyclin B1 degradation in late mitosis through phosphorylation of APC/C[108,111,112]. Alternatively, the sequestered cyclin B1–CDK1$^{T14/Y15}$ might be reintroduced into the nuclear–cytoplasmic cycle and subsequently further dephosphorylated by a yet unidentified phosphatase, allowing reactivation of CDK1 by CAK[113]. The ability of CDC14 to dephosphorylate CDK1 upon mitotic exit together with its cytoplasmic localization during G2 phase make it a potential candidate for this action, although both PP1 and PP2A have also emerged as likely candidates for CDK1 dephosphorylation[77,108].

IMPLICATIONS OF THE NODE-BASED MODEL

The node-based model of the G2 checkpoint represents a tightly controlled biomolecular switch. The Wee1 and CDC25C nodes are two arms of a scale that is influenced by the CHK1 and PLK1 nodes (depicted as weights and hydraulic arms) to tip to either the active or inactive form of CDK1 (**Figure 7**). Even under normal growth conditions, cells will always be halted upon arrival at the G2 checkpoint because of high CHK1 activity as a result of replication stress. This arrest allows for DNA repair. With successful repair of each DNA damage lesion PLK1 levels will rise, continuously bringing more balance to the scale. Once PLK1 activity exceeds CHK1 activity, the balance is tipped towards G2/M progression and feedback loops between CDK1 and CDC25C, Wee1 and CHK1 ensure that the balance cannot be restored and essentially becomes an irreversible biomolecular

switch. In line with this, recent work demonstrated that G2 checkpoint recovery is dependent on a PLK1 activity threshold and can occur in presence of a range of residual DNA damage signaling, resulting in heterogeneity in checkpoint fidelity[23].

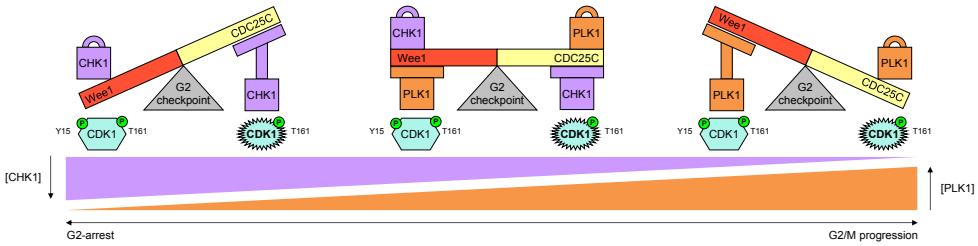

Figure 7 | Functional implications of the G2 checkpoint balance. The G2 checkpoint can be considered as a scale, where both arms are represented by the primary regulatory Wee1 and CDC25C nodes that pivot around the central CDK1 node and tip towards either active or inactive CDK1. The arms of the scale are in turn balanced by the secondary regulatory CHK1 and PLK1 nodes that act as either weights or hydraulic pumps. Following completion of S and G2 phase, high activity of the CHK1 node tips the scale in favor of inactive CDK1. With increasing DNA repair, CHK1 node activity gradually diminishes while PLK1 node activity complementarily increases. This shift first levels the balances and ultimately tips the G2 checkpoint in favor of CDK1 activity and G2/M progression.

Although not yet all details of the G2 checkpoint have been resolved, the model of the G2 checkpoint as proposed here already offers support in explaining some of the thus far poorly understood observations in studies using inhibitors interfering in the checkpoint. The interplay between the different G2 checkpoint nodes is predominantly determined by influencing the decision states of Wee1, CDC25C and CDK1 (**Figure 8**). Consequently, inhibition of key proteins influencing certain decision states might result in subcellular accumulation or, alternatively, changes in the level of degradation of the target.

For instance, as has been reported, inhibition of CHK1 would result in enhanced nuclear-to-cytoplasmic export and subsequent degradation of Wee1 since its competition with CDK1 is compromised. On the other hand, however, inhibition of the kinase domain of Wee1 by a small molecule would not affect the decision states and therefore does not change cellular Wee1 levels[114]. The effect of CHK1 inhibition on CDC25C would be exactly opposite. Since CHK1 normally affects the CDC25C NDS by signaling for nuclear-to-cytoplasmic export, inhibition of CHK1 using small molecules would result in nuclear accumulation of CDC25C and thus increased cellular levels as a result of decreased degradation. This has been reported for its homolog CDC25A and could thus likewise be true for CDC25C[62,115,116]. Moreover, the proposed nuclear–cytoplasmic cycling of CHK1 implies that inhibition of nuclear localized CHK1 results in nuclear accumulation and therefore prevention of CHK1 degradation, thus resulting in increased cellular CHK1 levels, as has been observed[117]. Inhibition of PLK1 would result in cytoplasmic accumulation of CDC25C since nuclear uptake of CDC25C is inhibited while being unavailable for degradation, as has been demonstrated using antisense mRNAs[118]. As a final example, PLK1 inhibition would also result

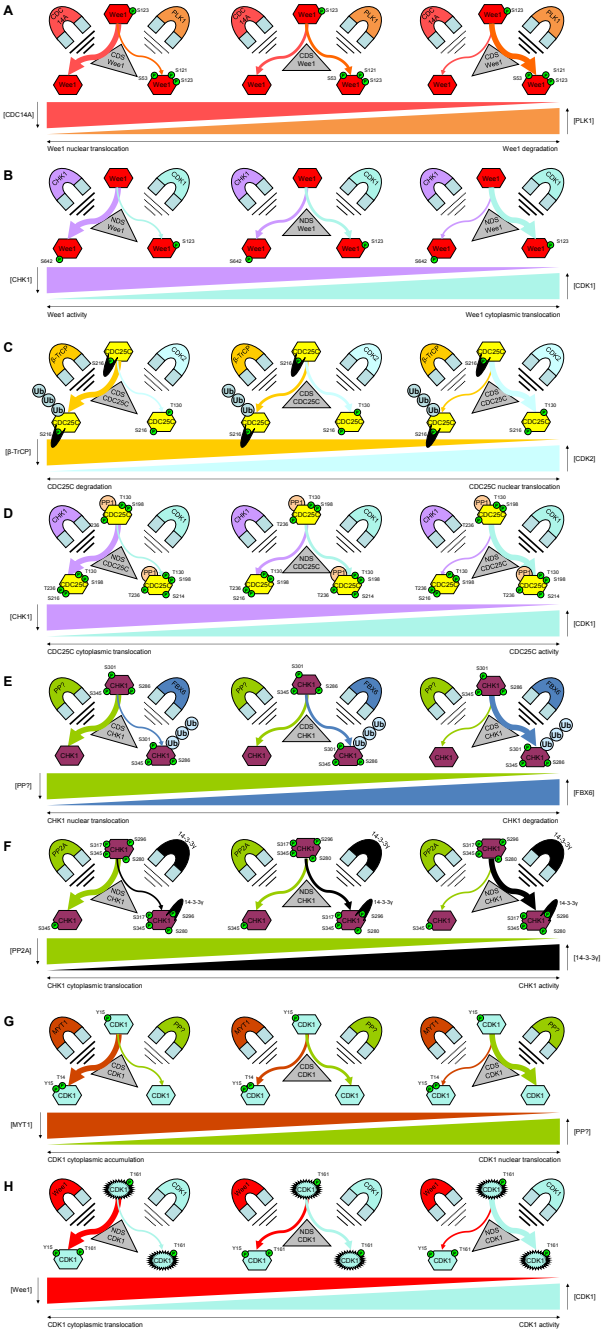

Figure 8 | Functional outcome of the decision states involved in the G2 checkpoint. The nuclear and cytoplasmic decision states (NDS, CDS) can be seen as conformations of a protein that are targeted by competing factors that determine the functional effect of a node on G2 checkpoint. The competing factors can be regarded as magnets that pull with varying strength, thereby routing the protein to a specific conformation. Subsequently are depicted the (**A**) Wee1 CDS, (**B**) Wee1 NDS, (**C**) CDC25C CDS, (**D**) CDC25C NDS, (**E**) CHK1 CDS, (**F**) CHK1 NDS, (**G**) CDK1 CDS and (**H**) CDK1 NDS.

in increased Wee1 protein levels since degradation of Wee1 is attenuated at the CDS of Wee1. Together, the proposed model allows for accurate prediction of the effects of interfering in the G2 checkpoint, making it a highly informative tool for the development of therapies focused on interfering in the G2 checkpoint.

CONCLUSIONS AND FUTURE DIRECTIONS

Although the last two decades have generated a framework of the biomolecular network of the G2 checkpoint, many interesting questions remain. Several steps of the G2 network remain to be elucidated in full detail, among which the factor responsible for the cytoplasmic phosphatase activity on cyclin B1–CDK1, the signal priming cyclin B1–CDK1 for extra-nuclear transport, the E3-ligase responsible for CDC25C degradation and the specific PP2A regulatory subunit determining CHK1 substrate recognition. Moreover, the cytoplasmic activation of the cyclin B1–CDK1 complex has interesting implications for the regulatory effect of CDK1 on the Wee1 and CDC25C nodes, although the extent to which these implied mode of actions truly influence the nodal balance of the G2 checkpoint has yet to be determined. On the one hand, cytoplasmically active CDK1 might already activate CDC25C for CDK1 targeted activity prior to nuclear entry, possibly preventing nuclear phosphorylation by CHK1 and thereby loosening the control of CHK1 on the NDS of CDC25C. On the other hand, it might directly counteract the effect of the phosphatase CDC14A on cytoplasmic Wee1, promoting Wee1 to re-enter the NDS of Wee1 by phosphorylating it and subsequently promoting degradation of Wee1. Together, this would allow CDK1 to simultaneously promote G2/M progression in the nucleus and the cytoplasm, adding to the strength of the G2 molecular switch.

Although beyond the scope of this review, it is intriguing to note that, many reports suggest a role for several G2 checkpoint players or homologs thereof in the regulation of the G1 or intra-S checkpoints. Among these are cyclin A, CDK2, CDC25A, CAK, PP2A, PP1, CHK1/2, PLK2/3 and Wee1[39,119-124]. This plethora of similarities to the G2 checkpoint therefore suggests that the G1 checkpoint is comprised of a similar nodal system with nuclear–cytoplasmic cycling, decision states and important degradation steps. Interesting questions are therefore raised about the similarities and differences between the G1 and G2 checkpoints and their implications for the effect of G2 checkpoint interference on the G1 checkpoint.

In summary, the G2 checkpoint is an ingenious node-based molecular switch which outcome is determined by the interplay of the PLK1, CHK1, Wee1, CDC25C and CDK1 nodes that are influenced by DNA damage and repair signaling. Together, this system allows the cell to intricately relay DNA status information to the cell cycle machinery, making it a pivotal process in maintaining cellular integrity.

REFERENCES

1. Elledge, S.J. Cell cycle checkpoints: preventing an identity crisis. *Science* **274**, 1664-1672 (1996).
2. Medema, R.H. & Macurek, L. Checkpoint control and cancer. *Oncogene* **31**, 2601-2613 (2012).
3. Jackson, S.P. & Bartek, J. The DNA-damage response in human biology and disease. *Nature* **461**, 1071-1078 (2009).
4. Malumbres, M. & Barbacid, M. Cell cycle, CDKs and cancer: a changing paradigm. *Nat Rev Cancer* **9**, 153-166 (2009).
5. Stewart, M. Molecular mechanism of the nuclear protein import cycle. *Nat Rev Mol Cell Biol* **8**, 195-208 (2007).
6. Deibler, R.W. & Kirschner, M.W. Quantitative reconstitution of mitotic CDK1 activation in somatic cell extracts. *Mol Cell* **37**, 753-767 (2010).
7. Pines, J. & Hunter, T. Human cyclins A and B1 are differentially located in the cell and undergo cell cycle-dependent nuclear transport. *J Cell Biol* **115**, 1-17 (1991).
8. Jackman, M., *et al.* Cyclin A- and cyclin E-Cdk complexes shuttle between the nucleus and the cytoplasm. *Mol Biol Cell* **13**, 1030-1045 (2002).
9. Reinhardt, H.C. & Yaffe, M.B. Phospho-Ser/Thr-binding domains: navigating the cell cycle and DNA damage response. *Nat Rev Mol Cell Biol* **14**, 563-580 (2013).
10. De Witt Hamer, P.C., *et al.* WEE1 kinase targeting combined with DNA-damaging cancer therapy catalyzes mitotic catastrophe. *Clin Cancer Res* **17**, 4200-4207 (2011).
11. Heald, R., *et al.* Human wee1 maintains mitotic timing by protecting the nucleus from cytoplasmically activated Cdc2 kinase. *Cell* **74**, 463-474 (1993).
12. Watanabe, N., *et al.* Regulation of the human WEE1Hu CDK tyrosine 15-kinase during the cell cycle. *EMBO J* **14**, 1878-1891 (1995).
13. Boutros, R., *et al.* CDC25 phosphatases in cancer cells: key players? Good targets? *Nat Rev Cancer* **7**, 495-507 (2007).
14. Bulavin, D.V., *et al.* Dual phosphorylation controls Cdc25 phosphatases and mitotic entry. *Nat Cell Biol* **5**, 545-551 (2003).
15. Harvey, S.L., *et al.* Cdk1-dependent regulation of the mitotic inhibitor Wee1. *Cell* **122**, 407-420 (2005).
16. Watanabe, N., *et al.* Cyclin-dependent kinase (CDK) phosphorylation destabilizes somatic Wee1 via multiple pathways. *Proc Natl Acad Sci U S A* **102**, 11663-11668 (2005).
17. Toyoshima-Morimoto, F., *et al.* Plk1 promotes nuclear translocation of human Cdc25C during prophase. *EMBO Rep* **3**, 341-348 (2002).
18. Debatisse, M., *et al.* Common fragile sites nested at the interfaces of early and late-replicating chromosome bands: cis acting components of the G2/M checkpoint? *Cell Cycle* **5**, 578-581 (2006).
19. Sorensen, C.S. & Syljuasen, R.G. Safeguarding genome integrity: the checkpoint kinases ATR, CHK1 and WEE1 restrain CDK activity during normal DNA replication. *Nucleic Acids Res* **40**, 477-486 (2012).
20. Helmrich, A., *et al.* Transcription-replication encounters, consequences and genomic instability. *Nat Struct Mol Biol* **20**, 412-418 (2013).
21. Bermejo, R., *et al.* Preventing replication stress to maintain genome stability: resolving conflicts between replication and transcription. *Mol Cell* **45**, 710-718 (2012).
22. Macurek, L. *et al.* Polo-like kinase-1 is activated by aurora A to promote checkpoint recovery. *Nature* **455**, 119-123 (2008).
23. Liang, H. *et al.* Homeostatic control of polo-like kinase-1 engenders non-genetic heterogeneity in G2 checkpoint fidelity and timing. *Nat Commun* **5**, 4048 (2014).
24. Seki, A., *et al.* Bora and the kinase Aurora a cooperatively activate the kinase Plk1 and control mitotic entry. *Science* **320**, 1655-1658 (2008).
25. Lee, M.S., *et al.* Identification of a nuclear localization signal in the polo box domain of Plk1. *Biochim Biophys Acta* **1793**, 1571-1578 (2009).
26. Golsteyn, R.M. *et al.* Cell cycle analysis and chromosomal localization of human Plk1, a putative homologue of the mitotic kinases Drosophila polo and Saccharomyces cerevisiae Cdc5. *J Cell Sci* **107**, 1509-1517 (1994).
27. Foley, E.A. & Kapoor, T.M. Microtubule attachment and spindle assembly checkpoint signalling at the kinetochore. *Nat Rev Mol Cell Biol* **14**, 25-37 (2013).
28. Lens, S.M., *et al.* Shared and separate functions of polo-like kinases and aurora kinases in cancer. *Nat Rev Cancer* **10**, 825-841 (2010).
29. Beck, J., *et al.* Ubiquitylation-dependent localization of PLK1 in mitosis. *Nat Cell Biol* **15**, 430-439 (2013).
30. Bruinsma, W., *et al.* Spatial separation of Plk1 phosphorylation and activity. *Front Oncol* **5**, 132 (2015).
31. Watanabe, N., *et al.* M-phase kinases induce phospho-dependent ubiquitination of somatic Wee1 by SCFbeta-TrCP. *Proc Natl Acad Sci U S A* **101**, 4419-4424 (2004).
32. Nakajima, H., *et al.* Identification of a consensus motif for Plk (Polo-like kinase) phosphorylation reveals Myt1 as a Plk1 substrate. *J Biol Chem* **278**, 25277-25280 (2003).
33. Liu, F., *et al.* The human Myt1 kinase preferentially phosphorylates Cdc2 on threonine 14 and localizes to the endoplasmic reticulum and Golgi complex. *Mol Cell Biol* **17**, 571-583 (1997).
34. Villeneuve, J., *et al.* MEK1 inactivates Myt1 to regulate Golgi membrane fragmentation and mitotic entry in mammalian cells. *EMBO J* **32**, 72-85 (2013).
35. Toyoshima-Morimoto, F., *et al.* Polo-like kinase 1 phosphorylates cyclin B1 and targets it to the nucleus during prophase. *Nature* **410**, 215-220 (2001).
36. Vitale, I., *et al.* Mitotic catastrophe: a mechanism for avoiding genomic instability. *Nat Rev Mol Cell Biol* **12**, 385-392 (2011).
37. Shiloh, Y. & Ziv, Y. The ATM protein kinase: regulating the cellular response to genotoxic stress, and more. *Nat Rev Mol Cell Biol* **14**, 197-210 (2013).
38. Abraham, R. T. Cell cycle checkpoint signaling through the ATM and ATR kinases. *Genes Dev* **15**, 2177-2196 (2001).
39. Bartek, J. & Lukas, J. Chk1 and Chk2 kinases in checkpoint control and cancer. *Cancer Cell* **3**, 421-429 (2003).
40. Jazayeri, A., *et al.* ATM- and cell cycle-dependent regulation of ATR in response to DNA double-strand breaks. *Nat Cell Biol* **8**, 37-45 (2006).
41. Li, P., *et al.* P90 RSK arranges Chk1 in the nucleus for monitoring of genomic integrity during cell proliferation.

Mol Biol Cell **23**, 1582-1592 (2012).
42. Gatei, M., *et al.* Ataxia-telangiectasia-mutated (ATM) and NBS1-dependent phosphorylation of Chk1 on Ser-317 in response to ionizing radiation. *J Biol Chem* **278**, 14806-14811 (2003).
43. Sorensen, C.S., *et al.* Chk1 regulates the S phase checkpoint by coupling the physiological turnover and ionizing radiation-induced accelerated proteolysis of Cdc25A. *Cancer Cell* **3**, 247-258 (2003).
44. Zhao, H. & Piwnica-Worms, H. ATR-mediated checkpoint pathways regulate phosphorylation and activation of human Chk1. *Mol Cell Biol* **21**, 4129-4139 (2001).
45. Walworth, N.C. & Bernards, R. rad-dependent response of the chk1-encoded protein kinase at the DNA damage checkpoint. *Science* **271**, 353-356 (1996).
46. Clarke, C.A. & Clarke, P.R. DNA-dependent phosphorylation of Chk1 and Claspin in a human cell-free system. *Biochem J* **388**, 705-712 (2005).
47. Goto, H., *et al.* Novel regulation of checkpoint kinase 1: Is checkpoint kinase 1 a good candidate for anti-cancer therapy? *Cancer Sci* **103**, 1195-1200 (2012).
48. Lu, X., *et al.* PPM1D dephosphorylates Chk1 and p53 and abrogates cell cycle checkpoints. *Genes Dev* **19**, 1162-1174 (2005).
49. Shaltiel, I.A., *et al.* The same, only different - DNA damage checkpoints and their reversal throughout the cell cycle. *J Cell Sci* **128**, 607-620 (2015).
50. Carlessi, L., *et al.* A protein phosphatase feedback mechanism regulates the basal phosphorylation of Chk2 kinase in the absence of DNA damage. *Biochim Biophys Acta* **1803**, 1213-1223 (2010).
51. Kasahara, K., *et al.* 14-3-3gamma mediates Cdc25A proteolysis to block premature mitotic entry after DNA damage. *EMBO J* **29**, 2802-2812 (2010).
52. Perry, J.A. & Kornbluth, S. Cdc25 and Wee1: analogous opposites? *Cell Div* **2**, 12 (2007).
53. Lee, J., *et al.* Positive regulation of Wee1 by Chk1 and 14-3-3 proteins. *Mol Biol Cell* **12**, 551-563 (2001).
54. Peng, C.Y., *et al.* Mitotic and G2 checkpoint control: regulation of 14-3-3 protein binding by phosphorylation of Cdc25C on serine-216. *Science* **277**, 1501-1505 (1997).
55. Mumby, M. PP2A: unveiling a reluctant tumor suppressor. *Cell* **130**, 21-24 (2007).
56. Janssens, V. & Goris, J. Protein phosphatase 2A: a highly regulated family of serine/threonine phosphatases implicated in cell growth and signalling. *Biochem J* **353**, 417-439 (2001).
57. Margolis, S.S., *et al.* Role for the PP2A/B56delta phosphatase in regulating 14-3-3 release from Cdc25 to control mitosis. *Cell* **127**, 759-773 (2006).
58. Wong, P.Y., *et al.* MASTL(Greatwall) regulates DNA damage responses by coordinating mitotic entry after checkpoint recovery and APC/C activation. *Sci Rep* **6**, 22230 (2016).
59. Leung-Pineda, V., *et al.* Phosphorylation of Chk1 by ATR is antagonized by a Chk1-regulated protein phosphatase 2A circuit. *Mol Cell Biol* **26**, 7529-7538 (2006).
60. Palii, S.S., *et al.* Dissecting cellular responses to irradiation via targeted disruptions of the ATM-CHK1-PP2A circuit. *Cell Cycle* **12**, 1105-1118 (2013).
61. Dozier, C., *et al.* Regulation of Chk2 phosphorylation by interaction with protein phosphatase 2A via its B' regulatory subunit. *Biol Cell* **96**, 509-517 (2004).
62. Zabludoff, S.D., *et al.* AZD7762, a novel checkpoint kinase inhibitor, drives checkpoint abrogation and potentiates DNA-targeted therapies. *Mol Cancer Ther* **7**, 2955-2966 (2008).
63. Janssens, V., *et al.* PP2A holoenzyme assembly: in cauda venenum (the sting is in the tail). *Trends Biochem Sci* **33**, 113-121 (2008).
64. Yan, Y., *et al.* Protein phosphatase 2A has an essential role in the activation of gamma-irradiation-induced G2/M checkpoint response. *Oncogene* **29**, 4317-4329 (2010).
65. Enomoto, M., *et al.* Novel positive feedback loop between Cdk1 and Chk1 in the nucleus during G2/M transition. *J Biol Chem* **284**, 34223-34230 (2009).
66. Kramer, A., *et al.* Centrosome-associated Chk1 prevents premature activation of cyclin-B-Cdk1 kinase. *Nat Cell Biol* **6**, 884-891 (2004).
67. Zhang, Y.W., *et al.* The F box protein Fbx6 regulates Chk1 stability and cellular sensitivity to replication stress. *Mol Cell* **35**, 442-453 (2009).
68. Mir, S.E. *et al. In silico* analysis of kinase expression identifies WEE1 as a gatekeeper against mitotic catastrophe in glioblastoma. *Cancer Cell* **18**, 244-257 (2010).
69. O'Connell, M. J., *et al.* Chk1 is a wee1 kinase in the G2 DNA damage checkpoint inhibiting cdc2 by Y15 phosphorylation. *EMBO J* **16**, 545-554 (1997).
70. Baldin, V. & Ducommun, B. Subcellular localisation of human wee1 kinase is regulated during the cell cycle. *J Cell Sci* **108**, 2425-2432 (1995).
71. Trepel, J., *et al.* Targeting the dynamic HSP90 complex in cancer. *Nat Rev Cancer* **10**, 537-549 (2010).
72. Mollapour, M., *et al.* Swe1^{Wee1}-dependent tyrosine phosphorylation of Hsp90 regulates distinct facets of chaperone function. *Mol Cell* **37**, 333-343 (2010).
73. Goes, F.S. & Martin, J. Hsp90 chaperone complexes are required for the activity and stability of yeast protein kinases Mik1, Wee1 and Swe1. *Eur J Biochem* **268**, 2281-2289 (2001).
74. Mollapour, M., *et al.* Hsp90 phosphorylation, Wee1 and the cell cycle. *Cell Cycle* **9**, 2310-2316 (2010).
75. McGrath, D.A., *et al.* Cks confers specificity to phosphorylation-dependent CDK signaling pathways. *Nat Struct Mol Biol* **20**, 1407-1414 (2013).
76. Olsen, B.B., *et al.* Mapping of the interaction sites between Wee1 kinase and the regulatory beta-subunit of protein kinase CK2. *Int J Oncol* **36**, 1175-1182 (2010).
77. Ovejero, S., *et al.* Human Cdc14A regulates Wee1 stability by counteracting CDK-mediated phosphorylation. *Mol Biol Cell* **23**, 4515-4525 (2012).
78. Yde, C.W., *et al.* The regulatory beta-subunit of protein kinase CK2 regulates cell-cycle progression at the onset of mitosis. *Oncogene* **27**, 4986-4997 (2008).
79. Litchfield, D.W. Protein kinase CK2: structure, regulation and role in cellular decisions of life and death. *Biochem J* **369**, 1-15 (2003).
80. Lindqvist, A., *et al.* Cdc25B cooperates with Cdc25A to induce mitosis but has a unique role in activating cyclin B1–Cdk1 at the centrosome. *J Cell Biol* **171**, 35-45 (2005).
81. Ling, M.T., *et al.* Contributions Made by CDC25 Phosphatases to Proliferation of Intestinal Epithelial Stem and Progenitor Cells. *PloS One* **6**, e15561 (2011).
82. Bollen, M., *et al.* Mitotic phosphatases: from entry guards to exit guides. *Trends Cell Biol* **19**, 531-541 (2009).
83. Guadagno, T.M. & Newport, J.W. Cdk2 kinase is required for entry into mitosis as a positive regulator of Cdc2-

cyclin B kinase activity. *Cell* **84**, 73-82 (1996).
84. Margolis, S.S., *et al.* PP1 control of M phase entry exerted through 14-3-3-regulated Cdc25 dephosphorylation. *EMBO J* **22**, 5734-5745 (2003).
85. Graves, P.R., *et al.* Localization of human Cdc25C is regulated both by nuclear export and 14-3-3 protein binding. *Oncogene* **20**, 1839-1851 (2001).
86. Margolis, S.S., *et al.* A role for PP1 in the Cdc2/Cyclin B-mediated positive feedback activation of Cdc25. *Mol Biol Cell* **17**, 1779-1789 (2006).
87. Schwindling, S.L., *et al.* Mutation of a CK2 phosphorylation site in cdc25C impairs importin alpha/beta binding and results in cytoplasmic retention. *Oncogene* **23**, 4155-4165 (2004).
88. Trunnell, N.B., *et al.* Ultrasensitivity in the Regulation of Cdc25C by Cdk1. *Mol Cell* **41**, 263-274 (2011).
89. Zeng, Y. & Piwnica-Worms, H. DNA damage and replication checkpoints in fission yeast require nuclear exclusion of the Cdc25 phosphatase via 14-3-3 binding. *Mol Cell Biol* **19**, 7410-7419 (1999).
90. Thanasoula, M., *et al.* ATM/ATR checkpoint activation downregulates CDC25C to prevent mitotic entry with uncapped telomeres. *EMBO J* **31**, 3398-3410 (2012).
91. Chen, F., *et al.* Arsenite-induced Cdc25C degradation is through the KEN-box and ubiquitin-proteasome pathway. *Proc Natl Acad Sci U S A* **99**, 1990-1995 (2002).
92. Busino, L., *et al.* Degradation of Cdc25A by beta-TrCP during S phase and in response to DNA damage. *Nature* **426**, 87-91 (2003).
93. Donzelli, M., *et al.* Dual mode of degradation of Cdc25 A phosphatase. *EMBO J* **21**, 4875-4884 (2002).
94. Bailly, E., *et al.* Cytoplasmic accumulation of cyclin B1 in human cells: association with a detergent-resistant compartment and with the centrosome. *J Cell Sci* **101**, 529-545 (1992).
95. Takizawa, C.G. & Morgan, D.O. Control of mitosis by changes in the subcellular location of cyclin-B1-Cdk1 and Cdc25C. *Curr Opin Cell Biology* **12**, 658-665 (2000).
96. Shapiro, G.I. Cyclin-dependent kinase pathways as targets for cancer treatment. *J Clin Oncol* **24**, 1770-1783 (2006).
97. Larochelle, S., *et al.* Requirements for Cdk7 in the assembly of Cdk1/cyclin B and activation of Cdk2 revealed by chemical genetics in human cells. *Mol Cell* **25**, 839-850 (2007).
98. Garrett, S., *et al.* Reciprocal activation by cyclin-dependent kinases 2 and 7 is directed by substrate specificity determinants outside the T loop. *Mol Cell Biol* **21**, 88-99 (2001).
99. Fisher, R.P., *et al.* Alternative mechanisms of CAK assembly require an assembly factor or an activating kinase. *Cell* **83**, 47-57 (1995).
100. Takizawa, C.G., *et al.* Ran-independent nuclear import of cyclin B1-Cdc2 by importin beta. *Proc Natl Acad Sci U S A* **96**, 7938-7943 (1999).
101. Moore, J.D., *et al.* Nuclear import of Cdk/cyclin complexes: identification of distinct mechanisms for import of Cdk2/cyclin E and Cdc2/cyclin B1. *J Cell Biol* **144**, 213-224 (1999).
102. Kramer, A., *et al.* Checking out the centrosome. *Cell Cycle* **3**, 1390-1393 (2004).
103. Jackman, M., *et al.* Active cyclin B1-Cdk1 first appears on centrosomes in prophase. *Nat Cell Biol* **5**, 143-148 (2003).
104. Gavet, O. & Pines, J. Activation of cyclin B1–Cdk1 synchronizes events in the nucleus and the cytoplasm at mitosis. *J Cell Biol* **189**, 247-259 (2010).
105. Santos, S.D., *et al.* Spatial Positive Feedback at the Onset of Mitosis. *Cell* **149**, 1500-1513, (2012).
106. Yang, J., *et al.* Control of cyclin B1 localization through regulated binding of the nuclear export factor CRM1. *Genes Dev* **12**, 2131-2143 (1998).
107. Hagting, A., *et al.* MPF localization is controlled by nuclear export. *EMBO J* **17**, 4127-4138 (1998).
108. Wurzenberger, C. & Gerlich, D.W. Phosphatases: providing safe passage through mitotic exit. *Nat Rev Mol Cell Biol* **12**, 469-482 (2011).
109. Liu, F., *et al.* Overproduction of human Myt1 kinase induces a G2 cell cycle delay by interfering with the intracellular trafficking of Cdc2-cyclin B1 complexes. *Mol Cell Biol* **19**, 5113-5123 (1999).
110. Chow, J.P. & Poon, R.Y. The CDK1 inhibitory kinase MYT1 in DNA damage checkpoint recovery. *Oncogene* **32**, 4778-4788 (2013).
111. Pines, J. Cubism and the cell cycle: the many faces of the APC/C. *Nat Rev Mol Cell Biol* **12**, 427-438 (2011).
112. Izawa, D. & Pines, J. How APC/C-Cdc20 changes its substrate specificity in mitosis. *Nat Cell Biol* **13**, 223-233 (2011).
113. Coulonval, K., *et al.* Coupling of T161 and T14 phosphorylations protects cyclin B-CDK1 from premature activation. *Mol Biol Cell* **22**, 3971-3985 (2011).
114. Aarts, M., *et al.* Forced mitotic entry of S-phase cells as a therapeutic strategy induced by inhibition of WEE1. *Cancer Discov* **2**, 524-539 (2012).
115. Landau, H.J., *et al.* The checkpoint kinase inhibitor AZD7762 potentiates chemotherapy-induced apoptosis of p53-mutated multiple myeloma cells. *Mol Cancer Ther* **11**, 1781-1788 (2012).
116. Yang, H., *et al.* Inhibition of checkpoint kinase 1 sensitizes lung cancer brain metastases to radiotherapy. *Biochem Biophys Res Commun* **406**, 53-58 (2011).
117. Morgan, M.A., *et al.* Mechanism of radiosensitization by the Chk1/2 inhibitor AZD7762 involves abrogation of the G2 checkpoint and inhibition of homologous recombinational DNA repair. *Cancer Res* **70**, 4972-4981 (2010).
118. Schmidt, M., *et al.* Molecular alterations after Polo-like kinase 1 mRNA suppression versus pharmacologic inhibition in cancer cells. *Mol Cancer Ther* **5**, 809-817 (2006).
119. Lee, M.H. & Yang, H.Y. Regulators of G1 cyclin-dependent kinases and cancers. *Cancer Metastasis Rev* **22**, 435-449 (2003).
120. Myer, D.L., *et al.* The Plk3-Cdc25 circuit. *Oncogene* **24**, 299-305 (2005).
121. McCourt, P., *et al.* PP2A(Cdc55) regulates G1 cyclin stability. *Cell cycle* **12**, 1201-1210 (2013).
122. Ceulemans, H. & Bollen, M. Functional diversity of protein phosphatase-1, a cellular economizer and reset button. *Physiol Rev* **84**, 1-39 (2004).
123. Zitouni, S., *et al.* Polo-like kinases: structural variations lead to multiple functions. *Nat Rev Mol Cell Biol* **15**, 433-452 (2014).
124. Hughes, B.T., *et al.* Essential role for Cdk2 inhibitory phosphorylation during replication stress revealed by a human Cdk2 knockin mutation. *Proc Natl Acad Sci U S A* **110**, 8954-8959 (2013).

SUPPLEMENTARY FIGURES

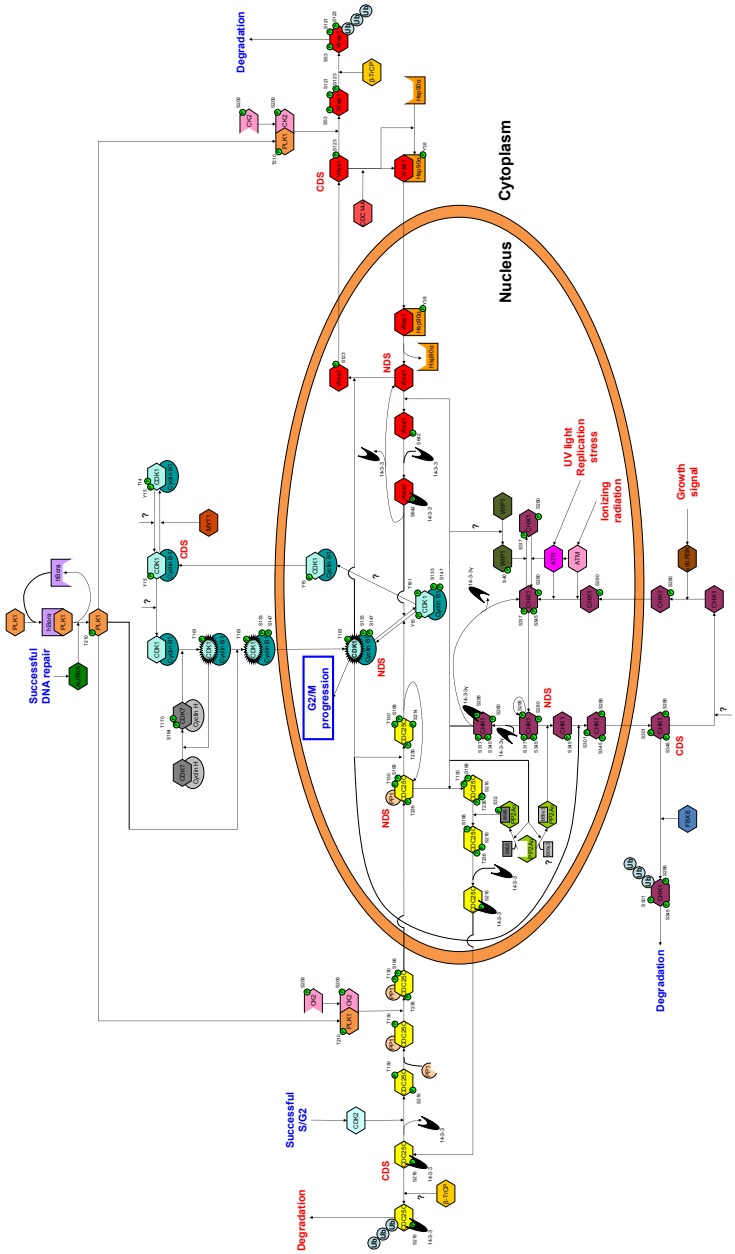

Supplementary Figure 1 | Complete overview of the G2 checkpoint network. All interactions described in **Figure 2** through **Figure 6** and simplified in **Figure 1** are depicted here. This intricate network is a delicate interplay between Wee1, CDC25C, PLK1, CHK1 and CDK1.

Supplementary Video 1 | https://febs.onlinelibrary.wiley.com/action/downloadSupplement?doi=10.1002%2F2211-5463.12206&attachmentId=124185424

Chapter 10

ATP-BINDING CASSETTE TRANSPORTERS LIMIT THE BRAIN PENETRATION OF WEE1 INHIBITORS

M.C. de Gooijer, L.C.M. Buil, J.H. Beijnen,
and O. van Tellingen

Investigational New Drugs. 2018;36(3):380-387

ABSTRACT

Introduction: Wee1 is an important kinase involved in the G2 cell cycle checkpoint and frequently upregulated in intracranial neoplasms such as glioblastoma (GBM) and diffuse intrinsic pontine glioma (DIPG). Two small molecules are available that target Wee1, AZD1775 and PD0166285, and clinical trials with AZD1775 have already been started. Since GBM and DIPG are highly invasive brain tumors, they are at least to some extent protected by the blood–brain barrier (BBB) and its ATP-binding cassette (ABC) efflux transporters. ***Methods:*** We have here conducted a comprehensive set of *in vitro* and *in vivo* experiments to determine to what extent two dominant efflux transporters in the BBB, P-gp (ABCB1) and BCRP (ABCG2), exhibit affinity towards AZD1775 and PD0166285 and restrict their brain penetration. ***Results:*** Using these studies, we demonstrate that AZD1775 is efficiently transported by both P-gp and BCRP, whereas PD0166285 is only a substrate of P-gp. Nonetheless, the brain penetration of both compounds was severely restricted *in vivo*, as indicated by a 5-fold (PD0166285) and 25-fold (AZD1775) lower brain–plasma ratio in wild-type mice compared to *Abcb1a/b;Abcg2*$^{-/-}$ mice. ***Conclusion:*** The brain penetration of these Wee1 inhibitors is severely limited by ABC transporters, which may compromise their clinical efficacy against intracranial neoplasms such as DIPG and GBM.

INTRODUCTION

The eukaryotic cell cycle is tightly regulated and consists of four phases. Cells predominantly spend time in the G1/G0 phase and subsequently progress through S and G2 phase before undergoing mitosis. Each of these four cell cycle phases is equipped with a checkpoint. These checkpoints are intricate molecular switches that govern the decision to progress to the next phase in the cycle and are pivotal to maintaining genomic integrity in healthy cells[1]. Cancer cells however, frequently harbor a deregulated cell cycle. Most often, the G1 checkpoint is abrogated (*e.g.*, due to loss of p53 function) and as a result cancer cells rely more heavily on the G2 checkpoint[2]. The G2 checkpoint is responsible for the decision to enter mitosis, and represents the final opportunity for the cell to minimize DNA damage before entering mitosis[3]. Inhibiting the G2 checkpoint in combination with DNA damage-inducing chemotherapy or radiotherapy has been postulated as a logical rationale to induce death of cancer cells harboring an abrogated G1 checkpoint. Forcing cells through division while sustaining considerable DNA damage creates high levels of genomic instability, ultimately resulting in mitotic catastrophe[4]. A promising target for this strategy is the kinase Wee1, a key enforcer of the G2 checkpoint.

Since the beginning of this century, two small molecule Wee1 inhibitors have been developed (**Figure 1**). PD0166285 was discovered in 2001 as a Wee1 inhibitor that also targets MYT1 and CHK1[5]. More recently, the specific Wee1 inhibitor AZD1775 (previously MK1775) was developed[6]. Both compounds have initially demonstrated preclinical efficacy in *TP53*-mutated tumor models as sensitizers to both chemotherapy[7] and radiotherapy[5,8]. Later, efficacy was also found in *TP53* wild-type tumors, and this effect was postulated to be mediated by intrinsic chromosomal instability[9] and replication stress[10,11].

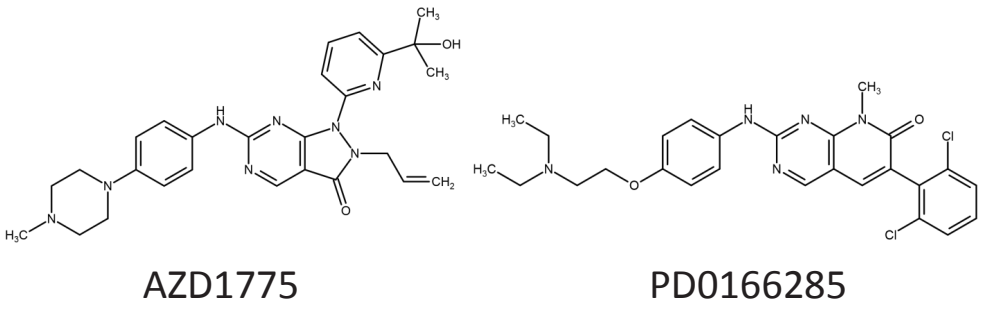

Figure 1 | Chemical structures of AZD1775 and PD0166285. Chemical structures of the Wee1 inhibitors AZD1775 and PD0166285. Both compounds contain the same core diphenylamine moiety.

Inhibition of Wee1 has initially been investigated in extracranial tumor models only, and these preclinical studies have now led to clinical development of AZD1775. The results of the first phase II trial investigating AZD1775 as a chemosensitizer in *TP53*-mutated ovarian cancer have now

been reported, and appear very encouraging[12]. More recently however, Wee1 has been gaining attention for treatment of various intracranial tumors, such as glioblastoma (GBM)[13,14], and diffuse intrinsic pontine glioma (DIPG)[15]. In these tumor types, Wee1 was shown to be one of the most overexpressed kinases and Wee1 inhibition could radiosensitize orthotopic preclinical GBM and DIPG models. These reports have now led to a number of clinical trials investigating AZD1775 in intracranial tumors such as GBM (ClinicalTrials.gov Identifiers NCT02207010, NCT01849146), DIPG (NCT01922076) and medulloblastoma, neuroblastoma and supratentorial embryonal tumors (NCT02095132).

When targeting intracranial tumors, at least one additional hurdle needs to be overcome, as these tumors are all to some extent protected by the blood–brain barrier (BBB)[16]. The brain microvascular endothelial cells form the core of the BBB and do not only prevent paracellular diffusion due to their lack of fenestrae and abundance of tight junctions, but are also equipped with a range of efflux transporters that actively pump out xenobiotics back into the bloodstream. These ATP-binding cassette (ABC) transporters, of which breast cancer resistance protein (BCRP; ABCG2) and P-glycoprotein (P-gp; ABCB1) are the most dominant, restrict the brain penetration of a wide range of xenobiotics, including many anticancer agents[17-19]. This impaired brain penetration has been demonstrated to limit therapeutic efficacy in several clinically relevant mouse models[20,21]. Importantly, studies testing a panel of inhibitors targeting PI3K have shown that the most brain penetrable compounds were the most likely candidates to achieve intracranial antitumor efficacy[22,23]. Since this might be similarly true for compounds targeting Wee1, we investigated the brain penetration of Wee1 inhibitors. We here show that both available Wee1 inhibitors, AZD1775 and PD0166285, are substrates of ABC transporters, potentially limiting their suitability for use against intracranial neoplasms such as GBM and DIPG.

METHODS

Drugs

PD0166285 was purchased from Sigma–Aldrich (St Louis, MO) and AZD1775 (MK1775) from Axon Medchem BV (Groningen, The Netherlands). Zosuquidar was obtained from Eli Lilly (Indianapolis, IN). Elacridar was generously provided by GlaxoSmithKline (Research Triangle Park, NC).

Cell culture

All used cell lines were previously generated in-house by dr. A.H. Schinkel[24-26]. Parental LLC–PK1 cells, and subclones overexpressing human ABCB1 (LLC–MDR1) or murine Abcb1a (LLC–Mdr1a), parental MDCK cells and sub-lines overexpressing human ABCG2 (MDCK–BCRP) or murine Abcg2

(MDCK–Bcrp1) were all cultured as described previously[18].

Concentration equilibrium transport assays

Concentration equilibrium transport assays (CETAs) were carried out using 500 nM of the Wee1 inhibitors and 5 μM of zosuquidar or elacridar was used to block transport, as described previously[18]. To prepare CETA samples for subsequent HPLC analysis, medium samples were mixed with two volumes of acetonitrile. After centrifugation, the supernatant was diluted 3-fold with water and the concentration of AZD1775 or PD0166285 was measured by High Performance Liquid Chromatography (HPLC) coupled to a UV detector (Model 996 UV Photodiode Array detector; Waters, Milford, MA) using a GraceSmart RP18 5μm column (150 x 2 mm) (Grace, Deerfield, IL). AZD1775 was detected at 340 nm using isocratic conditions with 45 % acetonitrile in 0.1% (v/v) formic acid in water delivered at a flow rate of 0.2 mL/min. PD0166285 was detected at 360 nm using the same column eluted with a gradient of methanol and 0.1% (v/v) formic acid in water ranging from 30% to 70% delivered at a flow rate of 0.2 mL/min.

Animals

All animal studies were approved by the animal experiment committee and adhered to national law and institutional guidelines. The animals had access to food and water *ad libitum*.

Pharmacokinetic studies

We used wild-type, *Abcg2*$^{-/-}$, *Abcb1a/b*$^{-/-}$ and *Abcb1a/b;Abcg2*$^{-/-}$ FVB mice. PD0166285 (5 mg/kg) and AZD1775 (20 mg/kg) were administered i.v. in DMSO. Blood was collected by cardiac puncture 1 hour after injection under isoflurane anesthesia, followed by brain tissue collection. Plasma was obtained by centrifugation (5 min, 5,000 rpm, 4 °C). Brains were weighed and homogenized using a FastPrep®-24 (MP-Biomedicals; Santa Ana, CA) in 1% (w/v) bovine serum albumin in water. All samples were stored at -20°C until analysis. AZD1775 and PD0166285 were extracted using diethyl ether and AZD8055 was used as internal standard. Organic phases were separated and dried by vacuum. Samples were reconstituted in methanol:water (20:80 v/v) and measured in an LC–MS/MS setup consisting of an Ultimate 3000 LC System (Dionex) and an API 4000 mass spectrometer (AB Sciex; Framingham, MA). Separation was performed on a ZORBAX Extend-C18 column (Agilent Technologies; Santa Clara, CA). Mobile phase A (0.1% formic acid in water) and B (methanol) was used in a 5 min gradient from 30 to 95%B maintained for 3 min followed by re-equilibration at 30%B. Multiple reaction monitoring (MRM) ion traces were 501.5 / 442.4 (AZD1775) and 512.2 / 438.9 (PD0166285) and 466.2 / 450.1 (AZD8055). Data were acquired and analyzed using Analyst® 1.6.2 software (AB Sciex).

Statistical analysis

CETA results were analyzed as described previously[18]. In short, the data was grouped by defining four sampling time points (30 min, 1 h, 2 h and 4 h) as a four-level within-subjects factor. Then, the general linear model repeated measures procedure of SPSS (v20; SPSS Inc; Chicago, IL) was used to determine whether the apical–basal differences were significantly increased by the factor of time. For *in vivo* pharmacokinetic experiments, one-way analysis of variance and *post hoc* Bonferroni was performed. In all experiments, differences were considered statistically significant when $p < 0.05$.

RESULTS

P-gp and BCRP transport AZD1775 in vitro

Transport affinity of AZD1775 for P-gp and BCRP was first investigated *in vitro* using concentration equilibrium transport assays (CETAs). AZD1775 is clearly transported by both P-gp and BCRP (**Figure 2**). First, an increasing difference in AZD1775 concentration over time between the apical and basolateral compartment was observed in both BCRP and Bcrp1-expressing cell lines. Notably, this translocation also occurred in the MDCK parental cell line. Inhibition of translocation in all BCRP-expressing cell lines by elacridar confirmed that BCRP was responsible for this translocation, although full inhibition of transport was not achieved in the Bcrp1-expressing cell line. This observation could be indicative of highly efficient AZD1775 transport by Bcrp1, since full inhibition could be achieved in the endogenous canine BCRP-expressing parental cell line and in the human BCRP expressing cell line.

AZD1775 transport assays with cell lines expressing P-gp yielded similar results as those using BCRP-expressing lines. AZD1775 translocation was found in all cell lines expressing P-gp, including the parental cell line that expresses endogenous porcine P-gp. Intriguingly, transport could be inhibited by the P-gp inhibitor zosuquidar in the Mdr1a and MDR1-expressing cell line, but not in the parental line, possibly indicating the presence of an additional unknown apically oriented transporter with substrate affinity for AZD1775 in this cell line.

PD0166285 is transported by P-gp, but not BCRP, in vitro

CETAs investigating translocation of PD0166285 revealed transport activity of P-gp, but not BCRP, *in vitro*. In none of the BCRP-expressing cell lines, translocation was observed (**Figure 3**). In contrast to BCRP, both Mdr1a and MDR1-expressing cell lines were found to transport PD0166285 while the parental porcine cell line was not. Again, loss of translocation in presence of the P-gp inhibitor zosuquidar is a further confirmation that P-gp was responsible for the

observed PD0166285 transport.

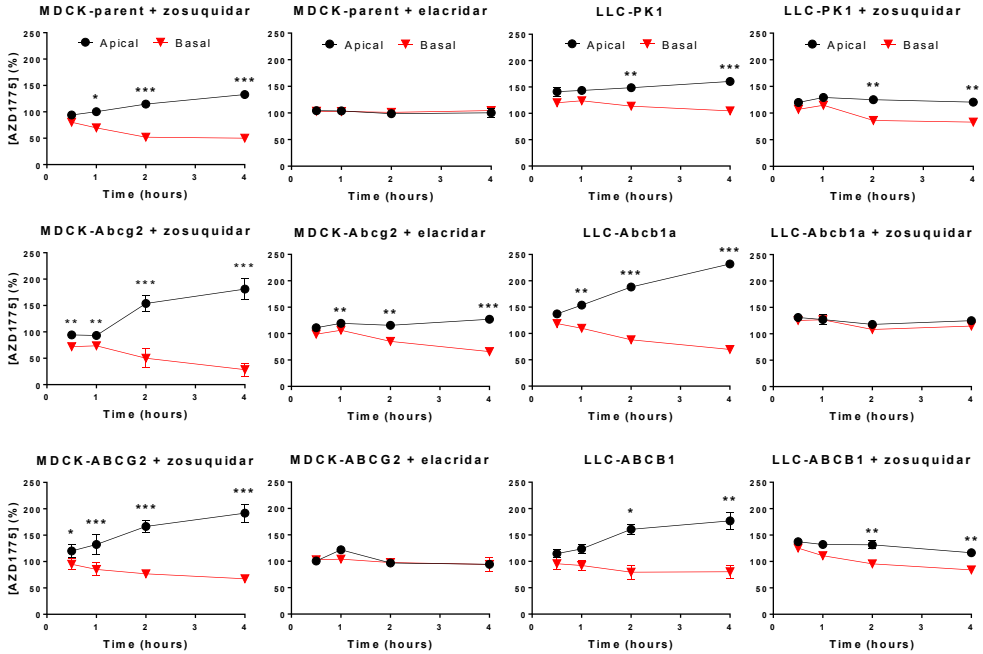

Figure 2 | *In vitro* transport of AZD1775 by P-gp and BCRP. Concentration equilibrium transport assays (CETAs) with various cell lines expressing murine or human P-gp or BCRP. AZD1775 showed profound basal to apical (B-to-A) translocation by Abcg2 and ABCG2. Interestingly, transport also occurred in the parental canine cell line. Note that any activity of endogenous canine P-gp in the MDCK lines was inhibited by adding 5 μM of zosuquidar. In all cell lines, BCRP transport was confirmed by inhibition with 5 μM of the BCRP/P-gp inhibitor elacridar. AZD1775 was transported by Mdr1a and MDR1, which could be inhibited by 5 μM of the P-gp inhibitor zosuquidar. Some residual B-to-A translocation of AZD1775 was observed in the LLC–PK1 and LLC–MDR1 that was not fully inhibited by 5 μM zosuquidar. Data are represented as mean ± SD (n ≥ 3); * $p < 0.05$, ** $p < 0.01$, *** $p < 0.001$.

P-gp and BCRP work in concert to limit the brain penetration of AZD1775 in vivo

The impact of the ABC transporters P-gp and BCRP on the brain penetration of AZD1775 was tested in a pharmacokinetic experiment using mouse strains that were genetically engineered to lack one or multiple transporters. Intravenous administration of 20 mg/kg AZD1775 resulted in major differences in brain levels between ABC transporter knockout mice 1 hour after injection, while the plasma levels were similar among all strains (**Figure 4A**). Compared to wild-type control mice the AZD1775 brain concentration was elevated in *Abcb1a/b*$^{-/-}$ but not in *Abcg2*$^{-/-}$ mice, suggesting that P-gp is the most dominant transporter limiting AZD1775 brain penetration. However, a further 6-fold increase in AZD1775 brain-plasma ratio that was observed in *Abcb1a/b; Abcg2*$^{-/-}$ compared to *Abcb1a/b*$^{-/-}$ mice demonstrates an important role for BCRP in AZD1775 efflux transport in the BBB *in vivo*. The presence of either one of these transporters is sufficient to cause a major reduction in the brain penetration of AZD1775.

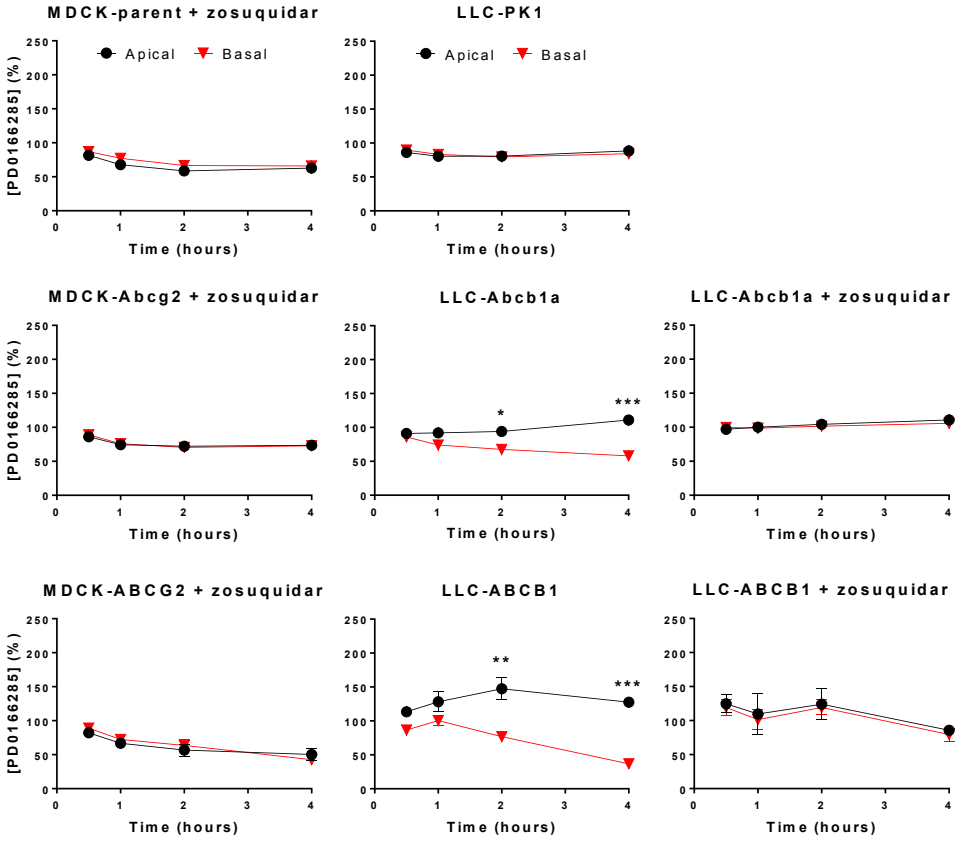

Figure 3 | *In vitro* transport of PD0166285 by P-glycoprotein. Concentration equilibrium transport assays (CETAs) with various cell lines expressing murine or human P-gp or BCRP. PD0166285 was transported by both Mdr1a and MDR1, which was inhibited by 5 μM of the P-gp inhibitor zosuquidar. PD0166285 was not transported by Bcrp1 or BCRP. No transport was observed in the parental porcine cell line. Data are represented as mean ± SD (n ≥ 3); * $p < 0.05$, ** $p < 0.01$, *** $p < 0.001$.

P-gp, but not BCRP, limits the brain penetration of PD0166285 in vivo

A similar pharmacokinetic experiment as described above for AZD1775 was conducted investigating the brain penetration of PD0166285. In this experiment, approximately 5-fold increased brain levels were observed in both *Abcb1a/b*$^{-/-}$ and *Abcb1a/b;Abcg2*$^{-/-}$ mice compared to wild-type mice (**Figure 4B**). Thus, this effect appeared to be solely caused by P-gp, since further elevated PD0166285 brain levels were not observed when Abcg2 was also absent. These differences in brain levels were also reflected in the brain–plasma ratios since plasma levels were similar in all genetic backgrounds. In summary, these results indicate that the brain penetration of PD0166285 *in vivo* is limited by P-gp, but not BCRP.

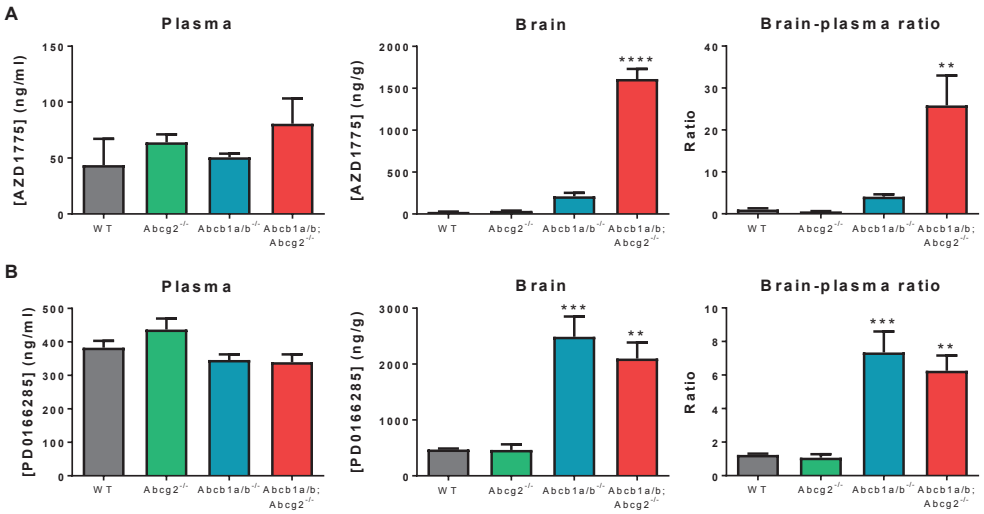

Figure 4 | The impact of P-gp and BCRP on the brain penetration of Wee1 inhibitors. (**A**) Wild-type (WT) FVB, *Abcg2*$^{-/-}$, *Abcb1a/b*$^{-/-}$ and *Abcb1a/b;Abcg2*$^{-/-}$ mice were intravenously injected with 20 mg/kg AZD1775. After one hour, brain and plasma levels were determined and brain-plasma ratios were calculated. In contrast to *Abcg2*$^{-/-}$ mice, brain levels in *Abcb1a/b*$^{-/-}$ mice were elevated compared to WT mice while plasma levels were similar in all strains. Compared to *Abcb1a/b*$^{-/-}$ mice, brain levels of AZD1775 were even further increased in *Abcb1a/b;Abcg2*$^{-/-}$ mice, indicating that P-gp and BCRP work in concert to limit brain penetration of AZD1775. (**B**) Plasma concentrations, brain concentrations and brain-plasma ratios were determined in various ABC transporter knockout mice 1 hour after i.v. administration of 5 mg/kg PD0166285. In contrast to *Abcg2*$^{-/-}$ mice, brain levels in *Abcb1a/b*$^{-/-}$ mice were elevated compared to WT mice at both time points while plasma levels were similar in all backgrounds. Compared to *Abcb1a/b*$^{-/-}$ mice, brain levels of PD0166285 were not further increased in *Abcb1a/b;Abcg2*$^{-/-}$ mice, indicating that P-gp, but not BCRP, limits the brain penetration of PD0166285. All data are represented as mean ± SD (n ≥ 4); * $p < 0.05$, ** $p < 0.01$, **** $p < 0.0001$.

DISCUSSION

This set of *in vitro* and *in vivo* studies together demonstrate that the brain penetration of the Wee1 inhibitors AZD1775 and PD0166285 is strongly restricted by ABC transporters. First *in vitro* transports assays demonstrate that AZD1775 is a substrate for both P-gp and BCRP, and that PD0166285 is a substrate for P-gp (**Figure 2 and Figure 3**). Next, pharmacokinetic experiments using wild-type and ABC transport knockout mice sampled for brain and plasma at 1 hour after drug administration clearly show that these same transporters are responsible for the very low brain penetration of the Wee1 inhibitors *in vivo* (**Figure 4**). Notably, in the absence of these transporters the brain-plasma ratio of both agents was remarkably high (approximately 25 for AZD1775 and 6 for PD0166285), whereas in wild-type mice AZD1775 and PD0166285 could only achieve a brain-plasma ratio of 1.0 and 1.2, respectively.

The finding of this study that AZD1775 is efficiently transported by P-gp and BCRP in the blood–brain barrier could explain the previous report by Pokorny *et al.* demonstrating that AZD1775 exhibits heterogeneous penetration in an preclinical orthotopic brain tumor model[27]. Importantly, these authors have demonstrated that this heterogeneous brain tumor distribution

limits antitumor efficacy in orthotopic glioma models, since efficacy could be observed against ectopic tumors. PD0166285 has not yet been investigated in a similar fashion, but the finding that it is an efficient P-gp substrate seems to predict that heterogeneous brain tumor distribution may likewise be found for PD0166285.

In contrast, a recent study by Wu *et al.* determined the brain–plasma ratio of AZD1775 in GBM patients by LC–MS/MS and found a brain–plasma ratio of approximately 7.5[28]. This ratio is about 7-fold higher that the ratio reported in the present study and also seems to contradict the study by Pokorny and colleagues. However, in the study by Wu *et al.* the brain–plasma ratio was measured in biopsies from the main mass of the brain tumor that is often leaky and thus might overestimate the general brain penetration[16]. Interestingly, the AZD1775 brain–plasma ratio in clinical specimens of the main tumor mass was similar to the brain–plasma ratio in *Abcb1a/b;Abcg2*$^{-/-}$ mice reported here, suggesting that the BBB was severely compromised in the regions of the tumor from which samples were collected by Wu and colleagues.

Even though the core of a GBM tumor is leaky, the BBB still remains an important hurdle to successful GBM treatment. Glioma is a disease that is systemic to the brain as these tumor cells invade into normal surrounding brain structures where they find shelter behind an intact BBB[16]. Since the leaky core of the tumor is often removed by surgery, adjuvant therapies should especially target those migrated cells. There is a strong biological rationale for a role of Wee1 inhibitors in such a systemic therapy, but these inhibitors thus need to overcome the BBB and its ABC transporters. In this light, PD0166285 might be a better candidate than AZD1775. Even though both compounds are substrates of P-gp, PD0166285 is not transported by BCRP. This difference might be more important in patients than in mouse models, since BCRP is more abundant in human brain endothelial cells than in murine brain[29]. Moreover, the therapy-resistant glioma stem-like cell (GSC) compartment is also protected by expression of BCRP[30].

A disadvantage of PD0166285 compared to AZD1775 may be its lower selectivity. PD0166285 has originally been described to not only inhibit Wee1, but also MYT1 and CHK1 at approximately equimolar potency[5]. AZD1775 on the other hand was developed as a more specific Wee1 inhibitor, although recent reports suggest that AZD1775 also targets PLK1[31,32]. However, since all these kinases fulfill overlapping and complimentary roles in the G2 checkpoint[3], more detailed mechanistic studies should shed light on the true disadvantage of this relative aspecificity.

Obviously, the ideal Wee1 inhibitor for treatment of intracranial neoplasms combines high target specificity and no affinity for P-gp and BCRP. However, until such a candidate is developed, alternative approaches should be investigated in an effort to make Wee1 inhibitors available for treatment of brain tumors. One such strategy involves combined administration with a P-gp/BCRP inhibitor such as elacridar[33]. Unfortunately however, AZD1775 doesn't appear to be the

most obvious candidate to investigate this approach in a clinical setting, because of its strong affinity for BCRP and the relative abundance of BCRP in the human BBB[29]. PD0166285 might be more promising for this treatment strategy, and our data suggest that this Wee1 inhibitor would potentially not need to be combined with a dual P-gp/BCRP inhibitor but could be investigated in combination with a potent P-gp inhibitor such as zosuquidar or tariquidar[34,35].

In summary, targeting Wee1 to treat intracranial neoplasms holds promise since Wee1 is overexpressed in various glioma types and several clinical trials have been started. However, since gliomas are highly invasive and thus to a considerable extent protected by the BBB, using a Wee1 inhibitor with sufficient brain penetration capacity is pivotal to the success of this treatment strategy. We demonstrate that both available Wee1 inhibitors, AZD1775 and PD0166285, are efficient substrates of ABC transporters in the BBB and it is therefore not very likely that they will be able to exhibit efficacy in patients.

REFERENCES

1. Malumbres, M. & Barbacid, M. Cell cycle, CDKs and cancer: a changing paradigm. *Nat Rev Cancer* **9**, 153-166 (2009).
2. Medema, R.H. & Macurek, L. Checkpoint control and cancer. *Oncogene* **31**, 2601-2613 (2012).
3. de Gooijer, M.C., *et al.* The G2 checkpoint—a node-based molecular switch. *FEBS Open Bio* **7**, 439-455 (2017).
4. Dixon, H. & Norbury, C.J. Therapeutic exploitation of checkpoint defects in cancer cells lacking p53 function. *Cell Cycle* **1**, 362-368 (2002).
5. Wang, Y., *et al.* Radiosensitization of p53 mutant cells by PD0166285, a novel G2 checkpoint abrogator. *Cancer Res* **61**, 8211-8217 (2001).
6. Hirai, H., *et al.* Small-molecule inhibition of Wee1 kinase by MK-1775 selectively sensitizes p53-deficient tumor cells to DNA-damaging agents. *Mol Cancer Ther* **8**, 2992-3000 (2009).
7. Rajeshkumar, N.V., *et al.* MK-1775, a potent Wee1 inhibitor, synergizes with gemcitabine to achieve tumor regressions, selectively in p53-deficient pancreatic cancer xenografts. *Clin Cancer Res* **17**, 2799-2806 (2011).
8. Bridges, K.A., *et al.* MK-1775, a novel Wee1 kinase inhibitor, radiosensitizes p53-defective human tumor cells. *Clin Cancer Res* **17**, 5638-5648 (2011).
9. Vriend, L.E., *et al.* WEE1 inhibition and genomic instability in cancer. *Biochim Biophys Acta* **1836**, 227-235 (2013).
10. Cuneo, K.C., *et al.* Wee1 kinase inhibitor AZD1775 radiosensitizes hepatocellular carcinoma regardless of TP53 mutational status through induction of replication stress. *Int J Radiat Oncol Biol Phys* **95**, 782-790 (2016).
11. Puigvert, J.C., *et al.* Targeting DNA repair, DNA metabolism and replication stress as anti-cancer strategies. *FEBS J* **283**, 232-245 (2016).
12. Leijen, S., *et al.* Phase II study of WEE1 inhibitor AZD1775 plus carboplatin in patients with TP53-mutated ovarian cancer refractory or resistant to first-line therapy within 3 months. *J Clin Oncol* **34**, 4354-4361 (2016).
13. Mir, S.E., *et al. In silico* analysis of kinase expression identifies WEE1 as a gatekeeper against mitotic catastrophe in glioblastoma. *Cancer Cell* **18**, 244-257, (2010).
14. De Witt Hamer, P.C., *et al.* WEE1 kinase targeting combined with DNA-damaging cancer therapy catalyzes mitotic catastrophe. *Clin Cancer Res* **17**, 4200-4207 (2011).
15. Caretti, V. *et al.* WEE1 kinase inhibition enhances the radiation response of diffuse intrinsic pontine gliomas. *Mol Cancer Ther* **12**, 141-150 (2013).
16. van Tellingen, O., *et al.* Overcoming the blood-brain tumor barrier for effective glioblastoma treatment. *Drug Resist Updat* **19**, 1-12 (2015).
17. Durmus, S., *et al.* Apical ABC transporters and cancer chemotherapeutic drug disposition. *Adv Cancer Res* **125**, 1-41 (2015).
18. de Gooijer, M.C., *et al.* P-glycoprotein and breast cancer resistance protein restrict the brain penetration of the CDK4/6 inhibitor palbociclib. *Invest New Drugs* **33**, 1012-1019 (2015).
19. Oberoi, R.K., *et al.* Pharmacokinetic assessment of efflux transport in sunitinib distribution to the brain. *J Pharmacol Exp Ther* **347**, 755-764 (2013).
20. Lin, F., *et al.* ABCB1, ABCG2, and PTEN determine the response of glioblastoma to temozolomide and ABT-888 therapy. *Clin Cancer Res* **20**, 2703-2713 (2014).
21. Parrish, K.E., *et al.* Efflux transporters at the blood-brain barrier limit delivery and efficacy of cyclin-dependent kinase 4/6 inhibitor palbociclib (PD-0332991) in an orthotopic brain tumor model. *J Pharmacol Exp Ther* **355**, 264-271 (2015).
22. Lin, F., *et al.* PI3K–mTOR pathway inhibition exhibits efficacy against high-grade glioma in clinically relevant mouse models. *Clin Cancer Res* **23**, 1286-1298 (2017).
23. Becker, C.M., *et al.* Decreased affinity for efflux transporters increases brain penetrance and molecular targeting of a PI3K/mTOR inhibitor in a mouse model of glioblastoma. *Neuro Oncol* **17**, 1210-1219 (2015).
24. Schinkel, A.H., *et al.* Absence of the mdr1a P-glycoprotein in mice affects tissue distribution and pharmacokinetics of dexamethasone, digoxin, and cyclosporin A. *J Clin Invest* **96**, 1698-1705 (1995).

25. Jonker, J.W., *et al.* Role of breast cancer resistance protein in the bioavailability and fetal penetration of topotecan. *J Natl Cancer Inst* **92**, 1651-1656 (2000).
26. Pavek, P., *et al.* Human breast cancer resistance protein: interactions with steroid drugs, hormones, the dietary carcinogen 2-amino-1-methyl-6-phenylimidazo(4,5-*b*)pyridine, and transport of cimetidine. *J Pharmacol Exp Ther* **312**, 144-152 (2005).
27. Pokorny, J.L., *et al.* The efficacy of the Wee1 inhibitor MK-1775 combined with temozolomide is limited by heterogeneous distribution across the blood–brain barrier in glioblastoma. *Clin Cancer Res* **21**, 1916-1924 (2015).
28. Wu, J., *et al.* An aqueous normal-phase chromatography coupled with tandem mass spectrometry method for determining unbound brain-to-plasma concentration ratio of AZD1775, a Wee1 kinase inhibitor, in patients with glioblastoma. *J Chromatogr B, Analyt Technol Biomed Life Sci* **1028**, 25-32 (2016).
29. Uchida, Y., *et al.* Quantitative targeted absolute proteomics of human blood-brain barrier transporters and receptors. *J Neurochem* **117**, 333-345 (2011).
30. Bleau, A.M., *et al.* PTEN/PI3K/Akt pathway regulates the side population phenotype and ABCG2 activity in glioma tumor stem-like cells. *Cell Stem Cell* **4**, 226-235 (2009).
31. Wright, G., *et al.* Dual targeting of WEE1 and PLK1 by AZD1775 elicits single agent cellular anticancer activity. *ACS Chem Biol* **12**, 1883-1892 (2017).
32. Zhu, J.Y., *et al.* Structural basis of Wee kinases functionality and inactivation by diverse small molecule inhibitors. *J Med Chem* **60**, 7863-7875 (2017).
33. Hyafil, F., *et al. In vitro* and *in vivo* reversal of multidrug resistance by GF120918, an acridonecarboxamide derivative. *Cancer Res* **53**, 4595-4602 (1993).
34. Dantzig, A.H., *et al.* Reversal of P-glycoprotein-mediated multidrug resistance by a potent cyclopropyldibenzosuberane modulator, LY335979. *Cancer Res* **56**, 4171-4179 (1996).
35. Martin, C., *et al.* The molecular interaction of the high affinity reversal agent XR9576 with P-glycoprotein. *Br J Pharmacol* **128**, 403-411 (1999).

10

Chapter 11

P-GLYCOPROTEIN AND BREAST CANCER RESISTANCE PROTEIN RESTRICT THE BRAIN PENETRATION OF THE CDK4/6 INHIBITOR PALBOCICLIB

M.C. de Gooijer, P. Zhang, N. Thota, I. Mayayo-Peralta, L.C.M. Buil, J.H. Beijnen, and O. van Tellingen

Investigational New Drugs. 2015;33(5):1012-1019

ABSTRACT

Introduction: Palbociclib is a cyclin dependent kinase (CDK) 4/6 inhibitor with nanomolar potency and was recently approved for treatment of breast cancer. The drug may also be useful in glioblastoma (GBM) and diffuse intrinsic pontine gliomas (DIPG), which often have an activated CDK4/6–retinoblastoma signaling pathway. However, GBM and DIPG spread widely into the surrounding brain, which calls for a CDK4/6 inhibitor with sufficient blood–brain barrier penetration. ***Methods:*** We first performed *in vitro* transwell assays and demonstrate that palbociclib is a substrate of both P-gp and BCRP. Next, we conducted pharmacokinetic studies using wild-type (WT), *Abcg2*$^{-/-}$, *Abcb1a/b*$^{-/-}$ and *Abcb1a/b;Abcg2*$^{-/-}$ mice. ***Results:*** The plasma levels were about 3000 and 500 nM and similar in all genotypes at 1 and 4 hours after i.v. administration of 10 mg/kg. At 4 h the brain-to-plasma ratios were 0.3 in WT and *Abcg2*$^{-/-}$ mice versus 5.5 and 15 in *Abcb1a/b*$^{-/-}$ and *Abcb1a/b;Abcg2*$^{-/-}$ mice, respectively. The oral bioavailability of palbociclib was high (63%) in WT mice and increased only modestly and non-significantly in *Abcb1a/b;Abcg2*$^{-/-}$ mice. The plasma level after oral dosing of 150 mg/kg was already much higher than observed in patients (200–400 nM) and exceeded 2500 nM for up to 24 hours. This latter dose is commonly used in preclinical studies, which calls into question their predictive value as they were conducted at dose levels causing a clinically non-relevant systemic drug exposure. ***Conclusion:*** Thus, the brain penetration of palbociclib is restricted by P-gp and BCRP, which may restrict the efficacy against GBM and DIPG. Moreover, preclinical studies with this agent should be conducted at a more clinically relevant dose level.

INTRODUCTION

Palbociclib (PD-0332991) is a potent dual cyclin-dependent kinase 4/6 (CDK4/6) inhibitor that exhibits IC_{50}s in the low nanomolar range. It efficiently induces a G1 cell cycle arrest and subsequent cytostasis *in vitro* and *in vivo*[1-5]. Palbociclib has recently received FDA approval for treatment of estrogen receptor positive, human epidermal growth factor receptor 2 negative (ER+/HER2-) advanced breast cancer[6]. Many other clinical trials are ongoing, including one for treatment of retinoblastoma-associated protein (RB)-proficient glioblastoma (GBM) (ClinicalTrials.gov Identifier NCT01227434). GBM is a devastating primary brain tumor with a very poor outcome. Even with optimal surgery and intensive chemo-radiation therapy the median overall survival is only about 15 months[7]. Palbociclib is receiving considerable interest for its potential use in treatment of GBM since more than 50% of tumors harbor a loss of the *CDKN2A/B* locus or *CDK4* amplification[8,9]. Moreover, Michaud *et al.* demonstrated the potential efficacy of palbociclib against preclinical orthotopic GBM mouse models[4]. Similarly, diffuse intrinsic pontine glioma (DIPG), a highly invasive pediatric neoplasm of the brainstem, has recently been found to harbor RB pathway amplifications in 30% of all cases[10,11]. Dependency of tumor cells on this pathway would render CDK4/6 inhibition a potentially attractive therapeutic target for treatment of GBM and DIPG.

GBMs and DIPGs are both incurable brain tumors, because of their location and the widespread infiltration of normal surrounding brain tissue that prevents complete surgical resection. Moreover, the many tumor cells that invaded the surrounding normal brain are protected by the blood–brain barrier (BBB). The BBB restricts the brain entry of therapeutic agents including many candidate drugs that have been considered for treatment of intracranial neoplasms[12]. The BBB is formed by the endothelial cells in the brain that are closely connected by tight junctions preventing paracellular movement. Small solutes with appropriate lipophilicity may gain access to the brain by lipid-mediated passive transcellular diffusion. However, in many cases transcellular entry of such compounds into the brain is restricted by the action of ATP-binding cassette (ABC) transporters expressed at the apical membrane of the microvascular endothelium in the brain. Of these, P-glycoprotein (P-gp/ABCB1) and breast cancer resistance protein (BCRP/ABCG2) are the two dominant ABC transporters at the BBB that together restrict the brain penetration of numerous compounds[13]. Moreover, the same transport proteins are also active in the gastro-intestinal tract and involved in limiting the oral bioavailability of substrate drugs[14]. Based on preliminary in vitro assays, we generated data suggesting that palbociclib is a substrate of both P-gp and BCRP. Consequently, we have performed detailed *in vitro* and *in vivo* studies to establish the impact of these drug transporters on the oral bioavailability, plasma levels and the brain distribution of palbociclib. Our work will help to better evaluate the potential of this compound for treatment of intracranial neoplasms.

METHODS

Drugs

Palbociclib (PD-0332991) was obtained from Active Biochem (Bonn, Germany). Zosuquidar was purchased from Eli Lilly (Indianapolis, IN). Elacridar was kindly provided by GlaxoSmithKline (Research Triangle Park, NC).

Cell culture

Parental and human (ABCB1; MDR1) and murine P-gp (Abcb1a: Mdr1a) overexpressing LLC cells were cultured in MEM supplemented with 10% FBS, 1% L-glutamine, 1% sodium pyruvate, 1% MEM vitamins, 1% non-essential amino acids and 1% penicillin/streptomycin (all Life Technologies; Carlsbad, CA) under 37 °C and 5% CO_2 conditions. Likewise, parental and human (ABCG2; BCRP) and murine BCRP (Abcg2; Bcrp1) overexpressing Madine–Darby canine kidney (MDCK) cells were cultured.

Concentration equilibrium transport assays

Concentration equilibrium transport assays (CETAs) were performed as described previously[15]. In short, MDCK or LLC cells were seeded onto Transwell microporous polycarbonate membrane filters (3.0 μm pore size, 24 mm diameter; Costar Corning; Corning, NY) at a density of 2×10^6 cells per well in complete MEM medium and allowed to grow into a monolayer. At the start of the experiment, medium in both the apical and basolateral compartment was replaced with palbociclib containing medium (1 μM) and samples were taken from both compartments at specific time points. When appropriate, specific transport was inhibited using the P-gp inhibitor zosuquidar (5 μM) or the dual P-gp/BCRP inhibitor elacridar (5 μM). Monolayer integrity was assessed by translocation of Carboxyl-[^{14}C]-inulin (approximately 1.6×10^6 DPM/ml) as measured using a Tri-Carb 2800TR Low Activity Liquid Scintillation Analyzer (Perkin Elmer; Waltham, MA). Medium samples of 50 μL were mixed with 100 μL of acetonitrile. After centrifugation the supernatant was diluted 1 + 2 with water and the palbociclib concentration was measured by High Performance Liquid Chromatography (HPLC) with UV detection at 365 nm (Model 996 UV Photodiode Array detector; Waters; Milford, MA) using a GraceSmart RP18 5μm column (Grace; Deerfield, IL). The mobile phase A comprised of 0.1% (v/v) formic acid and 0.025% (v/v) Triethylamine in water and mobile phase B was 80% (v/v) acetonitrile in water. Elution was done using 48% A and 52% B delivered at a flow rate of 0.2 ml/min.

Animals

All animal housing and studies were conducted according to national and institutional guidelines and approved by the animal experimental committee. Food and water was provided *ad libitum*.

Pharmacokinetic studies

Wild-type (WT), *Abcg2*$^{-/-}$, *Abcb1a/b*$^{-/-}$ and *Abcb1a/b;Abcg2*$^{-/-}$ FVB mice were used in pharmacokinetic studies. Palbociclib was administered p.o. or i.v. at a dose of 10 mg/kg in a formulation containing 2 mg/ml palbociclib in DMSO:Cremophor EL:water (1:1:8). Alternatively, it was given p.o. at a dose of 150 mg/kg in a formulation containing 7.5 mg/ml palbociclib in DMSO:Cremophor EL:water (1:1:3.25) containing 15 mM HCL. Blood was collected from the tip of the tail at serial time points, while terminal bleeding was done by cardiac puncture under isoflurane anesthesia, followed by tissue collection (brain, liver, and kidney). Plasma was obtained by centrifugation (5 min, 5,000 rpm, 4 °C). Tissues were weighed and homogenized using a FastPrep®-24 (MP-Biomedicals; Santa Ana, CA) in 1% (w/v) bovine serum albumin in water. All samples were stored at –20 °C until analysis.

Tissue and blood sample preparation and LC–MS/MS analysis

Plasma and tissue homogenates were mixed (1+2) with acetonitrile: formic acid (100:1; v/v), centrifuged (20,000 g, 5 min, 4 °C) and the clear supernatant was mixed with water (1 + 4). Of this solution, 50 µL was subjected to an LC–MS/MS system comprised of an UltiMate 3000 LC Systems (Dionex; Sunnyvale, CA) and an API 3000 mass spectrometer (Sciex; Framingham, MA). Separation was performed on a Symmetry C_{18} column (2.1×150 mm, particle size 3.5 µM; Waters; Milford, MA). Mobile phase A (0.1% formic acid in water) and B (methanol) was used in a 5 min gradient from 20 to 95% B maintained for 3 min followed by re-equilibration at 20% B. Multiple reaction monitoring was performed at 448.4/380.3. System control and data analysis was done using Analyst® 1.5.1 software (AB Sciex; Foster City, CA). The lower limit of quantification (LLQ) for palbociclib was 3 nM for plasma and 30 pmol/g for tissue homogenates.

Pharmacokinetic and statistical analysis

CETA results were analyzed with the General linear model repeated measures procedure of SPSS (v20; SPSS Inc; Chicago, IL). The differences of the percentage ratio of peak area of the measured samples to the references between apical and basal compartments were considered as the values from repeated measurements. The data was grouped by defining five sampling time points (5 min, 30 min, 1 h, 2 h and 4 h) as a five-level within-subjects factor. Simple contrast was selected to compare the differences between the mean observed values of 30 min, 1 h, 2 h and 4 h and 5 min. Then, the multivariate significance tests were performed to determine whether the apical–basal differences of palbociclib levels were significantly increased by the factor of time.

Pharmacokinetic parameters were calculated by PKSolver[16]. For *in vivo* experiments with two groups (WT *vs Abcb1a/b;Abcg2*$^{-/-}$ mice) we used two-tailed student's t-test. For the other *in vivo* experiments with four strains, Dunnett's test or two-way analysis of variance and *post hoc* Bonferroni was performed. Differences were considered statistically significant when $p < 0.05$.

RESULTS

Human and murine P-gp and BCRP transport palbociclib in vitro

To investigate substrate affinity of palbociclib for human and murine P-gp and BCRP, concentration equilibrium transport assays (CETAs) were conducted. Compared to the parental porcine kidney epithelial cell line (LLC–PK1), palbociclib was apically translocated over time by Mdr1a and MDR1 overexpressing cell lines (**Figure 1**). This translocation could be completely abrogated by the specific P-gp inhibitor zosuquidar, confirming substrate affinity of palbociclib for murine and human P-gp. Similar results were obtained for BCRP, since parental canine kidney epithelial cells (MDCK–parent) did not exhibit any palbociclib translocation while it was detected in murine and human, although to a lesser extent, over-expressing lines. Again, substrate affinity was confirmed by abrogating translocation using elacridar, a dual P-gp/BCRP inhibitor.

P-gp and BCRP restrict the brain penetration of palbociclib in vivo

Using WT and various ABC transporter knockout mice, a potential role for P-gp and BCRP in restricting the brain penetration of palbociclib was first analyzed at 1 h and 4 h following i.v. administration of 10 mg/kg. Whereas palbociclib plasma levels were similar in all mouse strains, marked differences in brain concentrations between the strains were observed (**Figure 2A**). Compared to WT mice, brain concentrations were 19- and 60-fold higher in *Abcb1a/b*$^{-/-}$ and *Abcb1a/b;Abcg2*$^{-/-}$ mice, respectively, at four hours after injection, leading to corresponding differences in brain–plasma ratios. The deficiency of *Abcg2* alone did not change the brain concentration relative to WT mice. Just like in plasma, palbociclib levels in other tissues (*e.g.*, liver, kidney) were also similar between genotypes (**Figure 2B**). Of note, the brain–plasma ratio in *Abcb1a/b;Abcg2*$^{-/-}$ mice after four hours was similar to tissue–plasma ratios of generally well equilibrated tissues such as the kidney and liver. Therefore, these studies show that P-gp and BCRP markedly restrict palbociclib brain penetration *in vivo*.

P-gp and BCRP marginally affect the oral bioavailability of palbociclib

To assess the impact of P-gp and BCRP on the oral bioavailability, the plasma pharmacokinetics of palbociclib in WT and *Abcb1a/b;Abcg2*$^{-/-}$ mice were established following p.o. and i.v. administration (**Figure 2C**). Serial blood samples from animals (n = 4 per group) were collected until 7 h after

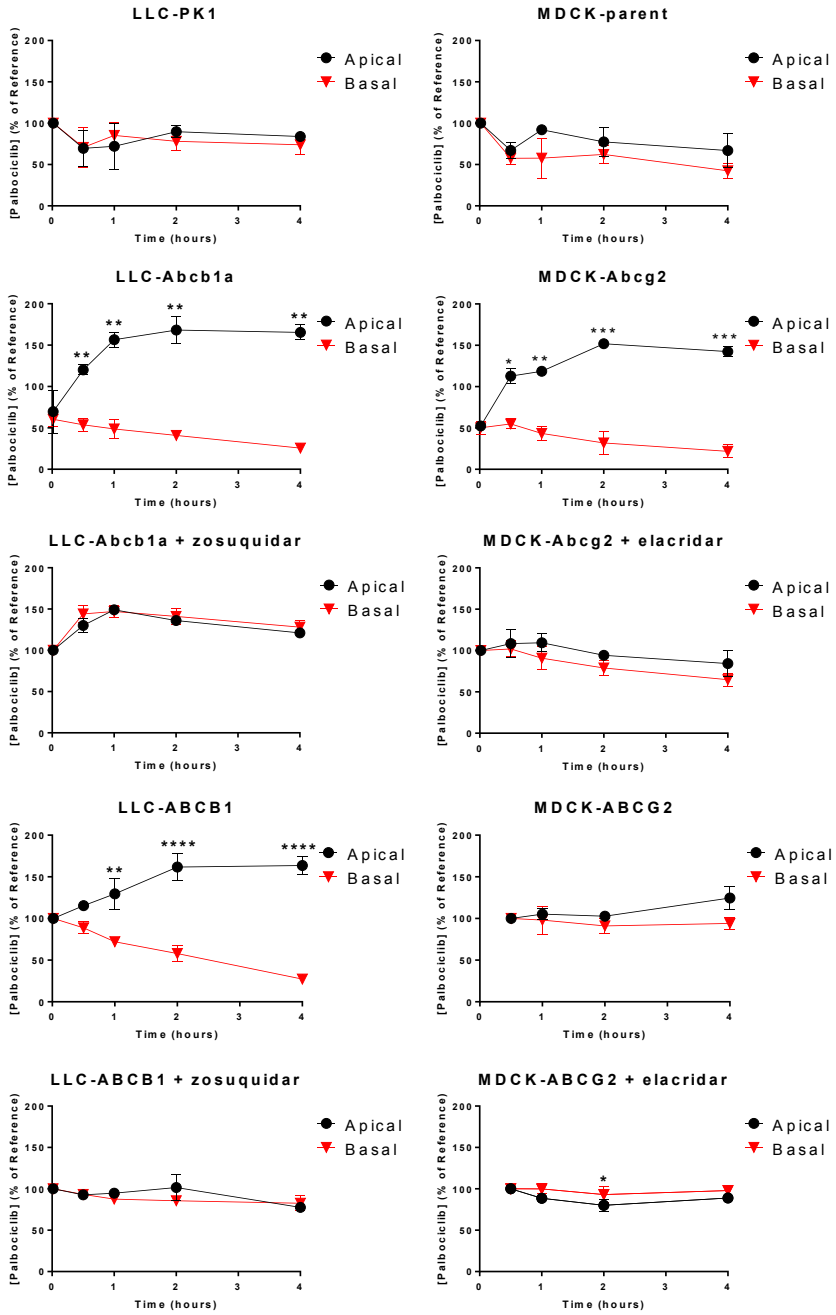

Figure 1. ***In vitro*** **transport of palbociclib by P-gp and BCRP**. Concentration equilibrium transport assays (CETAs) using LLC or MDCK cells overexpressing murine or human P-gp or BCRP. Palbociclib was shown to be transported *in vitro* by Mdr1a, MDR1, Bcrp1 and to a lesser extent BCRP, as indicated by basolateral-to-apical translocation observed in transporter overexpressing cell lines but not their parental counterparts. Transporter specificity was confirmed by absence of translocation in presence of specific P-gp (zosuquidar) or BCRP/P-gp (elacridar) inhibitors. Data are represented as mean ± SD (n = 3); * $p < 0.05$, ** $p < 0.01$, *** $p < 0.001$, **** $p < 0.0001$.

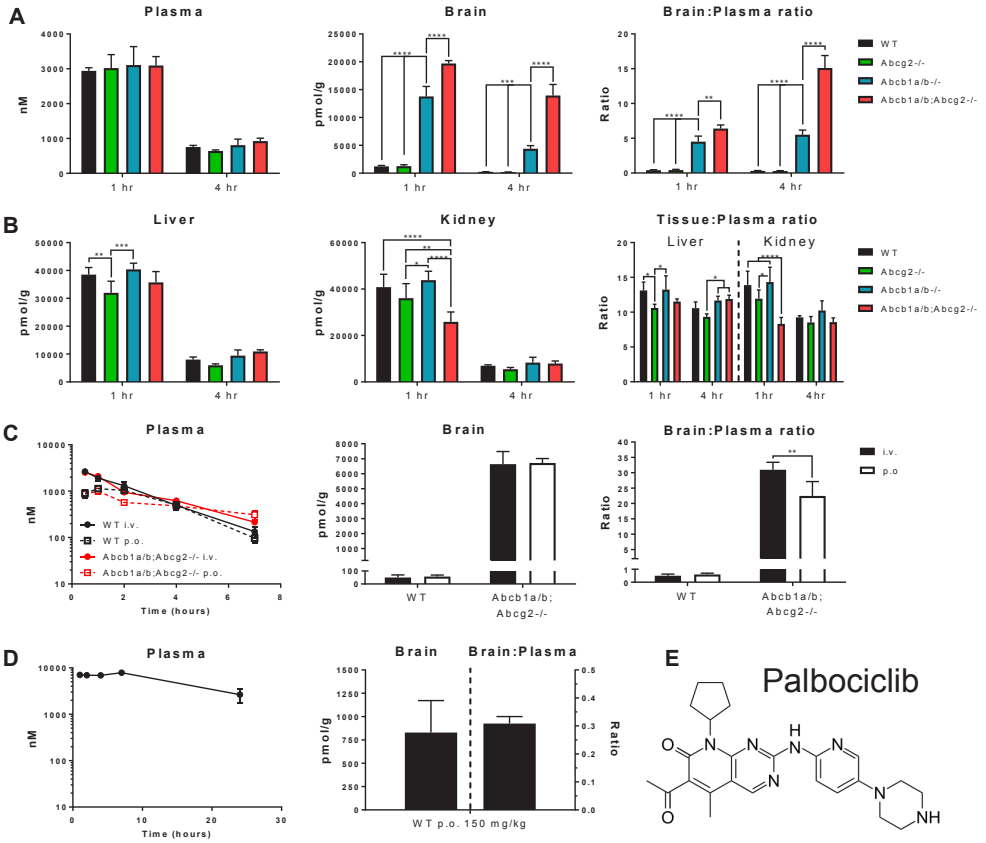

Figure 2 | The impact of P-gp and BCRP on the brain penetration and oral bioavailability of palbociclib. (**A**) Plasma concentration, brain concentration and brain–plasma ratio in various ABC transporter knockout mice 1 and 4 hours after i.v. administration of 10 mg/kg palbociclib. While plasma levels were similar between all strains, *Abcb1a/b*$^{-/-}$ and *Abcb1a/b;Abcg2*$^{-/-}$ displayed 19- and 60-fold increased brain levels compared to WT mice respectively after 4 hours. Brain-plasma ratios varied accordingly. (**B**) Palbociclib liver concentration, kidney concentration and tissue–plasma ratio of the experiment depicted in (**A**). All strains showed similar tissue–plasma ratios as were achieved in the brains of *Abcb1a/b;Abcg2*$^{-/-}$ mice. (**C**) Plasma curves up to 7 hours and brain concentration and brain-plasma ratio in WT and *Abcb1a/b;Abcg2*$^{-/-}$ mice 7 hours after i.v. or p.o. administration of 10 mg/kg palbociclib. No differences in i.v. plasma curves were observed between the strains whereas there was a slight increase in the oral plasma AUC of the *Abcb1a/b;Abcg2*$^{-/-}$ compared to the WT mice. Palbociclib brain levels were not different between the two administration routes. (**D**) Plasma curves up to 24 hours and brain concentration and brain–plasma ratio in WT mice 24 hours after p.o. administration of 150 mg/kg palbociclib. Similar brain–plasma ratios were measured as in the 10 mg/kg p.o. group depicted in (**C**). (**E**) Chemical structure of palbociclib. All data are represented as mean ± SD (n = 4); * $p < 0.05$, ** $p < 0.01$, *** $p < 0.001$, **** $p < 0.0001$.

drug administration and the pharmacokinetic parameters were calculated for each animal. In line with the first study, the plasma pharmacokinetics of palbociclib after i.v. administration was similar between the two genotypes. The absence of Abcg2 and Abcb1 increased the terminal half-life from 1.49 ± 0.12 h to 2.30 ± 0.15 h (p = 0.0002) but this did not significantly increase the $AUC_{0-\infty}$. After oral administration, the half-life was similar in WT mice (1.49 ± 0.15 h), but much longer in *Abcb1a/b;Abcg2*$^{-/-}$ mice (5.80 ± 2.11 h; $p < 0.007$). Overall, the oral bioavailability of palbociclib in WT mice was already 63%, and predominantly due to the longer terminal half-life, it further

increased in *Abcb1a/b;Abcg2*$^{-/-}$ mice to 85%, but this was not significant (**Table 1**). In line with the good oral bioavailability, both the brain concentration and brain–plasma ratio of palbociclib were similar after 7 hours between the different administration routes. Together, these data might suggest a minimal role for P-gp and BCRP in restricting palbociclib uptake in the gut, and palbociclib demonstrates good oral bioavailability even in ABC transporter-proficient animals.

	Parameter	Time (h)	Genotype	
			WT	*Abcb1a/b;Abcg2*$^{-/-}$
	Plasma $AUC_{i.v.}$ (nM·h)	0-∞	7400 ± 880	7600 ± 490
	C_{max} (nM)		2400 ± 550	2530 ± 180
i.v.	t_{max} (h)		0.5	0.5
10 mg/kg	V_{ss} (L/kg)		5.4 ± 1.3	6.3 ± 0.2
	C_{brain} (pmol/g)	7	50 ± 20	6640 ± 850****
	P_{brain} ($\times 10^{-3}$·h^{-1})		7.9 ± 0.4	870 ± 76****
	Plasma $AUC_{p.o.}$ (nM·h)	0-∞	4470 ± 370	6400 ± 1600
	C_{max} (nM)		1175 ± 96	1000 ± 140
p.o.	t_{max} (h)		1.5 ± 0.6	1.0
10 mg/kg	F (%)		63 ± 8.1	85 ± 20
	C_{brain} (pmol/g)	7	57 ± 11	6720 ± 300****
	P_{brain} ($\times 10^{-3}$·h^{-1})		13 ± 2.8	1090 ± 270***
	Plasma $AUC_{p.o.}$ (µM·h)	0-24	136 ± 14	
	C_{max} (nM)		7950 ± 480	
p.o.	t_{max} (h)		5.8 ± 2.5	
150 mg/kg	C_{brain} (pmol/g)	24	830 ± 340	
	P_{brain} ($\times 10^{-3}$·h^{-1})		6.0 ± 1.9	

Table 1 | Pharmacokinetic parameters after oral and i.v. administration of palbociclib to WT and *Abcb1a/b;Abcg2*$^{-/-}$ mice. AUC, area under the curve; C_{max}, maximum concentration in plasma; t_{max}, time to reach maximum plasma concentration; V_{ss}, volume of distribution at steady state; C_{brain}, brain concentration; P_{brain}, brain accumulation; F, oral bioavailability. Data are represented as mean ± SD (n = 4); *** $p < 0.001$, **** $p < 0.0001$.

Pharmacokinetics of oral palbociclib at a high dose

All preclinical *in vivo* efficacy studies using palbociclib reported so far have used daily dosing of 100 to 150 mg/kg p.o., but plasma pharmacokinetics have not yet been reported. We therefore also investigated the palbociclib plasma pharmacokinetics at this much higher dose level using WT mice (**Figure 2D**). The plasma C_{max} was 8000 nM and did not increase linearly with the dose (relative to 10 mg/kg), but the plasma level remained high and was still 2500 nM at 24 hours, the time of the next subsequent dosing (**Table 1**). Correspondingly, the palbociclib level in the brain

at 24 h after administration was about 800 pmol/g. This is in line with the level in the brain at the lower dose, as indicated by similar brain–plasma ratios between the two dose levels in WT (**Figures 2A, D**).

DISCUSSION

These *in vitro* and *in vivo* studies demonstrate that P-gp and BCRP together profoundly limit the brain penetration of palbociclib. The absence of P-gp alone caused a 19-fold increased palbociclib brain–plasma ratio, which increased to 60-fold when both transport proteins were absent. Notably, the palbociclib concentration in brains of *Abcb1a/b;Abcg2*$^{-/-}$ mice was similar as in other well perfused organs (liver, kidney).

Next to restricting the brain penetration, P-gp and BCRP are also known for their ability to limit the oral bioavailability of various (anti-cancer) agents through their presence and efflux function in the gut epithelium[17]. To assess whether palbociclib oral bioavailability was likewise affected, plasma pharmacokinetics were compared between i.v. and p.o. administration in both WT and *Abcb1a/b;Abcg2*$^{-/-}$ mice. No differences in $AUC_{0-\infty}$ were observed after i.v. administration between the two strains although plasma $AUC_{0-\infty}$ after oral dosing non-significantly increased by 1.4-fold in the *Abcb1a/b;Abcg2*$^{-/-}$ mice compared to WT mice. This trend suggests that P-gp and BCRP may limit the oral bioavailability of palbociclib, although a more detailed analysis of the clearance would be needed to confirm this finding since the terminal elimination phase appeared to contribute mostly to the differences in $AUC_{0-\infty}$ after oral dosing. However, this would require more animals and was not considered relevant enough as the oral bioavailability of palbociclib was already high in WT mice (F = 63%) superseding that of many clinically used anticancer agents[18]. As has been elaborated upon previously, there may be several reasons why ABC transporters may have much greater impact on the brain penetration in comparison to oral bioavailability, although these transporters are expressed on both the blood–brain barrier and the gastro-intestinal barrier. Among these are local drug concentration and the presence of uptake transporters[19]. Because of its good solubility (especially under acidic conditions due to the presence of nitrogen moieties) and permeability, Palbociclib can be categorized as a BCS class I drug (**Figure 1 and Figure 2E**)[20]. These data confirm the suitability of oral dosing of palbociclib in patients.

Patients receive palbociclib daily at a dose of 125 mg orally for a period of 21 days. The major dose limiting toxicity of palbociclib is myelosuppression, which is in line with the mechanism of action, *viz.* G1 cell cycle arrest of proliferating tissues. The clinical pharmacokinetic data that have been reported thus far show that plasma levels in patients generally do not exceed 100 ng/ml (about 200 nM)[21-23]. Such levels contrast sharply to the levels that we have found in mice, especially at the dose level of 150 mg/kg that is commonly used in preclinical efficacy studies[1-5]. In this work, brain penetration studies have been performed at a dose level (10 mg/kg) that

yielded clinically more relevant plasma levels, albeit still at the high end. At this dose level, the brain concentration of palbociclib in WT mice did not exceed 1200 pmol/g (≈600 ng/g) and dropped to 250 and 50 pmol/g at 4 and 7 hours, respectively, after drug administration and was much lower than in tissues that are not protected by a barrier (liver, kidney). In *Abcb1a/b;Abcg2*$^{-/-}$ mice the brain penetration is increased by 60-fold, which is in the range of other preliminary data reported recently[24]. In general, poor BBB penetration negates antitumor activity against invasive brain tumors[12]. Our finding calls into question the antitumor efficacy observed in previous *in vivo* studies that have been conducted at clinically irrelevant dose levels. Michaud *et al.*[4] have demonstrated efficacy of palbociclib against intracranial U87 tumors and against a primary xenograft GBM. Similarly, Barton *et al.*[5] have demonstrated efficacy against a PDGF-B driven, *p16*^{Ink4a}*/p19*^{Arf}-deficient intracranial tumor model growing in the brainstem. However, both studies used this high dose of 150 mg/kg of daily oral palbociclib. Moreover, next to these unrealistic drug levels in plasma and normal brain, the selected tumor models will or may have leaky vasculature (BBB). U87 forms non-invasive lesions with open vasculature as shown by magnetic resonance imaging (MRI)[25], which explains the 30-fold higher drug levels within the U87 lesion relative to brain adjacent to tumor tissue in the same animal[4]. Similarly, PDGF-B driven models can become very leaky when they develop into high grade tumors, as will likely occur in tumors that also don't express the p16^{Ink4a} and p19^{Arf} proteins[26]. The good accessibility of the tumor cells for the high palbociclib concentration in plasma may cause a further over-estimation of the efficacy of palbociclib. Although the single agent activity of palbociclib against intracranial models at lower doses has not been reported, dose levels of 12.5 mg/kg/day were only marginally effective against subcutaneous Colo-205 and MDA-MB-435 tumor models[1]. The clinical study with palbociclib in GBM has recently been completed (NCT01227434) and waits reporting, but based on these preclinical data, the prediction would be a lack of response of single agent palbociclib in GBM.

In summary, targeting CDK4/6 in treatment of GBM and DIPG holds promise given the likely dependence of a substantial subgroup of these tumors on the CDK4/6–RB signal transduction pathway. However, the intracranial localization of GBM and DIPG and the invasive character of these tumor cells into surrounding brain structures favor the protection of these tumor cells by the BBB and calls for a CDK4/6 inhibitor with sufficient brain penetration capacity. We demonstrate that P-gp and BCRP profoundly restrict the brain penetration of palbociclib and this will most likely limit the single agent efficacy in patients.

REFERENCES

1. Fry, D.W., *et al.* Specific inhibition of cyclin-dependent kinase 4/6 by PD 0332991 and associated antitumor activity in human tumor xenografts. *Mol Cancer Ther* **3**, 1427-1438 (2004).
2. Baughn, L.B., *et al.* A novel orally active small molecule potently induces G1 arrest in primary myeloma cells and prevents tumor growth by specific inhibition of cyclin-dependent kinase 4/6. *Cancer Res* **66**, 7661-7667 (2006).
3. Finn, R.S., *et al.* PD 0332991, a selective cyclin D kinase 4/6 inhibitor, preferentially inhibits proliferation of luminal estrogen receptor-positive human breast cancer cell lines in vitro. *Breast Cancer Res* **11**, R77 (2009).

4. Michaud, K., *et al.* Pharmacologic inhibition of cyclin-dependent kinases 4 and 6 arrests the growth of glioblastoma multiforme intracranial xenografts. *Cancer Res* **70**, 3228-3238 (2010).
5. Barton, K.L., *et al.* PD-0332991, a CDK4/6 inhibitor, significantly prolongs survival in a genetically engineered mouse model of brainstem glioma. *PloS One* **8**, e77639 (2013).
6. Dhillon, S. Palbociclib: first global approval. *Drugs* **75**, 543-551 (2015).
7. Stupp, R., *et al.* Radiotherapy plus concomitant and adjuvant temozolomide for glioblastoma. *N Engl J Med* **352**, 987-996 (2005).
8. The Cancer Genome Atlas Research Network. Comprehensive genomic characterization defines human glioblastoma genes and core pathways. *Nature* **455**, 1061-1068 (2008).
9. Brennan, C.W., *et al.* The somatic genomic landscape of glioblastoma. *Cell* **155**, 462-477 (2013).
10. Paugh, B.S., *et al.* Genome-wide analyses identify recurrent amplifications of receptor tyrosine kinases and cell-cycle regulatory genes in diffuse intrinsic pontine glioma. *J Clin Oncol* **29**, 3999-4006 (2011).
11. Wu, G., *et al.* The genomic landscape of diffuse intrinsic pontine glioma and pediatric non-brainstem high-grade glioma. *Nat Genet* **46**, 444-450 (2014).
12. van Tellingen, O., *et al.* Overcoming the blood-brain tumor barrier for effective glioblastoma treatment. *Drug Resist Updat* **19**, 1-12 (2015).
13. Lin, F., *et al.* Targeting core (mutated) pathways of high-grade gliomas: challenges of intrinsic resistance and drug efflux. *CNS Oncol* **2**, 271-288 (2013).
14. Sparreboom, A., *et al.* Limited oral bioavailability and active epithelial excretion of paclitaxel (Taxol) caused by P-glycoprotein in the intestine. *Proc Natl Acad Sci U S A* **94**, 2031-2035 (1997).
15. Lin, F., *et al.* Dual mTORC1 and mTORC2 inhibitor Palomid 529 penetrates the blood-brain barrier without restriction by ABCB1 and ABCG2. *Int J Cancer* **133**, 1222-1233 (2013).
16. Zhang, Y., *et al.* PKSolver: an add-in program for pharmacokinetic and pharmacodynamic data analysis in Microsoft Excel. *Comput Methods Programs Biomed* **99**, 306-314 (2010).
17. Shukla, S., *et al.* Improving cancer chemotherapy with modulators of ABC drug transporters. *Curr Drug Targets* **12**, 621-630 (2011).
18. Oostendorp, R.L., *et al.* The biological and clinical role of drug transporters at the intestinal barrier. *Cancer Treat Rev* **35**, 137-147 (2009).
19. de Vries, N.A., *et al.* Blood-brain barrier and chemotherapeutic treatment of brain tumors. *Expert Rev Neurother* **6**, 1199-1209 (2006).
20. Dahan, A., *et al.* Prediction of solubility and permeability class membership: provisional BCS classification of the world's top oral drugs. *AAPS J* **11**, 740-746 (2009).
21. Flaherty, K.T. *et al.* Phase I, dose-escalation trial of the oral cyclin-dependent kinase 4/6 inhibitor PD 0332991, administered using a 21-day schedule in patients with advanced cancer. *Clin Cancer Res* **18**, 568-576 (2012).
22. Niesvizky, R., *et al.* Phase 1/2 study of CDK4/6 inhibitor palbociclib (PD-0332991) with bortezomib and dexamethasone in relapsed/refractory multiple myeloma. *Leuk Lymphoma*, 1-21 (2015).
23. Schwartz, G.K., *et al.* Phase I study of PD 0332991, a cyclin-dependent kinase inhibitor, administered in 3-week cycles (Schedule 2/1). *Br J Cancer* **104**, 1862-1868 (2011).
24. Parrish, K.E., *et al.* BBB efflux pump activity limits brain penetration of palbociclib (PD0332991) in glioblastoma. *Mol Cancer Ther* **12 Suppl 11**, C81 (2013).
25. Kemper, E.M., *et al.* Development of luciferase tagged brain tumour models in mice for chemotherapy intervention studies. *Eur J Cancer* **42**, 3294-3303 (2006).
26. McConville, P., *et al.* Magnetic resonance imaging determination of tumor grade and early response to temozolomide in a genetically engineered mouse model of glioma. *Clin Cancer Res* **13**, 2897-2904 (2007).

11

Chapter 12

DISCONNECT BETWEEN IN VITRO AND IN VIVO EFFICACY OF THE MPS1 INHIBITOR NTRC 0066-0 AGAINST GLIOBLASTOMA

M.C. de Gooijer, P. Zhang, L.C.M. Buil, C.H. Çitirikkaya, H. Çolakoğlu, A.R.R. Maia, P.L.G. Slangen, I. Bockaj, M. Espitia-Ballestas, J.H. Beijnen, and O. van Tellingen

Manuscript submitted

ABSTRACT

Glioblastoma (GBM) is the most common adult primary brain tumor for which new therapeutic strategies are desperately needed. Monopolar spindle 1 (MPS1) is a mitotic kinase that plays a pivotal role in the spindle assembly checkpoint (SAC). GBM appears to be dependent on SAC fidelity, as MPS1 is overexpressed in many GBM patients. Thus, inhibiting MPS1 seems a viable therapeutic strategy to enhance mitotic cell death by attenuating SAC fidelity. NTRC 0066-0 is a recently developed MPS1 inhibitor that combines low nanomolar potency with a relatively long on-target residence time. We here investigate the potential of NTRC 0066-0 as monotherapy and in combination with chemo-radiation for treatment of GBM. We show that NTRC 0066-0 efficiently induces GBM cell death *in vitro*, following continuous exposure with IC_{50}s in the low nanomolar range. In contrast to previous reports of studies with other TTK inhibitors, we did not observe synergy *in vitro* with anti-microtubule drugs, such as docetaxel and vincristine. We demonstrate that NTRC 0066-0 has a high brain penetration, despite being a substrate of the efflux transporter P-glycoprotein. However, even when using recipient *Abcb1a/b;Abcg2*$^{-/-}$ mice with superior brain penetration and administering NTRC 0066-0 using a dose-dense regimen, we did not observe antitumor efficacy against an orthotopic GBM mouse model, neither as monotherapy nor in combination with standard-of-care temozolomide chemotherapy and radiotherapy. These data indicate that GBM is probably not a suitable indication for developing MPS1 inhibitors.

INTRODUCTION

Glioblastoma (GBM) is the most common adult primary brain tumor and has a dismal median survival of only 15 months[1]. Since the addition of the alkylating agent temozolomide to the standard of care in 2005, no other drugs have significantly improved the survival of glioblastoma patients[1]. New therapeutic options are thus needed, and several avenues are currently being explored. One of these is targeting monopolar spindle 1 (MPS1; HUGO name: TTK), a serine/threonine kinase that is an integral part of the spindle assembly checkpoint (SAC)[2]. MPS1 safeguards genomic integrity throughout mitosis by inducing and maintaining a mitotic arrest when chromosomes are improperly connected to the mitotic spindle, thereby preventing missegregation events that may result in chromosomal instability (CIN)[3]. GBMs seem to depend more heavily on the SAC, as several SAC components are overexpressed in GBM compared to low-grade gliomas and healthy brain tissue, including budding uninhibited by benomyl 1 (BUB1) and MPS1[4,5]. As replication stress increases the chance of missegregations[6], the upregulation of critical SAC components may reflect a strategy of GBMs to cope with increased intrinsic levels of DNA damage. Attenuating SAC signaling by inhibiting MPS1 might therefore force GBM cells to continue division without proper chromosome arrangement, resulting in CIN and ultimately cell death. Importantly, GBM cells might even depend more heavily on the SAC following exposure to the standard of care chemo-radiotherapy, as this induces genome-wide DNA damage.

Several MPS1 inhibitors have been developed to date[7-9], and one compound, MPS1-IN-3, has even demonstrated modest efficacy in a preclinical model of GBM when combined with the microtubule poison vincristine[5]. While these early results with MPS1-IN-3 were encouraging, it has not been taken into further clinical development. Notably, the intrinsic potency of this MPS1 inhibitor is relatively low, with IC_{50}s reported in the micromolar range. This might complicate clinical development of MPS1-IN-3, as micromolar concentrations might be difficult to achieve in the brains of glioblastoma patients. The brain is well-protected by drug efflux transporters that are present at the blood–brain barrier (BBB) and restrict brain entry of exogenous compounds, even when BBB integrity is compromised[10,11]. In fact, vincristine is one of many drugs that are efficiently transported by efflux transporters[12,13], and multiple clinical trials investigating vincristine against glioblastoma have failed[14,15]. In contrast, temozolomide is only a relatively weak substrate and is able to penetrate the brain at sufficient concentrations to achieve antitumor efficacy[16], and active against GBM in the clinic[1]. Thus, in order to show the potential of MPS1 inhibitors for treatment of GBM, preclinical studies should focus on highly potent compounds that have good BBB penetration, used either as monotherapy or in combination with the standard-of-care temozolomide chemo-radiotherapy.

Recently, a small-molecule drug (NTRC0066-0) was developed that possesses superior potency compared to 11 other MPS1 inhibitors that were evaluated in parallel, including BAY 1217389,

reversine, MPS1-IN-3 and NMS-P715[17]. NTRC 0066-0 demonstrated markedly increased target residence time and the lowest IC_{50}s of all MPS1 inhibitors against a panel of 66 cell lines. This makes NTRC 0066-0 a clear frontrunner among MPS1 inhibitors and a promising candidate to be tested in preclinical models of GBM. We here report that NTRC 0066-0 exhibits low nanomolar potency against a panel of GBM cell lines *in vitro*. NTRC 0066-0 does not synergize with microtubule poisons or DNA damaging chemotherapeutics. Although we found that NTRC 0066-0 is a substrate of the efflux transporter P-glycoprotein (P-gp; ABCB1), it has a good brain penetration and good oral bioavailability in mice. We investigated the *in vivo* antitumor efficacy of NTRC0066-0 using several dosing schedules and combination therapy settings, namely: dosing NRTC0066-0 at the maximum tolerated dose (MTD) every other day and twice-daily; as monotherapy in treatment-naïve tumors and at recurrence following temozolomide chemo-radiotherapy; and in a neo-adjuvant setting combined with temozolomide and radiotherapy. Although signs of tumor growth delay were observed in individual mice receiving treatment in a recurrent GBM setting, NTRC 0066-0 could not improve survival of mice carrying orthotopic GBM tumors in any of the settings tested. These findings indicate that developing MPS1 inhibitors for treatment of GBM will be challenging and future studies should aim to identify a population of GBM patients that might benefit from MPS1 inhibitor therapy in the recurrent setting.

METHODS

Drugs

NTRC 0066-0 was synthesized at the Netherlands Translational Research Center B.V. (Oss, The Netherlands) according to the procedure described in de Man *et al*.[18]. Temozolomide was purchased from Sigma–Aldrich (St. Louis, MO) for *in vitro* assays and TEVA Pharma (Haarlem, The Netherlands) for *in vivo* experiments. Vincristine was obtained from Pfizer (New York, NY), docetaxel from Hospira (Lake Forest, IL) and hydroxyurea from Sigma. Elacridar was provided by GlaxoSmithKline (Research Triangle Park, NC) and zosuquidar by Eli Lilly (Indianapolis, IN).

Cell culture

The serum-cultured GBM cell lines U87 and HS683 were purchased from the ATCC (Manassas, VA). T98G and LN-428 cells were kindly provided by dr. Conchita Vens (Netherlands Cancer Institute, Amsterdam, The Netherlands), E98 cells were obtained from prof. dr. William Leenders (Radboud University Medical Center, Nijmegen, The Netherlands), and LN-751 were generously made available by prof. dr. Monika Hegi (Centre Hospitalier Universitaire Vaudois, Lausanne, Switzerland). GSC lines were isolated from murine tumors that were generated by stereotactic injection of Lenti–Cre vector in the striatum of $Egfr^{vIII};p15^{Ink4b}/p16^{Ink4aF/F}$ (GSC750), $Egfr^{vIII};p15^{Ink4b}/p16^{Ink4aF/F};Pten^{F/F}$ (GSC578) or $Egfr^{vIII};p15^{Ink4b}/p16^{Ink4aF/F};Pten^{F/F};Tp53^{F/F}$ (GSC556) mice, as

previously described[19].

All MDCK and LLC cell lines were previously developed and provided by dr. A.H. Schinkel[20-22]. All non-GSC lines were cultured in MEM supplemented with 10% FBS, 1% L-glutamine, 1% sodium pyruvate, 1% MEM vitamins, 1% non-essential amino acids and 1% penicillin/streptomycin (all from Life Technologies; Carlsbad, CA) under 37 °C and 5% CO_2 conditions. GSC lines were cultured as neurospheres on ultra-low attachment plates (Corning Inc.; Corning, NY) in 50% Neurobasal medium and 50% DMEM/F12 + GlutaMAX supplemented with 1% penicillin/streptomycin, 2% B-27 minus vitamin A (all Life Technologies), 10 ng/ml EGF and 10 ng/ml bFGF (both PeproTech; London, UK).

Cell survival assays

Cells were plated in 24-wells plates at low cell densities (2,000–10,000 cells/well) and exposed to different drugs 24 hours later. Wells were pre-coated with poly-ornithine (15 µg/ml for 3 hours at room temperature) and subsequently with laminin (7.5 µg/ml for 1 hours at 37°C) prior to seeding GSCs to make them adherent without inducing differentiation. NTRC0066-0 was dissolved in DMSO (Sigma–Aldrich) for *in vitro* experiments and final DMSO concentrations never exceeded 0.1%. When untreated wells were confluent (approximately 6–10 days after seeding, dependent on the cell line), cells were fixed and stained using a solution containing crystal violet (5% w/v; Sigma–Aldrich) and glutaraldehyde (6% v/v; Honeywell; Morris Plains, NJ). Plates were imaged using a Chemi-Doc XRS+ (Bio-rad; Hercules, CA) and analyzed using the Colony Area plugin of ImageJ[23]. IC_{50} curves were fitted and plotted using the 'log(inhibitor) *vs.* normalized response – Variable slope' fitting procedure of GraphPad Prism v7 (GraphPad Software; La Jolla, CA). Combination indices (CI) were calculated according to the method described by Chou and Talalay, in which CI < synergism, CI = 1 additivity and CI > antagonism[24].

In vitro transport assays

Conventional bidirectional transport assays (CTAs) and concentration equilibrium transport assays (CETAs) were conducted as described previously[25]. NTRC 0066-0 was used at a concentration of 100 nM. Elacridar (5 µM; GlaxoSmithKline), NaN_3 and 2-deoxyglucose (both 10 mM; Sigma–Aldrich) were added to CTAs, and zosuquidar (5 µM) was added to MDCK CETAs to inhibit endogenous P-gp. Carboxyl-[^{14}C]-inulin (PerkinElmer; Waltham, MA) was added to all transport assays to determine membrane leakiness. Radioactivity was measured in Ultima Gold solution (Sigma–Aldrich) using a Tricarb 2800TR Liquid Scintillation Analyzer (PerkinElmer). Wells displaying inulin translocation exceeding 1.5% per hour were excluded from analysis.

Animals

Mice were housed at 20.9 °C on a 12 hour light/dark cycle with food and water *ad libitum*. All animal housing and studies were approved by the Animal Experiments Committee of the Netherlands Cancer Institute and conducted according to national law and institutional guidelines.

Pharmacokinetic studies

The pharmacokinetics of NTRC 0066-0 were analyzed in wild-type (WT), *Abcb1a/b*$^{-/-}$, *Abcg2*$^{-/-}$, *Abcb1a/b;Abcg2*$^{-/-}$ and *Abcb1a/b;Abcg2;Abcc4*$^{-/-}$ FVB mice. All knockout mouse strains have been developed at the Netherlands Cancer Institute[26-29]. For i.v. administration, NTRC0066-0 was formulated in DMSO:Cremophor EL:saline (1:1:8 v/v) and injected at a dose of 5 mg/kg. For i.p. and oral administration, NTRC0066-0 was administered at 5, 10 or 20 mg/kg as indicated. Serial blood sampling was done by tail vein bleeding at specific time points. At terminal time points, blood was drawn by cardiac puncture followed by tissue collection. Plasma was obtained from whole blood by centrifugation (5 min, 5,000 rpm, 4°C) and tissues were weighed and homogenized using a FastPrep®-24 (MP-Biomedicals; New York, NY) in 1% (w/v) bovine serum albumin (Sigma–Aldrich) in water.

LC–MS/MS analysis

NTRC 0066-0 was extracted from *in vitro* and *in vivo* samples using liquid–liquid extraction with diethyl ether. Another MPS-1 inhibitor, Compound 5 (Cpd-5)[9], was added to the samples as an internal standard. The dried organic phase was reconstituted in 30% methanol in water (v/v)[30]. Samples were measured using an LC–MS/MS system comprising an UltiMate 3000 LC Systems (Dionex; Sunnyvale, CA) and an API 4000 mass spectrometer (Sciex; Framingham, MA). Samples were injected on to a Securityguard C18 pre-column (Phenomenex; Utrecht, The Netherlands) connected to a ZORBAX Extend-C18 column (Agilent; Santa Clara, CA). Elution was done at a flow rate of 0.2 mL/min using a 5 minute gradient from 20% to 95% B (mobile phase A was 0.1% HCOOH in water (v/v) and mobile phase B was methanol). 95% B was maintained for 3 min followed by re-equilibration at 20% B. Multiple reaction monitoring parameters were 566.2/391.4 (NTRC0066-0) and 581.6/397.0 (internal standard). Analyst® 1.6.2 software (Sciex) was used for system control and data analysis.

Orthotopic xenograft studies

Orthotopic GBM tumors were induced in *Abcb1a/b;Abcg2*$^{-/-}$ mice by stereotactic injection of E98 cells expressing firefly luciferase (200,000 cells in 2 µL HBSS (Life Technologies) at an injection speed of 1 µL/min) at 2 mm lateral, 1 mm anterior and 3 mm ventral to the bregma. Tumor

growth was monitored using bioluminescence imaging by injecting D-luciferin (150 mg/kg i.p.; Promega; Madison, WI) and subsequently imaging mice on an IVIS Spectrum Imaging System (PerkinElmer). Survival was monitored daily and the humane endpoint was defined as body weight loss exceeding 20%. Time-to-recurrence was defined as the number of days elapsed until the tumor regained its pre-treatment size. Tumors were treated with CT-guided radiotherapy using an X-RAD 225Cx system (Precision X-Ray; North Branford, CT), temozolomide (10 mg/kg p.o. freshly prepared from powder in an aqueous solution containing 10% v/v ethanol), NTRC0066-0 (20, 10 or 5 mg/kg p.o. in an aqueous solution containing 10% v/v DMSO and 10% v/v Cremophor EL (Life Technologies)) or different combinations thereof, as described per experiment in the **Figure legends**.

Quantification of mitotic errors

Tumor-bearing mouse brains were formalin-fixed, paraffin-embedded and coronal sections (10 μm) were sliced using an RM2255 microtome (Leica; Wetzlar, Germany). Sections were subsequently deparaffinized using xylene, incubated in citrate buffer for antigen retrieval, blocked with 4% (w/v) BSA in TBS-T, incubated with rabbit-α-pH3^{Ser10} (1:250 for 3 hours at room temperature; Merck Millipore; Burlington, MA), incubated with goat-α-rabbit-AF568 (1:250 for 45 minutes at room temperature; Thermo Fisher Scientific; Waltham, MA) and mounted with Vectashield hardset antifade mounting medium with DAPI (Vector Laboratories; Burlingame, CA). Mitotic errors were imaged and scored using a Deltavision ultra high resolution microscope (Applied Precision Inc.; Issaquah, WA).

Magnetic resonance imaging

Magnetic resonance imaging was done using a sequence consisting of T2-weighted, T1-weighted pre-contrast and T1-weighted post-gadoterate meglumine (Dotarem®; Guerbet; Villepinte, France) contrast imaging on a BioSpec 70/20 USR (Bruker; Billerica, MA) system, as described previously[16].

Histology and Immunohistochemistry

Mouse heads were fixed in 4% (v/v) formaldehyde and 5% (v/v) glacial acetic acid overnight, and subsequently decalcified in 6.5 % (v/v) formic acid at 37 °C for 4 days. Decalcified tissues were paraffin embedded and cut into 4 μm coronal sections that were stained with hematoxylin and eosin (H&E), and for human Vimentin (1:4,000; M0725; DakoCytomation; Glostrup, Denmark), P-gp (1:200; 13978; Cell Signaling Technology; Danvers, MA) and BCRP (1:400; ab24115; Abcam; Cambridge, UK). Sections were imaged and processed using an Aperio AT2 system and ImageScope software (v12; both Leica).

Pharmacokinetic and statistical analysis

CETA results were analyzed with the General linear model repeated measures procedure of SPSS (v22; SPSS Inc; Chicago, IL), as described before[25]. PK solver was used to determine pharmacokinetic parameters[31]. The standard error of the oral bioavailability was calculated using the formula below:

$$SE_F = F\sqrt{\left(\frac{SE_{AUC_{p.o.}}}{AUC_{p.o.}}\right)^2 + \left(\frac{SE_{AUC_{i.v.}}}{AUC_{i.v.}}\right)^2}$$

All comparisons involving more than two experimental groups were done using one-way analysis of variance followed by *post hoc* Bonferroni tests. Statistical differences between PK parameters were calculated as Bonferroni corrected *p*-values using multiple Student's t-tests. Kaplan–Meier survival curves were analyzed using the log–rank test. Differences were considered statistically significant when $p < 0.05$.

RESULTS

NTRC0066-0 is cytotoxic against GBM cell lines with low nanomolar potency but does not synergize with chemotherapeutics

We first established the cytotoxic potency of NTRC 0066-0 against a panel of GBM cell lines *in vitro* using continuous drug exposure. The IC_{50} of NTRC 0066-0 against six serum-cultured cell lines was very uniform and in the low nanomolar range, varying from approximately 20 nM to 40 nM (**Figure 1A**). Moreover, the IC_{50} curves were very steep, with cell survival declining from 100 to 0% within one decade of concentration. These results were validated using three independent *Egfr*^{vIII}-driven murine glioma stem cell (GSC) lines, as GSCs more accurately resemble human GBM than classical serum-cultured lines[32]. We observed similarly low nanomolar IC_{50}s against *Egfr*^{vIII}**;***p15*^{Ink4b}*/p16*$^{Ink4a-/-}$ (GSC750), *Egfr*^{vIII}**;***p15*^{Ink4b}*/p16*$^{Ink4a-/-}$*;Pten*$^{-/-}$ (GSC578) and *Egfr*^{vIII}**;***p15*^{Ink4b}*/p16*$^{Ink4a-/-}$*;Pten*$^{-/-}$*;Tp53*$^{-/-}$ (GSC556) GSCs, confirming the potent efficacy of NTRC0066-0 against GBM cells *in vitro* (**Figure 1B**).

We next investigated whether NTRC 0066-0 can synergize with other chemotherapeutics to induce cytotoxicity in GBM cell lines. NTRC 0066-0 was combined with the microtubule poison vincristine (**Figure 2A**), the microtubule stabilizing agent docetaxel (**Figure 2B**), the alkylating agent temozolomide that is part of the standard-of-care treatment for GBM (**Figure 2C**), and the ribonucleotide reductase inhibitor hydroxyurea that induces replication stress (**Figure 2D**). NTRC0066-0 did not synergize with any of the tested chemotherapeutics and even displayed moderate to, in some instances, strong antagonism, as indicated by Combination Indices (CIs) over 1.0 up to 2.9 (**Figure 2F**). Although NTRC 0066-0 was continuously present in the previous

experiments, exposure to 100 nM for about 8 h was already sufficient to reduce cell survival by 25%. The addition of vincristine or docetaxel did not change the required exposure time (**Figure 2E**).

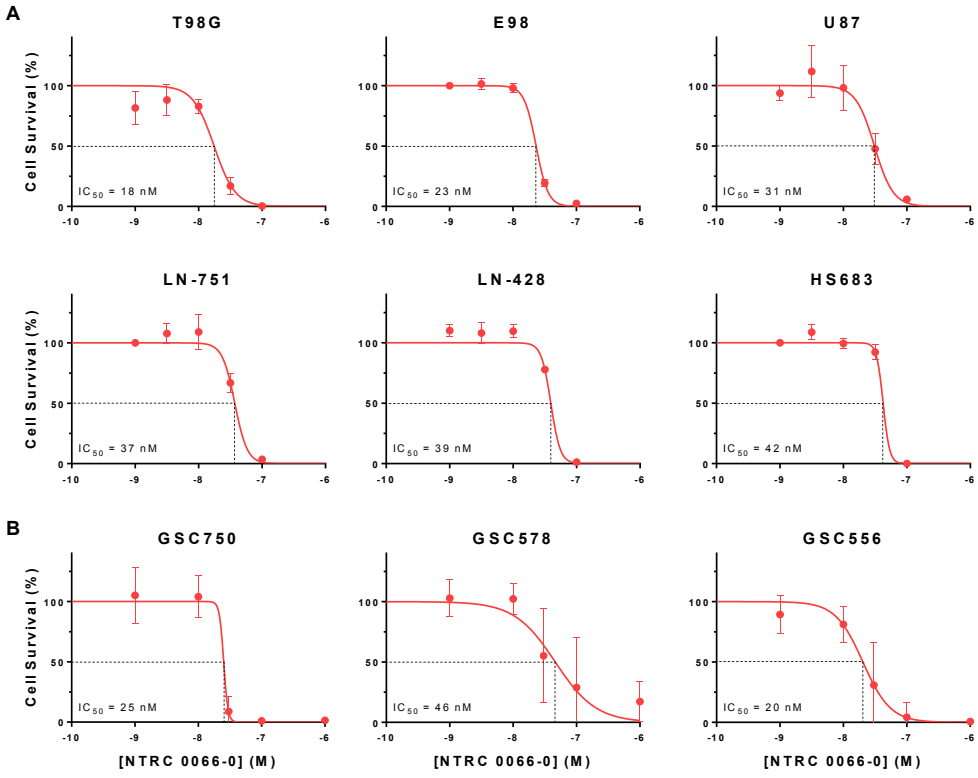

Figure 1 | *In vitro* cytotoxicity of NTRC 0066-0 against a panel of GBM cell lines. (**A**) IC_{50} curves of NTRC 0066-0 against six different serum-cultured GBM cell lines. Data are means ± SD; n ≥ 3. (**B**) IC_{50} curves of NTRC 0066-0 against *Egfr*^{vIII}*;p15*^{Ink4b}*/p16*$^{Ink4a-/-}$ (GSC750), *Egfr*^{vIII}*;p15*^{Ink4b}*/p16*$^{Ink4a-/-}$*;Pten*$^{-/-}$ (GSC578) and *Egfr*^{vIII}*;p15*^{Ink4b}*/p16*$^{Ink4a-/-}$*;Pten*$^{-/-}$*;Tp53*$^{-/-}$ (GSC556) glioma stem cell (GSC) lines. Data are means ± SD; n ≥ 8.

NTRC0066-0 achieves good brain penetration, despite being transported by P-gp in vitro and in vivo

ATP-binding cassette (ABC) efflux transporters are expressed at the BBB and limit the intracranial efficacy of anticancer agents by restricting their brain entry[10]. The most dominant ABC transporters at the BBB are P-gp (also known as MDR1 or ABCB1) and breast cancer resistance protein (BCRP; or ABCG2). Previously, it was shown that NTRC 0066-0 does not inhibit the activity of P-gp in a calcein-AM efflux assay[33]. Here, we determined whether NTRC 0066-0 (**Figure 3A**) is a substrate of human or murine P-gp or BCRP. NTRC 0066-0 displays sufficient membrane permeability across a cellular monolayer independent of direction (**Figure 2B**), and can thus

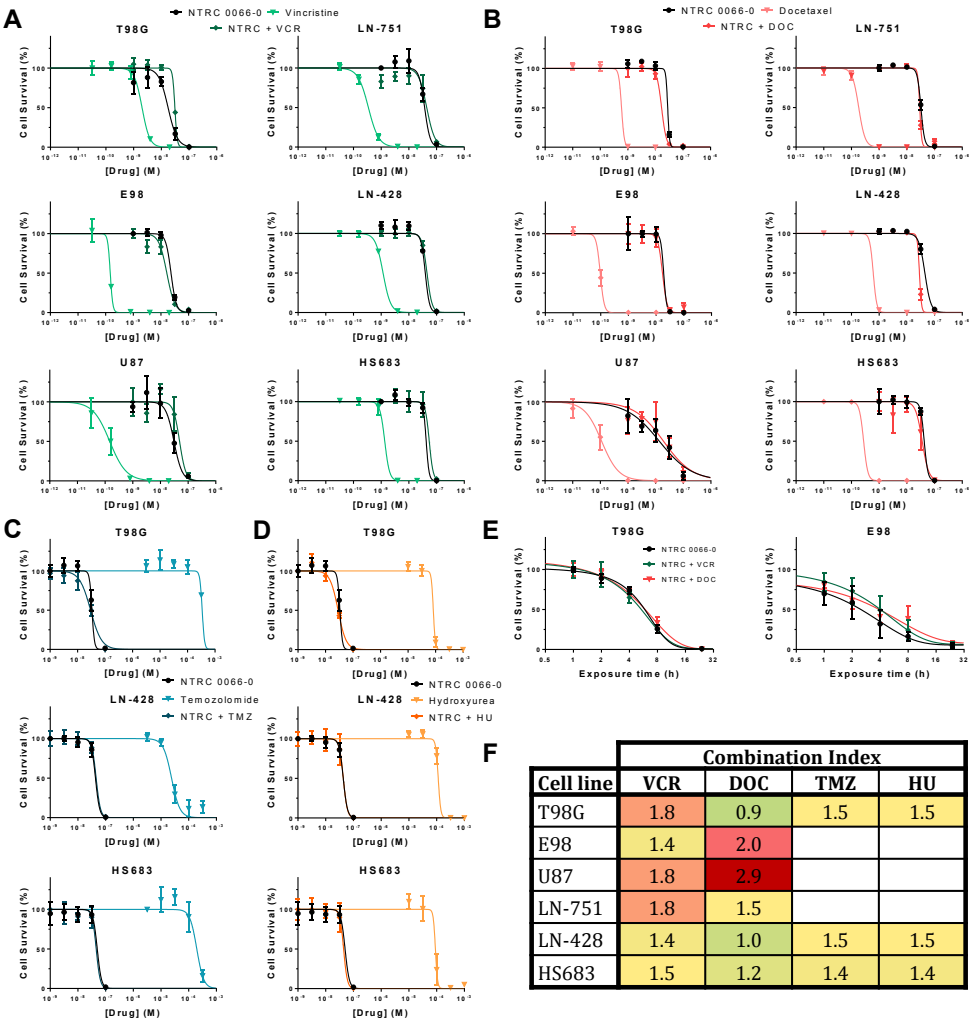

F

	Combination Index			
Cell line	VCR	DOC	TMZ	HU
T98G	1.8	0.9	1.5	1.5
E98	1.4	2.0		
U87	1.8	2.9		
LN-751	1.8	1.5		
LN-428	1.4	1.0	1.5	1.5
HS683	1.5	1.2	1.4	1.4

Figure 2 | NTRC 0066-0 does not synergize with classic chemotherapeutics *in vitro*. IC_{50} curves of NTRC 0066-0 in combination with (**A**) vincristine (VCR; 0.2 nM), (**B**) docetaxel (DOC; 0.2 nM for LN-428 and T98G, 0.1 nM for HS683 and LN-751, and 0.05 nM for E98 and U87), (**C**) temozolomide (TMZ; 200 µM for T98G, 100 µM for HS683 and 10 µM for LN-428) and (**D**) hydroxyurea (HU; 50 µM) against different serum-cultured GBM cell lines. (**E**) Exposure time–response curves of NTRC 0066-0 (100 nM) alone or in combination with VCR or DOC against T98 (0.2 nM VCR or DOC) and E98 (0.2 nM VCR or 0.05 nM DOC) GBM cells. (**F**) Combination indices (CI) of drug combinations depicted in (**A–D**), as described by Chou and Talalay: CI < 1 depicts synergism, CI = 1 additivity and CI > antagonism[24]. Data are means ± SD; n = 4.

be used in concentration equilibrium transport assays (CETAs) to determine ABC transporter substrate affinity as described previously[34]. The concentration of NTRC 0066-0 in the apical and basolateral compartment was similar after 4 h in CETAs using untransduced monolayers (MDCK–parent and LLC–PK1) or monolayers overexpressing murine BCRP (Bcrp1), human BCRP, or murine P-gp (Mdr1a), but we found moderate difference using human P-gp (MDR1) overexpressing monolayers (**Figure 3C**), indicating that NTRC 0066-0 can be transported by

human P-gp *in vitro*. Of note, we observed that the concentration decreased over time in both compartments to about 40% of the starting concentration, indicating that NTRC 0066-0 may be lost by non-specific binding to the plastic or degradation.

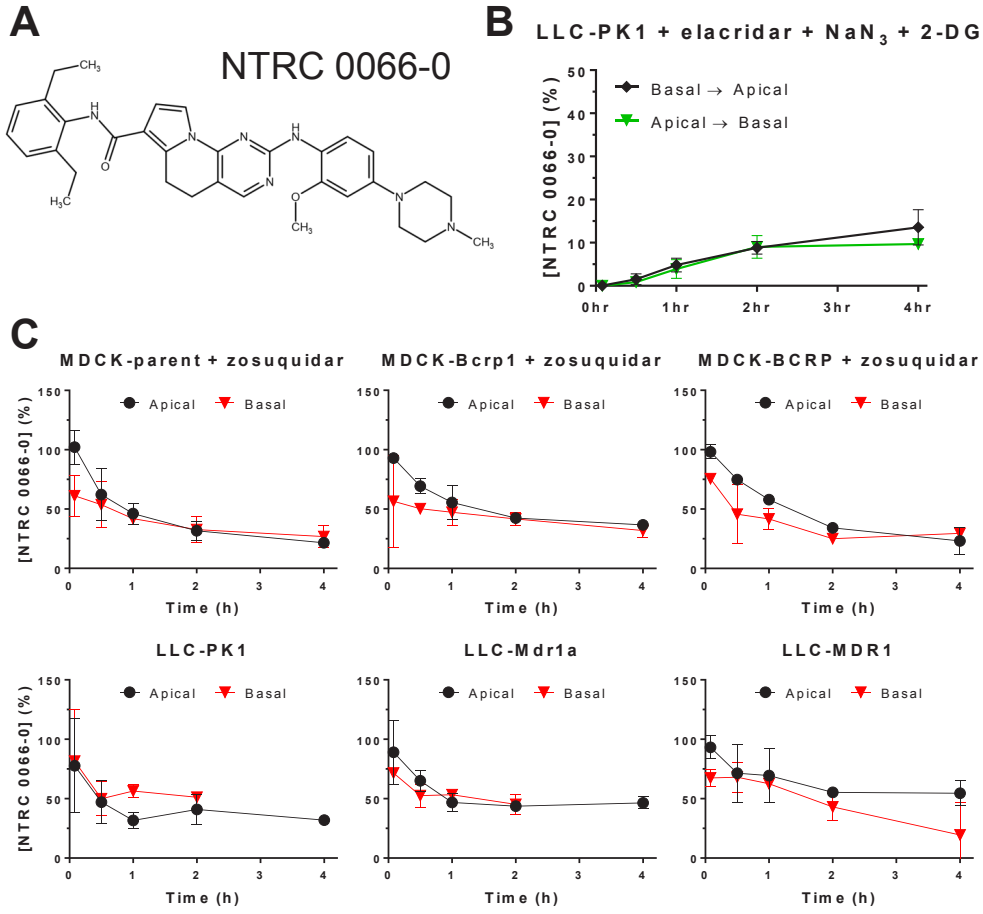

Figure 3 | *In vitro* transport of NTRC 0066-0 by P-glycoprotein. (**A**) Chemical structure of NTRC 0066-0. (**B**) Conventional transport assay in presence of elacridar, sodium azide (NaN_3) and 2-deoxyglucose (2-DG) to block ATP-dependent transporter activity. (**C**) Concentration equilibrium transport assays (CETAs) using MDCK or LLC cells that overexpress murine BCRP, (Bcrp1), human BCRP, murine P-gp (Mdr1a) or human P-gp (MDR1). Zosuquidar was used in MDCK cell lines to inhibit endogenous P-gp activity. Data are mean ± SD; n ≥ 2; * $p < 0.05$.

To study the impact of ABC transporters on the pharmacokinetics of NTRC 0066-0, we used mouse strains genetically lacking one or multiple transporters. We first studied the impact of P-gp, BCRP and multidrug resistance-associated protein 4 (MRP4; ABCC4) on the brain penetration of NTRC 0066-0 at 1 h after i.v. administration of 5 mg/kg. Compared to FVB WT mice, *Abcb1a/b*$^{-/-}$ mice had markedly increased NTRC 0066-0 brain concentrations and brain–plasma ratios,

while the plasma concentration was similar (**Figure 4A**). In contrast, no differences in plasma and brain concentrations were observed in *Abcg2*$^{-/-}$ mice. Furthermore, *Abcb1a/b;Abcg2*$^{-/-}$ and *Abcb1a/b;Abcg2;Abcc4*$^{-/-}$ mice did not display further increased NTRC 0066-0 brain concentration compared to *Abcb1a/b*$^{-/-}$ mice. Together, these data indicate that P-gp, but not BCRP and MRP4, limit the brain penetration of NTRC0066-0. Importantly, NTRC 0066-0 displayed a high brain–plasma ratio (approximately 4) in WT mice despite being transported by P-gp, suggesting that it might be a useful candidate MPS1 inhibitor to test for treatment of GBM.

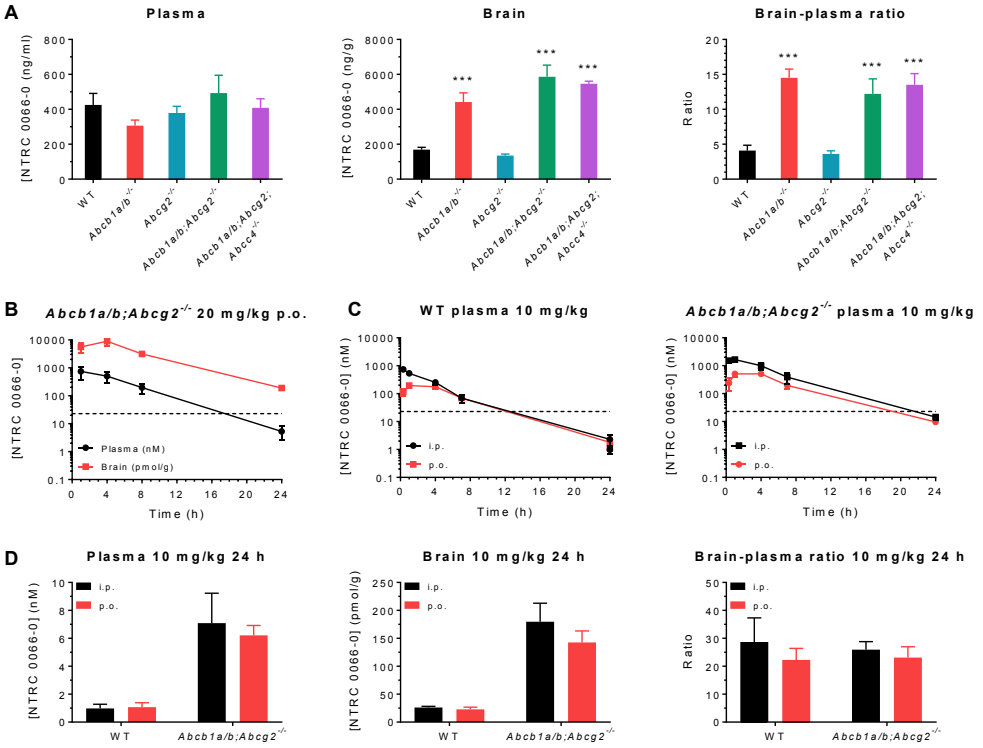

Figure 4 | Impact of P-gp, BCRP and MRP4 on the pharmacokinetics of NTRC 0066-0. (**A**) Plasma concentration, brain concentration and brain–plasma ratio of NTRC 0066-0 following intravenous adminstration of 5 mg/kg to wild-type (WT), *Abcb1a/b*$^{-/-}$, *Abcg2*$^{-/-}$, *Abcb1a/b;Abcg2*$^{-/-}$ and *Abcb1a/b;Abcg2;Abcc4*$^{-/-}$ mice. (**B**) Plasma and brain concentration–time curves following adminstration of 20 mg/kg NTRC 0066-0 p.o. to WT mice. (**C**) Plasma concentration–time curves following adminstration of 10 mg/kg NTRC0066-0 p.o. and i.p. to WT and *Abcb1a/b;Abcg2*$^{-/-}$ mice. (**D**) Plasma concentration, brain concentration and brain–plasma ratio 24 hours after adminstration of 10 mg/kg NTRC 0066-0 p.o. and i.p. to WT and *Abcb1a/b;Abcg2*$^{-/-}$ mice. Data are mean ± SD; n ≥ 4; *** $p < 0.001$.

We next determined the oral bioavailability of NTRC 0066-0 in *Abcb1a/b;Abcg2*$^{-/-}$ and WT mice relative to i.p. administered drug. We found that the plasma AUC of NTRC 0066-0 was about 2-fold higher both after i.p. and oral dosing in *Abcb1a/b;Abcg2*$^{-/-}$ mice *vs.* WT mice, resulting in a similar oral bioavailability of about 50% in both strains (**Figure 4C and Table 1**). The terminal half-life of NTRC 0066-0 was significantly longer in *Abcb1a/b;Abcg2*$^{-/-}$ mice compared to WT mice (**Figure**

4C and Table 1). At 24 hours, we collected the brains of these mice. Elimination of NTRC 0066-0 from the brain was slower than from the systemic circulation, as the brain–plasma ratio was approximately 20 at 24 hours. Interestingly, the brain–plasma ratio was similar in both strains, although the concentration in *Abcb1a/b;Abcg2*$^{-/-}$ mice at 24 h was about 5-fold higher than in WT mice (**Figures 4A, D**).

In view of the higher NTRC 0066-0 levels in the absence of P-gp, we conducted the first proof-of-concept studies in *Abcb1a/b;Abcg2*$^{-/-}$ mice (see below). We first established that 20 mg/kg NTRC 0066-0 every other day for 11 days (*q.*2*d.*x11d) could safely be given orally to *Abcb1a/b;Abcg2*$^{-/-}$ mice. This schedule has been used previously in a breast cancer model in WT FVB mice[33]. Next, we determined the brain and plasma levels at 1, 4, 8 and 24 h after oral dosing of 20 mg/kg and found that the brain concentration remained well above the threshold level of *in vitro* efficacy (**Figure 4B**).

	Parameter	Time (h)	Genotype	
			WT	*Abcb1a/b;Abcg*$^{2-/-}$
	Plasma $AUC_{i.p.}$ (nM·h)	0–∞	2800 ± 450	11000 ± 2200***
i.p.	C_{max} (nM)		780 ± 130	1700 ± 160***
10 mg/kg	t_{max} (h)		0.5 ± 0.3	0.8 ± 0.3
	$t_{1/2}$ (h)		2.5 ± 0.2	3.4 ± 0.4*
	MRT (h)		3.2 ± 0.4	4.3 ± 0.4*
	Plasma $AUC_{p.o.}$ (nM·h)	0–∞	1700 ± 150	4700 ± 710**
	C_{max} (nM)		180 ± 6.7	550 ± 52***
p.o.	t_{max} (h)		1.8 ± 1.5	3.3 ± 1.5
10 mg/kg	$t_{1/2}$ (h)		2.8 ± 0.2	3.6 ± 0.2**
	F (%)		59 ± 11	43 ± 11
	MRT (h)		4.7 ± 0.2	5.2 ± 0.5

Table 1 | Pharmacokinetic parameters after oral and i.p. administration of NTRC 0066-0 to WT and *Abcb1a/b;Abcg2*$^{-/-}$ mice. AUC, area under the curve; C_{max}, maximum concentration in plasma; t_{max}, time to reach maximum plasma concentration; $t_{1/2}$, plasma half-life; MRT, mean residence time; *F*, bioavailability. Data are represented as mean ± SD (n ≥ 4); ** $p < 0.01$, **** $p < 0.0001$.

NTRC 0066-0 does not improve survival of mice carrying orthotopic GBM tumors, although signs of tumor growth delay are observed in a recurrent GBM model

To study the *in vivo* antitumor efficacy of NTRC 0066-0 in relevant GBM models, we orthotopically injected E98 cells, as this cell line was one of the most sensitive to NTRC 0066-0 *in vitro* (**Figure 1A**) and robustly engrafts in nude mice. Moreover, orthotopic E98 tumors are only slightly visible on gadolinium-enhanced magnetic resonance imaging (**Figure 5A**) and well-perfused by

vessels expressing P-gp and BCRP (**Figure 5B**), indicating that the BBB in these tumors retains it functionality at least partly. We conducted all *in vivo* studies in *Abcb1a/b;Abcg2*$^{-/-}$ mice, as these have significantly higher NTRC 0066-0 exposure than WT mice (**Figure 4**) This allowed us to explore the concept of *in vivo* MPS1 inhibition therapy in the most optimal pharmacokinetic setting. Treatment was started when tumors were relatively small (bioluminescence signal of about 10^5 photons per second; p/s) to allow a sufficient window for a 21-day treatment period. However, treatment of therapy-naïve E98 tumors with 20 mg/kg NTRC 0066-0 *q.2d.*x11d did not result in reduced tumor growth (**Figure 6A**) or improved survival (**Figure 6B**).

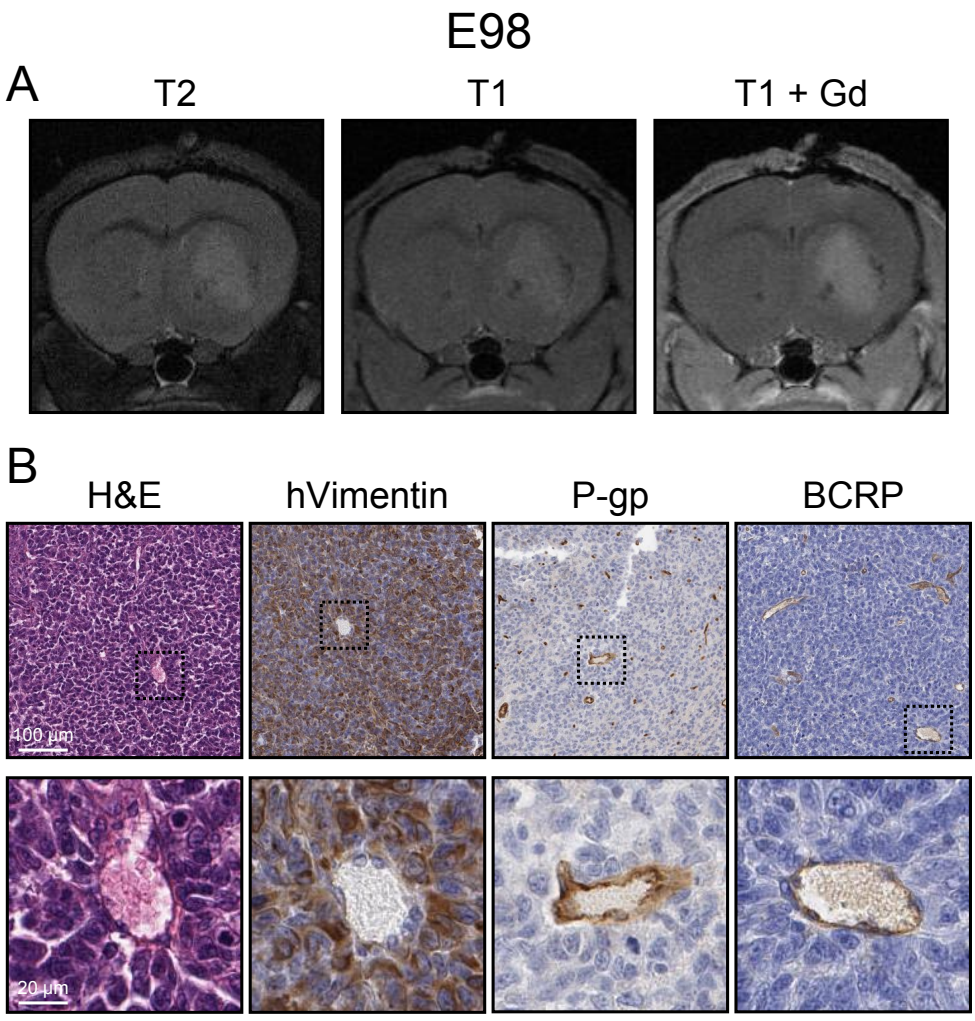

Figure 5 | Characterization of the intracranial orthotopic E98 GBM model. (**A**) Magnetic resonance imaging of an orthotopic E98 tumor using a sequence consisting of T2-weighted, T1-weighted pre-contrast and T1-weight gadolinium contrast-enhanced (T1 + Gd) imaging. (**B**) Coronal E98 tumor sections stained for hematoxylin and eosin (H&E), human vimentin (hVimentin), P-glycoprotein (P-gp) and breast cancer resistance protein (BCRP).

In the clinic, GBMs are treated with the DNA damaging therapies temozolomide (TMZ) and radiotherapy (RT), but uniformly recur. Since DNA damage is known to induce missegregations and aneuploidy[3], MPS1 is critical in protecting cells from mitotic cell death when encountering missegregations, and stable aneuploid cells are highly sensitive to MPS1 inhibition[35], we investigated whether NTRC 0066-0 could be effective against recurrent E98 tumors following TMZ + RT combination treatment (**Figure 6C**). TMZ + RT was given when tumors reached a size between 10^7 and 10^8 p/s and resulted in a substantial regression back to about 10^5 p/s. Administration of 20 mg/kg NTRC 0066-0 (*q.*2*d.*x11d) was started at the time of recurrence and resulted in remarkable growth delay in 2 out of 7 animals (**Figure 6D**) with one long-term survivor (**Figure 6E**), whereas the other tumors progressed as rapidly as vehicle treated animals. The reason for this heterogeneity is unclear, but could be related to the type and extent of DNA damage that was induced by TMZ + RT treatment in individual mice. Furthermore, the lack of efficacy in 5 out of 7 mice might be attributed to insufficient brain exposure. The plasma concentration at 24 h after administration of 20 mg/kg was only 6 nM (**Figure 4D**) and although the brain penetration of NTRC0066-0 in *Abcb1a/b;Abcg2*$^{-/-}$ mice is 20-fold higher, the every other day (*q.*2*d.*) dosing schedule will result in very low levels in the period between 24 and 48 h, which may allow tumor tissue recovery in these drug-free periods.

In an effort to achieve more continuous exposure to NTRC 0066-0 in mice, we investigated a more dose-dense administration schedule. We found that we could safely administer 5 mg/kg p.o. in the morning, and 10 mg/kg p.o. approximately 8 hours later for 7 consecutive days. Based on our pharmacokinetic studies, the lowest plasma trough concentration of NTRC 0066-0, which is reached in each morning just prior to the next dose, remained above 20 nM (**Figure 6F**). This concentration was effective against E98 cells *in vitro* and already higher than the plasma concentration observed 24 hours after administration of 20 mg/kg p.o. to *Abcb1a/b;Abcg2*$^{-/-}$ mice (**Figure 1A and Figure 4B**). Notably, the brain–plasma ratio is more than 20 in *Abcb1a/b;Abcg2*$^{-/-}$ mice. Treatment was started when the bioluminescence signal of the tumors was between 5–$10 \cdot 10^6$ p/s. Unfortunately, however, even under these most optimal conditions, we again did not observe any delay in tumor growth (**Figure 6G**) or survival (**Figure 6H**) when E98 tumors were treated with NTRC 0066-0 monotherapy. In fact, treatment with NTRC 0066-0 appeared to accelerate tumor growth and shorten survival. Although these effects were not statistically significant, this trend was seen in two independent experiments (**Figures 6A–B**; $p = 0.19$) and (**Figures 6G–H**; $p = 0.09$). In line with this lack of antitumor efficacy, NTRC0066-0 did not increase the number of mitotic errors in these tumors (**Figure 6I**). Notably, we only observed some cases of lagging anaphases, but very few chromatin bridges and multipolar anaphases.

In the same series, we also studied the dense NTRC 0066-0 dosing schedule (5/10 mg/kg *b.i.d.*x7d) in combination with chemo-radiotherapy. The recurrent tumor setting as performed above was not a feasible option, because a sufficiently powered study may require up to 40 animals in the

treatment cohort. We therefore tested it in an adjuvant setting where we started NTRC 0066-0 on day 3 following two days of RT + TMZ (2 Gy + 10 mg/kg *q.d.*x2d). In this setting, we again could not observe any effects on tumor growth (**Figure 6J**), as the time-to-recurrence was not different between treatment groups (**Figure 6K**). Concordantly, survival was also not affected (**Figure 6L**). In summary, NTRC 0066-0 did not improve survival of mice carrying orthotopic GBM tumors in any of the settings tested., although signs of tumor growth delay were observed in 2 out of 7 (30%) mice treated in the recurrent GBM setting (**Figures 6D–E**).

DISCUSSION

This study explored the potential of MPS1 inhibition as a therapeutic strategy for treatment of GBM, a devastating primary brain tumor. The MPS1 inhibitor NTRC 0066-0 efficiently induced cytotoxicity in multiple GBM and GSC cell lines with low nanomolar potency, obviously demonstrating the intrinsic potential of MPS1 inhibition to induce cytotoxicity in GBM cells. Moreover, the BBB penetration of NTRC 0066-0 is high, allowing good distribution throughout the brain. However, there was no good translation to *in vivo* antitumor efficacy, as we did not observe any robust tumor growth delay or improved survival, even in the most optimized pharmacokinetic settings using *Abcb1a/b;Abcg2*$^{-/-}$ mice and the highest tolerable dose-dense oral administration schedule. In contrast, other studies have reported promising efficacy of MPS1 inhibition in preclinical tumor models[5,8,9,33,36-39]. Single compound efficacy of NTRC 0066-0 was shown in orthotopic models of the triple-negative breast cancer cell line MDA-MB-231[33,40] and a subcutaneous model of the lung cancer cell line A427[40]. Several observations may help to explain the lack of efficacy of NTRC 0066-0 in GBM models , and understanding these may enable translation of the *in vitro* potential of MPS1 inhibition to *in vivo* treatment of GBM.

First, *in vivo* antitumor efficacy of MPS1 inhibition as monotherapy is rarely reported. In most studies, efficacy is only observed when MPS1 inhibitors are combined with classic chemotherapeutics that target microtubules such as vincristine[5], docetaxel[9,33] or paclitaxel[8,39]. Combination therapy with taxane drugs has only been studied in extracranial tumor models. However, such combinations are not attractive for treatment of GBM, as taxanes have a poor brain penetration as a result of efficient efflux by P-gp at the BBB[41,42]. Although vincristine combination therapy has shown some modest efficacy in preclinical GBM models, vincristine is also a P-gp substrate[13,43] and is clinically ineffective against GBM[14,15]. Combining MPS1 inhibitors with newer microtubule stabilizers that have improved brain penetration might offer a more promising perspective[44], albeit one that requires further investigation.

Second, most studies that report monotherapy efficacy of MPS1 inhibition used subcutaneous cancer models such as colorectal cancer, cervical cancer and triple-negative breast cancer[8,33,37-40]. There are several potentially important differences between subcutaneous tumor models and the

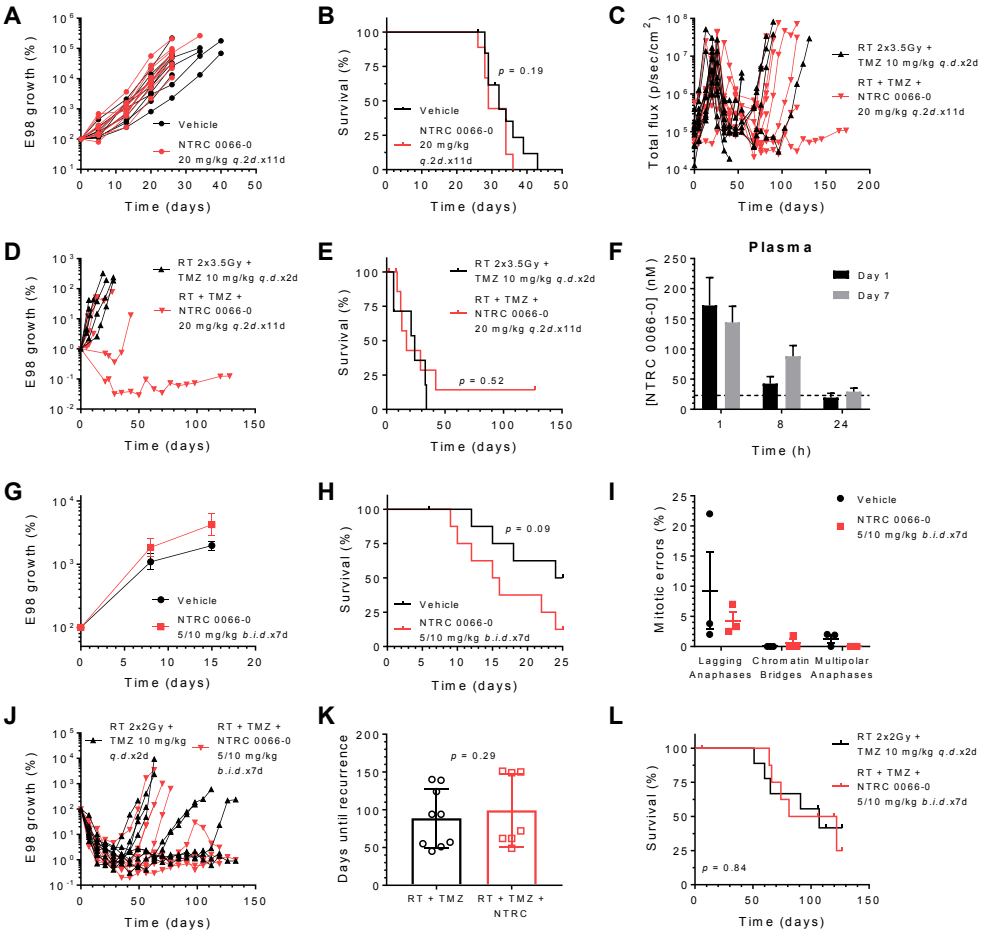

Figure 6 | NTRC 0066-0 antitumor efficacy studies against orthotopic E98 GBMs in *Abcb1a/b;Abcg2*$^{-/-}$ mice. (**A**) Tumor growth and (**B**) survival of mice treated with NTRC 0066-0 administered at 20 mg/kg every other day for 11 days (*q.2d.*x11d). n = 10. (**C**) Tumor growth from tumor induction, (**D**) tumor growth stratified to time-of-recurrence and (**E**) survival from time-of-recurrence of mice treated with NTRC 0066-0 administered at 20 mg/kg *q.2d.*x11d when recurrence occurred after treatment with 2 consecutive days (*q.d.*x2d) of 3.5 Gy radiotherapy (RT) and 10 mg/kg temozolomide (TMZ) chemotherapy, or RT + TMZ alone. Treatment with RT + TMZ was started when tumor reached 10^7 p/sec/cm^2; treatment with NTRC 0066-0 was started when recurrence was detected. n = 7. (**F**) Plasma concentrations of NTRC 0066-0 in *Abcb1a/b;Abcg2*$^{-/-}$ mice at several time points of day 1 and day 7 of treatment with 5 mg/kg NTRC0066-0 in the morning and 10 mg/kg NTRC 0066-0 approximately 8 hours later for 7 consecutive days (5/10 mg/kg *b.i.d.*x7d). Data are mean ± SD; n = 5. (**G**) Tumor growth and (**H**) survival of mice treated with NTRC 0066-0 administered at 5/10 mg/kg *b.i.d.*x7d. Data are mean ± SE; n = 9. (**I**) Percentages of various classes of mitotic errors in end-stage tumors from (**G**). Data are mean ± SD; n ≥ 50 cells/tumor, n = 3 mice/group. (**J**) Tumor growth, (**K**) time-of-recurrence (**L**) survival of mice treated with 2 Gy RT and 10 mg/kg TMZ *q.d.*x2d followed by NTRC 0066-0 administered at 5/10 mg/kg *b.i.d.*x7d, or RT + TMZ alone. Data are mean ± SD; n = 9.

brain tumor model that we used. Within the brain microenvironment, E98 cells need about 7–10 weeks to develop to a size of about 30 to 50 cubic mm. Although this size is large enough to kill the animal, it is considerably smaller than the 2000 cubic mm size that the subcutaneously growing tumors can reach in a much shorter period[33,40]. The more rapid expansion of those tumors may cause a higher replication stress in tumor cells. Moreover, due to their rapid expansion with

profound angiogenesis, subcutaneous cancer models are known to have a relatively aberrant vasculature[45]. This leaky vasculature facilitates intratumoral drug distribution and retention, leading to more continuous and relatively high local drug exposure. In fact, pharmacokinetic analysis of intratumoral drug concentrations show that MPS1 inhibitors can accumulate in subcutaneous tumors (unpublished data). The more long-term exposure could be one of the factors explaining the observed monotherapy efficacy in the subcutaneous setting. Such vascular artifacts of subcutaneous cancer models may not occur in orthotopic GBM models. Brain tumor models such as E98 grow relatively slow without evidence of necrosis as they are well perfused by vessels expressing BBB markers (**Figure 5**). Therefore, the drug concentration in the brain tumor likely follows the course of the drug level in normal brain. In the case of the intermittent (every other day) dose schedule this may result in considerable intervals of inadequate drug levels. Notably, however, when we changed to *b.i.d.* dosing, the efficacy did not improve. Instead, the trend towards a more rapid tumor progression that was already notable in the intermittent dose schedule (**Figures 6A–B**) became more pronounced with *b.i.d.* dosing (**Figures 6G–H**). This could imply that exposure to NTRC 0066-0 enables faster cycling of tumor cells by interference with checkpoint control, but without producing sufficient mitotic errors for causing cell death. In general, the level of mitotic errors that we observed in E98 tumors was low, as the majority of the tumors harbored less than 5% of mitotic errors. Since we analyzed only end-stage tumors, it could be that the absence of highly aberrant cells reflects the clearance from the general tumor population as a result of mitotic cell death. However, one would expect to observe a delayed tumor growth during NTRC 0066-0 treatment if the population encountering mitotic errors and subsequent cell death was substantial. Since we could not find such an effect, it is more likely that NTRC0066-0 5/10 mg/kg *b.i.d.*x7d did not induce mitotic errors in E98 cells in intracranial xenografts *in vivo*. If the induction of mitotic errors is more abundant *in vitro*, this might offer another explanation for the observed disconnect between the *in vitro* and *in vivo* efficacy of NTRC 0066-0 against these GBM cells.

Although the intracranial E98 xenograft propagates steadily (**Figures 6A, G**), the doubling time of these tumors is longer than cells cultured *in vitro*. Culturing in the presence of ample amounts of nutrients, growth factors and high oxygen levels may result in more pronounced replication stress due to higher intrinsic DNA damage levels and more mitotic segregation errors than occurs in the *in vivo* context. Under such conditions, GBM cells may depend more on proper control of cell cycle checkpoints. If so, this might also explain why we found some indications of efficacy when NTRC 0066-0 was given when E98 tumors recurred after RT + TMZ treatment, as these modalities are DNA damaging agents that are known to induce mitotic errors. Signs of efficacy were observed, even when NTRC 0066-0 was administered using the intermittent dosing scheme of 20 mg/kg *q.*2*d.*x11d. Using this scheme, clear antitumor responses were observed in 2 out of 7 mice. The level of heterogeneity in therapy response is striking, and might be related to substantial differences in intrinsic levels of mitotic errors (especially lagging anaphases) between

individual tumors that were observed even in untreated tumors (**Figure 6I**). On the one hand, understanding the requirement of this intrinsic heterogeneity might help to select a more optimal preclinical model to demonstrate the potential of MPS1 inhibition for treatment of GBM and could potentially contribute to identifying a patient group that is most likely to benefit from therapeutic strategies that involve MPS1 inhibition. On the other hand, the finding that MPS1 inhibition may cause an accelerated proliferation of a subpopulation of tumor cells is not an attractive prospect for further clinical development.

In summary, we observed profound cytotoxicity in GBM cells by the MPS1 inhibitor NTRC 0066-0 *in vitro*, but could not translate this finding to antitumor efficacy *in vivo*, despite a high brain penetration of NTRC 0066-0 and using the most dose-dense oral adminstration schedule that was tolerable. These data indicate that developing MPS1 inhibitors for treatment of GBM will be challenging.

REFERENCES

1. Stupp, R., *et al.* Radiotherapy plus concomitant and adjuvant temozolomide for glioblastoma. *N Engl J Med* **352**, 987-996 (2005).
2. Foley, E.A. & Kapoor, T.M. Microtubule attachment and spindle assembly checkpoint signalling at the kinetochore. *Nat Rev Mol Cell Biol* **14**, 25-37 (2012).
3. Vitale, I., *et al.* Mitotic catastrophe: a mechanism for avoiding genomic instability. *Nat Rev Mol Cell Biol* **12**, 385-392 (2011).
4. Mir, S.E., *et al.* In silico analysis of kinase expression identifies WEE1 as a gatekeeper against mitotic catastrophe in glioblastoma. *Cancer Cell* **18**, 244-257 (2010).
5. Tannous, B.A., *et al.* Effects of the selective MPS1 inhibitor MPS1-IN-3 on glioblastoma sensitivity to antimitotic drugs. *J Natl Cancer Inst* **105**, 1322-1331 (2013).
6. Burrell, R.A., *et al.* Replication stress links structural and numerical cancer chromosomal instability. *Nature* **494**, 492-496 (2013).
7. Lan, W. & Cleveland, D.W. A chemical tool box defines mitotic and interphase roles for Mps1 kinase. *J Cell Biol* **190**, 21-24 (2010).
8. Jemaa, M., *et al.* Characterization of novel MPS1 inhibitors with preclinical anticancer activity. *Cell Death Differ* **20**, 1532-1545 (2013).
9. Maia, A.R.R., *et al.* Mps1 inhibitors synergise with low doses of taxanes in promoting tumour cell death by enhancement of errors in cell division. *Br J Cancer* **118**, 1586-1595 (2018).
10. van Tellingen, O., *et al.* Overcoming the blood-brain tumor barrier for effective glioblastoma treatment. *Drug Resist Updat* **19**, 1-12 (2015).
11. Sarkaria, J.N., *et al.* Is the blood–brain barrier really disrupted in all glioblastomas? A critical assessment of existing clinical data. *Neuro Oncol* **20**, 184-191 (2018).
12. Allen, J.D., *et al.* Extensive contribution of the multidrug transporters P-glycoprotein and Mrp1 to basal drug resistance. *Cancer Res* **60**, 5761-5766 (2000).
13. Wang, F., *et al.* Influence of blood-brain barrier efflux pumps on the distribution of vincristine in brain and brain tumors. *Neuro Oncol* **12**, 1043-1049 (2010).
14. Perry, J., *et al.* Adjuvant chemotherapy for adults with malignant glioma: a systematic review. *Can J Neurol Sci* **34**, 402-410 (2007).
15. Nieder, C., *et al.* Combined radio- and chemotherapy of brain tumours in adult patients. *Clin Oncol* **21**, 515-524 (2009).
16. de Gooijer, M.C., *et al.* Improved brain penetration and antitumor efficacy of temozolomide by inhibition of ABCB1 and ABCG2. *Neoplasia* **20**, 710-720 (2018).
17. Uitdehaag, J.C.M., *et al.* Target residence time-guided optimization on TTK kinase results in inhibitors with potent anti-proliferative activity. *J Mol Biol* **429**, 2211-2230 (2017).
18. de Man, A.P.A., *et al.* (5,6-dihydro)pyrimido[4,5-e]indolizines. WO 2015/155042 A1 (ed. WIPO) (2015).
19. Lin, F., *et al.* ABCB1, ABCG2, and PTEN determine the response of glioblastoma to temozolomide and ABT-888 therapy. *Clin Cancer Res* **20**, 2703-2713 (2014).
20. Schinkel, A.H., *et al.* Absence of the mdr1a P-glycoprotein in mice affects tissue distribution and pharmacokinetics of dexamethasone, digoxin, and cyclosporin A. *J Clin Invest* **96**, 1698-1705 (1995).
21. Jonker, J.W., *et al.* Role of breast cancer resistance protein in the bioavailability and fetal penetration of topotecan. *J Natl Cancer Inst* **92**, 1651-1656 (2000).
22. Pavek, P., *et al.* Human breast cancer resistance protein: interactions with steroid drugs, hormones, the dietary carcinogen 2-amino-1-methyl-6-phenylimidazo(4,5-*b*)pyridine, and transport of cimetidine. *J Pharmacol Exp Ther* **312**, 144-152 (2005).
23. Guzman, C., *et al.* ColonyArea: an ImageJ plugin to automatically quantify colony formation in clonogenic assays. *PloS One* **9**, e92444 (2014).

24. Chou, T.C. Drug combination studies and their synergy quantification using the Chou-Talalay method. *Cancer Res* **70**, 440-446 (2010).
25. Zhang, P.*, et al.* ABCB1 and ABCG2 restrict the brain penetration of a panel of novel EZH2-Inhibitors. *Int J Cancer* **137**, 2007-2018 (2015).
26. Schinkel, A.H.*, et al.* Disruption of the mouse mdr1a P-glycoprotein gene leads to a deficiency in the blood-brain barrier and to increased sensitivity to drugs. *Cell* **77**, 491-502 (1994).
27. Jonker, J.W.*, et al.* The breast cancer resistance protein protects against a major chlorophyll-derived dietary phototoxin and protoporphyria. *Proc Natl Acad Sci U S A* **99**, 15649-15654 (2002).
28. Jonker, J.W.*, et al.* Contribution of the ABC transporters Bcrp1 and Mdr1a/1b to the side population phenotype in mammary gland and bone marrow of mice. *Stem Cells* **23**, 1059-1065 (2005).
29. Lin, F.*, et al.* Abcc4 together with abcb1 and abcg2 form a robust cooperative drug efflux system that restricts the brain entry of camptothecin analogues. *Clin Cancer Res* **19**, 2084-2095 (2013).
30. Caldarelli, M.*, et al.* Synthesis and SAR of new pyrazolo[4,3-h]quinazoline-3-carboxamide derivatives as potent and selective MPS1 kinase inhibitors. *Bioorg Med Chem Lett* **21**, 4507-4511 (2011).
31. Zhang, Y.*, et al.* PKSolver: An add-in program for pharmacokinetic and pharmacodynamic data analysis in Microsoft Excel. *Comput Methods Programs Biomed* **99**, 306-314 (2010).
32. Lee, J.*, et al.* Tumor stem cells derived from glioblastomas cultured in bFGF and EGF more closely mirror the phenotype and genotype of primary tumors than do serum-cultured cell lines. *Cancer Cell* **9**, 391-403 (2006).
33. Maia, A.R.R.*, et al.* Inhibition of the spindle assembly checkpoint kinase TTK enhances the efficacy of docetaxel in a triple-negative breast cancer model. *Ann Oncol* **26**, 2180-2192 (2015).
34. de Gooijer, M.C.*, et al.* Buparlisib is a brain penetrable pan-PI3K inhibitor. *Sci Rep* **8**, 10784 (2018).
35. Libouban, M.A.A.*, et al.* Stable aneuploid tumors cells are more sensitive to TTK inhibition than chromosomally unstable cell lines. *Oncotarget* **8**, 38309-38325(2017).
36. Maachani, U.B.*, et al.* Targeting MPS1 enhances radiosensitization of human glioblastoma by modulating DNA repair proteins. *Mol Cancer Res* **13**, 852-862 (2015).
37. Jemaà, M.*, et al.* Selective killing of p53-deficient cancer cells by SP600125. *EMBO Mol Med* **4**, 500-514 (2012).
38. Faisal, A.*, et al.* Characterisation of CCT271850, a selective, oral and potent MPS1 inhibitor, used to directly measure in vivo MPS1 inhibition vs therapeutic efficacy. *Br J Cancer* **116**, 1166-1176 (2017).
39. Wengner, A.M.*, et al.* Novel Mps1 kinase inhibitors with potent antitumor activity. *Mol Cancer Ther* **15**, 583-592 (2016).
40. Zaman, G.J.R.*, et al.* TTK Inhibitors as a targeted therapy for CTNNB1 (beta-catenin) mutant cancers. *Mol Cancer Ther* **16**, 2609-2617 (2017).
41. Kemper, E.M.*, et al.* Increased penetration of paclitaxel into the brain by inhibition of P-glycoprotein. *Clin Cancer Res* **9**, 2849-2855 (2003).
42. Kemper, E.M.*, et al.* Improved penetration of docetaxel into the brain by co-administration of inhibitors of P-glycoprotein. *Eur J Cancer* **40**, 1269-1274 (2004).
43. van Tellingen, O.*, et al.* P-glycoprotein and Mrp1 collectively protect the bone marrow from vincristine-induced toxicity in vivo. *Br J Cancer* **89**, 1776-1782 (2003).
44. Brunden, K.R.*, et al.* The characterization of microtubule-stabilizing drugs as possible therapeutic agents for Alzheimer's disease and related tauopathies. *Pharmacol Res* **63**, 341-351 (2011).
45. Jain, R.K. Normalization of tumor vasculature: an emerging concept in antiangiogenic therapy. *Science* **307**, 58-62 (2005).

12

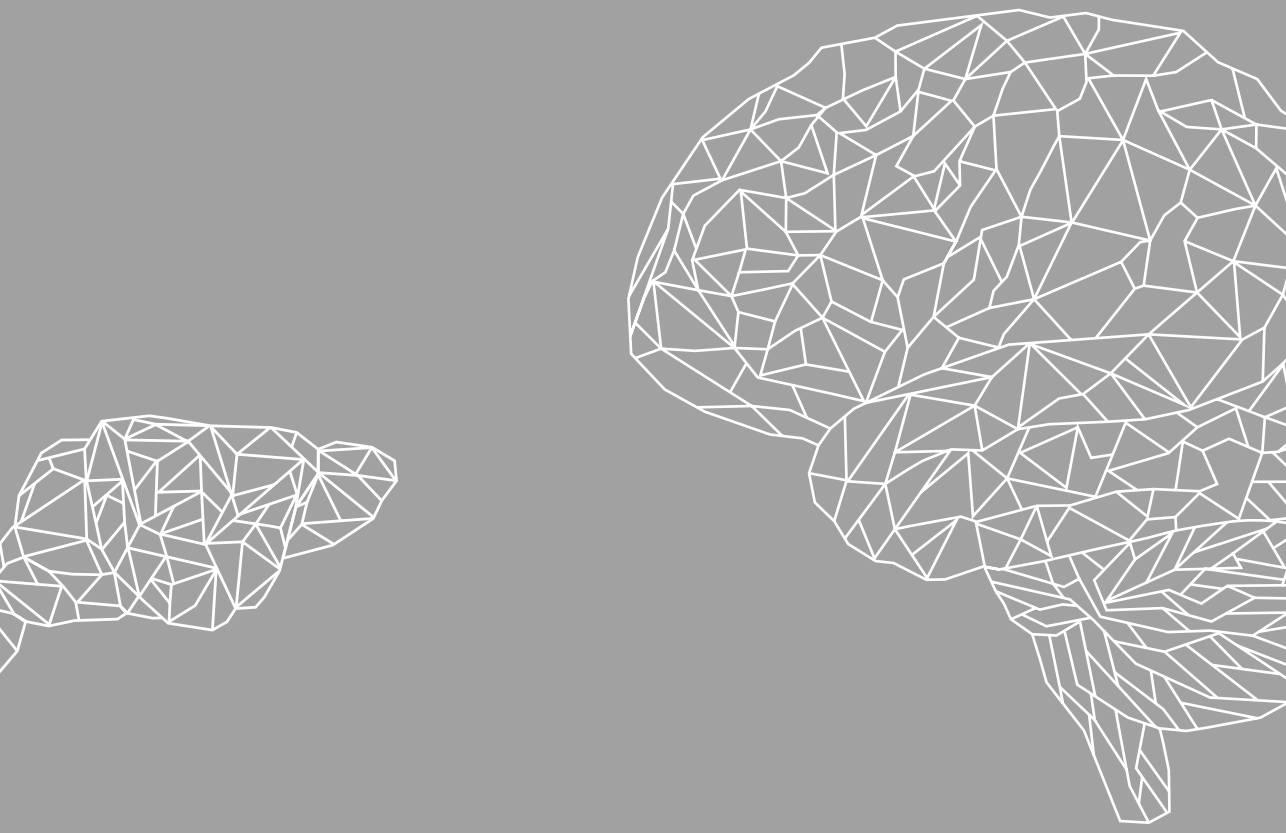

SECTION VI

INHIBITING PARP: ATTENUATING DNA REPAIR

Chapter 13

ABCB1, ABCG2 AND PTEN DETERMINE THE RESPONSE OF GLIOBLASTOMA TO TEMOZOLOMIDE AND ABT-888 THERAPY

F. Lin*, M.C. de Gooijer*, E. Moreno Roig, L.C.M. Buil, S.M. Christner, J.H. Beumer, T. Wurdinger, J.H. Beijnen, and O. van Tellingen

* These authors contributed equally

Clinical Cancer Research. 2014;20(10):2703-2713

ABSTRACT

Purpose: Little is known about the optimal clinical use of ABT-888 (veliparib) for treatment of glioblastoma. ABT-888 is a PARP inhibitor undergoing extensive clinical evaluation in glioblastoma, because it may synergize with the standard-of-care temozolomide (TMZ). We have elucidated important factors controlling ABT-888 efficacy in glioblastoma. ***Experimental design:*** We used genetically engineered spontaneous glioblastoma mouse models and allograft models that were orthotopically transplanted into wild-type (WT) and *Abcb1/Abcg2*-deficient (KO) recipients. ***Results:*** ABT-888/TMZ is not efficacious against *Tp53*$^{-/-}$*;p16*^{Ink4a}*/p19*$^{Arf-/-}$*;K-Ras*^{V12}*;Luc* allografts in WT recipients, indicating inherent resistance. Abcb1/Abcg2 mediated efflux of ABT-888 at the blood–brain barrier (BBB) causes a 5-fold reduction of ABT-888 brain penetration ($p < 0.0001$) that was fully reversible by elacridar. Efficacy studies in WT and KO recipients and/or concomitant elacridar demonstrate that Abcb1/Abcg2 at the BBB and in tumor cells impair TMZ/ABT-888 combination treatment efficacy. Elacridar also markedly improved TMZ/ABT-888 combination treatment in the spontaneous *Tp53*$^{F/F}$*;p16*^{Ink4a}*/p19*$^{ArfF/F}$*;K-Ras*^{V12}*;Luc* glioblastoma model. Importantly, ABT-888 does enhance TMZ efficacy in *Pten*-deficient glioblastoma allografts and spontaneous tumors, even in *Abcb1/Abcg2*-proficient WT mice. Loss of *PTEN* occurs frequently in glioblastoma (36%) and *in silico* analysis on glioblastoma patient samples revealed that it is associated with a worse overall survival (310 days *vs.* 620 days, n = 117). ***Conclusions:*** The potential of ABT-888 in glioblastoma can best be demonstrated in patients with *PTEN* null tumors. Therefore, clinical trials with ABT-888 should evaluate these patients as a separate group. Importantly, inhibition of ABCB1 and ABCG2 (by elacridar) may improve the efficacy of TMZ/ABT-888 therapy in all glioblastoma patients.

Translational relevance: Glioblastoma is a uniformly lethal disease and there is a great but yet unmet need for better therapies. There is a clear rationale for the clinical evaluation of PARP inhibitors such as ABT-888 (veliparib) in combination with the standard therapy in high-grade glioma patients. PARP inhibitors can augment the cytotoxic effects of DNA damage by interfering in DNA repair. Of all PARP inhibitors, ABT-888 is the clinically most advanced candidate agent for glioblastoma. Failure or success of these trials may not just determine the fate of ABT-888, but may set the stage for the whole concept of using PARP inhibitors in this disease. We here show that ABC transporters at the blood–brain barrier and tumor cells and *PTEN* status of tumor cells are important determinants of efficacy of ABT-888 and temozolomide combination therapy. This information need to be taken into account during the evaluation of ongoing clinical trials.

INTRODUCTION

Glioblastoma (GBM) is the most common and aggressive primary brain tumor and only very few chemotherapeutic agents are available that exert a meaningful response. The current standard-of-care is surgical resection followed by chemo-radiation therapy consisting of the DNA-alkylating agent temozolomide (TMZ) and radiotherapy. This DNA damaging treatment modality significantly increases the overall median survival to 14.6 months after diagnosis[1]. However, even with this aggressive treatment regimen the prognosis of GBM patients remains dismal and novel therapeutics are urgently needed.

Poly (ADP-ribose) polymerase (PARP) inhibitors enhance the activity of DNA damaging therapies, due to the critical function of PARP1 and PARP2 in base excision repair[2,3]. Several preclinical studies suggest that PARP inhibitors enhance the efficacy of TMZ in both sensitive and resistant tumors[4,5]. Moreover, their capacity to sensitize GBM cells to TMZ treatment and reverse TMZ resistance has been reported[6-8]. ABT-888 (veliparib) is a potent PARP1/2 inhibitor and the clinically most advanced candidate for glioblastoma, with several ongoing clinical trials. Obviously, the combination of ABT-888 with chemo-radiation therapy is receiving considerable interest, because it has shown promise in preclinical models, including intracranial models[9,10]. The outcome of these clinical trials may not only determine the fate of ABT-888, but may set the stage for the whole concept of using PARP inhibitors in the treatment of GBM. In order to maximize the chances for successful implementation of this drug, it is important to have a thorough understanding of the factors that may pose threats to this objective. Because we felt that critical information was lacking, we have performed comprehensive *in vivo* studies in a set of clinically relevant glioma models to interrogate the potential of ABT-888 in high-grade glioma and identified critical factors that may determine its success in the clinic.

A pitfall of many intracranial tumor models, including those that were used to demonstrate efficacy of ABT-888[9,10], is the very leaky tumor vasculature, resulting in excellent drug penetration throughout the whole tumor area. However, due to the invasive nature of gliomas, the permeability of the blood–brain barrier in such brain tumors (blood–brain tumor barrier; BBTB) is much more heterogeneous in GBM patients and may therefore compromise adequate drug exposure to a substantial fraction of GBM cells[11-13]. Especially agents that are recognized by ATP-binding cassette (ABC) drug efflux transporters expressed at the BBB are at risk. Of all efflux transporters present in the BBB, ABCB1 (also known as P-glycoprotein; P-gp or MDR1) and ABCG2 (breast cancer resistance protein; BCRP) are dominant[14]. Together, they are responsible for the efflux of a wide range of therapeutic agents, including many of the small molecule inhibitors that are currently under (clinical) investigation for brain cancer[15,16]. Moreover, ABCB1 and ABCG2 have established roles in conferring multidrug resistance by limiting intracellular drug accumulation in tumor cells[17,18]. Besides this issue of adequate drug exposure, many intracranial tumor models

also lack many important characteristics, including those involved in drug resistance, as a consequence of culturing cells in serum-containing medium[19,20]. By ignoring these intrinsic and extrinsic drug resistance mechanisms, these models may not be predictive for the clinical efficacy of potential GBM therapeutics, such as ABT-888.

We have previously developed a range of Cre–LoxP conditional transgenic mouse models of GBM for chemotherapy intervention studies[21]. These models allow interrogation of the influence of frequently altered genes in GBM (*e.g.*, *TP53* or *PTEN* status) on tumor sensitivity[22]. In the present study, we found that a serum-free cultured cell line derived from a spontaneous *Tp53*$^{F/F}$*;p16*^{Ink4a}*/p19*$^{ArfF/F}$*;K-Ras*^{V12}*;Luc* GBM and re-injected into nude mice did not respond to ABT-888 and temozolomide combination therapy. By using *Abcb1a/b* and/or *Abcg2*-deficient recipient mice and the dual ABC transporter inhibitor elacridar, we demonstrate that these drug efflux transporters are causing resistance in this clinically relevant model. Moreover, we found that ABT-888 is more active in *Pten*-deficient tumors in our *in vivo* models.

METHODS

See also **Supplementary Methods**.

Drugs

ABT-888 was obtained from Selleck Chemicals (Houston, TX), TMZ for *in vitro* experiments from Sigma–Aldrich (St Louis, MO) and TMZ for *in vivo* studies from TEVA Pharma (Haarlem, The Netherlands). Elacridar was kindly provided by GlaxoSmithKline (Research Triangle Park, NC) and zosuquidar by Eli Lilly (Indianapolis, IN).

Animals

Mice were housed and handled according to institutional guidelines complying with Dutch legislation. All experiments with animals were approved by the animal experiment committee of the institute. The animals used for pharmacokinetics studies were female wild-type (WT), *Abcb1a/b*$^{-/-}$, *Abcg2*$^{-/-}$, and *Abcb1a/b;Abcg2*$^{-/-}$ mice of FVB genetic background, between 9 and 14 weeks of age. *Pten*$^{F/F}$*;p16*^{Ink4a}*/p19*$^{ArfF/F}$*;K-Ras*^{V12}*;Luc* and *Tp53*$^{F/F}$*;p16*^{Ink4a}*/p19*$^{ArfF/F}$*;K-Ras*^{V12}*;Luc* conditional mice were genotyped as described previously[21]. Athymic (nude) WT and *Abcb1a/b;Abcg2*$^{-/-}$ mice of FVB background were used as recipient animals for orthotopic injection of neurosphere cultured GBM cells generated from the above mentioned conditional mouse models.

ABT-888 brain penetration

ABT-888 (10 mg/kg) was administered orally (p.o.) or intravenously (i.v.) and elacridar (100 mg/kg, p.o.) was given 15 min prior to ABT-888. Blood was collected by cardiac puncture or tail vein (for serial sampling). Brains were homogenized in 3 ml 1% (w/v) bovine serum albumin. ABT-888 plasma and brain samples were analyzed by LC–MS/MS as described[23] or for more sensitive quantitation over a concentration range of 0.3–100 ng/mL, a modified LC–MS/MS system utilizing an ABI4000 mass detector (m/z 245.2 to 84.2 for ABT-888, and 248.2 to 87.2 for [D_3]-ABT-888). Pharmacokinetic parameters were calculated using PKSolver[24].

Pharmacokinetic calculations and statistical analysis

Brain and plasma concentrations among multiple strains were compared by one-way analysis of variance (ANOVA) with Bonferroni *post hoc* test. Survival fractions were calculated according to the Kaplan–Meier method using GraphPad Prism v6 (GraphPad Software, Inc.; La Jolla, CA). The log–rank test was used to compare survival of groups.

Intracranial tumor models and bioluminescence imaging

The procedures of stereotactic intracranial injection of lentivirus or tumor cells and bioluminescence imaging (BLI) have been described in detail[21]. In short, *Pten$^{F/F}$;p16^{Ink4a}/p19$^{ArfF/F}$;K-Ras^{V12};Luc* and *Tp53$^{F/F}$;p16^{Ink4a}/p19$^{ArfF/F}$;K-Ras^{V12};Luc* mice were injected intracranially with 2 µl of CMV–Cre lentivirus suspension 2 mm lateral and 1 mm anterior to the bregma, 3 mm below the skull. For orthotopic transplantation models, 2 µl of cell suspension containing 5,000 cells was injected in athymic WT and *Abcb1a/b;Abcg2$^{-/-}$* nude mice. Tumor development was monitored by bioluminescence using the IVIS 200 (PerkinElmer; Waltham, MA). BLI values were log-converted. Mean and SE BLI values of each cohort were calculated for each time point, until most animals within the cohort had to be sacrificed due to disease progression. Mice were sacrificed when clear neurological symptoms occurred or weight loss (≥ 20%) was observed.

Drug formulation and treatment regimen

ABT-888 (in DMSO:saline; 1:10) was administered orally at a dose of 10 mg/kg *b.i.d.* for 5 days. TMZ (100 mg capsule) was dissolved just prior to administration in 2 ml of ethanol plus 18 ml saline, filtered and administered orally at a dose of 100 mg/kg *q.d.* x5 within 30 min after preparation. Elacridar was administered orally at a dose of 100 mg/kg 15 min prior to ABT-888 or TMZ administration.

GBM cell cultures and proliferation assays

GBM cell lines have been derived from tumors generated in *p16^{Ink4a}/p19$^{ArfF/F}$;K-Ras^{V12};Luc*, *Pten$^{F/F}$;*

p16^{Ink4a}/p19$^{ArfF/F}$;K-Ras^{V12};Luc, *Tp53$^{F/F}$;p16^{Ink4a}/p19$^{ArfF/F}$;K-Ras^{V12};Luc* and *Tp53$^{F/F}$;Pten$^{F/F}$;p16^{Ink4a}/p19$^{ArfF/F}$;K-Ras^{V12};Luc* conditional mice after lentiviral infection. Small amounts of tumor tissue were triturated mechanically in ice-cold Ca^{2+} and Mg^{2+} free HBSS (Life Technologies; Carlsbad, CA). Cell suspensions were cultured in ultra-low binding 6-well plates (Costar Corning; Corning, NY) in serum-free MHM (medium hormone mix) medium supplemented with 10 ng/ml EGF and bFGF (Sigma-Aldrich) as described previously[25].

Proliferation assays were carried out with GBM cells (2,000/well) seeded on laminin coated 96-well black-well/clear-bottom plates (Greiner Bio-One, Alphen, The Netherlands) in MHM medium supplemented with 10 ng/ml EGF and bFGF. Treatment was started after 1 day with MHM medium containing 0.1% DMSO (control), or 100 μM TMZ alone, or in combination with increasing concentrations of ABT-888 (0.3 μM to 30 μM). Cell density/viability was determined on day 0 (treatment start) and day 5 using bioluminescence imaging on an IVIS Lumina II Imaging System (PerkinElmer) with 150 μg/ml of beetle luciferin (Promega, Leiden, The Netherlands) in each well.

Histology and Immunohistochemistry

Brain tissue was fixed in 4% formaldehyde; paraffin embedded and cut into 4 μm coronal sections that were stained for hematoxylin and eosin (H&E) and for Abcg2/ABCG2 using the BXP-53 antibody (Abcam, Cambridge, UK).

Western blotting

For PARP inhibition analyses, GBM cells were cultured on laminin in 6-well plates until 80–90% cell confluency. Cells were incubated with drugs for 4 h and subsequently lysed with complete RIPA buffer containing phosphatase inhibitors. Lysates were processed for Western blotting. Primary antibodies used in this study are rabbit anti-PAR (1:1000; Trevigen; Gaithersburg, MD), mouse anti-β-tubulin isotype III (1:1000; Sigma-Aldrich) and Mdr (H-19) rabbit polyclonal (1:200; Santa Cruz Biotechnology; Santa Cruz, CA) and BXP-53 rat monoclonal (1:400; Abcam) for Abcb1 and Abcg2, respectively. Enhanced chemiluminescence (ECL) was used for detection using Molecular imaged ChemiDoc™ XRS+ system (Bio-Rad; Hercules, CA). Data was analyzed using ImageLab software (version 2.0.1) from Bio-Rad laboratories.

RESULTS

Tp53$^{-/-}$;p16^{Ink4a}/p19$^{Arf-/-}$;K-Ras^{V12};Luc GBM allografts are resistant to TMZ or ABT-888 and TMZ treatment

GSC457 cells were isolated from a lentivirally induced tumor in a *Tp53$^{F/F}$;p16^{Ink4a}/p19$^{ArfF/F}$;K-Ras^{V12};Luc* mouse. Tumors that developed after intracranial injection into nude mice resemble many features of human high-grade gliomas[21]. Mice received either vehicle, single treatment with 100 mg/kg TMZ *q.d.* or combined with 10 mg/kg ABT-888 *b.i.d.* for 5 days. Although a slight delay in tumor growth was observed, no significant difference in median survival was found between treated and control (**Figure 1A**; 11 *vs.* 11 days; $p = 0.37$) or the two treatment groups (12 *vs.* 11 days; $p = 0.22$).

Brain penetration of ABT-888 is restricted by Abcb1 and Abcg2 and can be enhanced by elacridar

We found that ABT-888 is transported by Abcb1, Abcg2 and ABCB1 *in vitro* (**Supplementary Figure 1**). Consequently, we evaluated the impact of Abcb1a/b and/or Abcg2 on the plasma and brain pharmacokinetics of ABT-888 using WT, *Abcb1a/b$^{-/-}$*, *Abcg2$^{-/-}$*, and *Abcb1a/b;Abcg2$^{-/-}$* mice. Following i.v. administration of 10 mg/kg of ABT-888, the AUC_{plasma} differed just 1.3-fold between the various strains (**Table 1 and Figure 2A**). Consequently, Abcb1 and Abcg2 do not a play critical role in the systemic clearance of ABT-888. In contrast, the AUC_{brain} of both *Abcb1a/b$^{-/-}$* and *Abcb1a/b;Abcg2$^{-/-}$* mice was significantly higher than in WT mice (3.7 and 4.9-fold, respectively; both $p < 0.0001$), demonstrating that Abcb1 and—to a lesser extent—Abcg2 at the BBB severely impair the brain entry of ABT-888. Interestingly, a profound continuous increase in the ABT-888 brain–plasma ratio was observed in *Abcb1a/b$^{-/-}$* and *Abcb1a/b;Abcg2$^{-/-}$* mice in a time course of 4 hours. This implies that the brain clearance does not keep up with the systemic clearance of ABT-888, demonstrating the importance of Abcb1 and Abcg2 in clearance of ABT-888 from the brain.

AUC_{0-4h}	Route	WT	Abcb1a/b $^{-/-}$	Abcg2$^{-/-}$	Abcb1a/b;Abcg2$^{-/-}$
Plasma	i.v.	1000 ± 31	1200 ± 70	1200 ± 47	1300 ± 59**
Brain	i.v.	860 ± 30	3100 ± 95****	910 ± 43	4200 ± 200****/####
AUC_{0-4h}	Route	WT	WT + elacridar	Abcb1a/b;Abcg2$^{-/-}$	Abcb1a/b;Abcg2$^{-/-}$ + elacridar
Plasma	p.o.	1500 ± 85	1800 ± 85^{+}	1400 ± 74	1800 ± 120^{++}

Table 1 | Plasma and brain AUC of ABT-888. WT, *Abcb1a/b$^{-/-}$*, *Abcg2$^{-/-}$* and *Abcb1a/b;Abcg2$^{-/-}$* mice received i.v. or p.o. ABT-888 (10 mg/kg). $AUC_{(0-4h)}$ in ng/ml·h or ng/g·h (mean ± SEM). ** $p < 0.01$, **** $p < 0.0001$ compared to WT mice. #### $p < 0.0001$ compared to *Abcb1a/b$^{-/-}$*. $^{+}$ $p < 0.05$, $^{++}$ $p < 0.01$, compared to *Abcb1a/b;Abcg2$^{-/-}$* mice not receiving elacridar. Oneway ANOVA with Bonferroni *post hoc* test.

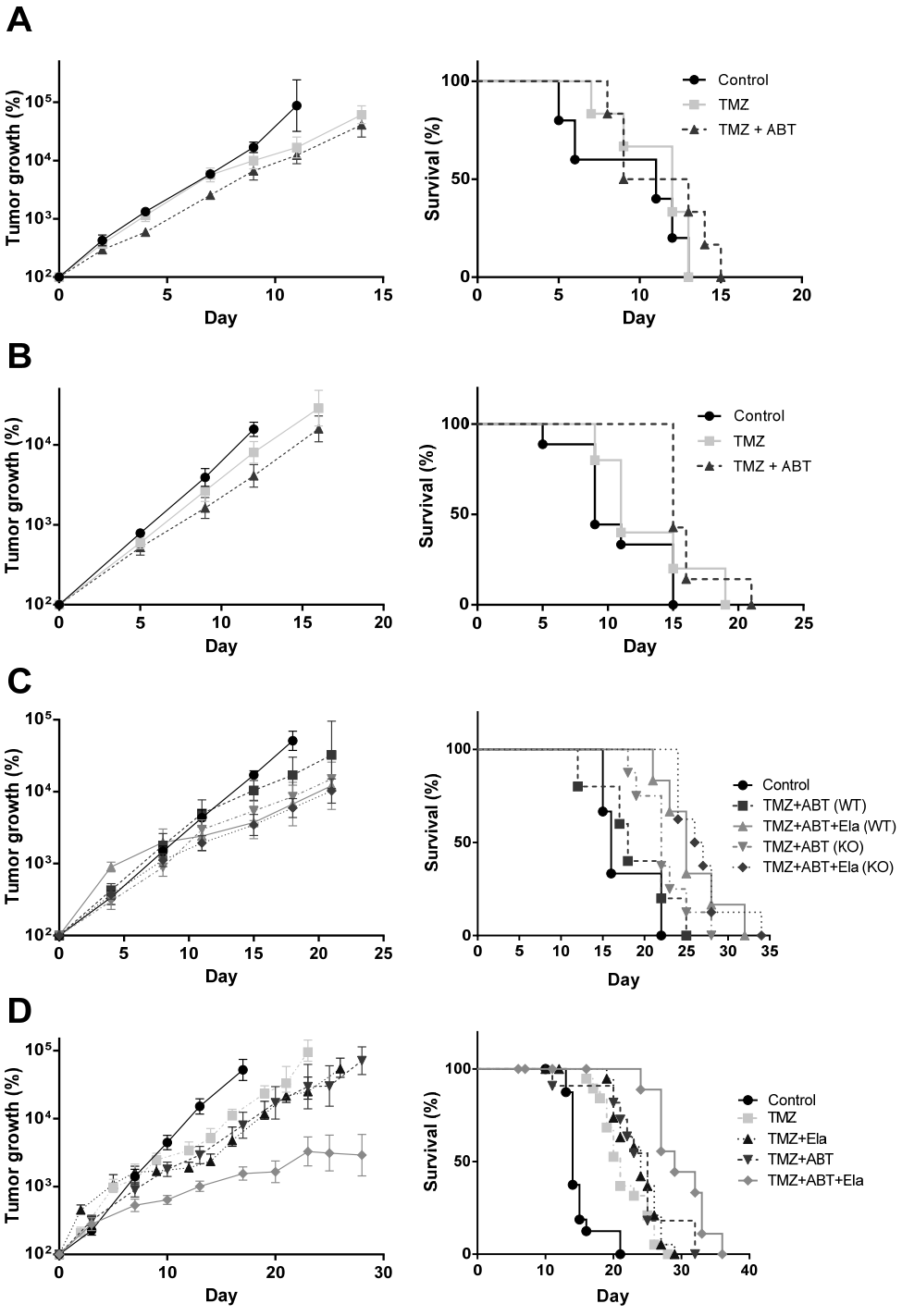
A
Tumor growth (%)
Day
Survival (%)
Control
TMZ
TMZ + ABT
B
Tumor growth (%)
Day
Survival (%)
Control
TMZ
TMZ + ABT
C
Tumor growth (%)
Day
Survival (%)
Control
TMZ+ABT (WT)
TMZ+ABT+Ela (WT)
TMZ+ABT (KO)
TMZ+ABT+Ela (KO)
D
Tumor growth (%)
Day
Survival (%)
Control
TMZ
TMZ+Ela
TMZ+ABT
TMZ+ABT+Ela

Figure 1 | Inhibition of Abcb1 and Abcg2 improve efficacy of ABT-888 + TMZ treatment. (**A**) Efficacy of TMZ vs TMZ+ABT-888 treatment against intracranial *Tp53*$^{-/-}$*;p16*^{Ink4a}*/p19*$^{Arf-/-}$*;K-Ras*^{V12}*;Luc* GSC457 cells injected into WT mice. (**B**). Same setup but now injected into *Abcb1a/b;Abcg2*$^{-/-}$ (KO) mice. (**C**) Efficacy of TMZ+ABT-888 with and without elacridar in both WT and KO mice. (**D**) Efficacy of TMZ or TMZ+ABT-888 with or without elacridar against (lentivirally induced) spontaneous *Tp53*$^{F/F}$*;p16*^{Ink4a}*/p19*$^{ArfF/F}$*;K-Ras*^{V12}*;Luc* tumors. TMZ p.o. at 100 mg/kg *q.d.* alone or concurrently with ABT-888 p.o. at 10 mg/kg *b.i.d.* and/or elacridar p.o. at 100 mg/kg *q.d.* 15 min prior to TMZ for 5 days. Left panels, relative tumor growth curves (bioluminescence imaging; means ± SEM). Right panels, Kaplan–Meier analysis of survival. Statistical significance was determined by Log-rank test. (**A**) n = 5, 6 and 6 WT mice in control, TMZ and TMZ+ABT-888 treated groups, respectively. (**B**) n = 9, 6 and 7 KO mice in control, TMZ and TMZ+ABT-888 groups respectively. (**C**) n = 3, 5, 6, 8, 8 for control, TMZ+ABT-888 (WT), TMZ+ABT-888+elacridar (WT) and both KO groups respectively. (**D**) n = 17, 19, 22, 11, 14 for control, TMZ, TMZ+elacridar, TMZ+ABT-888 and TMZ+ABT-888+elacridar groups respectively.

Similarly, inhibition of Abcb1 and Abcg2 by elacridar also increased ABT-888 brain accumulation. Concomitant elacridar slightly increased the AUC_{plasma} by 1.2-fold (**Table 1**; $p = 0.14$). This was also seen in *Abcb1a/b;Abcg2*$^{-/-}$ mice (1.3-fold; $p = 0.0099$) and thus most likely due to inhibition of other drug elimination pathways. Importantly, co-administration of elacridar in WT mice caused an 11-fold increased ABT-888 brain concentration ($p < 0.0001$) at 4 h after drug administration and a brain concentration-to-AUC_{plasma} ratio similar to that of *Abcb1a/b;Abcg2*$^{-/-}$ mice (with or without elacridar ($p = 0.25$ and $p > 0.99$ respectively)) and 9-fold higher than WT controls ($p < 0.0001$; **Figure 2B**). Thus, elacridar significantly enhances the brain accumulation of ABT-888 by inhibition of Abcb1 and Abcg2 at the BBB.

Co-administration of elacridar enhances the efficacy of TMZ and ABT-888 against GBM

To investigate whether absence of Abcb1 and Abcg2 at the BBB/BBTB would improve TMZ/ABT-888 treatment, we repeated the *in vivo* efficacy experiment with *Tp53*$^{-/-}$*;p16*^{Ink4a}*/p19*$^{Arf-/-}$*; K-Ras*^{V12}*;Luc* GSC457 cells in *Abcb1a/b;Abcg2*$^{-/-}$ nude mice. We observed a better overall survival with TMZ/ABT-888 treatment in *Abcb1a/b;Abcg2*$^{-/-}$ mice (**Figure 1B**) than in WT mice (**Figure 1A**). Mice receiving ABT-888+TMZ survived significantly longer than untreated controls (15 *vs.* 9 days; $p = 0.004$) whereas mice receiving TMZ alone did not (11 *vs.* 9 days; $p = 0.30$).

Besides the presence of Abcb1 and Abcg2 at the BBB/BBTB, their expression in tumor cells may also impair the intracellular accumulation and efficacy of ABT-888. Many of the murine derived GBM cell lines, including GSC457 express Abcg2 and also some Abcb1 and immunochemistry of Abcg2 revealed its presence in blood vessels and tumor cells (**Figure 3**). As assessed by western blotting, ABT-888 has PARP inhibitory activity in the sub-micromolar range in our GBM cell lines *in vitro*, which was modestly enhanced by elacridar (**Supplementary Figure 2**). To investigate whether elacridar can improve the efficacy of TMZ and ABT-888 *in vivo*, we administered TMZ and ABT-888 with or without elacridar to both WT and *Abcb1a/b;Abcg2*$^{-/-}$ mice bearing orthotopic *Tp53*$^{-/-}$*;p16*^{Ink4a}*/p19*$^{Arf-/-}$*;K-Ras*^{V12}*;Luc* GSC457. *Abcb1a/b;Abcg2*$^{-/-}$ mice receiving elacridar survived significantly longer than *Abcb1a/b;Abcg2*$^{-/-}$ mice not receiving elacridar (**Figure 1C**, median survival 26.5 *vs.* 22 days; $p = 0.025$). WT mice receiving elacridar in combination with TMZ and ABT-888 responded similarly as *Abcb1a/b;Abcg2*$^{-/-}$ mice receiving the combination. Elacridar

significantly prolonged the survival of WT mice receiving TMZ and ABT-888 treatment (median survival 25 *vs.* 18 days for WT mice receiving TMZ+ABT-888+elacridar *vs.* TMZ+ABT-888 respectively; $p = 0.039$). Together, these results support the idea that elacridar inhibited Abcb1 and Abcg2 both at the BBB and in tumor cells.

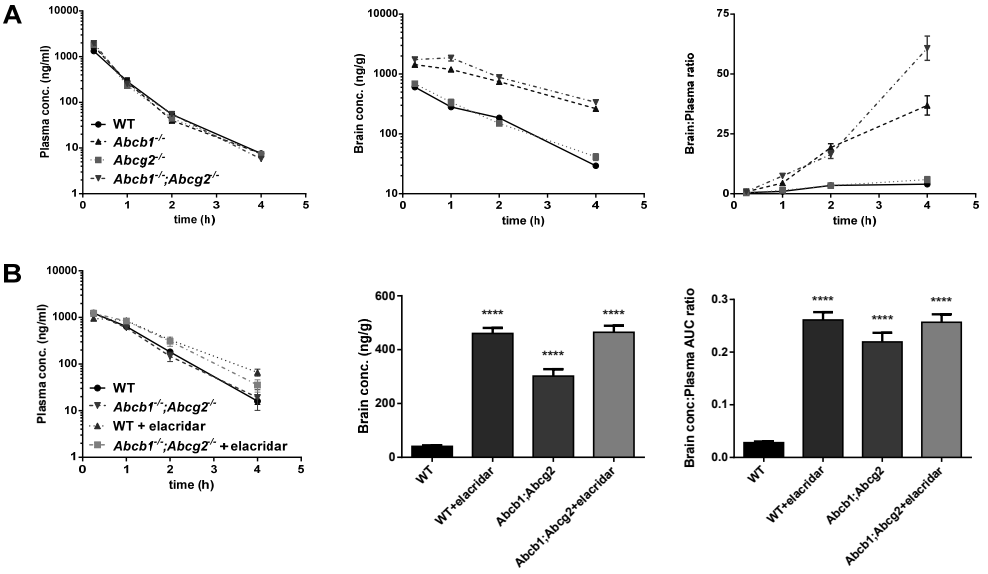

Figure 2 | The brain penetration of ABT-888 is limited by Abcb1 and Abcg2. (A) ABT-888 plasma concentrations, brain concentrations and brain–plasma ratios following i.v. administration of 10 mg/kg of ABT-888 (n = 5/time point/strain). (**B**) ABT-888 levels following 10 mg/kg p.o. administered to WT and *Abcb1a/b;Abcg2*$^{-/-}$ mice with/without co-administration of 100 mg/kg elacridar p.o. Blood samples were collected from the tail at 15 min, 1 h, 2 h and 4 h (n = 8/strain). Brain samples were harvested at 4 h after drug administration. Data are presented as means ± SEM, **** $p < 0.0001$ compared to WT. ANOVA followed by Bonferroni *post hoc* analysis.

As a second model, we used our spontaneous high-grade glioma model induced by lentivirus in LoxP conditional *Tp53*$^{F/F}$*;p16*^{Ink4a}*/p19*$^{ArfF/F}$*;K-Ras*^{V12}*;Luc* mice[21] (**Figure 1D**). TMZ alone has an effect on the survival in this model and elacridar enhances the efficacy of TMZ, because TMZ is a (weak) substrate of Abcb1 and Abcg2[26]. ABT-888 combined with TMZ only marginally improved median survival (25 *vs.* 21 days for TMZ+ABT-888 *vs.* TMZ respectively; $p = 0.14$). However, concomitant elacridar with TMZ+ABT-888 significantly improved median survival (33 *vs.* 25 days for TMZ+ABT-888+elacridar *vs.* TMZ+ABT-888 respectively; $p = 0.023$).

PTEN deficiency renders GBM sensitive to TMZ and ABT-888 treatment in vitro and in vivo

Deletion or inactivation of *PTEN* is a frequent event in GBM. By performing an *in silico* analysis on 117 glioblastoma patient samples, we found that patients whose tumor is deficient in *PTEN* have a significantly worse overall survival than patients whose tumors are proficient in *PTEN*, *viz.*

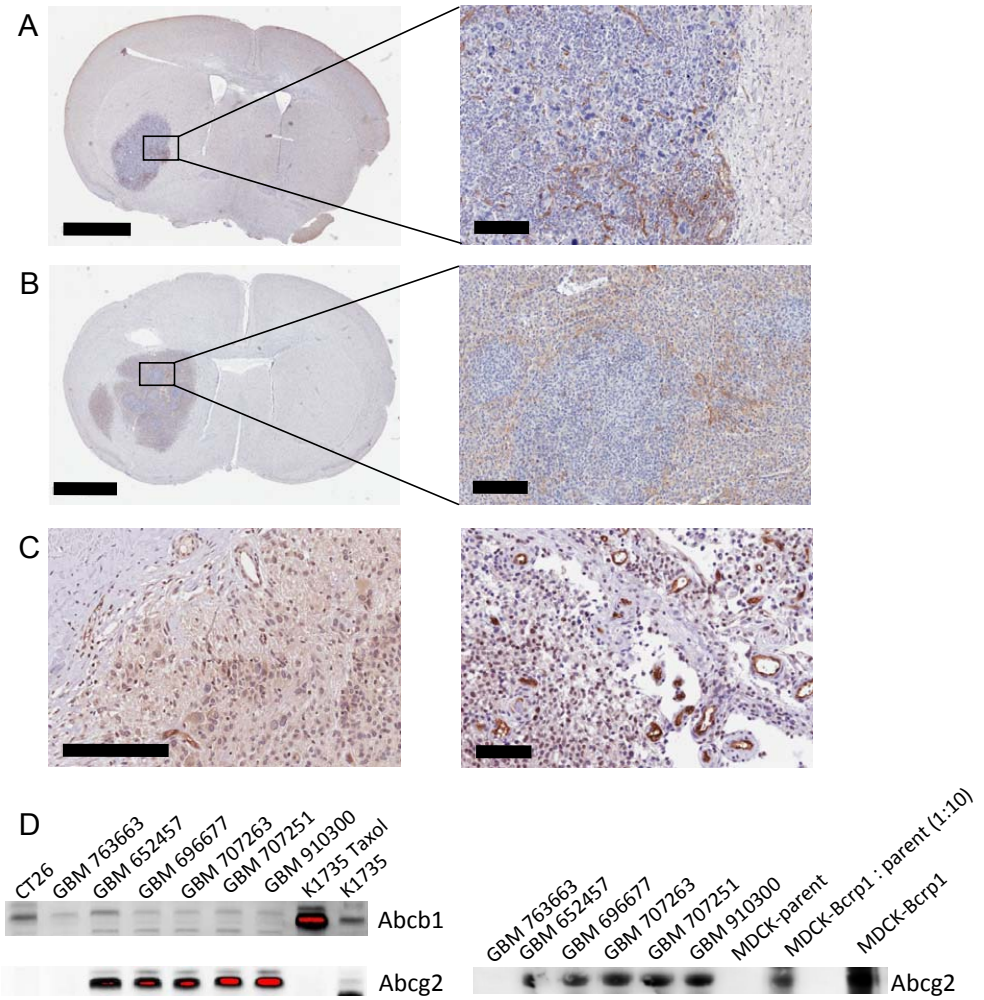

Figure 3 | Bcrp1/BCRP is present at the BBB/BBTB and also expressed in tumor cells. Bcrp1 staining in *Tp53*$^{-/-}$;*p16*^{Ink4a}/*p19*$^{Arf-/-}$;*K-Ras*^{V12};*Luc* GSC457 tumors in WT (**A**) and *Abcb1a/b;Abcg2*$^{-/-}$ nude mice (**B**). In WT mice Abcg2 is expressed at the BBB, in blood vessels throughout the tumor (BBTB) as well as on tumor cells. The presence of Abcg2 in tumor cells is even better visualized in the *Abcg2*-deficient *Abcb1a/b;Abcg2*$^{-/-}$ recipients. Notably, the expression in tumor cells is not uniform throughout the tumor. (**C**) Similar ABCG2 staining was observed in vessels and tumor cells in human GBM samples as depicted in these two examples. (Bar size: 2 mm (A,B left) and 200 um (all other panels). (**D**) Western blot analysis demonstrates the presence of Abcb1 and Abcg2 in GBM cell lines of different origins: *Tp53*$^{-/-}$;*p16*^{Ink4a}/*p19*$^{Arf-/-}$;*K-Ras*^{V12};*Luc* (GSC457, GSC300), *Pten*$^{-/-}$;*p16*^{Ink4a}/*p19*$^{Arf-/-}$;*K-Ras*^{V12};*Luc* (GSC677), *Tp53*$^{-/-}$;*Pten*$^{-/-}$;*p16*^{Ink4a}/*p19*$^{Arf-/-}$;*K-Ras*^{V12};*Luc* (GSC263, GSC251) and *p16*^{Ink4a}/*p19*$^{Arf-/-}$;*K-Ras*^{V12};*Luc* (GSC663). Control cell lines: CT26 is a non-drug selected murine colon cancer and K1735 is a non-drug selected murine melanoma cell line, both with endogenous expression of Abcb1, K1735–Taxol was drug-selected by stepwise increasing paclitaxel concentrations up to 0.5 μM, MDCK–Bcrp1 (murine Abcg2 transduced) and MDCK–parent (non-transduced) Madine–Darby canine kidney cells.

310 *vs.* 620 days; $p = 5.16 \times 10^{-6}$ (**Figure 4A**). On the other hand, it was recently shown by *in vitro* experiments that *PTEN*-null astrocytes have a compromised homologous recombination DNA repair pathway, rendering these more sensitive to treatment with TMZ and the PARP inhibitor ABT-888 due to synthetic lethality[27]. We have now used our GBM models to interrogate the role

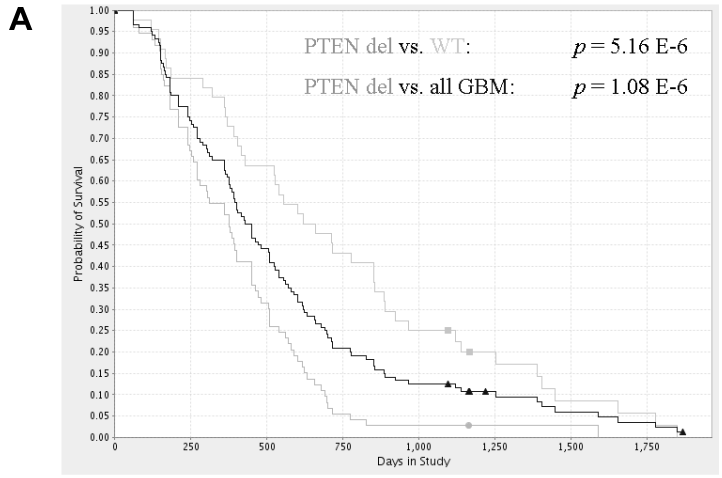
A
PTEN del vs. WT: p = 5.16 E-6
PTEN del vs. all GBM: p = 1.08 E-6
Probability of Survival
Days in Study
all GBM
PTEN del
PTEN WT

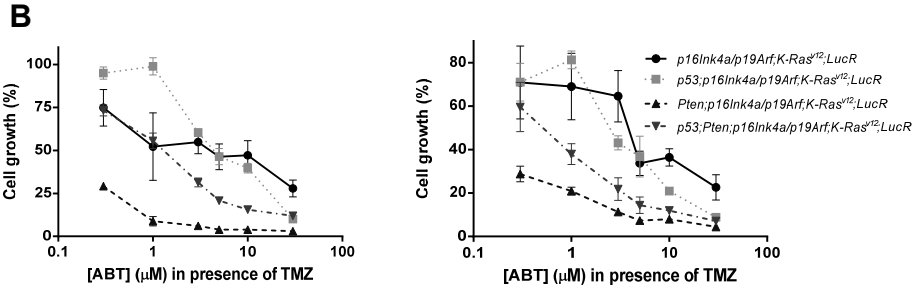
B
Cell growth (%)
[ABT] (μM) in presence of TMZ
p16Ink4a/p19Arf;K-Ras^V12;LucR
p53;p16Ink4a/p19Arf;K-Ras^V12;LucR
Pten;p16Ink4a/p19Arf;K-Ras^V12;LucR
p53;Pten;p16Ink4a/p19Arf;K-Ras^V12;LucR

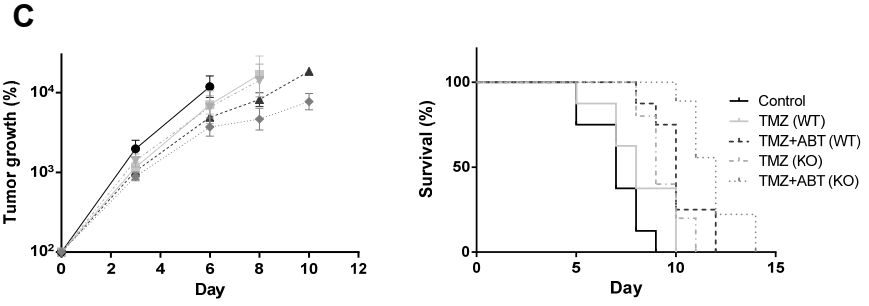
C
Tumor growth (%)
Day
Survival (%)
Control
TMZ (WT)
TMZ+ABT (WT)
TMZ (KO)
TMZ+ABT (KO)

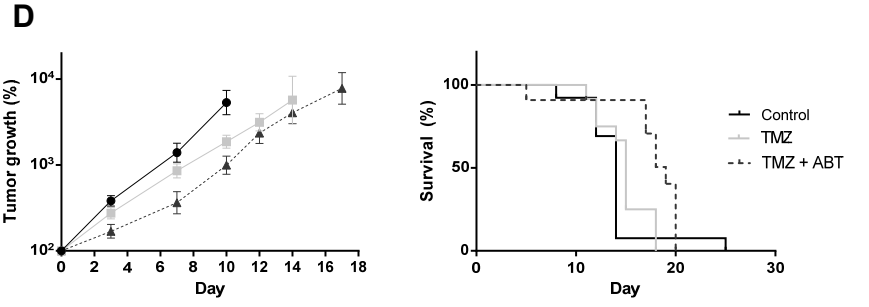
D
Tumor growth (%)
Day
Survival (%)
Control
TMZ
TMZ + ABT

Figure 4 | *PTEN*-deficient tumors are more sensitive to ABT-888 + TMZ treatment. (**A**) Kaplan–Meier analysis of *PTEN* deletion (≤ 1.8 copies) on overall survival of GBM patients (REMBRANDT database[36,37]). (**B**) Sensitivity (*in vitro*) of two panels of GBM cell lines of different genetic backgrounds exposed to 100 µM TMZ and increasing concentrations of ABT-888 for 5 days. Data (mean ± SEM; n = 4) growth percentage relative to treatment with TMZ alone. (**C**) Efficacy of ABT-888 in combination with TMZ against *Pten*$^{-/-}$*;p16*^{Ink4a}*/p19*$^{Arf-/-}$*; K-Ras*^{V12}*;Luc* GSC677 cells injected intracranially into WT or *Abcb1a/b;Abcg2*$^{-/-}$ (KO) mice and (**D**) (lentivirally induced) spontaneous *Pten*$^{F/F}$*;p16*^{Ink4a}*/p19*$^{ArfF/F}$*;K-Ras*^{V12}*;Luc* tumors. TMZ (100 mg/kg p.o. *q.d.*) alone or concurrently with ABT-888 (10 mg/kg p.o. *b.i.d.*) for 5 days. (**C**) and (**D**) left panels, relative tumor growth curves (means ± SEM). (**C**) and (**D**) right panels, Kaplan–Meier analysis of survival. Statistical significance was determined by Log-rank test. (**C**) n = 8, 8, 10, 9 for control, WT, TMZ (KO) and TMZ+ABT-888 (KO) groups respectively. (**D**) n = 13, 12, 11 for control, TMZ and TMZ+ABT-888 groups respectively.

of *PTEN* in the *in vivo* response to TMZ and ABT-888 treatment. GBM cell lines from spontaneous tumors including genotypes with additional *Pten* deletion demonstrate similar PARP inhibition by ABT-888 (**Supplementary Figure 2**). However, *Pten*$^{-/-}$*;p16*^{Ink4a}*/p19*$^{Arf-/-}$*;K-Ras*^{V12}*;Luc* GBM cells were much more sensitive to TMZ+ABT-888 than *Tp53;p16*^{Ink4a}*/p19*$^{Arf-/-}$*;K-Ras*^{V12}*;Luc* cells (**Figure 4B).** Likewise, additional deletion of *Pten* sensitized *Tp53*-deficient cells to ABT-888, albeit not to the level as of *Tp53*-proficient cells.

We treated intracranial *Pten*$^{-/-}$*;p16*^{Ink4a}*/p19*$^{Arf-/-}$*;K-Ras*^{V12}*;Luc* GSC677 GBM established in WT and *Abcb1a/b;Abcg2*$^{-/-}$ mice with TMZ or TMZ+ABT-888 (**Figure 4C**). The survival is short, due to the aggressive growth of these cells *in vivo*. In WT mice TMZ+ABT-888 treatment improved median survival relative to control group or TMZ treated animals (10, 8 and 7 days for TMZ+ABT-888, TMZ and controls, respectively; TMZ+ABT-888 *vs.* TMZ: $p = 0.044$; TMZ+ABT-888 *vs.* control: $p = 0.0004$). Note that such a therapeutic benefit of ABT-888 was not found in WT mice bearing *Tp53*$^{-/-}$*;p16*^{Ink4a}*/p19*$^{Arf-/-}$*;K-Ras*^{V12}*;Luc* GBM (**Figure 1A**). Importantly, *Abcb1a/b;Abcg2*$^{-/-}$ mice benefitted even more from treatment (median survival: 12 *vs.* 9 days for KO mice receiving TMZ+ABT-888 *vs.* TMZ respectively. $p = 0.0006$). Subsequently, we evaluated the effect of *Pten* deficiency in our lentivirally induced spontaneous *Pten*$^{F/F}$*;p16*^{Ink4a}*/p19*$^{ArfF/F}$*;K-Ras*^{V12}*;Luc* GBM model. Whereas the treatment effect in the *Tp53*$^{F/F}$*;p16*^{Ink4a}*/p19*$^{ArfF/F}$*;K-Ras*^{V12}*;Luc* GBM model generally becomes apparent not before some days after completion of the 5-day treatment, a marked effect in the spontaneous *Pten*-deficient tumors was already observed between days 0 and 7 (**Figure 4D**). Although there appears to be a trend toward a more accelerated growth later on, the median survival of mice receiving TMZ and ABT-888 combination treatment relative to TMZ alone increased significantly (19 *vs.* 15 days; $p = 0.0045$) while TMZ treatment alone did not affect median survival compared to vehicle control (15 *vs.* 14 days; $p = 0.15$).

DISCUSSION

This study, using clinically relevant *in vivo* high grade glioma mouse models, shows that the PARP inhibitor ABT-888 can improve the efficacy of TMZ chemotherapy against high-grade gliomas, but also identified two important factors that need to be considered when analyzing the clinical trials with ABT-888 in GBM. Firstly, ABCB1 and ABCG2 restrict both BBB penetration and tumor cell entry of ABT-888. Secondly, therapeutic benefit of ABT-888 added to TMZ in ABC transporter-

proficient WT mice was only significant in *Pten*-deficient tumors. Reassuringly, responses were observed at a dose level of ABT-888 yielding clinically relevant systemic exposure. Based on these results, we propose that the *PTEN* status of the tumor should be taken into account during the analysis of the clinical trials. Moreover, concomitant inhibition of ABCB1 and ABCG2 by elacridar may further improve the efficacy of ABT-888+TMZ combination treatment, so that *PTEN*-proficient tumors may also become responsive and *PTEN*-deficient tumors are sensitized even further.

TP53, *PTEN* and $p16^{INK4A}/p19^{ARF}$ are among the most frequently mutated or deleted genes in GBM[22]. We have previously developed high-grade glioma models using LoxP conditional transgenic mice that are deleted in brain cells following intracranial injection of lenti–Cre virus. These spontaneous tumors, as well as tumors from neurosphere cultured cell lines derived of these and reinjected into recipient mice, resemble many features that are characteristic for human GBM[21]. In the present study, we have used these models to evaluate the efficacy of ABT-888 to potentiate the activity of TMZ against high-grade glioma. Notably, the first study using WT mice injected with $Tp53^{-/-};p16^{Ink4a}/p19^{Arf-/-};K\text{-}Ras^{V12}$ GSC457 cells demonstrated only a very minor response to this combination therapy. We demonstrate that ABT-888 is a good substrate of the drug efflux transporters Abcb1 and Abcg2 and observed a more favorable response against GSC457 cells injected into $Abcb1a/b;Abcg2^{-/-}$ mice. Abcg2 was present in blood vessels of ABC transporter WT mice (**Figure 3**), but not in blood vessels of *Abcg2*-deficient $Abcb1a/b;Abcg2^{-/-}$ mice. The expression of ABCB1 in the tumor vessels of gliomas in patients is well documented[28-30]. Likewise, we were able to demonstrate the presence of ABCG2 in tumor vessels of patient specimens. Importantly, both in humans and in mice, ABCG2/Abcg2 was also found in tumor cells. Just recently, expression of ABCG2 in GBM was also demonstrated by Bahtia *et al.*[31], who reported nuclear localization of ABCG2 in a subpopulation of GBM cells. A similar pattern was also seen in some of our patient specimens (**Figure 3C**). Abcg2 staining was not uniform throughout the tumor. Considering that ABCG2 is a marker of early progenitor or stem cells, these Abcg2 positive regions may reflect the areas of the tumor enriched for tumor initiating cells. The presence of ABCB1 in GBM tumor cells is still debatable[32]. However, we successfully used elacridar in combination with TMZ and ABT-888 to further increase the efficacy in tumors grown in $Abcb1a/b;Abcg2^{-/-}$ recipient mice, which indicates that drug transporters in these cells form a secondary barrier, as schematically depicted in **Figure 5**.

Clearly, the response to ABT-888 that is observed in our high-grade glioma models is not as profound as reported previously[9,10] using other intracranial models. There are several reasons that may explain this discrepancy. First, our models have more tight BBTB properties, including the expression of ABC drug transporters, whereas the intracranial models in previously reported studies harbor leaky vessels, which may lead to over-prediction of their efficacy.

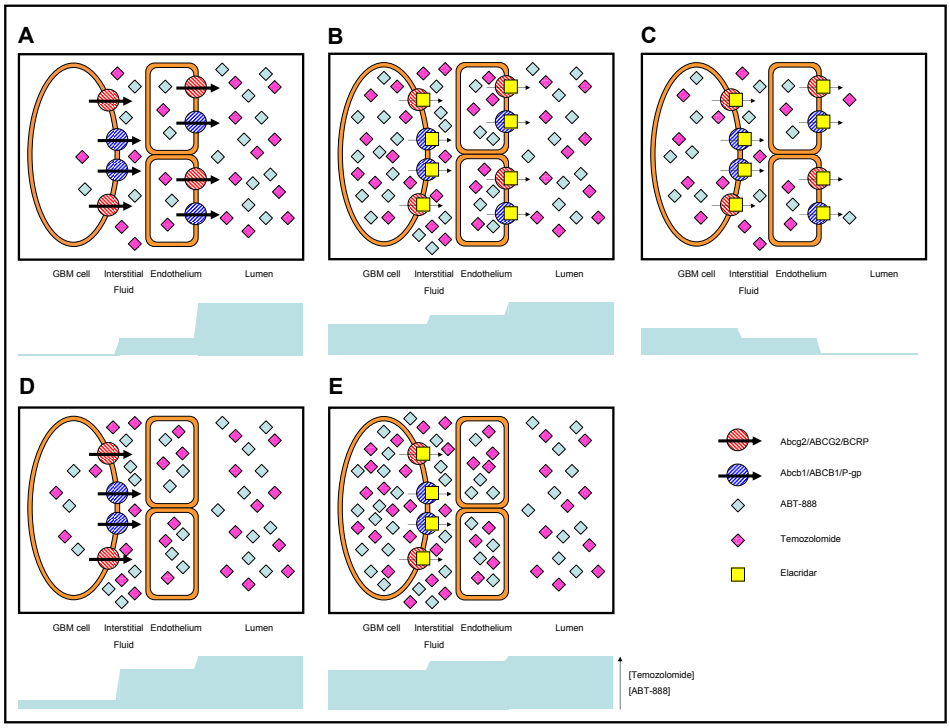

Figure 5 | ABCB1/ABCG2 at both the BBB/BBTB and in tumor cells limit drug entry and efficacy. (**A–C**) depicts the situation in WT mice, where drug penetration into tumors is higher when (**B**) elacridar inhibits ABCB1/ABCG2 at the BBB/BBTB and in tumor cells and (**C**) drug retention is prolonged when systemic clearance has taken place. (**D**) Drug penetration is higher in *Abcb1a/b;Abcg2*$^{-/-}$ (KO) mice but the best efficacy is achieved when (**E**) ABCB1/ABCG2 in tumor cells is inhibited by elacridar.

Secondly, the GBM cell lines used for the classical models have been maintained on serum containing media for many generations, which is known to cause loss of critical characteristics conserved within tumor stem cells. Importantly, these include chemotherapy resistance profiles such as expression of ABCG2, active DNA repair capacity, and resistance to apoptosis[33,34]. Most likely, the high-grade models (allograft and spontaneous) used in this study are much more stringent models for drug testing.

Finally, we used a dose of 10 mg/kg throughout all *in vivo* studies since this dose results in a clinically relevant systemic exposure of ABT-888. Recent clinical trials report a peak plasma level of 500 ng/ml with an AUC of 3500 ng/ml·h[35]. Previous preclinical studies have been using much higher doses of up to 50 mg/kg. Further increasing the dose in patients to improve efficacy, may result in unacceptable toxicity. Interestingly, co-administration of elacridar hardly affected the systemic exposure of ABT-888 (**Figure 2**), but enhanced the brain concentration of ABT-888 by 11-fold at 4 h. Consequently, this combination may enable improved local drug delivery to the brain, without increasing systemic exposure and possibly toxicity of ABT-888.

When exploring the efficacy of ABT-888 in our panel of spontaneous high-grade glioma derived cell lines, we also found that cell lines that are deficient in *Pten* were much more sensitive to TMZ and ABT-888 treatment. Our results are in line with the *in vitro* data showing that *PTEN*-null astrocytes have a disturbance in the homologous recombination DNA repair pathway causing synthetic lethality when base excision repair activity is inhibited by a PARP inhibitor[27]. Next, we took advantage of the fact that we could further explore the clinical relevance of this finding using our *in vivo* high-grade glioma models. Both WT and *Abcb1a/b;Abcg2*$^{-/-}$ mice bearing *Pten*$^{-/-}$;*p16*^{Ink4a}/*p19*$^{Arf-/-}$;*K-Ras*^{V12} GSC677 tumors responded better to the TMZ and ABT-888 treatment than the mice bearing *Tp53*-null, *Pten*-proficient tumors. Notably, however, although the *Pten*-deficient GSC677 cell line is more sensitive to TMZ and ABT-888 treatment, the effect of this combination on the tumor growth *in vivo* was not as dramatic as might have been hoped for based on the results obtained *in vitr*o. This finding on one hand reminds us that the tumor micro-environment of GBM cells proliferating *in vivo* can help these cells to escape from lethal drug effects. On the other hand, it highlights the importance of using the appropriate preclinical models to evaluate drug efficacy.

We expect that these preclinical findings will be useful to interpret the outcome of the currently ongoing clinical trials with ABT-888 in glioma patients (ClinicalTrials.gov Identifiers NCT01026493, NCT01514201, NCT00770471), In particular our data call for a subgroup analysis in GBM patients with *PTEN* deletion. *PTEN* loss is a frequent event in GBM (36% of cases). Notably, as assessed by an *in silico* analysis performed on 117 glioblastoma patients, *PTEN* loss is associated with a more dismal prognosis but our study provides reasonable evidence that this subgroup of patients may benefit most from ABT-888. This benefit, however, may get lost when analyzing all GBMs as one group. Furthermore, we have shown that the efficacy of ABT-888 and TMZ combination therapy is attenuated by ABCB1 and ABCG2, supporting the initiation of clinical trials investigating the potential of ABC transporter inhibitors (*e.g.*, elacridar) in glioma therapy.

REFERENCES

1. Stupp, R., *et al.* Radiotherapy plus concomitant and adjuvant temozolomide for glioblastoma. *N Engl J Med* **352**, 987-996 (2005).
2. Alexander, B.M., *et al.* Targeting DNA repair and the cell cycle in glioblastoma. *J Neurooncol* **107**, 463-477 (2012).
3. Jagtap, P. & Szabo, C. Poly(ADP-ribose) polymerase and the therapeutic effects of its inhibitors. *Nat Rev Drug Discov* **4**, 421-440 (2005).
4. Calabrese, C.R., *et al.* Anticancer chemosensitization and radiosensitization by the novel poly(ADP-ribose) polymerase-1 inhibitor AG14361. *J Natl Cancer Inst* **96**, 56-67 (2004).
5. Curtin, N.J., *et al.* Novel poly(ADP-ribose) polymerase-1 inhibitor, AG14361, restores sensitivity to temozolomide in mismatch repair-deficient cells. *Clin Cancer Res* **10**, 881-889 (2004).
6. Cheng, C.L., *et al.* Poly(ADP-ribose) polymerase-1 inhibition reverses temozolomide resistance in a DNA mismatch repair-deficient malignant glioma xenograft. *Mol Cancer Ther* **4**, 1364-1368 (2005).
7. Miknyoczki, S.J., *et al.* Chemopotentiation of temozolomide, irinotecan, and cisplatin activity by CEP-6800, a poly(ADP-ribose) polymerase inhibitor. *Mol Cancer Ther* **2**, 371-382 (2003).
8. Miknyoczki, S., *et al.* The selective poly(ADP-ribose) polymerase-1(2) inhibitor, CEP-8983, increases the sensitivity of chemoresistant tumor cells to temozolomide and irinotecan but does not potentiate myelotoxicity. *Mol Cancer Ther* **6**, 2290-2302 (2007).
9. Palma, J.P., *et al.* ABT-888 confers broad in vivo activity in combination with temozolomide in diverse tumors. *Clin Cancer Res* **15**, 7277-7290 (2009).
10. Donawho, C.K., *et al.* ABT-888, an orally active poly(ADP-ribose) polymerase inhibitor that potentiates DNA-damaging agents in preclinical tumor models. *Clin Cancer Res* **13**, 2728-2737 (2007).
11. Deeken, J.F. & Loscher, W. The blood-brain barrier and cancer: transporters, treatment, and trojan horses. *Clin*

Cancer Res **13**, 1663-1674 (2007).
12. de Vries, N.A., *et al.* Blood-brain barrier and chemotherapeutic treatment of brain tumors. *Expert Rev Neurother* **6**, 1199-1209 (2006).
13. Upadhyay, N. & Waldman, A.D. Conventional MRI evaluation of gliomas. *Br J Radiol* **84**, S107-111 (2011).
14. de Vries, N.A., *et al.* P-glycoprotein and breast cancer resistance protein: two dominant transporters working together in limiting the brain penetration of topotecan. *Clin Cancer Res* **13**, 6440-6449 (2007).
15. Agarwal, S., *et al.* Delivery of molecularly targeted therapy to malignant glioma, a disease of the whole brain. *Expert Rev Mol Med* **13**, e17 (2011).
16. Lin, F., *et al.* Targeting core (mutated) pathways of high-grade gliomas: challenges of intrinsic resistance and drug efflux. *CNS Oncol* **2**, 271-288 (2013).
17. Szakacs, G., *et al.* Targeting multidrug resistance in cancer. *Nat Rev Drug Discov* **5**, 219-234 (2006).
18. Kusuhara, H. & Sugiyama, Y. ATP-binding cassette, subfamily G (ABCG family). *Pflugers Arch* **453**, 735-744 (2007).
19. Zhou, B.B., *et al.* Tumour-initiating cells: challenges and opportunities for anticancer drug discovery. *Nat Rev Drug Discov* **8**, 806-823 (2009).
20. Lee, J., *et al.* Tumor stem cells derived from glioblastomas cultured in bFGF and EGF more closely mirror the phenotype and genotype of primary tumors than do serum-cultured cell lines. *Cancer Cell* **9**, 391-403 (2006).
21. de Vries, N.A., *et al.* Rapid and robust transgenic high-grade glioma mouse models for therapy intervention studies. *Clin Cancer Res* **16**, 3431-3441 (2010).
22. The Cancer Genome Atlas Research Network. Comprehensive genomic characterization defines human glioblastoma genes and core pathways. *Nature* **455**, 1061-1068 (2008).
23. Parise, R.A., *et al.* Liquid chromatography-mass spectrometric assay for the quantitation in human plasma of ABT-888, an orally available, small molecule inhibitor of poly(ADP-ribose) polymerase. *J Chromatogr B Analyt Technol Biomed Life Sci* **872**, 141-147 (2008).
24. Zhang, Y., *et al.* PKSolver: an add-in program for pharmacokinetic and pharmacodynamic data analysis in Microsoft Excel. *Comput Methods Programs Biomed* **99**, 306-314 (2010).
25. Bruggeman, S.W. *et al.* Bmi1 controls tumor development in an ink4a/arf-independent manner in a mouse model for glioma. *Cancer Cell* **12**, 328-341 (2007).
26. van Tellingen, O., *et al.* Inhibition of breast cancer resistance protein and P-glycoprotein enhances the brain penetration of temozolomide. *Cancer Res* **68 Suppl 9**, 3243 (2008).
27. McEllin, B., *et al.* PTEN loss compromises homologous recombination repair in astrocytes: implications for glioblastoma therapy with temozolomide or poly(ADP-ribose) polymerase inhibitors. *Cancer Res* **70**, 5457-5464 (2010).
28. Toth, K., *et al.* MDR1 P-glycoprotein is expressed by endothelial cells of newly formed capillaries in human gliomas but is not expressed in the neovasculature of other primary tumors. *Am J Pathol* **149**, 853-858 (1996).
29. Fattori, S., *et al.* Human brain tumors: multidrug-resistance P-glycoprotein expression in tumor cells and intratumoral capillary endothelial cells. *Virchows Arch* **451**, 81-87 (2007).
30. Guo, Z., *et al.* Expression and clinical significance of multidrug resistance proteins in brain tumors. *J Exp Clin Cancer Res* **29**, 122 (2010).
31. Bhatia, P., *et al.* Breast cancer resistance protein (BCRP/ABCG2) localises to the nucleus in glioblastoma multiforme cells. *Xenobiotica* **42**, 748-755 (2012).
32. Decleves, X., *et al.* Role of ABC transporters in the chemoresistance of human gliomas. *Curr Cancer Drug Targets* **6**, 433-445 (2006).
33. Liu, G., *et al.* Analysis of gene expression and chemoresistance of CD133$^+$ cancer stem cells in glioblastoma. *Mol Cancer* **5**, 67 (2006).
34. Dean, M., *et al.* Tumour stem cells and drug resistance. *Nat Rev Cancer* **5**, 275-284 (2005).
35. Kummar, S., *et al.* A Phase I study of veliparib in combination with metronomic cyclophosphamide in adults with refractory solid tumors and lymphomas. *Clin Cancer Res* **18**, 1726-1734 (2012).
36. Madhavan, S., *et al.* Rembrandt: helping personalized medicine become a reality through integrative translational research. *Mol Cancer Res* **7**, 157-167 (2009).
37. National Cancer Institute. *Rembrandt Home Page: http://rembrandt.nci.nih.gov* Accessed Sept 25, 2013.

SUPPLEMENTARY METHODS

In vitro transport experiments

To determine whether ABT-888 is a substrate of murine Abcb1a (Mdr1a) or human ABCB1 (MDR1), we analyzed the translocation of ABT-888 (0.5 μM) in a concentration equilibrium setting using the parental LLC pig-kidney cell line (LLC–parent) and sub-lines transduced with murine Abcb1a (LLC–Mdr1a) or human ABCB1 (LLC–MDR1). Similarly, the parental Madine–Darby canine kidney (MDCK) type II cell line (MDCK–parent) and murine Abcg2 (MDCK–Bcrp1) or human ABCG2 transduced sub-lines (MDCK–BCRP) were used to determine whether ABT-888 was a substrate of murine Abcg2 or human ABCG2. Cells were seeded on Transwell microporous polycarbonate membrane filters (3.0 μm pore size, 24 mm diameter; Costar Corning) at a density of 2×106 cells per well in complete MEM medium. Transwell experiments were performed Opti-

MEM medium. Zosuquidar (5 μM) was added to the medium to inhibit endogenous canine ABCB1 in all experiments with MDCK cell lines, and to inhibit the endogenous or exogenous ABCB1/Abcb1 activity in experiments with LLC cell when necessary. Elacridar was added to the medium to inhibit the endogenous or exogenous ABCG2/Abcg2 (and ABCB1/Abcb1) activity. Carboxyl-[14C]-inulin (PerkinElmer) was added to check the integrity of the membrane (approximately 1.6×106 DPM/ml). Samples of 50 μL were taken at 30, 120, 180 and 240 min and used for drug analysis. For *in vitro* transport assays, ABT-888 was analyzed by HPLCUV at 295 nm using a 10 min, 0.2 ml/min flow rate, 4% to 40% methanol in 0.1% formic acid in water gradient set-up.

The General Linear Model repeated measures procedure was applied to analyze the results of concentration equilibrium transport experiments using SPSS (v17.0; SPSS Inc; Chicago, IL). Data was grouped by defining 4 sampling time points (1, 2, 3 and 4 h) as a 4-level within-subjects factor. Simple contrast was selected to compare the differences between the mean observed values of 2 h, 3 h and 4 h and 1 h. Then, multivariate significance tests were performed to determine whether the apical–basolateral differences of the ABT-888 levels were significantly increased by the factor of time.

SUPPLEMENTARY FIGURES

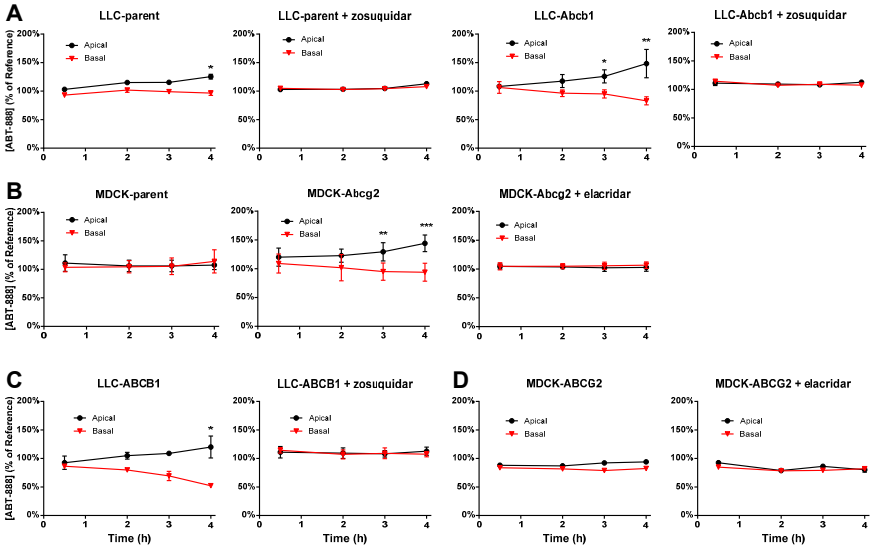

Supplementary Figure 1 | *In vitro* transwell assays. Transepithelial translocation of ABT-888 was assessed using (**A and C**) parental LLC–PK1 cells and cells transduced with mouse Abcb1a (LLC–Mdr1a) or human ABCB1 (LLC–MDR1), or (**B and D**) parental MDCKII cells (MDCK–parent) and cells transduced with mouse Abcg2 (MDCK–Bcrp1) or human ABCG2 (MDCK–BCRP). The setup was a concentration equilibrium assay, starting with an equal drug concentration in the apical and basolateral compartments. Zosuquidar (5 μM) was used for specific inhibition of Abcb1/ABCB1 mediated transport in LLC–PK1, LLC–Mdr1a or LLC–MDR1 cell lines and elacridar (5 μM) was used to inhibit transport mediated by Abcg2/ABCG2 in MDCK–Bcrp1 or MDCK–BCRP cell lines. Results are presented as the ratio of observed concentration in time to initial concentration. Data are means ± SD; n = 6 per experiment. * $p < 0.05$, ** $p < 0.01$, *** $p < 0.001$. Statistical significance was determined using the General Linear Model repeated measures procedure.

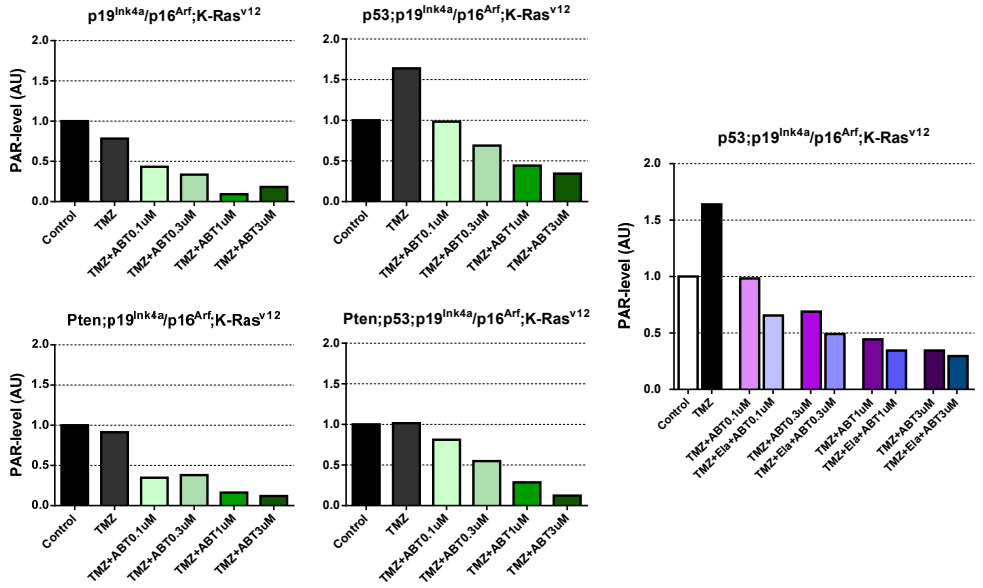

Supplementary Figure 2 | PAR levels by Western blot analysis. Poly ADP-ribose (PAR) Western Blotting results of GBM cell lysates after ABT-888 treatment. Laminin cultured GBM cells were exposed to TMZ (100 μM) alone or together with ABT-888 at concentrations of 0.1, 0.3, 1 and 3 μM for 4 hours after which PAR levels in cell lysates were determined by immunoblotting with an anti-PAR antibody and normalized by tubulin.

Chapter 14

ABCB1 ATTENUATES THE BRAIN PENETRATION OF THE PARP INHIBITOR AZD2461

M.C. de Gooijer, L.C.M. Buil, C.H. Çitirikkaya, J. Hermans, J.H. Beijnen, and O. van Tellingen

Molecular Pharmaceutics. 2018;15(11):5236-5243

ABSTRACT

Poly (ADP ribose) polymerase (PARP) inhibitors are a relatively new class of anticancer agents that have attracted attention for treatment of glioblastoma because of their ability to potentiate temozolomide chemotherapy. Previous studies have demonstrated that sufficient brain penetration is a prerequisite for efficacy of PARP inhibitors in glioma mouse models. Unfortunately however, most of the PARP inhibitors developed to date have a limited brain penetration due to the presence of P-glycoprotein (P-gp) and breast cancer resistance protein (BCRP) at the blood–brain barrier. AZD2461 is a novel PARP inhibitor that is unaffected by P-gp mediated resistance in breast cancer models and thus appears to have promising characteristics for brain penetration. We here use a comprehensive set of *in vitro* and *in vivo* models to study the brain penetration and oral bioavailability of AZD2461. We report that AZD2461 has a good membrane permeability. However, it is a substrate of P-gp and BCRP and P-gp in particular limits its brain penetration *in vivo*. We show that AZD2461 has a low oral bioavailability, although not affected by P-gp and BCRP. Together, these findings are not in favor of further development of AZD2461 for treatment of glioblastoma.

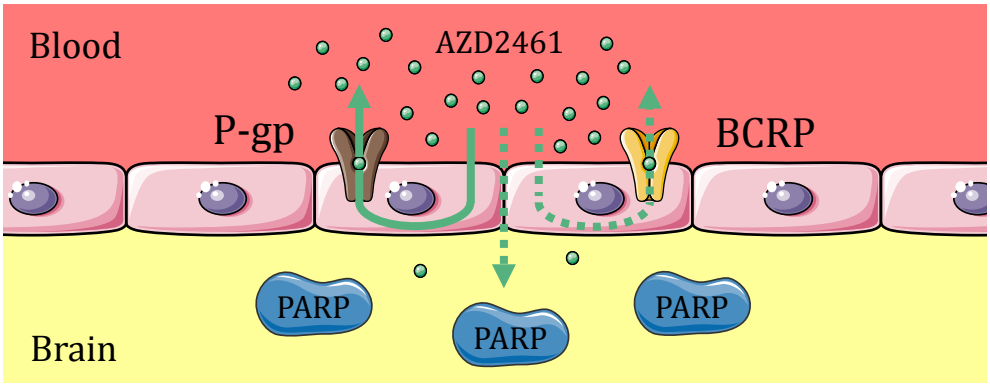

INTRODUCTION

Poly (ADP-ribose) polymerase (PARP) is an important enzyme in the DNA damage response[1]. It is mainly involved in base excision repair, but also plays a role in non-homologous end-joining. Cancer cells that lost a functional homologous recombination pathway depend more heavily on these DNA damage response pathways, and therefore PARP inhibitors have gained major interest for cancer treatment. The first breakthrough in the field of PARP inhibition came when olaparib, a first-in-class PARP inhibitor, demonstrated synthetic lethality in BRCA1-deficient triple negative breast cancer[2]. Unfortunately, preclinical studies have demonstrated that olaparib is a substrate for the efflux transporter P-glycoprotein (P-gp), and that upregulation of this transporter in tumor cells led to acquired resistance[2, 3].

P-gp and its relative breast cancer resistance protein (BCRP) have been discovered as factors conferring multidrug resistance to tumor cells, but they are also involved in the protection of healthy tissue throughout the body[4]. First, they are abundantly expressed in the liver and kidney where they are involved in excretion. Secondly, they are present in the intestinal wall and limit intestinal uptake of potentially harmful substances. Lastly and importantly, they are the dominant efflux transporters at various barrier sites such as the blood–brain barrier (BBB) and blood–testis barrier and reduce the distribution of xenobiotics into these organs. The BBB consists of the brain endothelial cells that are being supported by pericytes and astrocyte foot processes[5]. P-gp (ABCB1/MDR1) and BCRP (ABCG2) are expressed at the apical membrane of the brain endothelial cells and recognize and efflux many xenobiotics, including numerous anticancer agents, back into the blood stream when attempting to diffuse across the BBB[6].

The role of P-gp and BCRP in the BBB is of great interest for treatment of intracranial cancers such as glioblastoma (GBM), since these are all at least in part protected by a functional BBB[7]. Previous studies have shown that drugs inhibiting validated targets in GBM, such as Wee1 or CDK4/6, can be efficacious against extracranially transplanted GBM tumors or when BBB functionality is compromised as a result of genetic loss of ATP-binding cassette (ABC) transporters[8, 9]. However, many of these agents are much less efficacious when the tumor is situated behind a functionally intact BBB. PARP inhibitors have demonstrated promising preclinical results in treatment of GBM as a sensitizer to temozolomide chemotherapy, especially in PTEN-deficient tumors that may consequently have a compromised homologous recombination pathway[10, 11]. Unfortunately however, P-gp and BCRP at the BBB have already been shown to limit the brain penetration and prevent antitumor efficacy of earlier generation PARP inhibitors such as rucaparib[12, 13], talazoparib[14] and veliparib[10].

Recently, a new PARP inhibitor has been described that is not susceptible to P-gp mediated resistance in BRCA-deficient mammary tumors[15, 16]. Tumors that were fully resistant to olaparib

due to P-gp upregulation were still responsive to treatment with AZD2461. Based on these data, it was postulated that AZD2461 is not a substrate of P-gp, although pharmacokinetic data was not provided. Here, we investigate whether AZD2461 is a substrate of P-gp and BCRP and whether these transporters limit the brain penetration of AZD2461 to assess its potential for further clinical development for treatment of intracranial malignancies. We report that AZD2461 is mainly a P-gp substrate and that its brain penetration in wild-type mice is considerably reduced as a result of P-gp efflux activity at the BBB. As such, we conclude that AZD2461 is not an attractive candidate for further clinical investigation in the context of brain tumors.

METHODS

Drugs

AZD2461 was purchased from Syncom B.V. (Groningen, The Netherlands), zosuquidar from Eli Lilly (Indianapolis, IN) and olaparib from MedKoo (Research Triangle Park, NC). Elacridar was kindly provided by GlaxoSmithKline (Research Triangle Park, NC).

Cell culture

All cell lines used here were previously generated at the Netherlands Cancer Institute by dr. A.H. Schinkel[17-19]. All cells were cultured under 37 °C and 5% CO_2 conditions in minimal essential medium containing 10% FBS, 1% L-glutamine, 1% sodium pyruvate, 1% MEM vitamins, 1% non-essential amino acids and 1% penicillin/streptomycin (all from Life Technologies, Carlsbad, CA).

Concentration equilibrium transport assays

Conventional bidirectional transport assays (CTAs) and concentration equilibrium transport assays (CETAs) were carried out as described previously[20]. AZD2461 was used at a concentration of 100 nM. Zosuquidar (a P-gp inhibitor) and elacridar (a dual P-gp/BCRP inhibitor) were used at a concentration of 5 μM to block transport activity when needed, as this concentration is sufficient to fully inhibit P-gp and BCRP-mediated transport. Transwells exceeding 1.5% Carboxyl-[^{14}C]-inulin translocation per hour were excluded from the analysis as these were considered leaky.

To prepare AZD2461 transport assay samples for LC–MS/MS analysis, 10 μL medium samples were mixed with 30 μL of acetonitrile:formic acid (100:1 v/v). After centrifugation, the supernatant was 5-fold diluted in water. AZD2461 was subsequently measured using an LC–MS/MS system as described below.

Animals

Mice were housed on a 12 hour light/dark cycle. Food and water was provided *ad libitum*. Room temperature was maintained at 21 ºC. All animal housing and studies were approved by the institutional animal experimental committee and conducted according to national law and institutional guidelines.

Pharmacokinetic studies

We carried out pharmacokinetic studies with AZD2461 in wild-type (WT), *Abcg2*$^{-/-}$, *Abcb1a/b*$^{-/-}$ and *Abcb1a/b;Abcg2*$^{-/-}$ FVB mice[21-23]. AZD2461 was formulated in DMSO:Cremophor EL:water (1:1:8 v/v/v) for i.v. dosing at both 10 mg/kg and 50 mg/kg. For oral (100 mg/kg) administration, the drug was suspended in 0.5% hydroxypropyl methyl cellulose and mixed overnight at 4°C for optimal suspension. Bleeding from the tail vein was used to draw blood at intermediate time points, whereas at the terminal time point blood was also collected by cardiac puncture. Brain tissue was subsequently collected. Plasma was obtained from whole blood by centrifugation (5 min, 5,000 rpm, 4°C). After weighing, tissues were homogenized in 1% (w/v) bovine serum albumin using a FastPrep®-24 (MP-Biomedicals, NY). AZD2461 was extracted from plasma and brain homogenate via tert-butyl methyl ether liquid-liquid extraction. Olaparib was used as an internal standard for LC–MS/MS analysis.

LC–MS/MS analysis

AZD2461 concentrations were measured using an LC–MS/MS system that consisted of an UltiMate 3000 LC System (Dionex, Sunnyvale, CA) and an API 4000 mass spectrometer (Sciex, Framingham, MA). Samples were analyzed using a ZORBAX Extend-C18 column (Agilent, Santa Clara, CA), preceded by a Securityguard C18 pre-column (Phenomenex, Utrecht, The Netherlands). Elution was done using a mixture of mobile phase A (0.1% formic acid in water (v/v)) and mobile phase B (methanol) in a 5 minute gradient from 20% to 95%B, followed by 95%B that was maintained for 3 min and then re-equilibrated at 20%B. Multiple reaction monitoring parameters were 396.2/281.1 (AZD2461) and 435.2/281.2 (olaparib). System control and data analysis was done using Analyst® 1.6.2 software (AB Sciex; Foster City, CA). The accuracy and precision of the LC–MS/MS method were within the acceptable range. The detection limit was 0.3 nM, the lower limit of quantification was 2 nM and the upper limit of quantification was 100 nM AZD2461 in plasma.

Pharmacokinetic and statistical analysis

CETA results were analyzed with the General linear model repeated measures procedure of SPSS (v22; SPSS Inc, Chicago, IL) as described in detail before [20]. All other statistical analyses in this

study involved one-way analysis of variance followed by *post hoc* Bonferroni tests since more than two groups were compared. For all analyses, differences were considered statistically significant when $p<0.05$. The pharmacokinetic parameters of AZD2461 were determined using the PK solver plugin in Microsoft Excel[24]. The standard error of the oral bioavailability was calculated using the formula below:

$$SE_F = F\sqrt{\left(\frac{SE_{AUC_{p.o.}}}{AUC_{p.o.}}\right)^2 + \left(\frac{SE_{AUC_{i.v.}}}{AUC_{i.v.}}\right)^2}$$

RESULTS

P-gp and BCRP transport AZD2461 in vitro

We first established whether AZD2461 (**Figure 1A**) could be transported by P-gp and BCRP *in vitro*. To this end, we conducted a set of transport experiments using cell lines that overexpress human or murine P-gp or BCRP. We cultured these cells in a transwell system, essentially creating an apical and basolateral compartment being separated by a cellular monolayer. Before analyzing transporter substrate affinity, we first confirmed that AZD2461 is sufficiently permeable over the monolayer using a conventional transport assay (CTA) setup (**Figure 1B**), In this setup, a given compound is added to one compartment (the donor compartment) and the concentration in the other compartment (the acceptor compartment) is measured over time as a measure of a compound's cellular membrane permeability. The establishment of a compound's membrane permeability is important for the interpretation of the results of the more sensitive concentration equilibrium transport assay (CETA). In a CETA, a compound is added to both compartments of the transwell system at equal concentrations and the concentration in both compartments is again measured over time. However, without establishing a compound's potential to diffuse over the monolayer, absence of translocation in a CETA can also be caused by poor membrane permeability.

After we established that AZD2461 is membrane permeable, we measured AZD2461 translocation over ABC transporter-expressing cellular monolayers using the CETA setup. No translocation was observed in the parental cell lines, whereas AZD2461 was efficiently translocated by monolayers overexpressing murine Bcrp1, murine Mdr1a (P-gp) and human MDR1 (P-gp) (**Figure 1C**). These findings clearly indicate that AZD2461 is a substrate for murine BCRP and murine and human P-gp. No translocation occurred in human BCRP-overexpressing monolayers. It is a common finding, however, that compounds are more efficiently translocated by the murine Bcrp1 than the human BCRP expressing MDCK cells. We expect that this is caused by a lower and/or less polarized expression of BCRP in the MDCK–BCRP cell line. Consequently, it is still possible that AZD2461 can be transported by human BCRP, albeit that it is likely just a weak substrate.

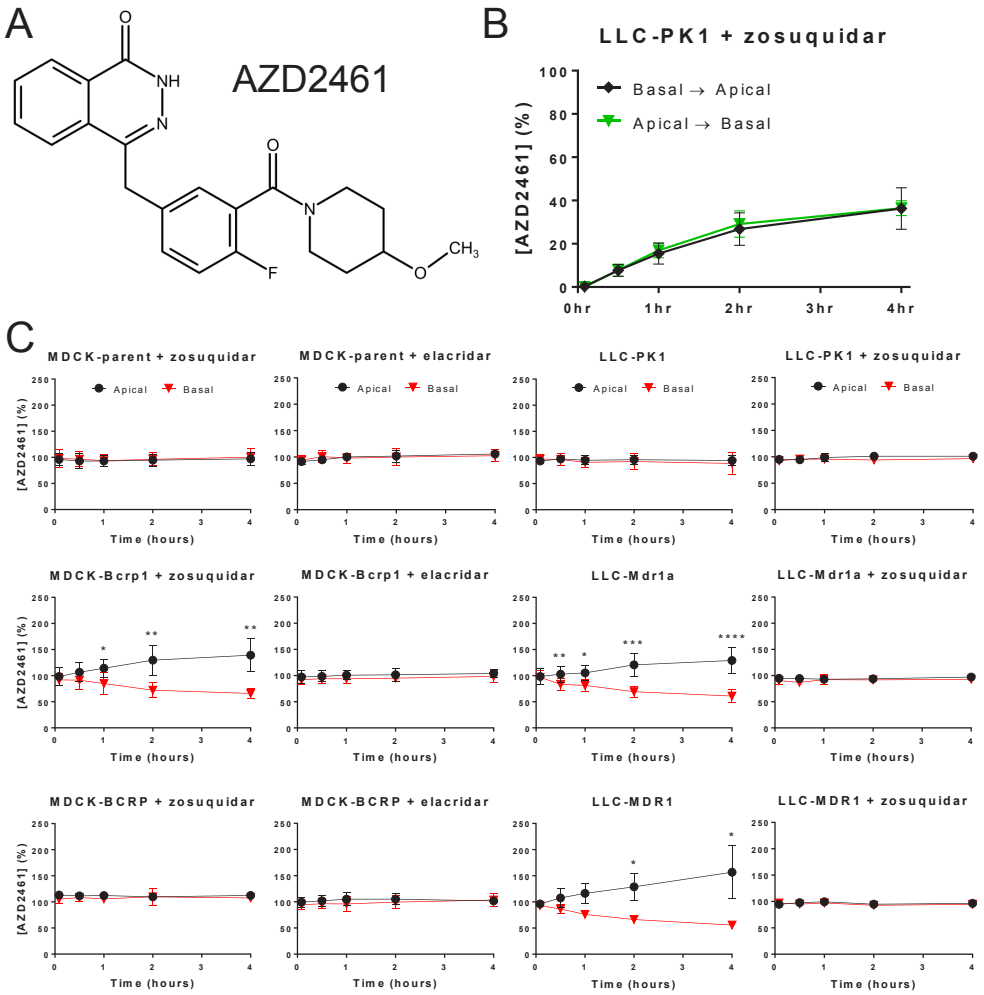

Figure 1 | Transport of AZD2461 by P-gp and BCRP *in vitro*. (**A**) The chemical structure of AZD2461. (**B**) A conventional transport assay (CTA) in presence of zosuquidar to block endogenous P-gp activity. In both directions, AZD2461 efficiently diffuses over an LLC–PK1 monolayer. Within 4 hours, the AZD2461 almost reached equilibrium. (**C**) Concentration equilibrium transport assays (CETAs) using MDCK or LLC cells that overexpress murine BCRP, (Bcrp1), human BCRP, murine P-gp (Mdr1a) or human P-gp (MDR1). Translocation of AZD2461 was observed over MDCK–Bcrp1, LLC–Mdr1a and LLC–MDR1 monolayers. In all cases, transport selectivity was confirmed by using the P-gp inhibitor zosuquidar or the dual P-gp/BCRP inhibitor elacridar. Zosuquidar was used in all MDCK cell lines to inhibit endogenous P-gp activity. Data are represented as mean ± SD (n ≥ 4); * $p < 0.05$, ** $p < 0.01$, *** $p < 0.001$, **** $p < 0.0001$.

P-gp restricts the brain penetration of AZD2461 in vivo

To investigate whether transport affinity for P-gp and BCRP has any impact on the brain penetration of AZD2461, we measured the AZD2461 brain concentration in wild-type (WT) FVB mice following intravenous administration and compared it to the concentrations obtained in mice that were genetically engineered to lack one or both of these ABC transporters. Mice lacking

Bcrp1 (*Abcg2*$^{-/-}$) did not have a higher brain concentration than WT mice, indicating that P-gp is able to fully compensate for the loss of Bcrp1 in these mice (**Figure 2**). In contrast, we could observe a 3-fold increased brain concentration in mice lacking P-gp (*Abcb1a/b*$^{-/-}$), indicating that this transporter restricts the brain penetration of AZD2461. A combined deletion of P-gp and BCRP (*Abc1a/b;Abcg2*$^{-/-}$) did not result in a further elevated AZD2461 brain level compared to *Abcb1a/b*$^{-/-}$ mice, suggesting that Bcrp1 does not efficiently transport AZD2461 at the BBB. Since Bcrp1 is able to transport AZD2461 *in vitro* (**Figure 1C**), it could be that a difference in the brain–plasma ratio of *Abcb1a/b*$^{-/-}$ and *Abc1a/b;Abcg2*$^{-/-}$ mice does exist. However, in order to reach statistical significance, many more mice will be required with these small differences. The expression of Bcrp1 at the murine BBB is about 5-fold lower compared to Mdr1a[25]. Therefore, the effects of P-gp are much easier to detect in mice than those of Bcrp1, especially when studying weak substrates. Notably, however, the expression of BCRP at the human BBB is higher than that of P-gp[26]. The observation that AZD2461 is a substrate of Bcrp1 therefore suggests that the effects of BCRP at the human BBB may be more pronounced.

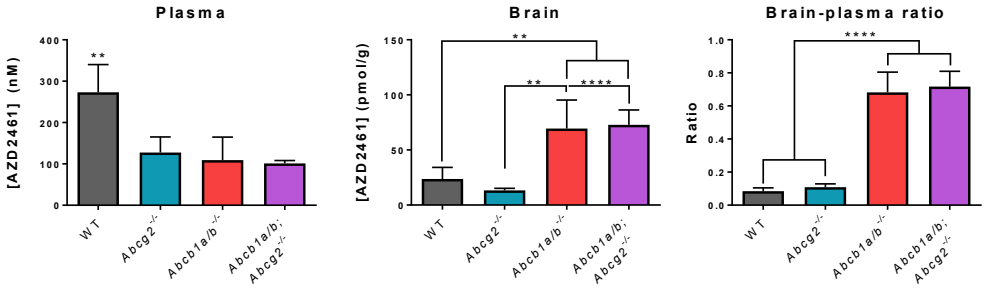

Figure 2 | P-glycoprotein restricts the brain penetration of AZD2461 *in vivo*. AZD2461 (10 mg/kg) was intravenously administered to wild-type, *Abcg2*$^{-/-}$, *Abcb1a/b*$^{-/-}$ and *Abcb1a/b;Abcg2*$^{-/-}$ mice. One hour after injection, blood and brain tissue was collected for LC–MS/MS analysis. A 3-fold increased brain concentration and corresponding brain–plasma ratio was observed in *Abcb1a/b*$^{-/-}$ and *Abcb1a/b;Abcg2*$^{-/-}$ compared to wild-type mice. Interestingly, wild-type mice had an approximately 2.5-fold increased plasma concentration compared to all knockout mouse strains. All data are represented as mean ± SD (n = 4); ** $p < 0.01$, **** $p < 0.0001$.

Interestingly, we observed an approximately 2.5-fold increased plasma concentration in WT mice compared to any of the ABC transporter knockout mice. The reason for this higher plasma concentration is unclear, but if we correct for this higher plasma concentration by calculating the brain–plasma ratio, the difference in AZD2461 brain penetration between WT and *Abcb1a/b*$^{-/-}$ and *Abc1a/b;Abcg2*$^{-/-}$ mice is even more pronounced at roughly 7-fold. Together, these data clearly show that the brain penetration of AZD2461 is restricted by P-gp, but not by BCRP.

AZD2461 has a poor oral bioavailability that is unaffected by P-gp and BCRP

Since PARP inhibitors are often administered orally to patients[27] and P-gp and BCRP can limit the oral uptake of pharmaceuticals[4], we also determined the oral bioavailability of AZD2461 in WT

and knockout mice. We applied 100 mg/kg of AZD2461 administered as a 10 mg/ml suspension in 0.5% hydroxypropyl methyl cellulose in water, as this dose and dose form were routinely used in preclinical studies[2, 3]. The plasma levels ranged between 1 and 10 micromolar (**Figure 3**), yielding an oral bioavailability in WT mice of only about 10% (**Table 1**). Compared to wild-type mice, no significantly increased oral bioavailability was found in any of the transporter knockout mouse strains (**Table 1**). In line with the previous i.v. results (**Figure 2**), we again found that wild-type mice had considerably higher plasma levels following intravenous administration of AZD2461, as indicated by an elevated AUC_{iv} and C_{max}. In summary, these data demonstrate that AZD2461 has a poor oral bioavailability, but this is not due to P-gp and BCRP.

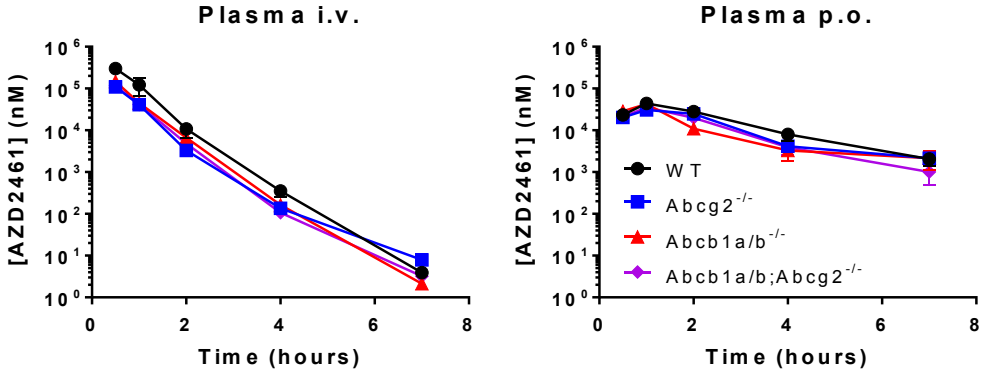

Figure 3 | No impact of P-gp and BCRP on the plasma concentrations of AZD2461 following intravenous and oral administration. AZD2461 was administered intravenously (50 mg/kg) and orally (100 mg/kg) to wild-type, *Abcg2*$^{-/-}$, *Abcb1a/b*$^{-/-}$ and *Abcb1a/b;Abcg2*$^{-/-}$ mice. No differences were observed in the plasma concentration time curves among the different mouse strains. The oral bioavailability of AZD2461 is poor, since oral administration to wild-type mice only yielded a dose-adjusted AUC of approximately 10% compared to intravenous administration (see **Table 1**). All data are represented as mean ± SD (n ≥ 4).

AZD2461 achieves similar brain–plasma ratios following oral and intravenous administration

We next studied the brain penetration of AZD2461 at several time points after oral administration. The brain penetration of AZD2461 in WT mice was again low, with a brain–plasma ratio never exceeding 0.1 (**Figure 4**). Similarly, the brain–plasma ratios were also low in *Abcg2*$^{-/-}$ mice. In contrast, the brain penetration in *Abcb1a/b*$^{-/-}$ and *Abcb1a/b;Abcg2*$^{-/-}$ mice was significantly higher. With steady brain–plasma ratios of approximately 0.5 at all measured time points, the difference in AUC_{brain}:AUC_{plasma} between WT and P-gp knockout mice was 10-fold. Taken together, we conclude that P-gp at the BBB restricts the brain penetration of AZD2461 following oral and intravenous administration.

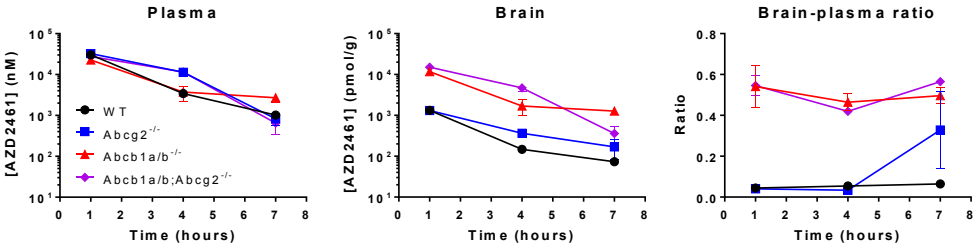

Figure 4 | P-glycoprotein restricts the brain penetration of AZD2461 following oral administration. AZD2461 was administered orally to wild-type, *Abcg2*$^{-/-}$, *Abcb1a/b*$^{-/-}$ and *Abcb1a/b;Abcg2*$^{-/-}$ mice at a dose of 100 mg/kg. A markedly increased brain concentration and brain plasma–ratio were observed in *Abcb1a/b*$^{-/-}$ and *Abcb1a/b;Abcg2*$^{-/-}$ mice, in line with the results obtained after intravenous administration (see **Figure 2**). All data are represented as mean ± SD (n ≥ 4).

DISCUSSION

PARP inhibitors are a relatively new class of anticancer agents that attenuate DNA damage repair by inhibiting poly (ADP ribose) polymerase. AZD2461 is a novel PARP inhibitor and its efficacy has been unaffected by P-gp in breast cancer models. We reasoned that AZD2461 might be an interesting candidate for treatment of GBM when its brain penetration is indeed not restricted by important efflux transporters expressed at the blood–brain barrier. This study, however, demonstrates that AZD2461 is a substrate of P-gp and BCRP and that P-gp in particular limits AZD2461 brain penetration *in vivo*. Moreover, we have also found that AZD2461 has a relatively low oral bioavailability. These findings are not in favor of further development of AZD2461 for treatment of GBM.

Glioblastoma is extensively treated, as standard-of-care consists of maximum surgical resection, followed by fractionated radiotherapy and concommitant temozolomide chemotherapy[28]. Temozolomide is an alkylating agent that exerts its cytotoxicity by forming methyl adducts on the DNA. Such adducts are often repaired by base excision repair, a process in which PARP plays a pivotal role. Consequently, PARP inhibition may be an attractive strategy to improve standard-of-care therapy for GBM. Encouraging results have been demonstrated using intracranial glioma mouse models[29, 30]. Moreover, Halford *et al.* very recently presented data in the American Society for Clinical Oncology meeting on the use of olaparib in patients with relapsed GBM[31]. However, olaparib is a substrate of P-gp and several studies have shown that P-gp and/or BCRP in the BBB can restict the efficacy of treatment with PARP inhibitors[10, 13, 14]. In order to fully exploit the potential of PARP inhibition in GBM, it is worthwhile to continue investing candidate PARP inhibitors that are not substrates of these ABC transporters. Recently, Chornenkyy *et al.* demonstrate efficacy of niraparib in orthotopic models of pediatric high-grade glioma and diffuse intrinsic pontine glioma[32]. This is in line with preliminary reports that niraparib displays a high brain–plasma ratio[33], although it is yet unknown if niraparib is recognized by P-gp or BCRP.

In contrast to previous studies showing that AZD2461 is not amenable to P-gp mediated resistance in breast cancer models, we here report that this PARP inhibitor is a substrate of P-gp. The reason why overexpression of P-gp was insufficient to confer AZD2461 resistance to a breast cancer model is unexplored. None of these studies included pharmacokinetic data in plasma and tumor samples. Considering that AZD2461 is a weaker substrate than olaparib, it might be that just enough AZD2461 is able to accumulate into these breast cancer cells to cause sufficient PARP inhibition, whereas this threshold of required PARP inhibition is not achieved with olaparib. However, at the BBB the hurdle of P-gp may be greater as P-gp may be more densely expressed in brain endothelial cells than in tumor cells. Furthermore, the AZD2461 influx into tumor cells might be higher than across the BBB as a result of higher pinocytic activity and the presence of additional uptake mechanisms. Additionally, AZD2461 needs to cross only cellular membrane to diffuse into a tumor cell, but has to diffuse across the apical and basloteral endothelial membrane to enter the brain. Together, these factors might allow more efficient efflux of weaker substrates at the BBB compared to tumor cells, as examplified by the 10-fold difference in AUC_{brain}–AUC_{plasma} ratio we observed between WT and *Abcb1a/b;Abcg2*$^{-/-}$ mice.

Route	Parameter	Time (h)	Genotype			
			WT	Abcg2$^{-/-}$	Abcb1a/b$^{-/-}$	Abcb1a/b;Abcg2$^{-/-}$
i.v. 50 mg/kg	AUC_{plasma} (μg/ml·h)	0-∞	200 ± 99	66 ± 18****	98 ± 22**	73 ± 5.2****
	C_{max} (μg/ml)		120 ± 53	43 ± 13*	58 ± 9.4	46 ± 5.8*
	t_{max} (h)		0.5	0.5	0.5	0.5
	$t_{1/2}$ (h)		0.44 ± 0.02	0.59 ± 0.14	0.42 ± 0.03	0.45 ± 0.06
	V_z (L/kg)		0.20 ± 0.11	0.68 ± 0.21	0.33 ± 0.10	0.44 ± 0.07
	CL (L/kg·h)		0.31 ± 0.16	0.79 ± 0.16	0.53 ± 0.13	0.69 ± 0.05
p.o. 100 mg/kg	AUC_{plasma} (μg/ml·h)	0-∞	45 ± 19	35 ± 7.2	32 ± 5.3	32 ± 6.3
	C_{max} (μg/ml)		17 ± 3.5	12 ± 2.9	18 ± 11	14 ± 3.2
	t_{max} (h)		1.0 ± 0.0	1.2 ± 0.4	0.8 ± 0.3	1.0 ± 0.0
	$t_{1/2}$ (h)		1.3 ± 0.3	1.5 ± 0.3	1.6 ± 0.6	1.1 ± 0.5
	F (%)		11 ± 7.5	27 ± 9.1	16 ± 4.5	22 ± 4.6
	V_z/F (L/kg)		4.8 ± 2.0	6.3 ± 2.0	7.9 ± 4.2	5.4 ± 3.3
	CL/*F* (L/kg·h)		2.5 ± 0.9	2.9 ± 0.5	3.2 ± 0.6	3.2 ± 0.6

Table 1 | Pharmacokinetic parameters of AZD2461 after oral and i.v. administration to WT, *Abcg2*$^{-/-}$, *Abcb1a/b*$^{-/-}$ and *Abcb1a/b;Abcg2*$^{-/-}$ FVB mice. AUC, area under the curve; C_{max}, maximum concentration in plasma; t_{max}, time to reach maximum plasma concentration; $t_{1/2}$, elimination half-life; V_z, apparent volume of distribution; *CL*, apparent clearance; *F*, oral bioavailability; V_z/F, apparent volume of distribution after oral administration; *CL*/*F*, apparent clearance after oral administration. Data are represented as mean ± SD (n ≥ 4); * $p < 0.05$, ** $p < 0.01$, **** $p < 0.0001$ relative to WT.

As we demonstrate here, the oral bioavailability of AZD2461 is only approximately 10%. Although not uncommon for small molecular targeted agents, a poor oral bioavailability is generally problematic for clinical development because it often leads to a high variability in exposure in patients[34]. Large variations in drug exposure increase the risk of over- and undertreatment, resulting in either toxicity or ineffective therapy. A similar low oral bioavailability has been found for olaparib in mice receiving olaparib in a microsuspension[35]. Notably, the oral bioavailability increased to 50% when using a soluble dosing form, suggesting that incomplete drug dissolution is the limiting factor. The formal bioavailability of olaparib in patients has not been established, due to the absence of an intravenous formulation. However, discrepancies in the relative oral bioavailability of olaparib between capsules and tablet solid dose forms were found[36], suggesting sub-optimal intestinal dissolution and uptake in patients. Based on our results, we expect that AZD2461 will have similar qualities as olaparib with respect to oral dose forms. A phase I study investigating the tolerability and pharmacokinetics of oral AZD2461 in refractory solid cancer patients has been completed, but unfortunately no data has yet been reported (ClinicalTrials.gov Identifier NCT01247168). Notably, some other clinically advanced PARP inhibitors seem to have substantially higher oral bioavailabilites than AZD2461[30, 37, 38], which would be an argument why AZD2461 might not be the preferred PARP inhibitor to develop further.

In summary, we have demonstrated that AZD2461 is a substrate of P-gp and BCRP, and that P-gp substantially limits the brain penetration of AZD2461 in mice. Moreover, AZD2461 has a low oral bioavailability, indicating that AZD2461 does not offer a pharmaceutical advantage over other PARP inhibitors. Together, these findings are not in favor of further clinical development of AZD2461 for treatment of glioblastoma.

REFERENCES

1. Rouleau, M., *et al.* PARP inhibition: PARP1 and beyond. *Nat Rev Cancer* **10**, 293-301 (2010).
2. Rottenberg, S., *et al.* High sensitivity of BRCA1-deficient mammary tumors to the PARP inhibitor AZD2281 alone and in combination with platinum drugs. *Proc Natl Acad Sci U S A* **105**, 17079-17084 (2008).
3. Jaspers, J.E., *et al.* BRCA2-deficient sarcomatoid mammary tumors exhibit multidrug resistance. *Cancer Res* **75**, 732-741 (2015).
4. Schinkel, A.H. & Jonker, J.W. Mammalian drug efflux transporters of the ATP binding cassette (ABC) family: an overview. *Adv Drug Deliv Rev* **64**, 138-153 (2012).
5. van Tellingen, O., *et al.* Overcoming the blood-brain tumor barrier for effective glioblastoma treatment. *Drug Resist Updat* **19**, 1-12 (2015).
6. Durmus, S., *et al.* Apical ABC transporters and cancer chemotherapeutic drug disposition. *Adv Cancer Res* **125**, 1-41 (2015).
7. Sarkaria, J.N., *et al.* Is the blood–brain barrier really disrupted in all glioblastomas? A critical assessment of existing clinical data. *Neuro Oncol* **20**, 184-191 (2018).
8. Pokorny, J.L., *et al.* The efficacy of the Wee1 inhibitor MK-1775 combined with temozolomide is limited by heterogeneous distribution across the blood–brain barrier in glioblastoma. *Clin Cancer Res* **21**, 1916-1924 (2015).
9. Parrish, K.E., *et al.* Efflux transporters at the blood-brain barrier limit delivery and efficacy of cyclin-dependent kinase 4/6 inhibitor palbociclib (PD-0332991) in an orthotopic brain tumor model. *J Pharmacol Exp Ther* **355**, 264-271 (2015).
10. Lin, F., *et al.* ABCB1, ABCG2, and PTEN determine the response of glioblastoma to temozolomide and ABT-888 therapy. *Clin Cancer Res* **20**, 2703-2713 (2014).
11. McEllin, B., *et al.* PTEN loss compromises homologous recombination repair in astrocytes: implications for glioblastoma therapy with temozolomide or poly(ADP-ribose) polymerase inhibitors. *Cancer Res* **70**, 5457-5464 (2010).
12. Durmus, S., *et al.* Breast cancer resistance protein (BCRP/ABCG2) and P-glycoprotein (P-GP/ABCB1) restrict oral availability and brain accumulation of the PARP inhibitor rucaparib (AG-014699). *Pharm Res* **32**, 37-46 (2015).
13. Parrish, K.E., *et al.* Efficacy of PARP Inhibitor rucaparib in orthotopic glioblastoma xenografts is limited by

ineffective drug penetration into the central nervous system. *Mol Cancer Ther* **14**, 2735-2743 (2015).
14. Kizilbash, S.H., *et al.* Restricted delivery of talazoparib across the blood-brain barrier limits the sensitizing effects of poly (ADP-ribose) polymerase inhibition on temozolomide therapy in glioblastoma. *Mol Cancer Ther* **16**, 2735-2746 (2017).
15. Jaspers, J.E., *et al.* Loss of 53BP1 causes PARP inhibitor resistance in Brca1-mutated mouse mammary tumors. *Cancer Discov* **3**, 68-81 (2013).
16. Henneman, L., *et al.* Selective resistance to the PARP inhibitor olaparib in a mouse model for BRCA1-deficient metaplastic breast cancer. *Proc Natl Acad Sci U S A* **112**, 8409-8414 (2015).
17. Schinkel, A.H., *et al.* Absence of the mdr1a P-glycoprotein in mice affects tissue distribution and pharmacokinetics of dexamethasone, digoxin, and cyclosporin A. *J Clin Invest* **96**, 1698-1705 (1995).
18. Jonker, J.W., *et al.* Role of breast cancer resistance protein in the bioavailability and fetal penetration of topotecan. *J Natl Cancer Inst* **92**, 1651-1656 (2000).
19. Pavek, P., *et al.* Human breast cancer resistance protein: interactions with steroid drugs, hormones, the dietary carcinogen 2-amino-1-methyl-6-phenylimidazo(4,5-*b*)pyridine, and transport of cimetidine. *J Pharmacol Exp Ther* **312**, 144-152 (2005).
20. Zhang, P., *et al.* ABCB1 and ABCG2 restrict the brain penetration of a panel of novel EZH2-Inhibitors. *Int J Cancer* **137**, 2007-2018 (2015).
21. Schinkel, A.H., *et al.* Disruption of the mouse mdr1a P-glycoprotein gene leads to a deficiency in the blood-brain barrier and to increased sensitivity to drugs. *Cell* **77**, 491-502 (1994).
22. Jonker, J.W., *et al.* The breast cancer resistance protein protects against a major chlorophyll-derived dietary phototoxin and protoporphyria. *Proc Natl Acad Sci U S A* **99**, 15649-15654 (2002).
23. Jonker, J.W., *et al.* Contribution of the ABC transporters Bcrp1 and Mdr1a/1b to the side population phenotype in mammary gland and bone marrow of mice. *Stem Cells* **23**, 1059-1065 (2005).
24. Zhang, Y., *et al.* PKSolver: An add-in program for pharmacokinetic and pharmacodynamic data analysis in Microsoft Excel. *Comput Methods Programs Biomed* **99**, 306-314 (2010).
25. Agarwal, S., *et al.* Quantitative proteomics of transporter expression in brain capillary endothelial cells isolated from P-glycoprotein (P-gp), breast cancer resistance protein (Bcrp), and P-gp/Bcrp knockout mice. *Drug Metab Dispos* **40**, 1164-1169 (2012).
26. Uchida, Y., *et al.* Quantitative targeted absolute proteomics of human blood-brain barrier transporters and receptors. *J Neurochem* **117**, 333-345 (2011).
27. Sonnenblick, A., *et al.* An update on PARP inhibitors—moving to the adjuvant setting. *Nat Rev Clin Oncol* **12**, 27 (2014).
28. Stupp, R., *et al.* Effects of radiotherapy with concomitant and adjuvant temozolomide versus radiotherapy alone on survival in glioblastoma in a randomised phase III study: 5-year analysis of the EORTC-NCIC trial. *Lancet Oncol* **10**, 459-466 (2009).
29. Tentori, L., *et al.* Systemic administration of GPI 15427, a novel poly(ADP-ribose) polymerase-1 inhibitor, increases the antitumor activity of temozolomide against intracranial melanoma, glioma, lymphoma. *Clin Cancer Res* **9**, 5370-5379 (2003).
30. Donawho, C.K., *et al.* ABT-888, an orally active poly(ADP-ribose) polymerase inhibitor that potentiates DNA-damaging agents in preclinical tumor models. *Clin Cancer Res* **13**, 2728-2737 (2007).
31. Halford, S.E.R., *et al.* Results of the OPARATIC trial: A phase I dose escalation study of olaparib in combination with temozolomide (TMZ) in patients with relapsed glioblastoma (GBM). *J Clin Oncol* **35 Suppl 15**, 2022 (2017).
32. Chornenkyy, Y., *et al.* Poly-ADP-ribose polymerase as a therapeutic target in pediatric diffuse intrinsic pontine glioma and pediatric high-grade astrocytoma. *Mol Cancer Ther* **14**, 2560-2568 (2015).
33. Mikule, K. & Wilcoxen, K. The PARP inhibitor, niraparib, crosses the blood brain barrier in rodents and is efficacious in a BRCA2-mutant intracranial tumor model. *Mol Cancer Ther* **14 Suppl 2**, B168 (2015).
34. Herbrink, M., *et al.* Variability in bioavailability of small molecular tyrosine kinase inhibitors. *Cancer Treat Rev* **41**, 412-422 (2015).
35. US Food and Drug Adminstration. Center for drug evaluation and research, Application number: 206162Orig1s000. Pharmacology Review(s). https://www.accessdata.fda.gov/drugsatfda_docs/nda/2014/206162Orig1s000PharmR.pdf (Accessed May 14, 2018),
36. Molife, L.R., *et al.* A phase I study to determine the comparative bioavailability of two different oral formulations of the PARP inhibitor, olaparib (AZD2281), in patients with advanced solid tumors. *J Clin Oncol* **28 Suppl 15**, 2599 (2010).
37. Molife, L.R., *et al.* A phase I study of oral rucaparib in combination with carboplatin. *J Clin Oncol* **31 Suppl 15**, 2586 (2013).
38. Shen, Y., *et al.* BMN 673, a novel and highly potent PARP1/2 inhibitor for the treatment of human cancers with DNA repair deficiency. *Clin Cancer Res* **19**, 5003-5015 (2013).

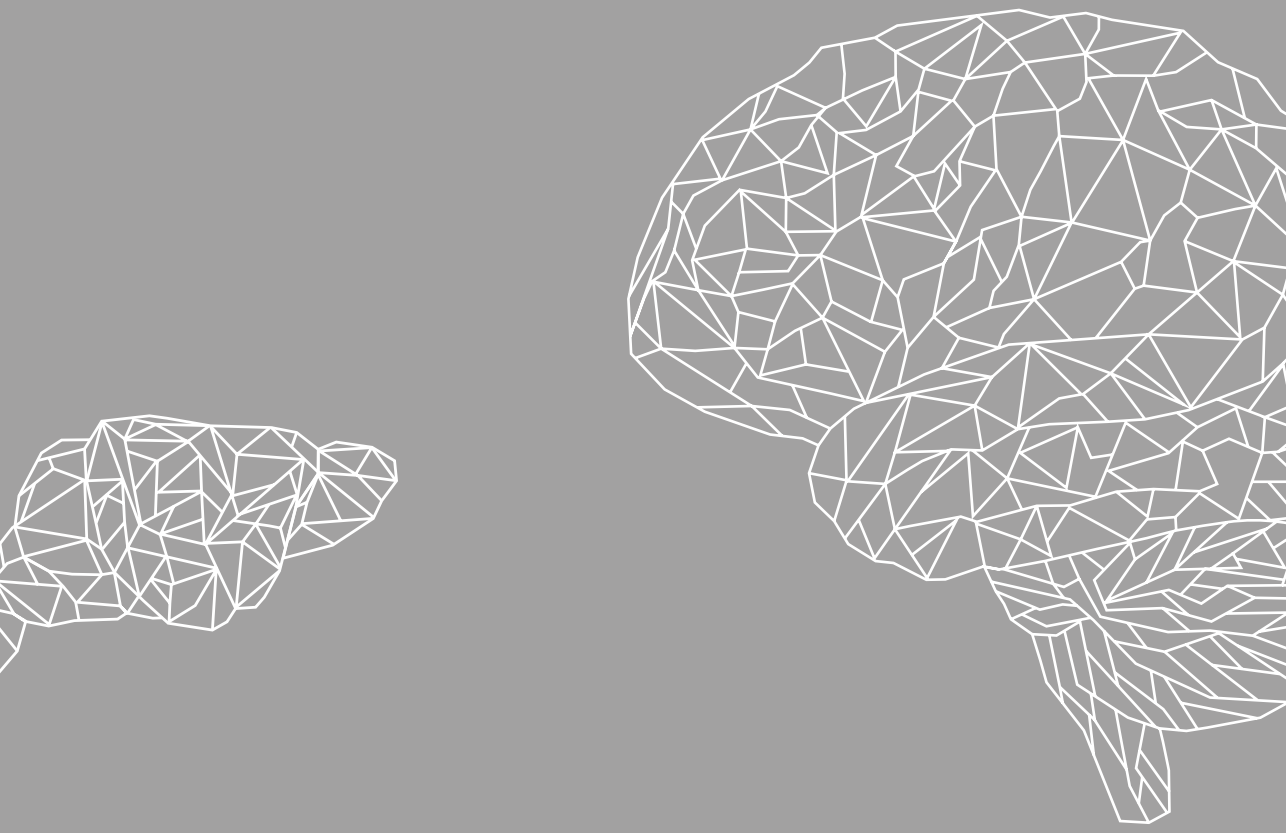

SECTION VII

TARGETING INVASION: TACKLING A DEVASTATING GBM HALLMARK

Chapter 15

AN EXPERIMENTER'S GUIDE TO GLIOBLASTOMA INVASION

M.C. de Gooijer*, M. Guillén Navarro*, R. Bernards, T. Wurdinger, and O. van Tellingen

* These authors contributed equally

Trends in Molecular Medicine. 2018;24(9):763-780

ABSTRACT

Glioblastoma is a highly aggressive brain tumor that is characterized by its unparalleled invasiveness. Invasive glioblastoma cells not only escape surgery and focal therapies, but also are more resistant to current radio- and chemo-therapeutic approaches. Thus, any curative therapy for this deadly disease likely should include treatment strategies that interfere with glioblastoma invasiveness. Understanding glioblastoma invasion mechanisms is therefore critical. We discuss the strengths and weaknesses of various glioblastoma invasion models and conclude that robust experimental evidence has been obtained on a pro-invasive role of Ephrin receptors, Rho GTPases and casein kinase 2 (CK2). Extensive interplay occurs between these proteins, suggesting the existence of a glioblastoma invasion signaling network that comprises several targets for therapy.

Highlights

- Glioblastoma (GBM) is a highly aggressive brain tumor that is characterized by an unparalleled invasion capacity.
- GBM cells invade the brain via the brain parenchyma, the perivascular space, white matter tracts and the leptomeningeal space.
- GBM invasion signaling is dependent on the brain microenvironment, including extracellular matrix composition.
- *In vitro*, *ex vivo* and *in vivo* models have been developed to study GBM invasion, each associated with their own strengths and limitations.
- A pro-invasive GBM signaling network is emerging from literature revolving around Ephrin receptors, Rho GTPases and casein kinase 2 that offers several druggable targets.

INVASION: AN OMINOUS HALLMARK OF GLIOBLASTOMA

Glioblastoma (GBM; see **Glossary**) is the most common and fatal adult brain tumor and is classified as a grade IV glioma[1]. GBM is highly aggressive and characterized by an unparalleled **invasion** capacity. Current therapeutic strategies are insufficient to control the disease, as reflected by a dismal median survival of less than 15 months from diagnosis[2]. The standard of care consists of maximal surgical resection followed by radiotherapy and **temozolomide** chemotherapy. However, this strategy does not target the diffuse infiltrative nature of the tumor. The invasiveness of GBM is a major obstacle for curative treatment, since it makes complete surgical resection impossible. GBM cells typically invade up to several centimeters away from the tumor mass and can even cross into the contralateral hemisphere[3,4]. GBM contains a subset of **glioma stem cells** (GSCs), and these may have an elevated invasive potential compared to non-stem tumor cells[5]. Moreover, GSCs are thought to be more resistant to radiotherapy and chemotherapy than more differentiated bulk tumor cells[6]. This hypothesis is corroborated by the observations that recurrent and chemotherapy-resistant tumors are enriched in the highly invasive **mesenchymal GBM** subtype[7-9]. Consequently, proximal and distant tumor recurrence occurs in GBM patients within two years after completion of the treatment[3,10].

The infiltrative tumor growth in GBM is orchestrated by the interaction of tumor cells within the brain microenvironment. Gliomas have unique features of invasion compared to other solid tumors. GBM cells typically only invade the brain and rarely metastasize to other tissues[11]. Notably, gliomas seem to prefer single-cell **migration** and invade over longer distances than other tumors that metastasize in the brain[12]. Moreover, GBM cells seem to populate the brain as an interconnected network via tumor microtubes that appear to facilitate invasion[13]. Invasion is a dynamic process, and brain tumor cells have evolved the ability to remodel the **extracellular matrix** (ECM) to assist in invasion[14]. The neural ECM occupies roughly 20% of the adult brain volume and varies in composition among brain structures[12,15]. The normal brain parenchyma is mainly composed of hyaluronan, thrombospondin, proteoglycans and tenascin-C[12]. Common ECM components found in other tissues such as collagens, laminin, and fibronectin are not found in the normal brain parenchyma, in line with its soft consistency. However, these ECM components are present in the vascular basement membranes where heparan sulfate, vitronectin, and entactin are also found[15]. The adaptation of GBM cells to the unique brain environment and their ability to induce heterogenic ECM alterations enable glioblastoma cells to invade the brain via multiple different **invasion routes**[14], resulting in an unparalleled invasive potential compared to that of other solid tumors (see **Figure I** in **Box 1**).

KEY PATHWAYS IN GLIOBLASTOMA INVASION

Glioblastoma invasion can be studied using a spectrum of models, with each having its own strengths and weaknesses: *in vitro* 2D (**Box 2**), *in vitro* 3D (**Box 3**), *ex vivo* (**Box 4**), and *in vivo* (**Box 5**). Although more complex models are expected to be more relevant physiologically, complexity usually comes at the cost of reduced throughput and less straightforward data interpretation. A good understanding of the advantages and limitations of each model (**Table 1**) and their suitability to study different invasion processes (**Table 2**) is required to select the most appropriate model to study a research question related to GBM invasion. For example, the influence of composition and biophysical properties of different matrices on invasion can be conveniently evaluated using *in vitro* 3D models. However, mapping of tumor–ECM–stroma interactions requires using *ex vivo* and *in vivo* models that retain the physiological brain environment.

Now, many studies are still conducted with traditional cell lines in 2D migration or 3D invasion assays, and they use artificial matrices that do not completely recapitulate the native brain microenvironment[16]. Obviously, studying invasion routes through the brain can best be done in the context of the original microenvironment. To address complex questions regarding GBM invasion, it is important to confirm *in vitro* findings by using *ex vivo* **organotypic brain slice models** and/or *in vivo* models. Furthermore, many papers still report findings on traditional serum-cultured cell lines such as U87 and U251, without further validation using GSC lines. These GSCs more closely mirror genotypic and phenotypic characteristics of GBM in patients, including invasiveness following injection into the mouse brain[17].

Below, we discuss the pro-invasive pathways for which robust data have been generated using a combination of *in vitro*, *ex vivo*, and *in vivo* models of GBM invasion. We address the known interplay between these pathways; highlight which important questions remain to be answered; and, based on this information, sketch a pro-invasive GBM signaling network that appears to emerge from the current body of work. In particular, we discuss the potential existence of a GBM invasion signaling network revolving around **Ephrin receptors**, **Rho GTPases** and **casein kinase 2** (CK2).

Eph receptors and ephrins: bi-directional signaling in GBM invasion

Erythropoietin-producing human hepatocellular carcinoma (Eph) receptors are the largest family of **receptor tyrosine kinases** in the human genome[18]. They are classified as type A (EphA) or type B (EphB) subfamilies according to sequence similarity and ligand affinity. Ephrin ligands are also divided in two subclasses. EphA and EphB receptors typically bind A-type ephrins and B-type ephrins, respectively, although a few exceptions exist[19]. Eph receptors and ephrins mediate cell-to-cell signaling that controls spatiotemporal tissue organization. The signal

	Invasion model	Advantages	Disadvantages
2D in vitro See Box 2	Scratch assay 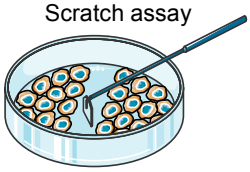	- Technically easy - Low-cost - High-throughput - Real-time cell tracking	- Low physiological relevance - Does not mimic invasion, only migration - Lacks 3D environment - Coating and scratch width influence migration
3D in vitro See Box 3	Transwell assay 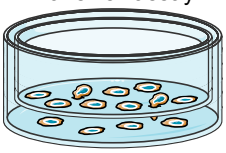	- Technically easy - Low-cost - High-throughput	- Does not mimic invasion, only migration - Lacks 3D environment - Results dependent on chemoattractant used - End-point assay
	Transwell + matrix 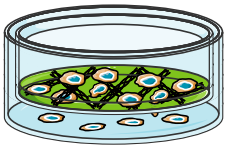	- Technically easy - High-throughput - Allows studying matrix interactions	- Difficult to distinguish between migration and invasion - End-point assay - Lacks tumor complexity
	3D bioscaffolds 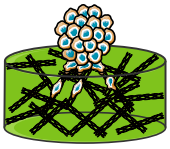	- High-throughput - 3D microenvironment - Real-time cell tracking - Recapitulates invasion, not migration	- Lacks tumor complexity - Lacks tumor-stroma interactions - Lacks brain structures (*e.g.* vasculature)
	Microfluidic co-culture 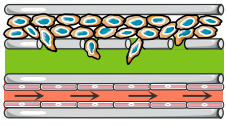	- 3D microenvironment - Real-time cell tracking - Allows studying interactions between different cell types - Mimics blood flow	- Does not completely recapitulate tumor complexity - Lacks native brain environment - Expensive
Ex vivo See Box 4	Organotypic brain slices 	- Native microenvironment - Real-time cell tracking - Preserves interactions between different cell types - Recapitulates different invasion routes	- Ethical issues associated with animals studies - Limited tissue stability - Intra- and interanimal variability - Lacks blood flow
In vivo See Box 5	Orthotopic xenograft 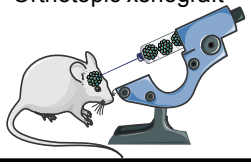	- Native microenvironment - Recapitulates different invasion routes - Allows studying effects of blood flow and the immune system on invasion	- Animal ethics - Time-consuming - Difficult to scale-up - Expensive - Limited image resolution - Less experimental control

Table 1 | The main advantages and disadvantages of common GBM invasion models. This table was prepared using Servier Medical Art under a Creative Commons Attribution 3.0 Unported License.

transduction mechanism is complex and creates bi-directional cell-to-cell communication. Upon ligand binding, Eph receptors get activated by phosphorylation, generating 'forward signaling'. Ephrins are membrane-bound ligands that can also signal in the host cell upon activation, a process known as 'reverse signaling'. In the brain, Eph receptors and ephrins are crucial for nervous system development since they regulate cell migration and axon guidance[20,21].

Several observations strongly connect both EphA and EphB signaling to GBM invasion. In GBM specimens, the Eph/ephrin pathway is overactivated in invasive cells compared to the stationary cells at the tumor core[22]. High protein expression of Eph receptors A2, A3, A4 and A7 has been associated with poorer patient outcome, but only EphA2 and EphA3 have been clearly linked to invasiveness and identified as preferentially expressed in mesenchymal and classical subtypes[23-29]. In addition, high EphA2 protein expression has been detected in tumor-propagating cells and has been linked to stemness and tumorigenesis[26,28]. Higher mRNA expression of the receptors EphB2, EphB3, and EphB4 was detected in GBM than in normal brain, although EphB1 expression was similar[30]. The pro-invasive role of the EphB2 receptor has been validated by comparing EphB2 and mock-transfected GBM and GSC cell lines by using *ex vivo* organotypic brain slices and *in vivo* intracranial injection[31,32].

		Invasion-related topic of interest			
		Signaling pathways	Influence of ECM	Cell-cell interactions	Route of invasion
2D in vitro see Box 2	Scratch assay	+	-	-	-
	Transwell assay	+	++	-	-
3D in vitro see Box 3	3D bio-scaffolds	++	+++	-	+
	Microfluidic co-culture	++	+++	++	++
Ex vivo see Box 4	Organotypic brain slices	+++	+	+++	+++
In vivo see Box 5	Orthotopic xenograft	+++	+	+++	+++

Table 2 | The suitability of common GBM invasion models to study different aspects of GBM invasion. "-":unsuitable, "+++": most suitable. The influence of the ECM can best be studied in 3D *in vitro* models, as these models allow for detailed manipulation of the matrix to study mechanistic effects of individual ECM components. By contrast, *ex vivo* and *in vivo* models are most suitable to study signaling pathways, cell–cell interactions and different invasion routes, as they best recapitulate the complexity of human GBM.

The overexpression of ephrin-B ligands is also associated with increased invasiveness, tumor grade, and poor outcome[22,33,34]. Previous studies demonstrated that ephrin-B2 and ephrin-B3 expressed on tumor cells mediate GBM invasion, which was first shown using *in vitro* transwell and *ex vivo* brain slices using serum-cultured cell lines[22,34]. Further studies using GSCs demonstrated an additional role of ephrin-B2 in facilitating **perivascular invasion** of GSCs *in vivo* using intra-vital microscopy in mice[35]. Eph receptors and ephrins are normally expressed on the basolateral membrane of vascular endothelial cells, where ephrin-B2 expression inhibits the migration of normal stem cells, a process known as **vascular compartmentalization**. However, GSCs upregulate ephrin-B2, causing desensitization of their own EphB receptors. This causes decreased recognition of endothelial ephrin-B2 by EphB receptors on GBM cells and creates a constitutive autocrine activation of proliferation signaling in GBM cells. Together, these interactions allow GBM cells to escape vascular compartmentalization[35].

In contrast to the role of ephrin-Bs, ephrin-As seem to function as tumor suppressors, since higher expression correlates with a less aggressive phenotype and better patient prognosis, although a specific role in invasion has not been demonstrated[36,37]. Day *et al.* proposed an interesting model for the spatiotemporal regulation of perivascular invasion by EphA/ephrin-A in GBM[38]. According to their model, an inversely correlated EphA and ephrin-A expression gradient may exist in GBM that is regulated by environmental cues. Cells expressing higher amounts of EphA receptors are poorly activated due to low ligand expression and acquire a more de-differentiated mesenchymal GSC-like phenotype, leading to increased invasiveness. In contrast, EphA expression diminishes as tumor cells migrate away from the vascular niche. In these cells, increased ephrin-A expression correlates with a more differentiated, less aggressive phenotype.

The current body of evidence suggests that Eph/ephrins spatiotemporally regulate GBM cell behavior through intercellular interactions, but more research is needed to elucidate the exact role of Eph receptors and ephrins in regulating various aspects of GBM invasion. Although still controversial, Eph/ephrins may also play a role in proliferation signaling in GBM. Wang *et al.* suggested that EphB2 controls the proliferation/migration dichotomy in GBM, in line with the 'go-or-grow' hypothesis that suggests that cells either migrate or proliferate[31]. They compared mock and EphB2-transduced human GSCs by using *in vitro* migration and invasion assays and *in vivo* intracranial xenografts and showed that EphB2 overexpression not only increases invasion but also inhibits proliferation, whereas EphB2 silencing increases proliferation, presumably by forward signaling mechanisms. In contrast, the upregulation of ephrin-B2, the ligand partner of EphB2, was shown to enhance tumor proliferation by reverse signaling in the absence of normal anchorage signals, thus independently of cell-to-cell interactions[35]. Regardless of the exact question to be studied, future studies investigating the role of Eph/ephrin in GBM should be done using models that conserve the brain microenvironment, since Eph/ephrin signaling is context-dependent and intercellular communication is crucial for their regulation.

Rho GTPases: spatial regulation of GBM invasion

The Rho family of GTPases are monomeric, low molecular weight proteins that belong to the Ras superfamily[39]. Mammalian Rho protein members are divided into subfamilies that include Rho-A-, Rac1- and Cdc42-similar proteins and also those that lack GTPase activity. They bind to the cell membrane, where their activation is tightly controlled by regulatory proteins. They become active when GDP is exchanged by GTP, a process promoted by guanine nucleotide exchange factors (GEFs). Conversely, GTPase-activating proteins inactivate them by catalyzing the hydrolysis of GTP to GDP. Guanine nucleotide dissociation inhibitors offer an additional level of regulation by sequestering inactive GDP-bound Rho proteins in the cytoplasm, thus preventing subsequent downstream effector binding. Rho GTPases regulate several cellular processes, including the control of actin-mediated cytoskeleton rearrangements that promote cell migration[39,40].

The Rho GTPase pathway is deregulated in tumors, including glioblastoma, which contributes to the invasiveness of malignant cells[39,41]. Increased activity of Rac1, Cdc42, RhoA and RhoG has been reported in GBM as a result of GEF overexpression, promoting *in vitro* migration and *ex vivo* and *in vivo* invasion[42-51]. Conversely, knockdown of Rac1, as well as its upstream activator PREX1, diminished invasion of GSCs in a Matrigel-coated **Boyden chamber**[52]. Biosensors that visualize active Rho family members have revealed that GBM cells differentially regulate the Rho GTPases Rac1, Cdc42, and RhoA dependent on the preferred route of invasion[47]. Cells penetrating the brain parenchyma had lower RhoA and higher Rac1 and Cdc42 activity than cells invading perivascular areas, as shown using two-photon microscopy on brain slices obtained 7 days after **orthotopic** injection of C6 GBM reporter cells. Moreover, Rho GTPase regulation established a cellular hierarchy, in which invading cells expressing more Rac1 and Cdc42 proteins guided other GBM cells through the invasive trail. Another study showed that Tax-interacting protein 1 (Tip-1) coordinates the spatiotemporal activation of Rho GTPases in the cell[49]. Tip-1 knockdown concordantly inhibited the infiltrative growth of human GBM cells *in vivo*, although possible effects on the preferred invasion route of these cells were not investigated.

The downstream effectors of Rho GTPases include several kinases and scaffold proteins. A detailed description of all downstream effectors has been extensively reviewed previously[39,41]. We here focus on the downstream effectors that are relevant in the context of GBM invasion, such as the RhoA effectors mammalian Diaphanous (mDia) and ROCK and the Cdc42 effector neural Wiskott-Aldrich syndrome protein (N-WASP)[53-55]. The mDia family of Rho GTP-binding formins and their interacting partner ROCK have a function in cell polarity and motility by regulating F-actin cytoskeleton dynamics[54,56,57]. In GBM, they seem to have a role in determining whether migration occurs randomly or in a certain direction. For example, ROCK was shown to promote glioma invasion toward the subventricular zone in response to chemo-attractants released by neural precursor cells (NPCs), as shown in orthotopic xenograft models[58]. Paradoxically, whereas

inhibition of mDia abrogates directional migration and invasion but preserves intrinsic random migration of U251cells *in vitro*, mDia agonists suppressed both random and directional migration, diminishing U87 spheroid invasion *ex vivo* on rat brain slices[55]. Furthermore, the Cdc42 effector N-WASP promotes low oxygen-induced invasion in gliomas, and its knockdown diminished the invasion of GBM cells *in vitro* in Boyden chambers and in *ex vivo* mouse brain slices[53].

Transcriptional regulators involved in GBM invasion signaling: a central role for CK2?

Several transcriptional regulators have been described to regulate GBM invasion. Historically, most studies have focused on how specific transcriptional regulators control migration-related expression programs in *in vitro* models only. Recently, however, several studies have demonstrated in *ex vivo* and *in vivo* models that transcriptional regulators play important roles in GBM invasion.

First, Pencheva *et al.* demonstrated the importance of interferon regulatory factor 3 (IRF3) in invasion. RNA-sequencing of highly versus poorly invasive U87 cells in organotypic brain slices, further supported by knockdown and overexpression experiments in U87 and GSCs, revealed that IRF3 represses the expression of a network of collagens and collagen-interacting proteins[59]. This repressive role of IRF3 in GBM invasion is negatively regulated by CK2. CK2 is a ubiquitous serine/threonine kinase with a large number of targets. It is a master regulator of numerous cellular processes, including transcription, signaling, and maintenance of cell viability[60]. CK2 is overexpressed in glioblastoma, promoting tumorigenesis. However, its role in GBM invasion has not been extensively studied. CK2 might facilitate the invasion process by increasing the rigidity of the ECM by promoting the deposition of collagens, since GBM cells typically invade rigid structures such as white matter tracts more easily than the softer brain parenchyma[61]. Pencheva *et al*. showed that therapeutic inhibition of CK2 represses ECM target genes by re-activating IRF3 and, as a result, suppresses GSC invasion in *ex vivo* organotypic brain slices and *in vivo* following brain implantation of mesenchymal GSCs in NOD/SCID mice, without affecting proliferation[59].

Second, Amodeo *et al.* showed that promyelocytic leukemia protein (PML) promotes cell migration in both normal NPCs and primary human GSC cells[62]. PML is a scaffold protein, induced by the oncogene Ras. Ras maintains expression of the EZH2 and SUZ12 subunits of the PRC2 complex, resulting in increased H3K27 trimethylation of SLIT promotor regions and subsequent repression of SLIT1 and SLIT2 transcription in GSC cells and NPCs, respectively. In line with a role in invasion, PML expression was found to be enriched in the highly invasive mesenchymal GBM subtype and inversely correlated with SLIT1 expression. Notably, PML degradation is induced via phosphorylation by CK2[63]. Theoretically, this suggests that CK2 should repress GBM invasion in the study by Amodeo *et al.*, in contrast to the findings by Pencheva *et al.*[59]. The reason for this discrepancy is unclear, but seems to suggest that the impact of CK2 on GBM invasion is context-dependent.

CK2 might regulate a broader invasive transcriptional program in GBM, since it is also involved in additional pathways that were previously linked to invasion and the expression of a mesenchymal program, such as the nuclear factor-κB (NF-κB) and the Janus kinase/signal transducer and activator of transcription (JAK/STAT) pathways[64,65]. CK2 directly regulates NF-κB transcriptional activity by phosphorylating key components of the complex[66]. NF-κB is constitutively activated in GSC lines as well as in GBM mouse models and has an important role in controlling GBM pathobiology[67,68]. As shown using freshly resected tumor tissue transplanted in NOD/SCID mice, NF-κB promotes conversion to mesenchymal GBM, the most invasive subtype, by controlling the expression of genes associated with a mesenchymal program (*e.g.*, STAT3, CCAAT-enhancer binding protein β (C/EBPβ)) and radiation response in patients[69,70]. Unfortunately, the direct role of NF-κB in migration has been solely evaluated using *in vitro* systems[68]. Recently, however, a study investigated the expression of several transcription factors in 44 GBM biopsy samples[71]. In this study, researchers detected high NF-κB protein expression in invasive GBM cells at the tumor rim compared to non-invasive GBM cells at the tumor core, which had increased Myc expression. Notably, Myc is also a direct target of CK2[72]. Using an organotypic brain slice model, Dhruv *et al.* demonstrated that NF-κB inhibition decreases cell invasion with no effect on cell proliferation. By contrast, Myc inhibition decreased cell proliferation and, in turn, increased cell migration. The authors suggested that this dual transcription system might control the proliferation/migration dichotomy in GBM[71].

As mentioned, the JAK/STAT axis is another downstream target of CK2 in orthotopic GSC xenografts in mice[65] and has been described to be involved in GBM invasion in orthotopic U87 tumors[73]. Unbiased genome profiling has demonstrated that STAT3 is a master regulator of mesenchymal transformation and cell migration[8,74]. Moreover, knockdown of STAT3 and C/EBPβ reduced fibronectin and COL5A1 protein expression in SNB-19 tumors in NOD/SCID mice[74]. JAK/STAT was also identified as a regulator of migration by controlling focal adhesion kinase (FAK)-mediated focal adhesions, by using *in vitro* 'scratch assays' and Boyden chambers with U87-EGFRvIII overexpressing cells[73]. EGFRvIII overexpression also increased invasion of orthotopically implanted tumors[73]. In another study using various serum-cultured cell lines in *in vitro* scratch assays and Boyden chambers, STAT3 seems to regulate the expression of pro-invasive factors such as matrix metalloproteinases, well-known remodelers of the ECM that aid in the migration process[75]. More substantial evidence has recently been reported, demonstrating that silencing of *STAT3* reduced single-cell infiltration in an *ex vivo* organotypic brain slice model[76]. Notably, crosstalk exists between the NF-κB and JAK/STAT pathways, since NF-κB and STAT3 directly interact in the nucleus of glioma cells[77]. In GBM, the nuclear translocation of both NF-κB and STAT3 is enhanced after irradiation, and this has been linked to increased migration (using *in vitro* scratch assays) and invasion (in Matrigel-coated Boyden cambers) of serum-cultured GBM cell lines[78].

An integrated view on GBM invasion signaling?

We have thus far discussed the most extensively validated pathways that are involved in GBM invasion signaling: the Eph/ephrins signaling axis; the Rho GTPase family; and a group of transcriptional regulators, namely, IRF3, PRC2, NF-κB and STAT3, that appear to have common upstream regulators. Although less extensively studied, convincing *in vivo* data on a role in GBM invasion have also been produced for two other receptors, integrin β8 (ITGB8) and transforming growth factor (TGF)-β receptor 1 (TGFBR1). Inhibition of TGFBR1 by LY2109761 strongly reduced the invasiveness of orthotopic NMA-23 GSCs grafted in mice[79]. ITGB8 promoted invasion of LN-229 serum-cultured GBM cells in an orthotopic mouse model. Knockdown of ITGB8 resulted in more proliferative, less invasive tumors[80,81]. Although interactions between most of these pathways have previously been described, recent literature has provided key discoveries that seem to suggest the existence of an integrated GBM invasion signaling network revolving around these pathways.

Various downstream effectors of the Eph/ephrin axis have been identified as mediators of GBM invasion. The family of Rho GTPases are direct downstream mediators of Eph/ephrin bi-directional signaling[82]. R-Ras was shown to be downstream of EphB2 in GBM invasion signaling [83]; and by intracranial injection of oncogenic H-Ras-transformed $PML^{+/-}$ and $PML^{-/-}$ neural progenitor cells, H-Ras was demonstrated to have pro-invasive effects via PML/SLIT1[62]. It is unclear whether Ras and PML interact directly, and these effects could possibly be mediated by CK2 as this kinase can act downstream of K-Ras[84]. Another regulator of Rho GTPases, FAK, is also implicated in Eph/ephrin signaling in cancer. FAK was found to be associated with and highly activated by EphB2 overexpression, mediating both cytoskeletal re-arrangements and focal adhesion formation that resulted in invasion of GSCs in laminin-coated Boyden chambers[31]. Another deregulated protein in GBM, AKT, seems to be involved in the Eph forward signaling that regulates GBM invasion[28]. A recent proteomics approach demonstrated that Ras, Rac1, PAK1, and AKT are all downstream targets of FAK in glioma cells in response to neuroligin-3 secretion by neurons, as investigated by comparing orthotopic injection of GSCs in wild-type and *Nlgn3*$^{-/-}$ mice[85].

Several interactions between Rho GTPases and CK2 have been described in contexts beyond GBM invasion. First, the Rho GTPase Rac1 has been described to regulate TBK1 and IRF3 during the antiviral type-I interferon response through PAK1 in human embryonic kidney cells and canine kidney cells[86]. PAKs are Rho effectors that have been described to be regulated by Rac1 and ROCK in the context of GSC invasion and hypoglossal neuron signaling, respectively[52,87]. As PAK1 appears to be a phosphorylation target of CK2[88], and TBK1 and IRF3 have been demonstrated to mediate the effects of CK2 on GBM invasion[59], Rac1 and ROCK might indirectly regulate PAK1 via CK2. Supporting this hypothesis are the observations that Rac1 interacts with CK2 at the neuromuscular synapse in the murine hind limb and that CK2 prevents activation of Rac1 by Wnt signaling in

mouse embryonic fibroblast and *Xenopus laevis* oocytes[89,90]. Second, RhoK appears to promote the downstream effects of CK2 on cytoskeleton remodeling in human astrocytes and vascular endothelial cells[91]. Third, CK2 phosphorylates RanGAP1 in cervical carcinoma cells, promoting its activity by stabilizing its complex with Ran and RanBP1[92]. Fourth, CK2 phosphorylates N-WASP and forms a complex with N-WASP in the context of clathrin-mediated endocytosis, diminishing the activity of both[93]. Moreover, CK2 phosphorylates WASP family verprolin-homologous protein (WAVE), an N-WASP homolog, on five different sites[94]. Finally, the formation of an interconnected network of GBM cells in *in vivo* orthotopic mouse models is dependent on GAP43[13], which is likely a direct target of CK2. Murine and bovine Gap43 are phosphorylated by CK2 on two distinct sites[95] and recombinant human CK2 phosphorylates rat Gap43 on five distinct sites *in vitro* and in neuronal growth cones[96]. GAP43 can also function downstream of several Rho GTPases, since GAP43 accumulation at the cell membrane is dependent on Cdc42 and N-WASP in rat pheochromocytoma cells[97] and the GEF TIAM2 induces GAP43 protein expression in neuroblastoma cells in a Rac1-dependent manner[98].

ITGB8 can signal to Rho GTPases in several contexts, including GBM invasion. In an orthotopic glioblastoma mouse model, knockdown of ITGB8 resulted in increased activation of Rac1, PAK1, and Cdc42. In addition, hyperactivation of Rac1 and knockdown of ARHGDIA, a Rho GTPase that interacts with ITGB8, both lead to decreased invasion of LN-229 cells in a Boyden chamber coated with Matrigel[80,81]. This interaction has also been observed in myofibroblasts, where ITGB8 binds ARHGDIA, leading to activation of Rac1[99]. Moreover, ITGB8 regulates the subcellular localization and activity of Rac1, Cdc42, and ARHGDIA via complex formation with protein tyrosine phosphatase (PTP)-PEST in migrating mouse astrocytes and fibroblasts[100].

Although not yet reported in a GBM invasion context, a link between TGFBR1 signaling and CK2 has been described in several other cell types. For example, TGF-β1, the canonical TGFBR1 ligand, inhibited CK2 activity and expression in immortalized murine hepatocytes[101]. Furthermore, pharmacological inhibition of CK2 rescued the TGF-β1 induced epithelial-to-mesenchymal transition of A549 human lung adenocarcinoma cells[102] and the TGF-β-induced expression of apolipoprotein E in a human monocytic leukemia cell line[103]. CK2 also mediated the induction of collagen IV gene transcription by TGF-β1 in murine mesangial cells[104]. Of note, induction of collagen gene transcription by CK2 has been demonstrated to mediate GBM invasion[59].

Taken together, there are strong indications for a bidirectional crosstalk between CK2 and Rho GTPases, although the specific interaction and direction appear to be context-dependent. Similarly, although CK2 appears to be a common upstream regulator of many transcriptional regulators involved in GBM invasion, little is known about the crosstalk between different transcriptional regulators and their exact roles in the pro-invasive signaling network in the context of invasion type and invasion route. Finally, ITGB8 signals upstream of Rho GTPases in the context of GBM

invasion and TGFBR1 downstream signaling appears to be mediated by CK2, but this still needs confirmation in a GBM invasion context. Although not all pieces of the GBM invasion signaling puzzle have been solved, combining all known interactions between Eph/ephrins, Rho GTPases, CK2, ITGB8, TGFBR1 and their downstream transcriptional regulators yields a putative integrated model of GBM invasion signaling (**Figure 1**, Key Figure).

DRUGGABILITY OF GBM INVASION PATHWAYS

Elucidation of GBM invasion pathways provides handles for designing therapeutic interventions. However, inhibiting GBM invasion on itself is unlikely to have considerable impact on survival. Extensive invasion has already occurred at the time of diagnosis, forming the seeds for later recurrence and just preventing invasion will not kill these cells. Thus, anti-invasion therapies need to be combined with other treatments. The benefit of such combinations may come from the creation of more compact tumors with a more drug-penetrable blood-brain barrier (BBB)[105] and from switching cells to a more proliferative phenotype that may render them more sensitive to anti-proliferative therapies such as chemoradiation.

At first glance, the GBM invasion signaling network offers several druggable targets. Inhibitors against TGFBR1, Ephrin receptors, FAK, ROCK, CK2, AKT, JAK, NF-κB, STAT3, and the EZH2 subunit of the PRC2 complex are available. However, not all of these targets appear to be specific to GBM invasion signaling. In our opinion, inhibitors of TGFBR1, Ephrin receptors, FAK, ROCK, or CK2 appear to hold the most promise to specifically target GBM invasion. Notably, the distribution of all such therapeutics may be restricted because the BBB in invasive tumor areas may be relatively intact[105].

Various TGF-β receptor inhibitors are in clinical development. Vactosertib (TEW7197) is tested in a phase I/II trial against myelodysplastic syndrome (ClinicalTrials.gov Identifier NCT03074006). Galunisertib (LY2157299)[106] is more advanced and already being tested against glioma (NCT01220271, NCT01682187, and NCT01582269). Galunisertib combined with lomustine in recurrent GBM did not increase overall survival[107]. However, the efficacy of lomustine against recurrent GBM is limited at best and lomustine may thus not be the ideal candidate to investigate combination therapies that include galunisertib. A phase I/II study combining galunisertib with temozolomide and ionizing radiation, the standard-of-care therapy against GBM, is ongoing (NCT01220271).

Ephrin receptor inhibitors are relatively early in development. The small molecule EphB4 inhibitor NVP-BHG712 has been studied pre-clinically, but so far for inhibition of angiogenesis[108]. In contrast, a phase I study investigating KB004, a recombinant monoclonal antibody against EphA3, against GBM is ongoing (NCT03374943).

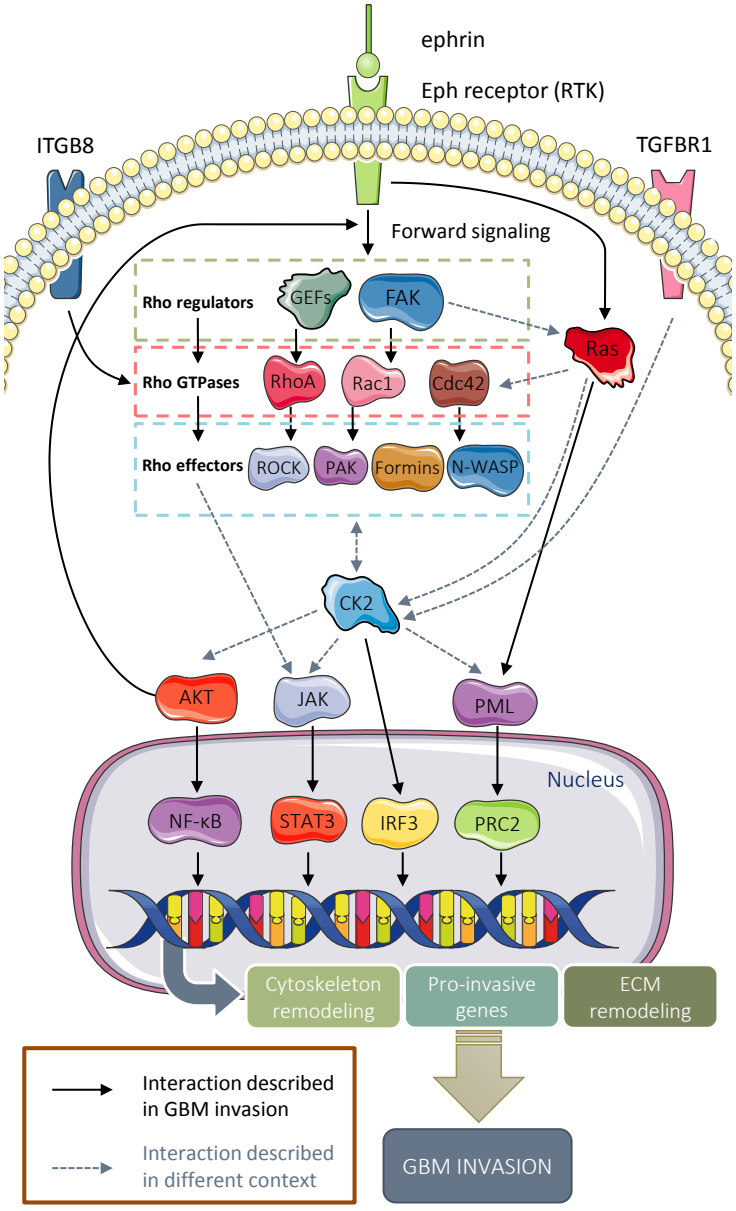

Figure 1, Key Figure. An integrated view on GBM invasion signaling. Schematic of the main pathways in glioblastoma (GBM) invasion and their interplay. Black arrows indicate known interactions in GBM signaling; dashed arrows indicate interactions that have been described in different contexts. Ephrin (Eph) receptors, integrin-β8 (ITGB8), and TGF-β receptor 1 (TGFBR1) are located at the cell membrane and signal downstream via Rho regulators, Rho GTPases, Rho effectors, and casein kinase 2 (CK2) to various transcriptional regulators that induce the expression of pro-invasive genes. CK2 appears to be a pivotal central node in GBM invasion signaling, on which various upstream pathways converge. FAK, focal adhesion kinase; GEFs, guanine nucleotide exchange factor; IRF3, interferon regulatory factor 3; JAK, Janus kinase; NF-κB, nuclear factor-κB; N-WASP, neural Wiskott-Aldrich syndrome protein; PAK, p21-activated kinase; PML, promyelocytic leukemia protein; PRC, polycomb repressive complex; ROCK, Rho-associated protein kinase; RTK, receptor tyrosine kinase; STAT, signal transducer and activator of transcription 3. This figure was prepared using Servier Medical Art under a Creative Commons Attribution 3.0 Unported License.

The development of FAK inhibitors for treatment of cancer is further advanced [109]. Several phase II trials are ongoing, mostly investigating defactinib (VS-6063) and GSK2256098 (*e.g.*, NCT01951690, NCT02523014) . No studies in glioma are yet being conducted.

ROCK inhibitors are already in phase III clinical development, albeit mainly for ophthalmological disorders and not for cancer (NCT03248037, NCT00498615). Preclinical studies have shown promising anti-invasive effects of ROCK inhibitors in several cancers, but convincing data for these effects in GBM are still lacking[110,111].

The CK2 inhibitor silmitasertib (CX4945) has shown to inhibit invasion in preclinical orthotopic mouse models of mesenchymal GBM[59], and is currently being clinically evaluated in several phase I trials for solid tumors and multiple myeloma (NCT00891280, NCT01199718).

CONCLUDING REMARKS

In this feature review, we focused on signaling pathways for which the role in GBM invasion has been extensively validated using *in vitro* systems and *ex vivo* and *in vivo* assays. Several other pathways have been linked to GBM migration *in vitro*, but require further research to demonstrate their *in vivo* relevance (see **Supplementary Table 1**). Most of these pathways have traditionally been evaluated using 2D *in vitro* systems, although many are known to be involved in 3D interactions in the brain microenvironment. We conclude that robust evidence has been generated supporting a pro-invasive role of Ephrin receptors, TGFBR1, ITGB8, Rho GTPases, and CK2.

Important questions in the field remain to be answered (see **Outstanding Questions**). We propose to work toward the integrative mapping of the signaling networks that regulate different types and routes of invasion depending on environmental cues. A recent example of this is the finding that Wnt7 is involved in the perivascular route of GBM invasion[112]. Finally, a standing issue in GBM invasion research is the often ambiguous roles that signaling pathways play in proliferation and invasion signaling. We appreciate the increased use of relevant GBM invasion models that recapitulate key aspects of GBM invasion routes and invasion types. The use of these models will help to discern which of the known pathways truly uncouple invasion signaling from proliferation signaling. Increasing our understanding of context-dependent, invasion-specific signaling will be an important step toward therapeutically targeting this detrimental hallmark of glioblastoma (**Box 6**). The field of therapeutic targeting of GBM invasion is still in its infancy, but several potential drug candidates are under development. However, more in-depth knowledge of GBM invasion signaling is necessary to fully exploit their potential.

REFERENCES

1. Louis, D.N., *et al.* The 2016 World Health Organization classification of tumors of the central nervous system: a summary. *Acta Neuropathol* **131**, 803-820 (2016).
2. Stupp, R., *et al.* Effects of radiotherapy with concomitant and adjuvant temozolomide versus radiotherapy alone on survival in glioblastoma in a randomised phase III study: 5-year analysis of the EORTC-NCIC trial. *Lancet Oncol* **10**, 459-466 (2009).
3. Prados, M.D., *et al.* Toward precision medicine in glioblastoma: the promise and the challenges. *Neuro Oncol* **17**, 1051-1063 (2015).
4. Kallenberg, K., *et al.* Glioma infiltration of the corpus callosum: early signs detected by DTI. *J Neurooncol* **112**, 217-222 (2013).
5. Cheng, L., *et al.* Elevated invasive potential of glioblastoma stem cells. *Biochem Biophys Res Commun* **406**, 643-648 (2011).
6. Bao, S., *et al.* Glioma stem cells promote radioresistance by preferential activation of the DNA damage response. *Nature* **444**, 756-760 (2006).
7. Verhaak, R.G., *et al.* Integrated genomic analysis identifies clinically relevant subtypes of glioblastoma characterized by abnormalities in PDGFRA, IDH1, EGFR, and NF1. *Cancer Cell* **17**, 98-110 (2010).
8. Phillips, H.S., *et al.* Molecular subclasses of high-grade glioma predict prognosis, delineate a pattern of disease progression, and resemble stages in neurogenesis. *Cancer Cell* **9**, 157-173 (2006).
9. Segerman, A., *et al.* Clonal variation in drug and radiation response among glioma-initiating cells is linked to proneural-mesenchymal transition. *Cell Rep* **17**, 2994-3009 (2016).
10. Milano, M.T., *et al.* Patterns and timing of recurrence after temozolomide-based chemoradiation for glioblastoma. *Int J Radiat Oncol Biol Phys* **78**, 1147-1155 (2010).
11. Lun, M., *et al.* The natural history of extracranial metastasis from glioblastoma multiforme. *J Neurooncol* **105**, 261-273 (2011).
12. Bellail, A.C., *et al.* Microregional extracellular matrix heterogeneity in brain modulates glioma cell invasion. *Int J Biochem Cell Biol* **36**, 1046-1069 (2004).
13. Osswald, M., *et al.* Brain tumour cells interconnect to a functional and resistant network. *Nature* **528**, 93-98 (2015).
14. Cuddapah, V.A., *et al.* A neurocentric perspective on glioma invasion. *Nat Rev Neurosci* **15**, 455-465 (2014).
15. Gritsenko, P.G., *et al.* Interstitial guidance of cancer invasion. *J Pathol* **226**, 185-199 (2012).
16. Rao, S.S., *et al.* Toward 3D biomimetic models to understand the behavior of glioblastoma multiforme cells. *Tissue Eng Part B Rev* **20**, 314-327 (2014).
17. Lee, J., *et al.* Tumor stem cells derived from glioblastomas cultured in bFGF and EGF more closely mirror the phenotype and genotype of primary tumors than do serum-cultured cell lines. *Cancer Cell* **9**, 391-403 (2006).
18. Kania, A. & Klein, R. Mechanisms of ephrin–Eph signalling in development, physiology and disease. *Nat Rev Mol Cell Biol* **17**, 240 (2016).
19. Himanen, J.P., *et al.* Repelling class discrimination: ephrin-A5 binds to and activates EphB2 receptor signaling. *Nat Neurosci* **7**, 501-509 (2004).
20. Todd, K.L., *et al.* EphA4 regulates neuroblast and astrocyte organization in a neurogenic niche. *J Neurosci* **37**, 3331-3341 (2017).
21. Jiao, J.W., *et al.* Ephrins as negative regulators of adult neurogenesis in diverse regions of the central nervous system. *Proc Natl Acad Sci U S A* **105**, 8778-8783 (2008).
22. Nakada, M., *et al.* The phosphorylation of ephrin-B2 ligand promotes glioma cell migration and invasion. *Int J Cancer* **126**, 1155-1165 (2010).
23. Day, B.W., *et al.* EphA3 maintains tumorigenicity and is a therapeutic target in glioblastoma multiforme. *Cancer Cell* **23**, 238-248 (2013).
24. Wang, L.F., *et al.* Increased expression of EphA2 correlates with adverse outcome in primary and recurrent glioblastoma multiforme patients. *Oncol Rep* **19**, 151-156 (2008).
25. Wang, L.F., *et al.* Increased expression of EphA7 correlates with adverse outcome in primary and recurrent glioblastoma multiforme patients. *BMC Cancer* **8**, 79 (2008).
26. Binda, E., *et al.* The EphA2 receptor drives self-renewal and tumorigenicity in stem-like tumor-propagating cells from human glioblastomas. *Cancer Cell* **22**, 765-780 (2012).
27. Liu, F., *et al.* A genome-wide screen reveals functional gene clusters in the cancer genome and identifies EphA2 as a mitogen in glioblastoma. *Cancer Res* **66**, 10815-10823 (2006).
28. Miao, H., *et al.* EphA2 promotes infiltrative invasion of glioma stem cells *in vivo* through cross-talk with Akt and regulates stem cell properties. *Oncogene* **34**, 558-567 (2015).
29. Wykosky, J., *et al.* EphA2 as a novel molecular marker and target in glioblastoma multiforme. *Mol Cancer Res* **3**, 541-551 (2005).
30. Teng, L., *et al.* Ligand-dependent EphB1 signaling suppresses glioma invasion and correlates with patient survival. *Neuro Oncol* **15**, 1710-1720 (2013).
31. Wang, S.D., *et al.* EphB2 receptor controls proliferation/migration dichotomy of glioblastoma by interacting with focal adhesion kinase. *Oncogene* **31**, 5132-5143 (2012).
32. Nakada, M., *et al.* The phosphorylation of EphB2 receptor regulates migration and invasion of human glioma cells. *Cancer Res* **64**, 3179-3185 (2004).
33. Tu, Y., *et al.* Expression of EphrinB2 and EphB4 in glioma tissues correlated to the progression of glioma and the prognosis of glioblastoma patients. *Clin Transl Oncol* **14**, 214-220 (2012).
34. Nakada, M., *et al.* Ephrin-B3 ligand promotes glioma invasion through activation of Rac1. *Cancer Res* **66**, 8492-8500 (2006).
35. Krusche, B., *et al.* EphrinB2 drives perivascular invasion and proliferation of glioblastoma stem-like cells. *Elife* **5**, e14845 (2016).
36. Hatano, M., *et al.* EphA2 as a glioma-associated antigen: a novel target for glioma vaccines. *Neoplasia* **7**, 717-722 (2005).
37. Li, J.J., *et al.* EphrinA5 acts as a tumor suppressor in glioma by negative regulation of epidermal growth factor receptor. *Oncogene* **28**, 1759-1768 (2009).
38. Day, B.W., *et al.* Eph receptors as therapeutic targets in glioblastoma. *Br J Cancer* **111**, 1255-1261 (2014).

39. Sahai, E. & Marshall, C.J. RHO-GTPases and cancer. *Nat Rev Cancer* **2**, 133-142 (2002).
40. Ridley, A.J. Rho GTPase signalling in cell migration. *Curr Opin Cell Biol* **36**, 103-112 (2015).
41. Fortin Ensign, S.P., *et al.* Implications of Rho GTPase signaling in glioma cell invasion and tumor progression. *Front Oncol* **3**, 241 (2013).
42. Tran, N.L., *et al.* Increased fibroblast growth factor-inducible 14 expression levels promote glioma cell invasion via Rac1 and nuclear factor-kappaB and correlate with poor patient outcome. *Cancer Res* **66**, 9535-9542 (2006).
43. Chuang, Y.Y., *et al.* Role of synaptojanin 2 in glioma cell migration and invasion. *Cancer Res* **64**, 8271-8275 (2004).
44. Feng, H., *et al.* Activation of Rac1 by Src-dependent phosphorylation of Dock180(Y1811) mediates PDGFRα-stimulated glioma tumorigenesis in mice and humans. *J Clin Invest* **121**, 4670-4684 (2011).
45. Feng, H., *et al.* EGFRvIII stimulates glioma growth and invasion through PKA-dependent serine phosphorylation of Dock180. *Oncogene* **33**, 2504-2512 (2014).
46. Fortin, S.P., *et al.* Cdc42 and the guanine nucleotide exchange factors Ect2 and trio mediate Fn14-induced migration and invasion of glioblastoma cells. *Mol Cancer Res* **10**, 958-968 (2012).
47. Hirata, E., *et al. In vivo* fluorescence resonance energy transfer imaging reveals differential activation of Rho-family GTPases in glioblastoma cell invasion. *J Cell Sci* **125**, 858-868 (2012).
48. Murray, D.W., *et al.* Guanine nucleotide exchange factor Dock7 mediates HGF-induced glioblastoma cell invasion via Rac activation. *Br J Cancer* **110**, 1307-1315 (2014).
49. Wang, H., *et al.* Tax-interacting protein 1 coordinates the spatiotemporal activation of Rho GTPases and regulates the infiltrative growth of human glioblastoma. *Oncogene* **33**, 1558-1569 (2014).
50. Salhia, B., *et al.* The guanine nucleotide exchange factors trio, Ect2, and Vav3 mediate the invasive behavior of glioblastoma. *Am J Pathol* **173**, 1828-1838 (2008).
51. Kwiatkowska, A., *et al.* The small GTPase RhoG mediates glioblastoma cell invasion. *Mol Cancer* **11**, 65 (2012).
52. Gont, A., *et al.* PREX1 integrates G protein-coupled receptor and phosphoinositide 3-kinase signaling to promote glioblastoma invasion. *Oncotarget* **8**, 8559-8573 (2017).
53. Tang, Z., *et al.* c-Src and neural Wiskott-Aldrich syndrome protein (N-WASP) promote low oxygen-induced accelerated brain invasion by gliomas. *PloS One* **8**, e75436 (2013).
54. Watanabe, N., *et al.* Cooperation between mDia1 and ROCK in Rho-induced actin reorganization. *Nat Cell Biol* **1**, 136-143 (1999).
55. Arden, J.D., *et al.* Small-molecule agonists of mammalian Diaphanous-related (mDia) formins reveal an effective glioblastoma anti-invasion strategy. *Mol Biol Cell* **26**, 3704-3718 (2015).
56. Chesarone, M.A., *et al.* Unleashing formins to remodel the actin and microtubule cytoskeletons. *Nat Rev Mol Cell Biol* **11**, 62-74 (2010).
57. Riento, K. & Ridley, A.J. Rocks: multifunctional kinases in cell behaviour. *Nat Rev Mol Cell Biol* **4**, 446-456 (2003).
58. Qin, E.Y., *et al.* Neural precursor-derived pleiotrophin mediates subventricular zone invasion by glioma. *Cell* **170**, 845-859.e819 (2017).
59. Pencheva, N., *et al.* Identification of a druggable pathway controlling glioblastoma invasiveness. *Cell Rep* **20**, 48-60 (2017).
60. Olsten, M.E. & Litchfield, D.W. Order or chaos? An evaluation of the regulation of protein kinase CK2. *Biochem Cell Biol* **82**, 681-693 (2004).
61. Ulrich, T.A., *et al.* The mechanical rigidity of the extracellular matrix regulates the structure, motility, and proliferation of glioma cells. *Cancer Res* **69**, 4167-4174 (2009).
62. Amodeo, V., *et al.* A PML/Slit axis controls physiological cell migration and cancer invasion in the CNS. *Cell Rep* **20**, 411-426 (2017).
63. Scaglioni, P.P., *et al.* A CK2-dependent mechanism for degradation of the PML tumor suppressor. *Cell* **126**, 269-283 (2006).
64. Ji, H. & Lu, Z. The role of protein kinase CK2 in glioblastoma development. *Clin Cancer Res* **19**, 6335-6337 (2013).
65. Zheng, Y., *et al.* Targeting protein kinase CK2 suppresses prosurvival signaling pathways and growth of glioblastoma. *Clin Cancer Res* **19**, 6484-6494 (2013).
66. Parhar, K., *et al.* The role of protein kinase CK2 in intestinal epithelial cell inflammatory signaling. *Int J Colorectal Dis* **22**, 601-609 (2007).
67. Friedmann-Morvinski, D., *et al.* Targeting NF-kappaB in glioblastoma: a therapeutic approach. *Sci Adv* **2**, e1501292 (2016).
68. Cahill, K.E., *et al.* Nuclear factor-kappaB in glioblastoma: insights into regulators and targeted therapy. *Neuro Oncol* **18**, 329-339 (2016).
69. Bhat, K.P.L., *et al.* Mesenchymal differentiation mediated by NF-kappaB promotes radiation resistance in glioblastoma. *Cancer Cell* **24**, 331-346 (2013).
70. Lee, D.W., *et al.* The NF-kappaB RelB protein is an oncogenic driver of mesenchymal glioma. *PloS One* **8**, e57489 (2013).
71. Dhruv, H.D., *et al.* Reciprocal activation of transcription factors underlies the dichotomy between proliferation and invasion of glioma cells. *PloS One* **8**, e72134 (2013).
72. Channavajhala, P. & Seldin, D.C. Functional interaction of protein kinase CK2 and c-Myc in lymphomagenesis. *Oncogene* **21**, 5280-5288 (2002).
73. Zheng, Q., *et al.* JAK2/STAT3 targeted therapy suppresses tumor invasion via disruption of the EGFRvIII/JAK2/STAT3 axis and associated focal adhesion in EGFRvIII-expressing glioblastoma. *Neuro Oncol* **16**, 1229-1243 (2014).
74. Carro, M.S., *et al.* The transcriptional network for mesenchymal transformation of brain tumours. *Nature* **463**, 318-325 (2010).
75. Senft, C., *et al.* Inhibition of the JAK-2/STAT3 signaling pathway impedes the migratory and invasive potential of human glioblastoma cells. *J Neurooncol* **101**, 393-403 (2011).
76. Priester, M., *et al.* STAT3 silencing inhibits glioma single cell infiltration and tumor growth. *Neuro Oncol* **15**, 840-852 (2013).
77. Gray, G.K., *et al.* NF-kappaB and STAT3 in glioblastoma: therapeutic targets coming of age. *Expert Rev Neurother* **14**, 1293-1306 (2014).
78. Kesanakurti, D., *et al.* Essential role of cooperative NF-kappaB and Stat3 recruitment to ICAM-1 intronic consensus elements in the regulation of radiation-induced invasion and migration in glioma. *Oncogene* **32**, 5144-5155 (2013).
79. Zhang, M., *et al.* Blockade of TGF-beta signaling by the TGFbetaR-I kinase inhibitor LY2109761 enhances radiation response and prolongs survival in glioblastoma. *Cancer Res* **71**, 7155-7167 (2011).

80. Reyes, S.B., *et al.* alphavbeta8 integrin interacts with RhoGDI1 to regulate Rac1 and Cdc42 activation and drive glioblastoma cell invasion. *Mol Biol Cell* **24**, 474-482 (2013).
81. Tchaicha, J.H., *et al.* Glioblastoma angiogenesis and tumor cell invasiveness are differentially regulated by beta8 integrin. *Cancer Res* **71**, 6371-6381 (2011).
82. Noren, N.K. & Pasquale, E.B. Eph receptor–ephrin bidirectional signals that target Ras and Rho proteins. *Cell Signal* **16**, 655-666 (2004).
83. Nakada, M., *et al.* EphB2/R-Ras signaling regulates glioma cell adhesion, growth, and invasion. *Am J Pathol* **167**, 565-576 (2005).
84. Basu, S.K., *et al.* Oncogenic RAS-induced perinuclear signaling complexes requiring KSR1 regulate signal transmission to downstream targets. *Cancer Res* **78**, 891-908 (2018).
85. Venkatesh, H.S., *et al.* Targeting neuronal activity-regulated neuroligin-3 dependency in high-grade glioma. *Nature* **549**, 533 (2017).
86. Christina, E., *et al.* Rac1 and PAK1 are upstream of IKK-ε and TBK-1 in the viral activation of interferon regulatory factor-3. *FEBS Lett* **567**, 230-238 (2004).
87. Gonzalez-Forero, D., *et al.* Endogenous Rho-kinase signaling maintains synaptic strength by stabilizing the size of the readily releasable pool of synaptic vesicles. *J Neurosci* **32**, 68-84 (2012).
88. Shin, Y.J., *et al.* Protein kinase CK2 phosphorylates and activates p21-activated kinase 1. *Mol Biol Cell* **24**, 2990-2999 (2013).
89. Herrmann, D., *et al.* Protein kinase CK2 interacts at the neuromuscular synapse with rapsyn, Rac1, 14-3-3γ, and Dok-7 proteins and phosphorylates the latter two. *J Biol Chem* **290**, 22370-22384 (2015).
90. Bryja, V., *et al.* β-Arrestin and casein kinase 1/2 define distinct branches of non-canonical WNT signalling pathways. *EMBO Rep* **9**, 1244-1250 (2008).
91. Kramerov, A.A., *et al.* Cell rounding in cultured human astrocytes and vascular endothelial cells upon inhibition of CK2 is mediated by actomyosin cytoskeleton alterations. *J Cell Biochem* **113**, 2948-2956 (2012).
92. Takeda, E., *et al.* Phosphorylation of RanGAP1 stabilizes its interaction with Ran and RanBP1. *Cell Struct Funct* **30**, 69-80 (2005).
93. Galovic, M., *et al.* Interplay between N-WASP and CK2 optimizes clathrin-mediated endocytosis of EGFR. *J Cell Sci* **124**, 2001-2012 (2011).
94. Pocha, S.M. & Cory, G.O. WAVE2 is regulated by multiple phosphorylation events within its VCA domain. *Cell Motil Cytoskeleton* **66**, 36-47 (2009).
95. Apel, E.D., *et al.* Phosphorylation of neuromodulin (GAP-43) by casein kinase II. Identification of phosphorylation sites and regulation by calmodulin. *J Biol Chem* **266**, 10544-10551 (1991).
96. Dokas, L.A., *et al.* Regulation of *in vitro* phosphorylation of the casein kinase II sites in B-50 (GAP-43). *Brain Res* **781**, 320-328 (1998).
97. Golub, T. & Caroni, P. PI(4,5)P2-dependent microdomain assemblies capture microtubules to promote and control leading edge motility. *J Cell Biol* **169**, 151-165 (2005).
98. Matsuo, N., *et al.* Characterization of STEF, a guanine nucleotide exchange factor for Rac1, required for neurite growth. *J Biol Chem* **277**, 2860-2868 (2002).
99. Lakhe-Reddy, S., *et al.* Beta8 integrin binds Rho GDP dissociation inhibitor-1 and activates Rac1 to inhibit mesangial cell myofibroblast differentiation. *J Biol Chem* **281**, 19688-19699 (2006).
100. Lee, H.S., *et al.* Protein tyrosine phosphatase-PEST and beta8 integrin regulate spatiotemporal patterns of RhoGDI1 activation in migrating cells. *Mol Cell Biol* **35**, 1401-1413 (2015).
101. Cavin, L.G., *et al.* Inhibition of CK2 activity by TGF-beta1 promotes IkappaB-alpha protein stabilization and apoptosis of immortalized hepatocytes. *Hepatology* **38**, 1540-1551 (2003).
102. Kim, J. & Hwan Kim, S. CK2 inhibitor CX-4945 blocks TGF-beta1-induced epithelial-to-mesenchymal transition in A549 human lung adenocarcinoma cells. *PloS One* **8**, e74342 (2013).
103. Singh, N.N. & Ramji, D.P. Transforming growth factor-beta-induced expression of the apolipoprotein E gene requires c-Jun N-terminal kinase, p38 kinase, and casein kinase 2. *Arterioscler Thromb Vasc Biol* **26**, 1323-1329 (2006).
104. Ždunek, M., *et al.* Protein kinase CK2 mediates TGF-beta1-stimulated type IV collagen gene transcription and its reversal by estradiol. *Kidney Int* **60**, 2097-2108 (2001).
105. van Tellingen, O., *et al.* Overcoming the blood–brain tumor barrier for effective glioblastoma treatment. *Drug Resist Updat* **19**, 1-12 (2015).
106. Giannelli, G., *et al.* Transforming growth factor-beta as a therapeutic target in hepatocellular carcinoma. *Cancer Res* **74**, 1890-1894 (2014).
107. Brandes, A.A., *et al.* A Phase II randomized study of galunisertib monotherapy or galunisertib plus lomustine compared with lomustine monotherapy in patients with recurrent glioblastoma. *Neuro Oncol* **18**, 1146-1156 (2016).
108. Martiny-Baron, G., *et al.* The small molecule specific EphB4 kinase inhibitor NVP-BHG712 inhibits VEGF driven angiogenesis. *Angiogenesis* **13**, 259-267 (2010).
109. Sulzmaier, F.J., *et al.* FAK in cancer: mechanistic findings and clinical applications. *Nat Rev Cancer* **14**, 598-610 (2014).
110. Rath, N., *et al.* Rho kinase inhibition by AT13148 blocks pancreatic ductal adenocarcinoma invasion and tumor growth. *Cancer Res* **78**, 3321-3336 (2018).
111. Patel, R.A., *et al.* RKI-1447 is a potent inhibitor of the Rho-associated ROCK kinases with anti-invasive and antitumor activities in breast cancer. *Cancer Res* **72**, 5025-5034 (2012).
112. Griveau, A., *et al.* A glial signature and Wnt7 signaling regulate glioma-vascular interactions and tumor microenvironment. *Cancer Cell* **33**, 874-889 e877 (2018).
113. Friedl, P. & Alexander, S. Cancer invasion and the microenvironment: plasticity and reciprocity. *Cell* **147**, 992-1009 (2011).
114. Zhong, J., *et al.* Mesenchymal migration as a therapeutic target in glioblastoma. *J Oncol* **2010**, 430142 (2010).
115. Cha, J., *et al.* Strategies of mesenchymal invasion of patient-derived brain tumors: microenvironmental adaptation. *Sci Rep* **6**, 24912 (2016).
116. Rao, J.S. Molecular mechanisms of glioma invasiveness: the role of proteases. *Nat Rev Cancer* **3**, 489-501 (2003).
117. Farin, A., *et al.* Transplanted glioma cells migrate and proliferate on host brain vasculature: a dynamic analysis. *Glia* **53**, 799-808 (2006).
118. Scherer, H.J. Structural development in gliomas. *Am J Cancer* **34**, 333-351 (1938).
119. Pedersen, P.H., *et al.* Migratory patterns of lac-z transfected human glioma cells in the rat brain. *Int J Cancer* **62**,

767-771 (1995).
120. Zimmermann, D.R. & Dours-Zimmermann, M.T. Extracellular matrix of the central nervous system: from neglect to challenge. *Histochem Cell Biol* **130**, 635-653 (2008).
121. Zhang, H., *et al.* Expression of a cleaved brain-specific extracellular matrix protein mediates glioma cell invasion *in vivo*. *J Neurosci* **18**, 2370-2376 (1998).
122. Xia, S., *et al.* Tumor microenvironment tenascin-C promotes glioblastoma invasion and negatively regulates tumor proliferation. *Neuro Oncol* **18**, 507-517 (2016).
123. Valster, A., *et al.* Cell migration and invasion assays. *Methods* **37**, 208-215 (2005).
124. Justus, C.R., *et al. In vitro* cell migration and invasion assays. *J Vis Exp* **88**, e51046 (2014).
125. Friedl, P., *et al.* New dimensions in cell migration. *Nat Rev Mol Cell Biol* **13**, 743-747 (2012).
126. Levin, V.A., *et al.* Protein and phosphoprotein levels in glioma and adenocarcinoma cell lines grown in normoxia and hypoxia in monolayer and three-dimensional cultures. *Proteome Sci* **10**, 5 (2012).
127. Heffernan, J.M., *et al.* Bioengineered scaffolds for 3D analysis of glioblastoma proliferation and invasion. *Ann Biomed Eng* **43**, 1965-1977 (2015).
128. Thomas, T.W. & DiMilla, P.A. Spreading and motility of human glioblastoma cells on sheets of silicone rubber depend on substratum compliance. *Med Biol Eng Comput* **38**, 360-370 (2000).
129. David, L., *et al.* Reticulated hyaluronan hydrogels: a model for examining cancer cell invasion in 3D. *Matrix Biol* **23**, 183-193 (2004).
130. Rao, S.S., *et al.* Glioblastoma behaviors in three-dimensional collagen-hyaluronan composite hydrogels. *ACS Appl Mater Interfaces* **5**, 9276-9284 (2013).
131. Yang, Y.L., *et al.* Influence of chondroitin sulfate and hyaluronic acid on structure, mechanical properties, and glioma invasion of collagen I gels. *Biomaterials* **32**, 7932-7940 (2011).
132. Wang, L., *et al.* Astrocytes directly influence tumor cell invasion and metastasis *in vivo*. *PloS One* **8**, e80933 (2013).
133. Coniglio, S.J. & Segall, J.E. Review: molecular mechanism of microglia stimulated glioblastoma invasion. *Matrix Biol* **32**, 372-380 (2013).
134. Chonan, Y., *et al.* Endothelium-induced three-dimensional invasion of heterogeneous glioma initiating cells in a microfluidic coculture platform. *Integr Biol* **9**, 762-773 (2017).
135. Fernandes, J.T.S., *et al.* A novel microfluidic cell co-culture platform for the study of the molecular mechanisms of parkinson's disease and other synucleinopathies. *Front Neurosci* **10**(2016).
136. Gao, Y., *et al.* A versatile valve-enabled microfluidic cell co-culture platform and demonstration of its applications to neurobiology and cancer biology. *Biomed Microdevices* **13**, 539-548 (2011).
137. Ogawa, J., *et al.* Glioblastoma model using human cerebral organoids. *Cell Rep* **23**, 1220-1229 (2018).
138. Jung, S., *et al.* Brain tumor invasion model system using organotypic brain-slice culture as an alternative to *in vivo* model. *J Cancer Res Clin Oncol* **128**, 469-476 (2002).
139. Jung, S., *et al.* Tracking the invasiveness of human astrocytoma cells by using green fluorescent protein in an organotypical brain slice model. *J Neurosurg* **94**, 80-89 (2001).
140. Yoshida, D., *et al.* Tracking cell invasion of human glioma cells and suppression by anti-matrix metalloproteinase agent in rodent brain-slice model. *Brain Tumor Pathol* **19**, 69-76 (2002).
141. Ohnishi, T., *et al.* A novel model of glioma cell invasion using organotypic brain slice culture. *Cancer Res* **58**, 2935-2940 (1998).
142. Jensen, S.S., *et al.* Establishment and characterization of a tumor stem cell-based glioblastoma invasion model. *PloS One* **11**, e0159746 (2016).
143. Holtkamp, N., *et al.* Brain slice invasion model reveals genes differentially regulated in glioma invasion. *Biochem Biophysical Res Commun* **336**, 1227-1233 (2005).
144. Yamada, K.M. & Cukierman, E. Modeling tissue morphogenesis and cancer in 3D. *Cell* **130**, 601-610 (2007).
145. Moser, K.V., *et al.* Brain capillaries and cholinergic neurons persist in organotypic brain slices in the absence of blood flow. *Eur J Neurosci* **18**, 85-94 (2003).
146. Hutter-Schmid, B., *et al.* Organotypic brain slice cultures as a model to study angiogenesis of brain vessels. *Front Cell Dev Biol* **3**, 52 (2015).
147. Guillamo, J.S., *et al.* Migration pathways of human glioblastoma cells xenografted into the immunosuppressed rat brain. *J Neurooncol* **52**, 205-215 (2001).
148. Yoshida, D., *et al.* Inhibition of glioma angiogenesis and invasion by SI-27, an anti-matrix metalloproteinase agent in a rat brain tumor model. *Neurosurgery* **54**, 1213-1222 (2004).
149. Sampetrean, O., *et al.* Invasion precedes tumor mass formation in a malignant brain tumor model of genetically modified neural stem cells. *Neoplasia* **13**, 784-791 (2011).
150. Zhang, F., *et al. In vivo* MRI tracking of cell invasion and migration in a rat glioma model. *Mol Imaging Biol* **13**, 695-701 (2011).
151. Ricard, C. & Debarbieux, F.C. Six-color intravital two-photon imaging of brain tumors and their dynamic microenvironment. *Front Cell Neurosci* **8**, 57 (2014).
152. Pittet, M.J. & Weissleder, R. Intravital Imaging. *Cell* **147**, 983-991 (2011).
153. Joo, K.M., *et al.* Patient-specific orthotopic glioblastoma xenograft models recapitulate the histopathology and biology of human glioblastomas *in situ*. *Cell Rep* **3**, 260-273 (2013).

Outstanding questions

- How is invasion signaling regulated in different glioblastoma (GBM) subtypes? GBM is classified into three distinct subtypes: proneural, mesenchymal, and classical GBM. Of these subtypes, mesenchymal GBM appears to be the most invasive. However, we do not know whether different subtypes use mesenchymal invasion programs to different extents or whether they use entirely different signaling programs.

- To what extent do cerebral organoids mimic the multicellular complexity of the brain and to what extent do they recapitulate the brain extracellular matrix?
- Does casein kinase 2 (CK2) interact with Rho GTPases, TGFBR1, JAK, PML, and AKT in the context of GBM invasion?
- Which signaling pathways uncouple proliferation signaling from invasion signaling? And is this context-dependent? Many pathways have been implicated in invasion signaling, but oftentimes these pathways simultaneously have strong effects on proliferation signaling, making it difficult to assess whether the impact on invasion is direct or indirect. The continued use of appropriate models that allow dissecting invasion from proliferation should elucidate these questions in the future.
- Can we generate an integrative map of GBM invasion signaling in the context of different invasion routes and different invasion types? Given the complexity of GBM invasion signaling, including both intracellular and intercellular communication, a systems biology approach will provide a more general overview of GBM invasion signaling. Such an overview may provide key vantage points for developing therapeutics that target GBM invasion.
- Does anti-invasive therapy sensitize GBM cells to anti-proliferative therapies? As some studies in orthotopic *in vivo* models suggest, inhibition of invasion induces proliferation, in line with the go-or-grow hypothesis. If so, anti-invasive therapy could make GBM cells more sensitive for therapeutic strategies that target proliferating cells, such as chemotherapy and radiotherapy.

Box 1. Invasion routes of GBM

In cancer, several **invasion types** have been described: single cancer cells can invade surrounding tissue in an amoeboid or mesenchymal manner, whereas groups of cancer cells can migrate as mesenchymal chains, clusters, or multicellular sheets[113]. Studies performed in 3D *in vitro* assays, *ex vivo* brain slice cultures, and *in vivo* mouse models have shown that GBM cells predominantly invade in a mesenchymal manner[114,115]. Cells develop protrusions in the direction of migration that depend on receptor-mediated focal adhesion points[113], secrete proteases to degrade the ECM and create new routes for movement[116,] and eventually remodel the cytoskeleton to make new connections that push the cell forward and promote migration. To aid this process of movement, glioma cells use pre-existent brain structures as trails for invasion. Early in the 20th century, it was already observed that GBM cells use different routes for invasion, namely, via white matter tracts, the brain parenchyma, the perivascular space, and the leptomeningeal space, which notably differ in structure and composition[117,118]. White matter tracts are made up of myelinated axons, that are physiologically used by cells to migrate. The corpus callosum is the biggest of these structures and

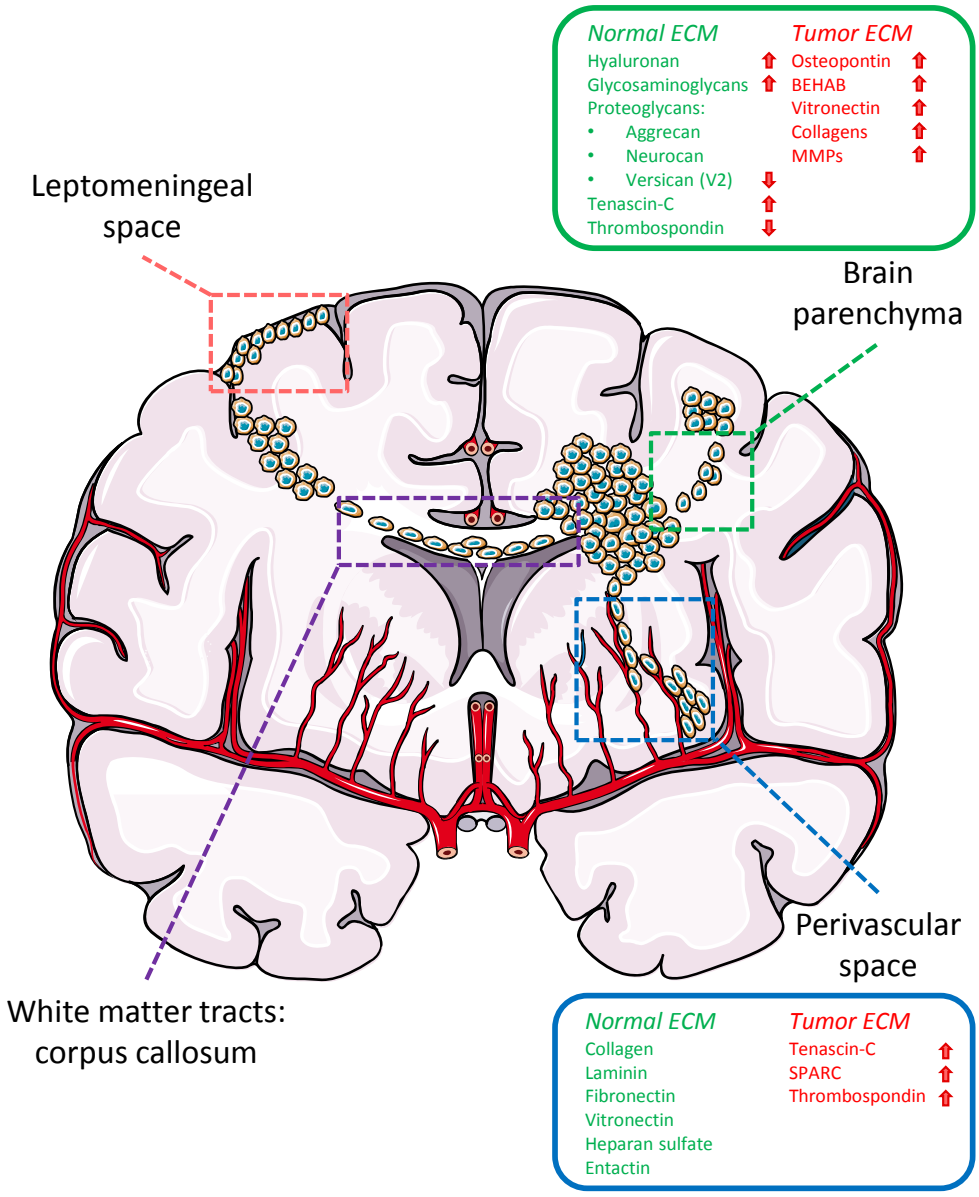

Figure I | Routes of invasion in GBM and topology-specific changes in tumor brain extracellular matrix (ECM) versus normal brain ECM. Four different routes of invasion have been described: via the brain parenchyma, perivascular space, white matter tracts and leptomeningeal space. In green are ECM components present in physiological 'normal ECM' conditions. In red are components only present in the tumor ECM. Red arrows indicate known changes in tumor ECM composition compared to normal ECM. BEHAB, brain-enriched hyaluronan-binding protein; MMPs, matrix metalloproteinases; SPARC, secreted protein acidic and rich in cysteine. This figure was prepared using Servier Medical Art under a Creative Commons Attribution 3.0 Unported License.

is often used by GBM cells as a highway to invade the opposite brain hemisphere[119]. The perivascular space surrounding the blood vessels is filled with fluid and also comprises more rigid matrix components. Both the perivascular space and white matter tracts are frequently used migratory routes for neuroblasts and neurons, suggesting that GBM cells might use similar mechanisms for invasion as neuroblasts[14]. In contrast, the parenchyma accommodates more densely arranged neurons and glia in a softer matrix, thereby making the extracellular space a narrow and tortuous compartment that provides higher physical resistance than the perivascular space[14,15]. GBM cells, however, can actively change the ECM composition. They are able to change the brain parenchyma composition by upregulating hyaluronan, osteopontin, vitronectin, collagens, and tenascin-C and by downregulating thrombospondin and versican (V2). In the perivascular space, tumor cells can upregulate tenascin-C, thrombospondin, and SPARC[12,59,120-122]. ECM that has been remodeled by GBM cells is referred to as 'tumor ECM'. The ability of GBM to use all these different invasion routes implies that different signaling cues must be available to them. This context-dependent invasion signaling is getting more and more appreciated, but much still remains to be elucidated.

Box 2. Two-dimensional in vitro models to study GBM invasion

Cell migration studies in 2D are the simplest model in which the behavior of GBM cells can be studied. The most popular technique is the 'monolayer wound-healing assay' or 'scratch assay'. GBM cells are grown as 2D monolayers on a plastic surface. After a scratch is made, the time that the cells require to migrate and fill the gap is measured. Although this gives an estimation of the migratory capacity of these cells, easily variable parameters, such as the width of the scratch, can change the migration velocity of the cells[123,124]. More importantly, scratch assays are particularly ill-suited to distinguish between proliferative and invasive effects, as proliferation is not measured and being corrected for. As an adaptation to the scratch assay, wells can be coated with ECM components and then used to study the influence of ECM components on molecular pathways involved in GBM migration. Note, however, that commonly used ECM components such as collagen and laminin are only present in the vascular basal membrane, making these assays only relevant for the perivascular invasion route (**Box 1**)[15]. Importantly, these scratch assays model cell migration rather than invasion, since cells can freely move using the open space, whereas invasion implies the need to make room for securing a spot in adjacent structures. Moreover, they fail to recapitulate the complexity of the brain microenvironment, making them unsuitable to assess the influence of the topology or biochemical composition of different parts of the brain on invasion[16].

Box 3. 3D in vitro models to study GBM invasion

3D *in vitro* models are a step forward in the direction of mimicking brain structures in a dish. Several studies have shown important discrepancies between 2D and 3D migration studies,

most likely due to the influence of different substrates and matrices on invasion[125,126]. The most common of these techniques is the Boyden chamber assay that evaluates invasion through a porous insert. Cells are seeded on top of the insert and movement into the bottom compartment is quantified over time. In an effort to better approach physiological conditions, inserts can be coated with a 3D-matrix. The most commonly used are the mouse sarcoma-derived Matrigel and collagen-based matrices. However, Matrigel is made of laminin, entactin, and collagen, which are not brain parenchyma ECM components. Moreover, these matrices are static and, in most cases, the addition of serum or chemo-attractants in the lower compartment is required to speed up the migration, which may not be physiologically relevant[16].

Bioengineered scaffolds are more complex artificial matrices that aim to better recapitulate the brain ECM. Hyaluronan-based hydrogels are popular, since hyaluronan is one of the most abundant components of the brain tumor microenvironment[12,127]. Importantly, bioengineered scaffolds can be devised to study the influence of physical matrix properties such as elasticity, density, or stiffness on GBM migration and invasion[61,128-131]. The physical properties of different brain compartments differ greatly and may therefore have important implications for GBM invasion (**Box 1**).

Even the most complex bioengineered scaffolds are unable to include multiple cell types that are naturally present in the brain environment and have been described to influence GBM invasion[132,133]. Microfluidic co-culture platforms, consisting of a gel scaffold flanked by two parallel channels in which different types of cells can be seeded, can resolve this limitation[134-136]. Using this platform, it is possible to assess the impact of intercellular interactions on GBM invasion. For example, GSCs were found to be more invasive when co-cultured with endothelial cells than when cultured alone and to form an invasive hierarchy. Cells positive for nestin, a stem cell marker, predominantly led the way and were followed by cells expressing the early neural differentiation marker TUBB3[134]. Cerebral organoids were recently developed as a 3D *in vitro* model and although current organoid systems do not have vasculature, co-culturing with endothelial cells could yield complex 3D invasion models in the future that do not require mechanic platforms[137].

Box 4. Ex vivo models to study GBM invasion

Organotypic brain slice cultures combine the relevant *in vivo* brain environment with the throughput of *in vitro* models and have been used since the beginning of this century[83,123,138-141]. In this setup, brain tissue slices are prepared postmortem from animal brains by using a vibratome. The slices are usually cultured on porous inserts in transwell plates. Tumor cells are seeded adjacent to the slice and cell invasion can then be quantified by measuring the distance and penetration depth into the brain slice. A study compared organotypic brain slice invasion models to *in vivo* orthotopic xenograft invasion models and found that these *ex vivo* models recapitulated

the *in vivo* invasion patterns of GBM and that GSCs retained their stem cell characteristics in this setting[142].

The major advantage of organotypic *ex vivo* assays is that the native brain structure creates a physiological microenvironment. This assay allows the evaluation of topological cues, making it a good platform to study tumor–stroma–ECM interactions. It can be used to investigate different invasion routes[117], and to identify genes that are differentially expressed in invasive and non-invasive glioma cells[59,143]. Organotypic *ex vivo* assays offer technical advantages over *in vivo* models, since imaging tissue slices is simpler and allows imaging at a higher resolution than in living organisms[144]. It also requires fewer animals than *in vivo* studies, since multiple slices can be generated from one brain. Although it lacks the flexibility offered by *in vitro* studies to interrogate the influence of different matrices, genetically modified rodent models can be used to alter the expression of some components of the brain microenvironment[35]. Conversely, deterioration of tissue viability in culture conditions is a concern, and limits the useful time span up to 7 to 14 days[59,138]. Another important limitation is the lack of blood supply, implying that endothelial cells are not exposed to shear stress. However, it has been demonstrated that capillaries survive in brain slices in the absence of circulation and that they might still be able to secrete various molecules[145,146]. Overall, despite technical limitations, this *ex vivo* model allows studying invasion in a more physiologically relevant model that preserves the native brain microenvironment.

Box 5. In vivo models to study GBM invasion

In vivo orthotopic xenograft models in mice and rats most closely mimic tumor development inside the complex native brain microenvironment and have been extensively used to study important features of GBM, such as the cellular invasion pattern, the different routes of invasion, and the *in vivo* response to therapy[35,147-149]. In these models, invasion can be assessed using histology or imaging techniques[142,150]. While histological analysis only delivers fixed data points, intravital imaging provides spatiotemporal data per animal, offering dynamic insight into the behavior of tumor cells and their interaction with brain structures[151,152]. Serum-cultured cells injected in the brain display very low invasiveness and these models can only be used to demonstrate increased invasiveness as a consequence of the studied interaction. Importantly, injecting GSCs in the brains of recipient mice yields GBM models that retain the invasive potential found in GBM patients[142,153]. Limitations of *in vivo* studies include ethical concerns, inter-animal variability and the difficulty to scale up experiments. In addition, although intravital imaging allows *in vivo* single-cell resolution, tissue penetration is limited and prevents studying more deeply located invasion routes. Although invasion is usually measured as the distance between satellite cells and the main tumor mass, there is currently no consensus method, hampering robust comparisons between studies. Developing standardized methods such as algorithms that discriminate invasive cells from stationary cells will help to more robustly quantify invasion in the future[149].

Box 6. Clinician's Corner

- Glioblastoma is the most common and aggressive brain tumor and has a dismal prognosis of 12–15 months median survival.
- Glioblastoma is characterized by an unparalleled invasive capacity, making complete surgical resection impossible, conferring resistance to radiotherapy and chemotherapy, and resulting in tumor recurrence in all patients within 2 years after completion of treatment.
- Glioblastoma invasiveness is regulated dependent on the route via which the tumor cells invade the brain: via the brain parenchyma, the perivascular space, white matter tracts, or the leptomeningeal space. Each route has a different local tissue composition that influences how glioblastoma cells convey their pro-invasive signals.
- In the future, any curative therapy for this deadly disease likely includes treatment strategies that interfere with glioblastoma invasiveness. Ephrin receptors, TGF-β receptor 1, Rho GTPases, and casein kinase 2 are attractive targets for such a therapeutic strategy.

GLOSSARY

Boyden chamber: *in vitro* invasion model that evaluates the movement of cells through a porous insert in a transwell system, either in absence or presence of extracellular matrices such as Matrigel.

Casein kinase 2: a constitutively active intracellular kinase that is most known for its role in regulating immunological signaling but is emerging as a player in GBM invasion signaling.

Ephrin receptors: receptor tyrosine kinases that convey intracellular signaling and play important roles in vascular compartmentalization.

Extracellular matrix: the network of proteins and structures that make up the space that is available between cells.

Glioblastoma: the most common adult brain tumor. Despite extensive treatment, patients have dismal prognosis as the disease is uniformly lethal.

Glioma stem cells: an undifferentiated subpopulation of GBM cells that is thought to drive GBM proliferation and growth because of their unlimited replicative potential and high therapeutic resistance.

Invasion: the ability of a cell to remodel its microenvironment, to penetrate and move into its surroundings.

Invasion routes: the routes a cancer cell takes to invade. In the brain, these can be through the parenchyma, along vasculature, via white matter tracts, or in the leptomeningeal space.

Invasion types: the ways in which cancer cells invade surrounding tissue. Single cells can invade in an amoeboid or mesenchymal manner, whereas groups of cancer cells can migrate as mesenchymal chains, clusters, or multicellular sheets.

Mesenchymal GBM: a glioblastoma subtype that is characterized by the overexpression of genes characteristic of the migratory cells of the undifferentiated mesenchyme. This subtype accounts for approximately 30% of primary GBMs and has been related with a higher invasive potential and worse prognosis than other subtypes.

Migration: the ability of a cell to move around in a space that is freely available.

Organotypic brain slice models: preclinical experimental models using brain slices as a matrix for seeding of tumor cells.

Orthotopic: at the site of the native tissue. In the case of glioblastoma xenograft models, this reflects injection of tumor cells into the brains of recipient animals.

Perivascular invasion: invasion along the basement membranes of pre-existent vasculature, often referred to as vessel co-option.

Receptor tyrosine kinases: transmembrane proteins that have a crucial role in regulating intracellular communication. They consist of an extracellular ligand-binding domain and an intracellular region with tyrosine kinase activity. Binding of an exogenous ligand induces activation of the receptor by autophosphorylation of tyrosine residues, ultimately triggering an intracellular signal transduction cascade.

Rho GTPases: enzymes belonging to the Rho family of proteins that convey intracellular signaling using GTP as an energy source.

Temozolomide: a chemotherapeutic that alkylates the O^6 and N^7 residues of guanine, leading to DNA mismatches, futile DNA repair cycles, and ultimately double-strand breaks.

Vascular compartmentalization: a physiological process that prevents cells from invading into the vasculature when this is not desired.

SUPPLEMENTARY TABLES

Reference	Pathway	Invasion model	Cell line*
Amos *et al.*, 2010[1]	PLAU	Boyden chamber + collagen IV *In vivo* orthotopic mouse model difficult to distinguish proliferation and invasion effects	U1242
Anand *et al.*, 2011[2]	MMP1	Boyden chamber + matrigel	T98G
Auf *et al.*, 2010[3]	IRE1/CTGF/ SPARC,THBS1, VEGFA, IL6, IL8	Boyden chamber Chick chorioallantoic membrane assay *In vivo* orthotopic mouse model	U87
Bernhart *et al.*, 2013[4]	PRKD2	Boyden chamber + matrigel	U87
Blandin *et al.*, 2016[5]	ITGA5/ITGAV/ ITGB1/FN1	Spheroid invasion assay	U87, LN-229
Breyer *et al.*, 2000[6]	CD44	*In vivo* orthotopic rat model difficult to distinguish proliferation and invasion effects	C6
Cai *et al.*, 2016[7]	miR-124/CAPN4	Scratch assay Boyden chamber + matrigel	U87, U251
Catalano *et al.*, 2015[8]	BECLIN/ATG5	Scratch assay Boyden chamber + matrigel	GL15
Chahal *et al.*, 2012[9]	MGMT	Boyden chamber + matrigel	U87, T98G, P-GM7, P-GM13
Chen *et al.*, 2017a[10]	HA/CD44 inhibition by anti-CD44	3D bioscaffold assay	U251
Chen *et al.*, 2017b[11]	EGF/MMP9	Boyden chamber + matrigel	A172
Chetty *et al.*, 2012[12]	CD44/MMP9	Scratch assay Boyden chamber + matrigel	4910, 5310
Chigurupati *et al.*, 2010[13]	TRPC6	Boyden chamber + matrigel	U373
D'Alessandro *et al.*, 2016[14]	KCNN4 inhibition by TRAM-34	Scratch assay Boyden chamber + matrigel	GL261
D'Alessandro *et al.*, 2013[15]	CXCL12/CXCR4/ KCNN4	Boyden chamber + matrigel *In vivo* orthotopic mouse model	GL15
DeSouza *et al.*, 2013[16]	HA/MOES	Scratch assay	U87, U373
Di *et al.*, 2013[17]	TRIM11	Scratch assay Boyden chamber + matrigel	D-54MG, U251

Diao *et al.*, 2010[18]	EGFR/VEGFR2 inhibition by DC101	*In vivo* orthotopic mouse model	Patient material propagated in mice
Dikshit *et al.*, 2013[19]	FAT1/PDCD4	Boyden chamber + matrigel	U87, A172
Ding *et al.*, 2011[20]	AQP4/EGF	Scratch assay Boyden chamber + matrigel *In vivo* orthotopic mouse model mention xenograft invasion frequency, data is unclear	LN229
Dong *et al.*, 2012[21]	miR-10b/miR21	Boyden chamber + matrigel	U87
Duan *et al.*, 2015[22]	HOXA13	Boyden chamber + matrigel	U87, U251, LN-229
Enloe and Jay, 2011[23]	PVR	Spheroid invasion assay + collagen I	A172
Eskilsson *et al.*, 2016[24]	EGFRviii/c-SRC	*In vivo* orthotopic rat model	Patient material propagated in rats
Feng *et al.*, 2017[25]	miR-330-5p/ITGA5	Scratch assay Boyden chamber + matrigel	U251
Florczyk *et al.*, 2013[26]	HA	Boyden chamber + collagen I	U118
Fowler *et al.*, 2011[27]	miR-124a	Scratch assay	A172
Friese *et al.*, 2004[28]	TGFB/MMP2/MMP3	Spheroid invasion assay Boyden chamber + matrigel	LNT-229
Galavotti *et al.*, 2013[29]	DRAM1/ATG5/ ATG7/SQSTM1	Scratch assay Boyden chamber + matrigel	G166 GSC line
Gallo-Oller *et al.*, 2016[30]	TGFB inhibition by P144	Scratch assay Boyden chamber +matrigel	U87, A172
Ghosh *et al.*, 2016[31]	TGFB/HMOX1/CD47	Boyden chamber	U87
Gilder *et al.*, 2015[32]	PLAUR/sPLAUR	Boyden chamber + vitronectin	U373
Grazia *et al.*, 2018[33]	SK1	Boyden chamber + matrigel Spheroid invasion assay + collagen	U87
Guo *et al.*, 2013[34]	ID1	Scratch assay Boyden chamber + matrigel difficult to distinguish proliferation and invasion effects	U87
Guo *et al.*, 2015[35]	LRIG3	Scratch assay Boyden chamber difficult to distinguish proliferation and invasion effects	U87, U251
Han *et al.*, 2017[36]	TAGLN2	Spheroid invasion assay + BME *In vivo* orthotopic mouse model	U87, U251, GBM#P3 GSC line

Hou *et al.*, 2016[37]	CSN6	Scratch assay Boyden chamber + matrigel difficult to distinguish proliferation and invasion effects	U87, LN-229
Hsieh *et al.*, 2012[38]	Hypoxia/Nox4	Boyden chamber + matrigel *In vivo* orthotopic mouse model	U87
Hu *et al.*, 2003[39]	ANG2/MMP2	Boyden chamber + matrigel *In vivo* orthotopic mouse model	U87
Hu *et al.*, 2006[40]	ANG2/ITGAV/ ITGB1/FAK/MMP2	Boyden chamber + matrigel *In vivo* orthotopic mouse model	U87
Huang *et al.*, 2018[41]	RAC1/ROCK inhibition by NSC23766 and Y27632	Scratch assay 3D bioscaffold assay	U87
Huijbers *et al.*, 2010[42]	MRC2	Boyden chamber + collagen I 3D bioscaffold assay	SF188
Jabouille *et al.*, 2015[43]	IRE1	*In vivo* orthotopic mouse model	U87
Ji *et al.*, 2018[44]	miR-615	Boyden chamber	U87, U251, SHG-44
Jiang *et al.*, 2017[45]	HSP47	Boyden chamber + matrigel	GBM1, GBM2 GSC lines
Johnson *et al.*, 2015[46]	HGC/MET	Spheroid invasion assay + matrigel	U87
Joseph *et al.*, 2014[47]	TGFB/ZEB1	Scratch assay Boyden chamber + matrigel	U87, U251, GG7, GG14 last two are GSC line
Kegelman *et al.*, 2017[48]	SDCBP inhibition by PDZi	Boyden chamber + matrigel *In vivo* orthotopic mouse model	U87 only *in vitro*, GBM6 GSC line, only *in vivo*
Keunen *et al.*, 2011[49]	VEGF/hypoxia/ HIF-1a inhibition by bevacizumab	*In vivo* orthotopic mouse model	Patient material propagated in mice
Khoshyomn *et al.*, 1999[50]	PLCG1 inhibition by U73122	Spheroid invasion assay + fetal rat brain spheroids	U87, C6
Kim and Kumar, 2014[51]	HA/CD44	Boyden chamber + hyaluronic acid, fibronectin	U373
Kohutek *et al.*, 2009[52]	CDH2/ADAM10	Boyden chamber	U251, U1242
Lamszus *et al.*, 2005[53]	TGFa/CDH5/EGFR/ VEGR2 inhibition by DC101/C225/E4G10	Boyden chamber + collagen *In vivo* orthotopic mouse model	G55
Lan *et al.*, 2015a[54]	MET/miR-144-3p	Boyden chamber + matrigel	U87, U251, LN-229, LN-18

Lan *et al.*, 2015b[55]	POMGNT1/PTPRB	Boyden chamber + matrigel	U251
Lecointre *et al.*, 2015[56]	UTS2/GNA13	Boyden chamber + fibronectin	U87, SW1088
Leng *et al.*, 2015[57]	TRPM7	Boyden chamber + matrigel	A172
Lewis-Tuffin *et al.*, 2010[58]	CDH1	Boyden chamber + collagen I difficult to distinguish proliferation and invasion effects	SF767
Li *et al.*, 2009[59]	PTEN/HGF/c-Met	Scratch assay Boyden chamber + collagen IV	U87/ A172
Li *et al.*, 2011[60]	EGFR/GBP1/MMP1	Boyden chamber + matrigel *In vivo* orthotopic mouse model	U178, A1207, SNB-19
Li *et al.*, 2014a[61]	MUC4/EGFR	Scratch assay Boyden chamber + matrigel	SNB-19, T98G
Li *et al.*, 2014b[62]	DIAPH1	Scratch assay Boyden chamber +matrigel difficult to distinguish proliferation and invasion effects	U87
Li *et al.*, 2017[63]	CXCL12, miR-137	Scratch assay Boyden chamber	U87, U251
Liang *et al.*, 2013[64]	STAT3	Boyden chamber + matrigel	U87, U251
Lin *et al.*, 2015[65]	HRH3	Scratch assay Boyden chamber + matrigel	U87
Lin *et al.*, 2018[66]	SAA1/ITGAV/ITGB3	Scratch assay Boyden chamber + matrigel	U87, A172, patient line 1-3
Liu *et al.*, 2016a[67]	RND3/SNAI1	Scratch assay	U251
Liu *et al.*, 2016b[68]	EGFRviii/hypoxia/ VTN/ITGB3/FAK/ SRC	Boyden chamber + matrigel	U87
Liu *et al.*, 2014[69]	TRPM7	Scratch assay Boyden chamber	A172
Lu *et al.*, 2012[70]	VEGF/VEGFR2/ HGF/MET	Scratch assay *In vivo* orthotopic mouse model difficult to distinguish proliferation and invasion effects	Mouse GSCs
Lucio-Eterovic *et al.*, 2009[71]	VEGF/VEGFR inhibition by bevacizumab	Boyden chamber + matrigel *In vivo* orthotopic mouse model	U87, NSC23 GSC line, only *in vitro*
Lv *et al.*, 2013[72]	TGFB1/CRKL	Scratch assay	U87, U251
Ma *et al.*, 2018[73]	FAM107A	Boyden chamber + matrigel	U373, SHG44

Madan *et al.*, 2016[74]	FAT1	Boyden chamber + matrigel	U87, U373, GOS3
Maugeri *et al.*, 2016[75]	PACAP/VIP	Scratch assay	U87
Mercurio *et al.*, 2017[76]	PC-PLC inhibition by D609	Boyden chamber + matrigel	U87
Micallef *et al.*, 2009[77]	MARCKS	Boyden chamber + matrigel	U373
Miekus *et al.*, 2012[78]	HSP90 inhibition by 17AEP-GA	Boyden chamber	LN-18, LN-229
Mikheeva *et al.*, 2010[79]	TWIST1	Boyden chamber + matrigel *Ex vivo* organotypic brain slice *In vivo* orthotopic mouse model difficult to distinguish proliferation and invasion effects	T98G, SNB-19, GBM6, GBM8 last two are GSC lines
Misek *et al.*, 2017[80]	MLK3/DOCK180	Scratch assay Boyden chamber Spheroid invasion assay + collagen I	LN-229, LN-18
Motiani *et al.*, 2013[81]	STIM1/ORAI1	Boyden chamber	GBM1, GBM8
Mu *et al.*, 2015[82]	IGF2BP2	Scratch assay Boyden chamber + matrigel	U87, U251, GBM-P
Mukherjee *et al.*, 2009[83]	CRMP1	Boyden chamber + gelatin	U87, U373
Munson *et al.*, 2013[84]	CXCR4/CXCL12	Boyden chamber + hyaluronan, collagen I	RT2, U87, C6, 9L
Murray *et al.*, 2014[85]	DOCK7/GAB1	Boyden chamber + fibronectin *Ex vivo* organotypic brain slice	U87, SNB-19
Nager *et al.*, 2015[86]	CTNNB	Boyden chamber + matrigel	U87
Nakada *et al.*, 2013[87]	ITGA3	Boyden chamber + fibronectin, laminin	U87, U251, SNB-19
Newman *et al.*, 2017[88]	IL13RA2	Boyden chamber + matrigel *In vivo* orthotopic mouse model	U87, Gli36
Onken *et al.*, 2016[89]	AXL inhibition by BMS-777607	Boyden chamber *Ex vivo* human GBM slice culture difficult to distinguish proliferation and invasion effects	U118, SF126
Parker *et al.*, 2013[90]	EGFR amplification	*Ex vivo* human GBM slice culture	Patient GBM slices
Patil *et al.*, 2015[91]	IGFBP2	Scratch assay Boyden chamber + matrigel	U87, U251
Praveen Kumar *et al.*, 2014[92]	IGFBP4	Boyden chamber + matrigel	U251, U343

Qin *et al*., 2014a[93]	RDX	Boyden chamber + matrigel difficult to distinguish proliferation and invasion effects	U251
Qin *et al*., 2014b[94]	EMP2	Scratch assay Boyden chamber + fibronectin, collagen I *In vivo* orthotopic mouse model difficult to distinguish proliferation and invasion effects	U373, T98G, U87 only *in vivo*
Roos *et al*., 2018[95]	TNFRSF12A	Boyden chamber + matrigel, collagen	U373
Rosa *et al*., 2018[96]	Hypoxia/KCNM inhibition by paxilline	Scratch assay Boyden chamber	U87, PAL GSC lines
Rosa *et al*., 2017[97]	KCNM inhibition by paxilline and IbTx	Boyden chamber	U87, U87-GSC
Ruiz-Ontanon *et al*., 2013[98]	RAC1/RAC3/ROCK/ ITGAV/ITGB3 inhibition by H1152 and anti-αVβ3	Spheroid invasion assay + matrigel Chick chorioallantoic membrane assay	GIC1-3 GSC lines
Saunders *et al*., 2015[99]	EGFRvIII/JNK2/ HGF/c-MET	Boyden chamber + BME	U87
Sciaccaluga *et al*., 2010[100]	CXCL12/CXCR4/ KCNN4	Boyden chamber	GL15, U251
Serres *et al*., 2014[101]	FN1/ITGA5/ITGB1	Boyden chamber + matrigel, matrigel + HA Spheroid invasion assay + matrigel	U87, U118, U138
Shi *et al*., 2013[102]	miR-21 inhibition by AC1MMYR2	Boyden chamber + matrigel *In vivo* orthotopic mouse model difficult to distinguish proliferation and invasion effects	U87
Sloan *et al*., 2004[103]	PVR/ITGB1	Boyden chamber	U87
Song *et al*., 2003[104]	MIIP/IGFBP2	Boyden chamber + matrigel *In vivo* orthotopic mouse model	LN-229
Song *et al*., 2018[105]	TGFB1/ZEB1/ZEB2	Scratch assay Boyden chamber +matrigel	U87, LN-18
Sulzmaier *et al*., 2016[106]	RSK2	Scratch assay Spheroid invasion assay + matrigel, collagen *Ex vivo* organotypic brain slice	U373, GBM8 GSC line, scratch assay only
Talasila *et al*., 2013[107]	EGFR inhibition by cetuximab	*In vivo* orthotopic rat model	Patient spheroids propagated in rats
Tate *et al*., 2012[108]	BMP7v	*In vivo* orthotopic mouse model difficult to distinguish proliferation and invasion effects	GSLC GSC line

Thomas *et al*., 2010[109]	PTEN/SPARC	Scratch assay + fibronectin *In vivo* orthotopic rat model	U87
Vehlow *et al*., 2017[110]	ITGB1/JNK inhibition by AIIB2 and SP600125	Spheroid invasion assay + collagen I	U343, DD-T4, DK32, DK41, GS-8 last three are GSC lines
Vouri *et al*., 2016[111]	AXL inhibition by BGB234/TIMP1	Boyden chamber + BME	SNB-19
Wang *et al*., 2015[112]	GATA2/ELK1	Boyden chamber + BME	U87
Wang *et al*., 2018[113]	miR-596/MACC1	Boyden chamber + matrigel	U87, U251
Weaver *et al*., 2006[114]	BK channels inhibition by IbTX and paxilline	Boyden chamber	U251
Weber *et al*., 2011[115]	PIK3CA/PI3R1	Boyden chamber + matrigel difficult to distinguish proliferation and invasion effects	SKMG26, D54
Wei *et al*., 2016[116]	miR-373/CD44/TGBR2	Scratch assay Boyden chamber + matrigel	U251
Wong *et al*., 2017[117]	TRPM7 activation by naltriben	Scratch assay Boyden chamber + matrigel	U87
Wu *et al*., 2014[118]	ANXA5	Boyden chamber + BME	U87, U118
Xu *et al*., 2016[119]	FRMD6	Boyden chamber + matrigel	U87, U251
Xu *et al*., 2018a[120]	USP15	Boyden chamber + matrigel difficult to distinguish proliferation and invasion effects	U87, U251
Xu *et al*., 2018b[121]	HOXB3	Boyden chamber + matrigel difficult to distinguish proliferation and invasion effects	U87, U251
Yan *et al*., 2010[122]	SPP1/ITGAV/ITGB3	Boyden chamber + matrigel	U87, U251
Yang *et al*., 2011[123]	L1CAM	Chick chorioallantoic membrane assay	T98G
Yang *et al*., 2017[124]	EGFRviii	Boyden chamber	U87, LN-229, N5
Yen *et al*., 2017[125]	AXL	Scratch assay Boyden chamber + matrigel	1XM
Yen *et al*., 2016[126]	AXL inhibition by m-butylidenephthalide	Scratch assay Boyden chamber + matrigel *In vivo* orthotopic rat model difficult to distinguish proliferation and invasion effects	DBTRG-05MG
Yoshida *et al*., 2004[127]	MMPs by inhibition by SI-27	*In vivo* orthotopic rat model	U251

Yu *et al*., 2016[128]	SPOCK1	Scratch assay Boyden chamber + matrigel	U87, U251
Zanotto-Filho *et al*., 2017[129]	IL6/IL8/CXCR2/ MMP2/RELA	Boyden chamber + BME difficult to distinguish proliferation and invasion effects	U251
Zhang *et al*., 2017[130]	TGFB2/ATG5/ATG7	Scratch assay Boyden chamber +matrigel *In vivo* orthotopic mouse model inhibition by LY2157299, difficult to distinguish proliferation and invasion effects	U87, U251, T98
Zhao *et al*., 2010[131]	MMP9/RAS	Boyden chamber + collagen IV *In vivo* orthotopic mouse model difficult to distinguish proliferation and invasion effects	U1242
Zhuang *et al*., 2013[132]	PLAUR/MMP9	Scratch assay Spheroid invasion assay + agar Boyden chamber + matrigel	U251, 5310
Ziv-Av *et al*., 2015[133]	GLIPR1/N-WASP/ HNRNPK	Boyden chamber +matrigel	U87, U251, A172

Supplementary Table 1 | Overview of pathways that are described in literature to be involved in glioblastoma invasion, but for which robust evidence is still lacking. Only pathways that are functionally validated are included in the overview. If specified, functional validation occurred only using pharmacological inhibitors. In all other instances, functional validation experiments consisted of knockout, knockdown, overexpression studies or a combination of these. In general, it is difficult to distinguish between proliferation and invasion effects in most assays reported in literature. A separate mention of this is included in the table when it was particularly difficult to assess whether an observed effect on invasion was an indirect effect of reduced proliferation. *Cell lines are all serum-cultured lines unless otherwise stated. *GSC*, glioma stem-cell like serum-free cell line; *BME*, basement membrane extract.

SUPPLEMENTARY REFERENCES

1. Amos, S., *et al*. Epidermal growth factor receptor-mediated regulation of urokinase plasminogen activator expression and glioblastoma invasion via C-SRC/MAPK/AP-1 signaling pathways. *J Neuropathol Exp Neurol* **69**, 582-592 (2010).
2. Anand, M., *et al*. Epidermal growth factor induces matrix metalloproteinase-1 MMP-1 expression and invasion in glioma cell lines via the MAPK pathway. *J Neurooncol* **104**, 679-687 (2011).
3. Auf, G., *et al*. Inositol-requiring enzyme 1alpha is a key regulator of angiogenesis and invasion in malignant glioma. *Proc Natl Acad Sci U S A* **107**, 15553-15558 (2010).
4. Bernhart, E., *et al*. Protein kinase D2 regulates migration and invasion of U87MG glioblastoma cells *in vitro*. *Exp Cell Res* **319**, 2037-2048 (2013).
5. Blandin, A.F., *et al*. Glioma cell dispersion is driven by alpha5 integrin-mediated cell-matrix and cell-cell interactions. *Cancer Lett* **376**, 328-338 (2016).
6. Breyer, R., *et al*. Disruption of intracerebral progression of C6 rat glioblastoma by *in vivo* treatment with anti-CD44 monoclonal antibody. *J Neurosurg* **92**, 140-149 (2000).
7. Cai, J.J., *et al*. miR-124 suppresses the migration and invasion of glioma cells *in vitro* via Capn4. *Oncol Rep* **35**, 284-290 (2016).
8. Catalano, M., *et al*. Autophagy induction impairs migration and invasion by reversing EMT in glioblastoma cells. *Mol Oncol* **9**, 1612-1625 (2015).
9. Chahal, M., *et al*. O6-Methylguanine-DNA methyltransferase is a novel negative effector of invasion in glioblastoma multiforme. *Mol Cancer Ther* **11**, 2440-2450 (2012).
10. Chen, J.E., *et al*. The combined influence of hydrogel stiffness and matrix-bound hyaluronic acid content on glioblastoma invasion. *Macromol Biosci* **17**, 1700018 (2017a).
11. Chen, X.C., *et al*. EGF stimulates glioblastoma metastasis by induction of matrix metalloproteinase-9 in an EGFR-dependent mechanism. *Oncotarget* **8**, 65969-65982 (2017b).
12. Chetty, C., *et al*. MMP-9 induces CD44 cleavage and CD44 mediated cell migration in glioblastoma xenograft cells. *Cell Signal* **24**, 549-559 (2012).
13. Chigurupati, S., *et al*. Receptor channel TRPC6 is a key mediator of Notch-driven glioblastoma growth and invasiveness. *Cancer Res* **70**, 418-427 (2010).
14. D'Alessandro, G., *et al*. KCa3.1 channels are involved in the infiltrative behavior of glioblastoma *in vivo*. *Cell Death Dis* **4**, e773 (2013).
15. D'Alessandro, G., *et al*. KCa3.1 channel inhibition sensitizes malignant gliomas to temozolomide treatment. *Oncotarget* **7**, 30781-30796 (2016).
16. DeSouza, L.V., *et al*. Role of moesin in hyaluronan induced cell migration in glioblastoma multiforme. *Mol Cancer* **12**, 74 (2013).
17. Di, K., *et al*. TRIM11 is overexpressed in high-grade gliomas and promotes proliferation, invasion, migration and glial tumor growth. *Oncogene* **32**, 5038-5047 (2013).
18. Diao, Y., *et al*. Enhanced cancer therapy with the combination of EGFR and VEGFR-2 targeting in an orthotopic glioblastoma model. *J Chemother* **22**, 407-412 (2010).
19. Dikshit, B., *et al*. FAT1 acts as an upstream regulator of oncogenic and inflammatory pathways, via PDCD4, in glioma cells. *Oncogene* **32**, 3798-3808 (2013).
20. Ding, T., *et al*. Role of aquaporin-4 in the regulation of migration and invasion of human glioma cells. *Int J Oncol* **38**, 1521-1531 (2011).
21. Dong, C.G., *et al*. Co-inhibition of microRNA-10b and microRNA-21 exerts synergistic inhibition on the proliferation and invasion of human glioma cells. *Int J Oncol* **41**, 1005-1012 (2012).
22. Duan, R., *et al*. HOXA13 is a potential GBM diagnostic marker and promotes glioma invasion by activating the Wnt and TGF-beta pathways. *Oncotarget* **6**, 27778-27793 (2015).
23. Enloe, B.M. & Jay, D.G. Inhibition of Necl-5 CD155/PVR reduces glioblastoma dispersal and decreases MMP-2 expression and activity. *J Neurooncol* **102**, 225-235 (2011).
24. Eskilsson, E., *et al*. EGFRvIII mutations can emerge as late and heterogenous events in glioblastoma development and promote angiogenesis through Src activation. *Neuro Oncol* **18**, 1644-1655 (2016).
25. Feng, L., *et al*. miR-330-5p suppresses glioblastoma cell proliferation and invasiveness through targeting ITGA5. *Biosci Rep* **37,** BSR20170019 (2017).
26. Florczyk, S.J., *et al*. Porous chitosan-hyaluronic acid scaffolds as a mimic of glioblastoma microenvironment ECM. *Biomaterials* **34**, 10143-10150 (2013).
27. Fowler, A., *et al*. miR-124a is frequently down-regulated in glioblastoma and is involved in migration and invasion. *Eur J Cancer* **47**, 953-963 (2011).
28. Friese, M.A., *et al*. RNA interference targeting transforming growth factor-β enhances NKG2D-mediated antiglioma immune response, inhibits glioma cell migration and invasiveness, and abrogates tumorigenicity *in vivo*. *Cancer Res* **64**, 7596-7603 (2004).
29. Galavotti, S., *et al*. The autophagy-associated factors DRAM1 and p62 regulate cell migration and invasion in glioblastoma stem cells. *Oncogene* **32**, 699-712 (2013).
30. Gallo-Oller, G., *et al*. P144, a transforming growth factor beta inhibitor peptide, generates antitumoral effects and modifies SMAD7 and SKI levels in human glioblastoma cell lines. *Cancer Lett* **381**, 67-75 (2016).
31. Ghosh, D., *et al*. TGFbeta-responsive HMOX1 expression is associated with stemness and invasion in glioblastoma multiforme. *Stem Cells* **34**, 2276-2289 (2016).
32. Gilder, A.S., *et al*. Soluble urokinase receptor is released selectively by glioblastoma cells that express epidermal growth factor receptor variant III and promotes tumor cell migration and invasion. *J Biol Chem* **290**, 14798-14809 (2015).
33. Grazia, C.M., *et al*. Cross-talk between sphingosine-1-phosphate and EGFR signaling pathways enhances human glioblastoma cell invasiveness. *FEBS Lett* **592**, 949-961 (2018).
34. Guo, D., *et al*. LRIG3 modulates proliferation, apoptosis and invasion of glioblastoma cells as a potent tumor suppressor. *J Neurol Sci* **350**, 61-68 (2015).
35. Guo, P., *et al*. ID1 regulates U87 human cell proliferation and invasion. *Oncol Lett* **6,** 921-926 (2013).
36. Han, M.Z., *et al*. TAGLN2 is a candidate prognostic biomarker promoting tumorigenesis in human gliomas. *J Exp Clin Cancer Res* **36**, 155 (2017).

37. Hou, J., *et al*. CSN6 controls the proliferation and metastasis of glioblastoma by CHIP-mediated degradation of EGFR. *Oncogene* **36**, 1134 (2016).
38. Hsieh, C.H., *et al*. Imaging the impact of Nox4 in cycling hypoxia-mediated U87 glioblastoma invasion and infiltration. *Mol Imaging Biol* **14**, 489-499 (2012).
39. Hu, B., *et al*. Angiopoietin-2 induces human glioma invasion through the activation of matrix metalloprotease-2. *Proc Natl Acad Sci U S A* **100**, 8904-8909 (2003).
40. Hu, B., *et al*. Angiopoietin 2 induces glioma cell invasion by stimulating matrix metalloprotease 2 expression through the $\alpha_v\beta_1$ integrin and focal adhesion kinase signaling pathway. *Cancer Res* **66**, 775-783 (2006).
41. Huang, Y., *et al*. Three-dimensional hydrogel is suitable for targeted investigation of amoeboid migration of glioma cells. *Mol Med Rep* **17**, 250-256 (2018).
42. Huijbers, I.J., *et al*. A role for fibrillar collagen deposition and the collagen internalization receptor endo180 in glioma invasion. *PloS One* **5**, e9808 (2010).
43. Jabouille, A., *et al*. Glioblastoma invasion and cooption depend on IRE1alpha endoribonuclease activity. *Oncotarget* **6**, 24922-24934 (2015).
44. Ji, Y., *et al*. MiR-615 inhibits cell proliferation, migration and invasion by targeting EGFR in human glioblastoma. *Biochem Biophys Res Commun* **499**, 719-726 (2018).
45. Jiang, X., *et al*. HSP47 promotes glioblastoma stemlike cell survival by modulating tumor microenvironment extracellular matrix through TGF-beta pathway. *ACS Chem Neurosci* **8**, 128-134 (2017).
46. Johnson, J., *et al*. Genomic profiling of a hepatocyte growth factor-dependent signature for MET-targeted therapy in glioblastoma. *J Transl Med* **13**, 306 (2015).
47. Joseph, J.V., *et al*. TGF-beta is an inducer of ZEB1-dependent mesenchymal transdifferentiation in glioblastoma that is associated with tumor invasion. *Cell Death Dis* **5**, e1443 (2014).
48. Kegelman, T.P., *et al*. Inhibition of radiation-induced glioblastoma invasion by genetic and pharmacological targeting of MDA-9/Syntenin. *Proc Natl Acad Sci U S A* **114**, 370-375 (2017).
49. Keunen, O., *et al*. Anti-VEGF treatment reduces blood supply and increases tumor cell invasion in glioblastoma. *Proc Natl Acad Sci U S A* **108**, 3749-3754 (2011).
50. Khoshyomn, S., *et al*. Inhibition of phospholipase C-gamma1 activation blocks glioma cell motility and invasion of fetal rat brain aggregates. *Neurosurgery* **44**, 568-577 (1999).
51. Kim, Y. & Kumar, S. CD44-mediated adhesion to hyaluronic acid contributes to mechanosensing and invasive motility. *Mol Cancer Res* **12**, 1416-1429 (2014).
52. Kohutek, Z.A., *et al*. ADAM-10-mediated N-cadherin cleavage is protein kinase C-alpha dependent and promotes glioblastoma cell migration. *J Neurosci* **29**, 4605-4615 (2009).
53. Lamszus, K., *et al*. Inhibition of glioblastoma angiogenesis and invasion by combined treatments directed against vascular endothelial growth factor receptor-2, epidermal growth factor receptor, and vascular endothelial-cadherin. *Clin Cancer Res* **11**, 4934-4940 (2005).
54. Lan, F., *et al*. miR-144-3p exerts anti-tumor effects in glioblastoma by targeting c-Met. *J Neurochem* **135**, 274-286 (2015a).
55. Lan, J., *et al*. Role of glycosyltransferase PomGnT1 in glioblastoma progression. *Neuro Oncol* **17**, 211-222 (2015b).
56. Lecointre, C., *et al*. Signaling switch of the urotensin II vasoactive peptide GPCR: prototypic chemotaxic mechanism in glioma. *Oncogene* **34**, 5080-5094 (2015).
57. Leng, T.D., *et al*. Suppression of TRPM7 inhibits proliferation, migration, and invasion of malignant human glioma cells. *CNS Neurosci Ther* **21**, 252-261 (2015).
58. Lewis-Tuffin, L.J., *et al*. Misregulated E-cadherin expression associated with an aggressive brain tumor phenotype. *PloS One* **5**, e13665 (2010).
59. Li, Y., *et al*. Interactions between PTEN and the c-Met pathway in glioblastoma and implications for therapy. *Mol Cancer Ther* **8**, 376-385 (2009).
60. Li, M., *et al*. Guanylate binding protein 1 is a novel effector of EGFR-driven invasion in glioblastoma. *J Exp Med* **208**, 2657-2673 (2011).
61. Li, W., *et al*. MUC4 modulates human glioblastoma cell proliferation and invasion by upregulating EGFR expression. *Neurosci Lett* **566**, 82-87 (2014a).
62. Li, Z., *et al*. Mammalian diaphanous-related formin 1 is required for motility and invadopodia formation in human U87 glioblastoma cells. *Int J Mol Med* **33**, 383-391 (2014b).
63. Li, D., *et al*. miR-137 acts as a tumor suppressor via inhibiting CXCL12 in human glioblastoma. *Oncotarget* **8**, 101262-101270 (2017).
64. Liang, Q., *et al*. Inhibition of STAT3 reduces astrocytoma cell invasion and constitutive activation of STAT3 predicts poor prognosis in human astrocytoma. *PloS One* **8**, e84723 (2013).
65. Lin, C.Y., *et al*. Serum amyloid A1 in combination with integrin alphaVbeta3 increases glioblastoma cells mobility and progression. *Mol Oncol* **12**, 756-771 (2018).
66. Lin, J.J., *et al*. Inhibition of histamine receptor 3 suppresses glioblastoma tumor growth, invasion, and epithelial-to-mesenchymal transition. *Oncotarget* **6**, 17107-17120 (2015).
67. Liu, B., *et al*. RND3 promotes Snail 1 protein degradation and inhibits glioblastoma cell migration and invasion. *Oncotarget* **7**, 82411-82423 (2016a).
68. Liu, Z., *et al*. EGFRvIII/integrin beta3 interaction in hypoxic and vitronectin enriching microenvironment promote GBM progression and metastasis. *Oncotarget* **7**, 4680-4694 (2016b).
69. Liu, M., *et al*. TRPM7 channels regulate glioma stem cell through STAT3 and Notch signaling pathways. *Cell Signal* **26**, 2773-2781 (2014).
70. Lu, *et al*. VEGF inhibits tumor cell invasion and mesenchymal transition through a MET/VEGFR2 complex. *Cancer Cell* **22**, 21-35 (2012).
71. Lucio-Eterovic, A.K., *et al*. Mediators of glioblastoma resistance and invasion during antivascular endothelial growth factor therapy. *Clin Cancer Res* **15**, 4589-4599 (2009).
72. Lv, S., *et al*. CrkL efficiently mediates cell proliferation, migration, and invasion induced by TGF-beta pathway in glioblastoma. *J Mol Neurosci* **51**, 1046-1051 (2013).
73. Ma, Y.S., *et al*. DRR1 promotes glioblastoma cell invasion and epithelial-mesenchymal transition via regulating AKT activation. *Cancer Lett* **423**, 86-94 (2018).
74. Madan, E., *et al*. FAT1 is a novel upstream regulator of HIF1alpha and invasion of high grade glioma. *Int J Cancer* **139**, 2570-2582 (2016).
75. Maugeri, G., *et al*. PACAP and VIP inhibit the invasiveness of glioblastoma cells exposed to hypoxia through the regulation of HIFs and EGFR expression. *Front Pharmacol* **7**, 139 (2016).

76. Mercurio, L., *et al*. Phosphatidylcholine-specific phospholipase C inhibition down- regulates CXCR4 expression and interferes with proliferation, invasion and glycolysis in glioma cells. *PloS One* **12**, e0176108 (2017).
77. Micallef, J., *et al*. Epidermal growth factor receptor variant III-induced glioma invasion is mediated through myristoylated alanine-rich protein kinase C substrate overexpression. *Cancer Res* **69**, 7548-7556 (2009).
78. Miekus, K., *et al*. 17AEP-GA, an HSP90 antagonist, is a potent inhibitor of glioblastoma cell proliferation, survival, migration and invasion. *Oncol Rep* **28**, 1903-1909 (2012).
79. Mikheeva, S.A., *et al*. TWIST1 promotes invasion through mesenchymal change in human glioblastoma. *Mol Cancer* **9**, 194 (2010).
80. Misek, S.A., *et al*. EGFR signals through a DOCK180-MLK3 axis to drive glioblastoma cell invasion. *Mol Cancer Res* **15**, 1085-1095 (2017).
81. Motiani, R.K., *et al*. STIM1 and Orai1 mediate CRAC channel activity and are essential for human glioblastoma invasion. *Pflugers Archiv* **465**, 1249-1260 (2013).
82. Mu, Q., *et al*. Imp2 regulates GBM progression by activating IGF2/PI3K/Akt pathway. *Cancer Biol Ther* **16**, 623-633 (2015).
83. Mukherjee, J., *et al*. Loss of collapsin response mediator Protein1, as detected by iTRAQ analysis, promotes invasion of human gliomas expressing mutant EGFRvIII. *Cancer Res* **69**, 8545-8554 (2009).
84. Munson, J.M., *et al*. Interstitial flow in a 3D microenvironment increases glioma invasion by a CXCR4-dependent mechanism. *Cancer Res* **73**, 1536-1546 (2013).
85. Murray, D.W., *et al*. Guanine nucleotide exchange factor Dock7 mediates HGF-induced glioblastoma cell invasion via Rac activation. *Br J Cancer* **110**, 1307-1315 (2014).
86. Nager, M., *et al*. Nuclear phosphorylated Y142 beta-catenin accumulates in astrocytomas and glioblastomas and regulates cell invasion. *Cell Cycle* **14**, 3644-3655 (2015).
87. Nakada, M., *et al*. Integrin alpha3 is overexpressed in glioma stem-like cells and promotes invasion. *Br J Cancer* **108**, 2516-2524 (2013).
88. Newman, J.P., *et al*. Interleukin-13 receptor alpha 2 cooperates with EGFRvIII signaling to promote glioblastoma multiforme. *Nat Commun* **8**, 1913 (2017).
89. Onken, J., *et al*. Inhibiting receptor tyrosine kinase AXL with small molecule inhibitor BMS-777607 reduces glioblastoma growth, migration, and invasion *in vitro* and *in vivo*. *Oncotarget* **7**, 9876-9889 (2016).
90. Parker, J.J., *et al*. Gefitinib selectively inhibits tumor cell migration in EGFR-amplified human glioblastoma. *Neuro Oncol* **15**, 1048-1057 (2013).
91. Patil, S.S., *et al*. Novel anti IGFBP2 single chain variable fragment inhibits glioma cell migration and invasion. *J Neurooncol* **123**, 225-235 (2015).
92. Praveen Kumar, V.R., *et al*. Insulin like growth factor binding protein 4 promotes GBM progression and regulates key factors involved in EMT and invasion. *J Neurooncol* **116**, 455-464 (2014).
93. Qin, J.J., *et al*. Radixin knockdown by RNA interference suppresses human glioblastoma cell growth *in vitro* and *in vivo*. *Asian Pac J Cancer Prev* **15**, 9805-9812 (2014a).
94. Qin, Y., *et al*. Epithelial membrane protein-2 EMP2 activates Src protein and is a novel therapeutic target for glioblastoma. *J Biol Chem* **289**, 13974-13985 (2014b).
95. Roos, A., *et al*. EGFRvIII–Stat5 signaling enhances glioblastoma cell migration and survival. *Mol Cancer Res* **16**, 1185-1195 (2018).
96. Rosa, P., *et al*. BK channels blockage inhibits hypoxia-induced migration and chemoresistance to cisplatin in human glioblastoma cells. *J Cell Physiol* **233**, 6866-6877 (2018).
97. Rosa, P., *et al*. Overexpression of large-conductance calcium-activated potassium channels in human glioblastoma stem-like cells and their role in cell migration. *J Cell Physiol* **232**, 2478-2488 (2017).
98. Ruiz-Ontanon, P., *et al*. Cellular plasticity confers migratory and invasive advantages to a population of glioblastoma-initiating cells that infiltrate peritumoral tissue. *Stem Cells* **31**, 1075-1085 (2013).
99. Saunders, V.C., *et al*. Identification of an EGFRvIII-JNK2-HGF/c-Met-signaling axis required for intercellular crosstalk and glioblastoma multiforme cell invasion. *Mol Pharmacol* **88**, 962-969 (2015).
100. Sciaccaluga, *et al*. CXCL12-induced glioblastoma cell migration requires intermediate conductance Ca^{2+}-activated K^+ channel activity. *Am J Physiol Cell Physiol* **299**, C175-184 (2010).
101. Serres, E., *et al*. Fibronectin expression in glioblastomas promotes cell cohesion, collective invasion of basement membrane *in vitro* and orthotopic tumor growth in mice. *Oncogene* **33**, 3451-3462 (2014).
102. Shi, Z., *et al*. AC1MMYR2, an inhibitor of dicer-mediated biogenesis of Oncomir miR-21, reverses epithelial-mesenchymal transition and suppresses tumor growth and progression. *Cancer Res* **73**, 5519-5531 (2013).
103. Sloan, K.E., *et al*. CD155/PVR plays a key role in cell motility during tumor cell invasion and migration. *BMC Cancer* **4**, 73 (2004).
104. Song, S.W., *et al*. IIp45, an insulin-like growth factor binding protein 2 IGFBP-2 binding protein, antagonizes IGFBP-2 stimulation of glioma cell invasion. *Proc Natl Acad Sci U S A* **100**, 13970-13975 (2003).
105. Song, Y., *et al*. Metformin inhibits TGF-beta1-induced epithelial-to-mesenchymal transition-like process and stem-like properties in GBM via AKT/mTOR/ZEB1 pathway. *Oncotarget* **9**, 7023-7035 (2018).
106. Sulzmaier, F.J., *et al*. RSK2 activity mediates glioblastoma invasiveness and is a potential target for new therapeutics. *Oncotarget* **7**, 79869-79884 (2016).
107. Talasila, K.M., *et al*. EGFR wild-type amplification and activation promote invasion and development of glioblastoma independent of angiogenesis. *Acta Neuropathol* **125**, 683-698 (2013).
108. Tate, C.M., *et al*. A BMP7 variant inhibits the tumorigenic potential of glioblastoma stem-like cells. *Cell Death Diff* **19**, 1644-1654 (2012).
109. Thomas, S.L., *et al*. PTEN augments SPARC suppression of proliferation and inhibits SPARC-induced migration by suppressing SHC-RAF-ERK and AKT signaling. *Neuro Oncol* **12**, 941-955 (2010).
110. Vehlow, A., *et al*. Adhesion- and stress-related adaptation of glioma radiochemoresistance is circumvented by beta1 integrin/JNK co-targeting. *Oncotarget* **8**, 49224-49237 (2017).
111. Vouri, M., *et al*. Axl-EGFR receptor tyrosine kinase hetero-interaction provides EGFR with access to pro-invasive signalling in cancer cells. *Oncogenesis* **5**, e266 (2016).
112. Wang, N., *et al*. microRNA-598 inhibits cell proliferation and invasion of glioblastoma by directly targeting metastasis associated in colon cancer-1. *Oncol Res* (2018).
113. Wang, Z., *et al*. GATA2 promotes glioma progression through EGFR/ERK/Elk-1 pathway. *Med Oncol* **32**, 87 (2015).
114. Weaver, A.K., *et al*. Expression and function of calcium-activated potassium channels in human glioma cells. *Glia* **54**, 223-233 (2006).
115. Weber, G.L., *et al*. Abrogation of PIK3CA or PIK3R1 reduces proliferation, migration, and invasion in glioblastoma

multiforme cells. *Oncotarget* **2**, 833-849 (2011).
116. Wei, F., *et al*. miR-373 inhibits glioma cell U251 migration and invasion by down-regulating CD44 and TGFBR2. *Cell Mol Neurobiol* **36**, 1389-1397 (2016).
117. Wong, R., *et al*. Activation of TRPM7 by naltriben enhances migration and invasion of glioblastoma cells. *Oncotarget* **8**, 11239-11248 (2017).
118. Wu, L., *et al*. Annexin A5 promotes invasion and chemoresistance to temozolomide in glioblastoma multiforme cells. *Tumour Biol* **35**, 12327-12337 (2014).
119. Xu, K., *et al*. Ubiquitin-specific protease 15 promotes tumor cell invasion and proliferation in glioblastoma. *Oncol Lett* **15**, 3846-3851 (2018a).
120. Xu, K., *et al*. Homeobox B3 promotes tumor cell proliferation and invasion in glioblastoma. *Oncol Lett* **15**, 3712-3718 (2018b).
121. Xu, Y., *et al*. FRMD6 inhibits human glioblastoma growth and progression by negatively regulating activity of receptor tyrosine kinases. *Oncotarget* **7**, 70080-70091 (2016).
122. Yan, W., *et al*. Expression pattern of osteopontin splice variants and its functions on cell apoptosis and invasion in glioma cells. *Neuro Oncol* **12**, 765-775 (2010).
123. Yang, C., *et al*. EGFR/EGFRvIII remodels the cytoskeleton via epigenetic silencing of AJAP1 in glioma cells. *Cancer Lett* **403**, 119-127 (2017).
124. Yang, M., *et al*. L1 stimulation of human glioma cell motility correlates with FAK activation. *J Neurooncol* **105**, 27-44 (2011).
125. Yen, S.Y., *et al*. Biodegradable interstitial release polymer loading a novel small molecule targeting Axl receptor tyrosine kinase and reducing brain tumour migration and invasion. *Oncogene* **35**, 2156-2165 (2016).
126. Yen, S.Y., *et al*. n-butylidenephthalide regulated tumor stem cell genes EZH2/AXL and reduced its migration and invasion in glioblastoma. *Int J Mol Sci* **18**, E372 (2017).
127. Yoshida, D., *et al*. Inhibition of glioma angiogenesis and invasion by SI-27, an anti-matrix metalloproteinase agent in a rat brain tumor model. *Neurosurgery* **54**, 1213-1222 (2004).
128. Yu, F., *et al*. SPOCK1 is upregulated in recurrent glioblastoma and contributes to metastasis and temozolomide resistance. *Cell Prolif* **49**, 195-206 (2016).
129. Zanotto-Filho, A., *et al*. Inflammatory landscape of human brain tumors reveals an NF-κB dependent cytokine pathway associated with mesenchymal glioblastoma. *Cancer Lett* **390**, 176-187 (2017).
130. Zhang, C., *et al*. TGF-beta2 initiates autophagy via Smad and non-Smad pathway to promote glioma cells' invasion. *J Exp Clin Cancer Res* **36**, 162 (2017).
131. Zhao, Y., *et al*. An extensive invasive intracranial human glioblastoma xenograft model: role of high level matrix metalloproteinase 9. *Am J Pathol* **176**, 3032-3049 (2010).
132. Zhuang, T., *et al*. Involvement of nitric oxide synthase in matrix metalloproteinase-9- and/or urokinase plasminogen activator receptor-mediated glioma cell migration. *BMC Cancer* **13**, 590 (2013).
133. Ziv-Av, A., *et al*. RTVP-1 regulates glioma cell migration and invasion via interaction with N-WASP and hnRNPK. *Oncotarget* **6**, 19826-19840 (2015).

15

Chapter 16

IDENTIFICATION OF A DRUGGABLE PATHWAY CONTROLLING GLIOBLASTOMA INVASIVENESS

N. Pencheva*, M.C. de Gooijer*, D.J. Vis, L.F.A. Wessels, T. Wurdinger, O. van Tellingen#, and R. Bernards#

* These authors contributed equally # corresponding authors

Cell Reports. 2017;20(1):48-60

ABSTRACT

Diffuse and uncontrollable brain invasion is a hallmark of glioblastoma (GBM), but its mechanism is understood poorly. We developed a three-dimensional (3D) *ex vivo* organotypic model to study GBM invasion. We demonstrate that invading GBM cells upregulate a network of extracellular matrix (ECM) components, including multiple collagens, whose expression correlates strongly with grade and clinical outcome. We identify the interferon regulatory factor 3 (IRF3) as a transcriptional repressor of ECM factors and show that IRF3 acts as a suppressor of GBM invasion. Therapeutic activation of IRF3 by inhibiting casein kinase 2 (CK2)—a negative regulator of IRF3—downregulated the expression of ECM factors and suppressed GBM invasion in *ex vivo* and *in vivo* models across a panel of patient-derived GBM cell lines representative of the main molecular GBM subtypes. Our data provide mechanistic insight into the invasive capacity of GBM tumors and identify a potential therapy to inhibit GBM invasion.

Highlights

- Invading GBM cells induce a network of collagens and collagen-interacting proteins.
- IRF3 acts as a transcriptional repressor of pro-invasive ECM genes in GBM.
- IRF3 activation leads to robust inhibition of GBM invasion.
- CK2 is a negative regulator of IRF3; CK2 inhibition suppresses GBM invasiveness.

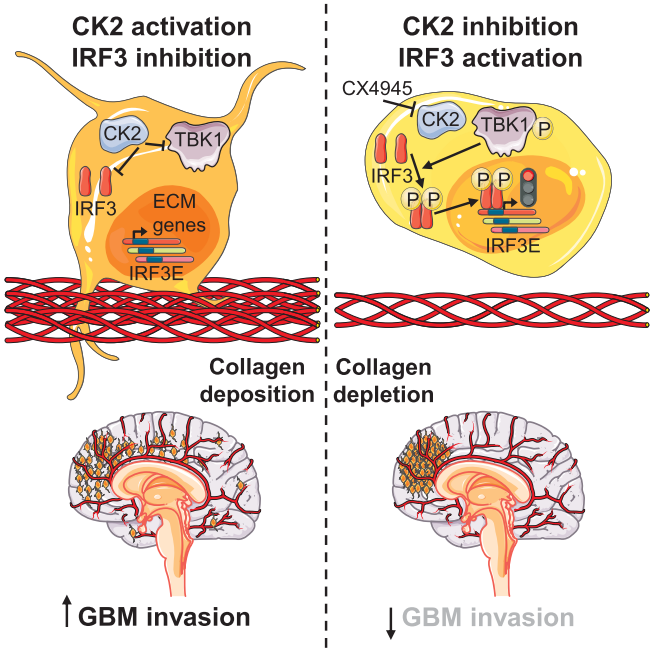

INTRODUCTION

Malignant brain tumors remain intractable, incurring over 140,000 deaths worldwide annually[1]. GBM is the most common and aggressive adult brain tumor typically arising in the glia, the cells providing homeostatic support to neurons. GBM tumors typically present with tentacle-like projections, which diffusely invade and destroy surrounding neural tissue, leading to a devastating outcome: less than 5% of patients survive past the 5-year mark[2,3]. The aggressive clinical manifestation of GBM is fueled by subsets of highly invasive neural stem-like glioma cells that can penetrate deep into the brain and escape therapy[4-6]. Even though integrated whole-genome analyses have catalogued a myriad of gene expression changes and genetic mutations in GBM[7-9], current knowledge of how such aberrations functionally contribute to GBM invasion and progression is incomplete.

Large-scale transcriptomic analyses have revealed that GBM tumors are highly heterogeneous and cluster into four molecularly defined subtypes: mesenchymal, proneural, neural, and classical—each of which is characterized by the distinct expression of 210 genes[8]. Interestingly, recent single-cell analyses have revealed that individual cells in the tumor can exhibit varying degrees of each expression subtype[10]. The mesenchymal subtype, which overexpresses genes characteristic of the loose and migratory cells of the undifferentiated mesenchyme, accounts for 30–50% of primary GBMs, displays one of the shortest survival times, and it is further enriched in recurrent and chemotherapy-resistant tumors[7-9,11]. The observation that mesenchymal genes are overexpressed in high-grade (invasive) versus lower grade gliomas begs the question whether specific mesenchymal pathways are causal to the GBM invasion.

In the past, multiple reports described glioma cell migration using 2D systems and have identified a number of signaling pathways such as the NF-κB, TGF-β and MAPK pathways[12-14]. Importantly, however, tumor cell invasion by definition requires interaction of tumor cells with the 3D extracellular environment, which is insufficiently recapitulated by the previously applied 2D systems. Here we describe the development of a clinically relevant 3D organotypic brain slice model for the *ex vivo* study of human GBM invasiveness. By implementing this model to systematically analyze highly invasive GBM cell populations, we have uncovered a network of ECM collagens and collagen-interacting proteins that are robustly upregulated in mesenchymal GBM tumors and drive GBM invasion. We identify IRF3 as a direct transcriptional repressor of ECM factors. We further show that CK2 acts as a negative regulator of IRF3 activity in human GBM. Therapeutic inhibition of CK2 represses ECM target genes by activating IRF3, resulting in the suppression of GBM invasion *ex vivo* and *in vivo*. Our findings provide a molecular handle on GBM invasiveness by identifying a clinically relevant ECM-driven invasion pathway and revealing a mechanistic rationale for the concerted suppression of pro-invasive ECM factors in GBM.

METHODS

See also **Supplementary Methods**.

Experimental model and subject details

All mouse studies were conducted in accordance with a protocol approved by the Institutional Animal Care and Use Committee at the Netherlands Cancer Institute (NKI) and in agreement with regulations by the European Union. All animals were provided with *ad libitum* supply of chow (RM3 (HDE), Cat# 831096; Special Diet Services; Essex, UK) and water and housed in a 12 h light/dark cycle at 21 °C temperature. Orthotopic glioma xenograft studies were conducted as previously described, using athymic nude or NOD/SCID female mice of approximately seven weeks of age[15]. For generating organotypic brain slices, 4-week old male athymic nude mice were used. NOD/SCID mice were obtained externally from Janvier Labs (Le Genest-Saint-Isle, France). Athymic nude mice were bred in house or ordered from Janvier. All mice ordered from Janvier were allowed to acclimate to the facility for one week before experiments. All experimental procedures were performed during the animals' light cycle. The health status of all mice was daily monitored by animal caretakers.

Patient-derived GNS cells lines (U3013MG, U3117MG, U3017MG, U3084MG, U3086MG, U3024MG, U3031MG, and U3054MG) were obtained through the Human Glioblastoma Culture Resource[16]. GBM8 and serum-cultured cell lines (U87, T98G, 42-MG-BA, and E98) were available in-house. Patient-derived GNS and GBM8 cells were cultured on 1% laminin (Sigma–Aldrich; St. Louis, MO) pre-coated plates and maintained in serum-free NSC media +bFGF/EGF (Thermo Fisher; Waltham, MA) supplemented with 1% GlutaMAX and 1% Pen/Strep. Serum-cultured GBM cells were grown in standard DMEM-based media supplemented with 10% FBS, 1% L-glutamine, and 1% Pen/Strep.

Quantification and statistical analysis

Statistical parameters associated with each figure are reported in the **Figure Legends**. All data are reported as the mean ± SEM, unless stated otherwise in the figure legend. Normalization and differential expression analysis of RNAseq datasets was performed using R and the DESeq2 statistical package with FDR rate set to 0.1package[17]. For pathway enrichment analysis in brain-invasive cell derivatives, we utilized the iPAGE software tool[18]. For discovery of DNA/RNA sequence motif enriched among genes upregulated in brain invasive cell derivatives, we used the FIRE software[19]. Both iPAGE and FIRE are freely available through the iGET portal at Columbia University (iget.c2b2.columbia.edu). The Mantel–Cox log–rank test was used for statistical comparisons in Kaplan–Meier survival analyses for the publicly available clinical

glioma cohort datasets[7,20,21]. The Kolmogorov–Smirnov test was employed in comparing IRF3 immunofluorescence intensity cumulative distributions. The Kruskal–Wallis test was used to compare U3054MG invasiveness and U87MG invasion distance *in vivo*. All other statistical comparisons were carried out using Student's t-tests (one-tailed (paired) for experiments with an *a priori* hypothesis on the direction of the effect and two-tailed (unpaired) for experiments without an *a priori* hypothesis). Throughout all figures: * $p < 0.05$, ** $p < 0.01$, and *** $p < 0.001$. Significance was concluded at $p < 0.05$. Statistical analyses were performed using the GraphPad Prism (v7; GraphPad Software; La Jolla, CA) software.

Accession numbers

Raw and processed data from the next generation RNA sequencing experiments have been deposited to NCBI Gene Expression Omnibus (GEO) under accession number GSE87535.

RESULTS

Development of an organotypic brain slice model of GBM invasion

Traditional models for assessing epithelial tumor cell invasion *in vitro* utilize matrigel, a solubilized basement membrane matrix[22]. Unlike epithelial cancers, invading GBM tumors, however, are not impeded by basement membranes within the brain parenchyma, which is fundamentally different in composition[23]. In order to develop a physiologically relevant brain tumor invasion model, we designed a 3D organotypic brain slice system to study the properties of invading GBM cells *ex vivo*. We established experimental conditions for culturing 300 µm thick organotypic brain slices up to 10 days *ex vivo* in serum-free neural stem-cell media following 1-day pre-treatment in serum-containing media, allowing for greater than 70% slice viability up to 10 days (**Supplementary Figures 1A–B**). In the invasion model, brain slices are cut into two symmetrical halves and GFP-expressing GBM cells are seeded on the insert adjacent to the inner side of each slice hemisphere and allowed to invade for 1 week (**Supplementary Figure 1C**). This approach permits spatial separation of non-invading and invading GBM cell populations. GBM cell invasion through the slice is visualized using confocal microscopy tools. The model also allows to simultaneously monitor cell proliferation/survival of non-invasive GBM cell populations by measuring GBM cell density on the insert surrounding the brain slice.

To test the relevance of the organotypic brain slice invasion model in recapitulating clinical GBM phenotypes, we tested the invasion capacity of a panel of patient-derived glioma neural stem-like (GNS) cells representative of the proneural, classical, and mesenchymal GBM subtypes[16]. Consistent with previous observations that highly invasive GBM tumors are enriched for mesenchymal stem-like properties[9], mesenchymal patient-derived GNS cells exhibited the

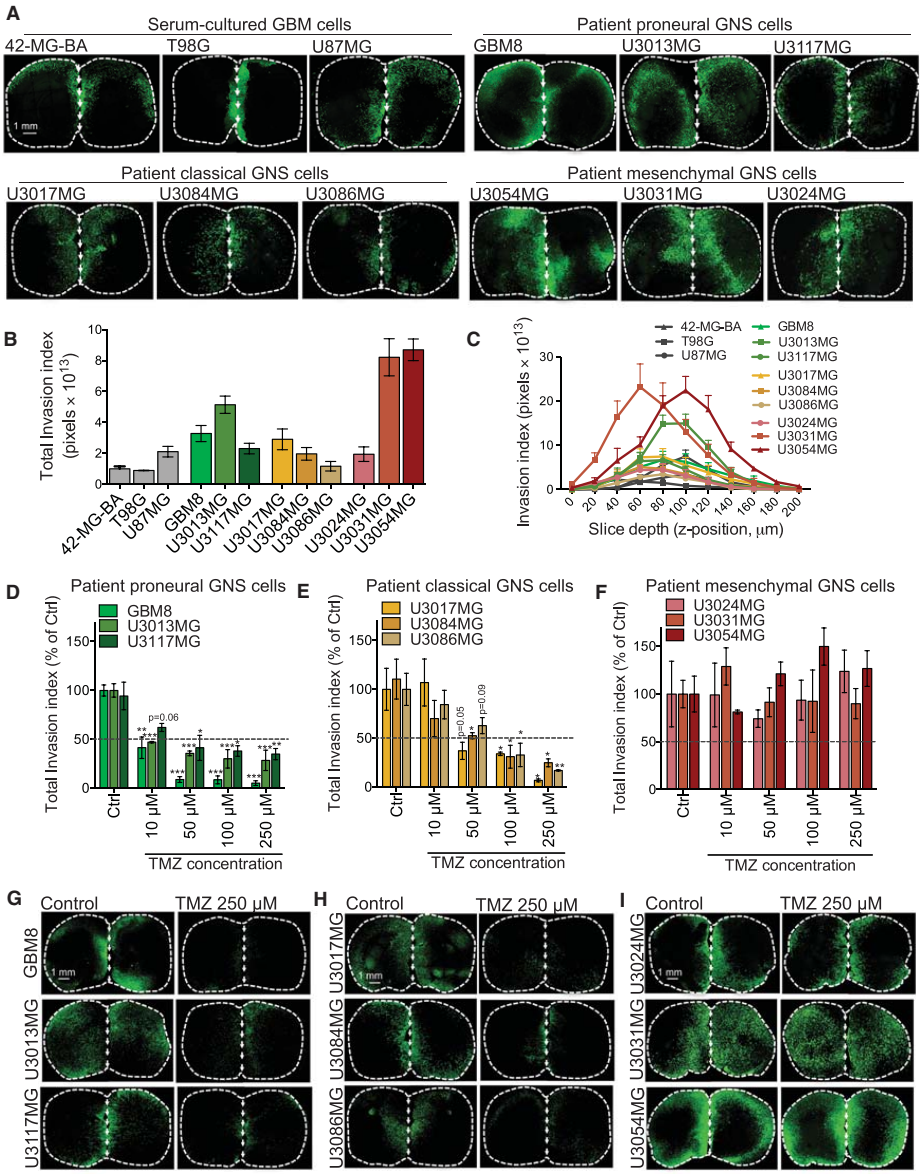

Figure 1 | An ex *vivo* brain slice model of GBM invasion. (**A**) Representative brain slice images, obtained by image tiling and whole-slice image reconstruction, depicting invasion by GFP-positive (GFP^+) GBM cell lines. Dotted lines outline slice contours; arrowheads indicate half-slice cut line. 1×10^5 GFP^+ GBM cells were seeded on the insert adjacent to the inner side of each slice hemispheres and allowed to invade the slices for one week. See also **Supplementary Figure 1C**. (**B**) Quantification of total invasion index by various GBM cell lines shown in (**A**). Invasion index was calculated as the background-corrected GFP^+ signal intensity (a measure of the total cell number in the slice) multiplied by the GFP^+ signal area (a measure of lateral cell invasion) for each z-plane. The total invasion index represents the sum of the invasion indexes across 11 z-planes taken at 20 μm depth increments in the slice. n ≥ 4. (**C**) Invasion index distribution as a function of slice depth/z-plane position. n ≥ 4. (**D–F**) Effect of TMZ treatment on brain slice invasion by patient-derived proneural (**D**), classical (**E**), and mesenchymal (**F**) GNS cell lines. n ≥ 3. (**G–I**) Representative brain slice images depicting invasion by GFP+ proneural (**G**), classical (**H**), or mesenchymal (**I**) GNS cells in response to TMZ treatment. All data are shown as mean ± SEM. * $p < 0.05$, ** $p < 0.01$, *** $p < 0.001$; p-values based on Student's t-tests. See also **Supplementary Figure 1**.

strongest invasion capacity across the cell line panel (**Figures 1A–C**).

We next sought to assess the response of invading GNS cells to temozolomide (TMZ) chemotherapy—the current standard of care for GBM patients. TMZ treatment suppressed the invasive capacity of patient-derived proneural and classical GNS cell lines by greater than 50% (**Figures 1D–E, G–H and Supplementary Figures 1D–E, G–H**). On the contrary, invading mesenchymal GNS cells were fully resistant to the TMZ treatment (**Figures 1F, I and Supplementary Figures 1F, I**). These findings are consistent with recent transcriptomic analyses on single-cell derived glioma-initiating clonal populations, revealing that therapy resistance is associated with a proneural-to-mesenchymal transition in GNS cell cultures[24].

Systematic identification of molecular pathways deregulated in GBM invasion

To systematically interrogate the molecular pathways governing GBM invasion, we performed an *ex vivo* selection screen to enrich for highly invasive GBM cell subpopulations from the poorly invasive U87MG parental cells. Transcriptomic profiling by next-generation RNA sequencing (RNA-Seq) of two independently derived U87MG brain-invasive derivatives (C1 and C2), which exhibited two-fold or higher increase in invasion capacity compared to the minimally invasive U87MG control cells (**Figure 2B**), revealed a common set of 71 upregulated genes (**Figure 2A and Supplementary Figure 2B**). Gene ontology analysis using the iPAGE software tool[18] showed that transcripts upregulated by the brain invasive derivatives were strongly enriched for ECM components (17 out of 71 genes), which consisted of multiple collagen members, including both subunits of collagen I (*COL1A1, COL1A2*) and collagen V (*COL5A1, COL5A2*) and *COL8A1*, as well as multiple collagen-interacting proteins (*CTGF, FBN1, MFAP4, SPARC, TGFBI, THBS1*) and collagen-processing enzymes (*LOX, LOXL1, LOXL3*) (**Figures 2A, C**). Notably, these ECM factors were expressed at higher levels in patient mesenchymal GBM tumors compared to proneural, neural, and classical GBM tumors (**Figure 2D and Supplementary Figure 2A**), revealing a significant association between this experimentally derived pro-invasive ECM signature and the mesenchymal GBM subtype. Additionally, the brain-invasive derivatives of two independent patient-derived mesenchymal GNS cell lines (U3031MG and U3054MG), which express high levels of mesenchymal ECM factors at baseline, exhibited even further induction of ECM collagens and collagen-interacting factors (**Figure 2E and Supplementary Figure 2C**). Consistent with a pro-invasive collagen function, exogenous addition of recombinant collagens I and V to the collagen-deficient proneural GBM8 GNS cells synergistically increased their brain slice invasion capacity without any effect on cell proliferation/survival (**Figure 2F and Supplementary Figure 2D**).

We next asked whether these pro-invasive ECM factors are prognostically relevant to clinical glioma outcomes. We focused on collagens I and V, as the genes encoding both subunits of each collagen were among the most upregulated transcripts both in mesenchymal GBM patient

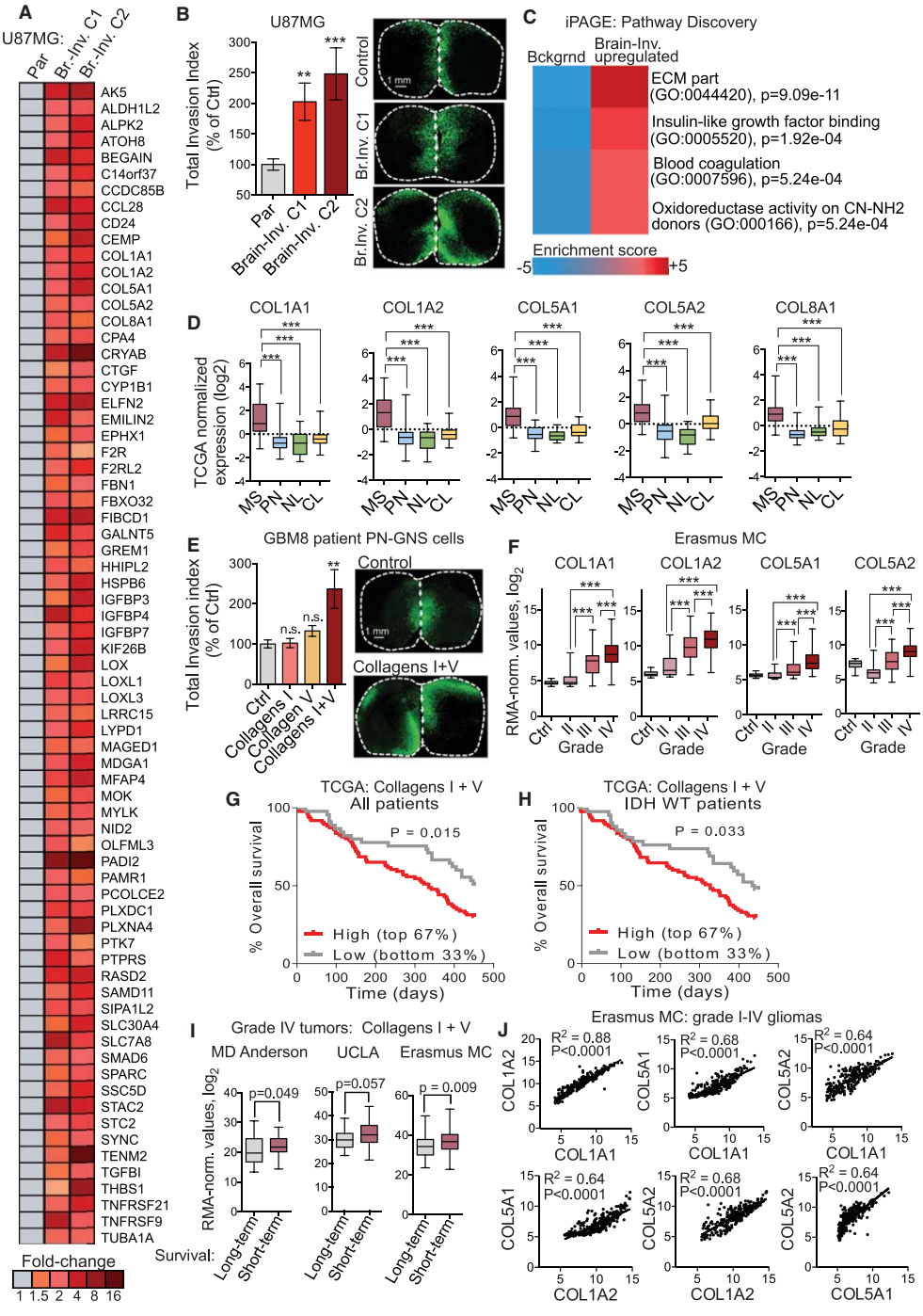
A
U87MG:
Par
Br.-Inv. C1
Br.-Inv. C2
AK5
ALDH1L2
ALPK2
ATOH8
BEGAIN
C14orf37
CCDC85B
CCL28
CD24
CEMP
COL1A1
COL1A2
COL5A1
COL5A2
COL8A1
CPA4
CRYAB
CTGF
CYP1B1
ELFN2
EMILIN2
EPHX1
F2R
F2RL2
FBN1
FBXO32
FIBCD1
GALNT5
GREM1
HHIPL2
HSPB6
IGFBP3
IGFBP4
IGFBP7
KIF26B
LOX
LOXL1
LOXL3
LRRC15
LYPD1
MAGED1
MDGA1
MFAP4
MOK
MYLK
NID2
OLFML3
PADI2
PAMR1
PCOLCE2
PLXDC1
PLXNA4
PTK7
PTPRS
RASD2
SAMD11
SIPA1L2
SLC30A4
SLC7A8
SMAD6
SPARC
SSC5D
STAC2
STC2
SYNC
TENM2
TGFBI
THBS1
TNFRSF21
TNFRSF9
TUBA1A
Fold-change
1 1.5 2 4 8 16
B
U87MG
Total Invasion Index (% of Ctrl)
Par
Brain-Inv. C1
Brain-Inv. C2
Control
Br.Inv. C1
Br.Inv. C2
1 mm
C
iPAGE: Pathway Discovery
Bckgrnd
Brain-Inv. upregulated
ECM part (GO:0044420), p=9.09e-11
Insulin-like growth factor binding (GO:0005520), p=1.92e-04
Blood coagulation (GO:0007596), p=5.24e-04
Oxidoreductase activity on CN-NH2 donors (GO:000166), p=5.24e-04
Enrichment score
-5
+5
D
COL1A1
COL1A2
COL5A1
COL5A2
COL8A1
TCGA normalized expression (log2)
MS
PN
NL
CL
E
GBM8 patient PN-GNS cells
Total Invasion index (% of Ctrl)
Ctrl
Collagens I
Collagen V
Collagens I+V
n.s.
Control
1 mm
F
Erasmus MC
RMA-norm. values, log2
Grade
G
TCGA: Collagens I + V
All patients
P = 0.015
% Overall survival
High (top 67%)
Low (bottom 33%)
Time (days)
H
TCGA: Collagens I + V
IDH WT patients
P = 0.033
I
Grade IV tumors: Collagens I + V
MD Anderson
UCLA
Erasmus MC
p=0.049
p=0.057
p = 0.009
Survival:
Long-term
Short-term
J
Erasmus MC: grade I-IV gliomas
R2 = 0.88
P<0.0001
R2 = 0.68
P<0.0001
R2 = 0.64
P<0.0001

Figure 2 | Systematic interrogation of molecular pathways deregulated in GBM invasion. (**A**) Heatmap depicting the fold-change in expression levels of transcripts identified as significantly upregulated (adj. $p < 0.05$) in two independently derived brain invasive cell clones (Br.Inv. C1 and Br.Inv.C2). Fold-changes were calculated from normalized RNAseq counts. (**B**) Total invasion index by U87MG control cells and two independently derived brain invasive U87MG derivatives (C1 and C2). Data are shown as mean ± SEM. n ≥ 3. *p*-values based Student's t-tests. (**C**) Heatmap depicting the enrichment score results from gene ontology (GO) pathway analysis, performed using the iPAGE software, on genes upregulated in U87MG brain invasive derivatives. (**D**) Box and whisker plots depicting microarray-based normalized expression levels for *COL1A1*, *COL1A2*, *COL5A1*, *COL5A2*, and *COL8A1* in mesenchymal (n = 56), proneural (n = 53), neural (n = 26), and classical (n = 38) GBM tumors from the TCGA cohort[8]. Whiskers represent min and max values; box extent corresponds to 25th–75th percentile. *p*-values based on Student's t-tests. (**E**) ECM target gene transcript levels, quantified by real-time quantitative polymerase chain reaction (RT-qPCR), in the brain invasive derivatives of mesenchymal U3031 GNS cells isolated from brain slices (Brain) and their respective control cells (Control). n ≥ 3. Data are shown as mean ± SEM. *p*-values based on Student's t-tests. (**F**) Total invasion index by proneural GBM8 GNS cells treated with control, collagen I (10 µg/ml), collagen V (10 µg/ml), or collagen I + V (10 µg/ml each). n ≥ 3. Data are shown as mean ± SEM. *p*-values based on Student's t-tests. (**G**) Box and whisker plots depicting microarray-based normalized expression values for *COL1A1*, *COL1A2*, *COL5A1*, and *COL5A2* as a function of glioma grade (normal control (Ctrl, n = 8); grade II (n = 24); grade III (n = 85); grade IV (n = 159) in the Erasmus Medical Center (MC) cohort[21]. n = 276. *p*-values based on Student's t-tests. Whiskers represent min and max values; box extent corresponds to 25th–75th percentile. (**H**) Kaplan–Meier curves depicting overall survival outcomes of GBM patients from the MD Anderson cohort[7] as a function of the combined collagen I + V expression levels in their tumors. The bottom 25th expression percentile was used as a stratification cut-off. n = 56. *p*-value based on log-rank (Mantel–Cox) test. (**I**) Box and whisker graphs showing combined collagen I and V expression levels in tumors of long-term GBM survivors (top 25% longest survival outcomes) and short-term survivors (remaining 75%) in the MD Anderson[7] (n = 56), UCLA[20] (n = 50), and Erasmus MC[21] (n = 150) cohorts. Whiskers represent min and max values; box extent corresponds to 25th–75th percentile. *p*-values based on Student's t-tests. (**J**) Pearson correlation analysis of *COL1A1*, *COL1A2*, *COL5A1*, and *COL5A2* expression levels in glioma tumors from the Erasmus MC cohort. n = 276. * $p < 0.05$, ** $p < 0.01$, *** $p < 0.001$. See also **Supplementary Figure 2**.

tumors as well as in multiple brain-invasive GBM cell line derivatives. Notably, the expression levels of *COL1A1, COL1A2, COL5A1*, and *COL5A2* significantly correlated with glioma progression stage and overall survival outcomes across three independent glioma cohorts (**Figure 2G and Supplementary Figures 2E–I**)[7,20,21].

We next examined the correlation between collagen I and V and survival outcomes among stage IV, high-grade GBM tumors only. Remarkably, the 25% of stage IV patients with the lowest tumor levels of collagens I and V exhibited significantly better survival outcomes (**Figure 2H**). Consistently, long-term GBM survivors, defined as the top 25% patients with longest survival times, had significantly reduced collagen I and V tumor levels (**Figure 2I**). Importantly, the individual expression levels of *COL1A1*, *COL1A2*, *COL5A1*, and *COL5A2* were significantly correlated with each other in patient glioma tumors from three independent clinical cohorts (**Figure 2J and Supplementary Figures 2J–K**), suggestive of a common upstream mechanism driving concerted ECM collagen expression in glioma tumors.

Discovery of IRF3 as a transcriptional repressor of pro-invasive ECM factors in GBM

To identify possible upstream regulators of pro-invasive ECM factors, we employed an unbiased computationally guided approach, using the FIRE motif discovery algorithm[19], to search for DNA/RNA regulatory motifs enriched in the regulatory sequences of the 71 genes upregulated by invasive GBM cell derivatives (**Figure 2A**). This approach yielded one motif (5'-T-A/G-GGGGC-3') that was significantly enriched in the promoters of genes upregulated by brain invasive U87MG derivatives (**Figure 3A**). Notably, this motif was present in the promoters of 42 of the 71 upregulated genes

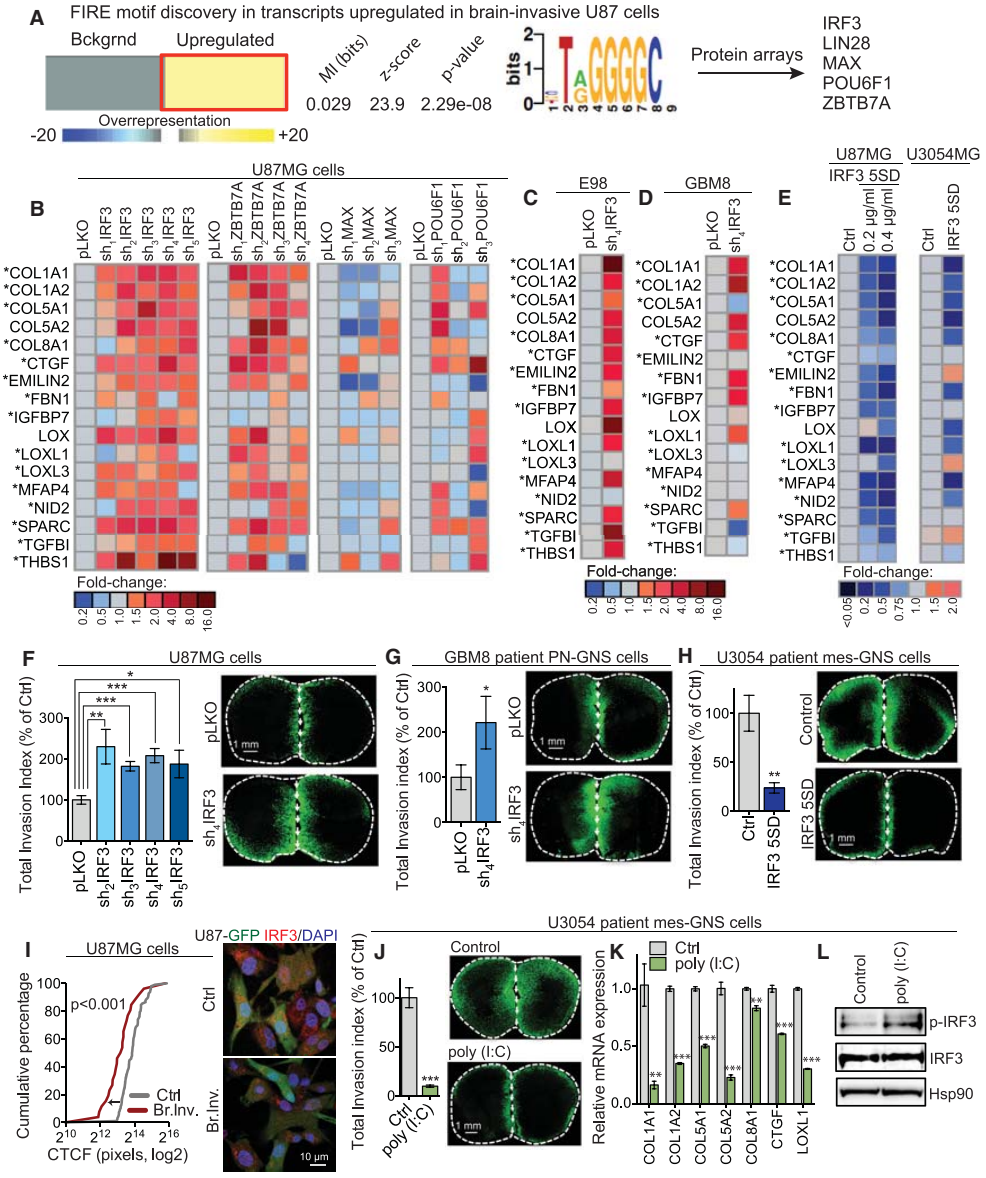

and 15 of the 17 ECM factors among these genes. Protein array data generated by the software suggested a set of five transcription factors (IRF3, LIN28A, MAX, POU6F1, and ZBTB7A) with binding activity for this DNA sequence. We performed loss-of-function experiments for all four factors expressed in U87MG cells (IRF3, ZBTB7A, MAX, and POU6F1) and observed that depletion of IRF3 led to robust upregulation of ECM target transcript levels (**Figure 3B and Supplementary Figures 3A, D–E**), implicating IRF3 as a transcriptional repressor of pro-invasive collagens and

Figure 3 | IRF3 acts as an endogenous suppressor of GBM invasion by transcriptionally repressing a pro-invasive ECM gene network. (**A**) Summary of results generated by the FIRE motif-finding algorithm on the 71 transcripts upregulated in the U87MG brain-invasive cell derivatives. Heatmap depicts the fold-enrichment score for the motif. Transcription factors previously found to bind DNA sequences containing the motif were identified in at least two independent protein array datasets. (**B–E**) Heatmaps of the fold-changes in mean expression levels, determined by RT-qPCR analyses, for ECM genes in: (**B**) U87MG cells stably expressing a control empty vector (pLKO) or a vector encoding an shRNA targeting IRF3, ZBTB7A. MAX, or POU6F1; (**C**) E98 cells expressing an empty vector or a vector containing an IRF3 shRNA; (**D**) GBM8 cells expressing a control vector or an IRF3 shRNA vector; (**E**) U87MG and U3054MG GNS cells transfected with an empty pRK5 vector (control) or a pRK5 vector containing constitutively active IRF3 5SD mutant. n ≥ 3. (**F–G**) Total invasion index by U87MG cells (**F**) and proneural GBM8 GNS cells (**G**) expressing an empty vector or an IRF3 shRNA vector. n ≥ 6 (**F**). n ≥ 3 (**G**). Data are shown as mean ± SEM. *p*-values based on Student's t-tests. (**H**) Total invasion index by U3054MG GNS cells transfected with a control or IRF3 5SD plasmid. n = 3. Data are shown as mean ± SEM. *p*-values based on Student's t-tests. (**I**) Cumulative fraction plot of the distribution of IRF3 background-corrected total cell fluorescence (CTCF), measured by IRF3 immunocytochemistry and confocal microscopy in U87MG control cells and their brain invasive derivatives. n ≥ 26 cells; *p*-value based on Kolmogorov–Smirnov test. (**J**) Total invasion index by U3054MG GNS cells treated with poly (I:C) (50 μg/ml) or control. n = 4. Data are shown as mean ± SEM; *p*-values based on Student's t-tests. (**K**) RT-qPCR analysis of the expression levels of *COL1A1*, *COL1A2*, *COL5A1*, *COL8A1*, *CTGF*, and *LOXL1* in U3054MG GNS cells treated with poly (I:C) (50 μg/ml) or control for 24 h. n = 3. Data are shown as mean ± SEM; *p*-values based on Student's t-tests. (**L**) Western blot analysis of phosphorylated IRF3 (p-IRF3), IRF3, and HSP90 in U3054MG GNS cells treated with poly (I:C) (50 μg/ml) or control for 3 h. HSP90 was used as a loading control. * $p < 0.05$, ** $p < 0.01$, *** $p < 0.001$. See also **Supplementary Figure 3**.

collagen-interacting factors in GBM. Knockdown of ZBTB7A also led to upregulation of multiple collagens and ECM factors, albeit its effect across the entire ECM gene signature was less robust than that of IRF3 loss. Knockdowns of MAX and POU6F1 did not have a clear unilateral effect on ECM gene expression (**Figure 3B and Supplementary Figure 3A**).

IRF3 acts as an endogenous suppressor of GBM invasion

Consistent with the robust effect of IRF3 loss on ECM transcript level induction, U87MG cells transduced with four independent short hairpin RNAs (shRNAs) targeting IRF3 exhibited a roughly two-fold increase in brain slice invasion without any corresponding effect on cell survival/proliferation (**Figure 3F and Supplementary Figures 3D–E, 3H–I**), revealing that endogenous IRF3 is required for invasion suppression. In comparison, knockdown of ZBTB7A did not yield a clear invasion phenotype, with only one out of four shRNAs conferring increase in invasion (**Supplementary Figures 3J–L**). The inferior effect of ZBTB7A depletion on GBM cell invasion could be due to the less pronounced effect of ZBTB7A loss on target induction across the entire ECM expression signature (**Figure 3B**). Alternatively, ZBTB7A could be targeting IRF3-independent factors, which could counteract the anti-invasive effects of ZBTB7A-driven ECM target repression.

Consistent with a requirement for endogenous IRF3 in suppressing GBM invasion, depletion of IRF3 in the independent E98 primary GBM cell line led to robust upregulation of ECM target gene expression (**Figure 3C and Supplementary Figure 3B**). Additionally, IRF3 silencing in the patient-derived proneural GBM8 cells caused significant induction in the levels of several collagens and collagen-interacting factors (**Figure 3D**) with a corresponding two-fold increase in brain slice invasion (**Figure 3G and Supplementary Figures 3C, M**).

Activation of IRF3 signaling is sufficient for suppressing GBM invasion

IRF3 is a latent transcription factor that normally resides in the cytosol. Upon signal activation, IRF3 is phosphorylated by its upstream kinase TBK1, homodimerizes, and translocates to the nucleus where it regulates target gene transcription[25,26]. To study the effect of transcriptionally active IRF3, we overexpressed a constitutively active form of IRF3, IRF3 5SD, where the C-terminal serine residues are converted into aspartate amino acids[27]. Overexpression of IRF3 5SD in two independent GBM cell lines led to repression of ECM gene expression (**Figures 3E and Supplementary Figures 3F–G**). Importantly, IRF3 5SD transfection elicited a marked inhibition in brain slice invasion, causing greater than 70% invasion suppression in the highly invasive U3054MG cells without any corresponding decrease in cell survival/ proliferation (**Figure 3H and Supplementary Figures 3N–P**). Taken together, these findings indicate that IRF3 is both required and sufficient for the suppression of GBM invasion.

Consistent with the invasion suppressive effect observed for IRF3, the brain invasive U87MG derivatives were enriched for single cells with lower total IRF3 levels compared to minimally invasive control cells. This decrease in IRF3 levels was pronounced for both cytoplasmic and nuclear IRF3 without an effect on IRF3 cytoplasmic-to-nuclear trafficking (**Figure 3I and Supplementary Figure 3Q**). These data suggest that clonal selection for cells with low total IRF3 levels could be enabling increased expression of pro-invasive ECM factors and ultimately conferring enhanced invasion capacity.

To determine if cell-extrinsic activation of IRF3 can suppress GBM invasion, we treated the highly invasive patient-derived mesenchymal GNS cells with poly (I:C), a synthetic double-strand RNA analogue that acts as an agonist for toll-like receptor 3 (TLR3) signaling—an activator of IRF3[28]. Consistent with our model, poly (I:C) treatment led to a significant decrease in brain slice invasion, downregulation of IRF3 ECM target gene expression, and a corresponding increase in IRF3 activation measured by IRF3 phosphorylation (**Figures 3J–L and Supplementary Figures 3R–V**). Collectively, these findings reveal that IRF3 activation is sufficient to strongly suppress GBM invasion.

CK2 inhibition activates IRF3 and represses IRF3 target ECM genes

Previous work identified CK2 as a negative regulator of IRF3 activation in murine fibroblasts and macrophages[29]. We hypothesized that if the negative regulation of IRF3 activity by CK2 is conserved in human GBM cells, then inhibition of CK2 should repress IRF3 target ECM genes by activating IRF3 and ultimately block tumor invasion. Consistent with this, treatment of U87MG cells and mesenchymal GNS cell lines with two structurally distinct CK2 inhibitors (CX4945 and TBB) caused significant reduction in expression levels for the vast majority of IRF3 ECM target

genes (**Figure 4A**). Additionally, genetic depletion of CSNK2A1, the catalytically active subunit of CK2, also caused repression of IRF3 ECM target genes (**Figure 4A**). Notably, two ECM genes, *EMILIN2* and *MFAP4*, were consistently upregulated upon CK2 inhibitor treatment, suggesting decoupling between CK2 inhibition and IRF3 activation. The observed upregulation in *EMILIN2* and *MFAP4* could be due to IRF3-independent CK2 targets or off-target effects of the CK2 inhibitor, as these two genes were not upregulated upon CSNK2A1 genetic inactivation.

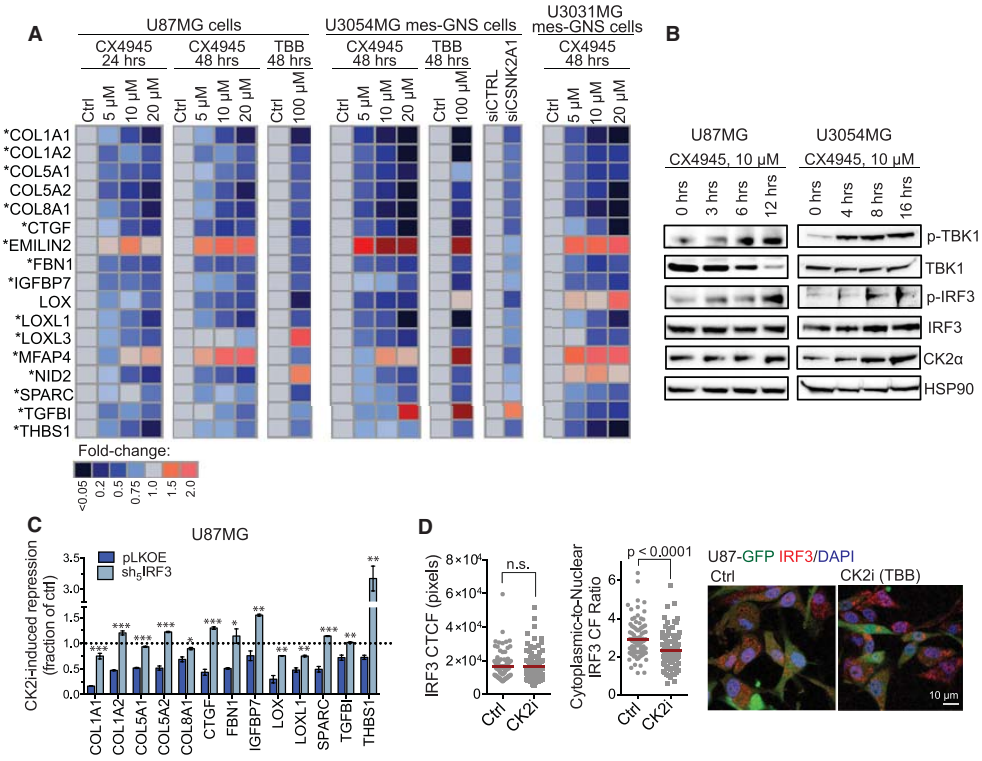

Figure 4 | CK2 is a negative regulator of IRF3 activation in GBM. (**A**) Heat-map of the fold-changes in mean expression levels, measured by RT-qPCR, of IRF3 ECM target genes in U87MG cells and U3054MG and U3031MG GNS cells that were treated with two CK2 inhibitors, CX4945 or TBB, at the indicated concentrations for 24 or 48 h. U3054MG cells were also transfected with an siRNA SMART pool targeting CSNK2A1 or a control non-targeting siRNA pool, and the expression levels of IRF3 ECM target genes were determined by RT-qPCR 72 h later. n = 3. (**B**) Western blot analysis of TBK1, phosphorylated TBK1 (p-TBK1), IRF3, phosphorylated IRF3 (p-IRF3), CK2α, and HSP90 loading control in U87MG cells and U3054 GNS cells in response to 10 µM CX4945 treatment for the indicated durations. (**C**) Transcript levels of IRF3 target genes in U87MG cells expressing an empty control vector or an IRF3 shRNA vector. Cells were treated with 100 µM TBB for 48 h, and the fold repression in gene expression upon CK2 inhibitor (CK2i) treatment relative to control was determined by RT-qPCR. Dotted line indicates absence of expression change. n = 3–4. (**D**) IRF3 CTCF (right graph) and cytoplasmic-to-nuclear background-corrected fluorescence (CF) ratio (left graph) were determined by IRF3 immunocytochemistry and confocal microscopy in U87MG cells treated with CK2i (100 µM TBB) or control for 16 h. n = 96 cells (control), n = 103 cells (CK2i). All data are shown as mean ± SEM. * $p < 0.05$, ** $p < 0.01$, *** $p < 0.001$; *p*-values based on Student's t-tests. See also **Supplementary Figure 4**.

Consistent with CK2 acting upstream of IRF3, CK2 inhibitor treatment led to an increase in the phosphorylated forms of both IRF3 as well as its main upstream kinase TBK1 (**Figure 4B**). To

determine if the effect of CK2 inhibition on pro-invasive ECM gene expression is mediated by increased IRF3 activation, we assessed the ability of the CK2 inhibitor to repress ECM gene levels in GBM cells depleted of IRF3. IRF3 loss abrogated the repressive effect of CK2 inhibition on ECM target gene expression (**Figure 4C**). Importantly IRF3 depletion partially attenuated U87MG invasion suppression by CK2 inhibition without affecting cell proliferation/survival (**Supplementary Figure 4**). These findings are consistent with IRF3 acting as a negative downstream mediator of the CK2 effects on invasion and ECM gene expression, while also pointing to potential additional CK2 targets that might contribute to GBM invasion suppression by CK2 inhibition.

IRF3 nuclear translocation, an event that occurs upon IRF3 phosphorylation, was increased in GBM cells treated with the CK2 inhibitor (**Figure 4D**), consistent with CK2 inhibition repressing ECM gene expression by increasing IRF3 phosphorylation and triggering IRF3 nuclear translocation. To determine if i.) IRF3 directly binds to its target ECM genes' promoters and ii.) IRF3 target binding is enhanced upon CK2 inhibition, we performed chromatin immunoprecipitation (ChIP) using anti-IRF3 or control IgG antibodies in U87MG cells treated with a CK2 inhibitor or control. Even in the absence of CK2 inhibition, anti-IRF3 ChIP resulted in a significant enrichment of chromatin fragments corresponding to the promoter regions of ECM genes harboring the IRF3 binding motif (**Figure 3A**), indicating that endogenous IRF3 directly binds to its target ECM genes (**Figure 5**). Importantly, CK2 inhibitor treatment triggered further increase in IRF3 promoter binding (**Figure 5**), consistent with CK2 inhibition activating IRF3-dependent transcriptional repression of ECM target genes.

CK2 inhibition suppresses GBM invasion ex vivo

CK2α (the catalytically active CK2 subunit) and IRF3 were broadly expressed across a panel of 14 serum-cultured GBM cell lines and patient-derived GNS cells representative of the main molecular subtypes in GBM (**Figure 6A**), suggesting that CK2 and IRF3 could be broadly targeted across multiple GBM subtypes. Interestingly, phosphorylated IRF3 was expressed at higher levels in serum-cultured GBM cells compared to patient-derived GNS cells (**Figure 6A**), consistent with the poor invasive capacity of serum-cultured cells in our model (**Figures 1A–C**).

We next evaluated the efficacy of CK2 inhibition in suppressing *ex vivo* brain invasion across multiple GBM cell line models. Notably, CK2 inhibitor treatment robustly suppressed brain slice invasion in a dose-dependent manner across nine independent patent-derived GNS cell lines representative of the mesenchymal, classical, and proneural GBM tumor subtypes (**Figures 6B–D and Supplementary Figures 5A–F**). Interestingly, at lower inhibitor concentrations (up to 5 μM CX4945), the effect of CK2 inhibition was on average two-fold stronger on invasion suppression compared to cell survival/proliferation inhibition across all cell lines tested (**Figures**

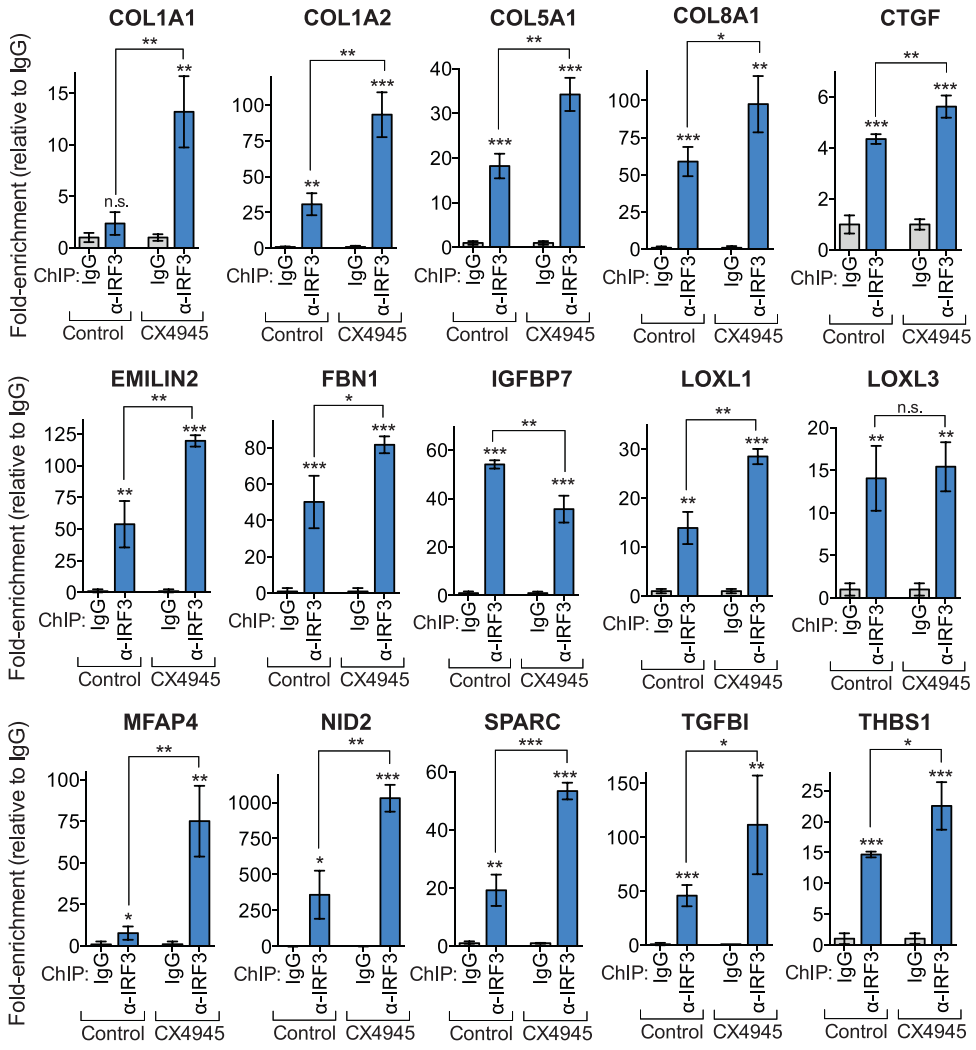

Figure 5 | IRF3 directly binds to ECM target genes' promoter regions. Fold-enrichment of genomic DNA fragments corresponding to gene promoter regions harboring the IRF3 motif (5'-T-A/G-GGGGC-3') following ChIP with anti-IRF3 antibody relative to IgG. ChIP reactions were performed using 25 µg of sheared chromatin prepared from U87MG cells pre-treated with 10µM CX4945 or control for 24 h. n = 3. All data are shown as mean ± SEM. * $p < 0.05$, ** $p < 0.01$, *** $p < 0.001$; p-values based on Student's t-tests.

6B–D and Supplementary Figures 5A–F). Notably, the U3031MG and U3054MG cells—the two mesenchymal patient-derived GNS cell lines with the highest invasion capacity in our cell line panel (**Figures 1A–C**)—were fully insensitive on cell proliferation/ survival at 5 µM CX4945, yet their brain slice invasion capacity was suppressed by 50% or more at 5 µM CX4945 (**Figures 6B–C**), indicative of decoupling between the CK2 inhibitor effects on cell invasion versus cell proliferation/survival.

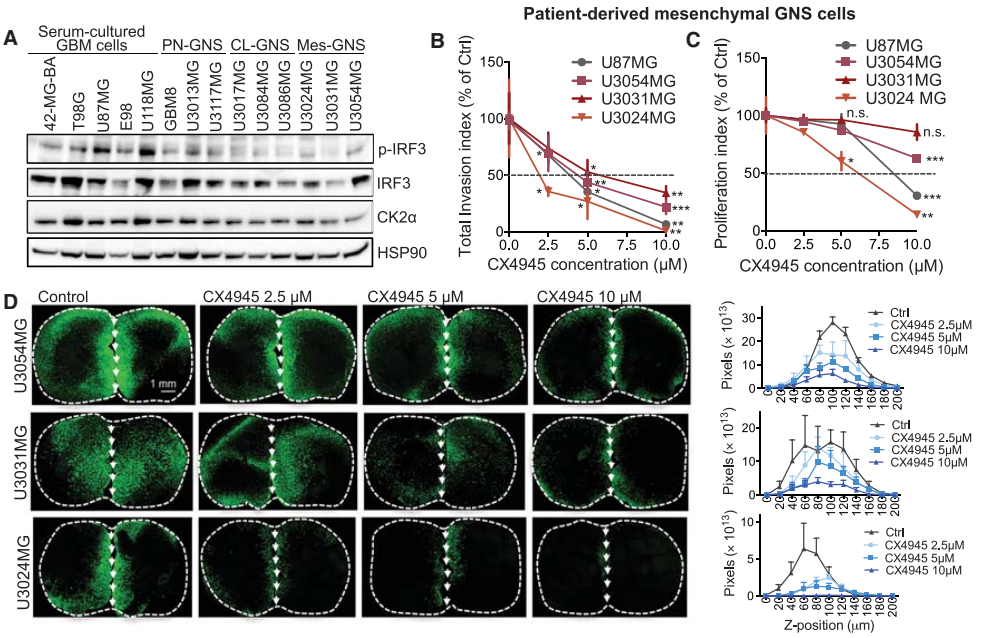

Figure 6 | CK2 targeting suppresses brain slice invasion by mesenchymal GNS cells. (**A**) The protein levels of phosphorylated IRF3 (p-IRF3), total IRF3, CK2α, and HSP90 were measured by western blotting in a panel of serum-cultured GBM cells and patient-derived proneural (PN), classical (CL), and mesenchymal (Mes) GNS cells. HSP90 was used as a loading control. (**B**) Total invasion index for U87MG, U3024MG, U3031MG, and U3054MG cells treated with CX4945 or control at the shown concentrations. n ≥ 3. (**C**) Proliferation/survival index for U87MG, U3024MG, U3031MG, and U3054MG cells in response to CX4945 or control treatment. Proliferation/survival index was calculated as the fraction of GFP^+ cell area on the insert. n ≥ 3. (**D**) Left panel: representative whole-slice reconstruction images illustrating the effect of CX4945 treatment on invasion by mesenchymal GNS cells quantified in (**B**). Right panel: distribution plots showing the invasion index as a function of z-plane position. All data are shown as mean ± SEM. * $p < 0.05$, ** $p < 0.01$, *** $p < 0.001$; p-values based on Student's t-tests. See also **Supplementary Figure 5**.

Therapeutic CK2 inhibition impedes GBM invasion in vivo

To validate our *ex vivo* findings on the effect of CK2 inhibition on GBM invasion in an i*n vivo* orthotopic glioma mouse model, we injected patient-derived mesenchymal U3054MG cells in the striatum of immunocompromised mice and, after tumors were established, stratified the mice into three groups receiving control chow or chow supplemented with CX4945 (25 or 75 mg/kg/day). Consistent with our *ex vivo* findings showing weak effect of the CK2 inhibitor on mesenchymal GBM cell proliferation/ survival, the total tumor mass *in vivo* was not affected by CX4945 treatment (**Supplementary Figures 6A–B**). Notably, we observed that CK2 inhibition strongly impeded U3054MG invasiveness *in vivo*. Post-mortem histological analysis revealed that in all CX4945-treated animals the U3054MG cells were confined to a single coronal brain section corresponding to the site of injection, indicating that tumor invasion was effectively blocked. In comparison, control U3054MG tumors displayed spreading to between 50–100% of coronal sections examined, indicative of tumor spreading along the rostral-caudal brain axis (**Figure 7A**). In line with this finding, control tumors appeared highly infiltrative and diffusely scattered,

whereas tumors of CX4945-treated animals appeared as confined dense lesions (**Figure 7B**). In an independent orthotopic xenograft model seeded with the patient-derived proneural GBM8 cell line, we consistently observed an increased GBM8 tumor density in the striatum and corpus callosum of CK2 inhibitor-treated mice. Importantly, GBM8 tumors cells found in the corpus callosum—a conduit used by GBM cells to spread from one brain hemisphere to the other—of CX4945-treated mice displayed a poorly invasive and rounded cell morphology compared to the spindle-shaped invasive morphology of their control-treated counterparts (**Supplementary Figure 6C**).

We next sought to determine if inhibition of IRF3—whose activity is negatively regulated by CK2—could conversely increase brain invasion by a poorly invasive GBM cell type. To this end, we orthotopically grafted immunocompromised mice with IRF3-depleted or control U87MG cells. Consistent with the poor invasive capacity observed for U87MG cells in the *ex vivo* invasion assay (**Figures 1A–C**), control U87MG brain tumors appeared minimally invasive and displayed a rounded morphology (**Figure 7C**). Importantly, IRF3 knockdown increased U87MG invasiveness *in vivo*, as indicated by the presence of single disseminated tumor cells that had invaded away from the tumor mass, corresponding to a >13-fold average increase in disseminated tumor cell distance from the main tumor (**Figures 7C–D**). Consistent with this, IRF3-depleted cells exhibited elongated and infiltrative/pro-invasive tumor cell morphology. These findings reveal IRF3 as an endogenous suppressor of GBM invasion *in vivo*.

DISCUSSION

GBM remains a devastating disease with a median survival time of 14–16 months. Diffuse invasion is a distinctive trait of GBM. Yet it is still not fully understood how GBM acquires such unprecedented invasive capacity. Frontline cytotoxic therapies—chemotherapy and radiotherapy—are largely ineffective in halting GBM invasion. In some cases, radiation could even increase the invasiveness of the tumor[30]. Here we report the systematic discovery of a pathway that specifically controls GBM invasion. We demonstrate that targeting a central node in this pathway allows for the functional decoupling of GBM invasion from cell proliferation/survival.

We describe the development of a clinically relevant *ex vivo* 3D organotypic invasion model, enabling us to systematically characterize the molecular pathways governing human GBM invasion. By integrating unbiased transcriptomic, computational, and functional analyses of invading GBM cells isolated from organotypic brain slices, we have uncovered an IRF3-repressed transcriptional ECM network. We demonstrate that IRF3 acts as a novel endogenous suppressor of GBM invasion and propose a therapeutic approach to activate IRF3 in GBM by targeting CK2—a negative IRF3 regulator[29].

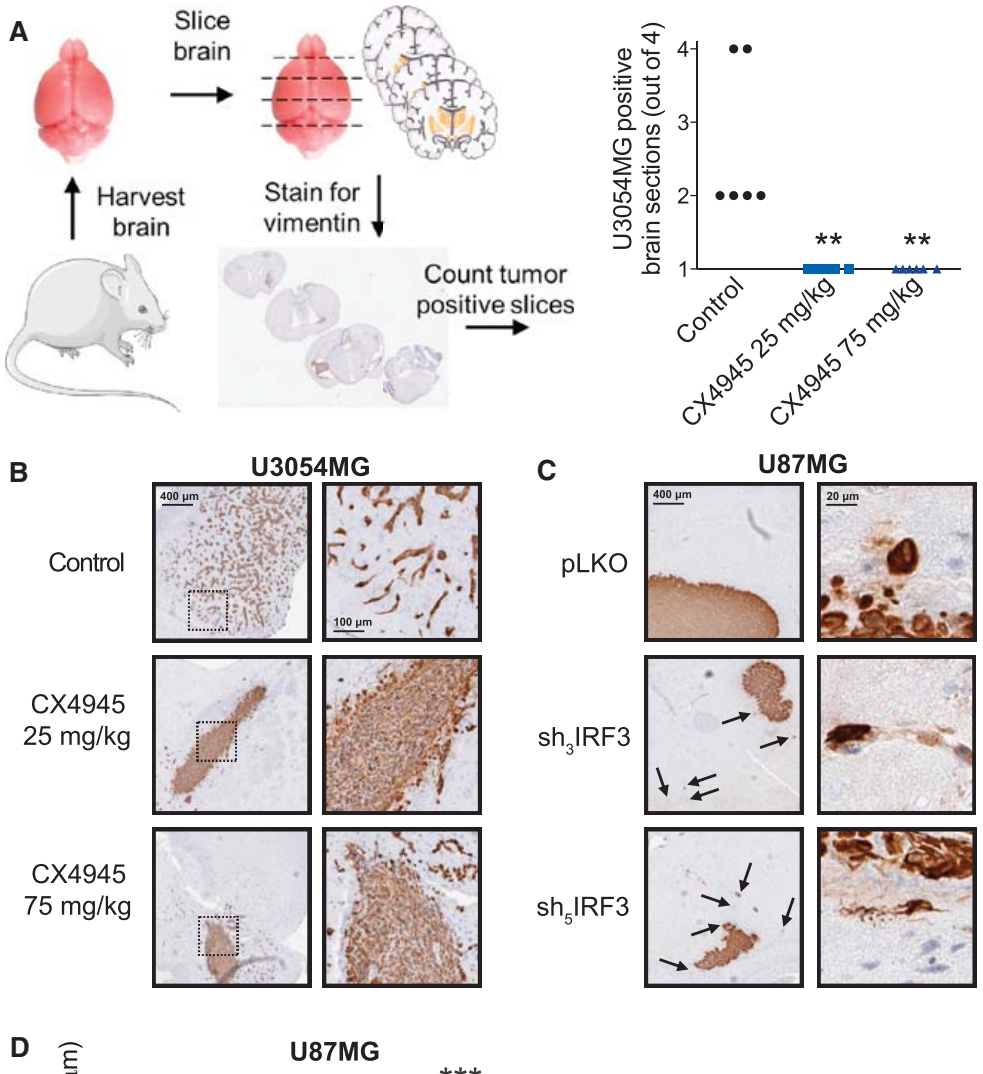
A
Slice brain
Harvest brain
Stain for vimentin
Count tumor positive slices
U3054MG positive brain sections (out of 4)
4
3
2
1
**
**
Control
CX4945 25 mg/kg
CX4945 75 mg/kg
B
U3054MG
Control
CX4945 25 mg/kg
CX4945 75 mg/kg
400 µm
100 µm
C
U87MG
pLKO
sh3IRF3
sh5IRF3
400 µm
20 µm
D
U87MG
Distance to tumor mass (µm)
1250
1000
750
500
250
0
***
***
pLKO
sh3IRF3
sh5IRF3

Figure 7 | CK2 inhibition impedes GBM invasion i*n vivo.* (**A**) Invasiveness of U3054MG cells in the brains of NOD/SCID mice orthotopically injected with 2 × 10^5 U3054MG cells and, after 1 week, assigned to either a control chow or CX4945-supplemented chow (25 or 75 mg/kg/day). At day 68 post-injection, brains were harvested and segmented into four coronal slices, which were analyzed for presence of U3054MG cells using human vimentin stain. n = 6. (**B**) Representative images from human vimentin immunostaining of U3054MG tumors from (**A**). Dashed squares indicate areas that are magnified in the right panels. (**C**) Representative images from human vimentin immunostaining of orthotopic GBM tumors formed in the brains of athymic nude mice following injection of 1 × 10^5 U87MG cells transduced with an empty control vector (pLKO)or a vector encoding an shRNA targeting IRF3(sh_3IRF3 or sh_5IRF3). n = 6. (**D**) Quantification of the distance traveled by single disseminated GBM cells from the main tumor mass for U87MG control tumors (pLKO) or U87MG tumors inactivated for IRF3 (sh_3IRF3 or sh_5IRF3). n = 15 cells, 2 tumors (pLKO), 61 cells, 2 tumors (sh_3IRF3), 37 cells, 2 tumors (sh_5IRF3). ** $p < 0.01$, *** $p < 0.001$; *p*-values based on Kruskal–Wallis test. See also **Supplementary Figure 6**.

In addition to the well-characterized role of IRF3 as an innate immune response-associated transcriptional *activator* mediating the rapid induction of type I interferon and interferon-stimulated genes, ISGs[25,26], our findings indicate that IRF3 plays a previously unappreciated role as a key invasion suppressor in GBM by acting in a non-canonical way as a transcriptional repressor of pro-invasive ECM factors expressed by invading GBM tumor cells. In light of previous evidence that ECM stiffness and composition could modulate the progression of epithelial cancers[31], the role of IRF3 in repressing ECM components in non-neural malignancies deserves further attention. IRF3 could also contribute to GBM suppression in a non-cell-autonomous manner by mediating the production of type I interferons and ISGs by GBM cells and thus engaging the anti-tumor properties of local microglia. Consistent with this, previous work showed that IRF3 overexpression led to enhanced production of IFNβ and IP-10 by GBM cells and caused a decrease in GBM migration in *in vitro* transwell assays[32].

A notable feature of the brain parenchyma is its deficiency in rigid ECM structures, including collagen, laminin and fibronectin constituents[23]. In light of the lack of ECM structural support in the brain microenvironment, we speculate that invading GBM tumors are faced with the challenge to synthesize and deposit their own collagen tracks, which they use as guides and a physical support matrix to facilitate their invasion. Consistent with our findings, previous studies have reported elevated levels of *COL3A1*, *COL4A1*, and *COL5A2* in GBM tumors[33], and *COL1A1*, *COL1A2*, and *COL5A2* are among the most highly expressed genes in mesenchymal GBM tumors[8].

Prior to our findings on a role for CK2 in controlling GBM invasion, CK2 was implicated as a therapeutic target in classical GBM. CK2 inhibitor was shown to decrease *in vitro* 2D cell migration and adhesion capacity, increase cellular apoptosis and inhibit classical GBM tumor growth[13]. Contrary to the report of Zheng *et al.* (2013), we did not observe an effect of the CK2 inhibitor on tumor growth, which could be attributed to the different GBM cell line models used—classical[13] versus mesenchymal and proneural in our study. CK2 is a pleiotropic kinase with many described cellular targets[34]. Our results that IRF3 depletion only partially attenuated the effect of the CK2 inhibitor on GBM invasion suggests that additional IRF3-independent CK2 targets might contribute to its effects. Previous studies have shown reduced Wnt-signaling[35] and decreased Sox2, Nestin, and EGFR expression levels[36] in glioma cells following CK2 inhibition, which could

explain the broad and diverse effects of CK2 inhibition on GBM progression phenotypes beyond invasion. Consistent with its pro-invasive role in GBM described here, CK2 has been shown to promote invasion by several epithelial cancer types including lung, colon, and liver cancers[37-40].

Our findings illustrate the power of functionally guided systematic approaches for uncovering master regulators of genetic pathways. Whereas simultaneous targeting of individual network components is challenging, targeting of their common upstream regulator can afford a simple way to coordinately modulate the pathway output. We establish IRF3 as a transcriptional repressor acting upstream an ECM gene network and show that IRF3 activation could serve as a promising therapeutic approach to inhibit GBM invasion—a currently intractable disease phenotype.

REFERENCES

1. Jemal, A., *et al.* Global cancer statistics. *CA Cancer J Clin* **61**, 69-90 (2011).
2. Ohgaki, H. & Kleihues, P. Population-based studies on incidence, survival rates, and genetic alterations in astrocytic and oligodendroglial gliomas. *J Neuropathol Exp Neurol* **64**, 479-489 (2005).
3. Wen, P.Y. & Kesari, S. Malignant gliomas in adults. *N Engl J Med* **359**, 492-507 (2008).
4. Pollard, S.M., *et al.* Glioma stem cell lines expanded in adherent culture have tumor-specific phenotypes and are suitable for chemical and genetic screens. *Cell Stem Cell* **4**, 568-580 (2009).
5. Suva, M.L., *et al.* Reconstructing and reprogramming the tumor-propagating potential of glioblastoma stem-like cells. *Cell* **157**, 580-594 (2014).
6. Rath, B.H., *et al.* Astrocytes enhance the invasion potential of glioblastoma stem-like cells. *PloS One* **8**, e54752 (2013).
7. Phillips, H.S., *et al.* Molecular subclasses of high-grade glioma predict prognosis, delineate a pattern of disease progression, and resemble stages in neurogenesis. *Cancer Cell* **9**, 157-173 (2006).
8. Verhaak, R.G., *et al.* Integrated genomic analysis identifies clinically relevant subtypes of glioblastoma characterized by abnormalities in PDGFRA, IDH1, EGFR, and NF1. *Cancer Cell* **17**, 98-110 (2010).
9. Tso, C.L., *et al.* Primary glioblastomas express mesenchymal stem-like properties. *Mol Cancer Res* **4**, 607-619 (2006).
10. Lee, J.K., *et al.* Spatiotemporal genomic architecture informs precision oncology in glioblastoma. *Nature Genet* **49**, 594-599 (2017).
11. Engstrom, P.G., *et al.* Digital transcriptome profiling of normal and glioblastoma-derived neural stem cells identifies genes associated with patient survival. *Genome Med* **4**, 76 (2012).
12. Joseph, J.V., *et al.* TGF-beta is an inducer of ZEB1-dependent mesenchymal transdifferentiation in glioblastoma that is associated with tumor invasion. *Cell Death Dis* **5**, e1443 (2014).
13. Zheng, Y., *et al.* Targeting protein kinase CK2 suppresses prosurvival signaling pathways and growth of glioblastoma. *Clin Cancer Res* **19**, 6484-6494 (2013).
14. Vitucci, M., *et al.* Cooperativity between MAPK and PI3K signaling activation is required for glioblastoma pathogenesis. *Neuro Oncol* **15**, 1317-1329 (2013).
15. Kemper, E.M., *et al.* Development of luciferase tagged brain tumour models in mice for chemotherapy intervention studies. *Eur J Cancer* **42**, 3294-3303 (2006).
16. Xie, Y., *et al.* The Human Glioblastoma Cell Culture Resource: Validated Cell Models Representing All Molecular Subtypes. *EBioMedicine* **2**, 1351-1363 (2015).
17. Love, M.I., *et al.* Moderated estimation of fold change and dispersion for RNA-seq data with DESeq2. *Genome Biol* **15**(2014).
18. Goodarzi, H., *et al.* Revealing global regulatory perturbations across human cancers. *Mol Cell* **36**, 900-911 (2009).
19. Elemento, O., *et al.* A universal framework for regulatory element discovery across all genomes and data types. *Mol Cell* **28**, 337-350 (2007).
20. Freije, W.A., *et al.* Gene expression profiling of gliomas strongly predicts survival. *Cancer Res* **64**, 6503-6510 (2004).
21. Gravendeel, L.A., *et al.* Intrinsic gene expression profiles of gliomas are a better predictor of survival than histology. *Cancer Res* **69**, 9065-9072 (2009).
22. Shaw, L.M. Tumor cell invasion assays. *Methods Mol Biol* **294**, 97-105 (2005).
23. Bellail, A.C., *et al.* Microregional extracellular matrix heterogeneity in brain modulates glioma cell invasion. *Int J Biochem Cell Biol* **36**, 1046-1069 (2004).
24. Segerman, A., *et al.* Clonal variation in drug and radiation response among glioma-initiating cells is linked to proneural-mesenchymal transition. *Cell Rep* **17**, 2994-3009 (2016).
25. Hiscott, J. Triggering the innate antiviral response through IRF-3 activation. *J Biol Chem* **282**, 15325-15329 (2007).
26. Ikushima, H., *et al.* The IRF family transcription factors at the interface of innate and adaptive immune responses. *Cold Spring Harb Symp Quant Biol* **78**, 105-116 (2013).
27. Xu, P., *et al.* Innate antiviral host defense attenuates TGF-beta function through IRF3-mediated suppression of Smad signaling. *Mol Cell* **56**, 723-737 (2014).
28. Yang, L. & Seki, E. Toll-like receptors in liver fibrosis: cellular crosstalk and mechanisms. *Front Physiol* **3**, 138 (2012).

29. Du, M., *et al.* Casein kinase II controls TBK1/IRF3 activation in IFN response against viral infection. *J Immunol* **194**, 4477-4488 (2015).
30. Shankar, A., *et al.* Subcurative radiation significantly increases cell proliferation, invasion, and migration of primary glioblastoma multiforme in vivo. *Chin J Cancer* **33**, 148-158 (2014).
31. Lu, P., *et al.* The extracellular matrix: a dynamic niche in cancer progression. *J Cell Biol* **196**, 395-406 (2012).
32. Tarassishin, L. & Lee, S.C. Interferon regulatory factor 3 alters glioma inflammatory and invasive properties. *J Neurooncol* **113**, 185-194 (2013).
33. Dong, H., *et al.* Integrated analysis of mutations, miRNA and mRNA expression in glioblastoma. *BMC Syst Biol* **4**, 163 (2010).
34. Filhol, O. & Cochet, C. Protein kinase CK2 in health and disease: Cellular functions of protein kinase CK2: a dynamic affair. *Cell Mol Life Sci* **66**, 1830-1839 (2009).
35. Nitta, R.T., *et al.* Casein kinase 2alpha regulates glioblastoma brain tumor-initiating cell growth through the beta-catenin pathway. *Oncogene* **34**, 3688-3699 (2015).
36. Rowse, A.L., *et al.* Protein kinase CK2 is important for the function of glioblastoma brain tumor initiating cells. *J Neurooncol* **132**, 219-229 (2017).
37. Benavent Acero, F., *et al.* CIGB-300, an anti-CK2 peptide, inhibits angiogenesis, tumor cell invasion and metastasis in lung cancer models. *Lung Cancer* **107**, 14-21 (2017).
38. Liu, Y., *et al.* CK2alpha' Drives Lung Cancer Metastasis by Targeting BRMS1 Nuclear Export and Degradation. *Cancer Res* **76**, 2675-2686 (2016).
39. Niechi, I., *et al.* Colon cancer cell invasion is promoted by protein kinase CK2 through increase of endothelin-converting enzyme-1c protein stability. *Oncotarget* **6**, 42749-42760 (2015).
40. Wu, D., *et al.* Stable knockdown of protein kinase CK2-alpha (CK2alpha) inhibits migration and invasion and induces inactivation of hedgehog signaling pathway in hepatocellular carcinoma Hep G2 cells. *Acta histochem* **116**, 1501-1508 (2014).
41. Schindelin, J., *et al.* Fiji: an open-source platform for biological-image analysis. *Nat Methods* **9**, 676-682 (2012).

SUPPLEMENTARY METHODS

Key Resources Table

Reagent or resource	Source	Identifier
Antibodies		
Rabbit polyclonal antibody anti-IRF3 (FL-425)	Santa Cruz	Cat#: sc9082 RRID: AB_2264929
Rabbit monoclonal antibody anti-phospho-IRF3 (4D4G)	Cell Signaling	Cat#: 4947S RRID: AB_823547
Rabbit polyclonal antibody anti-IRF3	Active Motif	Cat#: 39033
Rabbit monoclonal antibody anti-TBK1/NAK	Cell Signaling	Cat#: 3504S RRID: AB_2255663
Rabbit monoclonal antibody anti-phospho-TBK1/NAK	Cell Signaling	Cat#: 5483S RRID: AB_10695239
Rabbit polyclonal antibody anti-CK2 alpha	Cell Signaling	Cat#: 2656 RRID: AB_2236816
Mouse monoclonal antibody anti-c-Myc (9E10)	Santa Cruz	Cat#: sc-40 RRID: AB_627268
Rabbit polyclonal antibody anti-HSP90 (H114)	Santa Cruz	Cat#: sc-7947 RRID: AB_2121235
Normal rabbit IgG X	Santa Cruz	Cat#: sc-2027 X
Alexa Fluor® 568 goat anti-rabbit secondary antibody	Abcam	Cat#: 175471 RRID: AB_2576207
Mouse monoclonal antibody anti-vimentin	Dako	Cat#: M0725 RRID:AB_10015203
Chemicals, peptides, and recombinant proteins		
Neural Stem Cell Serum Free Medium	Thermo Fisher	Cat#: A1050901
GlutaMAX™ supplement	Thermo Fisher	Cat#: 35050061
Laminin	Sigma-Aldrich	Cat#: L2020
DRAQ5	eBioscience	Cat#: 65-0880-92
Hoechst 33342	Thermo Fisher	Cat#: 62249
EthD-1	Sigma-Aldrich	Cat#: 46043-1MG-F

Accutase	Sigma-Aldrich	Cat#: A6964
rCollagen I from human placenta	Sigma-Aldrich	Cat#: C7774
rCollagen V from human placenta	Sigma-Aldrich	Cat#: C3657
Lipofectamine 2000	Thermo Fisher	Cat#: 11668019
Poly(I:C)	Sigma-Aldrich	Cat#: P1530
Temozolomide (TMZ)	Selleckchem	Cat#: S1237
4,5,6,7-Tetrabromobenzotriazole (TBB)	Tocris	Cat#: 2275
CX4945	MedKoo	Cat#: 200843
Critical commercial assays		
ChIP-IT® Express Enzymatic kit	Active Motif	Cat#: 53009
TruSeq Stranded mRNA sample preparation kit	Illumina	Cat#: RS-122-2101/2
Total RNA isolation kit	Zymo Research	Cat#: R1055
Maxima First Strand cDNA Synthesis Kit for RT-qPCR	Thermo Fisher	Cat#: K1641
Deposited data		
RNA-Seq of U87 brain invasive derivatives: raw and processed data	This paper	GEO: GSE87535
Experimental models: cell lines		
Patient-derived GNS cell lines: U3013MG, U3117MG, U3017MG, U3084MG, U3086MG, U3054MG, U3031MG, U3024MG	The Human Glioblastoma Culture Resource (www.hgcc.se)	NA
Patient-derived GBM8 proneural GNS cell lines	Bakhos Tannous (MGH, Boston)	NA
Serum-cultured GBM cell lines: U87MG, T98G, 42-MG-BA	Bernards' lab (NKI)	NA
Primary serum-cultured E98 cell line	Pieter Wesseling (Radboud University MC, Nijmegen)	NA
Experimental models: organisms/strains		
Mouse: NOD/SCID (NOD.CB17/AlhnRj-*Prkdcscid*/Rj)	Janvier	Cat#: 2013-06-ENG-RM-33
Mouse: Athymic nude (RjOrl:NMRI-Foxn1nu /Foxn1nu)	NKI animal facility Janvier	NA Cat#: 2013-06-ENG-RM-29
Recombinant DNA		
pRK5 IRF3 5SD	Xu et al., 2014[27]	NA
Sequence-based reagents		
shRNA sequences		
sh*IRF3*: 5'-CCGGGATCTGATTACCTTCACGGAACTCGAGTTC CGTGAAGGTAATCAGATCTTTTT-3'	This paper	NA
sh*IRF3:* 5'-CCGGGCCAACCTGGAAGAGGAATTTCTCGAGAA ATTCCTCTTCCAGGTTGGCTTTTT-3'	This paper	NA

sh*IRF3:* 5′-CCGGGCAGGAGGATTTCGGAATCTTCTCGAGAA GATTCCGAAATCCTCCTGCTTTTT-3′	This paper	NA
sh*IRF3:* 5′-CCGGCGCAAAGAAGGGTTGCGTTTACTCGAGTA AACGCAACCCTTCTTTGCGTTTTT-3′	This paper	NA
sh*IRF3:* 5′-CCGGCCCTTCATTGTAGATCTGATTCTCGAGAAT CAGATCTACAATGAAGGGTTTTT-3′	This paper	NA
sh*ZBTB7A:* 5′-CCGGGCAGAAGGTGGAGAAGAAGATCTCGAGAT CTTCTTCTCCACCTTCTGCTTTTTTG-3′	This paper	NA
sh*ZBTB7A:* 5′-CCGGGCTGGACCTTGTAGATCAAATCTCGAGATT TGATCTACAAGGTCCAGCTTTTTTG-3′	This paper	NA
sh*ZBTB7A:* 5′-CCGGGCCACTGAGACACAAACCTATCTCGAGAT AGGTTTGTGTCTCAGTGGCTTTTTTG-3′	This paper	NA
sh*ZBTB7A:* 5′-CCGGCCAGTACTTCAAGAAGCTGTTCTCGAGAA CAGCTTCTTGAAGTACTGGTTTTTTG-3′	This paper	NA
sh*MAX*: 5′-CCGGACACACACCAGCAAGATATTGCTCGAGCA ATATCTTGCTGGTGTGTGTTTTTTG-3′	This paper	NA
sh*MAX*: 5-′CCGGCCACAGAATATATCCAGTATACTCGAGTAT ACTGGATATATTCTGTGGTTTTTG-3′	This paper	NA
sh*MAX*: 5′-CCGGCTGAGTGAATTGTACCTATTTCTCGAGAAA TAGGTACAATTCACTCAGTTTTTG-3′	This paper	NA
sh*POU6F1*: 5′-CCGGCCTCTGCTCCTATCCCAATTACTCGAGTAA TTGGGATAGGAGCAGAGGTTTTT-3′	This paper	NA
sh*POU6F1*: 5′-CCGGCTTCGCATTTAGCCCAGGAATCTCGAGATT CCTGGGCTAAATGCGAAGTTTTT-3′	This paper	NA
sh*POU6F1*: 5′-CCGGCGGGAGTTTGCCAAGAACTTTCTCGAGAA AGTTCTTGGCAAACTCCCGTTTTT-3′	This paper	NA
siRNA target sequences		
CSNK2A1 ON-TARGETplus SMART siRNA pool: 5′-GCAUUUAGGUGGAGACUUC-3′ 5′-GGAAGUGUGUCUUAGUUAC-3′ 5′-GCUGGUCGCUUACAUCACU-3′ 5′-AACAUUGUCUGUACAGGUU-3′	Dharmacon	Cat#: L-003475-00-0005
ON-TARGETplus non-targeting siRNA pool: 5′-UGGUUUACAUGUCGACUAA-3′ 5′-UGGUUUACAUGUUGUGUGA-3′ 5′-UGGUUUACAUGUUUUCUGA-3′ 5′-UGGUUUACAUGUUUUCCUA-3′	Dharmacon	Cat#: D-001810-10-05
Gene expression qPCR primer sequences		
GAPDH Forward: 5′-AGCCACATCGCTCAGACAC-3′	This paper	NA
GAPDH Reverse: 5′-GCCCAATACGACCAAATCC-3′	This paper	NA
18S Forward: 5′-GTAACCCGTTGAACCCCATT-3′	This paper	NA
18S Reverse: 5′-CCATCCAATCGGTAGTAGCG-3′	This paper	NA

COL1A1 Forward: 5'-GGGATTCCCTGGACCTAAAG-3'	This paper	NA
COL1A1 Reverse: 5'-GGAACACCTCGCTCTCCA-3'	This paper	NA
COL1A2 Forward: 5'-CTGGAGAGGCTGGTACTGCT-3'	This paper	NA
COL1A2 Reverse: 5'-AGCACCAAGAAGACCCTGAG-3'	This paper	NA
COL5A1 Forward: 5'- CCTGGATGAGGAGGTGTTTG-3'	This paper	NA
COL5A1 Reverse: 5'-CGGTGGTCCGAGACAAAG-3'	This paper	NA
COL5A2 Forward: 5'-ACAGGGTTTACAAGGACAGCA-3'	This paper	NA
COL5A2 Reverse: 5'-GGTCCAGGATCACCAGGTT-3'	This paper	NA
COL8A1 Forward: 5'-CCAACTCACCCTTGAAGTCAT-3'	This paper	NA
COL8A1 Reverse: 5'-GGCTGGTTTCTGTCTCTTCAG-3'	This paper	NA
CTGF Forward: 5'-GGCAAAAAGTGCATCCGTACT-3'	This paper	NA
CTGF Reverse: 5'-CCGTCGGTACATACTCCACAG-3'	This paper	NA
EMILIN2 Forward: 5'-CGTGAACAAGAATGTGAGCTG-3'	This paper	NA
EMILIN2 Reverse: 5'-CTAGGTCTGAAGTTCACTCGATACA-3'	This paper	NA
FBN1 Forward: 5'-GGCTCCTACAGATGTGAATGC-3'	This paper	NA
FBN1 Reverse: 5'-TCCGCATGTGTGTGTCAAC-3'	This paper	NA
IGFBP7 Forward: 5'-ACTGGCTGGGTGCTGGTA-3'	This paper	NA
IGFBP7 Reverse: 5'-TGGATGCATGGCACTCATA-3'	This paper	NA
LOX Forward: 5'-TGGGAATGGCACAGTTGTC-3'	This paper	NA
LOX Reverse: 5'-AAACTTGCTTTGTGGCCTTC-3'	This paper	NA
LOXL1 Forward: 5'-GCATGCACCTCTCATACCC-3'	This paper	NA
LOXL1 Reverse: 5'-CAGTCGATGTCCGCATTGTA-3'	This paper	NA
LOXL3 Forward: 5'-CAGGACCAGCACTCTTCTCC-3'	This paper	NA
LOXL3 Reverse: 5'-CACTGACAGGTCGCATGG-3'	This paper	NA
MFAP4 Forward: 5'-CGGCGTGTACCTCATCTACC-3'	This paper	NA
MFAP4 Reverse: 5'-GAGCCATTGAATCTCTTCTGGA-3'	This paper	NA
NID2 Forward: 5'-CCGGCATACTTGCATCTTG-3'	This paper	NA
NID2 Reverse: 5'-GCCTCCATGGTGAACACAC-3'	This paper	NA
SPARC Forward: 5'-TTCCCTGTACACTGGCAGTTC-3'	This paper	NA
SPARC Reverse: 5'-AATGCTCCATGGGGATGA-3'	This paper	NA
TGFBI Forward: 5'-CGAGTGCTGTCCTGGATATG-3'	This paper	NA
TGFBI Reverse: 5'-CCCAGGGTCTCGTAAAGGTT-3'	This paper	NA
THBS1 Forward: 5'-TCAGTTACCATCTGCAAAAAGG-3'	This paper	NA
THBS1 Reverse: 5'-ATCAGGAACTGTGGCATTGG-3'	This paper	NA
IRF3 Forward: 5'-AGAGGCTCGTGATGGTCAAG-3'	This paper	NA
IRF3 Reverse: 5'-TGTGCAGGTCCACAGTATTCTC-3'	This paper	NA
ZBTB7A Forward: 5'-GGCCACTGAGACACAAACCTA-3'	This paper	NA
ZBTB7A Reverse: 5'-AACCCCAGTCCGATCTCC-3'	This paper	NA

MAX Forward: 5'-CCAGCAAGATATTGACGACCT-3'	This paper	NA
MAX Reverse: 5'-TTCTCCAGTGCACGGACTT-3'	This paper	NA
POU6F1 Forward: 5'-CCCCTGCTAAGAGTGAGGTG-3'	This paper	NA
POU6F1 Reverse: 5'-TGGCAATGACCACAGCAG-3'	This paper	NA
CSKN2A1 Forward: 5'-GCGCCAATATGATGTCAGG-3'	This paper	NA
CSKN2A1 Reverse: 5'-TGGAACAGGCATCCCAAG-3'	This paper	NA
ChIP qPCR primers		
*COL1A1*_ChIP_F: 5'-GTGGACTCCCTTCCCTCCT-3'	This paper	NA
*COL1A1*_ChIP_R: 5'-CAATTTGGGAGTTGGAATGG-3'	This paper	NA
*COL1A2*_ChIP_F: 5'-GAGCCCCAAAGCTAGAGAAAA-3'	This paper	NA
*COL1A2*_ChIP_R: 5'-GGGAGGGAAGACTCGATAGC-3'	This paper	NA
*COL5A1*_ChIP_F: 5'-AGGAGTGAGGGGTGAGAGC-3'	This paper	NA
*COL5A1*_ChIP_R: 5'-GACGGGAACATCTGGGTTATT-3'	This paper	NA
*COL8A1*_ChIP_F: 5'-GGATGGGGCGATTTTCAC-3'	This paper	NA
*COL8A1*_ChIP_R: 5'-CACTGACATGGCCTGGAG-3'	This paper	NA
*CTGF*_ChIP_F: 5'-CAGTGTTCCCACCCTGACA-3'	This paper	NA
*CTGF*_ChIP_R: 5'-GCAAATGATTCTGTGTTGGGTA-3'	This paper	NA
*EMILIN2*_ChIP_F: 5'-CCGAGGAGGAAATTCGAGTC-3'	This paper	NA
*EMILIN2*_ChIP_R: 5'-GCGAATGAGGGACATGTTTA-3'	This paper	NA
*FBN1*_ChIP_F: 5'-GACACCCAGGGCAAGTGG-3'	This paper	NA
*FBN1*_ChIP_R: 5'-CCGGGAGGCTAAGACTGG-3'	This paper	NA
*IGFBP7*_ChIP_F: 5'-TCAAAAACCTCCTGGAATGC-3'	This paper	NA
*IGFBP7*_ChIP_R: 5'-CACGGAGGCACCTAAAGC-3'	This paper	NA
*LOXL1*_ChIP_F: 5'-CAGCCCCCAGTTTCATTTTA-3'	This paper	NA
*LOXL1*_ChIP_R: 5'-TCTGCATAGCCTGGGAATAA-3'	This paper	NA
*LOXL3*_ChIP_F: 5'-GTGGAGACCCCCGGATTA-3'	This paper	NA
*LOXL3*_ChIP_R: 5'-GCCAAAACCGAGGACTTTC-3'	This paper	NA
*MFAP4*_ChIP_F: 5'-GGCCCATCAGGAAGTAGGG-3'	This paper	NA
*MFAP4*_ChIP_R: 5'-ACCCACCCTGCTAGACCTGT-3'	This paper	NA
*NID2*_ChIP_F: 5'-CCGGATGAGAGGATGACC-3'	This paper	NA
*NID2*_ChIP_R: 5'-GAGCTGCCCCTTCCACTC-3'	This paper	NA
*SPARC*_ChIP_F: 5'-GACACTTGGGCCTGGTTCT-3'	This paper	NA
*SPARC*_ChIP_R: 5'-GGAGACTGCAAGGAATTACCC-3'	This paper	NA
*TGFBI*_ChIP_F: 5'-AAGATCAGTGAGGGAATCTTCG-3'	This paper	NA
*TGFBI*_ChIP_R: 5'-ACCTTGGGACTGAGGGACAG-3'	This paper	NA
*THBS1*_ChIP_F: 5'-CCCCCTTCACTTTCTAGCTG-3'	This paper	NA
*THBS1*_ChIP_R: 5'-CCAGTCTGGGCTCCTCTCT-3'	This paper	NA
Software and algorithms		

GraphPad Prism 7.0	GraphPad	NA
GENE-E	Broad Institute https://software.broadinstitute.org/GENE-E/index.html	NA
DESeq2	www.bioconductor.org[17]	NA
iPAGE	iget.c2b2.columbia.edu[18]	NA
FIRE	iget.c2b2.columbia.edu[19]	NA
Fiji/ ImageJ 1.48d	NIH: Imagej.nih.gov/ij	NA
Aperio ImageScope v12	Aperio Technologies Inc.	NA
Other		
Corning® Transwell® polyester membrane cell culture inserts	Corning	Cat#: 3450
Purina 5001 chow supplemented with CX4945	Research Diets, Inc.	NA

Organotypic brain slices

Brains were extracted from 4-week old male athymic nu/nu mice (euthanized by cervical dislocation), and organotypic brain slices were generated using a fully automated VT1200S vibratome (Leica Biosystems; Wetzlar, Germany). The cerebellum and olfactory bulb were removed, and the cerebrum was glued to the vibratome's cutting stage, using a small amount of cyanoacrylate glue (Leica Biosystems) enough to cover the caudal side of the brain lying over the glue. The tissue was fully submerged in ice-cold cutting media (HBSS, 1% Pen/Strep, 0.6% glucose, 25 mM HEPES), which was oxygenated by continuous airflow. 300 µm thick coronal brain slices were cut using vibratome speed of 0.08–0.1 mm/s and amplitude of 1.0. The slices were then sectioned into two symmetrical halves using a No. 10 scalpel, and the slice halves were transferred to 6-well 0.4 µm porous polyester membrane inserts (Costar Corning; Corning, NY) containing 2 mL of 25% serum-supplemented media (DMEM:F12, 25% FBS, 1% Pen/Strep, 1% L-glutamine, 5mM HEPES, 1.5% $NaHCO_3$). The transwell inserts were pre-coated in 1% laminin solution (in ddH_20) for 1 h at 37 °C prior to plating the brain slices. A maximum of 4 slice halves were cultured per 6-well insert. After the full brain was sliced and all the slices were transferred to the inserts, the media from the inserts was carefully removed and the 4 slice halves were oriented in a square position along the surface of the insert with about 1 cm distance between adjacent slice halves. 1 mL of 25% serum-supplemented media was added to the bottom well (top side of the insert with the slices being exposed to air), and the slices were incubated overnight. The following day, just prior to starting the invasion assay, the brain slices were washed twice in PBS by transferring the inserts to a new 6-well plate containing 2 mL of PBS in each well. After the last wash, the inserts with the slices were transferred to a 6-well plate containing 1 ml of NSC

media (Thermo Fisher; Waltham, MA; DMEM/F12, 2% StemPro supplement, 1% Pen/Strep, 1% Glutamax, 10 ng/mL EGF, 10 ng/mL bFGF) in the bottom well, allowing the top side of the slices to be exposed to air. Brain slice viability was measured by incubating the slices in 5 μM DRAQ5 (eBioscience; San Diego, CA), a cell-permeable dye that labels all cells in the sample, and 2 μM EthD-1 (Sigma–Aldrich), a live cell-impermeable dye that selectively labels dead cells, for 45 min at room temperature (RT) by gently shaking. Brain slices were imaged using Leica SP5 II confocal microscope at up to 40 μm slice depth, and the percentage of dead cells was quantified as the percentage of EthD-1-positive cells out of the total number of DRAQ5-positive cells for a total of 5 slice depths (z-planes), taken at 10 μm intervals.

Organotypic brain slice invasion assay

The brain slice invasion assay was designed as shown in **Supplementary Figure 1C**. GFP^+ GBM cells at a density of 1×10^5 cells in 2 μL media were seeded onto each insert adjacent to the corpus callosum on the inner side of each brain slice hemisphere. The inserts with the brain slices/GBM cells were fitted into a 6-well plate containing 1 mL of serum-free NSC media +bFGF/EGF in the bottom well (Thermo Fisher), allowing the upper side of the inserts with the slices to be exposed to air (liquid–air interface). NSC brain slice media was refreshed every 2–3 days. For drug treatment experiments, TMZ (Selleckchem; Houston, TX), poly(I:C) (Sigma–Aldrich), or CX4945 (MedKoo; Morrisville, TX) were added to the serum-free NSC brain slice media in the bottom well at the start of the invasion assay at concentrations as indicated in each figure. For recombinant protein treatment experiments, collagen I (Sigma–Aldrich) and/or collagen V (Sigma–Aldrich) were reconstituted in 0.01 M HCl (0.01 N) solution by heating at 50 °C for 5 min and were subsequently added to the NSC slice media at the start of the assay at the concentrations indicated in the legend of **Figure 2F**. Drug/recombinant protein-containing media was refreshed every 2–3 days.

The invasion assay was allowed to proceed for 1 week, after which the brain slices were fixed in 4% formaldehyde, counterstained in 10 μg/mL Hoechst 33342 (Thermo Fisher), and imaged using a Leica SP5 II confocal microscope. The whole brain slice surface was scanned at 10X magnification by performing a 200 μm z-stack with 20 μm z-plane increments. Whole brain slice images were reconstructed using image tiling. Hoechst staining was used to delimit the slice area and outline its boundaries. Total invasion index, quantified and summed across 11 z-planes taken at 20 μm increments for a total slice depth of 200 μm, was calculated as the total background-corrected GFP signal within a slice z-plane multiplied by the area of GFP signal detected in that z-plane. Proliferation/survival index was quantified as the density of GFP^+ GBM cells that had grown on the insert surrounding the brain slices, but did not invade the slices. All image quantification was performed using Fiji.

Generation of brain invasive derivatives

Brain invasive derivatives were generated by isolating all GBM cells that had invaded into organotypic brain slices at the end of the 1-week invasion assay. In order to isolate sufficient number of invading GBM cells for downstream analyses, roughly 12 brain slices were pooled to generate a single brain invasive derivative clone. The brain slices were gently removed from the inserts, transferred to a 10 cm plate containing 5 mL of PBS, chopped into small pieces using No.10 scalpels, and then transferred to a 15 mL falcon tube containing 6 mL of Accutase® solution (Sigma–Aldrich). The slice pieces were incubated in Accutase® for 30 min at 37 °C by mixing every 5 min. After the incubation, the cell suspension was filtered through 70 μm cell strainer, pelleted by centrifugation, and resuspended in cell media. Single-cell suspensions were plated, allowed to attach overnight, and the following day GBM cells were positively selected by applying a puromycin (1–2 μg/mL) drug selection (GBM cells expressing GFP also express a puromycin resistance gene). In parallel to isolating invasive GBM populations, we also processed the remaining inserts (after the brain slices had been removed) in an analogous manner as described above to isolate minimally invasive control GBM cell populations, which did not invade the brain slices but grew in parallel on the surrounding insert.

Next generation sequencing of brain invasive derivatives

In order to identify mRNA transcripts differentially expressed in U87MG brain invasive derivatives, cells were lysed in TRIzol (15596-018; Ambion; Foster City, CA) and submitted to the NKI deep sequencing core facility for RNA-seq analysis. Total RNA was extracted from two independently derived brain invasive U87 clones (C1 and C2) and their control minimally invasive cell population using TRIzol reagent according to the manufacturer's protocol. Briefly, 0.2x volumes of chloroform (Amylene; Biosolve; Valkenswaard, The Netherlands) was added to the Trizol homogenate and the tubes (Falcon, 15mL) were shaken vigorously. The tubes were incubated for 2–3 minutes at RT and centrifuged (rotanta 46 RS; Hettich; Kirchlengern, Germany) for 1 h at 4 °C. Approximately 70% of the upper aqueous phase was transferred to a clean 15 mL tube and 0.5x volume of isopropanol (33539; Sigma–Aldrich) was added. The tubes were incubated overnight at -20 °C and centrifuged for 30 minutes at 4 °C. The supernatant was removed and the pellet was washed twice with 80% ethanol (32221-2.5L; Sigma–Aldrich). The total RNA pellet was air-dried for 8 minutes and dissolved in an appropriate volume of nuclease-free water (AM9937; Ambion) and quantified using Nanodrop UV-VIS Spectrophotometer. The total RNA was further purified using the MinElute Cleanup Kit (74204; Qiagen; Hilden, Germany) according to the manufactures instructions. Quality and quantity of the total RNA was assessed by the 2100 Bioanalyzer using a Nano chip (Agilent; Santa Clara, CA). Total RNA samples having RIN>8 were subjected to library generation.

Strand-specific libraries were generated using the TruSeq Stranded mRNA sample preparation kit (RS-122-2101/2; Illumina Inc.; San Diego, CA) according to the manufacturer's instructions (Illumina, Part # 15031047 Rev. E). Briefly, polyadenylated RNA from intact total RNA was purified using oligo-dT beads. Following purification, the RNA was fragmented, random primed and reverse transcribed using SuperScript II Reverse Transcriptase (Invitrogen, part # 18064-014) with the addition of actinomycin D. Second strand synthesis was performed using Polymerase I and RNaseH with replacement of dTTP for dUTP. The generated cDNA fragments were 3' end adenylated and ligated to Illumina paired-end sequencing adapters and subsequently amplified by 12 cycles of PCR. The libraries were analyzed on a 2100 Bioanalyzer using a 7500 chip (Agilent), diluted and pooled equimolar into a 10 nM multiplex sequencing pool and stored at –20 °C. The libraries were sequenced with 65 base single reads on a HiSeq2500 using V4 chemistry (Illumina). Base calling was performed using Illumina RTA 1.18.64. Reads passing filter were converted to fastq reads using bcl2fastq (version 1.8.4). Sequenced reads were trimmed for adaptor sequence and masked for low-complexity or low-quality sequence. Filtered reads were mapped using tophat 2.0.12, using bowtie1, against the human genome build 38 (Ensembl) using a gene transfer file (GTF) version 77 (Ensembl). The parameters that were used by tophat were: --prefilter-multihits, --no coverage-search, --transcriptome index and --library-type first strand. Raw read counts were generated using a custom script, which is based on the same ideas as htseq-count. Reads that were uniquely mapped were used for determining gene expression in each sample.

Orthotopic xenograft studies

7-week old male NOD/SCID or athymic nude mice were intracranially injected as described previously[15]. In brief, firefly luciferase transduced 1×10^5 U87MG (expressing a control hairpin or an IRF3-targeting hairpin), 1×10^5 GBM8 or 2×10^5 U3054MG cells were injected into the striatum 2 mm laterally and 1 mm rostrally from the bregma, at a depth of 3 mm. Tumor growth was monitored weekly by bioluminescence (BL) using the IVIS Spectrum system (PerkinElmer; Waltham, MA). One week after injection, animals harboring GBM8 or U3054MG orthotopic tumors were assigned to control normal chow or chow supplemented with CX4945 (MedKoo) at 25 or 75 mg/kg/day (Research Diets Inc.; New Brunswick, NJ). At the end of each study, brains were collected and processed to generate FFPE coronal brain sections that were stained for human vimentin (V9, M0725; Dako; Glostrup, Denmark).

Immunohistochemistry figure preparation and quantification of invasion distance

All stained tissue slides were digitalized using the Leica Aperio AT2 system. All images were prepared for publication using Aperio ImageScope v12 (Aperio Technologies Inc.; Vista, CA). Quantification of U87MG invasion distance was carried out using FIJI[41]. Invasion distance was

defined as the distance of each disseminated tumor cell to the edge of the nearest observed tumor mass.

Lentiviral transduction

Lentiviral particles were produced by transfecting 1.5×10^6 293T cells (per well in a 6-well plate) with 1μg of 3rd generation packaging vectors, 1 μg of plasmid (pLKO–shRNA vector or a pLX304–GFP vector encoding GFP) and 9 μL of PEI transfection reagent. The media was refreshed 24 h after transfection, and the virus-containing media was harvested 48 h post-transfection. The virus was filtered through a 0.45 μm filter. The filtered virus was then used to transduce GBM cells at 1:10 dilution in the presence of polybrene (10 μg/ml). Puromycin selection (1–2 μg/mL) for cells that had successfully integrated the pLKO plasmid was carried out 72 h post-transduction. The sequences for the shRNAs used in gene knockdown experiments are listed under **Key Resources Table**.

Gene expression analysis by RT-qPCR

RNA was extracted from whole-cell lysates using a total RNA isolation kit (Zymo Research; Irvine, CA). 600 ng of total RNA was reverse transcribed into cDNA using the Maxima First Strand cDNA Synthesis kit (ThermoFisher), and 5 μL of the resulting 200 μL cDNA product was then mixed with SYBR® green PCR Master Mix (Applied Biosystems; Foster City, CA) and the appropriate forward and reverse PCR primers. Real-time quantitative PCR (RT-qPCR) amplification was performed using a 96-well plate system (Applied Biosystems). Each PCR reaction was carried out in triplicates. Gene expression was normalized to GAPDH or 18S, which were used as endogenous controls. Expression heat maps were generated using the GENE-E visualization software (https://software.broadinstitute.org/GENE-E/index.html). A list of RT-qPCR primers used is available in the **Key Resources Table**.

siRNA transfection

ON-TARGETplus SMART pool of siRNAs targeting CSNK2A1 or ON-TARGETplus non-targeting control siRNA pool (Dharmacon; Lafayette, CO) were transfected into U3054MG cells at a final concentration of 25 nM using lipofectamine 2000 transfection reagent according to the manufacturer's protocol (Thermo Fisher). After 6 h, the cell media was replaced with fresh media. Total RNA was extracted 72 h post-siRNA transfection, and the expression levels of CSNK2A1 and the IRF3 target ECM genes were quantified by RT-qPCR. Greater than 80% knockdown for CSNK2A1 was confirmed. Target siRNA sequences are listed in **Key Resources Table**.

Western blotting

Total cell lysates were prepared by lysing 1–3 × 10^6 GBM cells in ice-cold 300–400 µL of RIPA buffer, supplemented with proteinase and phosphatase inhibitors, on ice. Proteins were separated by SDS-PAGE, transferred to a PVDF membrane, and blotted with antibodies against total IRF3 (FL-425, sc9082; Santa Cruz Biotechnology; Santa Cruz, CA), phospho-IRF3 (4947), TBK1 (3504), phospho-TBK1 (5483), CK2α (2656; all Cell Signaling Technology; Danvers, MA), cMyc (9E10, sc-40), and HSP90 (sc-7947; both Santa Cruz Biotechnology).

IRF3 immunofluorescence

Cells were seeded at 50% confluence on poly-D-lysine-coated coverslips in a humid chamber and allowed to attach overnight at 37 °C. The next day, cells were washed once in PBS and fixed in 4% formaldehyde for 15 min at RT. Cells were washed once in PBS (5 min/wash) and permeabilized in 0.1% of triton for 10 min at RT. Cells were washed in PBS three times (5 min/wash) and incubated in blocking solution (1% BSA + 25.52 mg/mL glycine in PBS-T (0.1% Tween 20)) for 1 h at RT. Cells were then incubated in polyclonal rabbit anti-IRF3 primary antibody (sc9082; Santa Cruz Biotechnology) at 1:200 dilution in 1% BSA in PBS-T for 1.75 h at RT. Cells were washed three times in PBS-T (10 min/wash) and incubated in Alexa 568 anti-rabbit secondary antibody (ab175471; Abcam; Cambridge, UK) at 1:400 dilution in 1% BSA in PBS-T for 1 h at RT. Cells were then washed 3 times in PBS-T (5 min/wash) and counterstained with 1 µg/mL Hoechst 33342 (Thermo Fisher) nuclear stain for 5 min at RT. Coverslips were mounted on microscope slides using the VECTASHIELD hard-set mounting medium (H-1400; Vector Labs; Burlingame, CA), allowed to dry at RT overnight, and imaged using a Leica SP5 II confocal microscope. Background-corrected total, cytoplasmic, or nuclear cell fluorescence was calculated as the Integrated Density – (Area × Mean background) using Fiji.

Transient transfection of IRF3 5SD plasmid

U87MG cells were seeded at 10% confluency in a 10 cm plate. The respective amount of an empty control pRK5 plasmid or a pRK5 vector containing IRF3 5SD (as indicated in **Supplementary Figures 3F–G** and **Figure 3E**) was mixed with 1.5 mL of OMEM while 30 µL of lipofectamine 2000 transfection reagent (Thermo Fisher) was mixed with 1.5 mL of OMEM in a separate tube, and both were incubated for 5 min at RT. The plasmid/OMEM and lipofectamine/ OMEM solutions were then mixed together and incubated at RT for 20 min, after which the transfection mixture was added drop wise to a10 cm plate of cells, containing 7 mL of 10% serum-supplemented DMEM media (+1% L-glutamine, +1% Pen/Strep). Media was refreshed 8 h post-transfection. Protein and mRNA levels were assessed 72 h post-transfection. The cells were used for invasion assays starting at 72 h post-transfection.

IRF3 ChIP

To determine a potential interaction of endogenous IRF3 with the promoter regions of target ECM genes in human GBM cells, we performed chromatin immunoprecipitation (ChIP) using the ChIP-IT® Express Enzymatic kit (Active Motif; Carlsbad, CA) and a ChIP-optimized IRF3 antibody (39033; Active Motif) or a control IgG antibody (sc-2027; Santa Cruz Biotechnology). The ChIP experiment was carried out by following the precise recommendations of the kit's manufacturer. In brief, chromatin was extracted from ≈ 1.5 × 10^7 U87MG cells treated with DMSO or CX4945 (10 μM) for 24 h and cross-linked in formaldehyde-based cell fixation solution. Chromatin was sheared using the enzymatic shearing cocktail provided with the kit for 10 min at 37 °C. Chromatin shearing efficiency was confirmed by running ≈1 μg of reversely cross-linked sheared chromatin on an agarose gel. ChIP reactions were set-up by mixing 25 μg of sheared chromatin with anti-IRF3 (10 μL per reaction) or IgG antibody (3 μg per reaction) and ChIP buffer, containing protease inhibitors. The ChIP reactions were incubated on an end-to-end rotator for 16 h at 4 °C. The ChIP product was then filtered and bound to a column, eluted, reverse cross-linked, protein-digested, and DNA was column-purified and eluted in 100 μL of elution buffer. Purified DNA product was analyzed by RT-qPCR using 1 μL per reaction. Each reaction was done in triplicates. Primers spanning a short genomic region (70-110 bp) containing the IRF3 promoter motif (5'-T-A/G-GGGGC-3') were designed for each ECM target gene using Primer3 (http://bioinfo.ut.ee/primer3-0.4.0/). Standard curves for each primer set were generated using dilution series from known amounts (0.05–50 ng) of input chromatin and were used to extrapolate the amount of PCR product in each ChIP reaction. RT-qPCR primers used to analyze the ChIP product genomic DNA are listed in **Key Resources Table**.

Graphical Design

Figure 7A, **Supplementary Figure 1C** and the **Graphical Abstract** have been prepared using Servier Medical Art under a Creative Commons Attribution 3.0 Unported License.

SUPPLEMENTARY FIGURES

Supplementary Figure 1 | Development of a GBM brain slice invasion assay. (**A–B**) Brain slice viability, measured by quantifying the percentage of dead cells (marked by the live cell exclusion dye EthD-1) out of the total cell population (marked by the cell-permeable dye DRAQ5) in (**A**) 25% serum-containing media as a function of time up to 14 days across 5 different slice depth planes (z-position) and (**B**) after 10 days of culture in in 25% serum-containing media versus serum-free neural stem cell (NSC media) or NSC media following 1 day slice pre-incubation in 25% serum-containing media. n ≥ 3. (**C**) Schematic depicting the design of the brain slice invasion assay. (**D–F**) Effect of TMZ on cell survival/proliferation, expressed as proliferation index, by patient-derived proneural (**D**), classical (**E**), and mesenchymal (**F**) GNS cell lines. TMZ was added to the brain slice culture media at the indicated concentrations every two days for one week. Proliferation index was calculated as the density of GFP^+ GBM cells growing on the insert surrounding the brain slices. n ≥ 3. (**G–I**) Representative brain slice images depicting insert cell density of GFP+ proneural (**G**), classical (**H**), and mesenchymal (**I**) GNS cells in response to TMZ treatment. All numerical data are shown as mean ± SEM. * $p < 0.05$, ** $p < 0.01$, *** $p < 0.001$; p-values based on Student's t-tests.

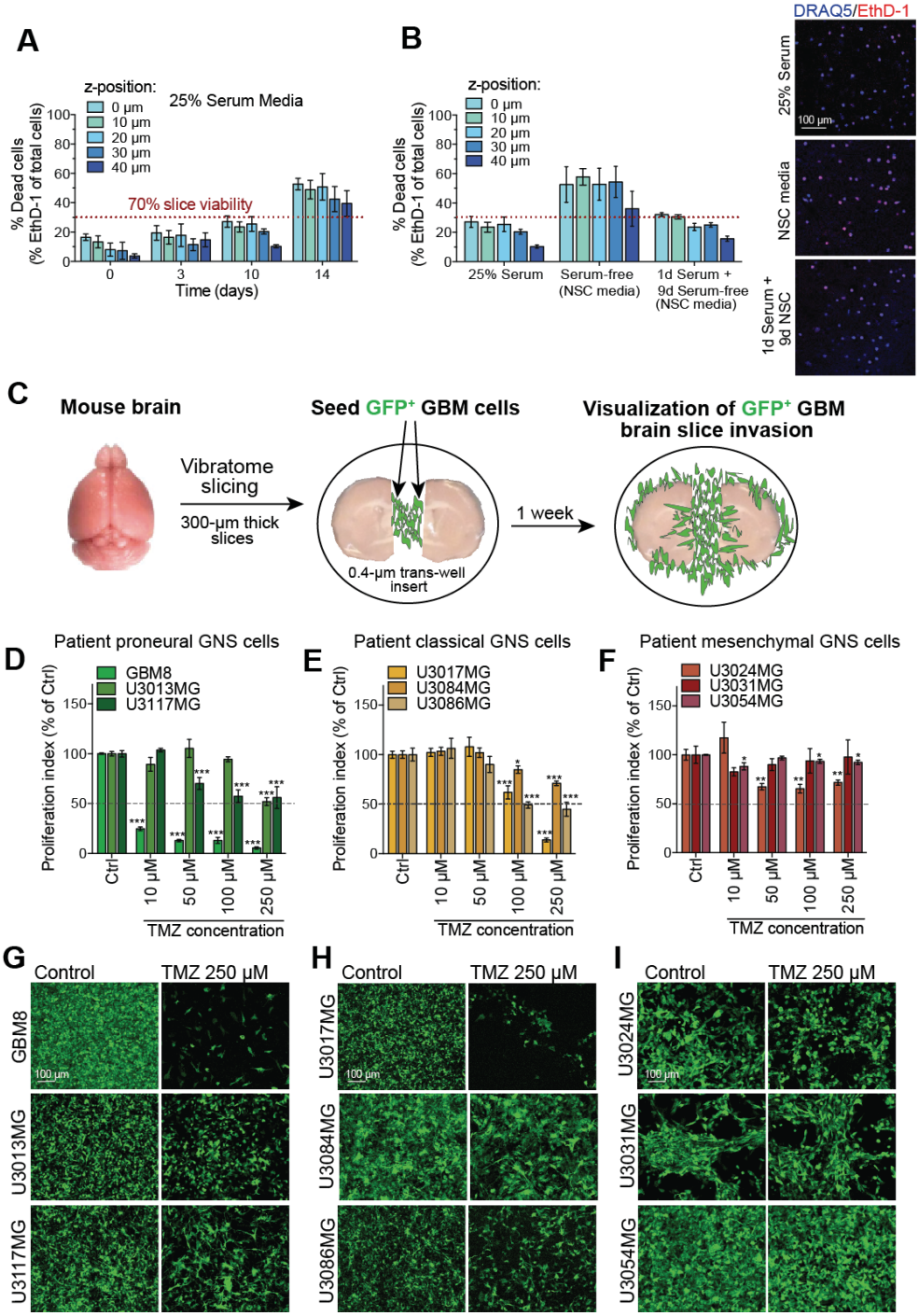

Supplementary Figure 1 | Development of a GBM brain slice invasion assay.

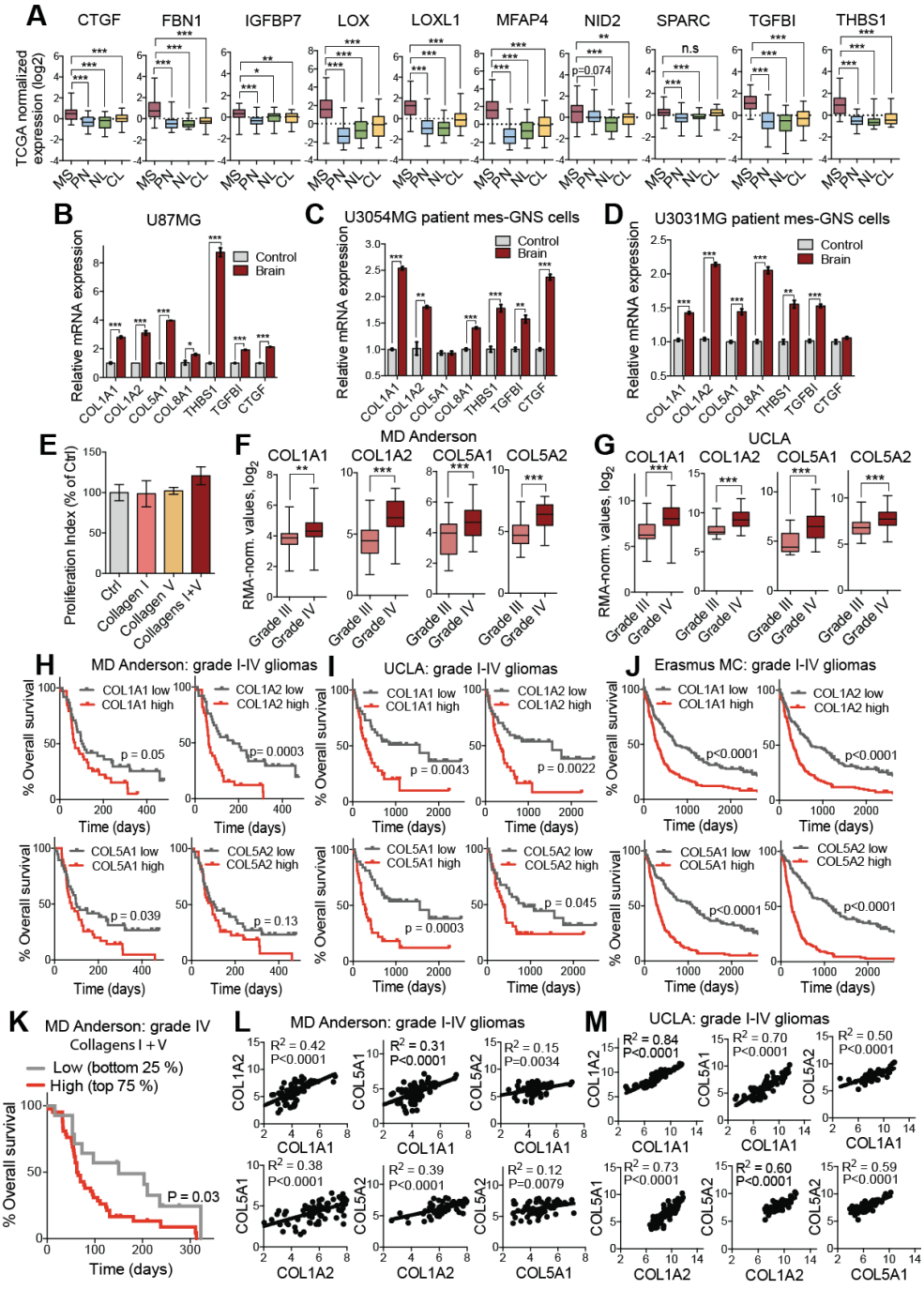

Supplementary Figure 2 | Clinical association of ECM collagens and collagen-interacting factors with glioma progression.

Supplementary Figure 2 | Clinical association of ECM collagens and collagen-interacting factors with glioma progression. (**A**) Box and whisker plots depicting microarray-based normalized expression levels for *CTGF*, *FBN1*, *IGFBP7*, *LOX*, *LOXL1*, *MFAP4*, *NID2*, *SPARC*, *TGFBI*, and *THBS1* in mesenchymal (n = 56), proneural (n = 53), neural (n = 26), and classical (n = 38) GBM tumors from the TCGA patient cohort[8]. n = 173. Whiskers represent min and max values, whereas box extent corresponds to 25th–75th percentile of the sample population. *p*-values based on Student's t-tests. (**B–C**) Transcript levels of *COL1A1*, *COL1A2*, *COL5A1*, *COL8A1*, *THBS1*, *TGFBI*, and *CTGF*, quantified by RT-qPCR, in U87MG control cells (**B**) and patient-derived mesenchymal U3054 GNS control cells (**C**) and their respective brain-invasive derivatives isolated from organotypic brain slices (Brain). n ≥ 3. Data are shown as mean ± SEM. *p*-values based on Student's t-tests. (**D**) Proliferation/survival index, quantified as the density of GFP$^+$ GBM cells growing on the insert outside of the brain slices, by patient-derived proneural GBM8 GNS cells treated with control, collagen I (10 µg/ml), collagen V (10 µg/ml), or a combination of collagen I and V (10 µg/ml each) for the 1-week duration of the invasion assay. n ≥ 3. Data are shown as mean ± SEM. *p*-values based on Student's t-tests. (**E–F**) Box and whisker plots depicting microarray-based normalized expression values for *COL1A1*, *COL1A2*, *COL5A1*, and *COL5A2* as a function of glioma tumor grade in the MD Anderson (**E**; grade III (n = 21), grade IV (n = 56)) and the UCLA (**F**; grade III (n = 24), grade IV (n = 50)) patient cohorts[7,20]. *p*-values based on Student's t-tests. Whiskers represent min and max values, whereas box extent corresponds to 25th–75th percentile of the sample population. (**G–I**) Kaplan–Meier curves for the MD Anderson (n = 77), UCLA (n = 74), and Erasmus MC (n = 263) cohorts[7,20,21] depicting overall survival outcomes of glioma patients as a function of individual *COL1A1*, *COL1A2*, *COL5A1*, and *COL5A2* expression levels in their tumors. Patients whose GBM tumors' collagen expression levels were greater or lower than the median for the population were classified as collagen expression high (red) or low (gray), respectively. *p*-values based on log-rank (Mantel–Cox) test. (**J–K**) Pearson correlation analysis of the individual expression levels of *COL1A1*, *COL1A2*, *COL5A1*, and *COL5A2* glioma tumors from the MD Anderson (n = 77) and UCLA (n = 74) patient cohorts[7,20]. * $p < 0.05$, ** $p < 0.01$, *** $p < 0.001$.

Supplementary Figure 3. IRF3 activation suppresses GBM cell invasion into organotypic brain slices. (**A**) Expression levels of *IRF3*, *ZBTB7A*, *MAX*, and *POU6F1*, quantified by RT-qPCR, in U87MG cells transduced with an empty pLKO vector or a pLKO vector encoding independent shRNAs targeting *IRF3*, *ZBTB7A*, *MAX*, or *POU6F1*, respectively. (**B–C**) *IRF3* transcript levels, determined by RT-qPCR, in (**B**) E98 and (**C**) GBM8 cells stably expressing an empty pLKO vector or a pLKO vector with an shRNA against *IRF3*. (**D**) IRF3 protein levels, determined by western blotting, in U87MG cells transduced with an empty pLKO vector or a pLKO vector encoding independent shRNAs targeting *IRF3*. HSP90 was used as a loading control. (**E**) Quantification of western blot measurements shown in (**D**). (**F–G**) Western blotting for IRF3, c-Myc, and HSP90 in (**F**) U87MG cells and (**G**) U3054MG cells transiently transfected with increasing amounts of a pRK5 vector expressing c-Myc-tagged IRF3 5SD construct, as indicated in the figures. HSP90 was used as a loading control. (**H**) Invasion index distribution as a function of slice depth/z-plane position in the slice for U87MG cells transduced with an empty pLKO vector (gray) or a pLKO vector encoding independent shRNAs targeting *IRF3* (blue tones). n ≥ 6. (**I**) Cell survival/proliferation index for U87MG cells transduced with an empty pLKO vector (gray) or a pLKO vector encoding independent shRNAs targeting *IRF3* (blue tones). n ≥ 8. (**J**) Total invasion index for U87MG cells expressing an empty pLKO vector (gray) or a pLKO vector encoding independent shRNAs targeting *ZBTB7A* (green tones). n ≥ 5. (**K**) Cell survival/proliferation index for U87MG cells transduced with an empty pLKO vector (gray) or a pLKO vector encoding independent shRNAs targeting *ZBTB7A* (green tones). n ≥ 8. (**L**) Invasion index distribution as a function of slice depth/z-plane position in the slice for U87MG cells transduced with an empty pLKO vector (gray) or a pLKO vector encoding independent shRNAs targeting *ZBTB7A* (green tones). n ≥ 5. (**M**) Cell survival/proliferation index for GBM8–pLKO control cells or GBM8–sh$_4$IRF3 cells. n = 3. (**N**) Total invasion index for U87MG cells transfected with a control (empty pRK5 vector) or IRF3 5SD containing plasmid. Invasion assay was carried out 72 h post-transfection for 1 week. n = 3. (**O–P**) Cell survival/proliferation index for (**O**) U87MG and (**P**) U3054MG cells transiently transfected with an empty pRK5 vector (control) or a pRK5 vector expressing IRF3 5SD and subjected to the invasion assay 72 h post-transfection for 1 week. n = 3. (**Q**) Cumulative fraction plot depicting the distribution of cytoplasmic-to-nuclear ratio of IRF3 CTCF, measured by confocal microscopy following immunocytochemical staining for IRF3 in minimally invasive U87MG control cells and their brain-invasive derivatives. n ≥ 26 cells. (**R**) Cell survival/proliferation index for U3054MG cells treated with poly (I:C) (50 µg/ml) or control added to the cell media every 2–3 days for the 1-week duration of the invasion assay. n ≥ 4. (**S**) Total invasion index quantified for patient-derived U3031MG mesenchymal GNS cells treated with poly (I:C) (50 µg/ml) or control added to the cell media every 2–3 days for the 1-week duration of the invasion assay. n = 4. (**T**) Cell survival/proliferation index for U3031MG cells treated with poly (I:C) (50 µg/ml) or control added to the cell media every 2–3 days for the 1-week duration of the invasion assay. n = 4. (**U**) RT-qPCR analysis of the expression levels of *COL1A1*, *COL1A2*, *COL5A1*, *COL8A1*, *CTGF*, and *LOXL1* in U3031MG GNS cells treated with poly (I:C) (50 µg/ml) or control for 24 h. n = 3. (**V**) Western blotting for phosphorylated IRF3 (p-IRF3), IRF3, and HSP90 in U3031MG GNS cells treated with poly (I:C) (50 µg/ml) or control for 3 h. HSP90 was used as a loading control. All data are shown as mean ± SEM. * $p < 0.05$, ** $p < 0.01$, *** $p < 0.001$; *p*-values based on Student's t-tests.

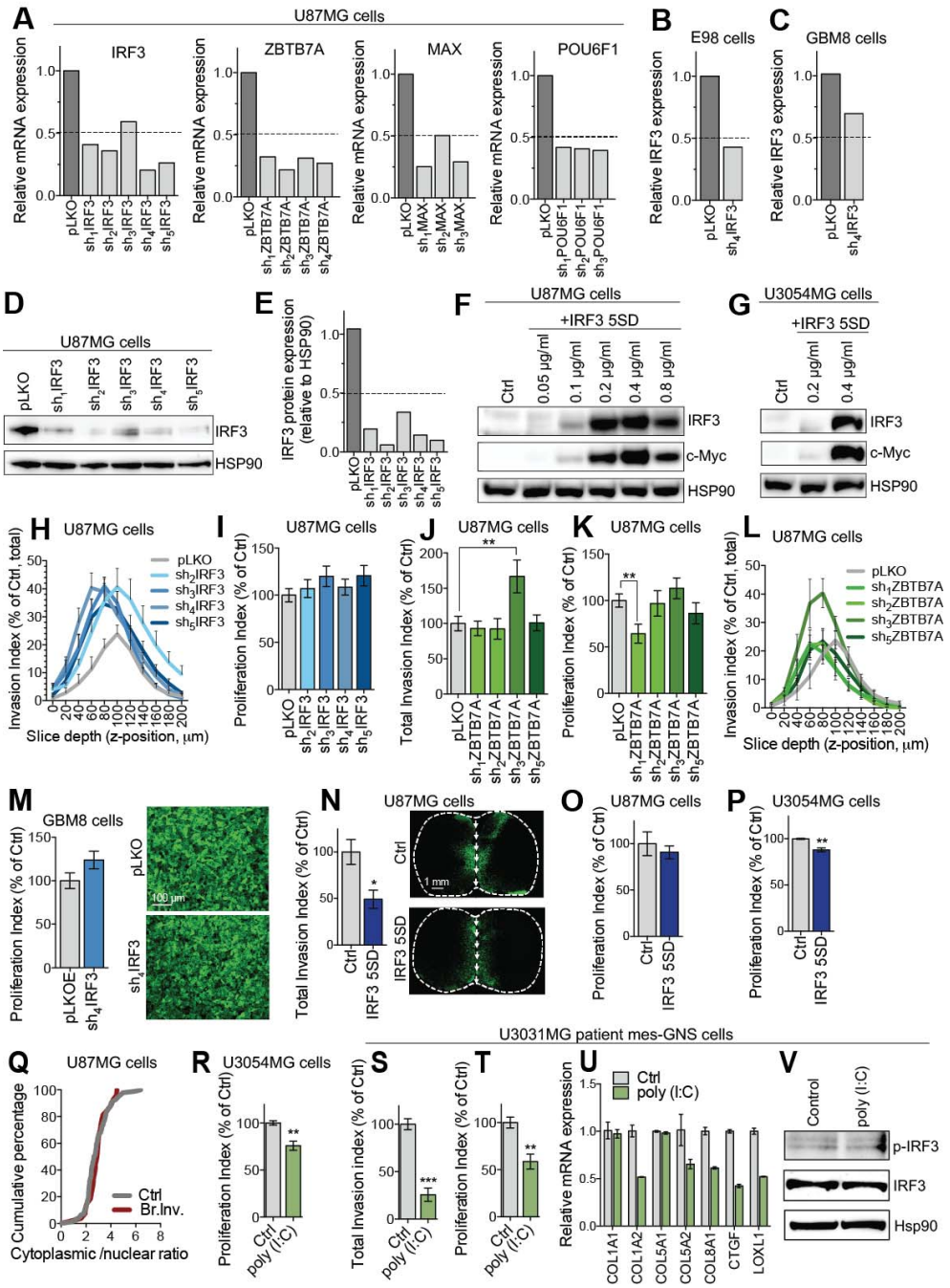

Supplementary Figure 3. IRF3 activation suppresses GBM cell invasion into organotypic brain slices.

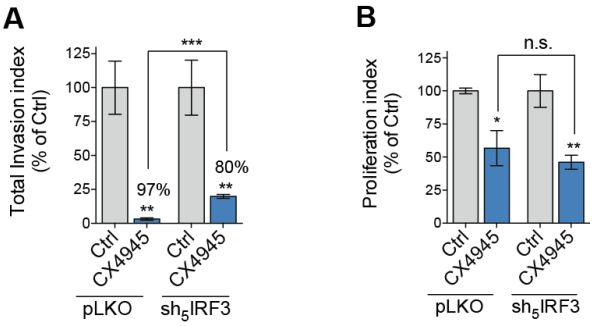

Supplementary Figure 4 | IRF3 knockdown partially occludes invasion suppression by CK2 inhibition. (**A**) Total invasion index calculated for U87MG cells stably expressing a control empty vector (pLKO) or a vector encoding an shRNAs targeting IRF3 in response to 10µM CX4945 treatment for 1 week. n ≥ 3. (**B**) Proliferation/survival index for U87MG cells expressing an empty pLKO vector or a pLKO vector with an IRF3-targeting shRNA, which grew on the inserts surrounding the brain slices, in response to 10µM CX4945 treatment for 1 week. n ≥ 3. All data are shown as mean ± SEM. * $p < 0.05$, ** $p < 0.01$, *** $p < 0.001$; p-values based on Student's t-tests.

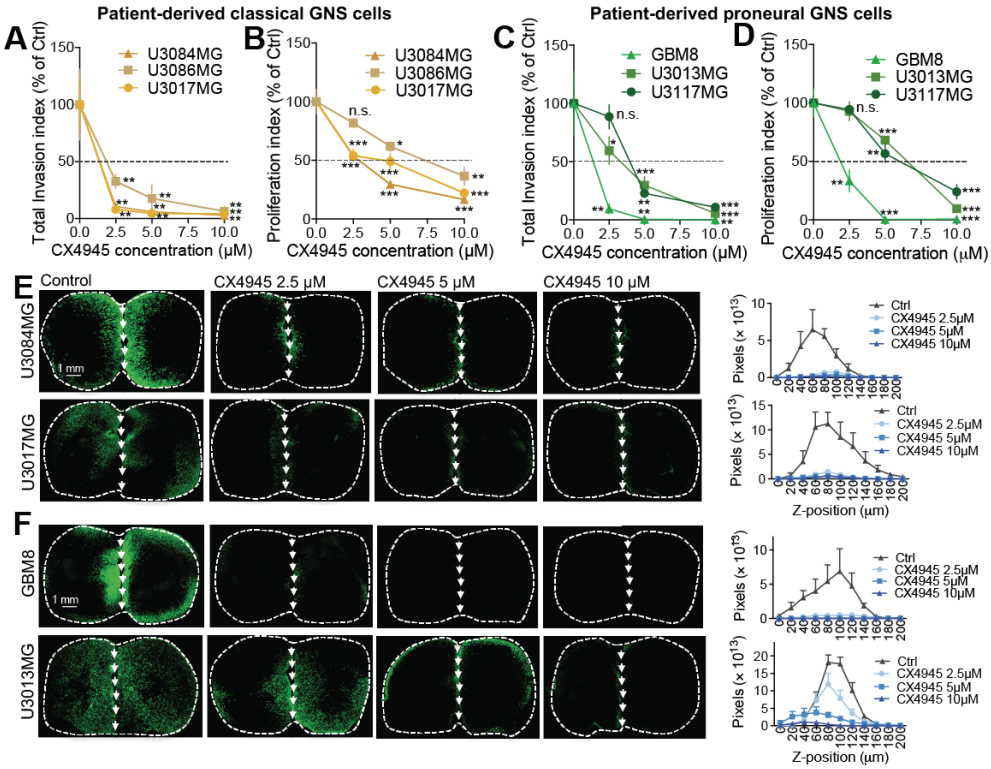

Supplementary Figure 5 | CK2 targeting suppresses brain slice invasion by proneural, and classical GNS cells. (**A, C**) Total invasion index calculated for patient-derived classical (**A**) and proneural (**C**) GNS cells in response to CX4945 treatment at the indicated concentrations for 1 week. n ≥ 3. (**B, D**) Proliferation/survival index for classical (**B**) and proneural (**D**) GNS cells, which grew on the inserts surrounding the brain slices, in response to CX4945 treatment at the indicated concentrations for 1 week. n ≥ 3. (**E, F**) Representative whole-slice reconstruction images illustrating the effect of CX4945 treatment on brain slice invasion by classical and proneural GNS cell lines quantified in (**A**) and (**C**), respectively (left panel). Distribution plots of invasion index as a function of z-plane position (right panel). All data are shown as mean ± SEM. * $p < 0.05$, ** $p < 0.01$, *** $p < 0.001$; p-values based on Student's t-tests.

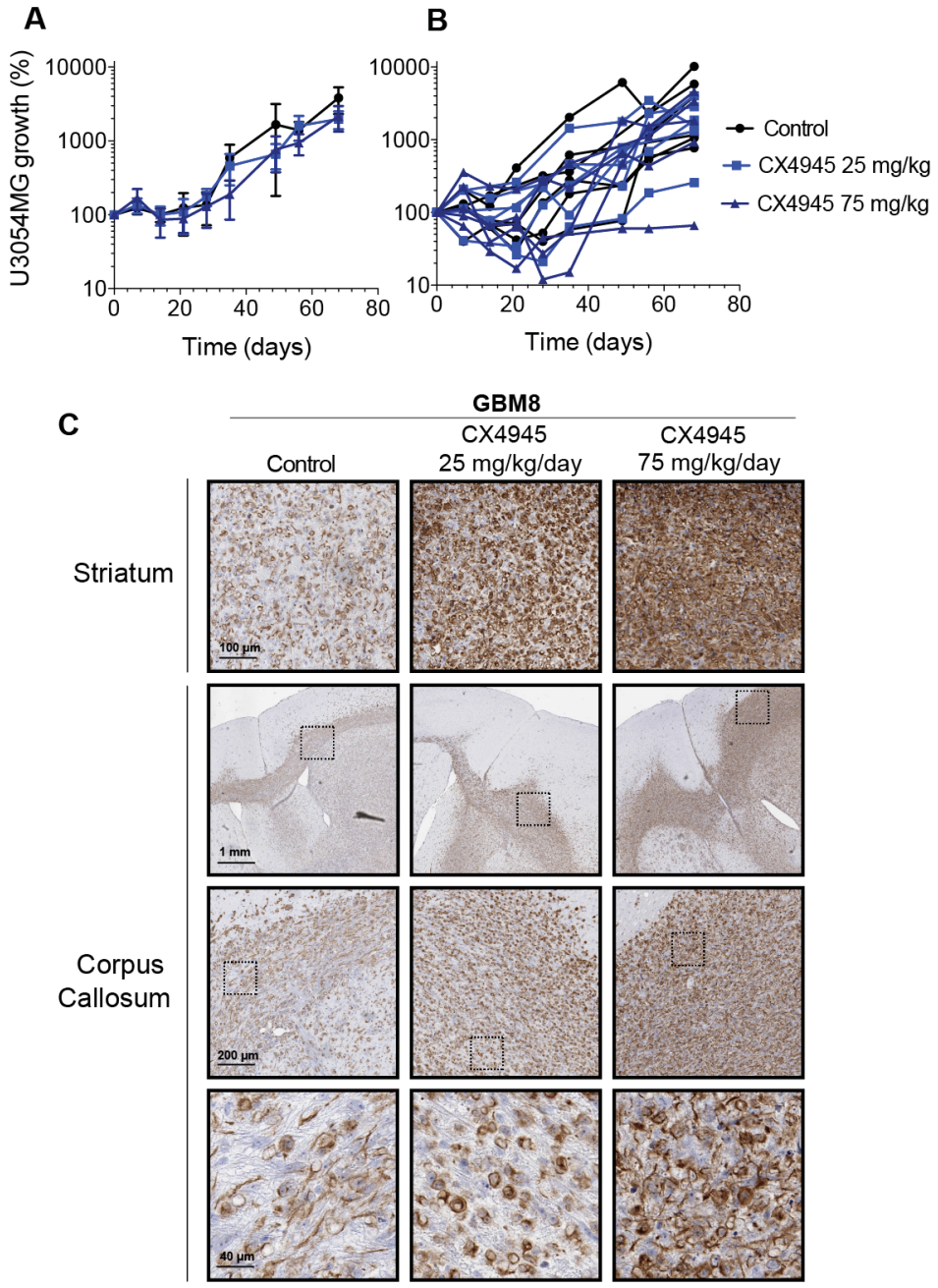

Supplementary Figure 6 | Effect of therapeutic CK2 inhibition on U3054MG tumor growth and GBM8 invasiveness *in vivo*. (**A**) Tumor growth of U3054MG tumors from **Figure 7A** was followed up using weekly bioluminescence measurements. n = 6. Data are shown as mean ± SEM. (**B**) Individual tumor growth curves from (**A**). (**C**) Representative images from human vimentin immunostaining of the striatum and corpus callosum of mice implanted with orthotopic GBM8 tumors and treated with control chow or CX4945-supplemented chow at a dose of 25 or 75 mg/kg/day. Dashed squares indicate the areas that are magnified and shown in the panels below each image.

16

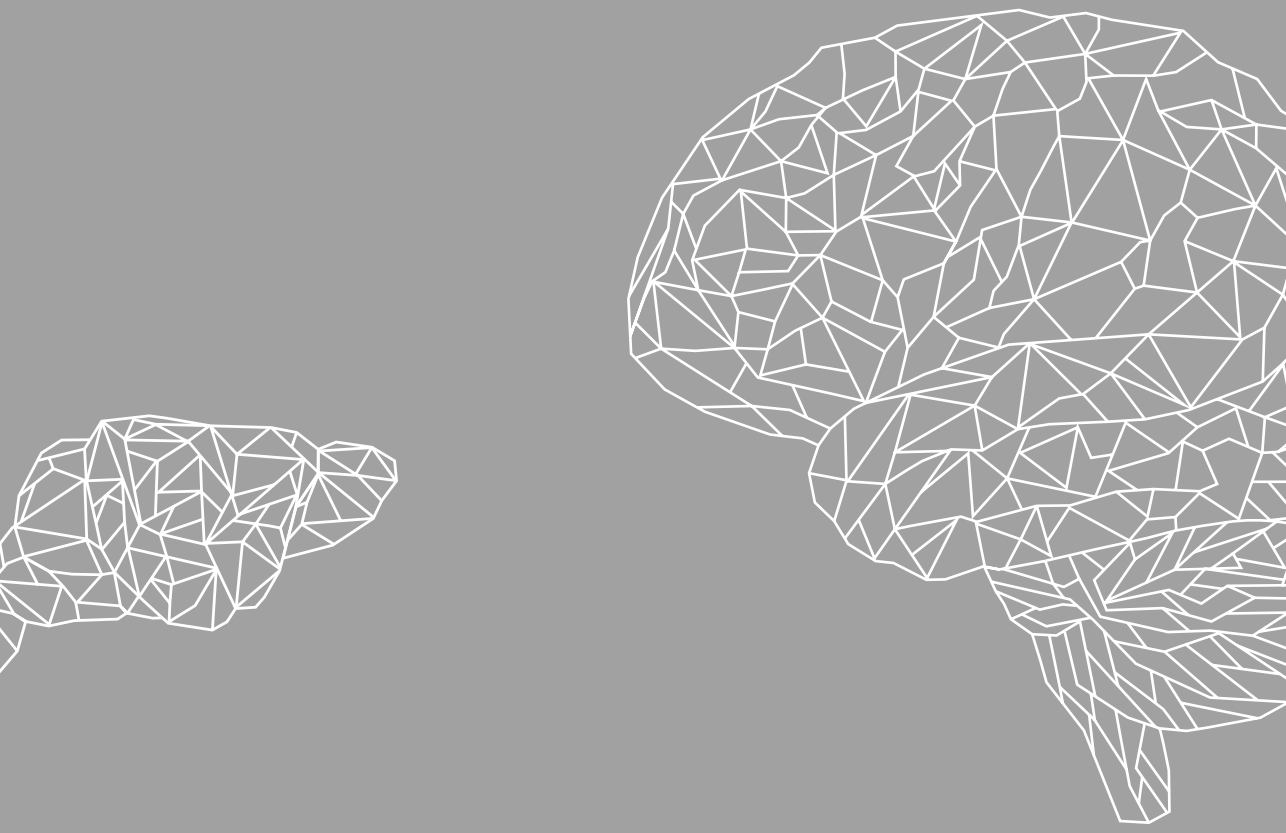

SECTION VIII

GENERAL DISCUSSION AND SUMMARY

GENERAL DISCUSSION

In recent years, considerable achievements have been made in the treatment of cancers that were notoriously intractable, such as metastatic melanoma and non-small cell lung cancer[1,2]. Yet, improvements in the therapy of glioblastoma (GBM) have only been incremental[3]. Why have we been doing so poorly and, even more importantly, what do we need to do to improve?

This thesis aimed to mount an attack on the three pillars of the glioblastoma triad: proliferation, invasion and resistance. Even though various seminal studies have recently allowed us to identify these pillars, several major challenges await us on the path towards translating our basic understanding of GBM biology to therapeutic approaches that can be meaningful for patients suffering from this devastating brain tumor. These challenges are both of biological and pharmacological nature, and are likely to evolve as our knowledge of GBM biology continues to expand.

Biological hurdles

Recent in-depth molecular characterizations have taught us that GBM is not one disease but a collection of subtypes defined by their specific biology[4–6]. GBMs are amongst the most heterogeneous tumors, and several subtypes are found within one patient almost without exception[7]. Of note, classical first-line chemo-radiotherapy can even further increase intratumoral heterogeneity due to their mutagenic nature[8]. Furthermore, GBMs are a 'moving target', as GBM cells have a high level of plasticity and the dominant subtype can switch upon selective therapeutic pressure[9,10]. It is therefore unlikely that we will ever find one 'golden bullet' for GBM. Rather, combination strategies will be required to exert meaningful antitumor efficacy. Importantly, because of its heterogeneity and plasticity, achieving complete cure may not be realistic even when using therapeutic combination strategies. More likely, we will be able to achieve durable responses by intelligently designing a multimodality approach. Subsequent monitoring of tumor relapse and companion diagnostics may pave the way to intelligent therapy switches when relapse occurs, thus turning GBM into a chronic disease. However, repeated molecular typing of relapsed GBM poses an additional challenge. Currently, diagnostics on GBM is performed on biopsies or surgical samples, requiring invasive procedures that cannot be repeated very often. Improving the power of non-invasive diagnostics to the level of invasive diagnostics will be essential to longitudinally monitor tumor evolution and select the appropriate alternate therapeutic intervention upon recurrence. Promising non-invasive diagnostic platforms include circulating tumor DNA and platelet-based platforms[11,12].

As mentioned, combination therapy strategies are likely required to exert meaningful responses in GBM. However, more research is necessary to investigate which therapeutic approach is

most effective for which GBM subtype. This thesis investigates classical chemotherapeutic (**Chapters 3, 4 and 13**) and radiotherapeutic approaches (**Chapter 12**), as well as more novel targeted strategies (**Chapters 6, 8 and 16**). DNA damaging approaches using chemotherapeutics and radiotherapy may be more generally applicable, but targeted agents are likely to achieve differential efficacy in different GBM subtypes depending on the genetic background of the tumor. Although the TCGA has provided highly valuable information and suggests that simultaneously interfering with the PI3K, MAPK and RB pathways can be of value in multiple GBM subtypes[4], the specific component of each pathway that needs to be targeted may vary per subtype. Most likely, future combination strategies will be multimodal approaches including common classical DNA damaging therapies as a general therapeutic backbone, supplemented with specific targeted agents depending on the GBM subtype.

Immunotherapeutic approaches have not been highlighted in this thesis. While immunotherapy has recently made significant advances in treatment of melanoma and some other cancers[1,2,13], results of immunotherapy clinical trials against GBM have thus far been disappointing[14]. An explanation for these failures may be the low abundance of neo-antigens in GBM, typically classifying them as 'cold' tumors[15]. Therefore, the clinically developed immunotherapy with checkpoint inhibitors that focus on restoring T cell activity may not be the most suitable approach for GBM. Instead, focusing on innate immune responses via macrophages or dendritic cells may be more promising[16,17]. Several studies have now reported that these cell types can influence therapy resistance in mouse models of GBM[18,19], and as such likely form an important part of the resistance pillar of the GBM triad. Therapeutic approaches focusing on these immune components may therefore in the future certainly be complimentary to drugs targeting the GBM cells themselves.

There is an increasing awareness that we need to improve the predictive value of preclinical model systems, in order to use them to direct translational cancer research. While the general predictive value of mouse models will be discussed below, *in vitro* GBM research brings an additional challenge. Traditionally, cancer cell cultures are established in serum-containing medium. However, a little over a decade ago a seminal paper in the field of *in vitro* GBM research has demonstrated that serum-cultured GBM cells poorly resemble the original tumors they were derived from[20]. Serum induces differentiation, and as a result surviving GBM cells acquire additional mutations to allow infinite proliferation as a cancer cell line under these conditions. The same paper remedied this problem by offering the recipe for a glioma stem cell (GSC) medium that allows GBM cells isolated from patients' tumors to maintain their characteristics. GSC models have since been accepted as the gold standard in GBM research. Due to the delicate, costly and time-consuming nature of GSC models, serum models will likely keep their place in GBM research in the near future. However, it is now clear that in order to increase the predictive value of preclinical GBM research, serum models should always be complimented with GSC models.

This thesis relies heavily on mouse models. Even though *in vitro* research is favored for ethical reasons, for now preclinical GBM research will likely continue to use *in vivo* models as these offer a level of biological complexity that cannot be achieved by *in vitro* systems. Even though *in vitro* systems become increasingly sophisticated[21,22], certain biological processes that have been demonstrated to be important for GBM biology cannot yet be modeled *in vitro*. These mostly include the micro-environmental context provided by, for instance, the immune system and stroma[23], blood–brain barrier (BBB)[24], stem cell niches and hypoxia[25] and metabolism[26].

Pharmacological hurdles

For any therapeutic strategy, delivery is key to achieving the desired pharmacodynamic effect. If a therapeutic cannot reach the tumor it cannot yield antitumor efficacy, as intrinsically potent as it may be. Especially in GBM, delivery poses an exceptional challenge, due to the presence of the BBB. The importance of the BBB in GBM is highlighted throughout this thesis as well as by other groups and these studies provide ample evidence that the BBB needs to be addressed to fully exploit the antitumor potential of a given therapy[24,27]. The potential of several circumvention strategies has been discussed in detail in **Chapter 1**. Two strategies appear to have the most potential. The first is simply selecting those candidate drugs whose brain penetration is least hampered by the BBB. **Chapters 5, 6, and 7** provide examples of these efforts. However, as becomes clear from numerous candidate drugs discussed in this thesis, the vast majority of drugs has a very poor brain penetration. Therefore, in order to increase the number of candidate drugs available for treatment of GBM, drug discovery programs in both academia and industry should put more emphasis on BBB penetration capacity.

A second promising strategy to increase the number of candidate drugs for GBM is pharmacological inhibition of drug efflux transporters that are expressed at the BBB. This strategy has successfully been employed in this thesis for GBM mouse models using the ABCB1/ABCG2 inhibitor elacridar (**Chapters 4 and 13**). Unfortunately however, the results of an initial clinical study using elacridar to boost the brain penetration of substrate drugs were not encouraging[28]. A plausible explanation for this discrepancy between mouse models and patients may be the interspecies differences in the oral bioavailability of elacridar[29]. The plasma concentrations that can be reached in patients after oral administration of elacridar are much lower than those achieved in mice[29,30]. Interestingly, the oral bioavailability does not appear to be linear in humans[30]. Possible causes of this low oral bioavailability include low solubility in the gastro-intestinal tract and rapid first-pass metabolism. Importantly, numerous mouse studies have demonstrated the intrinsic potential of using elacridar to boost the brain penetration of substrate drugs[31-33]. If similar effective elacridar plasma concentrations could also be reached in patients, this should greatly increase the number of available candidate drugs for treatment of GBM. Some efforts have already focused on overcoming the solubility issues of elacridar by turning to solid dispersion

formulations[34,35]. Although these have not yet yielded promising results[36], further improving the elacridar formulation and reducing its first-pass metabolism may be instrumental to providing GBM patients with several treatment options that are now only available to treat extracranial tumors.

As already mentioned above, the predictive value of cancer mouse models for treatment response in the clinic appears to be limited[37,38]. While there are several possible biological reasons underlying this disconnect, including those relevant for GBM research as discussed above, species differences in pharmacokinetics and tolerability of drugs are generally ignored . In most animal experiments investigating therapeutic interventions, mice are given as much as they can tolerate, analogous to phase I clinical trials. However, as mice have a higher metabolic rate than humans, the elimination half-life of drugs from plasma is generally much shorter than in humans. Consequently, intravenous or oral application of drugs usually result in plasma concentrations that are manifold higher than can be achieved in patients. Especially for targeted agents, single agent antitumor efficacy is often only seen at dose levels yielding these unrealistically high plasma concentrations. For instance, the CDK4/6 inhibitor palbociclib is only effective in mice when given at 150 mg/kg, yielding plasma concentrations that are approximately 40-fold higher than those achieved in patients (**Chapter 11**)[39,40]. Mimicking the plasma exposure of therapeutic agents more closely in cancer mouse models to those obtained in patients may likely contribute to increasing the predictive value of preclinical cancer research, potentially sparing patients and society from costly and futile larger clinical trials.

As highlighted in this thesis, the complexity of GBM calls for combination therapies. The future emphasis on combination therapies calls for changes in clinical trial design. First, combined toxicity of multiple drugs is an obvious concern. Traditionally, agents are given at the maximum tolerated dose (MTD) as determined in phase I clinical trials[41]. While this approach was useful for classic chemotherapeutic 'sledgehammers' for which more drug means more damage and thus more cell death, the introduction of targeted agents calls for a different endpoint, especially in combination trials. Often, targeted agents become toxic at dose levels that far exceed those required for target inhibition, essentially becoming untargeted agents. Indeed, combining multiple targeted agents at their MTD will almost without exception be too toxic for patients. However, these agents may not need to be used at their MTD, and pharmacodynamic endpoints such as target inhibition may be used to guide tolerable dosing of multiple targeted agents. Notably, mouse models may play an important role in establishing relationships between plasma concentrations and target inhibition in tumors.

A second issue when combining multiple drugs is their timing. Especially when also including multiple modalities such as radiotherapy, chemotherapy and targeted agents, potential synergism and interference needs to be investigated. For instance, cell cycle inhibitors may antagonize

radiotherapy when given concomitantly, but may delay recurrence when given adjuvantly. Preclinical in vivo models can provide valuable mechanistic insight and guide clinical trials design in this aspect.

A third and final issue is one of organization and collaboration. As multiple targets need to be simultaneously inhibited, and given the low number of drugs that are able to penetrate the BBB, it is unlikely that the portfolio of any pharmaceutical company will contain appropriate candidates for targets of the required combination. Therefore, collaborative efforts between different industrial and academic partners will be vital to making meaningful steps for GBM patients.

Concluding remarks

Over the years we have increasingly gained knowledge on the complexity of GBM biology, which allowed us to more rationally design treatment strategies. Major pillars of the malignancy of GBM are uncontrolled proliferation, unparalleled invasion and tremendous therapy resistance, and together these form the glioblastoma triad. Most likely, an intelligently designed therapeutic approach that attacks multiple components of the glioblastoma triad will be required to provide durable responses for patients. Although several biological and pharmacological challenges can already be identified that await us while bringing these combination strategies to the clinic, none of these seem insurmountable and we can therefore be justifiably optimistic about the future of GBM treatment.

REFERENCES

1. Luke, J.J., *et al.* Targeted agents and immunotherapies: optimizing outcomes in melanoma. *Nat Rev Clin Oncol* **14**, 463-482 (2017).
2. Gridelli, C. & Casaluce, F. Frontline immunotherapy for NSCLC: alone or not alone? *Nat Rev Clin Oncol* **15**, 593-594 (2018).
3. Stupp, R., *et al.* Radiotherapy plus concomitant and adjuvant temozolomide for glioblastoma. *N Engl J Med* **352**, 987-996 (2005).
4. Brennan, C.W., *et al.* The somatic genomic landscape of glioblastoma. *Cell* **155**, 462-477 (2013).
5. Ceccarelli, M., *et al.* Molecular profiling reveals biologically discrete subsets and pathways of progression in diffuse glioma. *Cell* **164**, 550-563 (2016).
6. Wang, Q., *et al.* Tumor evolution of glioma-intrinsic gene expression subtypes associates with immunological changes in the microenvironment. *Cancer Cell* **32**, 42-56 (2017).
7. Patel, A.P., *et al.* Single-cell RNA-seq highlights intratumoral heterogeneity in primary glioblastoma. *Science* **344**, 1396-1401 (2014).
8. Johnson, B.E., *et al.* Mutational analysis reveals the origin and therapy-driven evolution of recurrent glioma. *Science* **343**, 189-193 (2014).
9. Wang, J., *et al.* Clonal evolution of glioblastoma under therapy. *Nat Genet* **48**, 768-776 (2016).
10. Segerman, A., *et al.* Clonal variation in drug and radiation response among glioma-initiating cells is linked to proneural-mesenchymal transition. *Cell Rep* **17**, 2994-3009 (2016).
11. Best, M.G., *et al.* RNA-seq of tumor-educated platelets enables blood-based pan-cancer, multiclass, and molecular pathway cancer diagnostics. *Cancer Cell* **28**, 666-676 (2015).
12. Best, M.G., *et al.* Liquid biopsies in patients with diffuse glioma. *Acta Neuropathol* **129**, 849-865 (2015).
13. Motzer, R.J., *et al.* Nivolumab plus ipilimumab versus sunitinib in advanced renal-cell carcinoma. *N Engl J Med* **378**, 1277-1290 (2018).
14. Buerki, R.A., *et al.* Immunotherapy of primary brain tumors: facts and hopes. *Clin Cancer Res* **24**, 5198-5205 (2018).
15. Alexandrov, L.B., *et al.* Signatures of mutational processes in human cancer. *Nature* **500**, 415-421 (2013).
16. Lieberman, N.A., *et al.* Developing immunotherapeutic strategies to target brain tumors. *Expert Rev Anticancer Ther* **16**, 775-788 (2016).
17. Iglesia, M.D., *et al.* Genomic analysis of immune cell infiltrates across 11 tumor types. *J Natl Cancer Inst* **108**(2016).
18. Quail, D.F., *et al.* The tumor microenvironment underlies acquired resistance to CSF-1R inhibition in gliomas.

Science **352**, aad3018 (2016).
19. Garzon-Muvdi, T., *et al.* Dendritic cell activation enhances anti-PD-1 mediated immunotherapy against glioblastoma. *Oncotarget* **9**, 20681-20697 (2018).
20. Lee, J., *et al.* Tumor stem cells derived from glioblastomas cultured in bFGF and EGF more closely mirror the phenotype and genotype of primary tumors than do serum-cultured cell lines. *Cancer Cell* **9**, 391-403 (2006).
21. Chonan, Y., *et al.* Endothelium-induced three-dimensional invasion of heterogeneous glioma initiating cells in a microfluidic coculture platform. *Integr Biol (Camb)* **9**, 762-773 (2017).
22. Gao, Y., *et al.* A versatile valve-enabled microfluidic cell co-culture platform and demonstration of its applications to neurobiology and cancer biology. *Biomed Microdevices* **13**, 539-548 (2011).
23. Broekman, M.L., *et al.* Multidimensional communication in the microenvirons of glioblastoma. *Nat Rev Neurol* (2018).
24. Oberoi, R.K., *et al.* Strategies to improve delivery of anticancer drugs across the blood-brain barrier to treat glioblastoma. *Neuro Oncol* **18**, 27-36 (2016).
25. Aderetti, D.A., *et al.* The hypoxic peri-arteriolar glioma stem cell niche, an integrated concept of five types of niches in human glioblastoma. *Biochim Biophys Acta* **1869**, 346-354 (2018).
26. van Lith, S.A., *et al.* Glutamate as chemotactic fuel for diffuse glioma cells: are they glutamate suckers? *Biochim Biophys Acta* **1846**, 66-74 (2014).
27. Durmus, S., *et al.* Apical ABC transporters and cancer chemotherapeutic drug disposition. *Adv Cancer Res* **125**, 1-41 (2015).
28. Bauer, M., *et al.* Interaction of 11C-tariquidar and 11C-elacridar with P-glycoprotein and breast cancer resistance protein at the human blood-brain barrier. *J Nucl Med* **54**, 1181-1187 (2013).
29. Ward, K.W. & Azzarano, L.M. Preclinical pharmacokinetic properties of the P-glycoprotein inhibitor GF120918A (HCl salt of GF120918, 9,10-dihydro-5-methoxy-9-oxo-N-[4-[2-(1,2,3,4-tetrahydro-6,7-dimethoxy-2-isoquinolinyl)ethyl]phenyl]-4-acridine-carboxamide) in the mouse, rat, dog, and monkey. *J Pharmacol Exp Ther* **310**, 703-709 (2004).
30. Kuppens, I.E., *et al.* A phase I, randomized, open-label, parallel-cohort, dose-finding study of elacridar (GF120918) and oral topotecan in cancer patients. *Clin Cancer Res* **13**, 3276-3285 (2007).
31. Vaidhyanathan, S., *et al.* Factors influencing the central nervous system distribution of a novel phosphoinositide 3-kinase/mammalian target of rapamycin inhibitor GSK2126458: implications for overcoming resistance with combination therapy for melanoma brain metastases. *J Pharmacol Exp Ther* **356**, 251-259 (2016).
32. Durmus, S., *et al.* Oral availability and brain penetration of the B-RAFV600E inhibitor vemurafenib can be enhanced by the P-glycoprotein (ABCB1) and breast cancer resistance protein (ABCG2) inhibitor elacridar. *Mol Pharm* **9**, 3236-3245 (2012).
33. Traxl, A., *et al.* Breast cancer resistance protein and P-glycoprotein influence in vivo disposition of 11C-erlotinib. *J Nucl Med* **56**, 1930-1936 (2015).
34. Sawicki, E., *et al.* Pharmaceutical development of an amorphous solid dispersion formulation of elacridar hydrochloride for proof-of-concept clinical studies. *Drug Dev Ind Pharm* **43**, 584-594 (2017).
35. Sawicki, E., *et al.* Clinical pharmacokinetics of an amorphous solid dispersion tablet of elacridar. *Drug Deliv Transl Res* **7**, 125-131 (2017).
36. Verheijen, R.B., *et al.* Molecular imaging of ABCB1 and ABCG2 inhibition at the human blood-brain barrier using elacridar and (11)C-erlotinib PET. *J Nucl Med* **59**, 973-979 (2018).
37. Landgraf, M., *et al.* Rational design of mouse models for cancer research. *Trends Biotechnol* **36**, 242-251 (2018).
38. Day, C.P., *et al.* Preclinical mouse cancer models: a maze of opportunities and challenges. *Cell* **163**, 39-53 (2015).
39. Michaud, K., *et al.* Pharmacologic inhibition of cyclin-dependent kinases 4 and 6 arrests the growth of glioblastoma multiforme intracranial xenografts. *Cancer Res* **70**, 3228-3238 (2010).
40. Flaherty, K.T., *et al.* Phase I, dose-escalation trial of the oral cyclin-dependent kinase 4/6 inhibitor PD 0332991, administered using a 21-day schedule in patients with advanced cancer. *Clin Cancer Res* **18**, 568-576 (2012).
41. Iasonos, A. & O'Quigley, J. Adaptive dose-finding studies: a review of model-guided phase I clinical trials. *J Clin Oncol* **32**, 2505-2511 (2014).

SUMMARY

Glioblastoma (GBM) is the most common primary brain tumor and despite extensive treatment, patients are faced with a dismal prognosis. There is thus a great need for new treatment strategies that improve clinical responses and survival. Recent large-scale efforts have characterized many aspects of GBM biology and have highlighted three main pillars that underlie its malignancy: uncontrolled proliferation, unparalleled invasion and tremendous resistance to therapy. These pillars together form the glioblastoma triad, and this thesis has investigated all three pillars and demonstrates efficient ways to attack each separately. Hopefully, this knowledge will aid in designing an intelligent combination treatment strategy that attacks multiple components of the glioblastoma triad, as this will likely be required to provide long-term solutions for GBM patients.

Section I opens this thesis by introducing two of the pillars of the glioblastoma triad. **Chapter 1** gives an overview of available and developing therapeutic strategies to overcome the blood–brain tumor barrier (BBTB). The blood–brain barrier (BBB) protects the healthy brain from potentially harmful exogenous substances, by preventing paracellular diffusion and efficiently transporting unwanted compounds back into the bloodstream. In the context of a brain tumor, it is known as the BBTB and, although its integrity can be physically compromised, it provides GBM with protection from systemic anticancer treatments by limiting access of drugs to the tumor. Overcoming the BBTB is thus essential for efficiently delivery of systemic therapy to brain tumors. Chapter 1 discusses several strategies to achieve this goal, including osmotic BBB disruption, exploiting receptor-mediated transport systems and inhibition of drug efflux transporters and concludes that these latter two hold most promise for improving the delivery of treatment to brain tumors. **Chapter 2** focuses on the cellular signaling pathways that are deregulated in GBM and the potential treatment strategies to target these with molecularly targeted agents. It highlights three main pathways that harbor mutations in the majority of GBMs: the PI3K pathway, the MAPK pathway and the RB pathway. This chapter also provides an overview of inhibitors of components of these pathways with an emphasis on their potential to cross the BBB. Chapter 2 concludes that targeted therapy against one pathway is unlikely to be successful and combinations of targeted therapies should instead be explored.

Section II is the first section to explore a specific therapeutic strategy for GBM: improving the efficacy of classic chemotherapeutics. **Chapter 3** provides important evidence on the ongoing debate whether the BBB is relevant in the context of a brain tumor that compromises its physical integrity. We demonstrate that in mice bearing a 'leaky' brain tumor, the BBTB still expresses P-gp and BCRP, which reduces the antitumor efficacy of taxane chemotherapeutics, as these are kept away from the tumor by these drug efflux transporters. Importantly, we also show that these drugs can achieve efficacy in mice lacking these transporters or when the P-gp/BCRP inhibitor elacridar is co-administered. Therefore, we conclude that the BBB is still relevant in the context

of a brain tumor and that its barrier properties can be therapeutically targeted to improve tumor exposure to anticancer drugs. **Chapter 4** follows up on these studies by investigating the only chemotherapeutic with proven clinical efficacy against GBM: temozolomide (TMZ). Even though TMZ improves the median survival of GBM patients by approximately 4 months, this chapter demonstrates that TMZ is transported by P-gp and BCRP and that therapeutic inhibition of these transporters by elacridar improves its efficacy in GBM mouse models. These findings call for further clinical testing of temozolomide in combination with elacridar for the treatment of GBM.

Section III shifts the focus to newer targeted therapeutics and investigates inhibitors of the PI3K pathway. **Chapter 5** demonstrates that the PI3K inhibitor buparlisib is not a substrate of P-gp and BCRP and has an excellent brain penetration in mice. Importantly, intracranial target inhibition can be achieved at dose levels that result in clinically relevant plasma concentrations, suggesting that buparlisib is a prime candidate for clinical trials that aim to inhibit the PI3K pathway in GBM. **Chapter 6** addresses a panel of compounds that all target the PI3K pathway and selects NVP-BEZ235 and ZSTK474 as the most brain penetrable inhibitors. Using these brain penetrable inhibitors, we next demonstrate that even though efficient target inhibition can be achieved, the efficacy of single PI3K pathway inhibition against GBM mouse models is very modest. We therefore conclude that combined targeting of multiple pillars of GBM biology will be required to achieve durable clinical efficacy.

Section IV studies inhibitors of another proliferation pathway that is commonly activated in GBM: the MAPK pathway. **Chapter 7** investigates whether a panel of inhibitors targeting MEK, an important component of the MAPK pathway, can be transported by P-gp and BCRP and are able to cross the BBB. Unfortunately, all MEK inhibitors are substrates of P-gp and BCRP, albeit to varying extents. However, while most inhibitors exhibit rather poor brain penetration, PD0325901 reaches a brain–plasma ratio exceeding 0.5 and achieves intracranial target inhibition at dose levels that result in clinically relevant plasma concentrations. Together, these properties make PD0325901 the clear MEK inhibitor of choice for further clinical development for GBM. **Chapter 8** makes a sidestep from glioblastoma to melanoma brain metastases (MBMs). We first show that the BBTB in MBMs also express P-gp and BCRP. We also investigate vemurafenib, an inhibitor of mutated BRAF, and demonstrate that the BBB makes MBMs intrinsically more resistant to BRAF inhibitors compared to extracranial metastases. This intrinsic resistance can be diminished by co-administering the P-gp/BCRP inhibitor elacridar, offering a potential clinical solution for overcoming intrinsic resistance of MBMs. Intriguingly, this chapter also shows that MBMs rapidly acquire additional resistance mechanisms, in line with clinical observations. These resistance mechanisms appear to rely on non-canonical growth signaling. As some subsets of GBM also carry BRAF mutations, these findings may also be clinically relevant for primary brain tumors.

Section V moves away from proliferation pathways to investigate targeting the cell cycle.

Chapter 9 displays a new model that describes how the G2 checkpoint is regulated. The G2 checkpoint is situated at the transition of G2 phase to mitosis, and prevents cells from dividing when genomic integrity is compromised. The new model recognizes five key signaling nodes, centered around the cell cycle proteins PLK1, CHK1, CDC25C, Wee1 and CDK1. These nodes form an intricate signaling network that governs the decision to delay cell cycle progression by influencing the subcellular localization balance of key cell cycle proteins via 'nuclear and cytoplasmic decision states'. Importantly, this model offers explanations for several previously reported observations and may aid in predicting the effects of compounds targeting the G2 checkpoint. **Chapter 10** investigates two Wee1 inhibitors, which are a class of G2 checkpoint-targeting drugs. Wee1 inhibitors prevent cells from mounting a G2 cell cycle arrest and could thus force GBM cells to divide while sustaining considerable DNA damage, ultimately resulting in mitotic cell death. Unfortunately however, we find that both Wee1 inhibitors are efficiently kept out of the brain by P-gp and BCRP, making it unlikely that these compounds can be clinically effective against brain tumors. **Chapter 11** focuses on the G1 checkpoint, which occurs earlier in the cell cycle. Inhibition of CDK4 and CDK6 could be an efficient strategy to prevent GBM cells from progressing through the cell cycle. We study the brain penetration and efflux transporter substrate affinity of palbociclib, the first clinically developed CDK4/6 inhibitor. We show that palbociclib is very poorly brain penetrable, making it unlikely that this drug will be successfully developed for intracranial tumors. **Chapter 12** deals with another cell cycle checkpoint: the spindle assembly checkpoint (SAC) in mitosis. MPS1 is a key regulator of the SAC and prevents cells from completing mitosis when chromosomes are improperly attached to the mitotic spindle machinery. Overriding this failsafe by inhibiting MPS1 may result in missegregated chromosomes and, ultimately, cell death. The novel MPS1 inhibitor NTRC0066-0 is highly potent in inducing GBM cell death as a monotherapy *in vitro*. However, this efficacy cannot be translated to *in vivo* orthotopic GMB models, despite optimizing its brain exposure and dosing regimen. Interestingly, promising signs of durable antitumor efficacy are observed when NTRC0066-0 is combined with chemo-radiotherapy in as subset of mice. Although the reason for the discrepancy between *in vitro* and *in vivo* efficacy has not been resolved, this chapter highlights that the development of MPS1 inhibitors for treatment of GBM will be challenging.

Section VI shifts the focus back to the DNA, but instead of aiming to induce damage, we seek to diminish DNA repair by inhibiting the repair protein PARP. **Chapter 13** demonstrates that the PARP inhibitor ABT-888 (veliparib) modestly improves the efficacy of the alkylating chemotherapeutic temozolomide. Furthermore, we show that *PTEN*-deficient tumors are particularly sensitive to this treatment strategy. Lastly, we find that P-gp and BCRP located at the BBB and in the tumor itself reduce the efficacy of this strategy and that co-administration of elacridar can overcome this limitation. **Chapter 14** investigates an alternative PARP inhibitor, AZD2461, which would be less amenable to transport by efflux transport proteins than earlier developed PARP inhibitors. AZD2461 has been efficacious in murine breast cancer models that have developed resistance

to PARP inhibitors by upregulating P-gp. However, we find that AZD2461 is a substrate of P-gp, although it cannot be transported by BCRP at the BBB. Importantly, P-gp at the BBB severely limits the brain penetration of AZD2461, making it unlikely it will have a more favorable brain penetration than veliparib in GBM patients.

Section VII is the last section investigating a therapeutic strategy and focuses entirely on the last pillar of GBM biology: its unparalleled invasion capacity. **Chapter 15** provides an overview of the current knowledge on GBM invasion and the models that are available to study this aspect of GBM biology. It also lists the benefits and limitations of each model and concludes that robust experimental evidence requires the use of a combination of sophisticated *in vitro*, *ex vivo* and *in vivo* models. Previous literature that meets these criteria has provided evidence that Ephrin receptors, Rho GTPases and casein kinase 2 (CK2) play a role in GBM invasion signaling. Intriguingly, emerging evidence seems to suggest that these proteins form an invasion signaling network. **Chapter 16** describes the discovery of a pro-invasive role for CK2 in GBM. Through an unbiased approach aiming to characterize invasive GBM cells in an *ex vivo* organotypic model, we identify the CK2–TBK1–IRF3 axis as a pro-invasive signaling route in GBM. CK2 induces expression of various extracellular matrix (ECM) components, including multiple collagens. These ECM components provide GBM cells with a more rigid matrix to invade the normally softer brain tissue. Importantly, inhibition of CK2 using a small molecule inhibitor prevents GBM invasion *ex vivo* and *in vivo* in mice with a fully functional BBB.

In summary, therapeutically targeting GBM has proven to be very challenging. However, over the years we have increasingly gained knowledge on the complexity of GBM biology, which allowed us to more rationally design treatment strategies. Major pillars of the malignancy of GBM are uncontrolled proliferation, unparalleled invasion and tremendous therapy resistance, and together these form the glioblastoma triad. This thesis describes the results of our work on treatment strategies for all three pillars separately. We conclude that while modest efficacy can be achieved by individual targeting, an intelligently designed therapeutic approach that attacks multiple components of the glioblastoma triad will be necessary to provide durable responses for patients. Luckily, given the speed at which science advances and our current understanding of targeting individual components of the glioblastoma triad, we can justifiably be optimistic about future combination therapy approaches.

SAMENVATTING

Het glioblastoom (GBM) is de meest veelvoorkomende primaire hersentumor. Ondanks uitgebreide behandelingen worden patiënten met deze ziekte geconfronteerd met een erbarmelijke prognose. Er is dus grote behoefte aan nieuwe behandelstrategieën die klinische responsen en overleving verbeteren. Recente grootschalige onderzoeken hebben veel aspecten van de biologie van GBM gekarakteriseerd en hebben drie pijlers uitgelicht waarop de kwaadaardigheid van GBM rust: ongecontroleerde celdeling, een invasiecapaciteit die zijn gelijke niet kent en een aanzienlijke resistentie tegen therapieën. Deze pijlers vormen samen de glioblastoma triade, en dit proefschrift heeft al deze pijlers onderzocht en demonstreert efficiënte manieren om elke afzonderlijk aan te vallen. Deze kennis zal hopelijk helpen om een intelligente combinatiebehandelingsstrategie te ontwerpen die meerdere componenten van de glioblastoma triade aanvalt, aangezien dit waarschijnlijk nodig zal zijn om langetermijnoplossingen te bieden aan GBM patiënten.

Sectie I opent dit proefschrift met de introductie van twee pijlers van de glioblastoma triade. **Hoofdstuk 1** geeft een overzicht van de beschikbare en opkomende therapeutische strategieën om de bloed–hersentumor barrière (BHTB) te passeren. De bloed–hersen barrière (BHB) beschermt de gezonde hersenen tegen potentieel schadelijke stoffen die vreemd zijn voor het lichaam, door diffusie tussen cellen door te voorkomen en ongewenste stoffen efficiënt terug de bloedbaan in te transporteren. In de context van een hersentumor staat het bekend als BHTB en, hoewel zijn integriteit fysiek verstoord kan zijn, beschermt het GBM tegen systemische antikankerbehandelingen door de toegang van medicijnen tot de tumor te beperken. Het passeren van de BHTB is dus essentieel om systemische therapie de tumor efficiënt te laten bereiken. Hoofdstuk 1 bespreekt verschillende strategieën om dit te bereiken, waaronder osmotische BHB verstoring, het uitbuiten van receptor-gemedieerde transport systemen en remming van drug efflux transporters en concludeert dat deze laatste twee het meest veelbelovend zijn om de bereikbaarheid van hersentumoren voor systemische therapie te verbeteren. **Hoofdstuk 2** richt zich op de cellulaire signaalroutes die gedereguleerd zijn in GBM en manieren om deze gericht aan te pakken met doelgerichte geneesmiddelen. Het licht drie hoofroutes uit die mutaties bevatten in de meerderheid van de GBM's: de PI3K route, de MAPK route en de RB route. Dit hoofdstuk geeft ook een overzicht van remmers van componenten van deze routes en legt speciale nadruk op hun potentie om de BHB te passeren. Hoofdstuk 2 concludeert dat doelgerichte therapie tegen één signaalroute hoogstwaarschijnlijk niet succesvol zal blijken. In plaats van daarvan zouden combinaties van doelgerichte therapieën onderzocht moeten worden.

Sectie II is de eerste sectie die een specifieke therapeutische strategie voor GBM onderzocht: het verbeteren van de effectiviteit van klassieke chemotherapeutica. **Hoofdstuk 3** voorziet van belangrijk bewijs in het voortdurende debat of de BHB relevant is in de context van een hersentumor die de fysieke integriteit compromitteert. We demonstreren dat in muizen met

een 'lekke' hersentumor de BHTB nog steeds P-gp en BCRP bevat, en dat hierdoor de antitumor effectiviteit van chemotherapeutische taxanen verminderd wordt, aangezien deze efficiënt buiten de tumor worden gehouden door deze drug efflux transporters. Belangrijker nog, we laten ook zien dat deze medicijnen effectief kunnen zijn in muizen die deze transporters niet hebben of wanneer ze ook de P-gp/BCRP remmer elacridar krijgen. We concluderen daarom dat de BHB nog steeds relevant is in de context van een hersentumor en dat zijn barrière eigenschappen therapeutisch geremd kunnen worden om de blootstelling van de tumor aan antikankermedicijnen te verbeteren. **Hoofdstuk 4** vervolgt deze studies door de enige chemotherapie te onderzoeken die bewezen klinisch effectief is tegen GBM: temozolomide (TMZ). Ook al verlengt TMZ de mediane overleving van GBM patiënten met ongeveer 4 maanden, laat dit hoofdstuk zien dat TMZ wordt getransporteerd door P-gp en BCRP en dat therapeutische remming van deze transporters door elacridar zijn effectiviteit in GBM muismodellen verbetert. Deze bevindingen roepen op om temozolomide in combinatie met elacridar verder klinisch te testen als behandeling voor GBM.

Sectie III verlegt de focus naar nieuwere doelgerichte therapieën en onderzoekt remmers van de PI3K signaalroute. **Hoofdstuk 5** demonstreert dat de PI3K remmer buparlisib geen substraat is van P-gp en BCRP en dat het een uitstekende hersenpenetratie heeft in muizen. Nog belangrijker, intracraniële remming van het doelwit kan bereikt worden met doses die klinische relevante plasmaspiegels opleveren. Deze data suggereren dat buparlisib een uitgelezen kandidaat is om gebruikt te worden in klinische studies die als doel hebben om de PI3K signaalroute te remmen in GBM. **Hoofdstuk 6** bestudeert een panel van stoffen die allemaal de PI3K route remmen en selecteert NVP-BEZ235 en ZSTK474 als de remmers met de beste hersenpenetratie. Vervolgens demonstreren we dat hoewel deze twee remmers efficiënt hun doelwit bereikten, de effectiviteit van enkele remming van de PI3K route erg bescheiden is. We concluderen daarom dat het gecombineerd aanvallen van meerdere pijlers van de GBM biologie nodig zal zijn om langdurige klinische effectiviteit te bewerkstelligen.

Sectie IV bestudeert remmers van een andere groei signaalroute die over het algemeen geactiveerd is in GBM: de MAPK route. **Hoofdstuk 7** onderzoekt of een panel van remmers van MEK, een belangrijke component van de MAPK route, getransporteerd kunnen worden door P-gp en BCRP en de BHB kunnen passeren. Alle MEK remmers blijken helaas substraten van P-gp en BCRP te zijn, alhoewel in verschillende mate. Echter, ook al hebben de meeste remmers een slechte hersenpenetratie, bereikt PD0325901 een hersen–plasma ratio van meer dan 0,5 en kan het zijn doel remmen in de hersenen bij doses die klinisch relevante plasmaspiegels opleveren. Samengenomen maken deze eigenschappen PD0325901 tot de MEK remmer die duidelijk de voorkeur zou moeten genieten voor verdere klinische ontwikkeling tegen GBM. **Hoofdstuk 8** maakt een zijsprong van glioblastoom naar hersenuitzaaiingen van melanoom (MHU's). We laten eerst zien dat de BHTB in MHU's ook P-gp en BCRP bevat. Daarnaast onderzoeken we vemurafenib, een remmer van gemuteerde BRAF, en demonstreren we dat de BHB MHU's meer

resistent maakt tegen BRAF remmers vergeleken met extracraniële uitzaaiingen. Deze intrinsieke resistentie kan verminderd worden door gelijktijdige toediening van de P-gp/BCRP remmer elacridar. Deze strategie biedt een potentiële klinische oplossing om intrinsieke resistentie van MHU's te overwinnen. Intrigerend genoeg laat dit hoofdstuk ook zien dat MHU's snel additionele resistentie mechanismen vergaren, in lijn met klinische observaties. Deze resistentiemechanismen lijken te bogen op onconventionele groeisignalering. Aangezien sommige subgroepen van GBM ook BRAF mutaties hebben, kunnen deze bevindingen ook klinisch relevant zijn voor primaire hersentumoren.

Sectie V verlaat de groeisignaalroutes om het aanvallen van de celcyclus te bestuderen. **Hoofdstuk 9** geeft een nieuw model weer dat beschrijft hoe het G2 checkpunt wordt gereguleerd. Het G2 checkpunt bevindt zich op de overgang van de G2 fase naar mitose en voorkomt dat cellen delen als hun genomische integriteit is aangetast. Het nieuwe model herkent vijf cruciale signaleringsknooppunten die draaien om de celcycluseiwitten PLK1, CHK1, CDC25C, Wee1 en CDK1. Deze knooppunten vormen een ingewikkeld signaleringsnetwerk dat de beslissing om het doorlopen van de celcyclus uit te stellen bepaalt door de subcellulaire lokalisatie van cruciale celcycluseiwitten te beïnvloeden via 'nucleaire en cytoplasmatische beslissingstoestanden'. Dit model biedt verklaringen voor verscheidene eerder gerapporteerde observaties en zou kunnen helpen om de effecten van stoffen die zich op het G2 checkpunt richten te voorspellen. **Hoofdstuk 10** onderzoekt twee Wee1 remmers: een klasse van stoffen die zich op het G2 checkpunt richten. Wee1 remmers voorkomen dat cellen hun celcyclus kunnen stoppen in de G2 fase en kunnen dus GBM cellen forceren om te delen terwijl ze nog aanzienlijke hoeveelheid DNA schade hebben. Uiteindelijk zal dit leiden tot mitotische celdood. Jammerlijk genoeg vinden we dat beide Wee1 remmers efficiënt buiten de hersenen worden gehouden door P-gp en BCRP, waardoor het onwaarschijnlijk wordt dat deze stoffen klinische effectief kunnen zijn tegen hersentumoren. **Hoofdstuk 11** richt zich op het G1 checkpunt, dat zich eerder in de celcyclus bevindt. Remming van CDK4 en CDK6 kan een efficiënte strategie zijn om te voorkomen dat GBM cellen de celcyclus doorlopen. Dit hoofdstuk bestudeert de hersenpenetratie en mate van substraat affiniteit voor efflux transporters van palbociclib, de eerste klinisch ontwikkelde CDK4/6 remmer. We laten zien dat palbociclib een erg slechte hersenpenetratie heeft, waardoor het onwaarschijnlijk is dat dit medicijn succesvol ontwikkeld zal worden voor de behandeling van intracraniële tumoren. **Hoofdstuk 12** bestudeert nog een ander celcyclus checkpunt: het spoel assemblage checkpunt (SAC) in mitose. MPS1 is een cruciale regulator van de SAC en voorkomt dat cellen mitose voltooien terwijl chromosomen verkeerd verankerd zijn aan de mitotische spoel. Het platleggen van dit verzekeringsmechanisme door remming van MPS1 kan resulteren in verkeerd gescheiden chromosomen en, uiteindelijk, celdood. De nieuwe MPS1 remmer NTRC00660-0 induceert celdood van GBM cellen met hoge potentie als monotherapie *in vitro*. Echter, deze effectiviteit kan niet vertaald worden naar *in vivo* orthotope GBM modellen, ondanks het optimaliseren van de blootstelling in de hersenen en het doseringsschema. Interessant genoeg worden veelbelovende

tekenen van langdurige antitumor effectiviteit geobserveerd in een deel van de muizen die een combinatie behandeling met chemo-radiotherapie krijgen. Alhoewel de reden voor de discrepantie tussen *in vitro* en *in vivo* effectiviteit niet opgelost is, licht dit hoofdstuk duidelijk uit dat de ontwikkeling van MPS1 remmers voor de behandeling van GBM een uitdaging zal zijn.

Sectie VI verlegt de focus weer terug naar het DNA, maar in plaats van te proberen om schade te induceren trachten we het DNA herstel te beperken door het remmen van het hersteleiwit PARP. **Hoofdstuk 13** demonstreert dat de PARP remmer ABT-888 (veliparib) een bescheiden verhoging van de effectiviteit van het alkylerende chemotherapeuticum temozolomide oplevert. Daarnaast laat het zien dat *PTEN*-deficiënte tumoren extra gevoelig zijn voor deze behandelstrategie. Als laatste vind het dat P-gp en BCRP in de BHB en in de tumor zelf de effectiviteit van deze strategie verminderen en dat gelijktijdige toediening van elacridar deze beperking teniet kan doen. **Hoofdstuk 14** onderzoekt een alternatieve PARP remmer, AZD2461, waarvan wordt gerapporteerd dat deze minder vatbaar is voor transport door efflux transport eiwitten dan eerder ontwikkelde PARP remmers. AZD2461 is effectief gebleken in muismodellen van borstkanker die resistent zijn geworden tegen PARP remmers door P-gp meer tot expressie te brengen. Echter, we vinden dat AZD2461 een substraat is van P-gp, alhoewel het niet getransporteerd kan worden door BCRP in de BHB. Belangrijk is dat P-gp de hersenpenetratie van AZD2461 ernstig beperkt, waardoor het onwaarschijnlijk wordt dat het een gunstigere hersenpenetratie heeft in GBM patiënten dan veliparib.

Sectie VII is de laatste sectie die een therapeutische strategie onderzoekt en richt zich volledig op de laatste pijler van de GBM biologie: zijn invasiecapaciteit die zijn gelijke niet kent. **Hoofdstuk 15** verschaft een overzicht van de huidige kennis over GBM invasie en de modellen die beschikbaar zijn om dit aspect van de GBM biologie te bestuderen. Het somt ook de voordelen en beperkingen van elk model op en concludeert dat robuust experimenteel bewijs het gebruik van een combinatie van verfijnde *in vitro*, *ex vivo* en *in vivo* modellen vereist. Eerdere literatuur die aan deze criteria voldoet heeft bewijs geleverd dat Ephrin receptoren, Rho GTPases en casein kinase 2 (CK2) een rol spelen in GBM invasie signalering. Het is intrigerend dat opkomend bewijs lijkt te suggereren dat deze eiwitten een invasiesignaleringsnetwerk vormen. **Hoofdstuk 16** beschrijft de ontdekking van een pro-invasieve rol voor CK2 in GBM. Door middel van een onbevooroordeelde aanpak die zich richt op het karakteriseren van invasieve GBM cellen in een *ex vivo* organotypisch model identificeren we de CK2–TBK1–IRF3 as als een pro-invasieve signaleringsroute in GBM. CK2 induceert de expressie van verschillende extracellulaire matrix (ECM) componenten, waaronder meerdere collagenen. Deze ECM componenten voorzien GBM cellen van een meer rigide matrix om het normaal gesproken zachtere hersenweefsel binnen te dringen. Belangrijk voor de klinische relevantie van deze vinding is dat remming van CK2 met een klein molecuul GBM invasie *ex vivo* en *in vivo* in muizen met een volledig functionele BHB voorkomt.

Samengevat is gebleken dat het therapeutisch aanvallen van GBM een enorme uitdaging is. Echter, de afgelopen jaren hebben we steeds meer kennis verkregen over de complexiteit van de biologie van GBM, wat ons in staat heeft gesteld om behandelstrategieën meer rationeel te ontwerpen. Belangrijke pijlers van de kwaadaardigheid van GBM zijn ongecontroleerde celdeling, een invasiecapaciteit die zijn gelijke niet kent en een ongelooflijke resistentie tegen therapieën, en samen vormen deze de glioblastoom triade. Dit proefschrift beschrijft de resultaten van ons werk aan behandelstrategieën voor alle drie pijlers afzonderlijk. We concluderen dat terwijl bescheiden effectiviteit bereikt kan worden door individuele aanvallen, een intelligent ontworpen therapeutische aanpak die meerdere componenten van de glioblastoma triade aanvalt nodig zal zijn om langdurige effectiviteit te bieden voor patiënten. Gelukkigerwijs kunnen we gegeven de snelheid waarmee de wetenschap voortschrijdt en onze huidige kennis over het aanvallen van individuele componenten van de glioblastoma triade gerechtvaardigd optimistisch zijn over toekomstige combinatietherapie benaderingen.

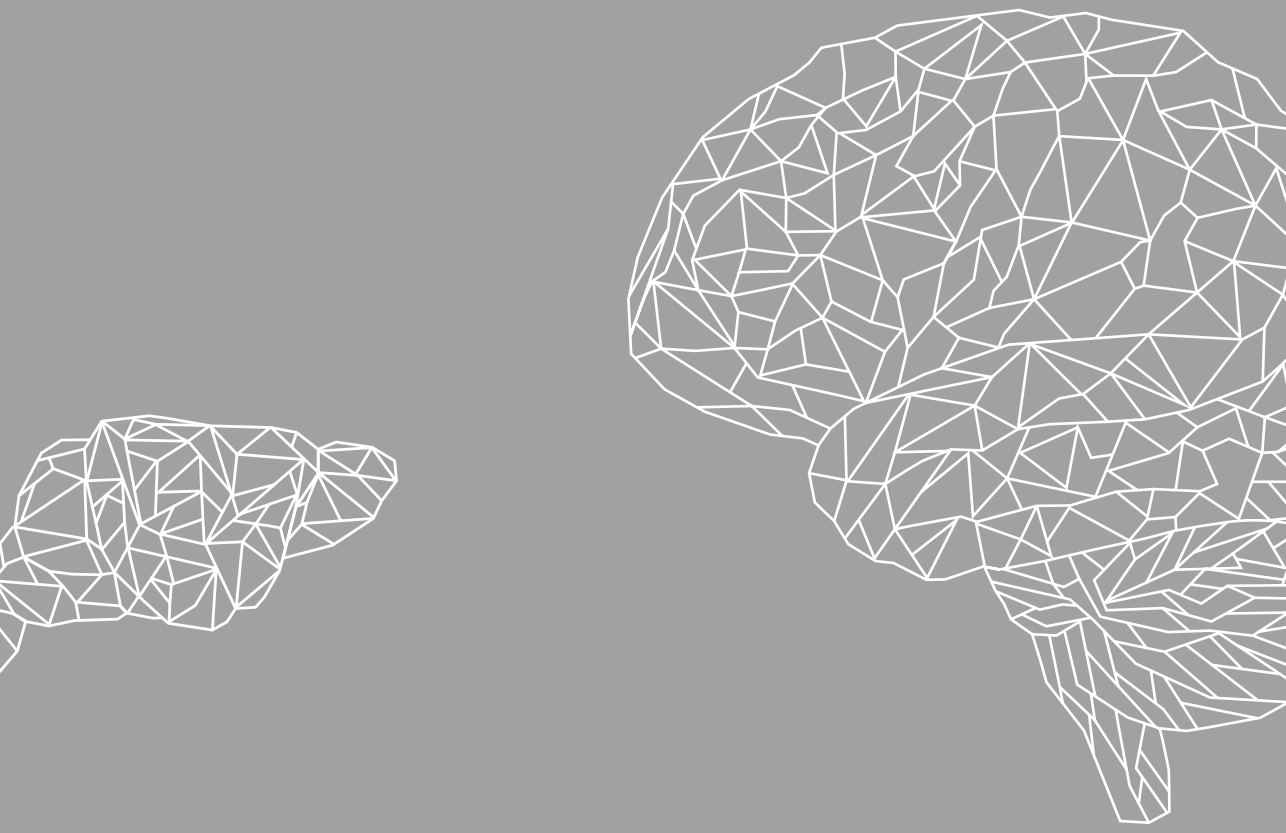

SECTION IX

ADDENDA

CURRICULUM VITAE

Mark Cornelis de Gooijer was born on October 5th of 1989 in Amsterdam and grew up in the neighboring town of Landsmeer. After obtaining his gymnasium diploma *cum laude* from Bernard Nieuwentijt College Damstede in 2007, he moved on to studying Biomedical Sciences at the Vrije Universiteit in Amsterdam. He received his Bachelor of Science degree *cum laude* in 2010 and subsequently enrolled in the Master's degree program in Oncology at the same university. During his graduate studies, he spent 9 months in the labs of dr. Olaf van Tellingen at the Netherlands Cancer Institute (NKI) and prof. dr. Thomas Wurdinger at the Cancer Center Amsterdam (CCA), studying ways to make brain tumors more sensitive to radiotherapy. He then relocated to Boston, Massachusetts for one year to work on resistance of brain tumors to chemotherapy under supervision of dr. Bakhos Tannous at Massachusetts General Hospital and Harvard Medical School, for which he was awarded a J. William Fulbright Graduate Student Scholarship. He obtained his Master of Science degree in 2012 and started his doctoral research in 2013 under supervision of his promotor prof. dr. Jos Beijnen and co-promotor dr. Olaf van Tellingen at the NKI and the Universiteit Utrecht, ultimately resulting in this thesis. During his doctoral studies, he became the treasurer of the investigators branch of the National Workforce for Neuro-Oncology (LWNO-i). After receiving his PhD title, Mark will continue to develop the research lines described in this thesis as a post-doctoral researcher at the NKI. His ultimate aim is to supply brain tumor patients with new sophisticated treatment options. Mark currently lives in his hometown Landsmeer with his newlywed wife and rebellious tiger-cat.

LIST OF PUBLICATIONS

de Gooijer, M.C., Buil, L.C.M., Çitirikkaya, C.H., Hermans, J., Beijnen, J.H., van Tellingen, O. ABCB1 attenuates the brain penetration of the PARP inhibitor AZD2461. *Mol Pharm* **15**, 5236-5243 (2018).

de Gooijer, M.C.*, Guillén-Navarro, M.*, Wurdinger, T., Bernards, R., van Tellingen, O. An experimenter's guide to glioblastoma invasion pathways. *Trends Mol Med* **24**, 763-780 (2018).

Meel, M.H., de Gooijer, M.C., Guillén-Navarro, M., Waranecki, P., Breur, M., Buil, L.C.M., Wedekind, L., Twisk, J.W.R., Koster, J., Hashizume, R., Raabe, E.H., Montero-Carcaboso, A., Bugiani, M., van Tellingen, O., van Vuurden, D.G., Kaspers, G.J.L., Hulleman, E. MELK inhibition in diffuse intrinsic pontine glioma. *Clin Cancer Res* **24**, 5645-5657 (2018).

de Gooijer, M.C., Zhang, P., Buil, L.C.M., Çitirikkaya, C.H., Thota, N., Beijnen, J.H., van Tellingen, O. Buparlisib is a brain penetrable pan-PI3K inhibitor. *Sci Rep* **8**, 10784 (2018).

de Gooijer, M.C., de Vries, N.A., Buckle, T., Buil, L.C.M., Beijnen, J.H., Boogerd, W., van Tellingen, O. Improved brain penetration and antitumor efficacy of temozolomide by inhibition of ABCB1 and ABCG2. *Neoplasia* **20**, 210-220 (2018).

Berenguer, J., Lagerweij, T., Zhao, X.W., Dusoswa, S., van der Stoop, P., Westerman, B., de Gooijer, M.C., Wedekind, L., López-López, À., Giovanazzi, A., Bruch-Oms, M., van der Meulen-Muileman, I., Reijmers, R.M., van Kuppevelt, T.H., García-Vallejo, J.J., van Kooyk, Y., Tannous, B.A., Wesseling, P., Koppers-Lalic, D., Vandertop, W.P., Noske, D.P., van Beusechem, V.W., van Rheenen, J., Pechtel, D.M., van Tellingen, O., Wurdinger, T. Glycosylated extracellular vesicles released by glioblastoma cells are decorated by CCL18 allowing for cellular uptake via chemokine receptor CCR8. *J Extracell Vesicles* **7**, 1446660 (2018).

Teng, J., Hejazi, S., Hiddingh, L., Carvalho, L., de Gooijer, M.C., Wakimoto, H., Barazas, M., Tannous, M., Chi, A.S., Noske, D.P., Wesseling, P., Wurdinger, T., Batchelor, T.T., Tannous, B.A. Recycling drug screen repurposes hydroxyurea as a sensitizer of glioblastomas to temozolomide targeting de novo DNA synthesis, irrespective of molecular subtype. *Neuro Oncol* **20**, 642-654 (2018).

de Gooijer, M.C., Buil, L.C.M., Beijnen, J.H., van Tellingen, O. ABC transporters limit the brain penetration of Wee1 inhibitors. *Invest New Drugs* **36**, 380-387 (2018).

de Gooijer, M.C., Zhang, P., Weijer, R., Buil, L.C.M., Beijnen, J.H., van Tellingen, O. The impact of P-glycoprotein and breast cancer resistance protein on the brain pharmacokinetics and pharmacodynamics of a panel of MEK inhibitors. *Int J Cancer* **142**, 381-391 (2018).

de Gooijer, M.C. & van Tellingen, O. Have we considered all barriers to mammalian target of rapamycin inhibition as treatment for diffuse intrinsic pontine glioma? *Transl Cancer Res* **6**, S1431-S1434 (2017).

de Gooijer, M.C. & Pencheva, N. Brain cancer cells build their own highways for invasion through the brain. *Amsterdam Sci* **6**, 7-8 (2017).

Pencheva, N.*, de Gooijer, M.C.*, Vis, D.J., Wessels, L.F.A., Wurdinger, T., van Tellingen, O., Bernards, R. Identification of a druggable pathway controlling glioblastoma invasiveness. *Cell Rep* **20**, 48-60 (2017).

de Gooijer, M.C., van den Top, A., Bockaj, I., Beijnen, J.H., Wurdinger, T., van Tellingen, O. The G2 checkpoint: a node-based molecular switch. *FEBS Open Bio* **7**, 439-455 (2017).

Lin, F.*, de Gooijer, M.C.*, Hanekamp, D., Chandrasekaran, G., Buil, L.C.M., Thota, N., Sparidans, R.W., Beijnen, J.H., Wurdinger, T., van Tellingen, O. PI3K-mTOR pathway inhibition exhibits efficacy against high-grade glioma in clinically relevant mouse models. *Clin Cancer Res* **23**, 1286-1298 (2017).

de Gooijer, M.C., Zhang, P., Thota, N., Mayayo-Peralta, I., Buil, L.C.M., Beijnen, J.H., van Tellingen, O. P-glycoprotein and breast cancer resistance protein restrict the brain penetration of the CDK4/6 inhibitor palbociclib. *Invest New Drugs* **33**, 1012-1019 (2015).

Zhang, P., de Gooijer, M.C., Buil, L.C.M., Beijnen, J.H., Li, G., van Tellingen, O. ABCB1 and ABCG2 restrict the brain penetration of a panel of novel EZH2-inhibitors. *Int J Cancer* **137**, 2007-2018 (2015).

van Tellingen, O.*, Arik-Yetkin, B.*, de Gooijer, M.C.*, Wesseling, P., Wurdinger, T., de Vries, E.H. Overcoming the blood-brain tumor barrier for effective glioblastoma treatment. *Drug Resist Updat* **19**, 1-12 (2015).

Lin, F.*, de Gooijer, M.C.*, Moreno Roig, E., Buil, L.C.M., Christner, S.M., Beumer, J.H., Wurdinger, T., Beijnen, J.H., van Tellingen, O. ABCB1, ABCG2 and PTEN determine the response of glioblastoma to temozolomide and ABT-888 therapy. *Clin Cancer Res* **20**, 2703-2713 (2014).

Lin, F., de Gooijer, M.C., Hanekamp, D., Brandsma, D., Beijnen, J.H., van Tellingen, O. Targeting core (mutated) pathways of high grade gliomas: challenges of intrinsic resistance and drug efflux transporters. *CNS Oncol* **2**, 271-288 (2013).

Degeling, M.H., Bovenberg, M.S., Lewandrowski, G.K., de Gooijer, M.C., Vleggeert-Lankamp, C.L., Tannous, M., Maguire, C.A., Tannous, B.A.. Directed molecular evolution reveals Gaussia luciferase variants with enhanced light output stability. *Anal Chem* **85**, 3006-3012 (2013).

Lin F, Chandrasekaran G, de Gooijer MC, Beijnen JH, van Tellingen O. Determination of NVP-BEZ235, a dual PI3K and mTOR inhibitor, in human and mouse plasma and in mouse tissue homogenates by reversed-phase high-performance liquid chromatography with fluorescence detection. *J Chromatogr B Analyt Technol Biomed Life Sci* **901**, 9-17 (2012).

**Authors contributed equally*

ACKNOWLEDGEMENTS

Science is teamwork, now more than ever. However, during the creation of my thesis it felt like much more than that, like familywork. I have been blessed with two wonderful families, who make me feel at home in and outside of science, support me unconditionally and make me enjoy life and science every single day.

My scientific family consists of many members, from my scientific *pater familias* and true second father Olaf to my godfather Jos, big brother Levi, little brother Paul, baby sisters Ceren and Hilâl, stepbrother Artur, and many uncles, aunts and cousins who I was able to collaborate with and supervise over the years. It truly was an honor and a privilege.

At least equally important are the people that I have been blessed to call family for the past 29 years (or at least it feels as long): all de Gooijers, van Essens and Bands. My gratitude is eternal, I would be nothing without you. I am overjoyed that we could recently celebrate the unison of one big family so beautifully. Lobke, it was you, it is you, and it will always be you. This work would have been a shadow of itself without you.

Words cannot convey the extent, sincerity and depth of my gratitude, so I will not attempt to do so on this paper. I hope I have already been able to express my gratitude to each of you personally. I will at least try my utmost to do so the next time we meet. Because trust me, this book may be finished, but the story is just about to begin.

DANKWOORD

Wetenschap is teamwork, nu meer dan ooit. Tijdens de totstandkoming van mijn proefschrift voelde het alleen als veel meer dan dat, als familiewerk. Ik ben gezegend met twee fantastische families, die me zowel binnen de wetenschap als daarbuiten thuis laten voelen, me onvoorwaardelijk steunen en me elke dag weer laten genieten van het leven en de wetenschap.

Mijn wetenschappelijke familie telt vele leden, van mijn wetenschappelijke *pater familias* en waarlijke tweede vader Olaf tot mijn peetvader Jos, grote broer Levi, kleine broertje Paul, baby zusjes Ceren en Hilâl, stiefbroer Artur, en vele ooms, tantes, neefjes en nichtjes met wie ik over de jaren heb mogen samenwerken en begeleiden. Het was een eer en een voorrecht.

Minstens net zo belangrijk zijn de mensen die ik gelukkig al 29 jaar (of anders voelt het ten minste net zo) tot mijn familie mag rekenen: alle de Gooijers, van Essens en Bandjes. Mijn dank is oneindig, ik zou niets zijn zonder jullie. Ik ben dolgelukkig dat we onlangs op zo'n prachtige wijze de verbintenis tot één grote familie hebben mogen vieren. Lobke, jij was het, jij bent het, en je zal het altijd zijn. Dit werk zou een schim zijn geweest van wat het nu is zonder jou.

Woorden doen geen recht aan de omvang en diepte van mijn dankbaarheid, dus ik zal ook geen poging doen ze hier op papier te zetten. Ik hoop dat ik ieder van jullie al persoonlijk mijn dankbaarheid heb over weten te brengen. Ik zal hiervoor in ieder geval mijn uiterste best doen de volgende keer dat we elkaar zien. Want geloof me, dit boek is dan wel uit, maar het verhaal gaat pas beginnen.